UNIVERSITÀ DEGLI STUDI DI MILANO

Dottorato di Ricerca in Scienze della Terra

Ciclo XXVI

Cancrinite-group minerals at non-ambient conditions: a model of the elastic behavior and structure evolution

Ph.D. Thesis

Paolo Lotti
Matricola R08990

Tutore
Prof. G. Diego Gatta

Co- Tutore
Prof. Alessandro Pavese

Anno Accademico
2012-2013

Coordinatore
Prof.ssa
Elisabetta Erba

Summary

Chapter 1

Introduction

1.1 THE [CAN]-FRAMEWORK TYPE

The [CAN]-framework type (Baerlocher et al. 2007) belongs to the so-called ABC-6 family of frameworks (Gies et al. 1999). In this family, the periodic building unit consists of six-membered rings of tetrahedra (S6R), not interconnected each other, arranged according to a hexagonal array (Fig. 1.1). The plane symmetry of such an arrangement is *P*6*mm*. Let us arbitrarily place the position of the ring at the coordinate (1/3,2/3) of a hexagonal cell and call it as an "A" position. Three kinds of stacking can occur: 1) the rings of new plane can be placed still at (1/3,2/3) giving rise to an "AA" stacking; 2) the new rings can be placed at (2/3,1/3) in a position arbitrarily called "B", giving rise to an "AB" stacking; 3) the rings can be placed at (0,0) in a position called "C", from which an "AC" stacking derives (Fig. 1.1). Then, a third plane of single six-membered rings can be stacked according to one of the three stacking options described above. If the stacking follows a periodic rule, a periodic three-dimensional framework is built up. Of the potentially infinite stacking sequences, many have effectively been found in natural minerals and/or in synthetic compounds (Baerlocher et al. 2007). The most simple sequence, the "AB" stacking, where "A" rings are centered at (1/3,2/3,*z*) and the "B" rings at (2/3,1/3,*z*), gives rise to the [CAN]-framework type (Fig. 1.2), *i.e.* to the framework of the cancrinite-group minerals, which are the object of the present study. Another class of widespread feldpathoids, the sodalite group, is structurally related to the cancrinite structure, as its framework ([SOD]-type) derives from an "ABC" stacking sequence. For both these groups, no superposition of the same ring type occurs. However, this is a common feature of several open-framework compounds. For example, in the [GME]-framework (AABB) of gmelinite, the [CHA]-framework (AABBCC) of chabazite, the [ERI]-framework (AABAAC) of erionite, or the [AFX]-framework (AABBCCBB) of the well-known synthetic zeolite SAPO-56. Although all these frameworks derive from different stackings of the same periodic building unit, their "secondary building-units" (*sensu* Barlocher et al. 2007) and the size and relative orientation of the structural voids can be significantly different. In addition, different can be the crystal-chemical and –physical properties of the related compounds. Therefore, it is not surprising that the natural feldpspathoids and zeolites, structurally related to the ABC-6 family, are widespread over a variety of geochemical and petrological environments. Before to introduce the structural features of the [CAN]-framework type, it is worth noting that there is a series of minerals showing different ABC-6 frameworks, which are, for geochemical and petrological reasons, closely related to the proper cancrinite-group. These minerals, although sometimes grouped within the cancrinite-group in the literature, were originally defined "cancrinite-like" by Leoni et al.

(1979), as reviewed by Bonaccorsi and Merlino (2005). Among them there are: bystrite ([LOS], ABAC, Pobedimskaya et al. 1991), liottite ([LIO], ABABAC, Ballirano et al. 1996a), afghanite ([AFG], ABABACAC, Ballirano et al. 1997), franzinite ([FRA], ABCABACABC, Ballirano et al. 2000), tounkite ([TOL], ABABACACABAC, Rozenberg et al. 2004), farneseite ([FAR], ABCABABACBACAC, Cámara et al. 2004), giuseppettite ([GIU], ABABABACBABABABC, Bonaccorsi 2004).

As previously described, the [CAN]-framework type is built from the simplest stacking sequence in the ABC-6 family: ···ABABAB···. In each plane (*e.g.* the "A" plane), the six-membered rings are not interconnected to each other (Fig. 1.1) and each ring is linked to three rings in the previous ("B") plane and to three rings in the next one (Fig. 1.2). The resulting structure is made by columns of base-sharing *can* units, also called "cancrinite cages", undecahedral cages or $4^6 6^5$ units according to the IUPAC recommendations (McCusker et al. 2001), where the bases correspond to the single six-membered rings perpendicular to the *c*-axis (S6R⊥[0001], Fig 1.2). These columns surround iso-oriented channels, parallel to [0001] and confined by twelve-membered rings of tetrahedra (12R) (Fig 1.2). Double *zigzag* chains of tetrahedra (*dzc* units), made by edge-sharing four-membered rings (S4R), run along the *c*-axis and border the single six-membered ring windows (hereafter S6R∠[0001]) acting as joint unit between cages and channels (Fig 1.2). Therefore, as reported in the literature (*e.g.* Pekov et al. 2011a), the [CAN]-framework can be described as made by two kinds of channels: 1) the large 12R-channel centered at (0,0,*z*) on the 6_3 screw axis and 2) the "narrow channels", corresponding to the columns of *can* units, centered at (1/3,2/3,*z*) and (2/3,1/3,*z*) on the 3-fold axes (Fig. 1.3). The topological symmetry of the [CAN]-framework is $P6_3/mmc$. The general symmetry is lowered to $P6_3$ in almost all the members of the group for the ordering of alternated SiO_4 and AlO_4 tetrahedra of the framework. In the $P6_3$ space group, along with the 6_3 and 3 axes, 2_1 screw axes occur at (1/2,0,z), (0,1/2,z) and (1/2,1/2,z) (Fig. 1.3). The framework is, therefore, made by two symmetry-independent T sites and four O sites, all placed in general 6*c* Wyckoff positions. In particular cases, (especially for davyne-subgroup minerals, see section 1.2.2) the $P6_3/m$ space group is observed, where mirror planes at $z = 0.25$ and $z = 0.75$ occur. In such a case, two T sites occupy special 6*h* positions (*x*,*y*,1/4) on the mirror plane, whereas the oxygen atoms lie at two 6*h* sites plus at a site in a general 12*i* position (see *International Tables for Crystallography, Vol. A*, Hahn 2002).

The type material of the CAN-group is cancrinite *sensu stricto*, which shows a framework density of 16.6 T/1000Å^3 (Baerlocher et al. 2007). The only "real" large channel system is that bound by the

twelve-membered rings and running along [0001] (Fig. 1.2). Although the channel is significantly large (with a free diameter of 5.9 Å, *sensu* Baerlocher et al. 2007), cancrinite-group minerals do not have high ionic exchange capacity and, more in general, zeolitic properties (see sections 1.4 and 1.5. This is in part due to structural features and in part to crystal chemical features. In fact, it is sufficient a single stacking fault with a "C-type" ring at (0,0,*z*) to interrupt the channels and to reduce the effective free diameter from 5.9 Å to those of the S6R⊥[0001] (*i.e.* 2.56 Å, maximum, and 1.44 Å, minimum) (Fig. 1.2). Similar values define the effective pore width of the S6R∠[0001] windows linking the channel walls to the *can* units (Fig. 1.2). Moreover, the presence of anionic groups surrounded by cations within the channel, as will be thoroughly discussed in the in the sections 1.2.1 and 1.2.2, acts as a further obstacle to ions mobility.

Many natural and synthetic compounds share the [CAN]-framework type, showing a significant crystal chemical variability, in terms of framework and extraframework compositions. In addition, is worth to report that the *can* unit (Fig. 1.2) is a structural composite building unit shared by a large number of zeolites with important technological applications (see *e.g.* Bish and Ming 2001). The variable crystal chemistry of the [CAN]-framework compounds will be overviewed in the next chapters of this PhD Thesis. In particular, a special attention will be paid to the crystal chemistry of the minerals of the cancrinite group.

Figure 1.1 (*Left side*) A hexagonal array of single six-membered rings in a plane. (*Right side*) Single six-membered rings in "A" (1/3,2/3,*z*), "B" (2/3,1/3,*z*) and "C" (0,0,*z*) positions.

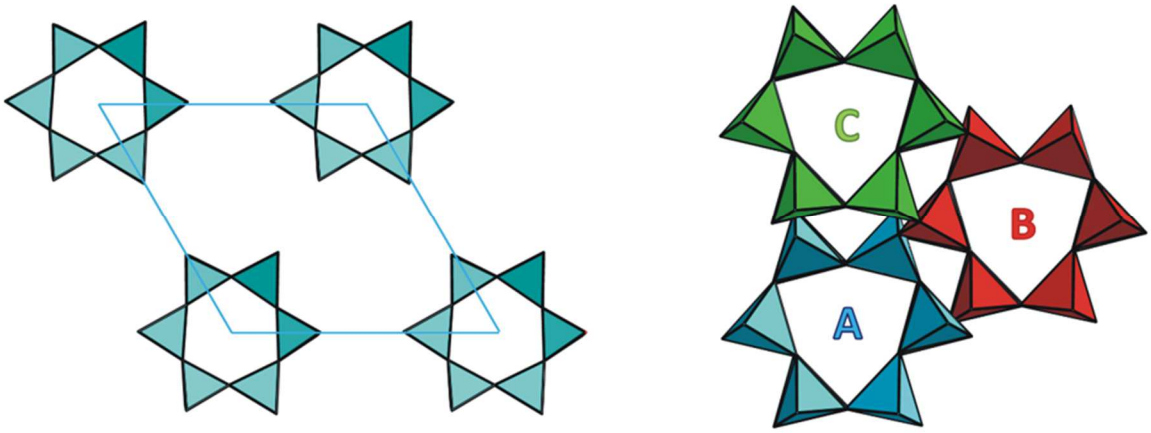

Figure 1.2 (*Left side*) The [CAN]-framework viewed down [0001]. The 6mR⊥[0001] cage bases, the large 12mR channel and the 4mR units are shown. (*Right side*) A portion of a column of *can* units. Two base-sharing cages are shown, along with a portion of a *dzc* chain and the 6mR∠[0001] windows.

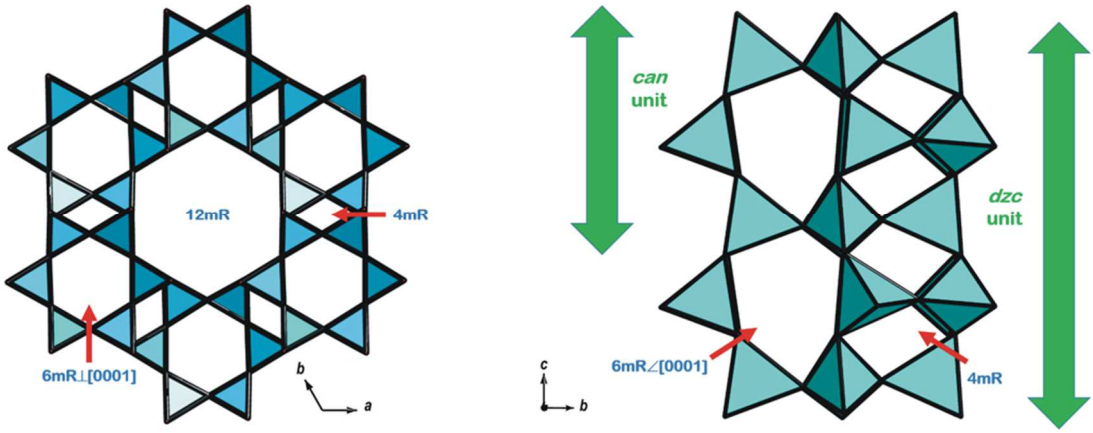

Figure 1.3 The symmetry operators of the *P*6$_3$ space group superimposed of the [CAN]-framework viewed down [0001]. The channel is centered on a 6$_3$ screw axis, the columns of *can* units on 3-fold axis, whereas the 4mR are centered on 2$_1$ screw axes.

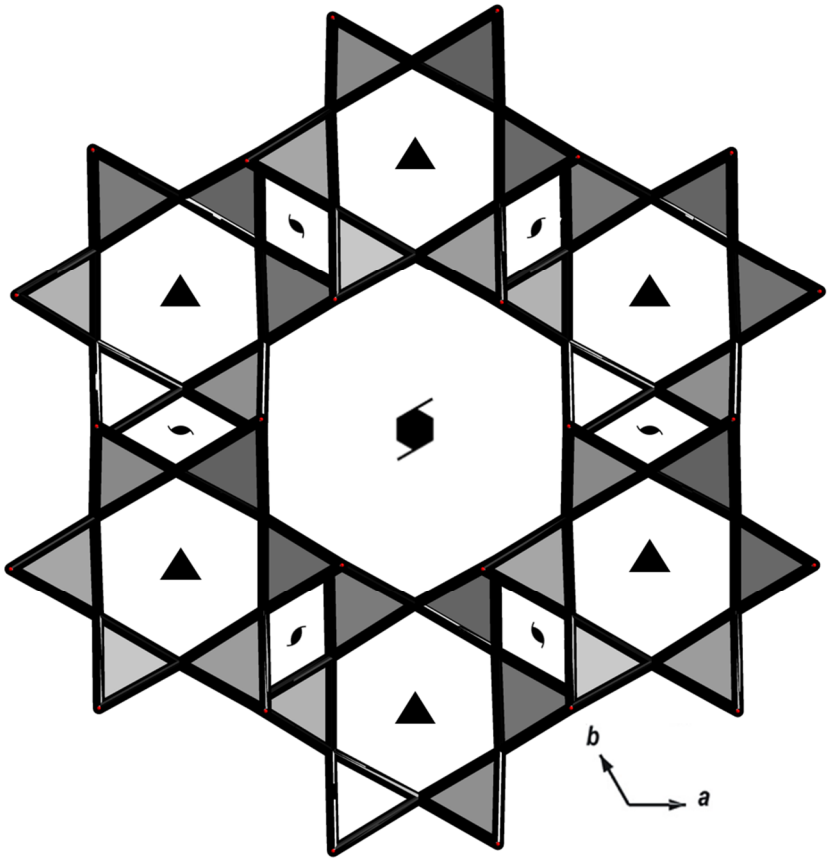

1.2 CRYSTAL-CHEMISTRY OF THE CANCRINITE-GROUP MINERALS

If we consider only the compounds showing the simplest ···ABAB··· stacking sequence of the layers made by six-membered rings (*i.e.* excluding the cancrinite-like compounds *sensu* Leoni et al., 1979), eleven mineralogical species have been reported up to now (Bonaccorsi and Merlino 2005; Pekov et al. 2011a). Ten of those show an aluminosilicate framework, with chemical formula $(Al_6Si_6O_{24})^{6-}$, whereas the eleventh, tiptopite, is the only cancrinite-group mineral with a different framework: it is a berillophosphate, with crystal-chemical formula $[(Li_{2.9}Na_{1.7}Ca_{0.7})(OH)_2(H_2O)_{1.3}](K_2)(Be_6P_6O_{24})$ (Peacor et al. 1987).

The $(Al_6Si_6O_{24})^{6-}$ framework is always perfectly ordered, with alternating SiO_4 andAlO_4 tetrahedra, as the Loweinstein's rule predicts, so that each S6R is made by three SiO_4 and three AlO_4. As a consequence of the order, the topological symmetry $P6_3/mmc$ is lowered to $P6_3/m$ or $P6_3$ in all the cancrinite-group minerals, with very rare exceptions (Rastsvetaeva et al. 2007). The excess of six negative charges of the framework is compensated by the extraframework population of the voids. These voids, as seen in the previous section can be divided in: 1) cages (*can* units) and 2) ideally uninterrupted channels parallel to [0001]. Besides a large crystal chemical variability (in part still unexplored) shown by the channel population, with several end-member compositions giving rise to complex solid solutions, only two ideally unmixable configurations are observed within the cages. One is given by the repetition of $[Na\cdot H_2O]^+$ clusters, so that chains along the columns of *can* units arise, and, similarly, the other configuration is made by chains of $[Ca\cdot Cl]^+$ clusters (Fig. 1.4). Therefore, a first classification among the cancrinite-group minerals is based upon the cage extraframework constituents. Following a scheme already adopted by Bonaccorsi and Merlino (2005) and by Pekov et al. (2011a) in their reviews, the cancrinite-group minerals can be partitioned in two subgroups: 1) the **cancrinite subgroup**, comprising all the minerals showing $[Na\cdot H_2O]^+$ chains and 2) the **davyne subgroup**, where $[Ca\cdot Cl]^+$ clusters occur. Since the crystal chemical formula of a cancrinite-group minerals embeds two clusters per formula unit, the cage population compensate for 1/3 of the framework negative charges, in both the subgroups. The remaining four negative charges must, therefore, be compensated by the channel population. As previously said, a higher chemical variability is possible for the population of these structural voids. However, a general scheme can be extrapolated. Cations, anions and molecular components can fill the channels, being that a characteristic feature of the cancrinite-group compounds, which largely influences the structure-properties. Na^+ is always the prevailing cation and can be partially substituted by Ca^{2+} and K^+. All of

them occupy crystallographic sites near the channel walls (Fig. 1.4), in order to be one-side bonded to the framework oxygen atoms. Anions and molecular groups occupy the center of the channel (Fig. 1.4), very often with split sites mutually exclusive, so that several possible configurations can occur within the same channel. These configurations can be ordered, leading to superstructures. The anionic and molecular groups most commonly occurring in Nature are CO_3^{2-}, SO_4^{2-}, Cl^-, H_2O, $C_2O_4^{2-}$, PO_4^{3-} and OH^-. Their relative ratio is conventionally used as the "species-defining criterion" (Bonaccorsi and Merlino 2005; Pekov et al. 2011a): *i.e.* the most abundant anion is species-defining, giving the name of the ideal end-member to the analyzed mineralogical sample. Due to the variable crystal chemistry, different channel configurations can occur among the cancrinite-group minerals and even among a mineralogical species itself. A schematic description of these channel configurations is reported below, along with a description of the structures of the mineralogical species belonging to the cancrinite- and davyne-subgroups. Below, a schematic list of these species (with the prevailing anions) is given:

- **Cancrinite-subgroup**: cancrinite (CO_3^{2-}), vishnevite (SO_4^{2-}), pitiglianoite (SO_4^{2-}), hydroxycancrinite (OH^-), kyanoxalite ($C_2O_4^{2-}$), depmeierite (PO_4^{3-}) and cancrisilite (CO_3^{2-}).
- **Davyne-subgroup**: davyne (SO_4^{2-}), balliranoite (CO_3^{2-}), microsommite (SO_4^{2-}) and quadridavyne (Cl^-).

1.2.1 Cancrinite-subgroup minerals

The minerals belonging to this subgroup all show chains made by subsequent clusters of $[Na\cdot H_2O]^+$ within the columns of *can* units. The Na^+ cation is located on a single site on the 3-fold axis (1/3,2/3,*z*), slightly displaced (along *z*) from the *can* unit basis, in almost the totality of the studied samples, with very rare exceptions (Zubkova et al. 2011; Pekov et al. 2011a). H_2O molecule occupies the center of the cage, generally positioning out of the 3-fold axis in three symmetry-equivalent and mutually exclusive positions (Fig. 1.4) (e.g. Jarchow 1965; Grundy and Hassan 1982; Hassan and Grundy 1991; Lindner et al. 1995; Hackbarth et al. 1999; Ballirano and Maras 2004; Shirinova et al. 2006; Della Ventura et al. 2009, Gatta et al. 2012; Lotti et al. 2012; chapters 4 and 5). In some cases, the H_2O oxygen was refined in a special 2*b* position on the 3-fold axis (Bresciani-Pahor et al. 1982; Hassan 1996a; Hassan et al. 2006). However, if not explicitly adopted as a strategy to stabilize the structure refinement under non-favorable conditions, the anomalously high values of the

displacement parameters suggest that the real position of the H_2O is out of the axis. Refined structures, having both the types of crystallographic H_2O have also been reported (Rastsvetaeva et al. 2007; Pekov et al. 2010, 2011a). The position of the H_2O hydrogen atoms has been located and refined by Della Ventura et al. (2009) by single-crystal neutron diffraction. The Authors reported a H_2O molecule plane only slightly inclined with respect to (0001), as also confirmed by polarized FTIR data. The H_2O molecule adopts a tetrahedral coordination given by two weak hydrogen bonds and two O-lone pairs directed towards the neighboring Na^+ cations (Della Ventutra et al. 2009). Both the symmetry-independent H-atoms show bifurcated bonds, giving rise to four possible H-bonds (Della Ventura et al. 2009). A further investigation based on polarized FTIR experiment on vishnevite was performed by Della Ventura et al. (2007). The H-bonding system is likely the driving force that displaces the H_2O molecule out from the 3-fold axis, as also proposed in other studies (Hassan and Grundy 1991; Pekov et al. 2010). The H_2O molecule is not placed halfway between the two neighboring Na^+ cations, but is closer to one of them. Therefore, the Na^+ cation has a "strong" tetrahedral coordination with the three O2 atoms of the cage basis and the closer H_2O oxygen atom, acting as the tetrahedral vertex (Fig. 1.5). In addition, the Na^+ shows longer bonds with the three O1 oxygen atoms of the cage basis and the further H_2O oxygen. (Fig. 1.5). The Na^+ coordination environment can, therefore, be viewed as a distorted (4+4) ditrigonal bipyramid. Pekov et al. (2011a) report that the majority of the studied samples belonging to the cancrinite-subgroup of minerals shows a full occupancy of the cage-H_2O sites (2 molecules p.f.u.). However, as already underlined by Pekov et al. (2010), the loss of H_2O does not perturb the charge balance, even though, in such a condition, neighboring not shielded and positively charged Na^+ cations would occur. Although rare, this configuration has been reported for a quasi-anhydrous natural cancrinite found in alkaline effusive rocks at Laacher See, Germany (Zubkova et al. 2011). Its structure refinement revealed the splitting of the Na^+ site over three mutually exclusive and statistically occupied positions along the [0001], likely in order to minimize charge repulsion.

The crystal chemistry of the channel in cancrinite-subgroup minerals is highly variable and, probably, still not completely explored. Overall, the [CAN]-framework channel is a system that was proved to be suitable to host a large number of clusters made by cations, anions and molecules. As previously mentioned, the general pattern is made by cations near the channel walls and anionic and molecular groups in the center or slightly displaced from the 6_3 axis (Fig. 1.4).

Cancrinite *sensu stricto*(*s.s*) is, by far, the most widespread mineral of the homonymous group. It was first described and named by Rosé (1839) and its crystal structure was first solved by Pauling (1930),

and then refined by Jarchow (1965). In cancrinite, cations can occupy a single crystallographic site in a general 6*c* position (*e.g.* Grundy and Hassan 1982; Pekov et al. 2011a; Della Ventura et al. 2009; Gatta et al. 2012; Lotti et al. 2012; chapter 4) or two mutually exclusive sites (Ballirano and Maras 2004; Hassan et al. 2006; Zubkova et al. 2011). Their coordination environment is made by three shorter bonds with the framework oxygen atoms O1, O3 and O4 on a side (along with two longer bonds with additional O3 and O4) and by a variable number of bonds (generally up to three) with the oxygen of the carbonate groups on the other side (Fig. 1.6). Ca^{2+} is always present in cancrinite *s.s.* (Pekov et al. 2011a) with a variable amount, generally not lower that 0.3 atoms per formula unit, whereas K^{+} is always absent or present as insignificant impurity (Pekov et al. 2011a). When two crystallographic cation sites are present, generally it is not possible to have a preferential partitioning of the Ca^{2+} cation, as deduced on the basis of the bond distances to the coordinated oxygen atoms. The CO_3^{2-} groups lie at the center of the channel in two mutually exclusive and iso-oriented configurations (Fig. 1.6). The C sites lie on the 6_3 axis, whereas the three O's are generated by symmetry in 6*c* positions around the C. The two configurations differ for the height within the asymmetric cell ($0 \leq z \leq 1/2$): the carbonate groups are generally split at $z \sim 0.17$ and 0.40 (C1-Oc1 and C2-Oc2). Obviously, for the very short distance between them, only one configuration can occur per each half-cell. Less often, up to four independent configurations are shown by the carbonate groups in cancrinite (Zubkova et al. 2011; Pekov et al. 2011a). A typical feature is a strongly anisotropic function of their displacement parameters, which are systematically elongated along [0001] (see *e.g.* Isupova et al. 2010 for a detailed description). An *in situ* low-*T* single-crystal X-ray diffraction study, performed in the framework of this PhD project (Gatta et al. 2012; section 4.1), reported that this feature is preserved, with no apparent change down to 100 K, suggesting that it is due to a positional rather than a dynamic disorder of the carbonate groups around their average positions. Several studies (Della Ventura et al. 2009; Gatta et al. 2012; Lotti et al. 2012; chapter 4) reported a non co-planar configuration of the atoms of the (CO_3^{2-})-group. However, the strong positional disorder hinders an unambiguous interpretation. The polarized FTIR data show a strong polarization of the carbonate stretching bands for $E \perp c$ (Della Ventura et al. 2009). The cations are positioned typically halfway between the two carbonates ($z \sim 0.27$). If the three shorter bonds to the framework oxygen atoms alone are taken into account, coupled with the bonds to the three Oc1 (or Oc2), belonging to two subsequent carbonates, two coordination-polyhedra are possible: a distorted trigonal prism or a distorted octahedron in response to the different carbonate oxygen atoms, *i.e.* Oc1 or Oc2. Superstructure reflections, characterized by different periods along the [0001] axis, are not

rare in cancrinite (Jarchow 1965; Foit et al. 1973; Grundy and Hassan 1982; Hassan and Buseck 1991) and tend to progressively disappear with increasing temperature (Foit et al. 1973). This superstructure was reported to arise from ordering of the [$(Na^+,Ca^{2+})_3(CO_3^{2-})$] clusters and their vacancies along the channel (Grundy and Hassan 1982; Hassan and Buseck 1991). In fact, if the C-C distance in aragonite (2.87 Å, De Villiers et al. 1971; Ungaretti and Dal Negro 1971) is considered as the shortest possible, the maximum amount of CO_3^{2-} in cancrinite is ~ 1.78 p.f.u., which is consistent with the chemical compositions reported in the literature (Bonaccorsi and Merlino 2005; Pekov et al. 2011a). The fit to the distance is, likely, the driving force for both the superstructure-ordering of vacancies and the positional disorder of the carbonate groups. It is interesting to notice that superstructure reflections, which affect the periodicity along *c*, are reported also for vishnevite and hydroxycancrinite (Grundy and Hassan 1984; Hassan and Grundy 1991).

Vishnevite, first described by Belyankin (1931), is the (SO_4^{2-})-dominant end-member and, like cancrinite, it is a quite common mineral in Nature. Reported structures show, for the cations within the channel, a single crystallographic site (Hassan and Grundy 1984) or two mutually exclusive sites (Della Ventura et al. 2007). The latter configuration can be considered more likely because of the interplay between the cations and the SO_4^{2-} tetrahedron. This anionic group occupies the center of the channel (Hassan and Grundy 1984; Della Ventura et al. 2007), where S is placed on the 6_3 axis. Two mutually exclusive configurations can occur: upward or downward (*i.e.* with the apical oxygen pointing up or down with respect to the S, see for example Fig. 1.6). The triangular base of the tetrahedron is given by three symmetry-related oxygen sites lying out of the 6_3 axis, whereas the apical oxygen is placed on it. Because of too short contacts, if a SO_4^{2-} tetrahedron occupies a position at a given height *z*, the symmetry related positions at $z + ½$ and $z – ½$ must be vacant. Therefore, only one SO_4^{2-} p.f.u. can be present. This drives to a lower negative charge within the vishnevite channel, if compared to the cancrinite one, where the amount of CO_3^{2-} is typically higher than 1 p.f.u., having an influence on the cations composition. In fact, Ca^{2+} is present only as a minor impurity in (SO_4^{2-})-cancrinites (Pekov et al. 2011a), whereas K^+ is more abundant than in cancrinite *sensu stricto*. In order to avoid too short K-O bonds, this cation cannot occupy a site at the same level of the SO_4^{2-} tetrahedron. Therefore, it must occupy the "internal" sites (farthest from the framework walls) in correspondence to the SO_4^{2-} vacant positions (see, for example, Fig. 1.6). In these sites, K^+ can be partially substituted by Na^+. When this substitution occurs, the SO_4^{2-} apical oxygen can be displaced from the 6_3 axis towards the Na^+ site, in order to give an ideal shorter Na-O bond (Merlino et al. 1991; Bonaccorsi et al. 2007). The "external" sites are occupied by Na^+ cations, in correspondence to the

SO_4^{2-} tetrahedron, bonded to 3+2 framework oxygen atoms on a side and one (Merlino et al. 1991; Bonaccorsi et al. 2007) or two (Hassan and Grundy 1984; Della Ventura et al. 2007) sulfate oxygen atoms on the other side (see, for example, Fig. 1.6). A channel can be internally ordered with a sequence of alternated $[Na_3(SO_4)]$ and $(K,Na)_3$ clusters. Two energetically equivalent configurations can occur: the first with $[Na_3(SO_4)]$ at z and $(K,Na)_3$ at $z + ½$, the second with the opposite configuration. If there is a long-range ordered distribution of these configurations among adjacent channels, a superstructure with a new unit-cell a parameter equal to $\sqrt{3}a_{vish}$ arises. This gives rise to a new mineralogical species called pitiglianoite. (Merlino et al. 1991; Bonaccorsi and Orlandi 1996; Della Ventura et al. 2005; Bonaccorsi et al. 2007), which shares with vishnevite a common c parameter and space group ($P6_3$). In pitiglianoite, three channels per unit-cell occur. Two of them are centered on the 3-fold axes and are symmetrically related by a 2_1 operator, so that being internally ordered with opposite configurations (Merlino et al. 1991; Bonaccorsi et al. 2007). The third channel is centered on the 6_3 axis and can randomly show one configuration or the other and appear being disordered from a diffraction analysis. However, if a long-range ordered configuration occurs also for this channel, the symmetry could be lowered from $P6_3$ to $P3$ and 000l reflections with $l = 2n+1$ would appear, as experimentally observed (although very weak) by Merlino et al. (1991). Pitiglianoite shares the same channel composition and superstructure features with microsommite, which differs for having $[Ca\text{-}Cl]^+$ clusters within the *can* units columns. A thorough study on the order-disorder phase transitions in microsommite has been carried out (Bonaccorsi et al. 2001) and will be reported below. It is worth noting that a synthetic pitiglianoite (referred to as "*synthetic sulfate hydrocancrinite of the microsommite type*") was synthetized several years before the first discovery of its occurrence in Nature, by Klaska and Jarchow (1977).

Hydroxycancrinite (or "basic cancrinite") is the (OH^-)-dominant end-member of the cancrinite subgroup and is often reported as a synthetic product . In Nature it is rare and usually represented by intermediate members of the cancrinite-hydroxycancrinite series in peralkaline plutons of the Kola peninsula, Russia (Pekov et al. 2011a). Its crystal structure is basically identical to that of cancrinite, differing for being Ca^{2+} depleted and for having OH^- and H_2O in place of the CO_3^{2-} at the channel center. Hydroxyl- and H_2O-oxygen atoms occupy the same positions of C and Oc in cancrinite: onto the 6_3 axis and out of it at ~ (0.12, 0.06, 0.17/0.40), respectively (Bresciani-Pahor et al. 1982; Hassan and Grundy 1991). As mentioned above, H_2O molecules are found as channel guests also in natural and synthetic (CO_3^{2-})-cancrinites (Pekov et al. 2011a; Zubkova et al. 2011; Hackbarth et al. 1999), suggesting an (at least partial) solid solution series. Although a rare species, many IR-spectra reported

in the literature show absorption bands typical of the OH^- stretching mode, as reported by Della Ventura et al. (2007).

Kyanoxalite is the ($C_2O_4^{2-}$) end-member. It is very rare; minerals of the cancrinite-kyanoxalite series have, up to now, been found only at the Lovozero alkaline pluton, Kola peninsula, Russia (Chukanov et al. 2010a; Olysych et al. 2011; Pekov et al. 2011a). Pure ($C_2O_4^{2-}$)- (Chukanov et al. 2010a) and mixed (CO_3^{2-},$C_2O_4^{2-}$)-members (Olysych et al. 2011) have been recognized by means of infrared spectroscopic analyses. The dumbbell-like oxalate groups are placed at the center of the channel, where two symmetry-independent groups can give rise to three symmetry-related and mutually exclusive configurations. Therefore, a total of six mutually exclusive configurations of the ($C_2O_4^{2-}$)-group is derived (Chukanov et al. 2010a). The reported C-C bond length is 1.50 Å, the C-O lengths 1.21-1.29 Å and the O-C-O angles 127-129° (Chukanov et al. 2010a). A similar configuration for the oxalate anion has been reported for a synthetic kyanoxalite-like compound, by Linares et al. (2011). Because of the too short contacts, one ($C_2O_4^{2-}$) per unit-cell (*i.e.* 1 p.f.u.) is the maximum amount possible. In the literature, the value is even lower (Chukanov et al. 2010a; Olysych et al. 2011; Pekov et al. 2011a), and a large fraction of channel vacancies were found to be occupied by H_2O molecules, as also suggested by IR-spectroscopic and structural data (Chukanov et al. 2010a). The cations are represented by Na^+ and minor K^+, occupying an "external" and an "internal" site, respectively.

Depmeierite is the (PO_4^{3-})-dominant member of the cancrinite subgroup and has been reported only from Mt. Karnasurt, Kola peninsula, Russia (Pekov et al. 2011b). The studied sample was characterized by a single cation site in the channels and by 0.47 PO_4^{3-} tetrahedra p.f.u., with two possible configurations: upward and downward, as observed for the sulfate-groups in vishnevite. The P is split in two sites (for the upward and downward tetrahedra, respectively) onto the 6_3 axis, whereas the oxygen atoms give two different triangular bases out of the 6_3 axis and an apical vertex on it. Minor amounts of H_2O and CO_3^{2-} are also present. Although extremely rare, it is worth noting that not irrelevant P_2O_5 contents have been reported in several cancrinite compositions (Pekov et al. 2011a, 2011b), suggesting the existence of a solid solution series.

Cancrisilite is the only member of the cancrinite group of minerals for which the species-defining criterion is not valid. Cancrisilite shows a [CAN]-framework enriched in Si^{4+}, with an ideal Si^{4+}:Al^{3+} ratio of 7:5. This leads to a disordering of the Si^{4+} and Al^{3+} in the framework tetrahedra, giving rise to an increase of symmetry from $P6_3$ to $P6_3mc$ (Khomyakov et al. 1991; Ogorodova et al. 2009; Pekov et al. 2011a). Cancrisilite is also a quite rare mineral, having been found only at the Khibiny-Lovozero

alkaline complexes, Kola Peninsula, Russia (Ogorodova et al. 2009). The extraframework crystal-chemistry of cancrisilite is analogous to that of cancrinite, with CO_3^{2-} as the dominant anionic group. Na^+ always prevails on Ca^{2+} and K^+. An exotic variety of cancrisilite, with symmetry reduction from $P6_3mc$ to $P3$ has been reported by Rastsvetaeva et al. (2007).

1.2.2 Davyne-subgroup minerals

The distinguishing feature of the davyne subgroup is represented by the chains of alternating Ca^{2+} and Cl^- ions, which fill the columns of *can* units in place of the Na-H_2O chains in cancrinite subgroup. The davyne subgroup comprises four mineralogical species: davyne, balliranoite, microsommite and quadridavyne. The first two species show the classical metrics of cancrinite-group compounds (*i.e*. a ~ 12.7, c ~ 5.2 Å), whereas the last two minerals show different kinds of superstructure affecting the a parameter: being $a_{mic} = \sqrt{3}a_{dav}$ and $a_{qua} = 2*a_{dav}$.

In all of them, the population of the cages shows the same configuration: the Ca^{2+} cation lies on the 3-fold axis and approximately centers (in heght) the S6R⊥[0001] (*i.e*. the basis of the *can* unit) bonding to all its six framework oxygen atoms (3*O1 + 3*O2) (Fig. 1.5). The Cl^- anion does not reside on the trigonal axis and gives rise to three symmetry-related and mutually exclusive positions almost halfway between the two neighboring Ca^{2+} cations (Fig. 1.5). This configuration is compatible with the occurrence of a mirror plane parallel to (0001) and, therefore, with the $P6_3/m$ space group, which has been reported for some davyne samples (Bonaccorsi et al. 1990, 1995) and quadridavyne (Bonaccorsi et al. 1994). Hassan and Grundy (1990) reported the structures of two davyne samples, in which Cl^- was placed in a special position onto the 3-axis. However, the Authors also reported a strong and highly anisotropic displacement parameter for the Cl^- site, which suggests a real positioning out of the trigonal axis. Chukanov et al. (2010b) reported for the holotype balliranoite both the configurations, as mutually exclusive. Therefore, the coordination polyhedron of the Ca^{2+} cation is a slightly distorted quasi-hexagonal bipyramid, where the neighboring chlorines act as the vertices (Fig. 1.5).

In davyne subgroup, the extraframework population of the channels not only determines the end-members, but is also responsible for the superstructure of microsommite and quadridavyne. The cationic content is represented by prevailing Na^+ and variable amounts of K^+ and Ca^{2+} (Ballirano et al. 1996b, 1998; Binon et al. 2004), while the reported anions are SO_4^{2-}, Cl^-, CO_3^{2-} and S_2^{2-}. Both

chemical and IR-spectroscopic analyses have shown that the sulfate, carbonate and chlorine groups can coexist within the channel (Ballirano et al. 1996b, 1998; Binon et al. 2004; Della Ventura et al. 2008). Their relative amount is the criterion used to define the end-members davyne and balliranoite (both showing a subcell metrics). If CO_3^{2-} is the prevailing anionic group, the sample is named balliranoite (ideal chemical formula $\{[(Na,Ca)_6(CO_3)_{1.2\text{-}1.7}][Ca_2Cl_2][Al_6Si_6O_{24}]\}$), as approved by the IMA Commission on New Minerals, Nomenclature and Classification (Chukanov et al. 2010b), otherwise the classical name davyne (ideal chemical formula $[(Na,K)_6(SO_4,Cl)][Ca_2Cl_2][Si_6Al_6O_{24}]$) is used. Due to the recent recognition as an independent mineralogical species and to the not trivial identification of C by chemical analysis, it cannot be excluded that the carbonate-rich balliranoite is not so rare. A more complex interplay between crystal chemistry and structural arrangement of the channel population leads to the mineralogical species microsommite and quadridavyne. From the chemical point of view, the first can be considered as the (SO_4^{2-})-end-member and the second as the (Cl^-)-one. However, this chemical feature needs to be coupled to the structural long-range order which will be discussed later.

The configuration of the extraframework population within the channel of davyne and balliranoite does not differ, at a first approximation, from that previously described for vishnevite and cancrinite, respectively. Cations always occupy two distinct and mutually exclusive positions. The external site at ~ (0.15, 0.30, 0.25) is occupied by Na^+ (or Ca^{2+}, Binon et al. 2004), while the inner one at ~ (0.11, 0.22, 0.25) is commonly referred to as a mixed (K^+, Na^+, Ca^{2+}) site (Bonaccorsi et al. 1990; Hassan and Grundy 1990; Binon et al. 2004; Rozenberg et al. 2009; Sapozhnikov 2010; Chukanov et al. 2010b). An additional (third) cationic site was reported for a balliranoite sample (referred to as [CO_3^{2-}]-davyne in Ballirano et al. 1998). The SO_4 tetrahedron can occur in both the upward and downward configurations (Fig. 1.6), where the sulfur site lies on the 6_3-axis and the apical oxygen is also positioned on the axis, or slightly displaced from it. The planar CO_3 group typically occupies two mutually exclusive and iso-oriented configurations disordered along [0001], as observed in the more common cancrinite, with C lying on the 6_3-axis. Interestingly, the triangular basis of the SO_4 tetrahedron is generally (Bonaccorsi et al. 1990; Hassan and Grundy 1990; Rozenberg et al. 2009; Chukanov et al. 2010b; Sapozhnikov 2010; chapter 7) rotated of 60° about the [0001] axis with respect to the planar CO_3 group (Ballirano et al. 1998; Chukanov et al. 2010b; Gatta et al. 2013; Lotti et al. 2013; chapter 6). As a consequence, when an $X \cdot CO_3$ cluster (where X is a cation) occurs at given height *z* in the channel, CO_3 group points an edge towards the X cation, so that two oxygen atoms are bonded to it in a sort of triangular XO_2 topology (Fig. 1.6). On the contrary, when an $X \cdot SO_4$

cluster occurs, the triangular basis of the SO_4 tetrahedron points a vertex towards the cation, giving rise to a single X-Os bond (Fig. 1.6). Obviously, if favorable distances occur, the X cation can also bond to the previous or the following anionic groups (*i.e.* at different *z*), leading to a large number of possible coordination environments (Fig. 1.6). The Cl^- anion, where present, is typically slightly displaced out of the 6_3-axis in a position that recalls that of the SO_4 tetrahedron apical oxygen (Bonaccorsi et al. 1990; Ballirano et al. 1998). Sapozhnikov (2010) reported a rather unusual "davyne" with the channels stuffed by SO_4^{2-}, CO_3^{2-} and S_2^{2-} anions, where the S of the sulfide group occupies three symmetry-related positions out of the 6_3-axis, giving rise to three possible configurations of the S_2^{2-} dimer.

The complicated history of microsommite (and davyne) is reported by Bonaccorsi et al. (1990). Briefly, davyne was first described by Monticelli and Covelli (1825), whereas microsommite was first reported, half century later, by Scacchi (1872). Later, they were considered two varieties of one species, differing in birefringence, by Zambonini (1906) and Lacroix (1907) and discredited to varieties of cancrinite in Deer et al. (1963). It was only with the work of Bariand et al. (1968) that davyne and microsommite were clearly recognized as independent mineralogical species. However, Bonaccorsi et al. (1990) wrote: "*… it remains unproved that samples defined microsommite by Scacchi (1872), as well as the large number of samples classified as microsommite in various mineralogical collections, are actually distinct from davyne"*. A re-investigation with modern techniques of this kind of minerals, classified more than a century ago, should provide a more clear scenario, as demonstrated by the recent work of Binon et al. (2004), who discredited "cavolinite", demonstrating that samples of davyne, quadridavyne and balliranoite were erroneously classified with that name. Microsommite and davyne share similar chemical compositions, with ideal chemical formulae $[Na_4K_2(SO_4)][Ca_2Cl_2][Si_6Al_6O_{24}]$ and $[(Na,K)_6(SO_4,Cl)][Ca_2Cl_2][Si_6Al_6O_{24}]$, respectively. However, they present significant metrical differences, being $a_{mic} = \sqrt{3}a_{dav}$, whereas they share a common *c* parameter ($c_{mic} = c_{dav}$). Therefore, microsommite can be identified by the occurrence of superstructure reflections having $h - k \neq 3n$, if the microsommite unit-cell is taken as a reference. This superstructure is due to the long-range ordering of the extraframework content within adjacent channels, as investigated by Bonaccorsi et al. (2001). This long-range order arises from geometrical constraints that limit the number of SO_4^{2-} groups to 1 per unit-cell translation (1/2 occupancy of the S site on the 6_3 axis). The SO_4^{2-} group can coexist with a cation lying at the "external" site at the same height, but it is mutually exclusive with the cations occupying the "internal" sites. If the maximum content of 1 SO_4^{2-} per formula unit is reached, the channel must be internally ordered, giving rise to

a sequence made of clusters of $[(Na,Ca)_3(SO_4)]$ at *z*, followed by clusters of $[(K,Na,Ca)_3]$ at *z* + 0.5, or *viceversa*. The two possible sequences, arbitrarily defined - and + by Bonaccorsi et al. (2001), are energetically equivalent. In microsommite at room-*T*, Bonaccorsi et al. (2001) reported that the order between adjacent channels can be described using a "triangular lattice", where two nodes (channels) are ordered with – and + sequences, respectively, and the third is disordered (*i.e.* can show both – or + sequences), as shown in Fig. 1.7. This ordering gives rise to the microsommite superstructure, keeping the $P6_3$ space group, where the "disordered" channel is centered on the 6_3 axis and the ordered ones on the two 3-fold axes. In davyne (and balliranoite), the internal order of the channel and, therefore, the long-range order are prevented by the insertion of Cl^-, according to the $SO_4^{2-} \leftrightarrow 2Cl^-$ substitution, or CO_3^{2-}, according to $SO_4^{2-} \leftrightarrow CO_3^{2-}$, or by a total amount of $SO_4^{2-} < 1$ p.f.u. Therefore, microsommite can also be seen as the SO_4^{2-} end-member of the subgroup.

The Cl^- almost pure end-members within the davyne subgroup show a different kind of superstructure (Bonaccorsi et al. 1994; Binon et al. 2004), with respect to microsommite. In this species, $a_{qua} = 2*a_{dav}$ and $c_{qua} = c_{dav}$, from which the name "quadridavyne", being the unit-cell volume four times that of davyne. A preliminary structure was reported by Bonaccorsi et al. (1994), since its complexity did not allow to refine a completely satisfactory model. The Authors reported three different cationic sites within the channels, labelled as "external", "middle" and "internal", and two possible sites for Cl^-, labelled "Cl(a)" and "Cl(b)". Two possible coordination schemes were proposed: if Cl(b) occurs, cations could occupy only the "external" and "internal" sites", if Cl(a) occurs, cations would be forced in the "middle" site. The quadridavyne superstructure leads to two crystallographically independent channels. In the channel centred on the 6_3-axis (0, 0, *z*) both the schemes could occur, whereas the channel at (½, ½, *z*) seems to favour the Cl(b) scheme.

Figure 1.4 (*Left side*) Schematic view of the Na-H_2O and Ca-Cl chains, in the columns of *can* units of cancrinite-subgroup and davyne-subgroup minerals, respectively. (*Right side*) The channel extraframework content of davyne, viewed along [0001]. The cations sites (Na1, Na2, K) are closer to the channel walls, whereas the anions (here SO_4^{2-}) occupy the channel center.

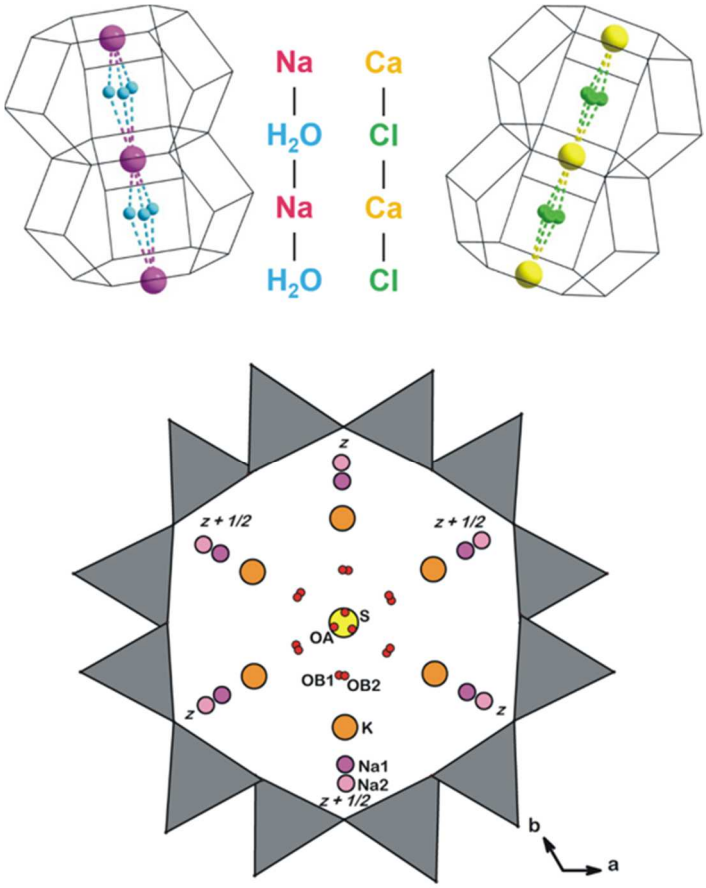

Figure 1.5 (*Left side*) The cage-Na^+ coordination environment in cancrinite. (*Right side*) The cage-Ca^{2+} coordination environment in davyne. Dashed lines represent mutually exclusive bonds

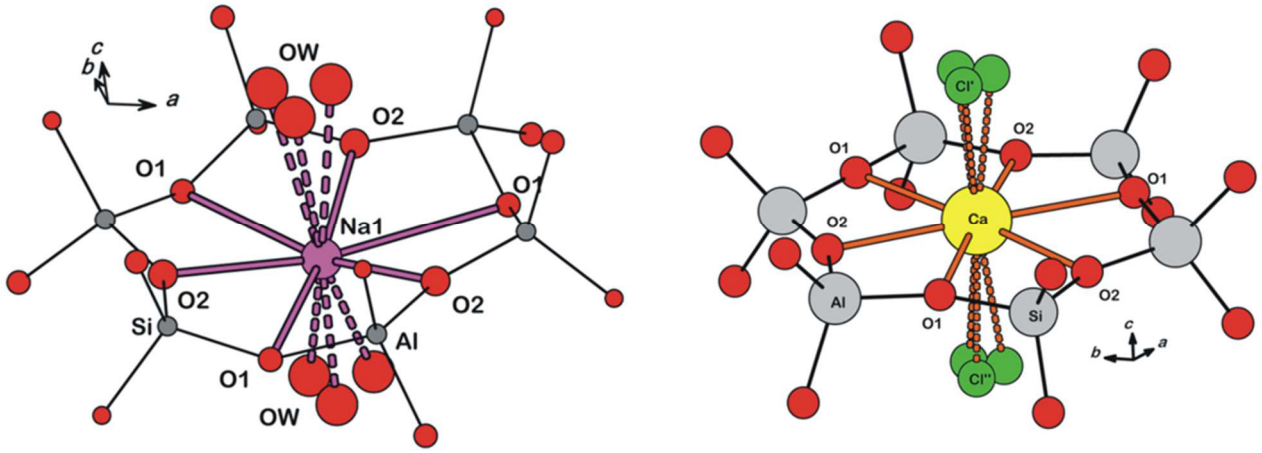

Figure 1.6 (*Left side*) Coordination shell of the (Na^+,Ca^{2+}) cations in the cancrinite channel. (*Right side*) Coordination shells of the "external" Na^+ and "internal" K^+ in the davyne channel. The possible upward and downward configurations of the SO_4^{2-} tetrahedra are shown. Dashed lines represent mutually exclusive bonds

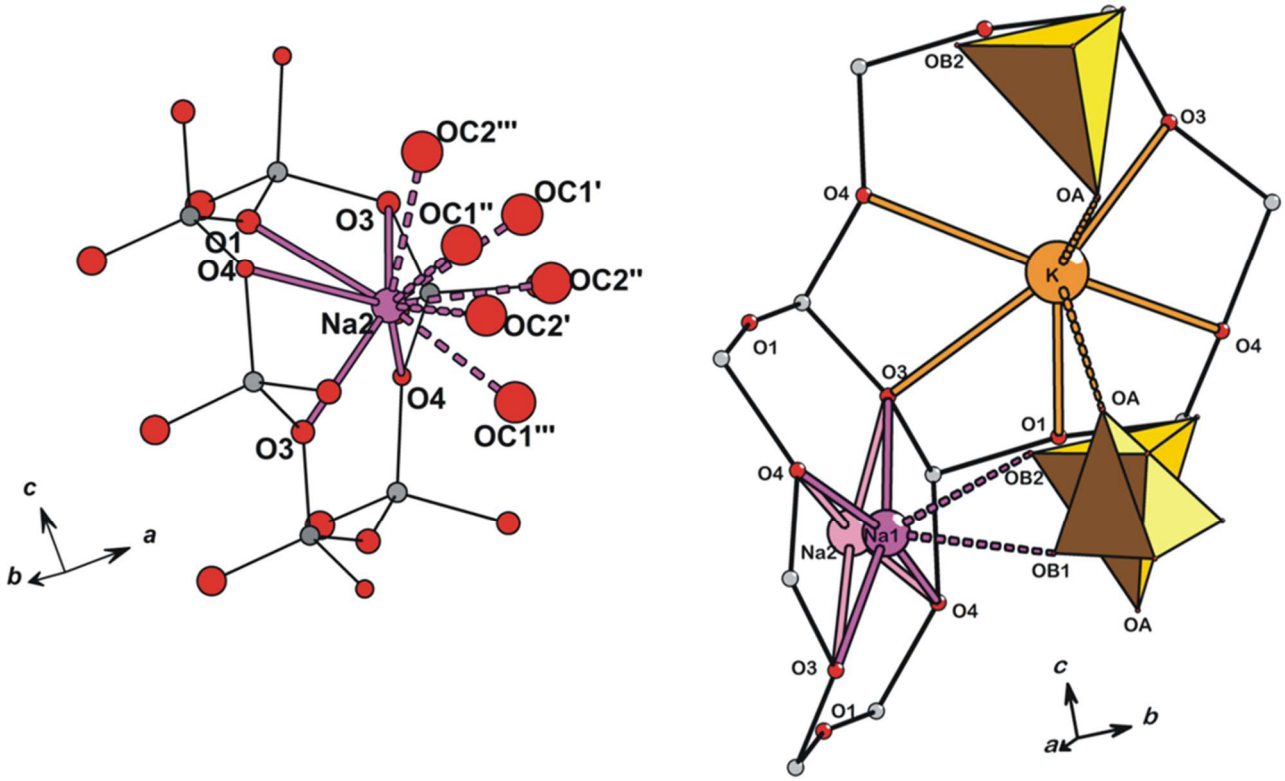

Figure 1.7 Schematic representation of the long-range ordered distribution of adjacent channels in microsommite and pitiglianoite. Each channel is internally ordered, showing the regular alternation of $[Na_3(SO_4)]$ and $[(Na,K)_3]$ clusters (+), or *viceversa* (-). The channels centered on the 6_3 screw axes, can randomly show both the sequences (*i.e.* ±).

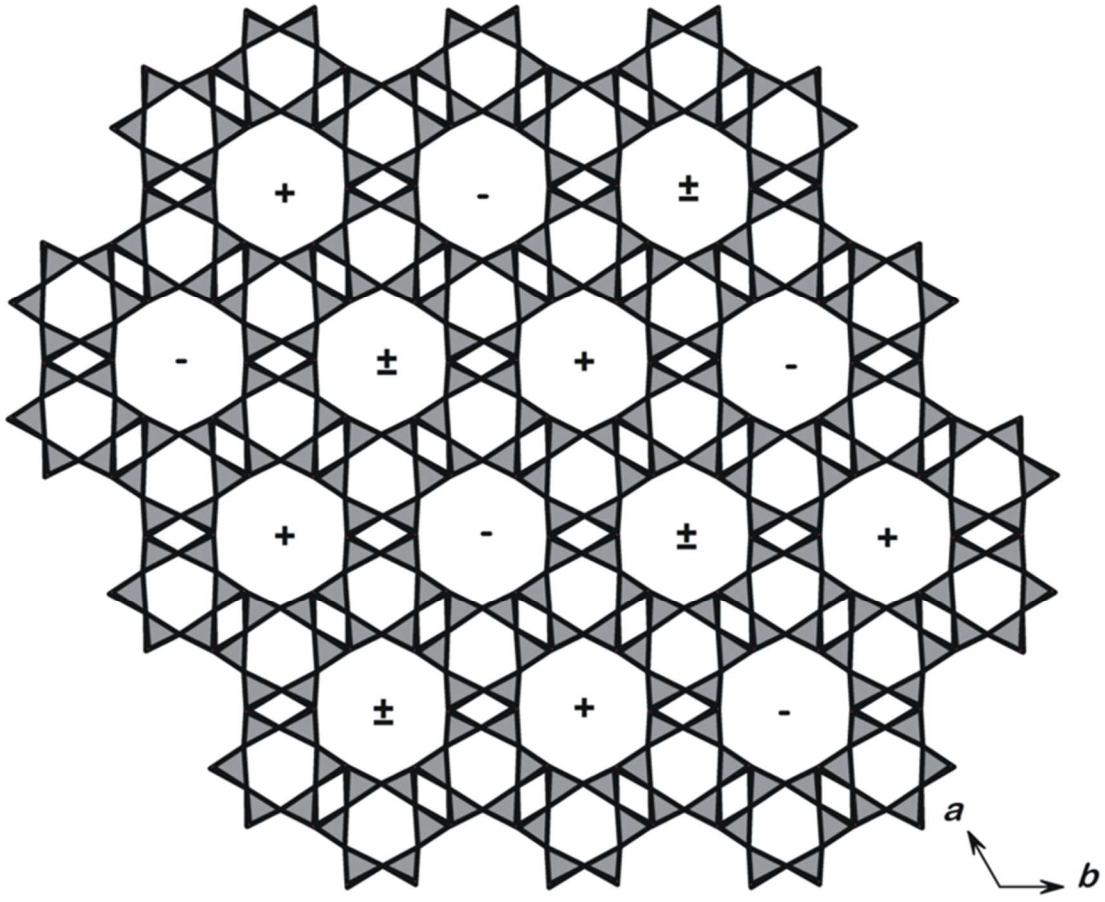

1.3 NATURAL OCCURRENCES OF CANCRINITE-GROUP MINERALS

Cancrinite-group minerals are mutually exclusive with SiO_2 polymorphs. Consequently, as reported by Deer et al. (2004), they are typical of geological environments 1) undersaturated in SiO_2, which, in addition, 2) must also be rich in alkalis, in particular Na^+, and 3) must supply the sufficient amount of volatile components, as CO_2, SO_2, Cl or F, which are fundamental for the crystallization of the cancrinite-group minerals. Large amounts of CO_2, SO_2 and halogens are typical of alkaline and peralkaline magmatism (Bailey and Hampton 1990). Therefore, it is not surprising that cancrinite-group minerals are strictly associated to geological settings related to alkaline magmatism. They are widespread both in intrusive environments, such as nepheline syenites, and in effusive settings, as phonolites. In addition, cancrinite-group minerals can be found in metasomatic environments related to alkaline magmas and/or limestone wallrocks. The various terms of the cancrinite- and davyne-subgroups can show substantial or subtle differences of genetic conditions. Below, an overview of the occurrence of these minerals in different geological settings is given, with a genetic classification scheme proposed by Pekov et al. (2011a), will be reported.

Cancrinite *sensu stricto* is, by far, the most common species of the group. It is widespread in intrusive alkaline magmatic complexes, where it can crystallize: 1) during the late-magmatic stage or 2) from hydrothermal alteration of pre-existing minerals. In the first case, cancrinite occurs in the last stage of magmatism, when a highly evolved magma, enriched in incompatible volatiles and alkalis, allows a direct crystallization, once the liquidus boundary is reached. This primary cancrinite is typical of vein- and dyke-intrusions or pegmatites. A secondary cancrinite can commonly form both during the late-magmatic stage and in post-magmatic hydrothermal conditions, from the alteration of nepheline- or sodalite-group minerals by the (CO_2)-rich fluids. Several examples can be found all over the world, representing the most common geological setting for cancrinite-group minerals. Primary and secondary cancrinite is widespread, both as rock-forming or accessory mineral, at the Lovozero alkaline pluton, Kola peninsula, Russia (Deer et al. 2004; Pekov et al. 2011a). At Alluaiv Mountain (Kola peninsula, Russia), cancrinite occurs in nepheline syenite (malignite) pegmatitic bodies, often replaced by natrolite and analcime (Deer et al. 2004). At the Alnö Island (Sweden) alkaline complex, it is found as a primary late liquidus phase (Deer et al. 2004), whereas is found as accessory mineral in the sodalite- and nepheline-syenites at Mount Sainte Hilaire, Quebec, Canada (Deer et al. 2004). At Iron Hill, Colorado, USA, a minor primary cancrinite is found in the nepheline syenites, but it is much more abundant as secondary alteration product of nepheline (Larsen 1942), as in the Cerro

Sarambì nepheline syenites (Amambay Area, Paraguay, Gomes et al. 2011) and at the Ice River alkaline complex (British Columbia, Canada). In the latter locality it is reported to replace also sodalite and microcline (Deer et al. 2004); a K-rich vishnevite can be hypothesized for the alteration product of the microcline. At the Ditrau alkaline complex (East Carpathians, Romania), cancrinite is reported as a hydrothermal alteration product of nepheline, after its reaction with (CO_2)-rich fluids, in the presence or not of neighboring calcite crystals (Fall et al. 2007). Similarly, at the Turiy massif (Kola Peninsula, Russia), cancrinite is a late-stage magmatic phase, crystallized at low temperature from CO_2-enriched fluids reacting with nepheline, in a nepheline-melilitolite (turjaite) (Bell et al. 1996). At Kandaguba (Kola Peninsula, Russia) cancrinite is a rock-forming mineral in nepheline and cancrinite-nepheline syenites related to a carbonatitic complex (Pilipiuk et al. 2001). Cancrinite occurrence in effusive environments is, by far, less common: primary cancrinite is found, associated with natrolite, in cavities of the phonolite sills at Point of Rocks (New Mexico, USA, Deer et al. 2004) and an almost anhydrous cancrinite occurs in small sanidinite xenoliths within alkali-rich basalts at Laacher See (Germany, Zubkova et al. 2011). In the latter case, the Authors proposed a secondary thermal-induced dehydration, for the roasting of the xenoliths during the basaltic eruption. Along with the occurrence as primary or secondary phase in alkaline intrusive rocks, cancrinite is also often found in metasomatic environments, mainly fenites and skarns. At the Alnö (Sweden) and Fen (Norway) areas can be found in the reaction zones between nepheline syenites and carbonatites (Deer et al. 2004), whereas at the Iivaara alkaline complex (Finland), abundant cancrinite is found in the most evolved fenite aureoles, where replaces alkali-feldspars of the granodioritic archean gneisses intruded by nepheline syenites (Sindern and Kramm 2000). Examples of metasomatic cancrinite in skarns, formed at the contact between limestone wallrocks and alkali-rich magmas, are: Bancroft (Ontario, Canada), primary constituent at the contact between Grenville marble and nepheline gneisses (Foit et al. 1973); Kishengarh (Rajputana, India), along nepheline syenite-limestone contact (Deer et al. 2004); Mt. Vesuvius (Italy), in limestone ejecta (Foit et al. 1973); Hsianghualing (Hunan, China), along with corundum at a granite-limestone contact (Deer et al. 2004) and Byram (Delaware River, USA), in nepheline hornfels at the contact between diabase and limestone (Deer et al. 2004).

Vishnevite share with cancrinite the same genetic settings. It forms as primary or secondary phase in alkaline magmatic environments undersaturated in SiO_2 and enriched in alkali and SO_2, during the late stage of magmatism or as product of hydrothermal alteration. Some examples of vishnevite occurrences are: Vishnevye Mountains (Southern Urals, Russia), the type locality, in veins of the alkaline complex (Deer et al. 2004); Loch Borolan (Scotland), where is disseminated in veins likely

replacing nepheline (Stewart 1941); Synnyr Massif (northern Pribaikal, Russia), as a high-K variety occurring in veins of the alkaline complex (Deer et al. 2004); Alnö Island (Sweden) and Oldoinyo Lengai (Tanzania) alkaline complexes (Deer et al. 2004); Zippa Mountain (British Columbia, Canada), as a product of late-stage magmatism in nepheline syenites and K-enriched trachyte (Coulson et al. 1999). At the Iivaara pluton (Finland), vishnevite is found in veins cross-cutting the intruding nepheline syenites, while cancrinite is abundant in the close fenitic aureoles (Sindern and Kramm 2000). At Kaminak Lake (Northwest Territories, Canada) is found, along with cancrinite, in nepheline syenites (Davidson 1970), whereas at Coyote Peak (California, USA) occurs in late-stage highly evolved alkaline mafic pegmatite (Erd and Czamanske 1983). As cancrinite, it is also found in metasomatic areas related to alkaline magmatism. At Zardalek (Turkestan-Alai mountain system, Kyrghyzistan), for example, where it is found, coupled with cancrinite, in skarn xenoliths of dolomites in nepheline syenites intrusions (Aleksandrov and Senin 2006). Similar occurrences are at various localities of Central Italy volcanic fields, in skarns related to trachytic and phonolitic magmas, locally enriched through contact with carbonate and evaporitic (sulfate) wallrocks (Della Ventura et al. 2005). Vishnevite is found in miarolitic cavities of nepheline syenites ejecta, within pyroclastites, at Pitigliano (Tuscany), Farnese and Alban Hills (Latium) (Della Ventura et al. 2007). The chemically related pitiglianoite is also found in similar settings at Pitigliano (type locality, Merlino et al. 1991) and Monte Cavalluccio (Latium), in a sanidine-rich ejected block (Della Ventura et al. 2005). It is interesting to note that the only cancrinite sample reported from the Alpine region, found in a metamorphic vein rich in Ca-silicates at Pizzo Tremogge (Valmalenco, Italy, Crespi et al. 1981), can be ascribed to pitiglianoite, for the kind of superstructure reflections reported by the Authors.

The other members of the cancrinite subgroup are, by far, less common. Cancrisilite is very rare and, up to now, has been found only in the Lovozero alkaline complex, Kola peninsula, Russia (Ogorodova et al. 2009). Thermochemical and thermal data, reported by Ogorodova et al. (2009), suggest that the formation of cancrinite should be thermodynamically favored over that of cancrisilite. Kyanoxalite and the intermediate members of the cancrinite-kyanoxalite series are only found at the Lovozero complex, where are late-stage primary minerals or secondary replacement of sodalite and nosean in nepheline syenites intrusions and pegmatites (Chukanov et al. 2010a). The crystallization of the oxalate-bearing terms of the series, both in intrusive dykes and pegmatites, coupled with the presence of reduced organic matter in pegmatites, marks the reductive conditions of the late-magmatic or hydrothermal fluids at the Lovozero alkaline complex (Chukanov et al. 2010a). According to Pekov et al. (2011b), these conditions are also responsible for the natural occurrence of two very rare

minerals of the group: depmeierite and hydroxycancrinite. The first is found as a hydrothermal alteration product, in association with natrolite, crystallized at *T* not higher than 250-300 °C from fluids particularly enriched in P_2O_5 (Pekov et al. 2011b). Pekov et al. (2011b) suggested that only under reductive conditions, inhibiting the crystallization of (CO_3^{2-})-bearing minerals, the crystallization of these rare terms is possible. In particular, hydroxycancrinite is considered, by these Authors, the less favored mineral, whose crystallization from the fluids is possible only when no other anion is available and no other chemically similar mineralogical phase is thermodynamically more stable. These reductive conditions appear to be typical only of the Lovozero complex. However, it should be noted that several end-members of the group are recognizable only by means of multiple analytical investigations, for the subtle chemical and structural differences. In particular, IR-analyses proved to be a valuable tool for a semi-quantitative identification of the different anionic groups trapped within the structural voids (Ballirano et al. 1998; Della Ventura et al. 2005, 2007; Chukanov et al. 2011). For example, the existence of the (CO_3^{2-})-rich balliranoite was recognized only recently (Ballirano et al. 1998; Binon et al. 2004; Chukanov et al. 2010b), whereas Pekov et al. (2011b) underlined that the paucity of the intermediate members of the cancrinite-depmeierite series has to be mainly assigned to the lack of sufficient analytical data reported in the literature. Therefore, even considering that the chemical features of the Lovozero pluton seem uncommon, it would be useful to consider that some minerals reported as cancrinite *sensu stricto* could bear anions in addition to the (CO_3^{2-}), being intermediate terms of solution series.

The davyne-subgroup minerals can be typically found in effusive environments. They are especially widespread in lithic blocks within pyroclastic, tephritic and pumice deposits at the alkaline volcanic fields of Central Italy (Monte Somma, Vesuvius, Monti Sabatini and Monti Vulsini) and at Laacher See, Germany (Deer et al. 2004). They generally occur in cavities of skarn-like rocks, likely formed as thermal metamorphic and metasomatic products, around the magmatic chamber walls (Deer et al. 2004; Fulignati et al. 2005). Davyne is also reported in lazurite-bearing skarns at the contact between alkaline intrusions and dolomite wallrocks at Badakhshan, Afghanistan (Rozenberg et al. 2009; Aleksandrov and Senin 2006) and, as a S^{2-} bearing sample, at Tultui, Baikal Area, Russia (Sapozhnikov 2010; Aleksandrov and Senin 2006). A different setting is shown by davyne occurring at Zabargad Island (Red Sea, Egypt), in veins cutting metabasalts, likely crystallized from hypersaline and hyperalkaline fluids (Deer et al. 2004). Microsommite is reported at Magureava Vaţei (Apuseni Mountains, Romania), in veins cutting the skarns developed at the contact between monzodioritic intrusions and marbles (Pascal et al. 2005). Quadridavyne seems to be the less common member of

the subgroup and has been found for the first time in metasomatized and hydrothermally altered lavas and scoriae, within ashes of the 1906 Vesuvius eruption (Bonaccorsi et al. 1994). The (CO_3^{2-})-rich balliranoite has been recognized from samples found in cavities of skarns (alkaline magma-limestone contact), occurring as lithic fragments in the volcanic deposits at Monte Somma, Naples, Italy (Chukanov et al. 2010b). A further occurrence was found in veins of alkaline fluids related to granite intrusions within marbles, at the Mogok Metamorphic Belt, Myanmar (Harlow and Bender 2013). Although apparently a rare member, it cannot be excluded that the (CO_3^{2-})-rich term balliranoite is more common than expected, due to its recent recognition (Ballirano et al. 1998; Binon et al. 2004; Chukanov et al. 2010b) and to the historical ambiguous classification of the minerals of this subgroup (see Bonaccorsi et al. 1990 for a review). In particular, balliranoite could be a common accessory mineral in metasomatized areas at the contact between alkaline magmas and carbonate wallrocks.

An overall description of the petrogenesis of the cancrinite-group minerals and solid solutions is not trivial. In fact, the occurrence of the cancrinite-group minerals is, quite often, poorly described as part of the paragenesis of different kinds of minerals. In many cases, the chemical composition and/or the basic crystallographic features of the reported cancrinite-group minerals (often cancrinite *sensu stricto*) are missing. On this basis, it cannot be guaranteed an unambiguous assignment to a given member of the group. However, a trend can be deduced from the occurrences of the several cancrinite-group members well described in the literature. A general scheme has been proposed by Pekov et al. (2011a), who classified the geological settings of cancrinite-group minerals into three groups: 1) the alkaline intrusive and related contact rocks, 2) the alkaline volcanic and related contact rocks and 3) the alkali-rich metamorphic and metasomatic rocks. Pekov et al. (2011a) suggest that the distinction of the cancrinite- and davyne-subgroups has not only crystal chemical, but also a geological basis. These Authors underline that the members of the cancrinite-subgroup are widespread in alkaline intrusive complexes, where are part of the post-magmatic derivatives, but are quite rare in alkaline effusive rocks. Alkali-rich effusive and metamorphic rocks are the main geological settings of the davyne-subgroup members, along with the lazurite-bearing metasomatic rocks. Moreover, Pekov et al. (2011a) assert that the cancrinite-subgroup minerals in alkaline intrusive complexes show a strong affinity for the (CO_3^{2-})-rich cancrinite *sensu stricto*, whereas the other members (with the exception of the quite common vishnevite) seem to occur only under low CO_2 activity, for example under the reductive conditions shown at the Lovozero complex (Chukanov et al. 2010a).

1.4 SYNTHETIC CANCRINITE-GROUP COMPOUNDS

The natural cancrinite-group minerals show a large variety in the chemistry of the extraframework population, opposed to an almost constant framework composition. The framework is always aluminosilicate, with the only exception of tiptopite ($K_2(Na,Ca)_2Li_3[Be_6P_6O_{24}](OH)_2*H_2O$). This is a hint of the flexibility of the [CAN] structure type, which is able to accommodate, within its voids, several kinds of cations, anions and molecular groups in various boding configurations. This feature is amplified by the even higher chemical variability shown by the synthetic cancrinite-group compounds.

The synthesis of cancrinite-group compounds is commonly performed under hydrothermal conditions and autogenous pressure (Fechtelkord et al. 2001a). These experimental conditions generally simulate the geochemical conditions of the late- and post-magmatic fluids in the geological environments in which cancrinite-group minerals occur. Several salts and oxides, or gels, can be selected as source of the chemical components. A key factor in the synthesis process is the alkalinity of the solution (Fechtelkord et al. 2001a), which must be kept high by an excess of NaOH, also used as a source of Na^+. Many combinations of cations, anions and molecular groups can be used as templating agents for the [CAN]-framework. Na^+ is a fundamental component in both natural and synthetic cancrinite-group compounds. According to Hackbarh et al. (1999), the type and geometry of the anions in solution act as structure-driving agents, where NO_3^-, $S_2O_3^{2-}$ and SO_3^{2-} promote the nucleation of the cancrinite structure, whereas the halogens favor the crystallization of sodalite-type structures. The same Authors note that, in the case of the CO_3^{2-} anion, cancrinite or sodalite or a phase with an intermediated structure can be synthesized, suggesting a relevant role played by kinetics. Aqueous solutions are common environments for the syntheses. However, organic solvents can also be used, like 1,3-butanediol, playing the double role of solvent and templating agent, which serve as backbone for the cancrinite channel and can be removed by calcination after the synthesis process (Burton et al. 1999; Fechtelkord et al. 2001a).

Several Authors reported that the synthesis of pure (CO_3^{2-})-cancrinite is not trivial. Burton et al. (1999) reported a cancrinite with a low (CO_3^{2-})-content, synthesized in organic solvent, starting from gels. Hackbarth et al. (1999) synthesized a carbonate cancrinite, with a low (CO_3^{2-})-content and H_2O molecules in the channels, from hydrothermal aqueous solutions at 473 K; at 353 K, the same Authors reported the occurrence of an intermediate cancrinite-sodalite structure. Kurdakova et al. (2013)

reported a (CO_3^{2-})-containing and Ca-free cancrinite, synthesized under hydrothermal conditions at 473 K and 10 MPa autogenous pressure, for 48 hours.

Synthetic hydrothermal counterparts of the very rare mineral hydroxycancrinite have been reported by Bresciani-Pahor et al. (1982) and Grundy and Hassan (1991). Fechtelkord et al. (2001a) synthesized the so-called "basic cancrinite" (synthetic hydroxycancrinite) in butanediol solvent, starting from gels of adequate composition. These Authors report that high OH^- concentrations favor the formation of sodalite structures, whereas a kinetics driven crystallization, governed by slowly dissolving reactants, leads to pure basic cancrinite. The interest towards hydroxycancrinite is due to the fact that the main obstacle to cation exchange capacity, in cancrinite-group compounds, is played by the presence of anions in the channel. The removal of these anions by annealing generally leads to the destruction of the cancrinite structure (Fechtelkord et al. 2003). This obstacle could be avoided in the case of basic cancrinite, for which hydroxyl anions and H_2O molecules may be removed under mild H*T* conditions (Fechtelkord et al. 2003).

The (NO_3^-)-cancrinite is another compound of large interest, since it crystallizes from high-alkaline nuclear wastes fluids and can potentially be used as stable storage material (see section 1.5). In addition, the (NO_3^-) anion is reported to strongly favor the crystallization of the cancrinite structure (Ocanto et al. 2009). The nitrate end-member of the cancrinite subgroup, never found in Nature, shows a high nucleation rate and a fast growth under very mild hydrothermal conditions, at temperatures not higher than 90°C (Liu et al. 2005), which correspond to the autogenous conditions in nuclear waste fluids. Buhl et al. (2000) synthesized (NO_3^-)-cancrinite under low-temperature (473 K) hydrothermal conditions, starting from different reactants, in order to investigate the feasibility of a large-scale industrial production, getting the best results using zeolite-X and a mixture of Na-silicate and aluminate as starting mixture. These Authors also synthesized single-crystals large enough for a structure determination, under hydrothermal conditions at 773 K and 0.15 GPa. The structure refinement showed strong similarities with the carbonate end-member, with a Na^+ site near the channel walls and two symmetry-independent and mutually exclusive configurations for the triangular nitrate anion at the channel center. An alternative synthesis route has been proposed by Ocanto et al. (2009), who took advantage of the redox reaction $3NO_2^- + 2MnO_4^- + H_2O \leftrightarrow 3NO_3^- + MnO_{2(s)} + 2H_2O$ in alkaline solutions, to get the (NO_3^-)-cancrinite starting from mixtures without the NO_3^- anion, at 80°C. Ocanto et al. (2009) also reported that starting from a pure (NO_2^-)-containing mixture, (NO_2^-)-sodalite is obtained at 8 mol/l NaOH and both (NO_2^-)-sodalite and cancrinite at 16

mol/l. Moreover, starting from pure (MnO_4^-)-containing mixtures a (MnO_4^-)-cancrinite is synthesized, showing the affinity of the [CAN]-framework also for this tetrahedral anion.

In addition to the triangular (CO_3^{2-}) and (NO_3^-) and to the tetrahedral (SO_4^{2-}) and (MnO_4^-), several other anionic groups have been enclathrated within the channels of synthetic cancrinite-group compounds. Shirinova et al. (2006) synthesized a (BO_3^{3-})-cancrinite under hydrothermal conditions at 653-673 K. A (CrO_4^{2-})-cancrinite has been synthesized, under hydrothermal conditions at 80°C, by Ocanto et al. (2008), from solutions with high CrO_4^{2-} and NaOH concentrations. The synthetic counterpart of the natural kyanoxalite ($C_2O_4^{2-}$ end-member) has been synthesized from hydrothermal solutions at 170 °C for 168 hours, using sodium oxalate in the starting mixtures of reactants, reaching 0.44 groups per formula unit (Linares et al. 2011). These Authors also reported that the smaller formate (HCO_2^-) and acetate ($C_2H_3O_2^-$) anions lead to the crystallization of sodalite structures. Lindner et al. (1995) synthesized a thiosulfate cancrinite at 300 °C and 85 bars, for 28 days, from hydrothermal solutions. The single-crystal diffraction data suggested a *P*3 space group and the structure refinement revealed several mutually exclusive configurations for the $S_2O_3^{2-}$ anion within the channel. The uncolored ($S_2O_3^{2-}$)-cancrinite turns into a yellow (S_2^-)-containing one after X-ray irradiation, whereas after annealing at 800 °C it transforms into a greenish-blue cancrinite with S_2^- and S_3^- radicals within the channels, as shown by IR-analysis. A literature-reported pure blue (S_3^-)-cancrinite is also cited by the Authors, showing the potential application of cancrinite-group compounds as colorant agents.

Another approach, which succeeded in the synthesis of cancrinite-group compounds, is given by the use of selected combinations of a large cation with a small cation, for example Cs^+ and Li^+, from which Fechtelkord et al. (2001b) synthesized a (Cs,Li)-basic cancrinite. In this case, the large Cs^+ cation fills the *can* unit cage, which results highly expanded, whereas the Li^+ cation occupies a site near the channel walls, tetrahedrally coordinating three framework oxygen atoms and a channel H_2O-oxygen, with a configuration similar to Na^+ in natural cancrinite (see for example Fig. 1.6). The center of the channel is occupied by mutually exclusive positions filled by H_2O molecules and hydroxyl anions. This approach has been extensively studied and improved by Colella and de' Gennaro (1989), who reported the synthesis of (Cs,Li)-, (Tl,Li)-, and (Rb,Li)- basic cancrinites under hydrothermal conditions at 200 °C and autogenous pressure. The Authors reported that the crystallization was very readily when using Cs^+, readily with Tl^+, whereas a lesser aptitude was shown by Rb^+, underlining the good fit of the couples (Cs,Li), (Cs,Na), and (Tl,Li) for the crystallization of the [CAN]-framework. The crystal structure of the synthesized (Cs,Li)-basic cancrinite was reported by Norby

et al. (1991). The Cs^+ ions occupy the center of *can* unit, coordinated by 12 framework oxygen atoms, Li^+ is placed near the channel walls, in a position resembling that of Na^+ in natural cancrinites, tetrahedrally coordinated with three framework oxygen atoms and a further oxygen belonging to H_2O molecules, which occupy mutually exclusive positions in the center of channel. A partial structure refinement of the (Tl,Li)-basic cancrinite was also reported (Norby et al. 1991). Tl^+, which has a shorter radius than Cs^+, was found to occupy three mutually exclusive positions within the *can* unit, likely in order to have adequate bonds to the framework oxygen atoms. Therefore, the poor fit of the (Tl-Li)-couple for the [CAN]-framework could be structurally explained by the lesser fit between Tl^+ and the *can* unit, with respect to the larger Cs^+. A further Tl^+-site was also found within the channel, whereas Li^+ and H_2O molecules were not located. Colella and de' Gennaro (1989) pointed out that both the small (Li^+) and large monovalent cations (Cs^+, Tl^+, Rb^+) are needed to play a templating role in the crystallization of the [CAN]-framework. The small cations, like Li^+ and Na^+, with their tetrahedral coordination, likely act as template in the formation of the [CAN]-channel. In the meanwhile, a filler for the *can* units columns (a large monovalent cation or a chain as Na^+-H_2O or Ca^{2+}-Cl^-) is needed. From the point of view of potential technological applications, extremely interesting results, from ion exchange studies, have been also reported by Colella and de' Gennaro (1989). Due to its position within the *can* cage (Norby et al. 1991), the Cs^+ ion turned to be not exchangeable, suggesting the potential application of cancrinite structures as host materials. Only partial Tl^+-Na^+ and Li^+-Na^+ exchange were reported for the cations located within the channel. The role of H_2O molecules and of the structural arrangement of the extraframework population remain unknown and should be investigated in this respect.

The same approaches, previously reported for aluminosilicates cancrinite-group compounds, can be applied for the synthesis of cancrinites showing a different framework chemistry. If in Nature only tiptopite (*i.e.* $K_2(Na,Ca)_2Li_3[Be_6P_6O_{24}](OH)_2*H_2O$) shows a non-aluminosilicate framework, several synthetic cancrinite-group compounds showing a different framework crystal chemistry have been reported. Their synthesis is of large interest for potential technological applications, since it allows to control the structure-property relationships of the zeolitic framework. In fact, the control over the framework crystal chemistry allows to modify the voids size and shape, without changing the topology (Lee et al 2000). Latham et al. (1996) synthesized a basic cancrinite with Fe^{3+} partially replacing Al^{3+} within the framework tetrahedra, leading to an increase in the unit-cell. More commonly, Si^{4+} and Al^{3+} are replaced by Ge^{4+} and Ga^{3+}, respectively. Lee et al. (2000) synthesized a (Cs,Na)-bearing aluminogermanate ($Na_6Cs_2[Al_6Ge_6O_{24}]*Ge(OH)_6$) and a gallogermanate

($Na_6Cs_2[Ga_6Ge_6O_{24}]$*$Ge(OH)_6$), under hydrothermal conditions at 170 and 110 °C, respectively. In both the compounds, Cs^+ fills the *can* unit cages, Na^+ lies near the channel walls and $Ge(OH)_6^{2-}$ octahedra occupy the channel center, with Ge^{4+} in a special site on the 6_3 screw axis (like S^{6+} in davyne or vishnevite). The replacement of framework tetrahedral cations had a "compressive" effect on the intertetrahedral angles, being the mean T-O-T angle 142.2° in cancrinite *sensu stricto*, 133.0° in (Al,Ge)-cancrinite and 128.9° in (GaGe)-cancrinite (Lee et al 2000). In this respect, a study on the thermal stability of this compound could be of large interest, since one can speculate on a potential larger margin for the structure expansion. Moreover, it is worth noting that Lee et al. (2000) observe that, due to its position within the *can* unit, the Cs^+ cation could be hardly exchanged under mild hydrothermal conditions, underlining a potentially exploitable feature. This, coupled with the strong affinity between the (NO_3^-) anion and the [CAN]-framework, suggest the potential applications of cancrinite-group compounds as large-scale disposal materials (*e.g.* Bao et al. 2005). A highly charged framework can also be synthesized combining P^{5+} with a divalent metal. Bieniok et al. (2005) synthesized a cobaltophosphate ($Na_6Cs_2[Co_6P_6O_{24}](OH)_2$*$1.4H_2O$) and a zincophosphate ($Na_6Cs_2[Zn_6P_6O_{24}](OH)_2$*$H_2O$) analogues of basic cancrinite, under hydrothermal conditions (140 and 250 °C, respectively) and using a large cation (Cs^+) and a small cation (Na^+) as templating agents, respectively, in analogy to the (Al,Ge)- and (Ga,Ge)-cancrinites. The Cs^+ ion fills the *can* units coordinating 12 framework oxygen atoms, whereas the Na^+ lies near the channel walls. A similar (Zn,P)-cancrinite, having the cage 82% occupied by Cs^+ and 18% by K^+ and with the Na^+ in the channels partially replaced by Fe^{2+}, was previously reported by Yakubovich et al. (1994).

A final remark, arising from the significant crystal chemical variability shown by cancrinite-group compounds is that the [CAN]-framework topology turns to be extremely versatile. A fundamental component appears to be a small monovalent cation (generally Na^+) occupying a channel site, which get a strong tetrahedral coordination to three framework oxygen atoms (O1, O3, O4) and one (or two) oxygen belonging to an anionic or molecular group in the channel center (Fig. 1.6). This geometrical structure-driving restraint seems to be confirmed by exchangeable capacity of Na^+ and Li^+ to act as templates for the [CAN]-framework and by the complete and reversible $Na^+ \leftrightarrow Li^+$ cationic exchange in basic cancrinite (Barrer and Falconer 1956). Alternatively, when highly expanded frameworks occur, as in the case of davyne subgroup, the previously cited three-fold coordination with framework-oxygen atoms is replaced by a four-fold coordination with two O3 and two O4 oxygen (Fig. 1.6). In addition, a large monovalent cation (as Cs^+) or dymers (*e.g.* Na^+-H_2O or Ca^{2+}-Cl^-) are required as fillers of the *can* unit columns. The "chemical flexibility" of cancrinite-group compounds,

when these conditions are fulfilled, allows the potential tailoring of structures, through several combinations of cations, anions and molecules. Once the relationships between crystal chemistry and structure, on a side, and (*P*,*T*)-stability fields, elastic behavior and chemical/zeolitic properties, on the other side, would be assessed, tailored cancrinite structures colud be proposed for potential technological applications.

1.5 CANCRINITE-GROUP COMPOUNDS IN RELEVANT TECHNOLOGICAL PROCESSES

Cancrinite-group compounds do not show typical zeolitic properties, such as high cation exchange capacity or molecular sieving (Fechtelkord et al. 2003). However, from the structural point of view, the [CAN]-framework shows a large channel (~ 5.9 Å free diameter, Baerlocher et al. 2007), in which the diffusion of cations, anions, molecules and even some hydrated complexes might be possible. On the contrary, the *can* units (cancrinite cages), with a cavity confined by six-membered rings of tetrahedra with effective pore width 1.5 - 2 Å, and can be considered as non-zeolitic voids. Despite the large 12-ring opening, the occurrence of stacking faults (with S6R occupying C positions, at 0,0,*z*,, Fig. 1.1) usually affect the isolated channels, along the [0001] direction (Bonaccorsi and Merlino 2005). Moreover, unlike most zeolites where the extraframework cations are weakly bound to H_2O-oxygen atoms, in cancrinite-group compounds the presence of cation-anion pairs gives rise to bonds more difficult to break, hindering the diffusion of ions (Fechtelkord et al. 2003). Attempts to expel the anionic population by annealing were tried, but always drove to the framework collapse and nucleation of more stable phases, like nepheline (Fechtelkord et al. 2003). For these reasons, cancrinites are not exploited for applications in industrial processes, as other open-framework materials. Moreover, they are not classified as proper zeolites (Armbruster and Gunter 2001; Deer et al. 2004; Bonaccorsi and Merlino 2005).

However, cancrinite-group compounds possess exchange capacities. Fechtelkord et al. (2003) pointed out that, disregarding the occurrence of stacking faults, in basic cancrinite (where the channel center is filled by hydroxyl groups and H_2O molecules) diffusion of ions can be achieved. In one of the first studies devoted to the synthesis and evaluation of physico-chemical properties of cancrinites, Barrer and Falconer (1956) succeeded in the synthesis of basic cancrinite and tested its exchange capacity with a set of monovalent and divalent cations. Among the tested combinations, the Authors reported a full and reversible exchange for the $Na^+ \leftrightarrow Li^+$, $Na^+ \leftrightarrow Ag^+$ and $Li^+ \leftrightarrow Ag^+$ pairs. However, the Authors suggested a solid solution immiscibility gap, with the co-existence of two phases, for the pairs involving the Ag^+ cation. Nevertheless, beside the full exchange capacity shown by basic cancrinite for these cations, a noticeably low diffusion coefficient was also reported (Barrer and Falconer 1956). On the other hand, the lack of significant ion exchange capacity, can be transformed from a disadvantage to an advantage, as will be shown below.

Although the cancrinite-group compounds cannot be grouped along with the materials showing good zeolitic properties, their occurrence in several processes of relevant environmental and industrial interests makes valuable the study of their physicochemical properties. The most relevant are: 1) the precipitation from Na-rich caustic nuclear waste solutions and from reactions between them and sediments, 2) the precipitation from the spent caustic liquors in Al-extraction processes.

Waste solutions, characterized by unique and extreme chemistries, have been reported from many nuclear sites in the United States, such as Hanford (Washington), Savannah River (South Carolina) and Oak Ridge (Tennessee) (Chorover et al. 2003). In particular, at the Hanford site, at least 67 waste tanks are known to have leaked into the subsurface sediments between 0.6 and 1.4 gallons of high-level waste solutions (Choi et al. 2006), byproducts of the processes used to extract U and Pu from the spent U-rods fuels (Bickmore et al. 2001). These solutions are characterized by high pH, high dissolved Na^+ and Al^{3+} content, NO_3^- and NO_2^- as major anions, with minor CO_3^{2-} and SO_4^{2-}, whereas Cs^+ and Sr^{2+} are the major radionuclides present (Bickmore et al. 2001; Deng et al. 2006). Zhao et al. (2004) reported that the solution temperature can be as high as 100°C, within the tanks, and 70°C in the subsurface sediments at 20 m depths. Several experiments have been carried out, using simulated solutions, to explore what reactions occur when these wastes are contact with the local sediments. (NO_3^-)-cancrinite has always been reported as the long-term (after some weeks) main precipitate (usually coupled with sodalite), after the reaction between the caustic solutions and quartz sand, kaolinite and natural local sediments (fluvial-glacial and fluvial-lacustrine gravels and sands) (*e.g.* Bickmore et al. 2001; Chorover et al. 2003; Zhao et al. 2004; Mon et al. 2005; Choi et al. 2006; Deng et al. 2006; Rivera et al. 2011). Moreover, Buck and McNamara (2004) reported the direct precipitation of (NO_3^-)-cancrinite from the solutions within the tanks. The same Authors also reported that similar findings had been already described at the Savannah River site. All these data represent a further proof for the strong structure-directing role shown by the NO_3^- anion towards the [CAN]-framework (Ocanto et al. 2009). The most interesting feature is the ability shown by the neo-formed feldspathoids (cancrinite overall) to incorporate large quantities of the Cs^+ ions initially present in solution, as reported by all the previously cited studies. In particular, Deng et al. (2006) suggested Cs^+ as a strong competitor for the cancrinite structure, whereas it tends to be excluded by sodalite, while Mon et al. (2005) reported that less than 55% of adsorbed/incorporated Cs^+ could be subsequently exchanged. This latter finding is an indirect proof that Cs^+ in cancrinite could be hardly removed under mild conditions, due to its position within the *can* units (Colella and de' Gennaro 1989; Norby et al. 1991; Lee et al. 2000; Bieniok et al. 2005). Less clear evidence in the literature

data concern the incorporation of Sr^{2+}. Recently, Wang and Um (2013) reported that a large quantity of Sr^{2+} co-precipitated is entrapped within the (NO_3^-)-cancrinite structure, whereas Choi et al. (2006) reported the preference of this cation in sodalite. Zhao et al. (2004) point out that the Cs^+ adsorption and/or incorporation capacity of cancrinite is significantly larger than that shown by kaolinite and clay minerals, naturally occurring in the Hanford sediments. Therefore, the secondary precipitation of cancrinite-group minerals, which incorporate in their crystal structures the dissolved radionuclides (at least Cs^+), can hinder their diffusion through the subsurface sediments. However, they can also act as a source of contaminants, once they dissolve in the case of varying geochemical conditions, as underlined by Mon et al. (2005) and Wang and Um (2013). In this light, Wang and Um (2013) noted that the characterization of the phase stability of secondary precipitates, as a function of varying geochemical conditions, is fundamental for a long-term evaluation of the radionuclides fate in subsurface sediments. A full characterization of the (*T*, *P*)-crystal chemistry of the cancrinite-group compounds might provide useful background data for this kind of evaluation.

The sequestrating properties shown by (NO_3^-)-cancrinite can also be applied for the tailoring of new materials for a safe storage of caustic waste solutions, potentially rich in Cs^+ radionuclides. Hydroceramics are materials made by a crystalline aluminosilicate matrix, mainly feldpsathoid and zeolite compounds, solidifying from a Na^+-rich caustic solution (Bao et al. 2005). Cancrinite was found to be one of the major mineral phases in hydroceramics, produced from simulated solutions through the addition of metakaolinite (as source for Si^{4+} and Al^{3+}, Bao et al. 2005). Hydroceramics have been considered for the safe and stable storage of waste solutions from the nuclear disposal sites, but can also be applied to any kind of alkaline waste. A benefit from the use of aluminosilicate-based waste forms, with respect to Portland cement-based ones, in given by the ability to fix the alkali cations in crystalline structures (and not in amorphous phases) (Bao et al. 2005). Riley et al. (2012) proposed Cl^--containing aluminosilicates as possible waste-storage form for the spent solutions of alkali-chloride salts used in a potential electrochemical process for nuclear fuel regeneration. These Authors pointed out that “cancrinite” (most properly davyne-subgroup compounds) has the highest storage potential for the incorporation of alkali-chlorides. However, the Authors report that during the sintering process, aimed to convert powders to a monolithic block, cancrinite became unstable transforming into sodalite, nepheline and low-carnegieite.

Another field, in which cancrinites play a relevant role, is given by the Al_2O_3 production (Bayer) process, from the digestion of bauxite ores in caustic solutions at high temperature. In this process, the used bauxite ores always show a minor amount of SiO_2 impurities, mainly as quartz and kaolinite,

which are also digested. When the spent Bayer liquor, which follows the gibbsite extraction, is re-heated for a new digestion cycle, Na-aluminosilicates precipitate on the heat-exchangers, reducing their efficiency and having a cost-impacting effect on the entire process. These precipitates are mainly composed by sodalite and cancrinite, where the latter is reported to be the thermodynamic most stable phase (Barnes et al. 1999a, 1999b, 1999c; Xu et al. 2010). As a consequence, cancrinite-group compounds are also one of the main components of the "red-mud", *i.e.* the sludge byproducts of the Al_2O_3 production processes. The disposal of red mud is a source of environmental concern, for its pollutant nature (Gelencsér et al. 2011), and of economic concern, for the costs involved which also affect the aluminum final cost. Therefore, its potential recycling has been investigated. Recently, the capacity of red mud to adsorb heavy metals (Pb^{2+}, Cd^{2+} and Zn^{2+}) and arsenate anion in solution was successfully tested, opening the way for a potential application in polluted soils (Santona et al. 2006; Castaldi et al. 2008, 2011). I was suggested that the adsorption of cations and anions within the cancrinite structural voids could be regarded as one of the possible sequestration mechanisms, even though a clear picture is still missing.

A further relevant field, in which cancrinite-group compounds are involved, is given by "geopolymers". Geopolymers are binder materials, alternative to Portland cement, produced from the reaction of (Si, Al)-containing industrial residues, as coal fly ashes for example, with alkaline solutions (Palomo et al. 1999). Geopolymers are made by crystalline zeolitic precursors surrounded by an amorphous matrix. Among the few reported zeolitic precursors, hydroxycancrinite can also be found (Oh et al. 2010). Although several studies on the bulk elastic behavior of geopolymers are available, Oh et al. (2011) pointed out the importance for a characterization of the elastic properties of the single zeolitic precursor phases, since the refined elastic parameters could be used in mechanical simulations.

The cancrinite microporous structure can be used as host matrix for several molecules showing exploitable properties. Among the others: Poborchii et al. (2002) reported synthesized Se_2^{2-} and Se_2^{-} dimers within the cancrinite-channels, showing photoluminescent properties; Hofmann et al. (2012) reported cancrinite structures entrapping oligosulfides chromophores; Miyake et al. (2005) reported synthesized and ion-exchanged cancrinites, entrapping Pb^{2+}-S^{2-} clusters within the channels, which showed photocatalytic properties.

Overall, the presence of cancrinite-group compounds in “technological” fields suggest how important is the knowledge of their physicochemical properties. Among those: the (*P*,*T*)-phase stability, the elastic properties and the structural response to non-ambient conditions of pressure and temperature.

Chapter 2

Non-ambient conditions: mineral physics and experimental techniques

2.1 TEMPERATURE AND PRESSURE MINERAL PHYSICS

2.1.1 Elastic parameters

When a crystalline compound is subject to a homogeneous change of applied temperature and/or pressure, a change of the size of its unit cell occurs. The change in size (and shape) of a finite spherical volume of a crystal is described by means of the so-called “strain ellipsoid”, which is characterized by three principal strain axes always mutually orthogonal. The symmetry of the crystal governs the strain ellipsoid: the strain of a cubic crystal, for example, is identical in any direction and the strain “ellipsoid” is, therefore, constrained to be a sphere. The strain ellipsoid of a uniaxial crystal (hexagonal, tetragonal or trigonal classes) is also constrained to be uniaxial and parallel to the unique crystallographic axis. In orthorhombic crystals, the three axes of the strain ellipsoid are co-axial to those of the unit cell, whereas in monoclinic crystals only the 2-fold crystallographic axis is co-axial to one of the principal strain axes. In triclinic crystals the principal strain axes do not necessarily coincide with the crystallographic ones. Therefore, for cubic, hexagonal, tetragonal, trigonal and orthorhombic crystals the change in the unit-cell edges is sufficient to describe the *T*- and *P*-induced strain of the material.

The elastic parameter that describes the fractional volume change as a function of temperature is the volume thermal expansion coefficient:

$$\alpha_V = \frac{1}{V} * \left(\frac{\partial V}{\partial T}\right)_P \qquad (1)$$

where the subscript *P* stands for constant pressure conditions. Similarly, the linear thermal expansion coefficient is defined as:

$$\alpha_l = \frac{1}{l} * \left(\frac{\partial l}{\partial T}\right)_P \qquad (2)$$

The fractional volume change in response to applied pressure is given by the isothermal volume compressibility:

$$\beta_V = -\frac{1}{V} * \left(\frac{\partial V}{\partial P}\right)_T \qquad (3)$$

whereas the fractional linear change as a function of applied pressure is defined as the isothermal linear compressibility:

$$\beta_l = -\frac{1}{l} * \left(\frac{\partial l}{\partial P}\right)_T \qquad (4)$$

The units are, therefore, K^{-1} for the thermal expansion coefficients and Pa^{-1} for the compressibilities.

For the description of the high-pressure elastic behavior of a solid, the compressibility is often substituted by its inverse, the isothermal bulk modulus, in [Pa] (often expressed in GPa for minerals, where 1 GPa = 10^9*Pa):

$$K_V = \frac{1}{\beta_V} = -V * \left(\frac{\partial P}{\partial V}\right)_T \qquad (5)$$

which can be viewed as a measure of the resistance of the substance to compression. It is worth noting that the isothermal bulk modulus is a physical parameter defined for a volume. However, the same concept can be applied to the linear compressibility using the "linearized bulk modulus", which describes the elastic resistance to compression of a fictive volume given by the cube of the linear unit. Since in cubic crystal $\beta_V = 3\beta_l$, the linearized bulk modulus is defined as:

$$K_l = \frac{1}{3\beta_l} = \frac{l}{3}\left(\frac{\partial P}{\partial l}\right)_T \qquad (6)$$

This fictive property, although meaningless from the physical point of view, it is very useful in the study of the elastic behavior of minerals and crystalline solids, in general. Not only because it allows the direct comparison of the unit-cell volume and linear edges elastic compliances, as will be shown in details later, but also because it allows to directly compare the elastic behavior of coordination polyhedra, planar molecular groups, interatomic bonds, etc.

2.1.2 Equations of state

An equation of state is a function that relates the state variables of a system and characterizes the state of a matter subject to a given set of physical conditions: $f(P,V,T)$.

The most known equation of state is that relating the state variables of ideal gases:

$$PV = nRT \qquad (7)$$

where n is the number of moles and R is the universal gas constant (~ 8.31 J*mol^{-1}*K^{-1}). From this equation it derives that, if the volume of n moles of ideal gas and the temperature of the system are known, only one value is possible for pressure: *i.e.* it is sufficient to know two state variables to fully characterize the state of matter.

In the case of solids and, therefore, of minerals, there is no thermodynamic basis that allows to derive a "unique" equation of state, as is the case for ideal gases. As a consequence, a number of semi-empirical equations have been proposed, starting from different assumptions, but no one can be considered as universally valid. The reliability of these equations of state has to be validated through the reproducibility of experimental data (Angel 2000). The equations of state represent a fundamental character of any compound, necessary to understand its behavior with varying (P,T)-conditions, and essentially reflect the nature of the compound's crystal structure. Although a full P-V-T equation is needed to characterize the states of a solid compound, the equation can be subdivided into independent components (Duffy and Wang 1998). Therefore, many equations of state are derived assuming constant one of the state variables, for example temperature or pressure. In this way, thermal $(T,V)_P$ and isothermal $(P,V)_T$ equations of state are defined.

2.1.3 Thermal $(T,V)_P$ equations of state

The volume behavior of a substance as a function of temperature, when pressure is kept constant, can be easily derived integrating the thermodynamic definition of the thermal expansion coefficient α_V:

$$\alpha_V = \frac{1}{V} * \left(\frac{\partial V}{\partial T}\right)_P \qquad (1)$$

$$\int_{T_0}^{T} \alpha_V dT = \int_{V_0}^{V} \frac{1}{V} dV \rightarrow \quad \alpha_V * (T - T_0) = \ln\frac{V}{V_0} \rightarrow \quad e^{[\alpha_V (T - T_0)]} = \frac{V}{V_0}$$

$$V(T) = V_0 * e^{[\alpha_V (T - T_0)]} \qquad (8)$$

where T_0 is a reference temperature, usually the room-T when experiments at $T \geq 293$ K are carried out, and V_0 is the volume at the reference temperature. Truncation of the exponential series to the second order allows the calculation of the "mean" thermal expansion coefficient (Fei 1995):

$$V(T) = V_0[1 + \bar{\alpha}(T - T_r)] \qquad (9)$$

If the thermal expansion coefficient is a constant ($\alpha_V = \alpha_0$), equation (8) fully describes the state of the solid as a function of temperature, when P is kept constant. If the thermal expansion coefficient varies with temperature, α_V can be expressed in several ways, as there is not thermodynamic restriction for the final formulation. Among those, a polynomial function is often used (Fei 1995):

$$\alpha_V = a_0 + a_1 * T + a_2 * T^{-2} \qquad (10)$$

where a_0, a_1 and a_2 are refinable parameters. However, Pawley et al. (1996) point out that the high-temperature experimental data are, often, not enough precise to justify the refinement of three parameters and suggested the following function for the thermal expansion coefficient:

$$\alpha_V = a_0 - a_1 * T^{-\frac{1}{2}} \quad (11)$$

This function allows the refinement of two parameters only (in addition to V_0) and binds the value of α_V to a_0 at high temperatures, as expected for its low-temperature dependence above the Debye-temperature (Pawley et al. 1996). The resulting thermal equation of state, after truncation of the exponential series to the second order, is (Pawlet et al. 1996):

$$V(T) = V_0[1 + a_0(T - T_r) - 2a_1(\sqrt{T} - \sqrt{T_r})] \quad (12)$$

Pawley et al. (1996) noted that, for several minerals, the values of the refined a_1 were found to be proportional to those of a_0, suggesting the relationship $a_1 = 10(\pm 2) * a_0$, from which the following function of the thermal expansion coefficient can be derived:

$$\alpha_V = a_0(1 - 10T^{-\frac{1}{2}}) \qquad (13)$$

The simplicity of the above formalism allows the refinement of only one parameter (in addition to V_0), which is particularly useful in the case of a limited number of experimental data (Pawley et al. 1996). Moreover, Holland and Powell (1998) noted that such simplification generally has negligible effects on the calculated molar volumes and molar Gibbs energies at high temperatures and elevated pressures, *i.e.* at conditions relevant for geological environments. The resulting equation of state, as adopted in the thermodynamic dataset of Holland and Powell (1998) is:

$$V(T) = V_0[1 + a_0(T - T_r) - 20a_0(\sqrt{T} - \sqrt{T_r})] \qquad (14)$$

It is worth noting that this formalism implies the refinement of the same number of parameters (two: V_0 and a_0) of the equation (8), but, differently from the latter, allows the thermal expansion coefficient to vary with temperature.

2.1.4 Isothermal $(P,V)_T$ equations of state

As reported above, none of the equations proposed for solids can be rigorously derived by thermodynamics. This fact led to the formulation of a significant number of semi-empirical isothermal equations of state, relating volume and pressure at a constant temperature, each of them arising from a specific set of assumptions (Duffy and Wang 1998; Angel 2000). The refinable parameters, usually involved in those equations, are the isothermal bulk modulus K_{V0} and its P-derivatives:

$$K_V' = \left(\frac{\partial K_V}{\partial P}\right)_T \qquad (15)$$

$$K_V'' = \left(\frac{\partial^2 K_V}{\partial P^2}\right)_T \qquad (16)$$

The Murnaghan equation of state (EoS) (Murnaghan 1937) is based on the assumption that K_V has a linear dependence to pressure and its simple form allows an algebraic solution of P as function of V and *viceversa* (Angel 2000):

$$P = \frac{K_{V0}}{K_V'}\left[\left(\frac{V_0}{V}\right)^{K_V'} - 1\right] \rightarrow \quad V = V_0\left(1 + \frac{K_V' P}{K_{V0}}\right)^{-\frac{1}{K_V'}} \qquad (17)$$

The Murnaghan EoS is reported to well describe compressions $\eta = (V/V_0)$ down to 0.9 (Angel 2000) and, due to its simple form, is incorporated in thermodynamic databases, as the one by Holland and Powell (1998).

A common approach in the formulation of $(P,V)_T$ equations of state is based on the assumption that the strain energy can be expressed as a Taylor's series in the "finite strain" (f) (Duffy and Wang 1998; Angel 2000). Despite several formulations of the finite strain exist, it was empirically demonstrated that the *Eulerian finite strain* (f_E) provides a good convergence for the Taylor's series (Duffy and Wang 1998):

$$f_E = \frac{\left[\left(\frac{V_0}{V}\right)^{\frac{2}{3}} - 1\right]}{2} \qquad (18)$$

The Birch-Murnaghan equation of state (Birch 1947) is derived as a Taylor's series in the Eulerian finite strain and its expansion to the fourth order gives:

$$P = 3K_{V0}f_E(1+2f_E)^{\frac{5}{2}}\left\{1+\frac{3}{2}(K_V{}'-4)f_E+\frac{3}{2}\left[K_{V0}K_V{}''+(K_V{}'-4)(K_V{}'-3)+\frac{35}{9}\right]{f_E}^2\right\} \quad (19)$$

The Birch-Murnaghan EoS is the most commonly used in mineralogy (Duffy and Wang 1998), for its good reproducibility of experimental data (not showing dramatic compressions) (Duffy and Wang 1998; Angel 2000) and for its versatility. In fact, since it is defined as a Taylor's series, it can be truncated to lower orders, reducing the number of refinable parameters. The Birch-Murnaghan EoS truncated to the third order, for which the coefficient of f_E^2 within the curly bracket in eq. (19) is set to zero, implies the refinement of three parameters: V_0, K_{V0} and K_V', whereas K_V'' is derived as:

$$K_V{}'' = -\frac{1}{K_{V0}}\left[(K_V{}'-4)(K_V{}'-3)+\frac{35}{9}\right] \quad (20)$$

A further approximation, often used when the number of experimental data and/or the range of compression are limited, is the truncation of the Birch-Murnaghan EoS to the second order:

$$P = 3K_{V0}f_E(1+2f_E)^{\frac{5}{2}} \quad (21)$$

for which $K_V' = 4$ and only the V_0 and K_{V0} are refined. This assumption is often found in the literature for not so pronounced expansion regimes.

Since in the experimental section of the present work, the Birch-Murnaghan EoS alone will be adopted to fit the *P*-*V* data of the studied cancrinite-group minerals, only some hints on the other isothermal equations of state will be given below.

Poirier and Tarantola (1998) proposed an equation of state in the form of a Taylor's series in the finite "natural strain":

$$f_N = \frac{1}{3}\left(\frac{V}{V_0}\right) \quad (22)$$

More details on the formulation of the *Natural strain* EoS can be found in Angel (2000). In general, the equations of state based on the finite strain do not accurately represent the elastic behavior at very high compressions ($\eta \leq 0.6$) (Angel 2000). Under extreme compressional regime Vinet et al. (1986, 1987) proposed a "universal" *P*-*V* EoS, based on an expression of the cohesive energy as a function of the interatomic potentials (Duffy and Wang 1998; Angel 2000):

$$P = 3K_0\frac{(1-f_V)}{{f_V}^2}e^{\left[\frac{3}{2}(K_V{}'-1)(1-f_V)\right]} \quad (23)$$

where $f_V = (V/V_0)^{1/3}$.

2.1.5 High-temperature and high-pressure *P-V-T* equations of state

All the equations of state reported above allow the characterization of the thermal expansion coefficient (α_V), coupled with its *T*-dependence, at a fixed pressure (usually the room-*P*) and of the compressibility (β_V, through the bulk modulus K_V), and its *P*-dependence, at a fixed temperature (usually the room-*T*). However, none of those parameters is sufficient to characterize the elastic behavior at a combined high-(*P*,*T*) condition. The *P*-dependence of α_V and the *T*-dependence of K_V are defined by the thermodynamic identity (Anderson 1989):

$$\left(\frac{\partial \alpha}{\partial P}\right)_T = \frac{1}{(K_{V(T)})^2}\left(\frac{\partial K_{V(T)}}{\partial T}\right)_P \quad (24)$$

A simple experimental approach, for the calculation of *P-V-T* equations of state for minerals, is given by performing a set of *n* compression isotherms at increasing temperature. In this manner, a series of *n* isothermal high-temperature Birch-Murnaghan equations of state can be refined, providing a set of $V_{0(T)}$, $K_{V0(T)}$ and $K_V'_{(T)}$ parameters, each of them referring to different temperature conditions. Once these parameters are known, the *T*-dependence of the bulk modulus can be refined from:

$$K_{V0}(T) = K_{V0}(T_0) + \left(\frac{\partial K_{V0}}{\partial T}\right)_P * (T - T_0) \quad (25)$$

if a linear *T*-dependence of the K_{V0} is assumed. If the refined K_V' values, from the different isotherms, are taken into account, a good approximation of a *P-V-T* equation of state is carried out.

Based on the data available in the literature, Holland et al. (1996) reported that the $(\partial K_0/\partial T)_P$ is proportional to the product $\alpha_V * K_{V0}$, which is a temperature-dependent parameter below the Debye temperature (Duffy and Wang 1998). Therefore, also $(\partial K_{V0}/\partial T)_P$ is a *T*-dependent parameter. However, Holland et al. (1996) reported that a good reproducibility of experimental data is shown approximating $(\partial K_{V0}/\partial T)_P$ to be constant and equal to:

$$\left(\frac{\partial K_{V0}}{\partial T}\right)_P = -3a_0 K_{V0(T0)} \quad (26)$$

where $K_{V0(T0)}$ is the refined bulk modulus at room-*T* and a_0 the refined parameter from the equation (14). Later, Holland and Powell (1998) simplified the formulation to

$$\left(\frac{\partial K_{V0}}{\partial T}\right)_P = -1.5 * 10^{-4} K_{V0(T0)} \qquad (27)$$

With these approximations, and assuming that the K_V' is independent from temperature, it is possible to obtain a *P*-*V*-*T* relationship starting only from the elastic parameters refined from $(T,V)_{\text{room-}P}$ and $(P,V)_{\text{room-}T}$ equations of state alone.

2.1.6 The F_E-f_E plot

The thermo-elastic behavior of a crystalline material can be assessed by a least-squares refinement of the parameters of an equation of state, through the fit to the experimental (*P*,*V*) and (*T*,*V*) data, obtained by *in situ* X-ray or neutron diffraction experiments. In this study, the fit of the isothermal $(P,V)_T$ Birch-Murnaghan equations of state to the experimental data of the studied cancrinite-group minerals, has been performed using the EoSFit v 5.2 software (Angel 2000, 2001). Several statistical parameters, a thorough description of which is reported by Angel (2000), allow the evaluation of how the refined equation of state reproduces the experimental data. A useful visual method to evaluate the EoS fit is given by the F_E-f_E plot, which is applicable to any isothermal EoS based upon a Taylor's series in the finite strain (Angel 2000). For the Birch-Murnaghan EoS, the f_E is the Eulerian finite strain, defined in the equation (18), and F_E is the normalized pressure:

$$F_E = \frac{P}{3f_E(1+2f_e)^{\frac{5}{2}}} \qquad (28)$$

The Birch-Murnaghan EoS itself can be re-written as:

$$F_E = K_{V0} + \frac{3}{2}(K_V' - 4)f_E + \frac{3}{2}\left[K_{V0}K_V'' + (K_V' - 4)(K_V' - 3) + \frac{35}{9}\right]{f_E}^2 \qquad (29)$$

which is a simple polynomial function of F_E in f_E. If the f_E and F_E values, calculated from the experimental (*P*,*V*) data, are plotted on a diagram, having f_E as the abscissa and F_E as the vertical axis (Fig. 2.1), the intercept on the F_E axis of the fit in the data represents K_{V0} and this value can be compared to the bulk modulus refined from the EoS fit. Moreover, the trend of the F_E- f_E plot gives useful indications on the order to which truncate the Taylor's series. In fact, from the equation (29), it derives that a sub-horizontal trend suggests that a 2nd order truncation, assuming (K_V' = 4), could be adequate; a linear non-horizontal trend suggests the truncation to the 3rd order, whereas a parabolic trend suggests a 4th order truncation as the most adequate. For a reasonable evaluation of the F_E-f_E

plot, the uncertainties on f_E (σ_f) and F_E (σ_F) have also to be reported (Angel 2000). The formulation of these parameters, reported below, is taken from Angel (2000), and Heinz and Jeanloz (1984):

$$\sigma_f = \frac{1}{3} * \eta^{-\frac{5}{3}} * \sigma_\eta \qquad (30)$$

$$\sigma_F = F_E \sqrt{\left(\frac{\sigma_P}{P}\right)^2 + (\sigma')^2} \qquad (31)$$

where η is the compression (V/V_0), σ_η its uncertainty and σ' the uncertainty in $f_E(1 + 2f_E)^{5/2}$ defined as:

$$\sigma' = \frac{\left[7\left(\eta^{-\frac{2}{3}}\right)-5\right]\sigma_\eta}{3\left(1-\eta^{-\frac{2}{3}}\right)\eta} \qquad (32)$$

From the equation (31), it derives that, since (σ_P/P) decreases with pressure, the same will be for σ_F, giving rise to larger uncertainties in the F_E-f_E plot at the lowest pressure data. Angel (2000) also underlines that the f_E and F_E values can be defined only if the experimental V_0 is known.

Figure 2.1 (*Left side*) The experimental *P*-*V* data of the mineral balliranoite fitted by a Birch-Murnaghan EoS truncated to the second order (*i.e.* $K' = 4$). The refined parameters V_0 and K_0 are shown. (*Right side*) The F_E-f_E plot derived from the same experimental data. The sub-horizontal trend corroborates the use of a second-order BM-EoS. The weighted linear fit through the data intercepts the F_E axis at a value comparable to the refined K_0.

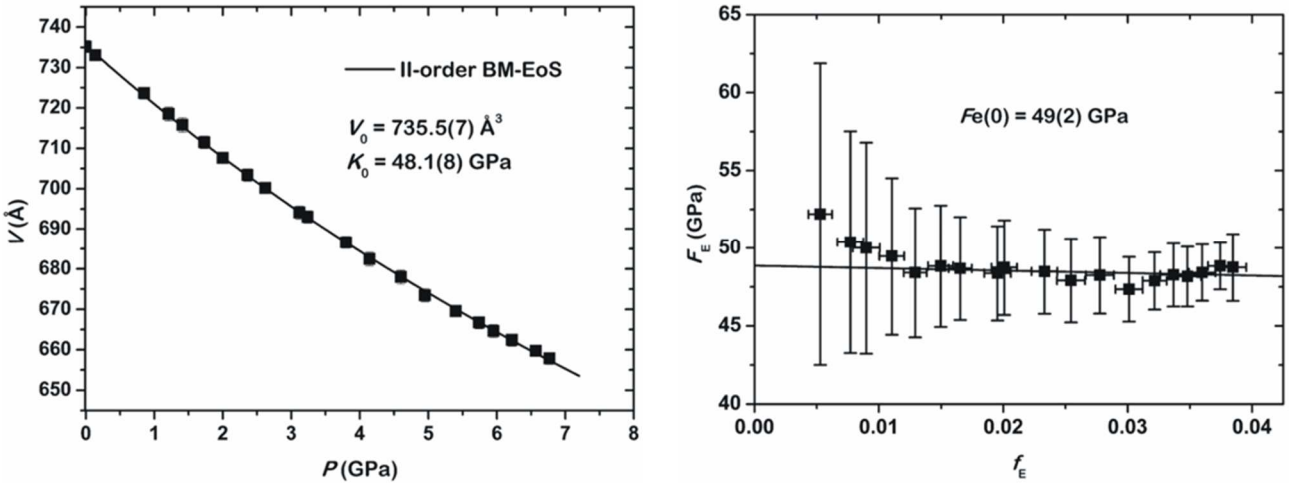

2.2 LOW-TEMPERATURE AND HIGH-PRESSURE SINGLE-CRYSTAL DIFFRACTION TECHNIQUES

The thermo-elastic behavior and the structure response to non-ambient (*P*,*T*)-conditions of a mineral or, more in general, of a crystalline compound, can be investigated by means of X-ray or neutron diffraction experiments, from single crystals or polycrystalline samples. Precise unit-cell parameters of the studied sample are obtained by least-squares refinement from the measured 2θ diffraction angles. The refinement of a crystal structure model is possible by minimizing, through least-squares methods, the calculated intensities of the diffraction peaks to those integrated from the experimental collection. In this work, the low-*T* and high-*P* elastic behavior and structure evolution of the studied cancrinite-group minerals have been analyzed using single-crystal diffraction methods. Conventional lab X-ray diffractometers and synchrotron radiation have been used.

The low-*T* data have been collected using an Oxford Diffraction Gemini Ultra single-crystal diffractometer, equipped with a Mo-*K*α X-ray source and a Ruby-CCD area detector. An area detector allows the simultaneous collection of multiple diffraction peaks, reducing the total time of the data collection and allowing a maximum coverage of the reciprocal space. In order to maximize the number of reciprocal nodes intercepting the Ewald sphere and to allow redundancy of diffraction data, both a rotation of the crystal and a displacement of the detector are needed. In a four-circle diffractometer this is obtained through the use of four goniometers: three rotating the sample and the fourth moving the detector. All the diffractometers used in this study are based on the κ geometry (Fig. 2.2). In this configuration, the 2θ-goniometer controls the rotation of the detector about an axis perpendicular to the basal plane. The three goniometers allowing the rotation of the sample are: the ω-goniometer (co-axial to 2θ), the κ-goniometer (showing a rotation axis having a ~ 50° incident angle on the basal plane) and the ϕ-goniometer (co-axial to the goniometer head's axis). When an area detector is employed, the typical collection strategy consists in a set of runs, in each of which a rotation about a goniometer axis is performed, keeping the others at constant angles. The detector records the frames in a stepwise method, where the step-angle and the collection-time per frame are editable parameters. When using a point-detector, a scan over each diffraction peak is performed, in order to refine its 2θ position and integrate the diffracted intensity. The unit-cell parameters, for the study of the high-pressure elastic behavior of cancrinite and balliranoite, have been obtained from the 2θ positions of selected sets of diffraction peaks centered using a KUMA KM4 point-detector diffractometer, equipped with a Mo-Kα X-ray source (Fig. 2.2). The intensity data, for the refinement

of the structure model of those two minerals were obtained using an Oxford Diffaction Xcalibur diffractometer, equipped with a Mo-Kα X-ray source and a CCD detector (Fig. 2.2). The use of a Mo-Kα X-ray source is preferable in high-pressure experiments. In fact, the lower wavelength (0.7107 Å), if compared to the Cu-Kα (1.5418 Å), allows a larger $2/\lambda$ radius of the limiting sphere (Giacovazzo 1992), partially counterbalancing the loss of reflections for the shadowing of large portions of reciprocal space, due to the diamond anvil cell (see next sections). The high-pressure diffraction data of vishnevite and davyne have been collected at the ID09A beamline of the European Synchrotron Radiation Source (ESRF), Grenoble, France, which is dedicated to the high-pressure conditions. The well-known advantage of using a synchrotron radiation is given mainly by the high brilliance of the beam, which allows the study of very small-volume samples, and by the possibility to choose a well-suited beam wavelength. At the ID09A beamline, the primary white beam, from an undulator insertion device, is vertically focused by a spherical mirror and horizontally by a bent Si(111)-monochromator allowing a 30*30 μm^2 beam size at the sample position. The simple and robust geometry consists of a single ω-goniometer, allowing the rotation of the sample about a vertical axis. The diffracted peaks are collected by an on-line Mar555 flat panel detector, 430*350 mm^2 in size.

2.2.1 *In situ* low-temperature devices

The *in situ* single-crystal low-temperature diffraction experiments have been performed using an Oxford Cryosystems 700 Series nitrogen-flow cryostat. This device allows the sample to be flowed by a flux of N_2 gas in a range of temperature between 80 and 400 K. The liquid nitrogen is taken up from an unpressurized dewar and flowed to a heater where it evaporates. Then, the gaseous nitrogen is re-cooled by a heat-exchanger and flowed out of the coldhead towards the sample, where a temperature stability of 0.2 K is maintained, with an absolute *T*-uncertainty within 2 K (Fig. 2.3).

2.2.2 *In situ* high-pressure devices

The *in situ* single-crystal high-pressure diffraction experiments have been performed using “diamond anvil cells” to compress the crystals hydrostatically (Fig. 2.3).

The study of the high-pressure behavior of solids is an active field of research by a long time, even though the pioneering experimental setups allowed the use of large-scale devices only (Fig. 2.4). The

advent of the diamond anvil cell (DAC) allowed a significant improvement in the field of high-pressure crystallography. In a diamond anvil cell a *P*-load system allows two diamond anvils to move to each other compressing a metal gasket, placed between them, upon which a hole is drilled, that contains the sample and a *P*-calibrant. A *P*-trasmitting fluid also fills the gasket hole, allowing the conversion of the non-hydrostatic pressure (applied by the diamond anvils through the gasket deformation) into a hydrostatic pressure on the sample and the calibrants. The volume of the gasket hole is large enough to allow X-ray diffraction experiments in conventional lab (Miletich et al. 2000).

Diamond anvil cell: the components

Diamonds are one of the fundamental components of the diamond anvil cells. Diamonds possess a series of suitable properties: besides the well-known hardness, they are transparent not only to the visible light, but also to a large range of electromagnetic radiations, including soft and hard X-rays (Miletich et al. 2000). Therefore, the DAC can be used for *in situ* spectroscopic and diffraction studies. In this respect, diamonds are classified in two categories. The type-I diamonds contain relevant impurities of nitrogen, which do not affect the use in diffraction experiments and are reported to improve the diamond resistance at very high-pressure conditions (Miletich et al. 2000). The type-II diamonds do not contain significant nitrogen impurities and, though more expensive, are needed in spectroscopic studies, for the nitrogen aggregates absorption in UV and IR-spectra (Miletich et al. 2000). The size and shape of the diamonds (Fig. 2.5) are also a critical factor (Miletich et al. 2000). The modified brilliant-cut and the Drukker-cut are among the most used (Miletich et al. 2000. The thickness of the diamond anvils has to be reduced to minimize background and Compton effects, but the ratio thickness/table cannot be reduced too much to avoid diamonds failure and the ratio table/culet must also be kept high to allow a suitable multiplicity between inward pressure (on the table) and outward pressure (from the culet). The culet edges are beveled, in order to reduce the stress at the gasket contact and prevent the diamond's failure.

The **backing plates** are the support to which the table of each diamond is attached (Fig. 2.5). They must be strong enough to support the diamonds and must also be relatively transparent to the X-rays. An optical access is needed, for example by a hole (Fig. 2.3) to be filled with a plug during diffraction experiments. Beryllium is the most used material for the backing plates, since it can be drilled to provide the optical access and is almost transparent to X-rays, giving rise to powder diffraction rings, which can be easily treated. On the other hand, it is not resistant to high temperature and very high

pressure and it is highly toxic to humans. Alternative materials for backing plates are tungsten carbide, boron or boron carbide and diamond itself (Miletich et al. 2000).

The **gasket** (Fig. 2.5) is made by a metal foil, usually a hardened stainless steel, which has a double role: it provides a support to the diamond anvils, at high-pressure conditions, and it provides the chamber where the *P*-transmitting fluid applies the hydrostatic pressure to the sample. The metal foil, generally 250 μm thick, is first pre-indented in the DAC, in order to achieve, at the pre-indented area between the diamond culets, the desired height for the chamber. Then, the sample chamber is created by drilling a hole at the center of this area, by means of a spark eroder or by a mechanical drill. The hole diameter can be variable and depends on the culet diameter, where a shorter culet diameter allows higher pressures. The hole dimensions are critical to define the maximum pressure achievable during the experiment: the lower the total surface area of the sample chamber, the higher the maximum pressure (Miletich et al. 2000). At high pressure, the fluid inside the chamber also transmits an outward force on the chamber walls, which is counterbalanced by an inward force generated by the gasket shear stresses and by the friction between the diamond anvils and the gasket (Miletich et al. 2000). The higher the total chamber surface area, the higher the outward force. Once the outward force becomes predominant, the hole begins to expand, causing a pressure drop inside the chamber. Usually, this leads to the end of the experiment. The chamber high-pressure resistance can be improved by the use of high-strength metals as gaskets, like tungsten or rhenium (Miletich et al. 2000).

A fundamental character of a diamond anvil cell is the mechanism adopted to apply the load to the anvils: *i.e.* how the anvils are pushed towards each other. Among the adopted solutions, a successful choice is given by the screw-bolts mechanism. In this case, the cell body is made by two opposing parts, which are pushed together simply by the tightening of some screws by Allen keys (Fig. 2.3, 2.5). Variable configurations of the screw system have been designed (Miletich et al. 2000), but in all the cases a particular care has to be taken when tightening the screws, in order to ensure a homogeneous load to the anvils. This can be easily ensured by the use of a *membrane-cell*, where the *P*-load is controlled by changing the gas pressure on a circular membrane, which, in turn, transmits the load to one of the anvils. Moreover, this mechanism is compatible with a setup allowing an online *P*-increase: *i.e.* without removing the cell from the experimental conditions (Miletich et al. 2000).

Pressure-transmitting medium

For a rigorous high-pressure study of a crystalline compound, it is fundamental to ensure a homogenous pressure without any deviatoric stress. These requirements are achieved if the pressure is transmitted to the sample by a fluid with hydrostatic behavior. Non-hydrostatic stresses affect the high-pressure behavior of the sample and of the *P*-calibrants (see next section), therefore biasing the pressure measurement (Angel et al. 2007). Several media that are liquid at room-*P* can be used, but none of them keeps its liquid form beyond 10-12 GPa (Miletich et al. 2000). For higher pressure regimes is, therefore, necessary the use of gaseous media at room-*P*, which become liquid at low-*P* under low-*T* and preserve a quasi-hydrostatic behavior even after the *P*-induced solidification. Moreover, the *P*-transmitting medium must ensure the chemical stability of the sample. When open-framework materials are studied, as is the case of this work, it should be considered the potential incorporation of the *P*-transmitting medium molecules into the sample crystal structure. Pure mono-component liquids are, usually, not suited, for their low-pressure glass transition (Miletich et al. 2000). Therefore, the *P*-transmitting media are, generally, mixtures of liquids. Among those, one of the most used is the methanol-ethanol mixture, with a 4:1 ratio proportion, which shows a liquid-to-glass transition at ~ 9.8-10.4 GPa (Piermarini et al. 1973; Angel et al. 2007), which increases to ~ 12 GPa for the 16:3:1 methanol:ethanol:water mixture (Angel et al. 2007). The most appropriate gaseous media at room-*P* are the noble gases, like He, Ar, Ne or Kr. The 4:1 methanol:ethanol mixture has been the only medium used in this study.

Pressure calibration

One of the most important issues in high-pressure experiments is the measurement of pressure. A direct relationship between the pressure at the sample position and the applied load is impossible, even for the remote controlled membrane-cells. Therefore, it is necessary the use of materials as pressure calibrants, for which the shift of a property as a function of pressure is known. Since diamond anvil cells allow the optical access to the sample chamber, an adopted solution is given by the laser-induced fluorescent sensors, for which the shift of a given emitted radiation wavelength as a function of pressure is known. The fluorescent sensors are placed inside the sample chamber and irradiated with a laser beam, passing through the optical access of the backing plates (Fig. 2.5). The most common sensors, as ruby or REE-doped compounds, can be excited by visible light radiations (*e.g.* the 514.5 nm radiation of Ar-ion lasers). Then, the emitted radiation must be measured by a

spectrometer. Since the parameter of interest is the $\Delta\lambda$, a careful measurement of the emitted wavelength at room-*P* is fundamental. In general, a fluorescent sensor must be highly luminescent, with small halfwidths of the peaks and a sensitive $\Delta\lambda$ *vs. P*. Ruby (*i.e.* Cr^{3+} doped corundum, Al_2O_3), is likely the most common fluorescent *P*-calibrant, since very small spheres (~ 10 μm in diameter) are sufficient, allowing the majority of the chamber volume to be free for the sample. Ruby spheres can be excited by a green-blue visible light and emit two characteristic lines: λ_1 at 694.2 nm and λ_2 at 692.8 nm at room-(*P*,*T*). The *P*-dependence of the λ_1 wavelength has been calibrated by Mao et al. (1986), who proposed the following function:

$$P\ [Mbar] = \frac{1904\left[\left(\frac{\lambda}{\lambda_0}\right)^B - 1\right]}{B} \quad (33)$$

where λ_0 is the emitted radiation wavelength at room-*P* and *B* an empirical parameter equal to 7.665, at quasi-hydrostatic conditions. The major disadvantages of the ruby pressure gauge consist in the strong dependence of the $\Delta\lambda$ on temperature (a ΔT = 6 K has the same effect of a ΔP = 0.1 GPa) and on non-hydrostatic conditions (Miletich et al. 2000). Therefore, care must be taken to keep temperature as constant as possible, when using a ruby sensor, also considering the laser-induced heating. Alternative fluorescent calibrants are the rare earth elements (REE)-doped sensors, which are, generally, low-sensitive to temperature and provide a stronger *P*-dependence. An example is provided by the (Sm^{2+})-doped oxydes and halogenides, showing an emitted radiation singlet, and the Sm^{3+}:YAG (Yttrium Aluminum Garnet, $Y_3Al_5O_{12}$), showing an intense doublet with increasing $\lambda_1 \leftrightarrow \lambda_2$ separation with pressure (Miletich et al. 2000).

The major advantage of fluorescent sensors is provided by the relative ease of measurement and by the small volume required by the calbrant materials within the pressure chamber. However, typical uncertainties in the measured pressure, range between 0.05 and 0.1 GPa (Miletich et al. 2000). Moreover, the emitted spectra need to be collected away from the diffractometer, in a standard experimental setup, allowing the onset of *T*-induced further uncertainties (Angel et al. 1997; Miletich et al. 2000). More accurate *P*-measurements are possible by the use of the internal diffraction standard. In this case, a crystal of the calibrant material is loaded into the chamber along with the sample under investigation. An accurate determination of the calbrant unit-cell parameters is possible through its diffraction pattern and, then, the pressure can be measured from the well-known equation of state of the material. The major disadvantage consists in a strong reduction of the chamber volume available to the sample. From a general point of view, an internal diffraction standard should be: 1)

highly symmetric with a small unit cell and strong diffraction peaks, to reduce interference with the sample diffraction pattern; 2) highly compressible and stable in a large *P*-range; 3) chemically stable in the *P*-transmitting medium. Even though cubic compounds, like NaCl and fluorite (CaF_2), can be used, the most common internal diffraction standard is quartz, K_0 = 37.12(9) GPa, K' = 5.99(4) from a III-order Birch-Munaghan EoS (Angel et al. 1997). Since quartz is hexagonal, it is important to load the calibrant crystal with the (10.0) face parallel to the DAC bisecting plane (see next section).

Diamond anvil cell shadowing: the accessible reciprocal lattice

When a diffraction experiment is performed using a crystal in air, all the diffraction peaks, for which $d_{hkl} \leq 2/\lambda$, can be moved to intersect the Ewald sphere by rotation of the crystal (Giacovazzo 1992). Therefore, for a crystal in air, the accessible reciprocal lattice for diffraction is a sphere centered on the origin and of radius $2/\lambda$. When a high-pressure experiment is performed using a diamond anvil cell, part of the reciprocal lattice will be hindered by the opaque components of the DAC (the gasket and the metal body). Only the X-ray photons passing through the backing plates and the diamonds during their incident and diffracted paths would be collected by the detector. The accessible volume is a function of the DAC's opening angle (2α) and of its orientation with respect to the incident beam, defined by the angle ψ_i (Fig. 2.6). In particular, the limiting diffraction conditions are given by:

$$2\theta \leq \alpha + \psi_i \quad (34)$$

These conditions, valid for diffraction experiments in transmission geometry, which has been adopted for the high-pressure studies in the present work, define a toroidal accessible area of reciprocal lattice (Miletich et al. 2000), where the rotation axis of the toroidal area is perpendicular to the bisecting plane of the DAC (*i.e.* perpendicular to the gasket plane, Fig. 2.6). Therefore, the reciprocal lattice [*hkl*] vectors oriented approximately parallel to the toroid axis will be inaccessible to diffraction. In the case of trigonal, tetragonal and hexagonal compounds, the uniaxial axis should be taken parallel to the bisecting plane of the DAC, in order to preserve information and resolution both along *a** and *c**. In the case of orthorhombic, monoclinic and triclinic compounds, unless two differently oriented crystals are loaded in to the cell, the loss of information and resolution along a set of [*hkl*] directions is unavoidable.

Figure 2.2 The single-crystal X-ray diffractometers at the Earth Sciences Dept., University of Milano. On the left, the point detector KUMA KM4. On the right, the CCD Xcalibur Oxford Diffraction. Both the diffractometers are based on the κ geometry: the goniometers axes are shown.

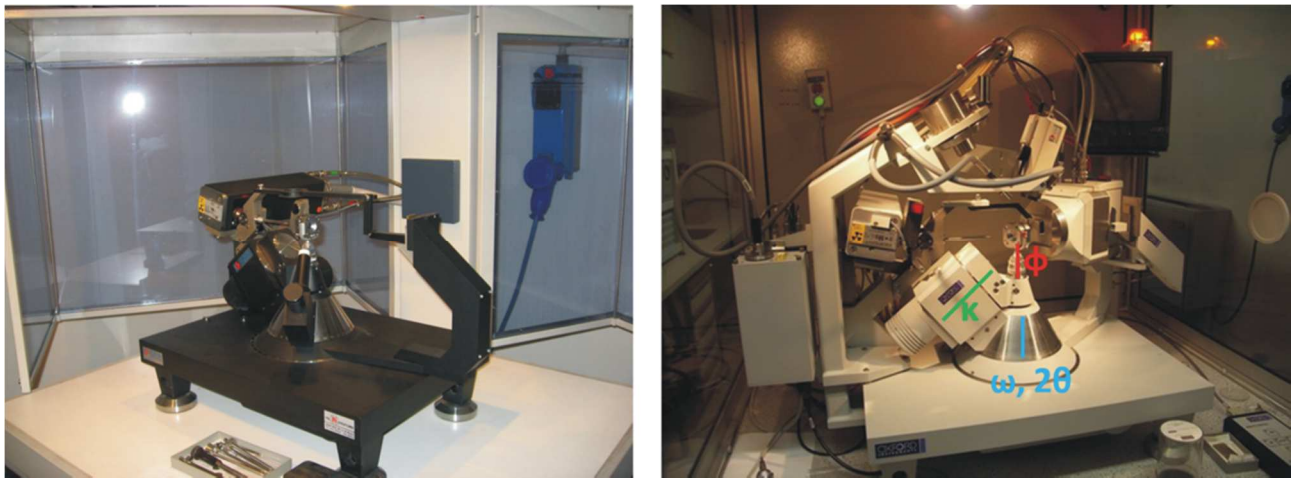

Figure 2.3 (*Left side*) The Oxford 700 series nitrogen-flow cryosystem, mounted on the Oxford Diffraction Gemini Ultra single-crystal diffractometer at the Institute of Mineralogy and Petrography, University of Innsbruck. (*Right side*) An ETH-type diamond anvil cell.

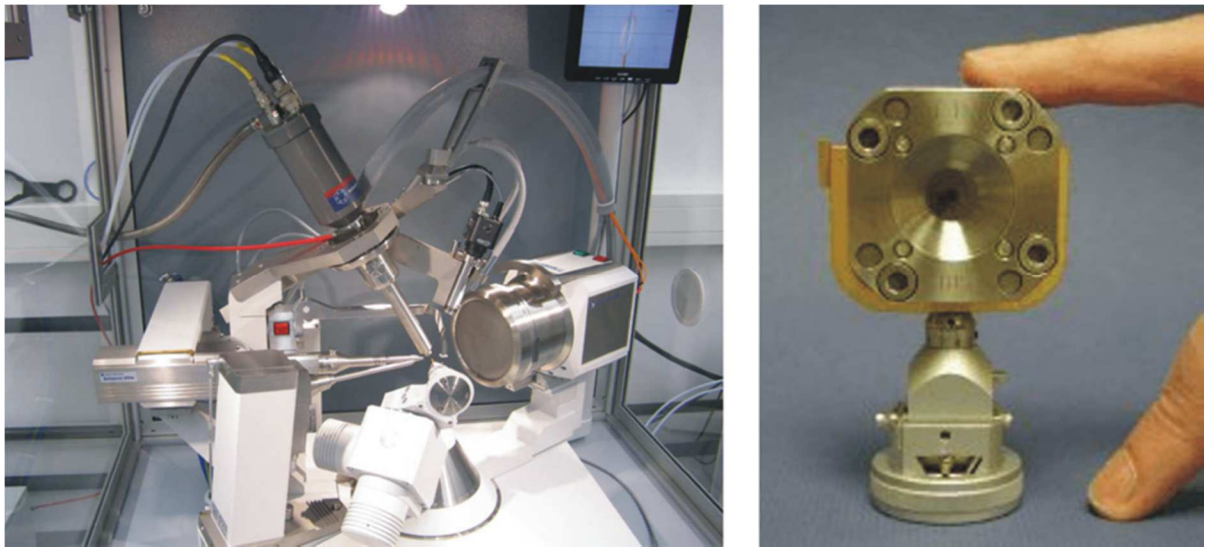

Figure 2.4 An early high-pressure experimental setup…

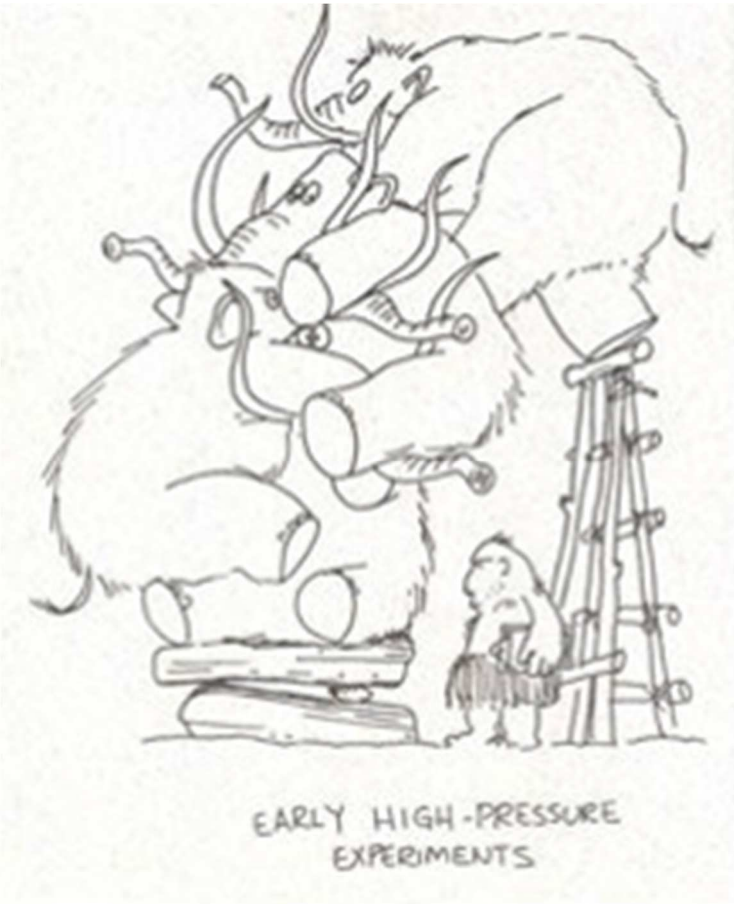

Figure 2.5 (*Top*) On the left, an ETH-type diamond anvil cell mounted on the KUMA KM4 point detector diffractometer. The optical access, drilled in the beryllium backing plate, can be seen. On the right, the components of an ETH-type diamond anvil cell. The four screws used to apply the load to the diamonds are shown. (*Bottom*) Schematic representation of a diamond anvil cell.

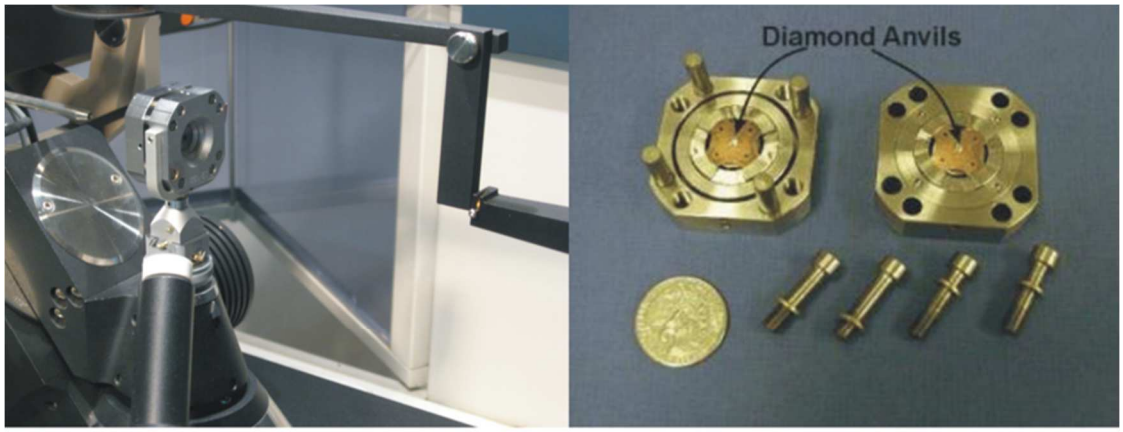

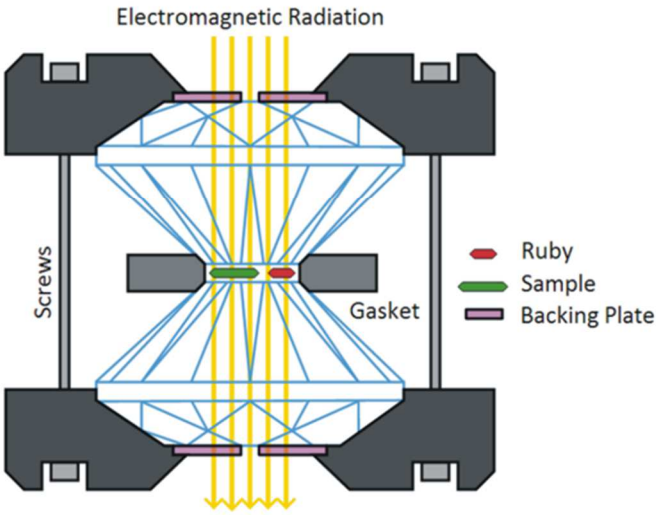

Figure 2.6 (*Left side*) The angle between the incident beam (red arrow) and the diamond anvil cell (ψ_i) and the DAC's opening angle (2α) are shown. (*Right side*) A view of the toroidal-shaped accessible reciprocal lattice volume for diffraction experiments with a DAC.

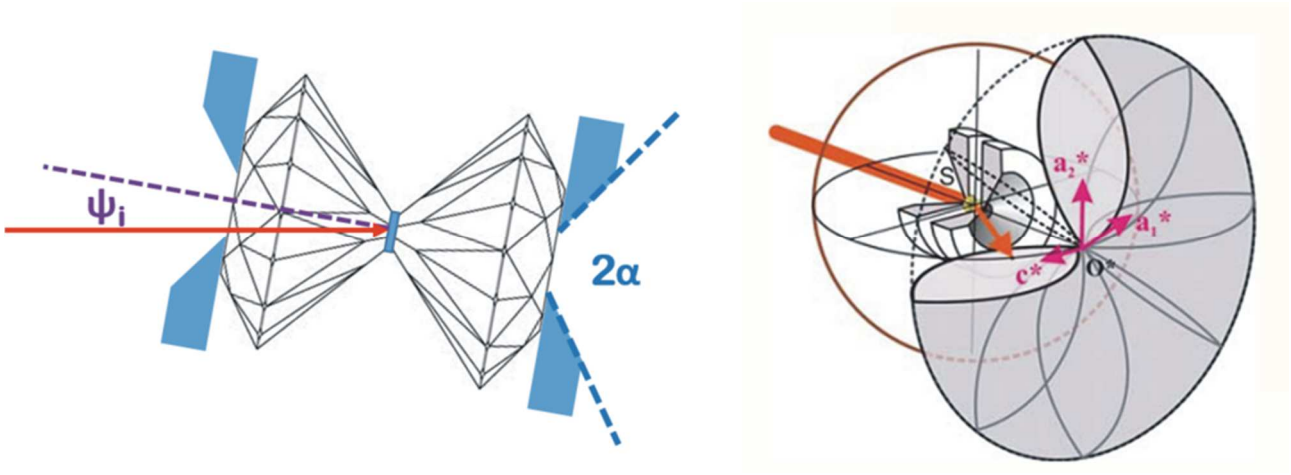

Chapter 3

Cancrinite-group minerals at non-ambient conditions

3.1 CANCRINITE-GROUP MINERALS AT NON-AMBIENT CONDITIONS: THE STATE-OF-THE-ART

In the previous chapters, the natural occurrence of the cancrinite-group minerals, the synthetic compounds sharing the [CAN]-topology along with their implications in several technological and industrial fields, have been overviewed. A characteristic feature, which emerges from both the natural and the synthetic species, is the significant chemical variability shown by the components of this group. In Nature, the cancrinite-group minerals are typical of hydrothermal and late-magmatic stages of (SiO_2)-undersaturated alkaline igneous environments, in intrusive or effusive rocks. In addition, they are also typical of related contact metamorphism. Pekov et al (2011a) proposed a genetic classification, in which the minerals of the cancrinite subgroup are characteristic of intrusive environments (as late nepheline-syenite dikes or pegmatites), whereas the minerals of the davyne subgroup are most commonly associated to effusive environments and related metasomatic rocks (like the skarns). As already reported in section 1.3, a more rigorous classification of the relationship between geological settings and different solid solutions is not trivial. In fact, a full characterization of the phase stability fields, and of the reactions at the field boundaries, is missing or limited to restricted experimental conditions (*e.g.* Sirbescu and Jenkins 1999). Della Ventura et al. (2007, 2008) reported, on the basis of micro-FTIR spectroscopic mapping, the zoning in volatile composition (*e.g.* CO_2 *vs*. CO_3) in crystals of cancrinite-group minerals, pointing out the potential application as a sensitive tool for monitoring the chemical conditions of crystallization. The characterization of the phase stability fields of the different terms of the solid solutions could also allow the monitoring of the (*P*,*T*)-conditions in the crystallization environments. In section 1.5, the occurrence of cancrinite-group compounds in various “technological” fields has been overviewed. The potential use of these compounds as stable storage materials for alkaline wastes (Bao et al. 2005; Riley et al. 2012), the potential recycling of red mud in the treatment of polluted water (Santona et al. 2006; Castaldi et al. 2008, 2011), along with other industrial applications, arise the importance for a deep knowledge of their (*P*,*T*)-phase stability fields and thermo-elastic behavior. For example, Riley et al. (2012) noted that, when subjected to a sintering process, the transformation of cancrinite-group compounds into sodalite and carnegieite occurred, highlighting the importance for the characterization of their high-temperature behavior. Several studies on the behavior at non-ambient (mainly high-temperature) conditions of natural and synthetic cancrinites can be found. In this respect, the state-of-the-art will be overviewed in the next paragraphs.

3.1.1 High-temperature studies on cancrinite-group compounds

The evolution of the unit-cell parameters with *T* of a natural cancrinite *s.s.* has been reported by Hassan (1996a, 1996b), from which only a higher expansivity of the *c* axis with respect to *a* could be derived, due to the severe scattering of the data. The thermogravimetric data (5 K/min heating rate) showed two main peaks ascribable to H_2O loss (Hassan 1996b), the first at 573 K and the second at 700 K. At 700 K, a significant change of the intensities of several diffraction peaks, suggested a structural re-arrangement induced by the new anhydrous form. The Author also reported the loss of CO_2 at 1223 K and the melting of the material at 1523-1527 K. Later, Hassan et al. (2006) performed an *in situ* high-temperature study of a natural cancrinite, based on synchrotron powder diffraction. At 777 K, a discontinuity in the unit-cell parameters, causing a temporary decrease in expansivity, was reported and assigned to the loss of the ordering of the [Ca·CO_3] clusters along [0001]. The dehydration was reported to occur at 898 K, according to the structure refinements. An analysis of the thermo-elastic behavior was also performed, from which the calculated volume thermal expansion coefficient at room conditions is α_V = 4.154(4)*10^{-5} K^{-1}, whereas the linear coefficients are α_a = 0.8960(8)*10^{-5} K^{-1} and α_c = 2.344(2)*10^{-5} K^{-1}, in the range 298-769 K. An X-ray powder diffraction experiment was performed on a natural cancrinite, previously heated at 873 K, by Ballirano et al. (1995). A decrease in the unit-cell parameters, if compared to the pre-heating data, and the structure refinement revealed a complete and irreversible dehydration, at the time-scale of the experiment. On the basis of an *in situ* single-crystal X-ray diffraction study in the range 173-823 K, Isupova et al. (2010) reported a discontinuity in the unit-cell parameters at 673 K, which was ascribed to the loss of H_2O. This assignment was confirmed by the structure refinement, which suggested an additional minor loss of CO_2. The Authors also reported thermogravimetric data showing a continuous loss of H_2O from 350 K up to the strong dehydration peak at 673 K. Sirbescu and Jenkins (1999) studied the phase stability field of cancrinite, in *T* and X_{CO2} at the constant pressure of 2.2 kbar. The Authors reported a univariant boundary, with a negative slope in *T* for increasing X_{CO2}, based on the reaction: cancrinite = 6 nepheline + 2 calcite + *n*H2O. At X_{CO2} < 0.2, the destabilization of cancrinite was reported to produce liquid and crystals of Na-rich melilite. Sirbescu and Jenkins (1999) also reported an interesting thermogravimetric study, with both an automated and a manual ramp; in the latter, the temperature was stepwise increased only after a constant weight was reached at each step. The results from the manual ramp, which needed a total experimental time of 10 days, always showed higher mass loss with respect to the automated ramp at the same temperature conditions, suggesting a low diffusion rate for the volatile constituents in cancrinite. Therefore it can be derived that the

thermogravimetric studies based on standard heating rates (~ 1-10 K/min) likely report data from non-equilibrium conditions. From the manual thermogravimetric ramp, Sirbescu and Jenkins (1999) reported a full dehydration at 1058 K. At $T > 1153$ K, the transformation of cancrinite into nepheline and haüyne was observed. Although it is not a proper high-temperature study, it is worth to report here the study on a natural almost anhydrous cancrinite, by Zubkova et al. (2011), for which more details are in the section 1.2.1. The Authors suggested the loss of H_2O and the consequent re-arrangement of cage-Na^+ to be a consequence of crystal roasting during the effusive process. The knowledge of the cancrinite dehydration behavior and phase stability would allow the temperature characterization of the associated effusive process.

Up to now, no studies on the high-temperature behavior of the (SO_4^{2-})-rich vishnevite have been performed. However, the high-temperature behavior of the K-rich pitiglianoite, chemically analogue to vishnevite, but with an ordered distribution of the extraframework components among the adjacent channels (see section 1.2.1), was studied by Bonaccorsi et al. (2007). The studied sample showed an increase of the unit-cell parameters up to 499 K, where the dehydration process, confirmed by *in situ* FTIR analysis, leads to a decrease of unit-cell volume in the range 499-676 K. At $T \geq 676$ K, a further increase of the unit-cell parameters was measured up to 914 K. Single-crystal X-ray structure refinements showed that the dehydration process was accompanied by a cation exchange between cages and channel: a large portion of the cage Na^+ was substituted by channel-K^+ and *viceversa*. This process was irreversible and a structure refinement from data collected at room-*T* after the heating experiment revealed that only a minor amount of H_2O could be re-adsorbed. FTIR spectroscopic data showed that CO_2 molecules were present at room conditions and were completely lost at $T \geq 723$ K.

Several studies on the high-temperature behavior of synthetic cancrinite-group compounds can be found in the literature. Thermogravimetric data on synthetic Ca-free (CO_3^{2-})-rich cancrinite have been reported by Hackbarth et al. (1999) and Kurdakova et al. (2013). Hackbarth et al. (1999) reported a reversible dehydration at 673 K, while Kurdakova et al. (2013) reported a three-stage weight loss: in the range 310-370 K the loss "of surface water", at 370-970 K the loss of "structural H_2O" and between 970 and 1370 K a stepwise loss of CO_2. Fecthelkord et al. (2001) reported a similar weight loss pattern for a (NO_3^-)-cancrinite, of large interest for the storage of nuclear wastes (see section 1.5): "surface water" was lost in the range 296-400 K, "structural H_2O" at 450-600 K and NO_3^- desorption was reported in the range 800-1000 K. Analogous temperature ranges were found by Liu et al. (2005). "Basic cancrinite" is, in principle, able to provide ion exchange capacity (Fechtelkord et al. 2003) and, therefore, its high-temperature behavior is of particular interest. In this respect,

Fechtelkord et al. (2003), reported a total loss of H_2O in the range 373-773 K and a decomposition of the starting material within 943-1003 K. The synthetic counterpart of the natural kyanoxalite, the ($C_2O_4^{2-}$)-rich term of the cancrinite subgroup, has been investigated by Linares et al. (2011). After heating the starting sample at 873 K, infrared spectroscopic analysis revealed the oxidation of the enclathrated $C_2O_4^{2-}$ to CO_3^{2-}. A thermogravimetric study showed a complex mechanism of CO_2 loss in the range 573-973 K. Particularly interesting are the high-temperature studies of Cs-bearing cancrinite analogues. Fechtelkord et al. (2001b) performed a thermogravimetric analysis of a (Cs,Li)-basic cancrinite (see section 1.4), reporting the loss of channel-H_2O in the range 350-900 K. At 943 K, the structure decomposition was observed. Lee et al. (2000) synthesized an aluminum-germanate (AlGe-CAN, $Na_6Cs_2[Al_6Ge_6O_{24}]*Ge(OH)_6$) and a gallium-germanate cancrinite (GaGe-CAN, $Na_6Cs_2[Ga_6Ge_6O_{24}]*Ge(OH)_6$). Thermogravimetric data showed the total loss of channel volatiles in the range 473-873 K for AlGe-CAN and 473-823 K for GaGe-CAN. *In situ* time-resolved synchrotron powder diffraction experiments revealed the transformation of GaGe-CAN into a nepheline-hydrate analogue at $T \geq 823$ K (Lee et al. 2000). Thermogravimetric data from synthetic cobalt-phosphate ($Na_6Cs_2[Co_6P_6O_{24}](OH)_2*1.4H_2O$) and zinc-phosphate ($Na_6Cs_2[Zn_6P_6O_{24}](OH)_2*H_2O$) cancrinites (Bieniok et al. 2005), revealed a total dehydration at $T \sim 965$ K.

Despite subtle differences, all the H*T* experimental findings reported above, show a dehydration process in cancrinite-group minerals, which, with some exceptions, is generally observed at 700-750 K and always precedes the transformation of the channel-anions.

The main interest on the high-temperature behavior of the davyne subgroup is due to the nominally anhydrous nature of its compounds. The thermal behavior of a microsommite and a davyne, both showing $P6_3$ symmetry and of a $P6_3/m$ davyne has been studied by Bonaccorsi et al. (1995). Microsommite can be considered as the (SO_4^{2-})-pure term of the subgroup, in which an ordered distribution of the extraframework population among the adjacent channels occurs, as in pitiglianoite. The (Cl^-)-pure term quadridavyne, on the contrary, shows a different kind of superstructure. More details are given in section 1.2.2. Bonaccorsi et al. (1995) reported that both davyne and microsommite having a $P6_3$ symmetry, showed a similar thermo-elastic behavior up to about 473 K, where a displacive phase transition to $P6_3/m$ occurred. In $P6_3/m$ space group, the intertetrahedral O3-O4-O3 angle (Figure 3.1) of the *dzc* chains is constrained by the mirrors (at $z = 0.25$ and 0.75) to be O3-O3-O3 = 180°. Therefore, a discontinuity with an abrupt drop in the thermal expansivity along the *c* axis also occurred. In the davyne sample showing a $P6_3/m$ symmetry at room conditions, the thermal expansivity along [0001] was found to be very low within the entire *T*-range investigated,

due to the aforementioned symmetry-induced constraint. In particular, the mean linear thermal expansion coefficient along the *a* axis of three studied sample was ~ $1.3*10^{-5}$ K^{-1}. The mean α_c of the $P6_3$ microsommite and davyne before the phase transition was $1.6*10^{-5}$ K^{-1}, whereas the mean α_c of the $P6_3/m$ compounds was ~ $0.25*10^{-5}$ K^{-1}. A comparison with the thermo-elastic data reported by Hassan et al. (2006) for a natural cancrinite, shows a different elastic anisotropy. Such a discrepancy will be thoroughly discussed in chapter 8, based on the results obtained in the present study.

3.1.2 High-pressure studies on cancrinite-group compounds

To our knowledge, before the present study on cancrinite-group minerals, only two studies on the high-pressure behavior of cancrinites were available in the open literature: the first, by Gatta and Lee (2008), on the $Na_6Cs_2[Ga_6Ge_6O_{24}]*Ge(OH)_6$ synthesized by Lee et al. (2000); the second, by Oh et al. (2011), on a synthetic hydroxycancrinite.

Gatta and Lee (2008) investigated the high-pressure behavior of the synthetic $Na_6Cs_2[Ga_6Ge_6O_{24}]*Ge(OH)_6$ by means of *in situ* synchrotron powder diffraction under hydrostatic conditions, using a modified Merril-Basset diamond anvil cell. The studied sample was found to keep its crystallinity up to the highest pressure investigated, *i.e.* 5.01 GPa. The elastic behavior was described by a Murnaghan EoS [K_0 = 36(2) GPa, K' = 9(1)] and by a III-order Birch-Munghan EoS [K_0 = 35(2) GPa, K' = 11(1)]. The reported elastic parameters were confirmed by the F_E-f_E plot, from which the $F_E(0)$ = 35(2) GPa and a calculated K' = 11(2) were derived. The Authors also reported linearized Murnaghan EoS fit for the compressibilities of the cell edges [K_{a0} = 40(2) GPa, K_a' = 11(1); K_{c0} = 31(1) GPa, K_c' = 7.4(8]), showing a low anisotropy at room-conditions (K_{a0}:K_{c0} = 1.29:1), increasing with pressure. The structure refinements revealed that the high-pressure structure evolution of this material is governed by both tilting and compression of the $(Ga,Ge)O_4$ tetrahedra; the compression likely influences the strong increase in stiffness with pressure, suggested by the high K' values. The tetrahedral compression is a characteristic feature of this compound and the Authors suggested that a lower compressibility would be expected for the aluminosilicate cancrinites, in which rigid tetrahedra occurr. The role of the framework crystal chemistry on the high-pressure behavior will be discussed in chapter 8. No significant change of the extraframework configuration was observed. The Authors reported a compression and distortion of the Cs- and Na-polyhedra within the cage and channel, respectively, whereas a strong undistorted compression of the $Ge(OH)_6$ octahedron, at the center of channel, was reported. Despite the use of a hydrous pressure-transmitting medium

(*i.e.* methanol:ethanol:water = 16:3:1), Gatta and Lee (2008) did not report any *P*-induced overhydration.

Oh et al. (2011) reported the high-pressure elastic behavior of a synthetic hydroxycancrinite, up to 6.1 GPa. Hydroxycancrinite is considered one of the zeolitic precursor in the matrix of geopolymers, binding materials alternative to Portland cement (Oh et al. 2011). The Authors performed an *in situ* synchrotron powder diffraction experiment, suggesting that the characterization of the elastic behavior of the single precursors would allow a better understanding of the intrinsic elasticity of geopolymers. The experimental data were fitted by a II-order Birch-Murnaghan EoS, as suggested by the zero-slope F_E-f_E plot, yielding a refined bulk modulus K_0 = 46(5) GPa. These data appear to confirm the hypothesis of a lower compressibility of aluminosilicate cancrinites, at least at low-*P* regimes, proposed by Gatta and Lee (2008).

Figure 3.1 The intertetrahedral O3-O4-O3 angle in $P6_3$ davyne (*left side*) is symmetry-induced to O3-O3-O3 = 180° in $P6_3/m$ davyne (*right side*), for the mirror planes at z = 0.25 and 0.75.

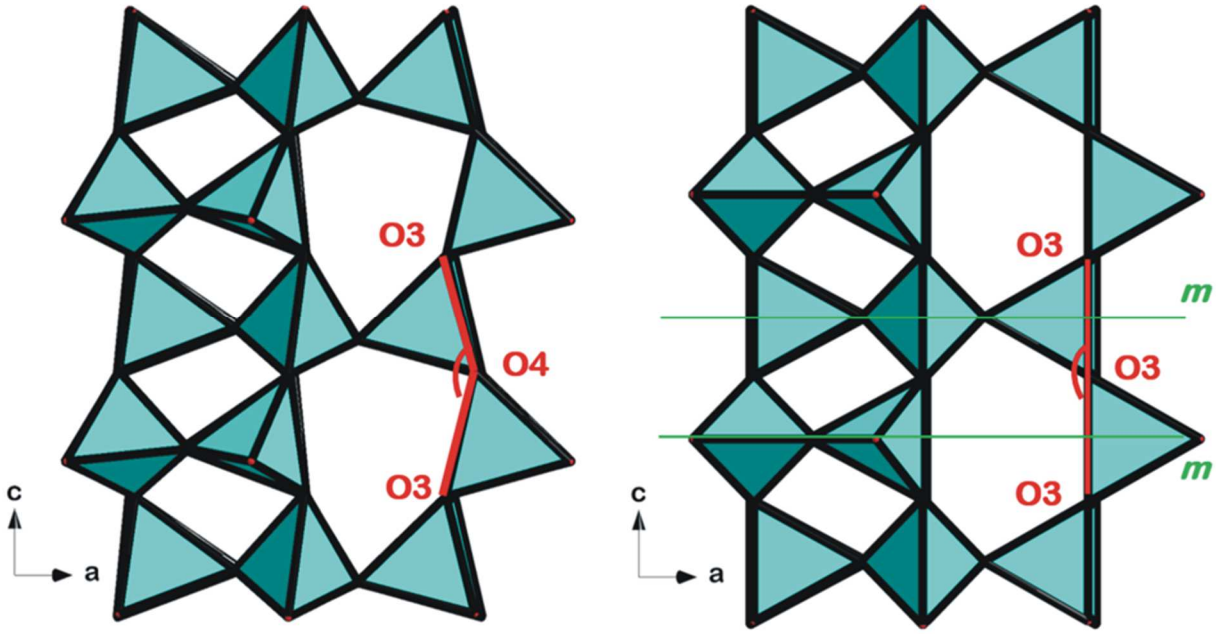

3.2 THE AIM OF THE PROJECT: A MODEL OF THE THERMO-ELASTIC BEHAVIOR AND STRUCTURE EVOLUTION OF CANCRINITE-GROUP MINERALS AT NON-AMBIENT CONDITIONS

The aim of this study is to provide a model of the thermo-elastic behavior and of the crystal structure evolution of cancrinite-group minerals, in response to non-ambient temperature and pressure conditions. In particular, the role played by the different extraframework population will be investigated. For the construction of a comprehensive model we decided to restrict the study to the compositions most common in Nature, corresponding to the (CO_3^{2-})-rich and (SO_4^{2-})-rich terms within the cancrinite and davyne subgroups, respectively: cancrinite {$[(Na,Ca)_6(CO_3)_{1.2\text{-}1.7}][Na_2(H_2O)_2][Al_6Si_6O_{24}]$} and vishnevite {$[(Na,Ca,K)_6(SO_4)][Na_2(H_2O)_2][Al_6Si_6O_{24}]$}, balliranoite {$[(Na,Ca)_6(CO_3)_{1.2\text{-}1.7}][Ca_2Cl_2][Al_6Si_6O_{24}]$} and davyne {$[(Na,Ca,K)_6((SO_4),Cl)][Ca_2Cl_2][Al_6Si_6O_{24}]$}. In order to keep a limited number of chemical and structural variables the terms pitiglianoite, microsommite and quadridavyne, all showing superstructures, have not been considered in this study.

Although only a minor portion of the crystal chemistry of cancrinite-group compounds is covered by the four selected minerals, a significant number of structural configurations will be taken into account. The substitution of the [Na·H_2O] by the [Ca·Cl] clusters within the *can* units leads to an expansion of the [CAN]-framework, as the unit-cell and structural parameters reported in the literature show. In particular, the expansion along the *c* axis in the davyne subgroup can lead to the displacive phase transition from the $P6_3$ to the $P6_3/m$ space group. The effects caused by the *P*-induced (inverse) phase transition on a natural davyne sample will be investigated in section 7.2. The different composition of the *can* units, within the two subgroups, not only causes the framework expansion, but also a significantly different coordination environment of the cage cations. In the cancrinite subgroup, the Na^+ shows a strong tetrahedral coordination to the three neighboring O1 atoms of the S6R⊥[0001] cage basis and the closer H_2O oxygen, and a weaker tetrahedral coordination to the three O2 and the farther Ow atoms, giving rise to a 4+4 environment (see *e.g.* Fig. 4.3 and 5.1). In the davyne subgroup, the Ca^{2+} shows a proper 8-fold ditrigonal bipyramidal coordination to the six S6R⊥[0001] oxygen and the two neighboring Cl^- atoms (see *e.g.* Fig 6.1 and 7.1). These different coordination environments are expected to have a significant effect on the structural and elastic behavior. A model of the role played by the population of the *can* units will be presented. If the selected minerals show for the *can* units two discrete and mutually exclusive configurations, the structural distribution of the

channel components is, by far, more complex. Nevertheless, the tetrahedral sulfate anion cannot occupy two subsequent asymmetric units along *c* (asymmetric unit: *c*/2), differently from the triangular and planar carbonate. The restraints induced by the tetrahedral SO_4^{2-} also affect the distribution and the type of the channel cations. In fact, Pekov et al (2011a) reported a strong affinity between CO_3^{2-} and Ca^{2+}, whereas only minor K^+ is observed in the (CO_3^{2-})-rich terms. On the contrary, the large K^+ cation is commonly associated to the SO_4^{2-} anion, likely coupled to the vacancies between two subsequent sulfate tetrahedra, for the favorable bond distances allowed by the resulting free volume at the center of the channel. The complex role played by the different channel configurations on the elastic behavior and structure evolution will also be investigated. The effects of the geometric shape of the anionic groups on the elastic and structural behavior could be applied to the other triangular and tetrahedral anions known in the cancrinite-group compounds (see section 1.4).

In order to provide a general model of the elastic behavior and structure evolution in cancrinite-group minerals a series of experiments at low temperature ($T \leq 293$ K) and high pressure have been performed by means of *in situ* single-crystal X-ray diffraction experiments. The results from the studies on cancrinite, vishnevite, balliranoite and davyne will be reported, along with the related discussions, in the chapters 4, 5, 6 and 7, respectively. In addition, the results from an *in situ* high-temperature single-crystal X-ray diffraction study on cancrinite will also be reported. Chapters 4, 5, 6 and 7 are all published or forthcoming papers. A comprehensive discussion, on the role played by the different crystal chemistries, will be reported in the chapter 8.

Chapter 4

Cancrinite

4.1 CANCRINITE BEHAVIOR AT LOW-TEMPERATURE

The experimental findings reported in the following paragraphs have been published in the following paper:

G.D. Gatta, P. Lotti, V. Kahlenberg and U. Haefeker (2012) The low-temperature behaviour of cancrinite: an *in situ* single-crystal X-ray diffraction study. *Mineralogical Magazine*, **76**, pp. 933-948.

4.1.1 Materials and experimental methods

A single crystal (130*120*90 μm^3) free of defects at the optical scale, from a centimetric gem-quality crystal of cancrinite from Cameroun used by Della Ventura et al. (2009), was selected for the X-ray diffraction experiments at low temperature. The chemical formula of the cancrinite sample was previously reported by Della Ventura et al. (2009) by electron microprobe analysis in wavelength dispersive mode: $Na_{6.59}Ca_{0.93}[Si_{6.12}Al_{5.88}O_{24}](CO_3)_{1.04}F_{0.41}\cdot 2H_2O$.

Intensity diffraction data were collected at 293, 250, 220, 180, 140, 100 and then again at 293 K using an Oxford Diffraction Gemini Ultra diffractometer, equipped with a Ruby CCD detector and graphite monochromator, operating at 50 kV and 40 mA with Mo*K*α radiation. Low temperature data collections were performed with the crystal cooled by an Oxford Cryosystems 700 series Plus open-flow nitrogen gas device (temperature stability better than 0.2 K, temperature absolute uncertainty within 2 K at the crystal position). A combination of ω and φ scans was used to maximize data coverage and redundancy, with 1° scan width, 29 s exposure time per frame and maximum 2θ of ~80°. The crystal was found to be metrically hexagonal within the entire *T*-range investigated, with the following unit-cell constants at room conditions: $a = b = 12.6018(3)$, $c = 5.1204(2)$ Å and $V = 704.21(2)$ $Å^3$. Systematic absences were compatible with the space group $P6_3$ at any temperature, and no evidence of superstructure or twinning was found. Lorentz-polarization corrections were applied to all the datasets using the Crysalis software (Agilent 2012). Further details pertaining to the data collection strategies are given in Table 4.1.

Unpolarized single-crystal Raman spectra at room temperature were collected from the same crystal used for the low-*T* X-ray diffraction experiments, using a Labram HR-800 confocal Raman-spectrometer by HORIBA equipped with an open-electrode charge-coupled detector (CCD). The sample was excited with a Nd:YAG laser (30 mW, 532 nm). The laser beam was focussed through a

100x objective (N.A. = 0.9) to a 1 micrometer spot on the sample. Laser power at the sample surface was approximately 5 mW. The regions from 100 to 1400 cm^{-1} and 3400 to 3800 cm^{-1} were investigated. Raman spectra were collected in backscattered geometry for 2 x 200 s (Fig. 4.1) with a resolution below 2 cm^{-1}. A grating with 1800 lines/mm was used to disperse the scattered Raman light. The accuracy of Raman line shifts was of the order of 0.5 cm^{-1} and emission lines of a Ne lamp were used for calibration.

4.1.2 Results

Thermoelastic behavior

The low-*T* behavior of the unit-cell volume of cancrinite is shown in Fig. 4.2. Cell volume decreases monotonically within the *T*-range investigated, and similar behavior is observed also along the unit-cell edges. No evidence of a phase transition was observed within the *T*-range investigated. The *V*-*T* data were fitted with the equation (8) derived from the thermodynamic definition of the thermal expansion coefficient (α) (Fig. 4.2), $V(T) = V_{T0}\exp(\alpha \cdot \Delta T)$, where α was considered to be constant with *T*. The refined parameters are: $\alpha_V = 3.8(7) \cdot 10^{-5}$ K^{-1} and $V_0 = 698.2(6)$ $Å^3$. The same protocol was applied to the *a*-*T* and *c*-*T* data, leading to the refined parameters $\alpha_a = 0.7(2) \cdot 10^{-5}$ K^{-1} and $a_0 = 12.580(3)$ Å, $\alpha_c = 2.1(3) \cdot 10^{-5}$ K^{-1} and $c_0 = 5.096(2)$ Å, where α_a and α_c are the linear expansion coefficients. The elastic anisotropy is $\alpha_a:\alpha_c = 1:3$. The mean thermal expansion coefficients between 293 and 100 K [$\overline{\alpha} = 1/x_0(\Delta x/\Delta T)$] were also calculated as $\overline{\alpha_V} = 4.1(2) \cdot 10^{-5}$ K^{-1}, $\overline{\alpha_a} = 0.81(4) \cdot 10^{-5}$ K^{-1} and $\overline{\alpha_c} = 2.48(7) \cdot 10^{-5}$ K^{-1}.

Despite the scattering of the data, a fit using the equation proposed by Pawley et al. (1996) was also done (eq. 14 in section 2.1), giving the following refined parameters (for $T = 100$ K as reference temperature): $V_0 = 698.5(4)$ $Å^3$, $a_{0V} = 1.5(2)*10^{-4}$ $K^{-1/2}$; $a_0 = 12.580(2)$ Å, $a_{0a} = 2.5(5)*10^{-5}$ $K^{-1/2}$; $c_0 = 5.097(2)$ Å, $a_{0c} = 9(1)*10^{-5}$ $K^{-1/2}$. The calculated thermal expansion coefficients at 293 K are: $\alpha_{V(293\ K)} = 6.8(8)*10^{-5}$ K^{-1}, $\alpha_{a(293\ K)} = 1.2(2)*10^{-5}$ K^{-1}, $\alpha_{c(293\ K)} = 3.7(4)*10^{-5}$ K^{-1}. The elastic anisotropy at room conditions is still $\alpha_a:\alpha_c \sim 1:3$.

Structure refinements

The structure refinement based on X-ray diffraction intensity data collected at 293 K was performed with the SHELXL-97 program (Sheldrick, 1997, 2008), using the atomic coordinates of Della Ventura et al. (2009) as starting model. Neutral atom scattering factors for Si, Al, Na, Ca, C and O from the *International Tables of Crystallography* (Wilson and Prince, 1999) were used. C-O bond distances were restrained to be 1.300 ± 0.005 Å, according to the refined values by single-crystal neutron diffraction of Della Ventura et al. (2009). Hydrogen positions were not refined. The first cycles were performed with isotropic atomic displacement parameters and only in a further stage were the displacement parameters refined anisotropically. Only the Ow site was kept isotropic. The structure refinement (99 refined parameters) converged to an agreement factor R_1 of 0.0378, based on 2260 intensity data with $Fo > 4\sigma(Fo)$, with no significant correlation in the variance-covariance matrix and residual peaks in the difference Fourier density map of +0.94/-0.67 e^{-}Å^{-3} (Table 4.1). Atom coordinates, occupancies and displacement parameters are listed in Table 4.2. The refined extraframework sites confirmed the model previously described: a sodium-rich site (Na1, *2b* Wyckoff position) in the cancrinite cage (Table 4.2), along with three mutually exclusive and symmetrically related H_2O oxygen sites (Ow), off the 3-fold axis (Fig. 4.3); the large channels are filled by a cationic site (Na2) occupied by Na (86.9(5)%) and Ca (13.1(5)%) (Table 4.2) in a general *6c* position and by two mutually exclusive carbonate groups (occ. 35(1) and 47(1)%, respectively, Table 4.2), with the C sites (C1 and C2) in the centre of the channel on *2a* special positions (1.25 Å apart on the 6_3 axis), and oxygen atoms on 6*c* general positions (Oc1 and Oc2 sites) (Fig. 4.3, Table 4.2).

The structure refinements at 250, 220, 180, 140 and 100 K were performed using the same strategy described above and constraining all the site occupancy factors (*sof*) to the values refined at 293 K, except for the two carbonate groups (C1-Oc1 and C2-Oc2 sites). All refinements achieved convergence with no significant correlation in the variance-covariance matrix of the refined parameters and insignificant residual peaks in the difference-Fourier electron density maps. No change of the extraframework population was detected (*e.g.*, site migration, ordering) within the *T*-range investigated. Further details pertaining to the structure refinements are listed in Table 4.1. Atom coordinates, site occupancies and U_{iso}/U_{eq} displacement parameters are given in Table 4.2. Anisotropic displacement parameters are in Table 4.3.

Test refinements were performed for any low-*T* dataset leaving the Ow *sof* free, in order to detect any potential N_2-flux-induced dehydration phenomena (Gatta and Lotti, 2011). However, no significant

change of the *sof* value was detected. A structure refinement based on the intensity data collected at room-*T* after the low-*T* experiments was also performed, showing that any low-*T* induced structure modification is completely reversible (Tables 4.1 and 4.2).

Low-*T* framework behavior

The S6R⊥[0001] units show a "ditrigonalization process" with decreasing temperature, as described by the "ditrigonal rotation angle" $\alpha_{S6R\perp[0001]}$ (Fig. 4.5, Table 4.4) [$\alpha_{S6R\perp[0001]} = (1/6)*\Sigma_i |120° - \theta_i|/2$, where θ_i is the angle between the basal edges of neighboring tetrahedra articulated in the six membered ring]. This parameter was originally defined to describe the deviation from the perfect hexagonal shape ($\alpha = 0$) of the six-membered rings in the tetrahedral sheet of phyllosilicates (Brigatti and Guggenheim 2002). The S4R joint units show a shortening along the $O3\text{-}O4_{S4R}$ distances (Figs. 4.4 and 4.5, Table 4.4). The channels size is controlled by the 12R distances $O1\text{-}O1_{12R}$, which undergo a shortening with decreasing temperature (Figs. 4.4 and 4.5, Table 4.4), and $O3\text{-}O4_{12R}$ (Fig. 4.4, Table 4.4), which are almost constant within the temperature range investigated. The cancrinite cages show a flattening with decreasing temperature, described by the closure of the O2-O2-O2 (Fig. 4.4, Table 4.4). In every plane (A or B) of S6R parallel to (0001), a decrease of the "corrugation" [defined as $\Delta z = [z(O)_{max} - z(O)_{min}]*c$, where $z(O)_{max}$ is the maximum *z* coordinate of the oxygen belonging to the rings, $z(O)_{min}$ the minimum one and *c* is the unit-cell edge length (Brigatti and Guggenheim, 2002)] with decreasing temperature is observed, along with the ditrigonalization of the rings (Table 4.4). An increase of the ditrigonal shape is also shown by the 6mR∠[0001] windows connecting channels and cages. The equivalent thermal parameters of the Si, Al and O sites decrease with decreasing temperature (Table 4.2).

Low-*T* extraframework behavior

The equivalent displacement parameters of the Na1 and Na2 sites show a linear decrease with decreasing temperature (Fig. 4.6), and a similar behavior is observed also for the Ow site. In contrast, the isotropic displacement parameters of the carbonate groups sites (*i.e.*, C1, Oc1, C2, Oc2) remain almost constant within the temperature range investigated (Table 4.2).

The coordination polyhedron of the Na1 site lying in the *can* unit is a distorted (4+4) bipyramid with a ditrigonal base (corresponding to the S6R⊥[0001] oxygen sites) and two H_2O oxygen atoms as apical vertices (Fig. 4.3). Its deformation is strictly controlled by the ditrigonalization of the rings,

which leads to a shortening of the three Na1-O2 bond distances and to the stretching of the three Na1-O1 bonds, whereas the two independent Na1-Ow bond distances do not show any significant change with temperature (Table 4.4).

The Na2 site (*i.e.*, the mixed Na/Ca site) is coordinated by five framework oxygen atoms and up to three carbonate oxygen atoms (max CN = 8) (Fig. 4.3). In each asymmetric unit (periodicity = *c*/2), two mutually exclusive and partially occupied carbonate groups were refined. This means that each asymmetric unit is actually occupied by one CO_3 group, and so three combinations for couples of successive units can occur, *i.e.* C1-C1, C2-C2 and C1-C2. For the first two, the C-C distance is equal to *c*/2 (2.56(2) Å at room-*T*); for the last combination, C-C is equal to 3.81(2) Å at room-*T*. As a consequence, three different configurations of the Na2 coordination shells are possible. However, both the chemical content of cancrinite and the refined site occupancies suggest that vacancies of the carbonate groups occur, leading to different polyhedral configurations with lower coordination number. The absence of superstructures suggests that these vacancies are randomly distributed. The structure refinements show the shortening of the Na2-O1, Na2-O3', Na2-O4' and Na2-Oc1'" and the stretching of the Na2-O3" and Na2-O4" bond distances with decreasing temperature (Table 4.4).

Raman spectra

In the spectroscopic range investigated in this study (*i.e.* 100-1400 and 3400-3800 cm^{-1}), 29 bands are distinguishable. These are designed from υ_1 to υ_{29} with increasing wavenumber and listed in Table 4.5. A fit with two Lorentzian profiles was used in order to resolve overlapping peaks. According to previous Raman investigations of open-framework silicates with zeolitic structures (Dutta and Del Barco, 1985; Dutta and Puri, 1987; Lindner et al., 1996; Wopenka et al., 1998; Mozgawa, 2001), the following general mode assignments can be outlined. The modes between 3000-3800 cm^{-1} are caused by O-H stretching of extraframework water molecules. The most intense Raman modes of the carbonate group are usually observed between 700 (in-plane bending mode) and 1100 cm^{-1} (symmetric stretching mode), whereas weak Raman peaks occur near 1400 cm^{-1} due to the asymmetric stretch (Nakamoto et al., 1957; Frost et al., 2009). Other modes between 900 and 1100 cm^{-1} are also assigned to inter-tetrahedral anti-symmetric T-O-T (T = Si or Al) stretching vibrations. Inter-tetrahedral symmetric T-O-T stretching vibrations range between 640 and 760 cm^{-1}. Bands below 550 cm^{-1} are assigned to various intra-tetrahedral δ(O-T-O) bending and rotational modes, and to lattice deformations too. For our cancrinite, the anisotropy of the Raman effect is extremely evident in terms of intensities of the bands, which vary significantly with crystal orientation (Fig. 4.1).

4.1.3 Discussion

Thermoelastic behavior

The low number and the scattering of the data prevented an accurate description of the elastic behavior of natural cancrinite at low temperature. The choice of fixing the thermal expansion coefficient α to a constant value using equation (8) is a necessary approximation due to the low number of *V*-*T* data. Refined α_V, α_a and α_c thermal expansion parameters compared to the co-respective mean thermal expansion parameters (*i.e.* $\overline{\alpha_V}$, $\overline{\alpha_a}$ and $\overline{\alpha_c}$) agree within 1σ. Moreover, no evidence of gas-flux induced dehydration phenomena (Gatta and Lotti, 2011) and no change of the deformation mechanisms were detected (see below), suggesting the absence of any kind of phase transition. The thermal expansion coefficient obtained in this study shows good agreement with that obtained by Hassan et al. (2006) for a natural cancrinite [$Na_{5.96}Ca_{1.52}[Al_6Si_6O_{24}](CO_3)_{1.57}\cdot 1.75H_2O$], within the *T*-range 298-769 K (*i.e.* $\alpha_V = 4.2(4)\cdot 10^{-5}$ K^{-1}). A thorough discussion on this point will be given in chapter 8.

Low-*T* framework behavior

The main deformation mechanisms, at low-*T*, of the cancrinite framework act through tetrahedral tilting, and in particular by anti-cooperative rotation of adjacent tetrahedra. For a given tetrahedron belonging to a given A plane which shows a clockwise rotation, the four adjacent vertex-sharing tetrahedra (three in the same A plane and one in the next B plane) will show an anti-clockwise rotation (Fig. 4.4). This mechanism is responsible for the ditrigonalization process of the S6R⊥[0001] and for the shortening of the O3-$O4_{S4R}$ distance, whereas the ditrigonalization itself gives rise to the shortening of the O1-$O1_{12R}$ channel diameter. Each pair of tetrahedra connected through the O2 hinge (Fig. 4.4) shares the upward O3 and O4 apices with the bases of two tetrahedra in the next plane, which shows in turn an opposite rotation: this forces the O3 and O4 apices to move towards each other, with a consequent decrease of the tilting angle between the tetrahedra bases and the (0001) plane and a reduction of the Δ*z* "corrugation" of the ring-planes.

The observed contraction in the (0001) plane reflects the shortening along the directions defined by the O1-$O1_{12R}$, O3-$O4_{S4R}$ and O2-$O2_{S6R\perp[0001]}$ distances, the latter in response of the ditrigonalization of the *can* unit basis. The decrease of the Δ*z* "corrugation" of the ring-planes in the (0001) plane,

related to the closure of the O3-O4-O3 angle (see Fig. 3.1), might explain the contraction along the *c* crystallographic direction (Table 4.4). Moreover, the flattening of the *can* units, defined by the closure of the O2-O2-O2 angle (Fig. 4.4, Table 4.4), also occurs in response to the contraction along [0001]. Since no change of <T-O> bond distances occurs with temperature (Table 4.4), we consider that the framework tetrahedra act as rigid units within the *T*-range investigated.

Low-*T* extraframework behavior

The equivalent displacement parameters of the carbonate group sites are almost constant within the temperature range investigated (Table 4.4) and, for all of them, the U_{33} parameter shows a value significantly higher than U_{11} and U_{22} (Fig. 4.3; Table 4.3). This nonrealistic configuration can be explained with a positional disorder along [0001] of the C1 and C2 sites (and the related oxygen sites), maintained at low-*T*. The equivalent displacement parameters of Na1 and Na2 linearly decrease with temperature, but the trend is steeper for Na1 (Fig. 4.6). This behavior could be due to a higher positional disorder of the Na2 site, someway related to the positional disorder of the carbonate groups along the *c* axis, coupled with the presence of different possible coordination polyhedra (*i.e.*, due to CO_3 group vacancies).

The chemical formula deduced on the basis of the structure refinement is $Na_{7.26}Ca_{0.65}[Al_6Si_6O_{24}][CO_3]_{1.63}(H_2O)_2$. If compared to the chemical formula reported by Della Ventura et al. (2009), it presents a higher Na content and a lower amount of Ca. However, the sum of electrons of the extra-framework cationic sites is similar, being 92.86 e^- from the structure refinement of this study and 91.09 e^- from the chemical analysis. The higher amount of CO_3 deduced from the structure refinement is partially due to the presence of F (Della Ventura et al., 2009), which was not considered in the refinement. However, the total positive charge of the refined model is 8.56 p.f.u. while the total negative charge (framework + extraframework population) is 9.26 p.f.u.. This discrepancy suggests an overestimation of the CO_3 sites occupancy factors, probably as a result of the positional disorder of the CO_3 groups coupled with their partial site occupancy (Tables 4.2 and 4.3).

Raman spectra

Raman spectra of our natural cancrinite from Cameroun shows strong similarities with those reported in the RRUFF database (i.e., RUFF ID: R100110, French River, Ontario, Canada; RRUFF ID: R050352, York River, Dungannon Township, Ontario, Canada) (Downs, 2006). The spectra that we

collected show two significantly broad vibrational modes active in the O-H stretching region, at 3536 (υ_{28}) and 3647 (υ_{29}) cm^{-1}, respectively (Table 4.5). A series of intense bands between 938 and 1057 cm^{-1} (υ_{20}- υ_{27}) are assigned to inter-tetrahedral anti-symmetric T-O-T stretching vibrations (Table 4.5). The intense bands at 1042 (υ_{26}) and 1057 cm^{-1} (υ_{27}) (Fig. 4.1, Table 4.5) appear not to be ascribable to the symmetric stretching mode of the carbonate group, as they occur in "nominally" CO_3-free compounds with CAN topology (*e.g.* vishnevite, RUFF ID: R061139; davyne, RUFF ID: R060305; Downs, 2006). Inter-tetrahedral symmetric T-O-T stretching vibrations, ranging between 630 and 760 cm^{-1}, are represented only by a couple of significantly intense bands (υ_{16}- υ_{18}, Fig. 4.1, Table 4.5). One of the most intense band of the spectrum, likely pertaining to the low-energy δ(O-T-O) bending mode, was found at 499 cm^{-1} (υ_{15}) (Table 4.5). Further significantly intense bands were found at 418 (υ_{11}) and 460 (υ_{13}) cm^{-1}, respectively. Such bands might be assignable to δ(O-T-O) bending modes or to "breathing" vibrations of the 4- and 6-membered rings of tetrahedra (Mozgawa, 2001). Between 200 and 400 cm^{-1}, some among the most intense Raman bands occur (υ_4-υ_{10}). The band at 277 cm^{-1} (υ_5) is the most intense band observed in the Raman spectrum shown in Fig. 4.1. Raman pleochroism is extremely evident (Fig. 4.1). The pleochroism likely reflects the orientation of S6R⊥[0001], their ··ABAB·· stacking sequence and the oriented configurations of the extraframework population.

4.1.4 Conclusions

This is the first investigation of the elastic behavior and structure evolution of a natural cancrinite at low temperature. No evidence of a phase transition, or change of deformational mechanisms were detected within the temperature range investigated ($100 < T$ (K) < 293). The structure refinement based on intensity data collected at room temperature after the low-*T* experiment confirmed that the low-*T* induced deformation processes are completely reversible.

The extraframework population does not show significant variations at least down to 100 K. The strong positional disorder of the carbonate groups along the *c* axis persists within the *T*-range investigated. The structure evolution of cancrinite at low-*T* appears to be mainly governed by continuous framework re-arrangement through tetrahedral tilting. In particular, the main deformational mechanisms are represented by the ditrigonalization of the S6R⊥[0001], contraction of the S4R joint units along the O3-$O4_{S4R}$ diameter, "compression" of the *dzc* chains through the closure of the O3-O4-O3 angle and the flattening of the *can* units.

Figure 4.1 Unpolarized single-crystal Raman spectra of cancrinite collected at room temperature in the regions 100-1400 and 3400-3800 cm^{-1} with the crystal in two different orientations (crystal rotated by 90º). The list of the frequencies of the main Raman bands is given in Table 4.5. None of the spectra are corrected for background.

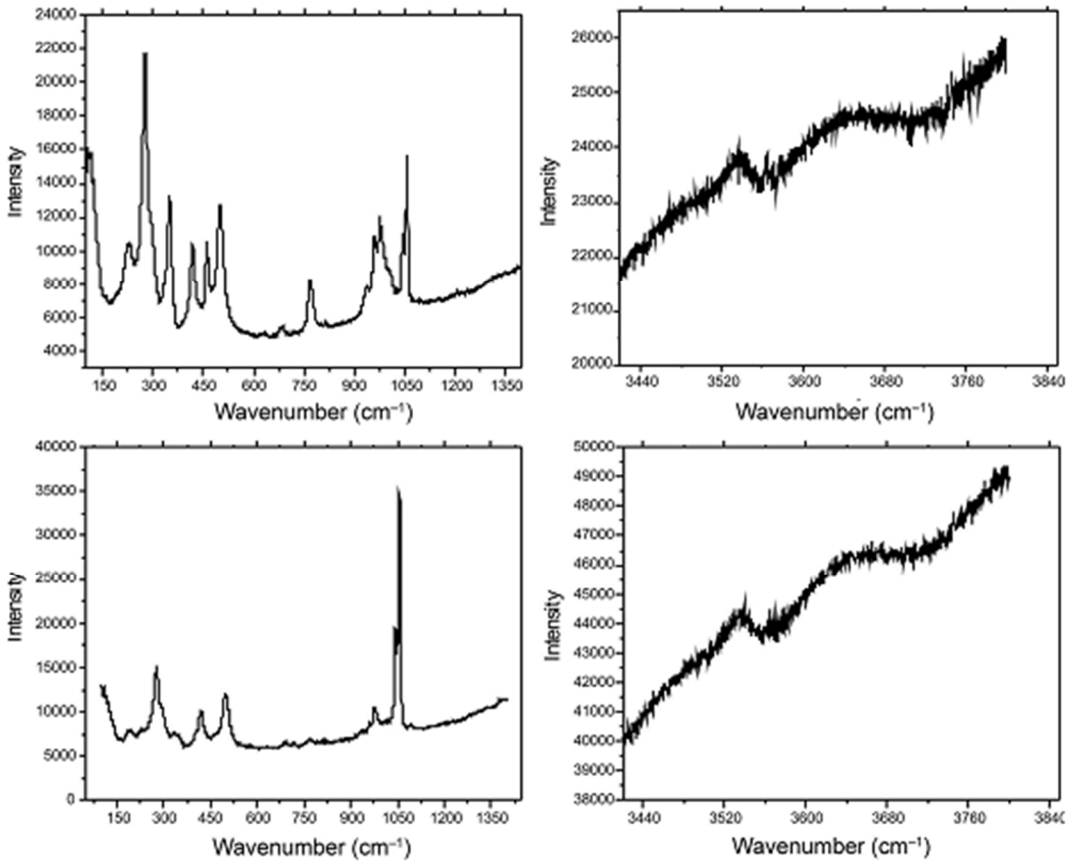

Figure 4.2 The unit-cell volume of cancrinite as a function of *T*. The solid line represents the *V*-*T* fit using the equation $V(T)=V(T_0)\exp(\alpha_V*\Delta T)$

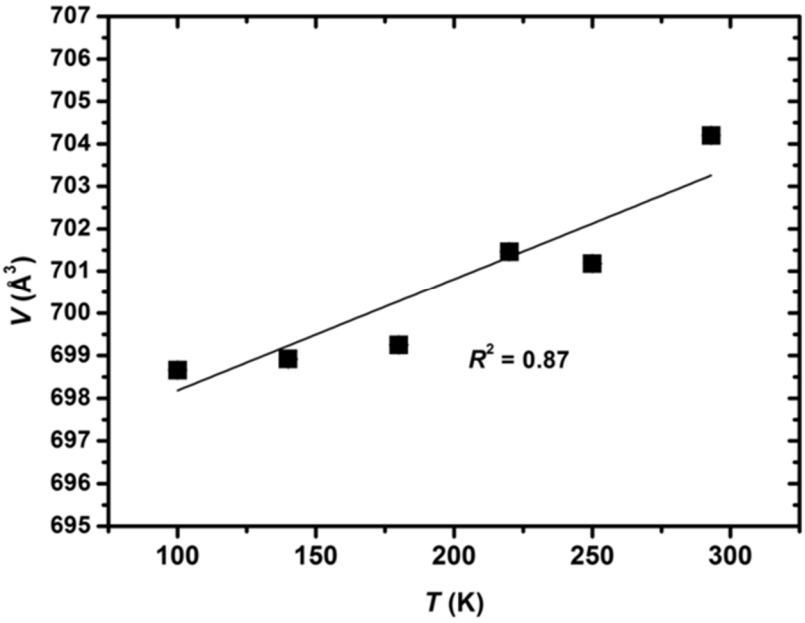

Figure 4.3 (A) The coordination shell of the Na1 site. Dashed lines represent mutually exclusive Na-Ow bond lengths. (B) The coordination shell of the Na2 site (*i.e.*, five framework oxygen on a side and up to three carbonate oxygen on the opposite side, maximum C.N. = 8). (C) The extraframework population of the 12mR channel, with the Na2 site close to the channel wall and the carbonate anions lying at the center. Different stacking sequences of the CO_3^{2-} groups and their vacancies are possible.

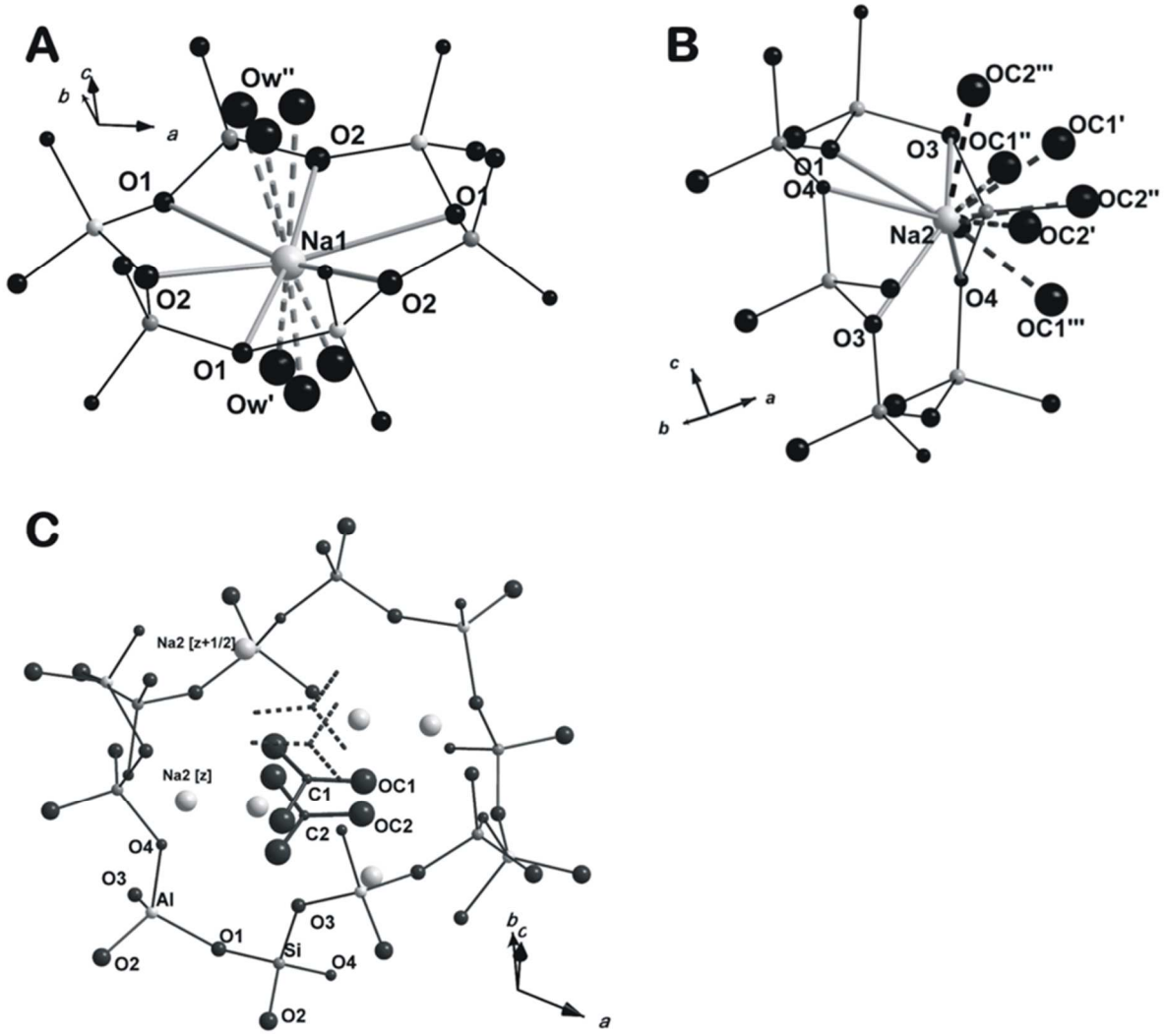

Figure 4.4 (*Left side*) The cancrinite framework viewed down [0001]. (*Right side*) The *can* unit, with a view of the O2-O2-O2 flattening angle.

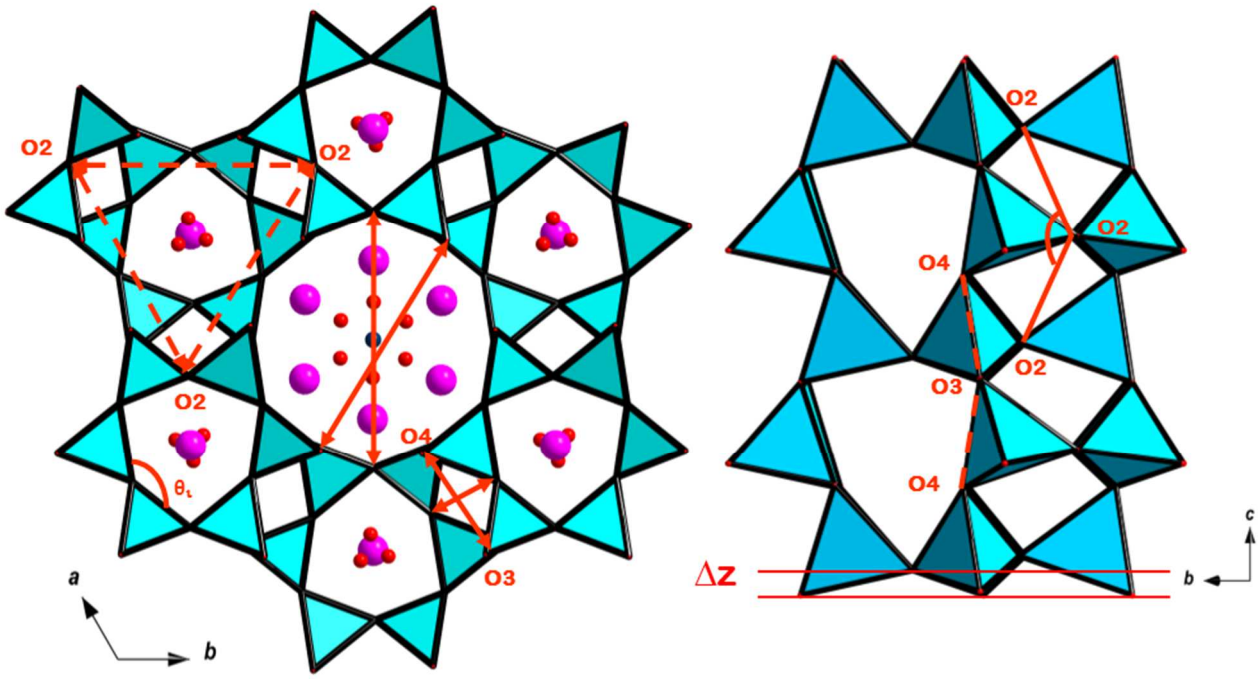

Figure 4.5 (*Left side*) Evolution of the''ditrigonal rotation angle'' ($\alpha_{S6R\perp[0001]}$) of the S6R⊥[0001] as a function of *T*. (*Right side*) Evolution of the O3-O4$_{S4R}$ and of the O1-O1$_{12R}$ diameters as a function of temperature.

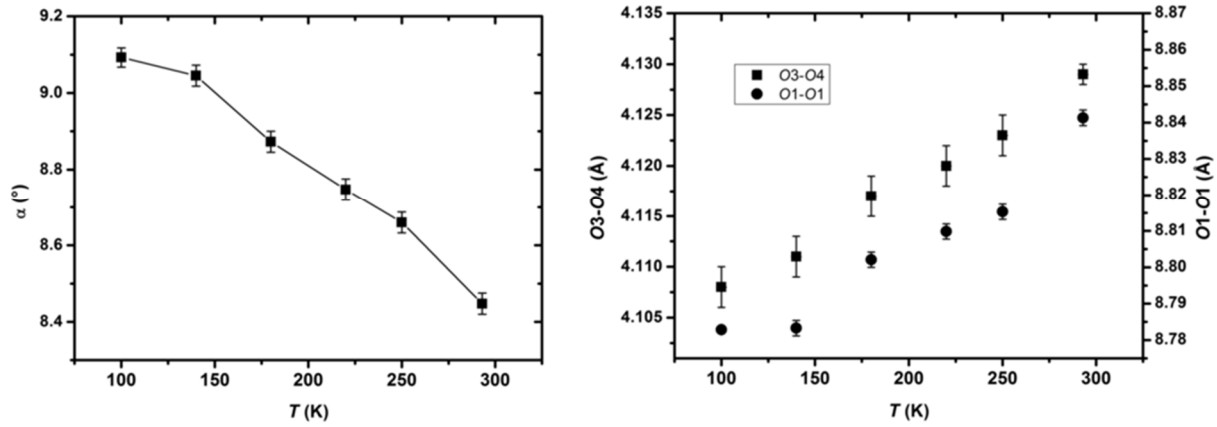

Figure 4.6 Evolution of the equivalent atomic displacement parameters (U_{eq}) of Na1 and Na2 sites as a function of temperature.

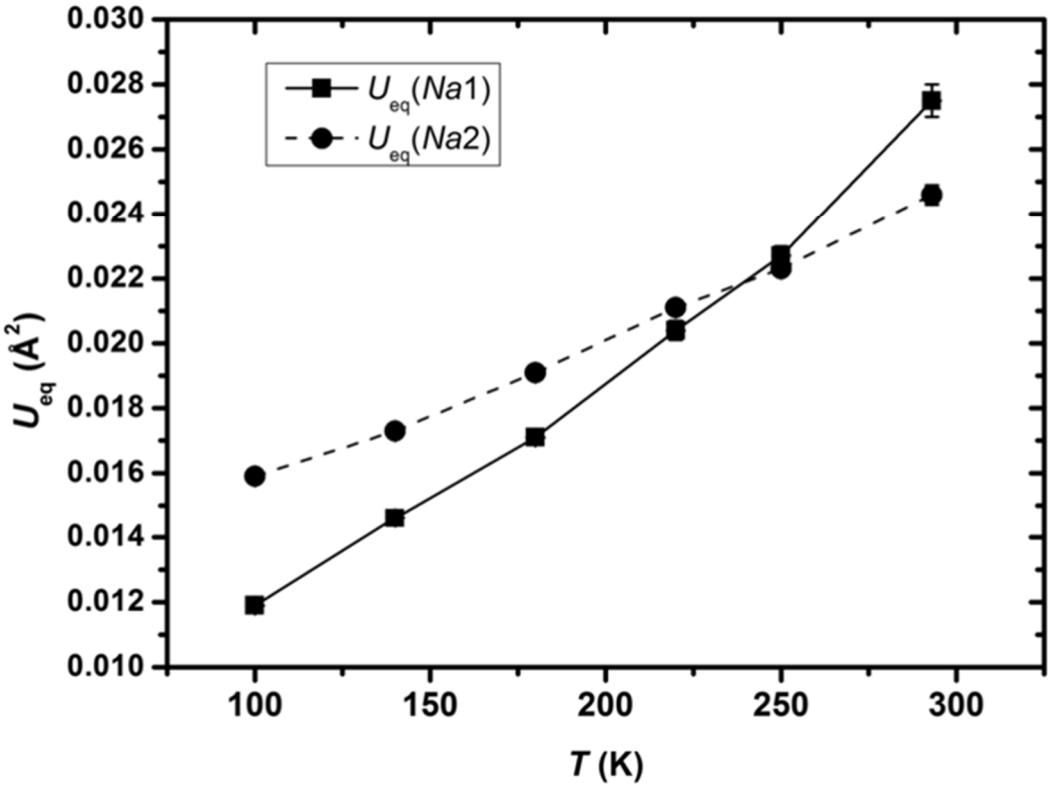

4.2 CANCRINITE BEHAVIOR AT HIGH PRESSURE

The experimental findings reported in the following paragraphs have been published in the following paper:

P. Lotti, G.D. Gatta, N. Rotiroti, F. Cámara (2012) High-pressure study of a natural cancrinite. *American Mineralogist*, **97**, pp. 872-882.

4.2.1 Materials and methods

The high-pressure single-crystal X-ray diffraction experiments were performed on a platy crystal of natural cancrinite (140*110*75 μm^3) free of defects under the polarized microscope, collected from the same gem-quality sample from Cameroun used by Della Ventura et al. (2009), for a single-crystal neutron diffraction experiment and polarized infra-red spectroscopy. The same sample was also used for the low-*T* single-crystal X-ray diffraction study reported in section 4.1. Cancrinite crystals from this sample do not show any evidence of superstructure reflections. The chemical composition is reported in section 4.1.1.

An intensity data collection with the crystal in air was first performed using an Xcalibur - Oxford Diffraction diffractometer equipped with a CCD detector, operating at 50 kV and 40 mA with a monochromatised Mo*K*α radiation source and a detector-sample distance fixed at 80 mm. A combination of ω and φ scans was chosen to maximize data coverage and redundancy. The step scan was 1°/frame along with an exposure time of 60 s/frame (Table 4.6). A total number of 19933 reflections, out of which 1933 unique for symmetry, were collected up to $2\theta_{max} = 70°$, showing a metrically hexagonal lattice with systematic extinctions consistent with the space group $P6_3$ (Table 4.6). The refined unit-cell parameters were: a = 12.5976(6) Å, c = 5.1168(2) Å and V = 703.2(1) $Å^3$ (Table 4.6). Intensities were then integrated, corrected for Lorentz-polarization (Lp) and for absorption effects (analytical absorption corrections by Gaussian integration based upon the physical description of the crystal) using the CrysAlis software package (Agilent 2012). Further details pertaining to the data collection strategy are in Table 4.6. A hydrogen-free structure refinement of cancrinite was then performed with the SHELXL-97 program (Sheldrick 1997), starting from the atomic coordinates of Della Ventura et al. (2009) in the space group $P6_3$. Neutral atomic scattering factors for Si, Al, Na, Ca, C and O from the *International Tables of Crystallography* (Wilson and Prince 1999) were used. A mixed scattering curve of Na and Ca was used to model the Na2 site, and

the site occupancy factors of C1 and C2 were constrained to be equal to that of Oc1 and Oc2, respectively. The H_2O oxygen site (Ow), lying off the 3-fold axis in three symmetry-related and mutually exclusive positions, was modeled with a site occupancy factor (*s.o.f.*) of 1/3. The C-Oc bond lengths were restrained to 1.300 ± 0.005 Å, on the basis of the neutron refinement reported by Della Ventura et al. (2009). In the last cycles of the refinement, the displacement parameters of all the atomic sites were refined anisotropically; only the displacement parameters of C, Oc and Ow sites were refined isotropically, due to a significant correlation among the refined parameters likely ascribable to the positional disorder of the carbonate groups and H_2O molecules (Grundy and Hassan 1982; Della Ventura et al. 2009). The refinement converged to an agreement factor R_1 of 0.056 for 1092 reflections with $F_o > 4\sigma(F_o)$. At the end of the refinement, no significant correlation was observed in the variance-covariance matrix and the residual peaks in the difference-Fourier function of the electron density were between +0.77/-0.55 $e^-/Å^3$. Further details pertaining to the structure refinement are in Table 4.6.

An ETH-type diamond anvil cell (Miletich et al. 2000), was used for the high-pressure experiments. A T301 steel foil, 0.250 mm thick, was used as a gasket, which was pre-indented to a thickness of about 0.110 mm before drilling a micro-hole (~ 0.300 mm in diameter) by spark-erosion. The same crystal of cancrinite previously investigated at ambient conditions was placed into the gasket hole along with some ruby chips and a single-crystal of quartz used as *P*-standards (Mao et al. 1986; Angel et al. 1997). A 4:1 mixture of methanol:ethanol was used as hydrostatic pressure-transmitting medium (Angel et al. 2007). Lattice parameters were measured between 0.0001 and 6.63(3) GPa (Table 4.7), by centering of 42 Bragg reflections with a KUMA KM4 point-detector diffractometer, operating at 50 kV and 40 mA with a graphite monochromatized Mo*K*α radiation source. Ten intensity data collections between 0.0001 GPa (with crystal in the DAC without any pressure medium) and 6.63(3) GPa (Table 4.6) were performed with an Xcalibur - Oxford Diffraction diffractometer equipped with a CCD (graphite-monochromatized Mo*K*α radiation). A combination of ω and φ scans was used, with step of 0.5 °/frame and an exposure time of 60 s/frame (Table 4.6). No violations of the reflection conditions expected for the space group $P6_3$ were observed within the *P*-range investigated. Integrated intensity data were corrected for Lp and absorption effects due to the crystal and the DAC using the ABSORB computer program (Angel 2004). The H*P* structure refinements based on the intensity data collected with the crystal in the DAC were performed with the SHELXL-97 program (Sheldrick 1997, 2008). The number of the refined parameters was reduced to 45: all the occupancy factors were constrained to the values refined with the crystal in air and the atomic displacement

parameters (*adp*'s) were all refined isotropically. In addition, the C1-C2 and Oc1-Oc2 *adp*'s. were, respectively, constrained to be equal. As for the structure model at room conditions, the C-Oc bond lengths were restrained to 1.300 ± 0.005 Å^3. The refinements converged for all the H*P* datasets with R_1 always lower than 0.088, with no significant correlation between the refined parameters and residual peaks in the difference-Fourier maps lower than ±0.96 e^-/Å^3.

Atomic fractional coordinates, site occupancy factors and atomic displacement parameters pertaining to the structure refinements at room-*P* and H*P* are given in Table 4.8; bond distances and angles are listed in Table 4.9. Refined anisotropic displacement parameters are in Table 4.10.

4.2.2 Results

Elastic behavior

The evolution of the unit-cell parameters of cancrinite up to 6.63(3) GPa is shown in Fig. 4.7. The unit-cell parameters measured in decompression showed that the pressure-induced structural evolution of up to ~ 6.6 GPa is completely reversible.

The *P*-*V* data, between 0.0001 and 6.63(3) GPa, were first fitted to an isothermal Birch-Murnaghan-type equation of state truncated to the 3rd-order (BM-III EoS, Birch 1947), using the EoS-Fit v5.2 program (Angel 2000). Weighted fit (by the uncertainty in *P* and *V*) gives the following elastic parameters: V_0 = 702.0(7) Å^3, K_{V0} = 51(2) GPa and K_V' = 2.9(4). The evolution of the Eulerian strain *vs.* the normalized pressure within the entire *P*-range investigated is shown in Fig. 4.7, suggesting that the isothermal volume compression in cancrinite can be described with a 3rd-order BM EoS, giving a bulk modulus at room-*P* of *Fe*(0) = 50(1) and its *P*-derivative of 3.2(3). A "linearized" BM-III equation of state was used to fit the *a*-*P* and *c*-*P* data (Angel 2000), giving the following refined parameters: a_0 = 12.593(5) Å, K_{a0} = 64(4) GPa, K_a' = 4.5(9), c_0 = 5.112(3) Å, K_{c0} = 36(1) GPa, K_c' = 1.9(3). The elastic anisotropy at room pressure is then: K_{a0}:K_{c0} = 1.78:1.

When one EoS is used over the entire *P*-range investigated, a modest misfit is observed for the *a*-axis and the unit-cell volume, respectively, suggesting a potential change of the compressional behavior between 4.62(3) – 5.00(2) GPa. On this basis, two different BM EoS fits were used to model the elastic behavior along the *a* and *c* axes and for the unit-cell volume, between 0.0001 – 4.62(3) and 5.00(2) – 6.63(3) GPa, respectively. The refined parameters for the range 0.0001-4.62(3) GPa, from

a III-BM EoS, are: a_0 = 12.603(7) Å, K_{a0} = 52(6) GPa and K_a' = 11(4); c_0 = 5.115(3) Å, K_{c0} = 34(2) GPa and K_c' = 2.8(8); V_0 = 703.3(7) Å^3, K_{V0} = 45(2) GPa and K_V' = 6(1). For the range 5.00(2)-6.63(3) GPa, the following parameters are obtained with a II-BM EoS: a_0 = 12.63(2) Å and K_{a0} = 58(4) GPa; c_0 = 5.196(16) Å and K_{c0} = 20.6(14) GPa; V_0 = 715(4) Å^3 and K_{V0} = 40(2) GPa. A further *fe-Fe* plot is shown in Fig. 4.7 with the refined V_0 obtained by the BM-III EoS fit [0.0001 – 4.62(3) GPa] and by the BM-II EoS fit [5.00(2) – 6.63(3) GPa], respectively.

Structure refinements

The structure refinement of cancrinite at room-*P* confirms the framework and extraframework configuration previously described (*e.g.* Della Ventura et al. 2009, section 4.1), with the *can* units stuffed by ⋯Na–H_2O—Na–H_2O⋯ chains. The 12R-channels show cation sites close to the walls (Na2), partially occupied by Na (85.4(6)%) and Ca (14.6(6)%), and CO_3^{2-} groups occupying the center in two mutually exclusive positions (*i.e.* C1 and Oc1 *s.o.f.* = 42.1(7)%; C2 and Oc2 *s.o.f* = 45.9(6)%; Table 4.8) (Fig. 4.3). The chemical formula deduced on the basis of the structure refinement is: $Na_{7.04}Ca_{0.88}[Al_6Si_6O_{24}](CO_3)_{1.76}\cdot 2H_2O$, and if we consider the amount of F obtained on the basis of the EMPA-EDS (*i.e.* 0.41 atoms per formula unit, Della Ventura et al. 2009), we obtain (after a recalculation of the C/F *s.o.f.*): $Na_{7.04}Ca_{0.88}[Al_6Si_6O_{24}](CO_3)_{1.15}F_{0.41}\cdot 2H_2O$. This chemical formula shows a slightly higher amount of Na and a lower amount of Ca with respect to the formula reported by Della Ventura et al. (2009). In fact, the sum of the electrons ascribable to the extraframework cations (Na and Ca) from the structure refinement is 95.4 e^-, slightly higher than 91.1 e^- from the experimental chemical analysis (Δe^- ~ 4.5%).

The H*P* structure refinements showed that the general configuration of framework and extraframework population was maintained within the *P*-range investigated; the main deformation mechanisms of the tetrahedral framework and of the channel and cage content are described below.

High-pressure framework behavior

At high pressure, the structure refinements show that the single 6-membered rings perpendicular to [0001] (S6R⊥[0001]) experience a ditrigonalization process (Fig. 4.8). A linear increasing of the ditrigonal rotation angle $\alpha_{S6R\perp[0001]}$ (Fig. 4.9; Table 4.9) is observed. Moreover, we observed a decrease of the (A,B)-plane corrugation Δz (Table 4.9). In addition, a closure of the O3-O4-O3 angle is also observed (Table 4.9).

The S4R joint-unit shows a compression along the $O3\text{-}O4_{S4R}$ diameter (Fig. 4.4, 4.9; Table 4.9). In the 12R-channel, an almost constant value of the symmetrically related $O3\text{-}O4_{12R}$ distances is observed with pressure, along with a shortening of the $O1\text{-}O1_{12R}$ distances (*i.e.* ~5.7%; Fig. 4.4, 4.9; Table 4.9). The S6R-windows connecting channels and cages (S6R∠[0001]) show a strong ditrigonalization. The *can* unit shows a pronounced flattening along [0001], governed by the closure of the O2-O2-O2 angle (Fig. 4.4, 4.9; Table 4.9), whereas its maximum width on the (0001) plane, defined by the three symmetry-related diameters O2-O2 (dashed lines in Fig. 4.4), is constant within the *P*-range investigated (Table 4.9).

The evolution of the channel- and cage-volumes with *P* was studied. The channel volume was modeled as $V_{ch} = (\pi R^2)*c$, where $R = [(O1\text{-}O1)_{12R}+(O3\text{-}O4)_{12R}]/4$; $(O1\text{-}O1)_{12R}$ and $(O3\text{-}O4)_{12R}$ being the independent channel diameters (Fig. 4.4, Table 4.9). The cage volume was modeled as $V_{cg} = (V_{cell} - V_{ch})/2$. The volumes thus defined are, at a first approximation, purely geometrical models, which do not represent the free void space of cages and channels, *sensu* Baerlocher et al. (2007). Both the V_{ch}-*P* and V_{cg}-*P* data (Table 4.9) were fitted with a truncated BM-III equation of state, fixing V_0 to the experimental value at P_0. The refined elastic parameters are: K_{V0ch} = 52(3) GPa, $K_{V'ch}$ = 1.4(10) for the channel, and K_{V0cg} = 53(4) GPa, $K_{V'cg}$ = 4(2) for the cage.

High-pressure extraframework behavior

The Na1 site, which lies in the *can* unit, coordinates the neighboring S6R oxygen atoms and two H_2O molecules, showing a distorted (4+4) ditrigonal bipyramid coordination shell (Fig. 4.3). The distortion of this polyhedron is strictly governed by the framework deformation. With increasing pressure, we observe a contraction of the Na1-O2 and an expansion of the Na1-O1 bond lengths (Table 4.9). The two Na1-Ow distances of the coordination polyhedron are symmetrically independent and both show a shortening with pressure (Table 4.9).

The sum of the refined site occupancies of the mutually exclusive carbonate groups is lower than 1 (Table 4.8), reflecting site vacancy. The absence of any superstructure reflections suggests that these vacancies are randomly distributed along the channels. Three combinations of subsequent CO_3 groups are possible: C1-C2 (3.85(7) Å at room-*P*), C1-C1 and C2-C2 (both spaced by *c*/2, 2.542(2) Å at room-*P*) (Fig. 4.3; Table 4.9).

The Na2 site is coordinated by 5 framework oxygen atoms on a side and up to 3 carbonate oxygen atoms on the opposite side (Fig. 4.3). With increasing pressure, we observe a decrease of the shorter

Na2-O3', Na2-O4' and Na2-O1 bond lengths and an expansion of the longer Na2-O3'' and Na2-O4'', whereas no significant change occurs for the Na2-Oc distances (Table 4.9).

4.2.3 Discussion

Elastic behavior

The refined isothermal bulk modulus at room-*P* (*i.e.* K_{V0} = 45-52 GPa) is similar to that of other microporous materials which share with cancrinite the presence of "6-membered rings" of tetrahedra as secondary building units (*sensu* Baerlocher et al. 2007) (Gatta 2008), among those: sodalite (*i.e.* K_{V0} = 51(1) GPa; Hazen and Sharp 1988), levyne (*i.e.* K_{V0} = 56(4) GPa for $P < 1$ GPa, 46(1) GPa for $P > 1$ GPa; Gatta et al. 2005), and chabazite (*i.e.* K_{V0} = 35(5) GPa for $P \leq 1$GPa, 62(1) GPa for $P \geq 1.4$ GPa; Leardini et al. 2010). The stiffer open-framework silicates show bulk moduli of 60-70 GPa (*e.g.* philippsite K_{V0} = 67(2) GPa, Gatta and Lee 2007; gismondine K_{V0} = 63.8(2), Ori et al. 2008), whereas for the softest the range is 18-40 GPa (*e.g.* Na-ZSM-5 K_{V0} = 18.2(6) GPa, Arletti et al. 2011; H-ZSM-5 K_{V0} = 23.7(4) GPa, Quartieri et al. 2011; zeolite-A K_{V0} = 22.1(3), Arletti et al. 2003; heulandite K_{V0} = 27.5(2), Gatta et al. 2003; mordenite K_{V0} = 41(2) GPa, Gatta and Lee 2006).

A subtle change in the elastic behavior of cancrinite appears to occur at $P > 4.60(3)$ GPa (Fig. 4.7). However, the accuracy and precision of our data, along with the modest *P*-range investigated, do not allow to have a unique picture of the elastic behavior. In addition, a potential change of the compressional mechanisms at $P > 4.60(3)$ GPa is not supported by the deformation mechanisms deduced on the basis of the H*P* structure refinements, by any change of the symmetry or by any evidence of satellite reflections (Fig. 4.9, Table 4.9). However, it is interesting to note that a clear change in compressibility, supported by a re-arrangement of the channel population, has been observed in vishnevite, as will be reported in chapter 5. On the contrary, no change in the elastic behavior has been observed for balliranoite and davyne (chapters 6 and 7).

High-pressure framework behavior

The main deformation mechanism in the cancrinite framework in response to the applied pressure is the anti-cooperative rotation of adjacent tetrahedra belonging to the S6R⊥[0001]. The S6R⊥[0001] ditrigonalization is the main effect of the anti-cooperative rotation mechanism, leading to the channel

contraction along the O1-$O1_{12R}$ distances (Fig. 4.4 and 4.9). The (O1-$O1_{12R}$ /O3-$O4_{12R}$) ratio decreases with *P* from 1.038(3) at 0.0001 GPa to 0.989(2) at 6.63(3) GPa (Table 4.9). On the whole, *a*) the channel O1-$O1_{12R}$ shortening coupled with *b*) the S4R joint-units compression along the O3-$O4_{S4R}$ direction and *c*) the S6R⊥[0001] compression (along O2-$O2_{S6R}$, Table 4.9) are the mechanisms responsible for the *P*-driven contraction on the (0001) plane (Fig. 4.4, 4.9), whereas the compression along the *c* axis is accommodated by compression of the *dzc* chains, well described by the closure of the O3-O4-O3 angle. (Figs. 4.4; Table 4.9). The compression of the *dzc* chain and the mechanisms accommodating the shortening within the (0001) plane govern the flattening of the *can* units.

The elastic parameters obtained from the compressional behavior of the channel and the cage (Table 4.9) show that these units have similar bulk moduli at room-*P*, but the cage becomes stiffer with increasing pressure, likely for the presence of the ···Na-H_2O··· chains, which can act as "pillars", hindering the compression of this unit.

High-pressure extraframework behavior

At high pressure, the variation of the Na1 to framework-oxygen bond lengths appears to be the effect of the S6R⊥[0001] ditrigonalization, whereas the compression along [0001] governs the bond lengths shortening along the ···Na–H_2O—Na–H_2O··· chains (Fig. 4.3; Table 4.9).

Different coordination shells, with maximum coordination number (C.N.) of 8, are possible for the Na/Ca mixed Na2 site, due to the different CO_3^{2-} ordering but with a fixed coordination with 5 framework oxygen (Fig. 4.3). At high pressure, the expansion of the longer Na2-O3" and Na2-O4" bonds leads an increasingly weaker interaction with these atoms, suggesting an actual C.N. = 6 at these conditions.

The contraction of the short C1-C1 and C2-C2 distances (equal to *c*/2) at high pressure suggests an increasing instability for these stacking configurations in favor of the longer C1-C2 one (~3.85 Å at room-*P*), if we consider the C-C distance in aragonite (~2.87 Å) as the shortest reported in carbonates (Bonaccorsi and Merlino 2005). However, previous structure refinements of natural cancrinites from X-ray and neutron diffraction data (*e.g.* Ballirano and Maras 2005; Della Ventura et al. 2009, Gatta et al. 2011) showed anisotropic displacement parameters of the CO_3 group significantly elongated along [0001], likely due to a positional disorder aimed to optimize the C-C distances at a local scale toward an energetically less-costly configuration.

Figure 4.7 Variation of the unit-cell parameters of cancrinite with pressure and Eulerian finite strain *vs*. normalized stress plot (f_E-F_E plot). For the unit-cell parameters *vs*. *P* plots, the dotted lines represent the axial and volume BM-EoS fits between 0.0001 and 6.63(3) GPa, whereas the solid lines represents the BM-EoS fitS between 0.0001–4.62(3) and 5.00(2)–6.63(3) GPa, respectively (see text for further details). The e.s.d. values are of the same size of the symbols.

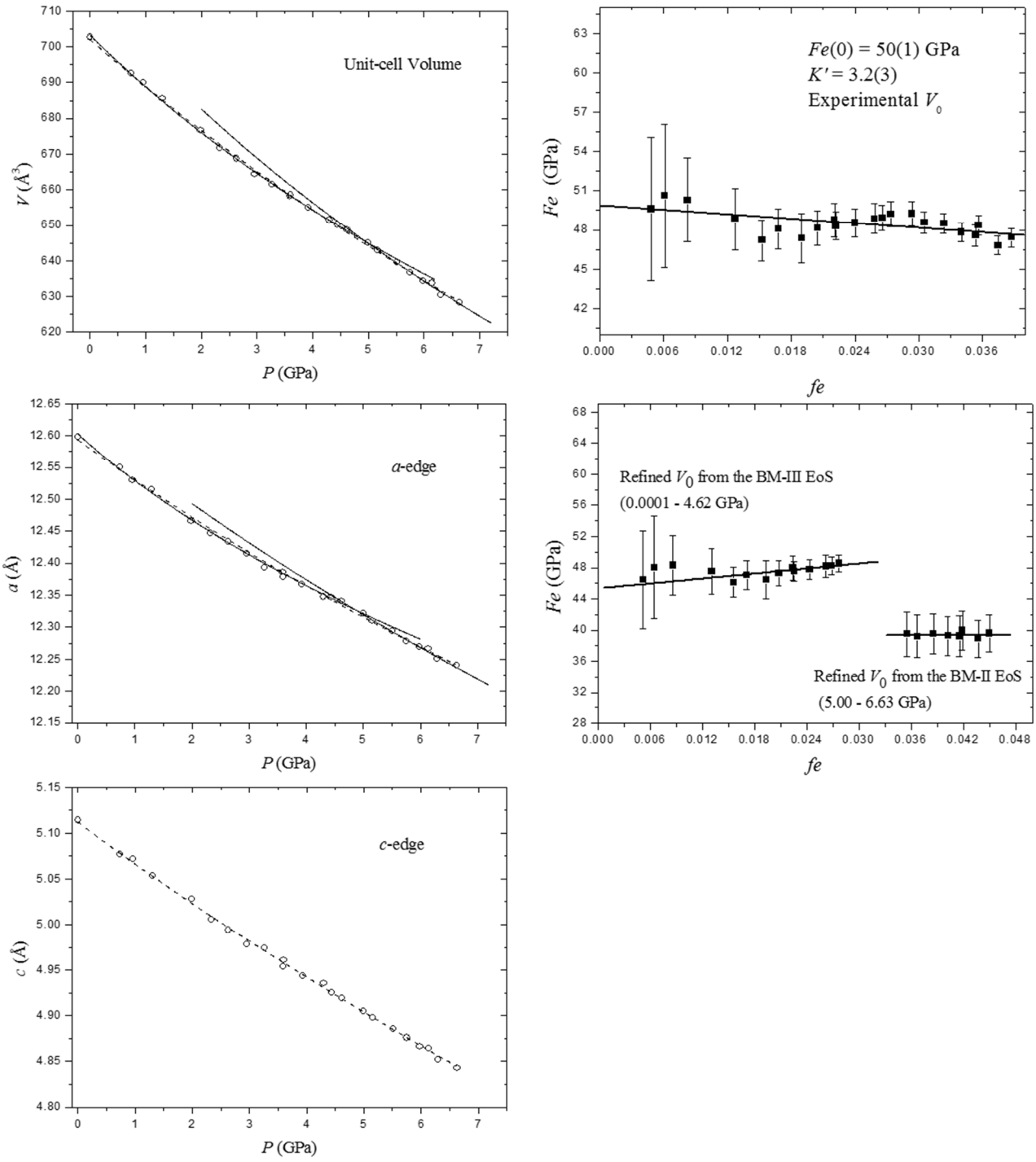

Figure 4.8 The S6R⊥[0001] at room *P* (*left side*) and at 6.63 GPa (*right side*). The *P*-induced anti-cooperative rotation of adjacent tetrahedra (ditrigonalization) is shown.

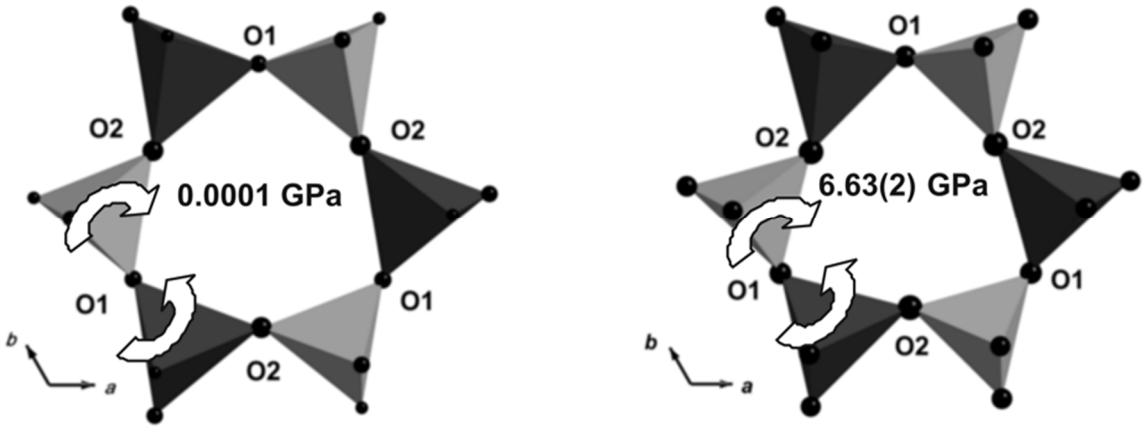

Figure 4.9 Evolution with *P* of: (A) the ditrigonal rotation angle $\alpha_{S6R\perp[0001]}$ of the S6R⊥[0001] unit, (B) the O3-$O4_{S4R}$ diameter of the S4R unit, (C) the O1-$O1_{12R}$ diameter of the channel, and (D) the O2-O2-O2 flattening angle of the *can* unit. The weighted linear fits through the data points are shown.

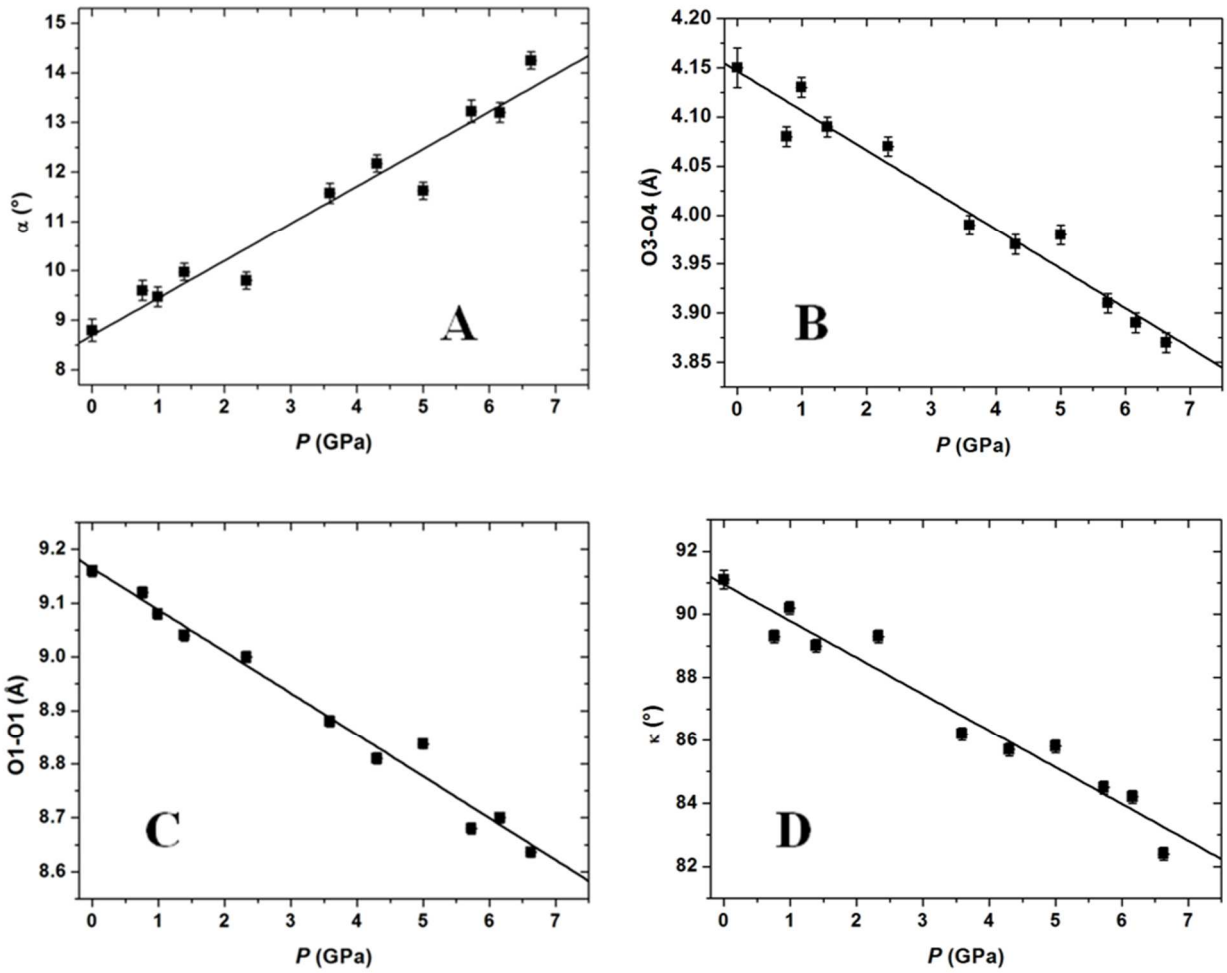

4.3 CANCRINITE BEHAVIOR AT HIGH TEMPERATURE

The experimental findings reported in the following paragraphs have been published in the following paper:

G.D. Gatta, D. Comboni, M. Alvaro, P. Lotti, F. Cámara, M.C. Domeneghetti, Thermoelastic behavior and dehydration process of cancrinite, *Physics and Chemistry of Minerals, in press*

4.3.1 Experimental methods

Sample preparation

The *in situ* high-temperature X-ray diffraction experiment was performed on a crystal fragment (300*200*150 μm^3), from the main batch already used by Della Ventura et al. (2009) and for the low-*T* and high-*P* studies reported in sections 4.1 and 4.2. The selected crystal showed sharp optical extinction with crossed polarized light under the microscope. The previous diffraction studies reported no superstructure reflections. The crystal was mounted inside a 0.3 mm inner diameter and 26 mm long quartz capillary (kept open), and held by quartz wool to avoid any mechanical stress. The capillary was mounted on a metal goniometer head on a Philips PW1100 diffractometer (Mo*K*α radiation), working at 30 mA/50 kV and using a 0.5 mm pinhole short collimator, operated with FEBO software (a local developed control software). On top was placed a microfurnace (controlled by a Eurotherm unit) with an H-shaped Pt–Rh resistance and a Pt:Pt–Rh thermocouple inside a steel cylindrical cage 1 inch wide closed with a Kapton film (*e.g.*, Redhammer et al. 2010, Alvaro et al. 2011).

Calibration of the furnace

Due to the low thermal conductivity of quartz and the distance between the thermocouple tip and the crystal inside the quartz vial (ca. 1.5 mm), the reading of the controller is not the actual temperature of the crystal. To overcome this problem, a temperature calibration was undertaken by: (i) observing the melting of selected pure salts, (ii) measuring the thermal expansion of quartz across the α – β phase transition. A spherical crystal of quartz was mounted on a quartz vial. Unit-cell parameters were collected at high temperature every 25 K. Linear fitting, performed on the observed melting

points and on the observed α –β transition temperature of quartz *vs.* the recorded temperature at the controller display, yielded the following equation:

$$T = 8.852(4.353) + 1.153(9)*T_{display}$$

with ±1 K on the reading of the thermocouple. Gaussian error propagation yielded a 6.75 K 1σ error at room-*T* and 7.04 K at 973 K. The temperature stability of the furnace while changing goniometer position was within a few K.

Unit-cell parameters and intensity data collections

Unit-cell parameters (Table 4.11, Figure 4.10) were refined using the Philips URF and LAT routines, by least-squares refinement of the UB-matrix on the basis of 24 and 60 selected intense reflections, respectively, in the θ-range 2-34° (Redhammer et al. 2010, Alvaro et al. 2011, Ferrari et al. 2014). Data were collected at intervals of 25 K in the *T* range 293-823 K. The UB matrix, and so the unit-cell parameters, were firstly refined by measuring the Bragg angles of the selected 24 most intense reflections, using horizontal and vertical slits. Afterward, the Philips LAT routine was used to obtain accurate and precise unit-cell parameters. The LAT routine allowed the position of different reflections (with different *nd*-values, where *d* is the interplanar distance and *n* = 1, 2, 3, 4, …), at positive and negative ω-2θ, to be measured. The reflection is first centered by using the vertical and horizontal slits, then a scan in ω-2θ is performed and the observed maxima are determined. The observed *nd*-values were fitted producing a relative *d*-value and its e.s.d.'s. The procedure was repeated for each temperature step on a group of 60 reflections, and lattice parameters were obtained by least-squares fitting of all the observed *d*-values.

The protocol applied at each temperature step consists in a small set of URF procedures (approx 10 minutes each) aimed to the refinement of the UB matrix until the complete relaxation is reached (*i.e.*, when the difference between the observed position for the 24 peaks in two subsequent measures are negligible). Only when the unit-cell parameters did not change anymore, the LAT procedure was performed. The results of the aforementioned protocol for the unit-cell edges measurements at each temperature step are reported in Tables 4.11 and 4.12 and in Figure 4.10. At 748 K, the unit-cell parameters achieved the relaxation only after 12 days. The isothermal data at 748 K are reported in Figure 4.11.

Intensity data collections were performed at 303, 448, and 748 K, respectively. Profiles of 2.1° in ω at fixed scan rate of $0.07°s^{-1}$ were integrated using the Lehmann and Larsen (1974) protocol, and the

integrated intensities were then corrected for Lorenz-polarization and absorption effects using a ψ-scan method (North et al. 1968).

Thermal Equation of State

In order to account for α_V variations with T, the fit of the unit-cell parameters trend with T was performed with a modified second-order polynomial equation proposed by Berman (1988), using the EoSFit software (courtesy of Ross J. Angel), as follows:

$$V(T) = V_{0(Pr,Tr)}\exp[a_0(T - T_r) + ½\cdot a_1(T^2 - T_r^2)] \quad (35)$$

where V_o, P_r and T_r are the reference volume, pressure and temperature, respectively, and the thermal expansion coefficient is described as: $\alpha_{V,Tr} = a_0 + a_1(T - T_r)$. In addition, in order to account for α_V saturation at high-T, a further fit was performed using a modified version of the equation proposed by Pawley et al. (1996) and Holland and Powell (1998) , rewritten as:

$$V(T) = V_{0(Pr,Tr)}[1 + a_0(T - T_r) - 2\cdot(10a_0+a_1)(\sqrt{T} - \sqrt{T_r})] \quad (36)$$

where V_o, P_r and T_r are the reference volume, pressure and temperature, respectively, and the thermal expansion coefficient is modeled as: $\alpha_{V,Tr} = a_0 - [(10a_0 + a_1)/\sqrt{T}]$ (see the manual of the EoSFit software at http://www.rossangel.com/ for further details). Even considering the small range of temperature investigated, all the volume-temperature data (Table 4.11) were fitted with the two aforementioned empirical equations (*i.e.* Berman 1988; Pawley et al. 1996) in order to select the best representative fitting model for our dataset (Table 4.13).

Structure refinements

Structure refinements have been performed from the intensity data collected at 303, 448 and 748 K, in the space group $P6_3$ (as suggested by the systematic extinctions) using the SHELXL-97 software (Sheldrick 1997, 2008) implemented in the WinGX suite of crystallographic programs (Farrugia 1999). Neutral X-ray scattering factors for Si, Al, Na, Ca, C and O were taken from the *International Tables of Crystallography, Vol. C* (Wilson and Prince 1999). The structure of cancrinite at 303 K was refined starting from the framework coordinates of Della Ventura et al. (2009). In order to get a stable refinement, some restraints were applied: i) the Na2 site was refined applying a mixed Na/Ca X-ray scattering curve and constraining their fractions to sum full occupancy (a test refinement with occupancy factors free to vary validated this as a good approximation, *i.e.* within 2σ); ii) the C1-OC1

and C2-OC2 bond distances were restrained to 1.300(5) Å following a previously reported procedure (sections 4.1 and 4.2); iii) the C1-C2 and OC1-OC2 sites were constrained to share the same atomic displacement parameters (*adp*'s), respectively. Convergence was achieved in the last cycles of refinement with anisotropic *adp*'s for all the sites, excluding Ow. Constraining C1-C2 and OC1-OC2, respectively, to share the same anisotropic *adp* was considered an acceptable compromise, as the *adp*'s of these sites are mainly influenced by the positional disorder along [0001], which equally involves the C1-OC1 and C2-OC2 groups as shown by the difference-Fourier maps in Figure 4.12 and described in sections 4.1 and 4.2. The structure refinement based on the 448 K dataset was performed constraining the Na and Ca fractions of the Na2 site to the values refined at 303 K and restraining the C1-C2 and OC1-OC2 *adp*'s to an isotropic function. A test refinement with the Ow occupancy factor (*sof*) free to vary suggested a full occupancy. The 748 K structure refinement was carried out with the same strategy, but refining the *sof*(Ow) and constraining its *adp* to the value refined at 478 K, for which a detailed discussion is given later. All the refinements converged with no significant residues in the difference-Fourier syntheses and no significant correlation between the refined parameters. Further details pertaining to the structure refinements are given in Table 4.14. Atomic site coordinates, occupancy factors and equivalent/isotropic *adp*'s are in Table 4.15; relevant bond distances, angles and structural parameters in Table 4.16. Anisotropic displacement parameters are in Table 4.17.

4.3.2 Results and discussion

Unit-cell parameters evolution with *T*

The unit-cell parameters evolution with *T* (Tables 4.11 and 4.12, Figures 4.10 and 4.11) shows three different expansion regimes: (i) the first trend, for the hydrated structure, from room-*T* (291 K) to 748 K, in which all the unit-cell parameters (*a*, *c*, *V*) expand almost linearly with increasing *T* (Figure 4.10); (ii) the dehydration regime (748 K), where a contraction of all the unit-cell parameters takes place (Figures 4.10 and 4.11); (iii) the second expansion regime, from 748 K to 823 K, where the quasi-dehydrated structure expands upon increasing *T* (Figure 4.10). A discussion about the quasi-dehydrated form is given below.

In order to test the quality of the fitting protocols (Table 4.13), in terms of difference between the unit-cell volume calculated from the thermal-equations fit and the actual measured volume, the δV

parameter, defined as the difference between observed and calculated volume, was calculated at different *T* (Figure 4.13). The δV clearly shows that both the modified equations of Pawley et al. (1996) and Berman (1988) reproduce very well the thermal expansion behavior within the entire hydrous expansion regime (from room-*T* to 748 K), with the exception of the last data points due to the impending dehydration (at 748 K) (arrows in Figure 4.13).

While the limited range of temperature investigated for the quasi-anhydrous thermal expansion regime (*i.e.*, 748K – 823K) allowed a good quality fit adopting the modified equation by Berman (1988), a low-quality was obtained with the modified equation by Pawley et al. (1996). For the sake of consistency, we thus adopted the modified equation by Berman (1988), being the most representative of our dataset for both the temperature regimes (Figure 4.13, Table 4.13).

Within the hydrous expansion regime (303 - 748 K), *a*, *c* and *V* expand almost linearly with increasing temperature by about 0.6, 1.3 and 2.5 %, respectively, with the following axial and volume thermal expansion coefficients: $\alpha_{a(\mathrm{hyd},303,1\mathrm{bar})} = 1.16(3)*10^{-5}\ \mathrm{K}^{-1}$; $\alpha_{c(\mathrm{hyd},303,1\mathrm{bar})} = 2.58(8)*10^{-5}\ \mathrm{K}^{-1}$; $\alpha_{V(\mathrm{hyd},303,1\mathrm{bar})} = 4.88\ (8)*10^{-5}\ \mathrm{K}^{-1}$ (Table 4.13). The thermal expansion in cancrinite is more pronounced along [0001], which expands more than twice than on (0001) (Table 4.11, Figure 4.10). This anisotropic thermal expansion scheme is in perfect agreement with the high-*T* data reported by Hassan (1996a) and Hassan et al. (2006), and with the low-*T* data reported in section 4.1.

At 748 K, the dehydration takes place, and the unit-cell edges accordingly decreased, reaching a relaxation only after 17100 min (about 12 days) (Table 4.12, Figure 4.11). Such a regime has been constantly monitored by measuring the unit-cell parameters as a function of time at constant temperature, shown in Figures 4.10 and 4.11. During such a contraction regime, the unit-cell volume undergoes a total reduction of 0.61%. In response to the loss of H_2O, most of the volume contraction is accommodated along [0001] which, being the softest direction, undergoes the most pronounced shortening (*i.e.*, 0.41%) compared to that on (0001) (*i.e.*, 0.1% along *a*) (Table 4.12, Figure 4.11). The anisotropy scheme is maintained during the whole dehydration process as shown in Figure 4.11.

At $T > 748$ K, the unit-cell parameters of the quasi-anhydrous structure show further expansion with a rate similar to that of hydrated structure (Figure 4.10). The unit-cell volume expands by 0.44% between 748 and 823 K. The anisotropic expansion scheme of the quasi-anhydrous structure is similar to that observed for the hydrous cancrinite (*i.e.* $\alpha_a < \alpha_c$), being *c* the direction with largest dilatation, with an expansion of 0.22% compared to 0.11% of the *a* edge in the temperature range between 748 and 823 K.

If we compare the Berman (1988) thermal equation of state fit for the hydrous (*i.e.*, 303 – 748 K) and quasi-anhydrous structures (*i.e.*, 748 – 823 K), the latter affected by higher uncertainty, we observe a difference (though not so pronounced) between the refined a_0 coefficients (*i.e.*, $4.88(8)\cdot10^{-5}$ and $3.1(6)\cdot10^{-5}$ K^{-1}, Table 4.13). The fitting results provided in Table 4.13 confirm that the anisotropy scheme is maintained even when the dehydration process at 748 K is completed.

The unit-cell parameters were also measured at 773, 673, 573, 473, 373 and 291 K by cooling the crystal, using the same protocol applied for the increasing temperature ramp (longer times were needed to reach the structure relaxation). Unfortunately, a significant decrease in the intensity of the diffraction peaks coupled with a shape broadening, already observed at 823 K, suggested an irreversible reduction in crystallinity, likely due to the impending decomposition, which led to large uncertainties on the measured parameters. However, an inspection of the data reported in Table 4.11 and Figure 4.10 suggests that the dehydration process is an irreversible process at the time scale of the experiment.

High-temperature structural evolution and the effects of the dehydration process

The structural model of our cancrinite at room conditions is consistent with those previously reported in the literature, and it is virtually identical to those obtained on crystals from the same locality (*i.e.*, Della Ventura et al. 2009; sections 4.1 and 4.2). The framework is completely ordered with alternating SiO_4 and AlO_4 tetrahedra, as the Lowenstein's rule predicts and as observed in nearly all cancrinite-group minerals with Si:Al = 1:1. The columns of cages are filled with a Na^+ site (*i.e.*, Na1) in a special position on the 3-fold axis (Figure 4.3), almost at the same height of the S6R⊥[0001] oxygen atoms (Table 4.15), and H_2O molecules (Ow, H_2O-oxygen site) lying at the center of the cage in three symmetry-related and mutually exclusive positions out of the axis (Figure 4.3, Table 4.15). The channel is stuffed with a single cationic site (*i.e.*, Na2) near the walls and CO_3^{2-} groups at the center, occupying two mutually exclusive iso-oriented configurations, both highly disordered along [0001] (Figures 4.3 and 4.12; Table 4.15). The crystal chemical formula from the structure refinement is: $Na_{7.30}Ca_{0.70}Si_6Al_6O_{24}(CO_3)_{1.69}\cdot2.00H_2O$, which is in good agreement with the formula from the chemical analysis (Della Ventura et al. 2009) reported in section 4.1.1.

The *sof*'s of the two independent CO_3^{2-} groups, which were set free to vary in the H*T*-refinement, did not show any evident CO_2-loss nor a redistribution between the sites with increasing temperature (Table 4.15). On the other hand, a test refinement suggested no significant loss of H_2O at 448 K,

consistent with the structure refinements of Hassan et al. (2006). The structure refinement at 748 K, based on intensity data collected when the dehydration process was completed, suggests that a minor amount of H_2O molecules still persists within the cages, as shown by the difference-Fourier syntheses phased without the Ow site (Figure 4.12). The maps show weak maxima located at the Ow site, which hosts the H_2O groups in the hydrous phase. The refinement of the Ow at 748 K, leaving both *sof* and *adp* free to vary was unstable. Consequently, the Ow *adp* was fixed to the value refined at 448 K and the *sof* set free to vary. With this strategy, the Ow *sof* refined to an occupancy of 5(1)% (*i.e.*, 0.30(6) H_2O molecules *p.f.u*) (Table 4.15), which cannot be considered as a quantitative measure of the H_2O content at 748 K (due to the bias induced by the fixed *adp*) but as a qualitative proof of a minor amount of H_2O persistency after the dehydration process. The 748 K refinement also shows a strong elongation (along [0001]) of the Na1 anisotropic *adp* (Table 4.17), which suggests thermal and/or positional disorder of the Na^+ cations, no more coordinated along the *can* unit columns by the H_2O molecules. It is worth noting that in the structure of a natural (almost) anhydrous cancrinite, found in small xenoliths in alkaline basalts of Laacher See (Eastern Eifel, Germany), the Na^+ site in the *can* units is split over three mutually exclusive positions along the 3-fold axis (Zubkova et al. 2011).

The loss of H_2O at 748 K seems to influence only the Si-O2-Al inter-tetrahedral angle, as shown by the T-O-T *vs*. *T* evolution shown in Figure 4.14 and Table 4.16. The behavior of the T-O-T angles suggests that the dehydration affects predominantly the cages (*can* units), as shown in Figure 4.14, where cage- and channel-volumes *vs. T* are shown (Table 4.16). These values have been modeled following the protocol reported in section 4.2.2.

The effects of the dehydration, manifested by the behavior of Si-O2-Al, can be described as a change in the tilting mechanism of the quasi-rigid $(Si,Al)O_4$ tetrahedra. This change can be followed through the evolution of several structural parameters of the *can* unit. The S6R⊥[0001] ditrigonal rotation angle $_{S6R\perp[0001]}$, first decreases (at 448 K) and then increases after the dehydration (Table 4.16). The loss of H_2O significantly affects the S4R units. The $O3\text{-}O4_{S4R}$ diameter (Figure 4.4) expands between 303 and 448 K, following the same, but opposite in sign, mechanism described at low-*T* (section 4.1) and high-*P* (section 4.2). At 748 K, we observe a shortening of this diameter (Table 4.16), as a consequence of the change in the tilting mechanism. The $O3\text{-}O4_{S4R}$ shortening likely governs the behavior of the cage volume, V_{cg}, between 448 and 748 K. This shortening is partially counterbalanced by the elongation of the $O3\text{-}O4_{12R}$ diameter in the 12-ring channel, which is, on the contrary, almost constant between 303 and 448 K (Figure 4.4, Table 4.16), as also observed at low-*T*

and high-*P*. The O1-$O1_{12R}$ channel diameter seems not to be affected by the dehydration, as it shows a continuous increase with temperature (Table 4.16). The *T*-induced structural response along *c* is driven by the expansion of the double chains of tetrahedra, well described by the O3-O4-O3 angle (Table 4.16), which induces a hexagonalization of the S6R-windows (S6R∠[0001]) linking cages and channels (Figure 4.4). In this case, excluding the effects due to the shortening of the unit-cell *c* parameter in response to dehydration, no change in the deformation mechanisms is shown.

A further deformation mechanism, observed in the low-*T* and high-*P* behaviors of cancrinite, is the flattening of the cage, described by the closure of the O2-O2-O2 angle (Figure 4.4) in response to the contraction of the double chains of tetrahedra along [0001], coupled with the constant value of the $(O2\text{-}O2)_{cw}$ diameter referred to as "cage width" (dashed lines in Figure 4.4). This mechanism acts as a marker of the change of tetrahedra tilting. Between 303 and 448 K, we observe an opening of O2-O2-O2, due to the constant O2-O2 "cage width" (Table 4.16), but between 448 and 748 K a slight flattening of the cage occurs, despite the expansion along [0001], due to a strong increase of the O2-$O2_{cw}$ (Table 4.16), which clearly marks a change in the framework deformation mechanisms.

Apparently, the channel-cations coordination environments do not seem to be affected by the dehydration process. An elongation of the shorter Na2-O1, Na2-O3′ and Na2-O4′ and a shortening of the longer Na2-O3″ and Na2-O4″ bond lengths is observed (Figure 4.3, Table 4.16). An increase in both the average < Na2-O_f> and < Na2-O_c> bond lengths with the framework- and (CO_3^{2-})-oxygen atoms, respectively, is observed (Table 4.16).

The reasons for the change in the tilting mechanism can be inferred by following the evolution of the Na1 coordination environment. At room conditions, the Na^+ cation is 8-fold bonded with four shorter lengths (to three O2 and one Ow) and four longer lengths (to three O1 and the other Ow) (Figure 4.3). At 448 K, we observe an increase in Na1-O2 and a decrease in Na1-O1 (Table 4.16), which is the same response, but opposite in sign, observed at low-*T* and high-*P* (sections 4.1 and 4.2). At 748 K, despite the continuous decrease in Na1-O1, an inversion of the Na1-O2 vs. *T* behavior is shown (Table 4.16). Therefore, we can infer that in the hydrous 303 – 448 K range, not affected by H_2O loss, the cancrinite structural evolution is driven by the same mechanism (but opposite in sign) which drives the framework re-arrangement at low temperature (down to 100 K) and high pressure (up to 6.63(3) GPa). The change in the tilting mechanism, induced by dehydration, is likely driven by the tendency to minimize the Na1-O1 and Na1-O2 distances, in order to compensate the loss in the bond-valence contribution of the H_2O oxygen site, Ow.

Comparison with previous studies

Hassan (1996a) and Hassan et al. (2006) described the thermo-elastic behavior of cancrinite on the basis of *in situ* powder diffraction data. A similar behavior can be deduced from our thermo-elastic parameters and those calculated on the basis of the data of Hassan et al. (2006), for the range 298-769 K, (*i.e.*, $\alpha_{V(303K,1bar)} = 4.7(8)*10^{-5}$ K^{-1}; $\alpha_{a(303K,1bar)} = 1.1(2)*10^{-5}$ K^{-1}; $\alpha_{c(303K,1bar)} = 2.4(5)*10^{-5}$ K^{-1}). However, our data about the dehydration process differ by those of Hassan (1996a, 1996b) and Hassan et al. (2006). Hassan (1996a, 1996b) and Hassan et al. (2006) set the heating rate as 60, 5 and 9.5 K/min, respectively. Sirbescu and Jenkins (1999) reported two comparative thermogravimetric analyses on a synthetic (CO_3^{2-})-cancrinite. In the first experiment, a computer-automated analysis, within the range 383-1623 K and a heating rate 2 K/min, was performed. For the second, a manual procedure was used with repeated weightings at each step until a constant weight was reached. The manual procedure required a period of 10 days, with an average heating rate of 0.06 K/min. Sirbescu and Jenkins (1999) reported a noticeable lower mass loss, at any given temperature, for the automated analysis. This was ascribed to the too faster heating rate (*i.e.*, 2 K/min), concluding that such a rate did not allow sufficient time for the volatiles to diffuse out of the cancrinite crystals. A release of "zeolitic H_2O" was reported within the range ~ 573-1058 K, with a dehydration rate that significantly decreases with increasing temperature (Sirbescu and Jenkins 1999). In our experiments, we increased temperature by step of 25 K, with a dwell time of about 30 minutes in order to achieve the structure relaxation. If we consider the slow mechanism of dehydration that we observed with our protocol, the heating rates adopted by Hassan (1996a, 1996b) and Hassan et al. (2006) appear to be too high, and so this might explain some differences on the dehydration process. Our experimental findings corroborate the results of Sirbescu and Jenkins (1999).

The protocol we used in this study was extremely useful to accurately bracket the dehydration-*T* and shed lights on the actual rate of the dehydration, which, to our knowledge, had not been reported so far. In fact, as shown in Table 4.12, the process of dehydration at 748 K took approximately 12 days. Moreover, a more detailed description of the *T*- and dehydration-induced structural re-arrangement has been carried out, since this was lacking or was not the main topic in the previous studies devoted to cancrinite behavior at high-temperature (Hassan 1996a, 1996b; Sirbescu and Jenkins 1999; Fechtelkord et al. 2001a; Hassan et al. 2006; Isupova et al. 2010). It is interesting to point out some similar findings between our structural data and those from Fechtelkord et al. (2001a) and Isupova et al. (2010). In particular: i) Fechtelkord et al. (2001a) reported two structure refinements of a NO_3-

cancrinite at room-*T* and its partially dehydrated form at 673 K, showing a decrease of Na1-O1 and a constant Na1-O2; ii) an inversion of the Si-O2-Al *vs*. *T* behavior following the dehydration process was reported by Isupova et al. (2010), showing strong similarities with T-O-T *vs*. *T* behavior from our data (Table 4.16).

Figure 4.10 The evolution of the unit-cell parameters of cancrinite as a function of temperature. Full symbols represent data collected with increasing-*T*, open symbols represent data collected during the cooling.

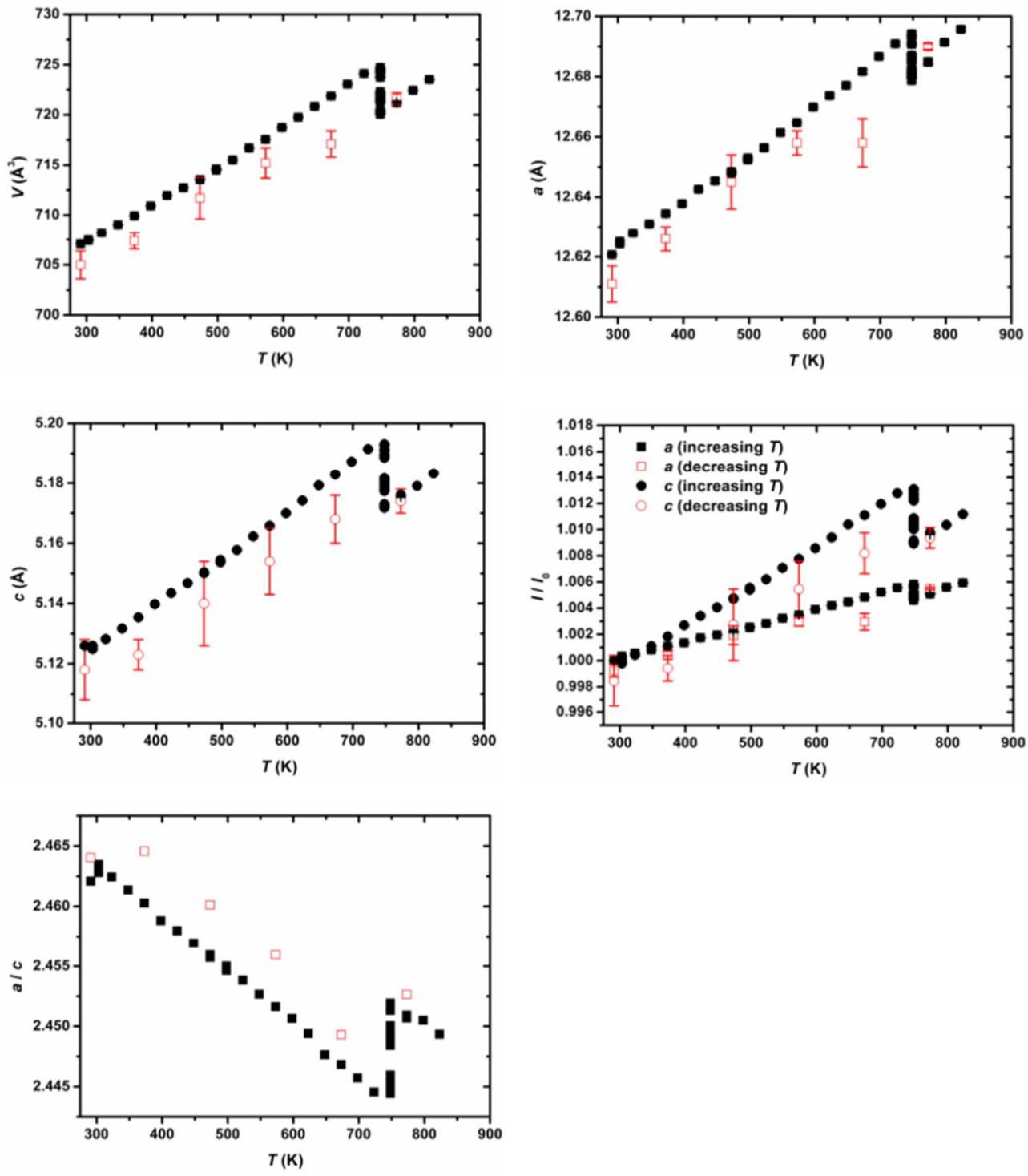

Figure 4.11 Variations of unit cell volume, a/a_0 and c/c_0, and a/c ratio with increasing time at constant temperature (748 K). The e.s.d.'s are smaller than the symbols.

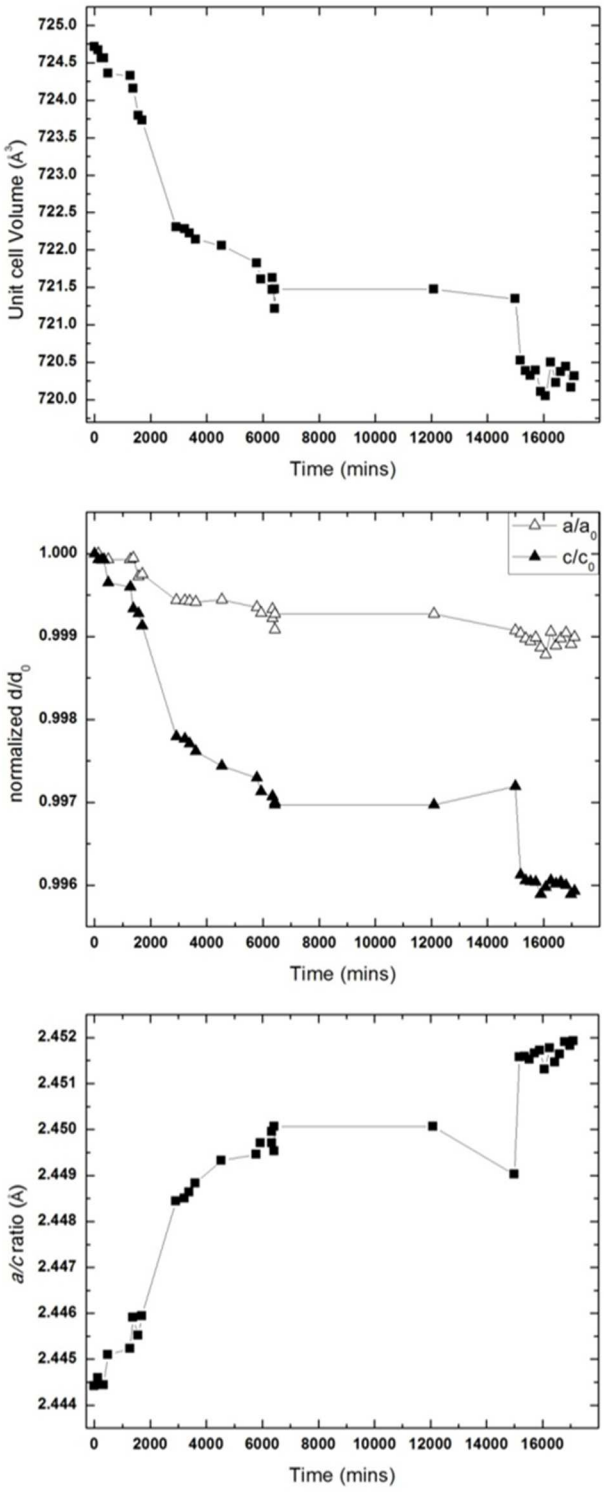

Figure 4.12 (*Top*) Difference-Fourier map of electron density phased without the CO_3^{2-} groups at T = 303 K; $0 < c < 1$, $-0.2 < x < 0.2$. (*Bottom*) Difference-Fourier map of electron density phased without the Ow sites at T = 748 K, showing the *can* unit content in a plane parallel to (0001) at z = 0.20 (H_2O molecules).

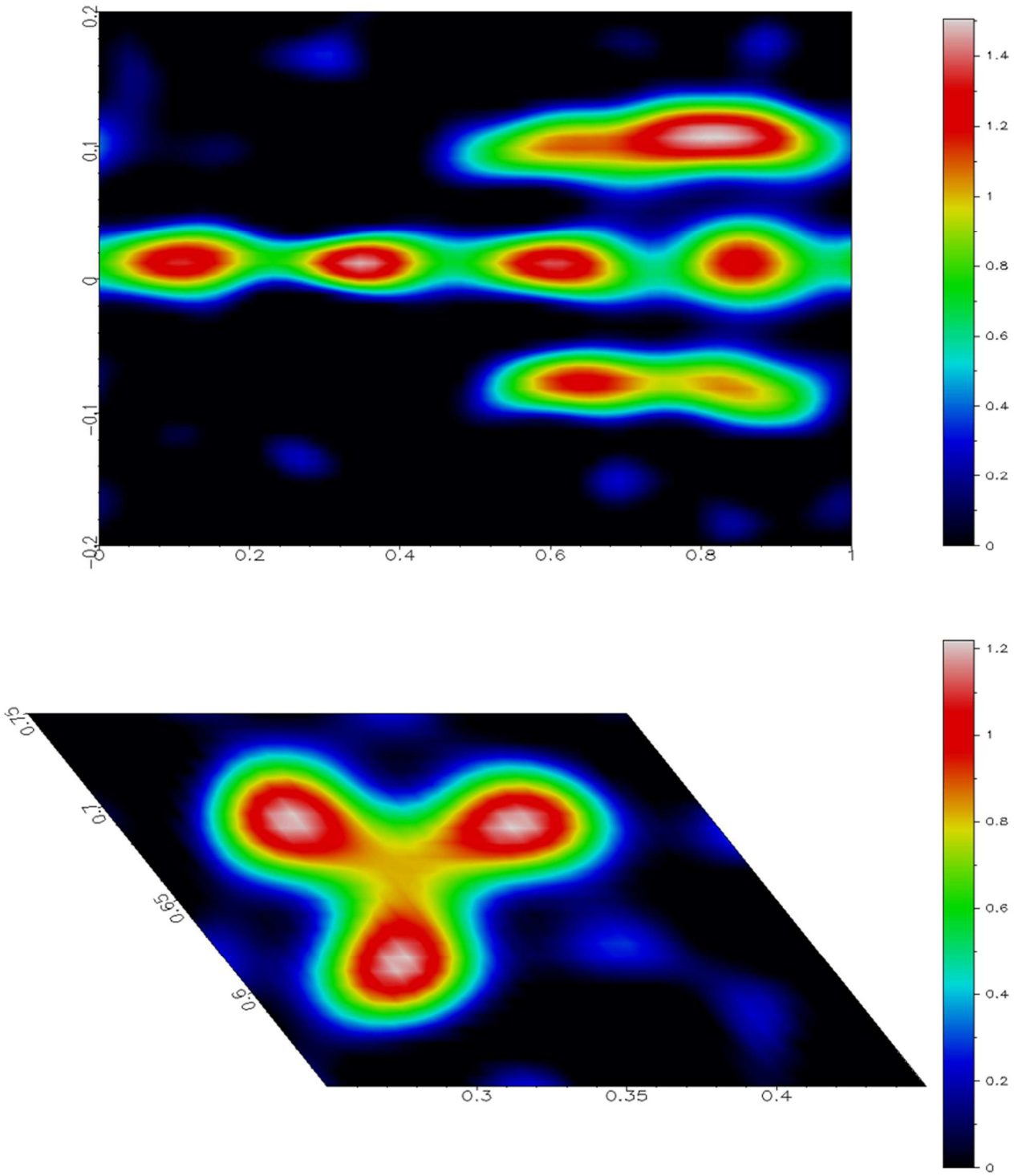

Figure 4.13 Difference between experimental and calculated volume (by thermal equation of state fit), δ*V*, as a function of temperature. The δ*V* clearly shows that both the modified equations of Pawley et al. (1996) and Berman (1988) reproduce very well the thermal expansion behavior from room-*T* to 748 K, with the exception of the last data points due to the impending dehydration (arrow). The grey area represents the average δ*V* *e.s.d.* deduced on the basis of the experimental and calculated *V* *e.s.d.*.

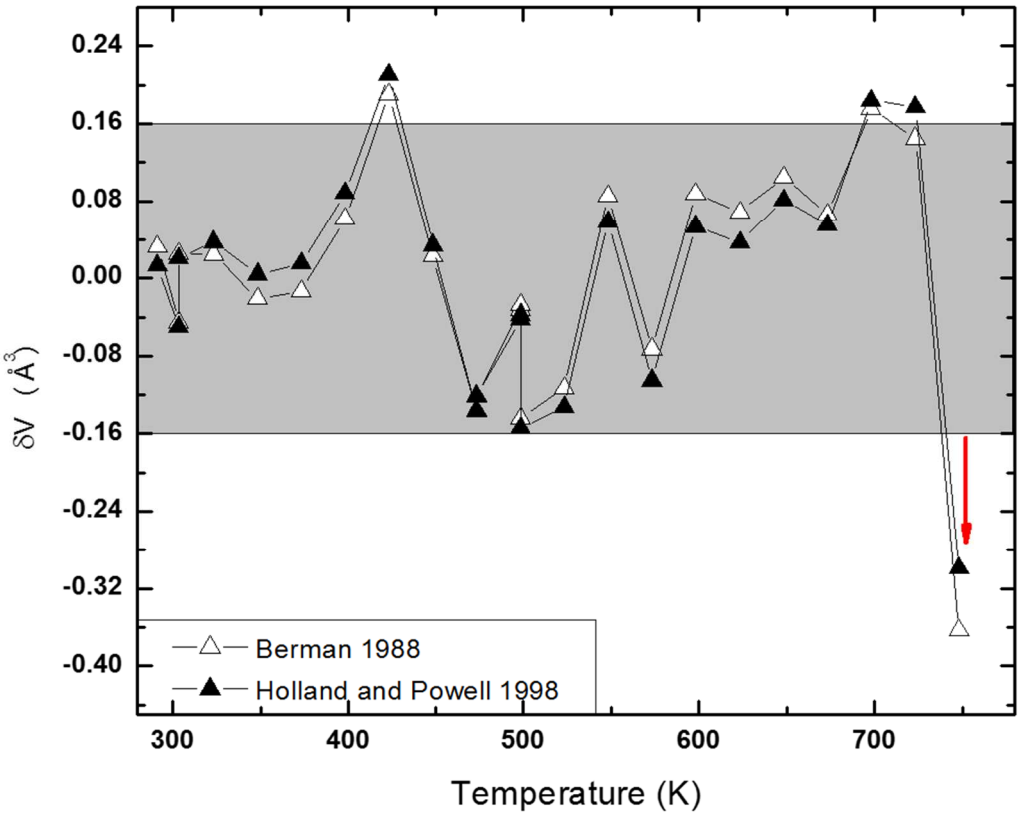

Figure 4.14 (*Left side*) Evolution of the Si-O-Al intertetrahedral angles (normalized to the values at 303 K) with *T*. (*Right side*) The variation with *T* of the channel (V_{ch}) and *can* unit (V_{cg}) volumes

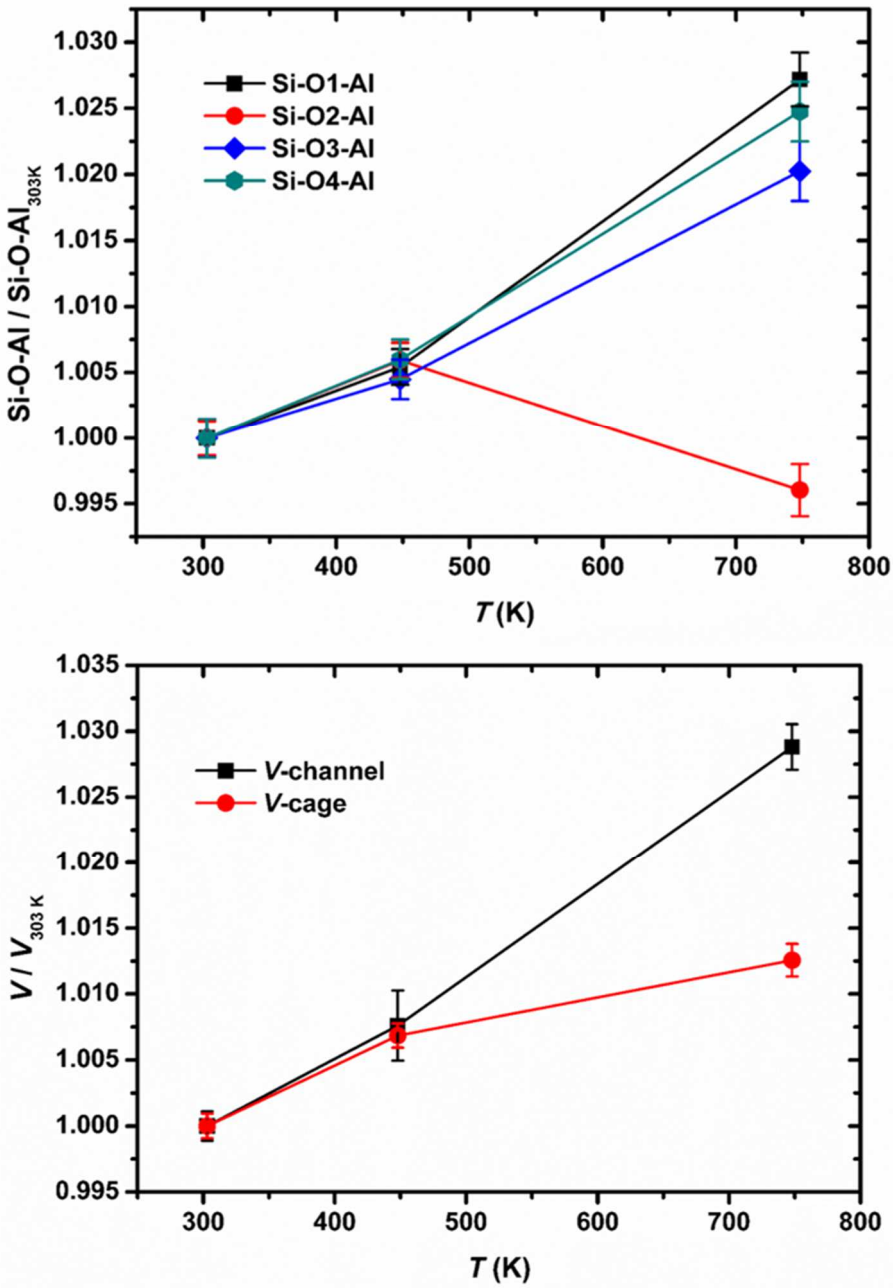

Chapter 5

Vishnevite

5.1 VISHNEVITE BEHAVIOR AT LOW TEMPERATURE AND HIGH PRESSURE

5.1.1 Materials and experimental methods

Small single-crystal fragments of vishnevite, from a sample of the type locality (Vishnevye Gory, Urals, Russia), have been selected for the low-temperature and high-pressure diffraction experiments. An inspection at the polarized light microscope did not show any defect at the optical scale. A fragment (120*100*80 μm^3) was selected for the chemical analysis, performed using a JEOL 8200 electron microprobe, operating at 15 kV acceleration voltage and 5 nA incident beam, with 3 μm beam size. The following natural standards were used: omphacite (Na), realgar (S), anorthite (Ca, Al), K-feldspar (K), wollastonite (Si) and celestine (Sr). The average chemical formula, based on five point analyses and calculated on the basis (Si + Al) = 12 a.p.f.u., is: $(Na_{5.22}K_{1.64}Ca_{0.07}Sr_{0.01})(Si_{6.13}Al_{5.87}O_{24})(SO_4)_{0.58}$ (Table 5.1).

The *in situ* low-*T* diffraction experiments have been performed using an Oxford Diffraction Gemini Ultra diffractometer, operating at 50 kV and 40 mA, with a graphite-monochromatized Mo-Kα radiation. A crystal ~ 130*105*90 μ^3 was used. Two intensity datasets, at 293 (room-conditions) and 110 K, were collected using a combination of ω scans, with 1° steps and 90 s exposure time per frame. The crystal was cooled using an Oxford Cryosystems 700 series nitrogen-flow cryostat, with 2 K absolute uncertainty and 0.2 K temperature stability at the crystal position. The diffraction peaks were compatible to the $P6_3$ space group and the following unit-cell parameters at 293 and 110 K, respectively, were measured: a_{293K} = 12.7613(7) Å , c_{293K} = 5.2231(2) Å and V_{293K} = 736.63(9) $Å^3$, a_{100K} = 12.7223(6) Å , c_{100K} = 5.1918(3) Å and V_{100K} = 727.75(8) $Å^3$. Intensity data have been integrated and corrected for Lorentz-polarization effect and crystal absorption using the CrysAlis software (Agilent 2012).

The high-pressure experiments have been performed at the ID09A beamline of the European Synchrotron Radiation Facility (ESRF), Grenoble, France. A parallel monochromatic beam (E ~ 30 kEv, λ = 0.414 Å) was used. The beam was vertically focused by a spherical mirror and horizontally by a bent silicon-(111) monochromator, in order to have a beam-size at the sample position of 30*30 μm^2. The diffraction pattern was collected by an online MAR555 flat panel detector. A single-crystal was selected and cut: a fragment ~ 110*110*90 $Å^3$ was selected to collect an intensity dataset in air. The data collection strategy consisted in a rotation of the crystal about a vertical ω-axis, within the

range -45° ≤ ω ≤ +45°, with 1° step scan and 1 s exposure time per frame. A further fragment, ~ 70*55*50 $Å^3$, was loaded, along with few ruby chips as pressure calibrants (Mao et al. 1986), in a membrane-controlled diamond anvil cell, with Boehler-Almax design, 600 μm diamond culet-size and cone-aperture of 60°. A stainless-steel gasket was first pre-indented to ~70 μm and a hole, 250 μm in diameter, was drilled by a spark-eroder as *P*-chamber. A nominally anhydrous 4:1 methanol:ethanol mixture was used as *P*-transmitting medium (Angel et al. 2007). Diffraction data have been collected at twenty-two different pressures, from 0.20(2) (P_1) to 7.40(4) (P_{22}) GPa., following an ω stepwise rotation from -30° to +30°, as delimited by the DAC opening angle, with 1° steps and 1 s exposure time per frame. Unit-cell parameters, from P_0 (air) to P_{22}, have been refined and are reported in Table 5.2. Intensity data have been integrated and corrected for Lp-effect using the CrysAlis software (Agilent 2012), the correction for absorption (from the DAC) and for different diffracting volume, as a function of ω rotation, was applied using the ABSPACK routine implemented in CrysAlis. Further details on the data collections are in Table 5.3.

5.1.2 Structure refinements and high-pressure structural re-arrangement

The structure refinements from the low-*T* datasets have been performed using the SHELXL software (Sheldrick 1998, 2008), implemented in the WinGX suite of crystallographic programs (Farrugia 1997). Neutral scattering factors for O, Si, Al, Na, K and S have been taken from the *International Tables for Crystallography, Volume C* (Wilson and Prince 1999). The framework coordinates of cancrinite refined from the room-*T* dataset of the present study (section 4.1) were used as starting model. The extraframework population was identified by Fourier synthesis. The *can* units are occupied by a cation site on the 3-axis (Na) and by three mutually exclusive H_2O oxygen sites (Ow) out of the triad (Fig. 5.1). Two mutually exclusive cation sites are close to the channel walls: an "internal" site (M1) occupied by K^+ and an "external" one (M2) occupied by Na^+ (Fig. 5.1), as previously reported in the literature. The difference-Fourier maps of electron density, phased without the anionic groups, showed a disordered distribution along the 6_3 axis at the channel center (Fig. 5.2). The same disordered distribution, from which two maxima emerged at different height, was also observed around the screw axis at positions compatible to the triangular basis of the sulfate tetrahedron. A configuration given by two SO_4^{2-} tetrahedra, the first showing the apical oxygen pointing downward and the second upward (Fig. 5.1), can be suggested, as already reported in the literature (Hassan and Grundy 1984; Della Ventura et al. 2007). In such a case, two split sites for the

sulfur (S1 and S2) have been modeled, along with two symmetry-independent sites for the basal oxygen (Ob1 and Ob2). The location of the apical oxygen atoms is not trivial, and their refinement is practically impossible, due to the too short distances of the sites along the 6_3 axis. Therefore, the sulfate apical oxygen was not added in the model. In order to stabilize the refinement, the site occupancy factors of the sulfate sites (*i.e.* S1, S2, Ob1 and Ob2) belonging to the same group were restrained and the two configurations (S1-Ob1 and S2-Ob2) were set as equally probable. In addition, the S1-Ob1 and the S2-Ob2 bond lengths have been restrained to 1.45(1) Å. The first cycles were performed using isotropic atomic displacement parameters, which were later turned to anisotropic for the framework sites and Na (the Na^+ site within *can* units). The refinement from the 110 K dataset has been performed starting from the room-*T* model, following the same strategy and constraining the occupancy of the extraframework sites to the values refined at 293 K. Both the refinements converged with residuals in the difference-Fourier map $\leq \pm 1.05$ $e^-/Å^3$ and no significant correlation between the refined parameters. Further details on the structure refinements are in Table 5.3. Atomic coordinates, occupancy factors and isotropic\equivalent atomic displacement parameters are in Table 5.4. Anisotropic atomic displacement parameters are listed in Table 5.5.

The structure refinement from the room-*P* dataset, collected at ESRF, has been performed using the JANA2006 software (Petricek et al. 2006). The starting model was set to the framework coordinates refined from the 293 K dataset. The extraframework population was identified through Fourier synthesis. A similar electron density distribution at the channel center was found (Fig. 5.2) and the same sulfate configurations, previously reported, were adopted. In addition, a strongly anisotropic (along [0001]) electron density distribution, related to the cage-Na, was also found. The cage-Na positional disorder was modeled through two split sites (Na1 and Na2). In the final cycles, only the framework sites were refined with anisotropic *adp*'s. In order to get a stable refinement, the same bond lengths and occupancy restrictions, described above for the sulfate sites, have been applied. In addition, Na1-Na2, M1-M2 and all the sulfate sites have been constrained to share the same *adp*, respectively. Twelve high-pressure datasets have been selected to perform the structure refinements. In order to compensate for the reduction in the number of observed reflections, due to the DAC shadowing, further restraints were applied. The Si-Al and the framework oxygen sites were also constrained to share the same *adp*, the Si-O and Al-O bonds were restrained to the P_0 refined values ± 0.01 Å and the occupancies were constrained to the P_0 values, except for Na1 and Na2, which were allowed to vary keeping the total sum constant. The (*x*,*y*)-coordinates of the sulfate-group basal oxygen sites (*i.e.* OB1 and OB2) and the isotropic *adp* shared by all the sites belonging to the sulfate

group were constrained to the values refined at room-*P*. At $P \geq 3.43(4)$ GPa, the refined parameters related to the sulfate tetrahedron suggested a change in the anion configuration. An inspection through the Fourier synthesis revealed a clearly different distribution of electron density, if compared to those observed up to 3.24(9) GPa (Fig. 5.2). The two maxima, emerging from the continuous distribution along the 6_3 axis, were assigned to the S site and to the apical oxygen site (Oa). A single upward configuration (Fig. 5.3) was adopted, after inspection of the Fourier peaks around the screw axis. The triangular base of the sulfate tetrahedron (Ob) was fixed at reasonable *x*,*y* coordinates (0.12,0.06), inferred from the Fourier maps, leaving *z* free to vary. If compared to both the configurations shown by the sulfate tetrahedra before the anion re-arrangement, the new sulfate tetrahedron is rotated by ~ 60° along [0001]. Further discussion on this subject is in the section 5.1.4. The occupancy of the new S, Ob and Oa sites was fixed accondingly to the P_0 values. All the refinements converged with no significant residuals in the difference-Fourier map of electron density and correlation between the refined parameters. Atomic coordinates, site occupancy factors and isotropic atomic displacement parameters are given in Table 5.4. Anisotropic atomic displacement parameters from the P_0 dataset are in Table 5.5. Both the low-*T* and high-*P* refinements showed a twinning of the crystal, with a' = 0 1 0, b' = 1 0 0, c' = 0 0 -1 and twin ratio about 0.60:0.40. Further details pertaining to the structure refinements are in Table 5.3.

5.1.3 Results

Elastic behavior

The studied sample of vishnevite keeps its crystallinity up to the highest pressure investigated, 7.40(4) GPa. Figure 5.4 shows the experimental unit-cell volume data as a function of pressure. Two subtle discontinuities can be found between 2.47(2) and 2.84(10) GPa and between 3.43(4) and 3.83(9) GPa, from which three pressure regimes can be defined. The bulk elastic behavior in the first *P*-regime [P_1-P_8, 0.20(1)-2.47(2) GPa] has been determined by fitting the experimental data to a Birch-Murnaghan equation of state truncated to the third order (III-BM EoS, Birch 1947, Angel 2000). Due to the limited number of experimental data, large uncertainties resulted in the refined parameters: V_0 = 733.8(8) Å^3, K_{V0} = 49(4) GPa, K_V' =5.4(33). The refinement of a second order BM-EoS yielded the following refined parameters: V_0 = 733.5(4) Å^3, K_{V0} = 50.8(10) GPa. The unit-cell linear elastic behavior, along the *a* and *c* directions, has been determined by the fit of "linearized" BM-EoS (Angel 2000). The fit

of III-BM EoS yielded: a_0 = 12.765(3) Å, K_{a0} = 56(4) GPa, K_a' = 7.3(32); c_0 = 5.202(2) Å, K_{c0} = 37(2) GPa, K_c' = 5.0(20). The fit of II-BM EoS gave: a_0 = 12.762(2) Å, K_{a0} = 59.8(9) GPa; c_0 = 5.2013(9) Å, K_{c0} = 38.0(6) GPa. Due to the very low number of experimental data within the second *P*-regime [P_9-P_{11}, 2.84(10)-3.43(4) GPa], a fit by an equation of state was impossible. However, the average volume and linear compressibilities could be calculated, from which the resulting average volume and "linearized" bulk muduli are derived: K_V = 47(2) GPa, K_a = 55(3) GPa and K_c = 37(1) GPa. The elastic behavior in the third *P*-regime [P_{12}-P_{22}, 3.83(9)-7.40(4) GPa] has been determined by fitting the experimental data to a III-BM-EoS. The following elastic parameters, for the volume and the *a* and *c* edges, have been refined: V_0 = 757(6) Å^3, K_{V0} = 30(3) GPa, K_V' =2.6(5); a_0 = 12.844(19) Å, K_{a0} = 40(3) GPa, K_a' = 1.8(4); c_0 = 5.325(29) Å, K_{c0} = 16(3) GPa, K_c' = 3.6(5). All the equations of state fits have been performed using the EoSFit v5.2 (Angel 2000).

The average thermal expansion coefficients between 293 and 110 K were calculated: $\alpha_V = 6.32(9)*10^{-5}$ K^{-1}, $\alpha_a = 1.59(5)*10^{-5}$ K^{-1}, $\alpha_c = 3.12(5)*10^{-5}$ K^{-1}.

High-pressure and low-temperature structure evolution

The pressure-driven structure evolution of vishnevite, with the exception of the channel population re-arrangement between 3.24(9) and 3.43(4) GPa, is mainly governed by the tilting of the quasi-rigid tetrahedra. The average (Si,Al)-O bond lengths evolution with pressure is constant within the estimated standard deviation (Table 5.6). The Si-O-Al intertetrahedral angles all show a closure with increasing pressure (Fig. 5.5, Table 5.6).

The mechanisms of structure deformation, at $P \leq 3.24(9)$ GPa can be described through the strain of the composite building units of the [CAN]-framework. The S6R⊥[0001], corresponding to the *can* unit basis, undergoes an increase in its ditrigonal rotation angle $\alpha_{S6R\perp[0001]}$ (section 4.1.2; Fig. 5.5 and 5.6, Table 5.6). The increase in the ditrigonal character of the ring also induces a shortening along the O2-O2$_{S6R\perp[0001]}$ diameter (Fig 5.6, Table 5.6). Both the symmetry-independent channel diameters, O1-O1$_{12R}$ and O3-O4$_{12R}$, are shortened with pressure, following a stronger trend for O1-O1$_{12R}$ (Fig. 5.5 and 5.6; Table 5.6). The S4R's, making the *dzc* chains, show a compression along the O3-O4$_{S4R}$ (Fig. 5.6, Table 5.6). Along [0001] the compression of the *dzc* chains, well described by the closure of the O3-O4-O3 angle (Fig. 5.6, Table 5.6), occurs. The cage behavior is mainly represented by a flattening, as confirmed by the closure of the O2-O2-O2 angle (Fig. 5.5 and 5.6, Table 5.6).

At $P \geq 3.43(4)$ GPa, the structural re-arrangement of the sulfate tetrahedron, previously described, occurs. The main effect on the tetrahedral tilting is given by a significant increase in the rate of some of the deformation mechanisms described above. An inspection of the Si-O-Al angles reveals a fall of the Si-O2-Al values at the highest experimental pressures (Fig. 5.5; Table 5.6). The most significant increase in the deformation rate is shown by the S6R⊥[0001] ditrigonal rotation angle $\alpha_{S6R\perp[0001]}$ (and the related O2-O2$_{S6R\perp[0001]}$ compression), the O1-O1$_{12R}$ channel diameter and the O3-O4-O3 angle, related to the compression of the *dzc* chain (Fig. 5.5; Table 5.6). In addition, a stronger flattening of the cage is also shown (Fig. 5.5, Table 5.6).

The most striking effect of the sulfate re-arrangement is, likely, the displacement of the M1 and M2 cations towards the center of the channel, which is significant at $P \geq 3.43(4)$ GPa, as the atomic fractional coordinates reported in Table 5.4 show. In general, a shortening of the M2-O3′ and M2-O4′ and an increase of the M2-O3″ and M2-O4″ bond lengths occurr (Fig. 5.1, Table 5.6). A compression of the M1-O3′ and M1-O4′ is shown up to the sulfate re-arrangement, after which a constant value is observed (Fig. 5.1, Table 5.6). On the contrary, a constant M2-O1 bond is shown up to 3.43(4) GPa, after which a clear compression occurs (Fig. 5.1, Table 5.6). With the exception of a slight shortening of the Na-O2 bonds, any significant change in the Na^+ coordination environment apparently occurs up to 3.43(4) GPa; at high-*P* a clear increase in the Na-O1 and a strong compression of the Na-O2 are shown (Fig. 5.1, Table 5.6).

Fig. 5.5 and Table 5.6 show the *P*-induced evolution of the channel and cage volumes, defined as in section 4.2.2. A visual inspection of the diagram allows the identification of an enhanced compression of the channel, if compared to the cage, following the sulfate re-arrangement. Despite the low number of experimental data (Table 5.6), obtained by the structure refinements from the selected datasets, a fit by a II-order BM-EoS has been done, using the EoSFit v.5.2 software (Angel 2000). For the "*pre*-sulfate re-arrangement" range, the following parameters were refined for the channel and the cage, respectively: V_{ch0} = 323.8(13) Å^3, K_{V0ch} = 35(3) GPa; V_{cg0} = 205.9(7) Å^3, K_{V0cg} = 57(6) GPa. For the "*post*-sulfate re-arrangement range", the refined parameters are: V_{ch0} = 371(8) Å^3, K_{V0ch} = 10.1(12) GPa; V_{cg0} = 208(2) Å^3, K_{V0cg} = 40(6) GPa.

Despite only two structure refinements are available for the low-*T* regime (i.e. 293 and 110 K), the good quality of the data allows to identify the same deformation mechanisms previously described (Table 5.6), even though with a different magnitude.

5.1.4 Discussion

Structure model

The models adopted for the vishnevite structure refinements, from both the low-*T* and high-*P* datasets, are consistent to those reported in the literature (Hassan and Grundy 1984; Della Ventura et al. 2007). As previously discussed, the disordered distribution of electron density along the 6_3 axis (Fig. 5.2) did not allow the refinement of the apical oxygen atoms of the two mutually exclusive sulfate tetrahedra, one pointing downwards and the other upwards (Fig. 5.1). The splitting of the sulfur site in two mutually exclusive positions was preferred. For the refinements from the high-pressure datasets, the Na^+ site within the cages was also split in two subsites. Although not usual in the literature, such a model is consistent with the strong anisotropic atomic displacement parameter of the Na site from the low-*T* refinements (Table 5.5). The occurrence of few vacancies, in both the Na^+ and H_2O positions, likely induces a slight displacement of the Na-H_2O clusters along the 3-axis, in order to optimize distances and bond lengths. The crystal chemical formula from the 293 K structure refinement is: $[Na_{3.49}K_{2.04}(SO_4)_{0.69}][Na_{1.68}(H_2O)_2][Si_6Al_6O_{24}]$. For the high-*P* datasets, if the M1 site occupancy (refined using the Na scattering factor alone) is transformed into the equivalent K value (*sof*(Na):*sof*(K) = 19:11), the crystal chemical formula from the room-*P* structure refinement is: $[Na_{3.38}K_{1.80}(SO_4)_{1.00}][Na_{1.62}(H_2O)_{1.85}][Si_6Al_6O_{24}]$. A good agreement, between the compositions of the *can* units, is shown by the two models. If we calculate the number of electrons at the channel cation sites, from the two refined formulae we obtain: (3.49*11) + (2.04*19) = 77.15 e^- and (3.38*11) + (1.80*19) = 71.38 e^-, respectively, which differ for 5.77 e^- only, equal to $Na_{0.52}$ or $K_{0.30}$. If we assume the Na content of the *can* units to be 1.65 atoms per formula unit (average between the two aforementioned models), the channel population from the chemical analysis is: $[Na_{3.57}K_{1.64}Ca_{0.07}Sr_{0.01}(SO_4)_{0.58}]$, from which 72.21 electrons of the cations sites can be derived, showing a good agreement with the structure refinements. The overestimated K content, in both the structure refinements formulae, suggests slight substitution of K^+ by Na^+ at the M1 site, as also shown by davyne (see chapter 7). On the contrary, a discordant and overestimated sulfate content is shown by the formulae from the structure refinements. However, if we consider the strong disorder of the electron density along [0001] and the adopted model, this is not surprising. In fact, it was impossible to avoid, in the refinement of the occupancies of the S sites, the contribution from the apical oxygen atoms, only partially compensated by the restraints to the Ob sites occupancies. As already reported in the literature (*e.g.* Bonaccorsi et al. 2001), the occurrence of two subsequent sulfate tetrahedra, at

z and *z* ± 0.5, is impossible, due to too shorts contacts. The occurrence of too short contacts also prevent the co-existence of neighboring sulfate and cations in M1, at the same height. Therefore, two kind of alternating clusters can occurr: [$^{M2}Na_3(SO_4)$] and [$^{M1}(K,Na)_3$]. The presence of vacancies at the anionic sites, suggested by both the chemical analysis and the low-*T* refinements, likely prevents an ordered distribution of these clusters along [0001].

Elastic behavior

The elastic behavior of vishnevite is characterized by a strong increase in compressibility, which likely follows the structural re-arrangement of the channel extraframework population, occurring between 3.24(9) and 3.43(4) GPa. This *P*-induced structural re-arrangement approximately occurs in the mid of the second elastic regime [P_9-P_{11}, 2.84(10)-3.43(4) GPa], as previously defined, which shows a volume compressibility approximately intermediate between those refined from the first and the third *P*-ranges. Therefore, it can be hypothesized that the experimental results from this second *P*-range could correspond to a metastable configuration related to the re-organization of the channel population.

In vishnevite, the most compressible direction is along *c*, with an elastic anisotropy at room conditions given by K_a:K_c = 1.51:1, which likely increases with pressure within the first *P*-range, as the refined K_l' and the data in Fig. 5.4 suggest. Interestingly, a comparison to the elastic behavior of cancrinite in the range 0.0001-4.62(3) GPa yields a very similar elastic anisotropy at room-*P*: K_a:K_c = 52(4):34(2) = 1.53:1. If we consider the average bulk moduli calculated for the second *P*-range, we obtain an elastic anisotropy K_a:K_c = 1.49:1, whereas the calculated elastic anisotropy at 3.83(9) GPa (at the beginning of the third *P*-range), from the refined III-BM EoS parameters, is $K_a(P_{12})$:$K_c(P_{12})$ = 46:28 = 1.64:1, which tends to decrease at the highest experimental pressures.

Despite the sample did not show any hint for a structure collapse nor for a loss of crystallinity, except for a decrease in the diffracted intensities from the very last high-*P* points, the elastic softening in the third *P*-range, suggest the onset of a metastable configuration, as will be further discussed in the next section.

About the thermo-elastic behavior in the range 110-293 K, it is interesting to note the strong thermo-elastic anisotropy, where *c* corresponds, by far, to the most expandable direction. Similarly, a strong anisotropy was shown by cancrinite (section 4.1), whereas the same is not valid for davyne and balliranoite (chapters 6 and 7).

An unambiguous interpretation of the high-pressure behavior of vishnevite is not trivial. As in the other studied cancrinite-group minerals, in vishnevite a quasi-rigid behavior of the $(Si,Al)O_4$ tetrahedra is observed. Therefore, the *P*-induced strain is accommodated by the tilting of the tetrahedra: as in cancrinite and differently from davyne and balliranoite, all the Si-O-Al intertetrahedral angles undergo a closure with pressure (Fig. 5.5, Table 5.6). The structure refinements up to 3.24(9) GPa describe the structure evolution responsible for the elastic behavior of the first *P*-range, and reveal a similar framework deformation as that observed in cancrinite. The strain in the (0001) plane is accommodated by several non-independent mechanisms: 1) a strong ditrigonal rotation of the S6R⊥[0001], which induces the shortening of the $O2\text{-}O2_{S6R\perp[0001]}$ diameter; 2) the channel compression along both the independent diameters $O1\text{-}O1_{12R}$ and $O3\text{-}O4_{12R}$; 3) the shrinking of the S4R units along $O3\text{-}O4_{S4R}$. The bulk compression along the [0001] crystallographic direction is accommodated by the *dzc* chains, which shorten through the tilting of the tetrahedra around the O3 and O4 "hinges", as well described by the closure of the O3-O4-O3 angle (Fig. 5.6; Table 5.6). Besides the shrinking of the almost circular channel, a significant flattening of the *can* units occurs, as confirmed by the closure of the O2-O2-O2 angle (Fig. 5.5 and 5.6; Table 5.6). The second elastic regime, described between 2.84(10) and 3.43(4) GPa, could be a hint for the upcoming structural re-arrangement. Between 3.24(9) and 3.43(4) GPa, the sulfate tetrahedron undergoes a reconfiguration, which likely triggers the observed increase in compressibility and clearly induces a change in the deformation mechanisms affecting the channel population. The refined model, from both the room-*P* and the 293 and 110 K datasets (Table 5.4), shows the sulfate tetrahedra pointing the vertices of the triangular basis more or less towards the neighboring Na^+ cations in M2, so that a single and strong M2-Ob bond occurs (Fig. 5.1). This is the same configuration observed for the davyne samples studied in this work (see chapter 7) and for davyne structures reported in the literature (*e.g.* Bonaccorsi et al. 1990, 1995; Hassan and Grundy 1990). A similar configuration was also reported for the long-range ordered pitiglianoite (Merlino et al. 1991), chemically analogous to vishnevite. On the contrary, in cancrinite and balliranoite (see chapters 4-6 and cited references), the triangular carbonate groups point their edges towards the neighboring Na^+ and Ca^{2+} cations (*i.e.* the O_{CO3} oxygen are rotated of about 60° with respect to the O_{SO4}), in order to have two (Na,Ca)-Oc bonds (see Fig. 4.3 and 6.2). The sulfate configuration in vishnevite, at room conditions, likely prevents both the shortening of the M1-O1 bond and the displacement of the cations towards the channel center. An increasing instability of the resulting cations coordination environment could lead to the re-arrangement of the sulfate

tetrahedron into a single upward configuration, with the triangular basis resembling that of the carbonate groups in cancrinite (Fig. 5.3). This is, apparently, confirmed by the strong displacement of the M1 and M2 sites towards the channel center at $P \geq 3.43(4)$ GPa, likely in order to fit energetically favorable bonds (Table 5.4). An inspection of the *P*-evolution of the cage-Na^+ coordination environment shows a compression of the shorter Na-O2 bond lengths (Table 5.6), within the entire *P*-range investigated, which reinforce the mainly tetrahedral character of the Na-coordination shell. The longer Na-O1 bonds are constant up to the sulfate re-arrangement and, later, undergo a clear elongation. We propose this behavior to be a consequence of the interaction between O1 and $^{M2}Na^+$, previously discussed. It is interesting to note that the re-configuration of the channel extraframework population is followed by a strong increase in the rate of several deformation mechanisms, in particular: the increase in the S6R⊥[0001] ditrigonal rotation angle $\alpha_{S6R\perp[0001]}$, the $O1\text{-}O1_{12R}$ channel diameter and the O3-O4-O3 angle compressions (Fig. 5.5; Table 5.6). These features and the anomalously low compressibility shown by the studied vishnevite at $P \geq 3.83(9)$ GPa, likely suggest that, though the apparent stability up to 7.40(4) GPa, the structural configuration following the channel population re-arrangement is probably metastable and unlikely to occur in a natural geological environment.

Despite a comprehensive analysis of the low-*T* structure evolution of vishnevite is impossible, an inspection of the change in the structural parameters between 293 and 110 K (Table 5.6) reveals that, though with a different magnitude, the bulk volume contraction is accommodated by the same deformation mechanisms which accommodate the strain in the previously described low-*P* regime.

5.1.5 Conclusions

The elastic behavior of vishnevite in the low-*P* regime (*i.e.* $P \leq 2.47(2)$ GPa) reveals strong similarities to the volume compressibility and elastic anisotropy shown by cancrinite in the same *P*-range. In addition, the same framework deformation mechanisms were found to govern the structure evolution at pressure up to 3.24(9) GPa. An apparent increase in compressibility in the range $2.84(10) \leq P$ (GPa) $\leq 3.43(4)$, possibly suggests the onset of structural instability, likely related to the occurrence of too short cation-oxygen contacts within the channels. Between 3.24(9) and 3.43(4)

GPa, a structural re-arrangement affects the sulfate tetrahedra and, more in general, the channel extraframework population. As a consequence, a migration of the cations towards the channel center occurs at $P \geq 3.43(4)$ GPa. This reconfiguration of the channel environment is followed by a strong increase in compressibility, as shown by the small values of the refined K_0 and K'. The elastic softening, coupled with the strong rate of deformation of several structure parameters, suggests a metastable nature of the high-pressure vishnevite structure.

Figure 5.1 (*Left side*) The Na-coordination environment within the *can* unit. A 4+4 coordination is shown, with a strong tetrahedral shell involving the three O2 and the closer Ow′ sites. (*Right side*) The K (M1) and Na (M2) coordination environments within the channel. The upward (S1-Ob1) and downward (S2-Ob2) sulfate anions (without the apical oxygen) are also shown. In both the pictures, dashed lines represent mutually exclusive bonds.

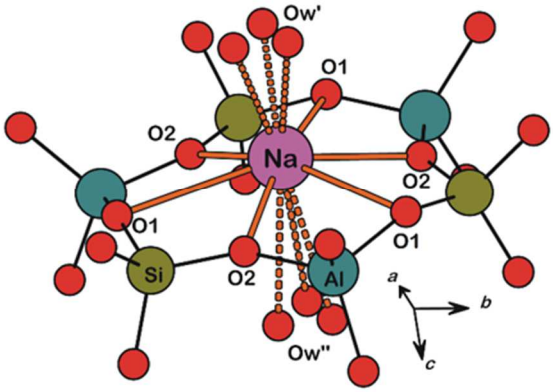

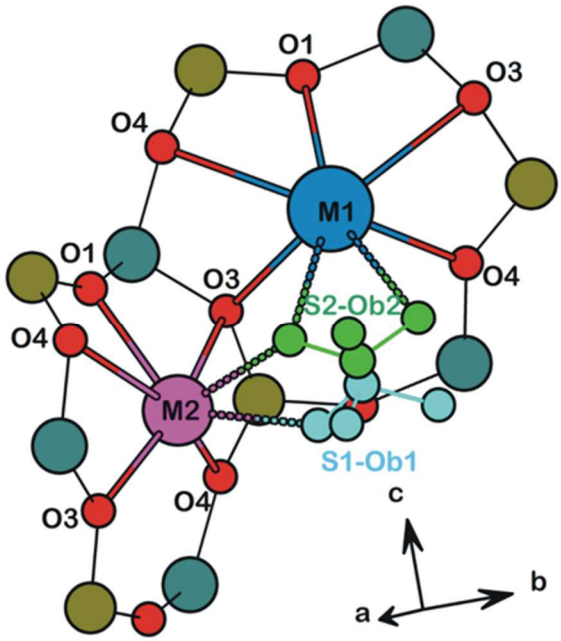

Figure 5.2 (A) Difference-Fourier map of electron density, phased without the sulfate anion, at the center of the channel, from the room-*P* dataset. The modeled positions for the S1 and S2 sites are shown. (B) Difference-Fourier map of electron density, phased without the sulfate anion, showing a section perpendicular to [10.0] at x = 0.06. Modeled positions for the Ob sites are shown. (C) Difference-Fourier map of electron density, phased without the sulfate anion, at the center of the channel, from the P_{11} [3.43(4) GPa] dataset. The modeled positions for the S and Oa sites are shown.

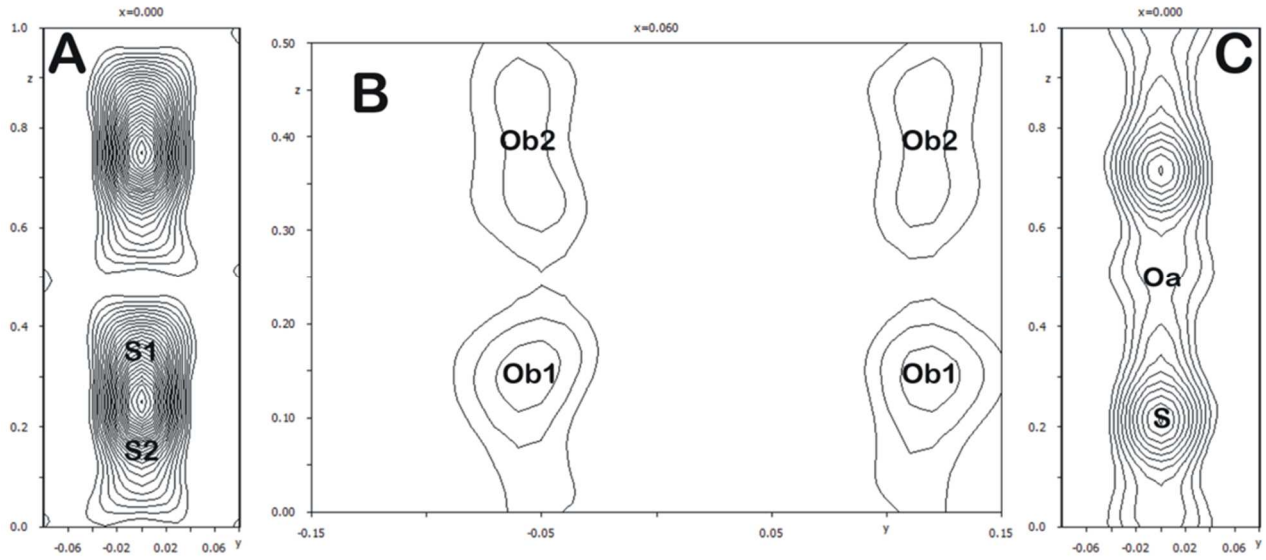

Figure 5.3 The configuration of the channel extraframework population at P_{11} [3.43(4) GPa]. The modeled upward sulfate tetrahedron, pointing an edge towards the neighboring Na^{+} cations in M2, is shown (see the text for further details).

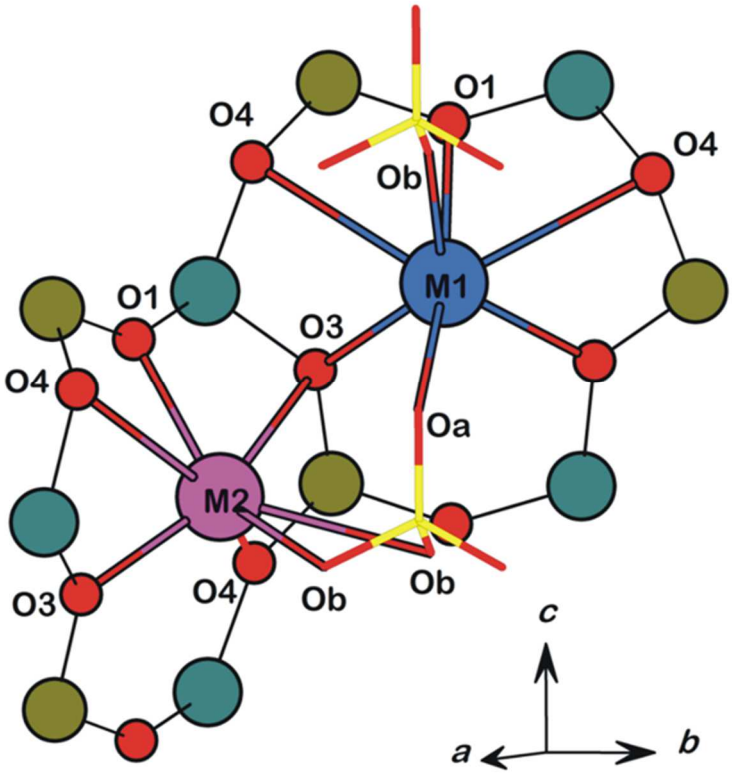

Figure 5.4 (*Left side*) The experimental *V-P* data. The blue line represents the fit with a III-BM EoS in the range P_1-P_8. The red line represents the fit with a III-BM EoS in the range P_{12}-P_{22}. The increase in compressibility is evident. (*Right side*) The experimental a/a_{P1} (blue) and c/c_{P1} (green) vs. *P* data. The fits with "linearized" III-BM EoS, in the same *P*-ranges described above, are shown.

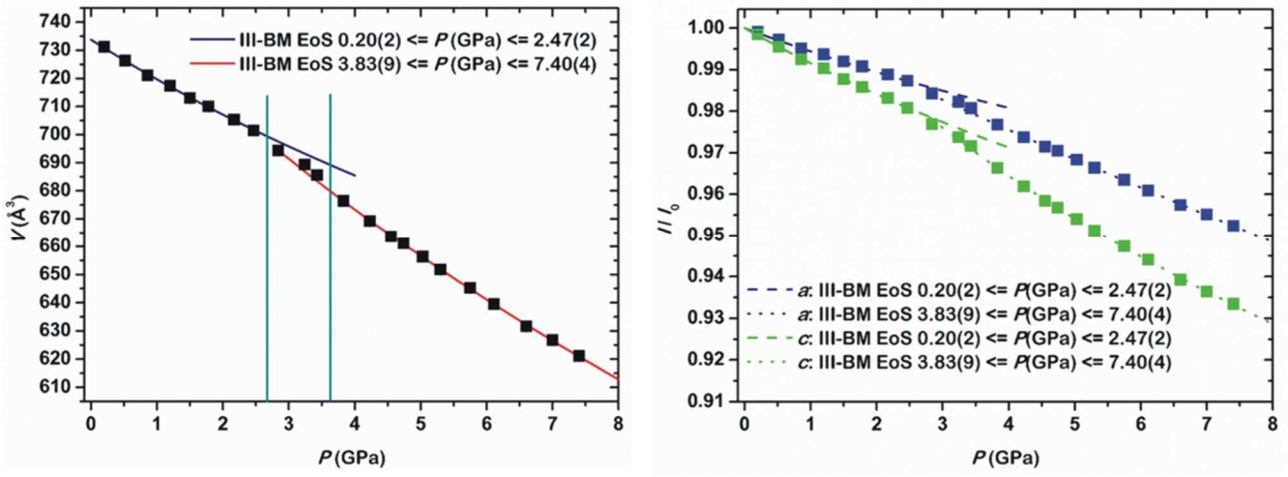

Figure 5.5 *P*-induced evolution of: (A) the Si-O-Al intertetrahedral angles; (B) the S6R⊥[0001] ditrigonal rotation angle $\alpha_{S6R\perp[0001]}$; (C) the O1-O1$_{12R}$ and O3-O4$_{12R}$ channel diameters, normalized to their P_2 values; (D) the O2-O2-O2 *can* unit flattening angle; (E) the channel- and cage-volumes, normalized to their P_2 values.

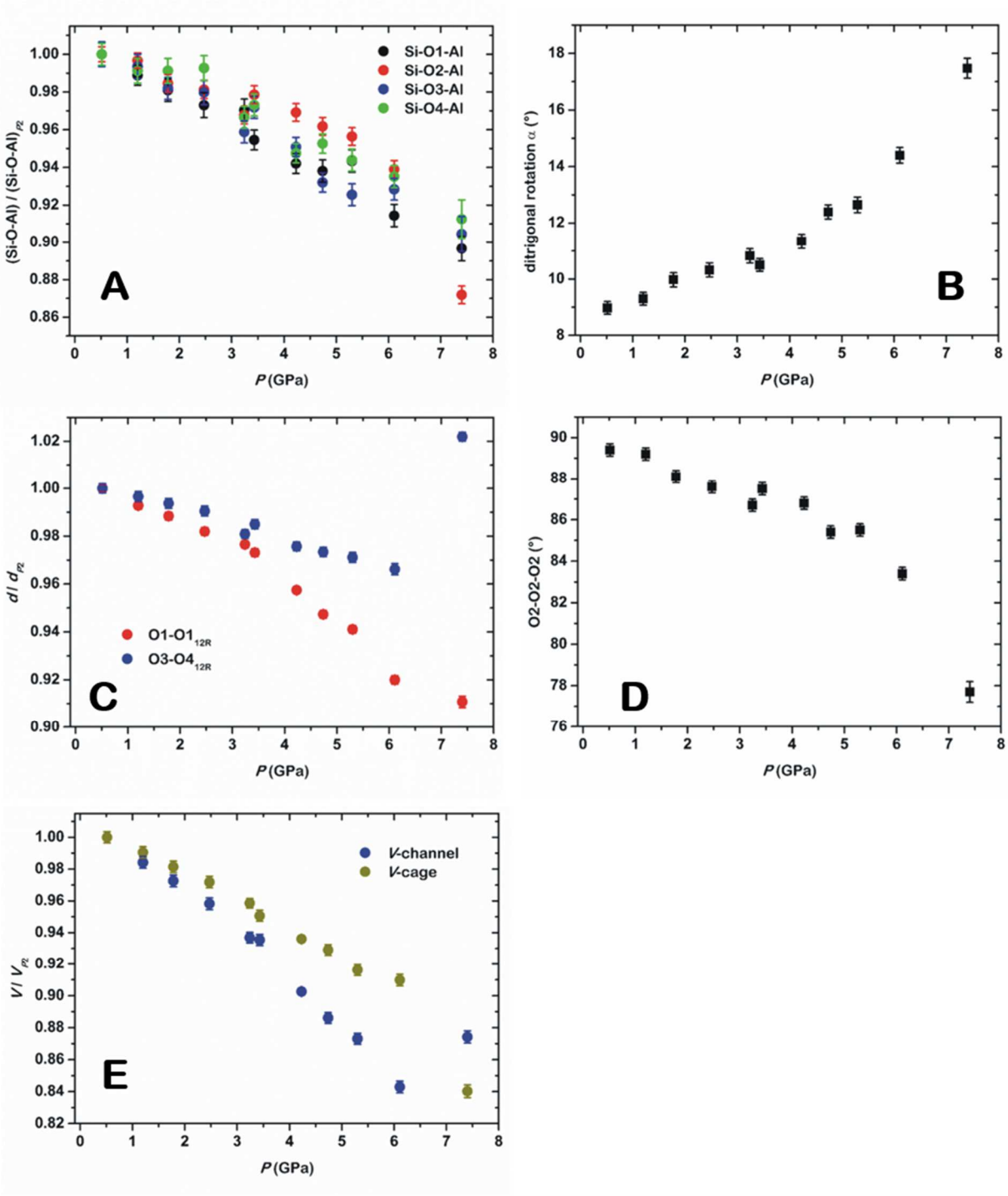

Figure 5.6 (*Left side*) The [CAN]-framework of vishnevite viewed down [0001]. (*Right side*) Two base-sharing *can* units. In both the pictures, relevant structural parameters are shown.

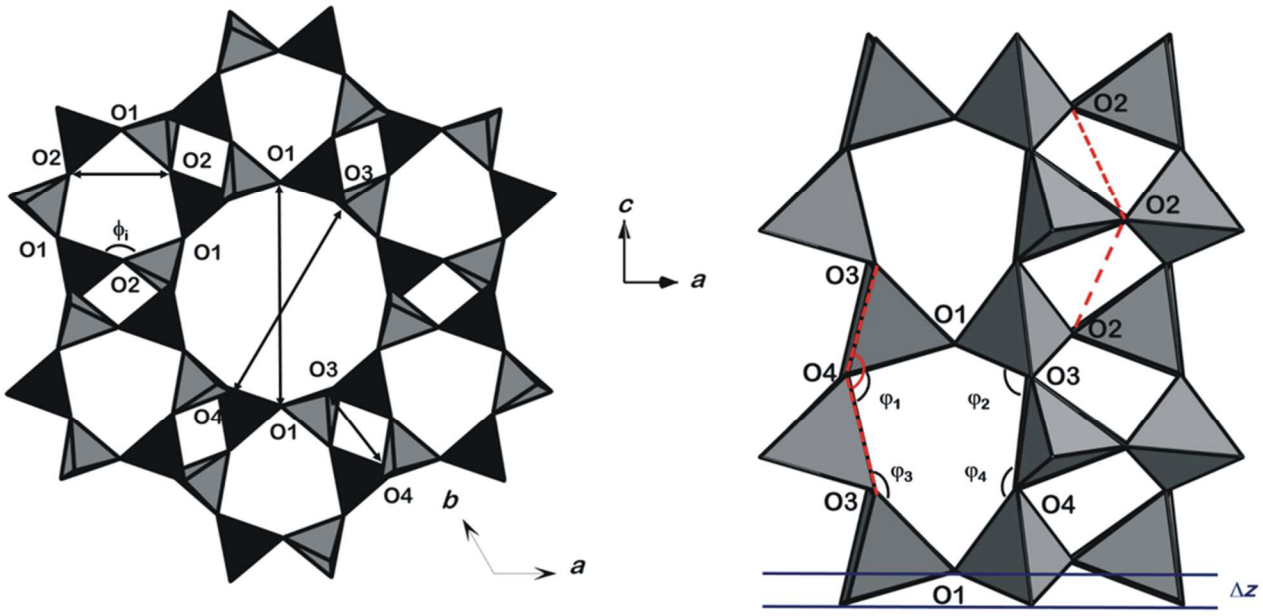

Chapter 6

Balliranoite

6.1 BALLIRANOITE BEHAVIOR AT LOW TEMPERATURE

The experimental findings reported in the following paragraphs have been published in the following paper:

G.D. Gatta, P. Lotti, V. Kahlenberg (2013) The low-temperature behavior of balliranoite (CAN topology): an *in situ* single-crystal X-ray diffraction study. *Microporous and Mesoporous Materials*, **174**, pp. 44-53.

6.1.1 Materials and experimental methods

The natural sample of balliranoite used in this study is from Dattaw, Mogok metamorphic belt, Myanmar (#108339, collection of the American Museum of Natural History, New York, USA), in an assemblage of corundum (ruby), marialite (mizzonite) and, presumably calcite (sample was trimmed before acquisition). Balliranoite likely crystallized in a skarn-like environment by the interaction of granite and its fluids with the marble wallrocks and corundum inclusions (Harlow and Bender 2013, and references therein). Some fragments have been selected from a centimeter-size gem-quality crystal for the chemical analysis and low-*T* diffraction experiments.

Chemical analysis was performed with a JEOL 8200 electron microprobe in wavelength dispersive mode with 15 kV acceleration voltage, 5 nA incident beam current and 3 μm beam size. The following natural standards were used: hornblende (F), omphacite (Na), realgar (S), anorthite (Ca, Al), K-feldspar (K), wollastonite (Si) and scapolite (Cl).

A single-crystal (180*160*135 μm^3) free of defects at the optical scale was selected for the *in-situ* low-temperature single-crystal X-ray diffraction experiments. Six intensity data collections were performed at 293 (room-*T*), 250, 220, 180, 140 and 108 K (Table 6.1) using an Oxford Diffraction Gemini Ultra diffractometer equipped with a Ruby CCD detector, operating at 50 kV and 40 mA with a graphite-monochromatized Mo-Kα radiation. The low-temperature conditions (T < 293 K) were obtained by cooling the crystal with an Oxford Cryosystems 700 Plus open-flow nitrogen gas device (temperature stability 0.2 K, absolute uncertainty within 2 K at the crystal position). A combination of ω-scans, with 1° step scan and 30 s/frame exposure time, was used to maximize data coverage and redundancy. The unit-cell was found to be metrically hexagonal within the *T*-range investigated, absence conditions always compatible with the $P6_3$ space group and no evidence for superstructure

reflections. The measured unit-cell parameters at 293 K were: a = 12.6701(3) Å, c = 5.3178(1) Å and V = 739.30(3) Å^3. Intensities from all the datasets were integrated and corrected for Lorentz-polarization effects using the Crysalis software (Agilent 2012). Further details about the data collection protocol and unit-cell parameters at different temperatures are in Table 6.1.

6.1.2 Results

Chemical composition and structure refinements

Table 6.2 reports the chemical composition of our balliranoite, yielding the following crystal-chemical formula: $(Na_{4.47}Ca_{2.86}K_{0.11})(Si_{5.96}Al_{6.04}O_{24})Cl_{2.03}(CO_3)_{0.78}(SO_4)_{0.33}$, based on (Si + Al) = 12 a.p.f.u..

The balliranoite structure refinements at different temperatures were performed using the SHELXL-97 software (Sheldrick 1997, 2008) integrated in the WinGX suite (Farrugia 1999). Neutral atomic scattering factors for O, Si, Al, Na, Ca, Cl and C were taken from the *International Tables for Crystallography vol. C* (Wilson and Prince 1999). The structure refinement based on the data collected at 293 K (room-*T*) was performed starting from the framework coordinates reported by Chukanov et al. (2010b). The extraframework sites were located by inspection of the difference-Fourier maps of electronic density. The *can* unit content is given by a Ca site (Ca), located on the 3-fold axis (1/3,2/3,*z*) at the center of the S6R⊥[0001] (Fig. 6.1), and by three symmetry-related and mutually exclusive Cl sites (Cl), out of the 3-axis (Fig. 6.1). Their site occupancy factors (*sof*'s) were initially refined, giving a full occupancy (1/3 for each Cl site), and then fixed to 1.0 (Ca) and 1/3 (Cl) in the late stages. Two mutually exclusive cation sites (M1 and M2) were found close to the channel walls (Fig. 6.2) as reported also by Chukanov et al. (2010b), whereas CO_3^{2-} groups were located at the center of the channel in two mutually exclusive configurations (C1-O5 and C2-O6 sites) (Fig. 6.2), where carbon atoms lie on the 6_3 axis (0,0,*z*) and the oxygen atoms out of it in a symmetry-induced triangular configuration, as in cancrinite (chapter 4) and in holotype balliranoite (Chukanov et al. 2010b). A diffuse electronic density along the 6_3 axis in the difference-Fourier maps (Fig. 6.3) did not allow to locate unambiguously the SO_4^{2-} group, expected on the basis of the chemical analysis. A test refinement was performed with the configuration of the SO_4^{2-} group reported by Chukanov et al. (2010b), but unsuccessfully. In other words, the SO_4^{2-} configuration found for the holotype of Chukanov et al. (2010b) is not applicable to our balliranoite. The first cycles of refinement were

conducted with isotropic displacement parameters (*adp*'s), which were set anisotropic in the last stages; only the M2 site was modeled as isotropic. Both M1 and M2 were refined using the scattering factor of Na, since a mixed Na/Ca scattering curve did not improve the figure of merit of the refinement. No constraints on the carbon (C1 and C2) and related oxygen (O5 and O6) site occupancy factors were applied, in order to consider any potential contribution due to the SO_4^{2-} groups. In order to get a stable refinement, O5 and O6 were constrained to share the same anisotropic *adp*'s. The refinement converged to an R_1 = 0.0301 for 2544 reflections with Fo > 4σ(Fo) (Table 6.1), with no significant correlation between the refined parameters and with highest residuals in the difference-Fourier maps of electron density equal to +0.98 $e^-/Å^3$ and -0.57$e^-/Å^3$ (Table 6.1). A racemic twinning with ratios of the twin components equal to 0.52(3):0.48(3) was found. However, the refined twinning did not affect the quality of the structure refinements both at room and low-*T* conditions. The same refinement strategy was applied to the low-temperature intensity data, restraining M1 and M2 to keep the total occupancy refined at room conditions and constraining the (CO_3^{2-})-group sites to the room-*T* occupancies. No change of the extraframework configuration was detected at low-*T*. All the refinements converged with no significant correlation between the refined parameters and with highest residuals in the difference-Fourier maps < ± 1.22 $e^-/Å^3$ (Table 6.1). Atomic coordinates, site occupancy factors and equivalent/isotropic displacement parameters of all the structure refinements are in Table 6.3. Anisotropic displacement parameters are in Table 6.4.

Thermoelastic behavior

Figure 6.4 shows the evolution of the balliranoite unit-cell volume *vs* temperature, which follows a monotonic trend with no evidence of phase transition or change of the thermal behavior. These experimental data were fitted with the equation (8) directly derived from the thermodynamic definition of the thermal expansion coefficient ($\alpha_V = 1/V_0*(\partial V/\partial T)_P$), already to describe the L*T* behavior of cancrinite (section 4.1): $V(T) = V_{T0}*\exp(\alpha_V*\Delta T)$, where α_V is assumed to be constant within the temperature range investigated and the reference-T_0 was fixed to the lowest experimental temperature (*i.e.* 108 K). The fit yielded the following refined parameters: V_{T0} = 732.7(3) $Å^3$ and α_V = 4.6(4)*10^{-5} K^{-1}. The experimental *a* and *c* unit-cell edges *vs* temperature (Fig. 6.4) were, in turn, fitted with the same "linearized" equation [$l(T) = l_{T0}*\exp(\alpha_l*\Delta T)$], giving the following refined parameters: a_{T0} = 12.636(3) Å and α_a = 1.4(2)*10^{-5} K^{-1}, c_{T0} = 5.300(1) Å and α_c = 1.7(2)*10^{-5} K^{-1}. The resulting α_a:α_c ratio, describing the anisotropic thermal volume expansion, is then 1:1.21.

A fit of the experimental data by the equation (14), proposed by Pawley et al. (1996), was also done, yielding the following refined parameters: V_r = 733.5(3) Å^3, a_{0V} = 1.6(2)*10^{-4} K$^{-1/2}$; a_r = 12.640(3) Å, a_{0a} = 4.6(7)*10^{-5} K$^{-1/2}$; c_r = 5.3015(4) Å, a_{0c} = 6.1(3)*10^{-5} K$^{-1/2}$. The calculated thermal expansion coefficients at room-*T* are: $\alpha_{V,293K}$ = 6.7(8)*10^{-5} K^{-1}, $\alpha_{a,293K}$ = 1.9(3)*10^{-5} K^{-1}, $\alpha_{c,293K}$ = 2.6(1)*10^{-5} K^{-1}, from which the elastic anisotropy $\alpha_{a,293K}$: $\alpha_{c,293K}$ = 1:1.37 is derived.

Low-*T* structure evolution

The balliranoite framework is built by perfectly ordered SiO_4 and AlO_4 tetrahedra as in cancrinite and almost all of the cancrinite-group minerals (Bonaccorsi and Merlino 2005; Pekov et al. 2011a). The low *T*-induced evolution of the intertetrahedral Si-O-Al angles is reported in Table 6.5 and Figure 6.5, which show that all but the Si-O2-Al angle decrease with decreasing temperature. The mean <Si-O> and <Al-O> bond lengths are constant within their estimated standard deviations (Table 6.5), suggesting a rigid behavior of the TO_4 tetrahedra.

Within the (0001) plane, several non-independent deformational mechanisms can be described. The S6R⊥[0001] (*i.e.* the cage basis) shows a small increase of the ditrigonal rotation angle $\alpha_{S6R\perp[0001]}$ (section 4.1.2; Fig. 6.6; Table. 6.5). This mechanism leads to a limited shortening of the O2-$O2_{S6R\perp[0001]}$ ring diameter (Fig. 6.6; Table 6.5). The "cage width", described by the three symmetrically related $(O2\text{-}O2)_{cw}$ diameters (dashed lines in Fig. 6.6), decreases with decreasing temperature (Fig. 6.5; Table 6.5), coupled with a shortening of both the independent channel diameters $(O1\text{-}O1)_{12R}$ and $(O3\text{-}O4)_{12R}$ (Fig. 6.5 and 6.6; Table 6.5), where $(O1\text{-}O1)_{12R}$ is calculated as the projection onto the (0001) plane of the O1-O1 distance.

A low-*T* induced shortening of the TO_4 *double zigzag* chains running along the [0001] direction, well described by the closure of the O3-O4-O3 angle (Table 6.5), reflects the ditrigonalization of the S6R∠(000l) windows and a decrease of the hexagonal layers "corrugation" ($\Delta z = (z(O)_{max} - z(O)_{min})*c$) (Fig. 6.6; Table 6.5).

The channel- and cage-volumes (calculated according to the protocol in section 4.2.2) behaviors with temperature have been described by the same equation (8) ($V(T) = V_{T0}*\exp(\alpha_V*\Delta T)$) previously used to fit the unit-cell volume. The refined thermoelastic parameters are: V_{ch0} = 321.1(1) Å^3 and α_{Vch} = 6.0(4)*10^{-5} K^{-1}, V_{cg0} = 205.9(1) Å^3 and α_{Vcg} = 3.4(4)*10^{-5} K^{-1}, respectively.

Table 6.3 shows that the equivalent\isotropic displacement parameters of both framework and extraframework sites undergo a decrease with decreasing temperature. The Ca coordination environment within the *can* unit is a ditrigonal bipyramid (C.N. = 8), where the S6R⊥(0001) oxygen atoms define the ditrigonal basis and two Cl atoms behave as apical verteces (Fig. 6.1). A small shortening of the Ca-Cl bond lengths can be observed with decreasing temperature, whereas Ca-O1 and Ca-O2 do not show any appreciable deviation from the room-*T* values (Table 6.5). The channel-cations M-O bond lengths with *T* are given in Table 6.5. For both M1 and M2, a shortening of the average <M-O> bond lengths with framework-O atoms is shown at low-*T* (Table 6.5), whereas no appreciable decrease is observed for the average <M1-O> bond lengths with carbonate oxygen atoms.

6.1.3 Discussion

Low-*T* structure evolution

The low-*T* induced structure evolution in balliranoite can be mainly described in terms of rigid tetrahedra rotation, as the average <T-O> bond lengths suggest (Table 6.5). The shortening of the structure within the (0001) plane can be ascribed to two independent mechanisms: 1) the cage width shortening along $(O2\text{-}O2)_{cw}$ and 2) the S6R⊥(0001) ditrigonal rotation through the $O2\text{-}O2_{S6R\perp[0001]}$ shortening (Fig. 6.5 and 6.6; Table 6.5). At the same time, the "compression" of the *double zigzag* chains (Fig. 6.6, Table 6.5) fully describes the shortening along the [0001] crystallographic direction. The refined cage- and channel-volume thermal expansion coefficients show that the highest contribution to the low-*T* induced unit-cell volume contraction is given by the channel voids, being $\alpha_{cg}:\alpha_{ch} = 1:1.76$.

A straightforward description of the channel extraframework population is not trivial, since both cations and anions occupy several mutually exclusive positions, giving rise to multiple possible configurations. Both the "M" sites have been refined using the neutral scattering curve of Na, giving site occupancy factors equal to 0.854(4) and 0.160(4) for M1 and M2 at room-*T*, respectively, which correspond to [(0.854+0.160)*11]*6 = 66.92 e^- per unit-cell. Assuming a full occupancy of the Ca site (Ca) within the cage, the chemical analysis (Table 6.2) shows that the channel cationic population is given by $Na_{4.47}Ca_{0.86}K_{0.11}$, corresponding to 68.46 e^- per unit-cell, in good agreement with the structure refinement. The channel-anions electronic content from the structure refinement (Table 6.3) is [(0.49+0.24)*6]*2 = 8.76 e^-/unit-cell for C and [(0.54+0.13)*8]*6 = 32.16 e^-/unit-cell for O, giving

a total of 40.92 e^-/unit-cell. On the basis of the chemical analysis, the channel anionic composition is $(CO_3)_{0.78}(SO_4)_{0.33}$, which corresponds to 40.33 e^-/unit-cell, in good agreement with the structure refinement. All the anionic sites show significantly anisotropic displacement parameters, with unrealistic U_{33} values (Fig 6.2; Table 6.4), which represent the positional disorder along [0001] suggested by the difference-Fourier maps (Fig. 6.3). As already proposed for cancrinite (Ballirano and Maras 2004; Della Ventura et al. 2009; section 4.1 of the present study), this is likely due to the displacing of C atoms from their average positions in order to avoid too short C-C distances. If the C-C distance in aragonite (2.88 Å) (De Villiers 1971) is assumed to be the shortest in minerals (Bonaccorsi and Merlino 2005), a positional displacing along with the occurrence of vacancies are needed in balliranoite, being C1-C1 and C2-C2 equal to $c/2$ = 2.6589(1) at room-*T*.

An inspection of the refined M-O bond lengths at room-*T* conditions (Table 6.5) highlights the M2 proximity to the channel walls (Fig. 6.2), and so its shorter bond lengths with the framework-oxygen atoms. On the contrary, M1 is slightly closer to the (CO_3^{2-})-oxygen sites and likely too far from O1 for an effective bond when it is occupied by Na, according to the bond-valence method (Brown 2002). If we assume that all the channel Ca and K occupy the M1 site, because of more favourable bond lengths (Table 6.5), it follows that M1 would be occupied by 57% Na, 14% Ca and 2% K, while 27% of vacancies occur. As a consequence, the 16% of the M2 site is occupied by the remaining Na atoms, possibly associated with vacancies in the closest anionic sites. A decrement of the distance between M1 and M2 is shown (Table 6.5), suggesting a tendency of the two sites to merge with decreasing *T*, though an apparent saturation of the decrease of the M1↔M2 distance at the lowest *T* do not allow a clear interpretation of the phenomenon.

The *can* units extraframework configuration is more simple: chains of alternated Ca and Cl develop along the [0001] direction. Three mutually exclusive upwards and three downwards Ca-Cl bonds can occur (Fig. 6.1), due to the Cl positioning out of the 3-fold axis, though the highly anisotropic Cl displacement parameters (Table 6.4) suggest a much more disordered configuration. Both the independent Ca-Cl bond lengths decrease with decreasing *T* (Table 6.5), showing a shortening of the Ca-Cl chains in response to the deformation of the tetrahedral framework.

Thermoelastic behavior and comparison with the cancrinite evolution at L*T*

To the best of our knowledge, this is the first study on the thermoelastic and structural behavior of the CO_3^{2-} end-member of davyne subgroup, *i.e.* balliranoite, at non-ambient conditions. However, a

comparison with the natural cancrinite thermoelastic behavior at low-*T* conditions (section 4.1) can be carried out. In cancrinite, the refined volume thermal expansion coefficient is $3.8(7)*10^{-5}$ K^{-1} within the range $100 \leq T$ (K) ≤ 293, which corresponds within 1σ to the α_V refined for balliranoite. If the linear thermal expansion coefficients α_a and α_c are compared, a different thermoelastic anisotropy between these two isotypic materials can be found: the α_a:α_c ratio being 1:1.21 in balliranoite and 1:3 in cancrinite. This difference is due to a weaker thermal expansion along [0001] and a stronger expansion within the (0001) plane in balliranoite with respect to cancrinite (α_a(Can) = $0.7(2)*10^{-5}$ K^{-1}; α_c(Can) = $2.1(3)*10^{-5}$ K^{-1}). However, the low number of data points and the scattering of the data lead to high estimated standard deviations of the refined axial thermal expansion coefficients.

Both these isotypic materials show, as expected, a decrease of the magnitude of the equivalent/isotropic atomic displacement parameters at low-*T*. However, if in cancrinite the equivalent *adp*'s of the (CO_3^{2-})-sites are kept constant with *T*, in balliranoite C1, C2 and (O5,O6) all show a decrease of their equivalent *adp*'s, suggesting a higher influence of the thermal disorder.

The largest difference between the low-*T* structural evolution of cancrinite and balliranoite can be found within the (0001) plane. In balliranoite, the deformation is mostly accommodated by the cage-width shortening along $O2\text{-}O2_{cw}$ (Fig. 6.5, Table 6.5). On the contrary, in cancrinite (section 4.1) the cage-width is constant with *T* and the deformation is completely accommodated by the ditrigonalization of the S6R⊥(0001), which leads to the shortening of the $O2\text{-}O2_{S6R\perp[0001]}$ diameter. A different behavior of the channel diameters is also observed: in balliranoite both $(O1\text{-}O1)_{12R}$ and $(O3\text{-}O4)_{12R}$ decrease with *T* (Fig. 6.5; Table 6.5), while in cancrinite only the longest $(O1\text{-}O1)_{12R}$ does (section 4.1). As a consequence, a continuous decrease of the shortest free diameter (along the $(O3\text{-}O4)_{12R}$ direction) occurs in balliranoite, whereas in cancrinite it remains constant with *T*. A different *can* unit behavior is also observed: in balliranoite, the cage-width shortening is accompanied by a same-magnitude "compression" along [0001], as confirmed by the constant value of the O2-O2-O2 flattening angle (Fig. 6.6, Table 6.5); in cancrinite, in contrast, the shortening along the *c*-axis is not counterbalanced within the (0001) plane, so leading to a pronounced flattening of the cage through the decrease of the O2-O2-O2 angle.

Appreciable differences can be observed between the Ca and Na coordination environments within the *can* units of balliranoite and cancrinite, respectively. In balliranoite, no changes are shown by the Ca-O1 and Ca-O2 bond lengths at low-*T*, whereas in cancrinite a considerable shortening of Na-O2

is due to the S6R⊥(0001) ditrigonalization. Furthermore, in cancrinite all the T-O-T intertetrahedral angles, including Si-O2-Al, undergo a closure with decreasing *T*. We do not observe a similar behavior in balliranoite, suggesting that the coordination environments of the *can* unit cations likely play a key role in low-*T* deformation of the [CAN] framework. No considerable differences are observed between the deformation mechanisms acting along [0001].

6.1.4 Conclusions

The thermoelastic behavior of balliranoite, the CO_3^{2-} end-member of davyne subgroup, in the range $108 \leq T\,(\mathrm{K}) \leq 293$, has been studied for the first time, showing a thermal expansion coefficient similar to that of cancrinite. A different thermoelastic anisotropy, between these isotypic materials, can be inferred from the linear expansion coefficients.

The low-*T* structure evolution of balliranoite is driven by rotation of the framework rigid tetrahedra, which accommodate the unit-cell deformation through the shortening of the *can* cage “width” and channel diameters within the (0001) plane, along with the *double zigzag* chains “compression” along [0001]. A comparison with the low-*T* cancrinite behavior shows significant differences of the mechanisms acting within the (0001) plane, where different cage and channel deformations are observed.

These results suggest that the nature of the *can* unit population and the coordination environments could influence the type of the [CAN] framework deformation at low-*T*.

Figure 6.1 The *can* unit extraframework population, showing the Ca site and three mutually exclusive Cl sites (out of the 3-fold axis). The Ca-coordination environment is drawn. Dashed lines represent mutually exclusive bonds.

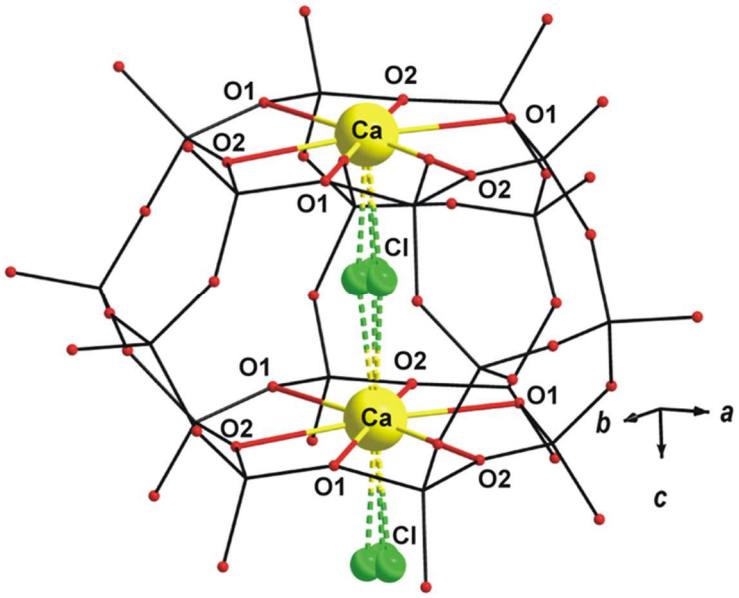

Figure 6.2 (A) Coordination shells of M1 and M2 channel-cations sites. Dashed lines represent mutually exclusive bonds. The C atoms show a triangular coordination perpendicular to the [0001] axis. (B) The channel extraframework population viewed down [0001]. Blue sticks at the center of the channel represent the CO_3^{2-} groups.

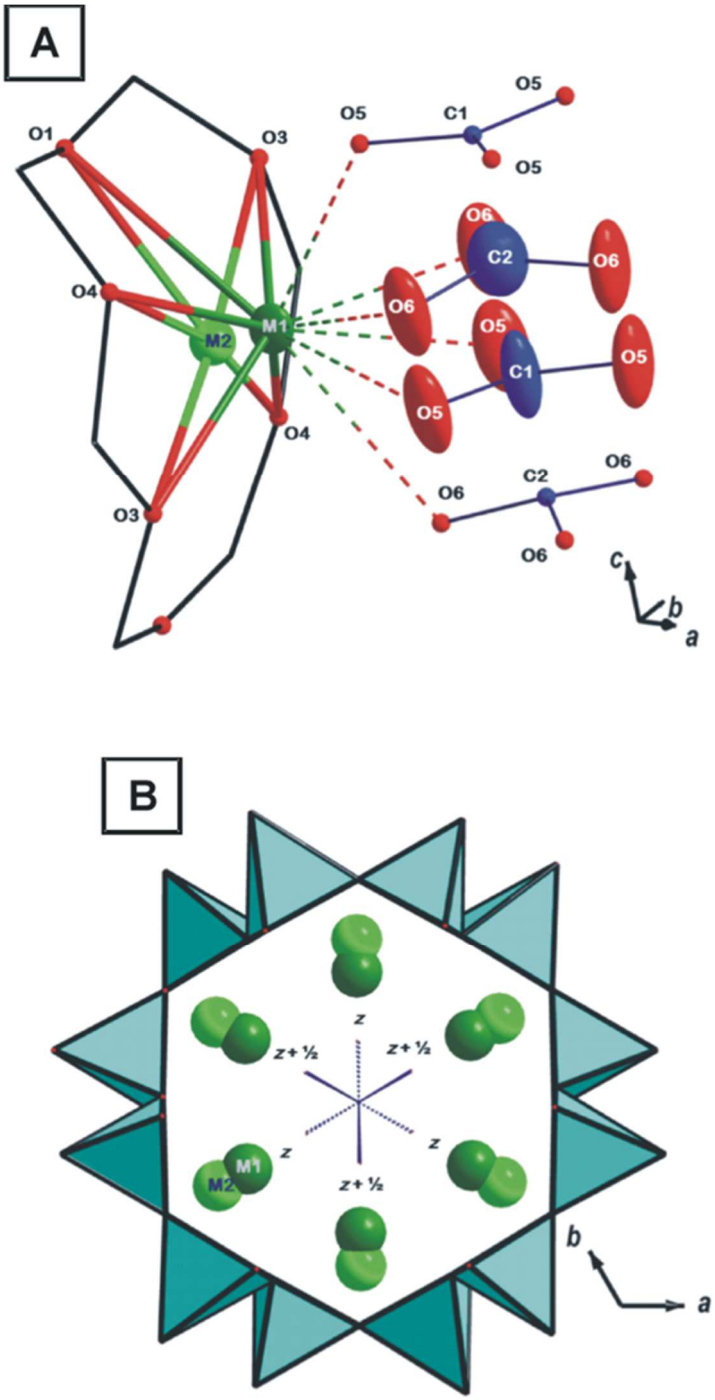

Figure 6.3 Difference-Fourier map of the electron density, phased without the CO_3^{2-} groups, showing the positional disorder along the 6_3 axis at the center of the 12R-channel, from the room-*T* (*left* side) and the room-*P* (*right side*) refinements.

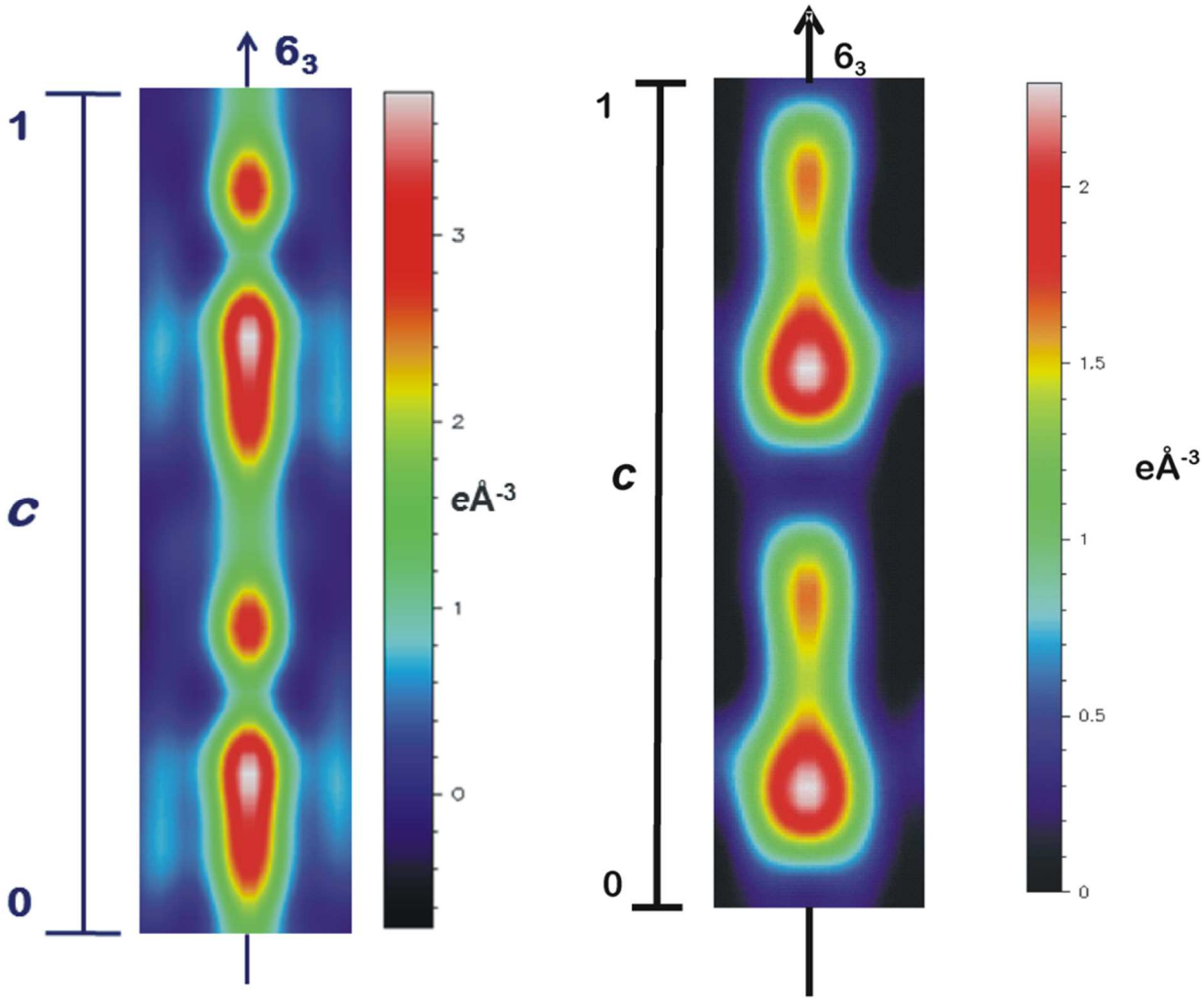

Figure 6.4 (*Top*) The unit-cell volume of balliranoite as a function of *T*. The solid line represents the fit using the equation (8) $V(T) = V_{T0}*\exp(\alpha_V*\Delta T)$. (*Center and bottom*) The unit-cell edges *a* and *c* of balliranoite as a function of *T*, respectively. The solid lines represents the fit using the linearized equation $l(T) = l_{T0}*\exp(\alpha_l*\Delta T)$ For all the diagrams the experimental errors are of the same magnitude as the symbols.

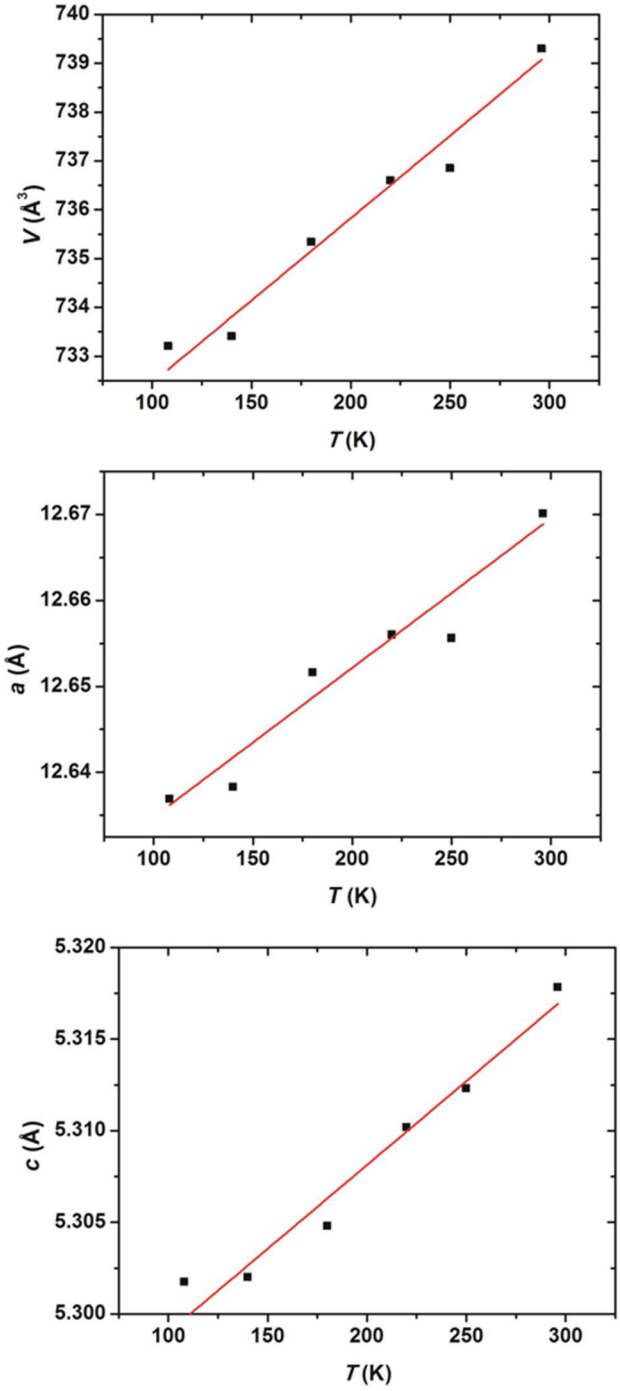

Figure 6.5 (*Top*) The intertetrahedral Si-O-Al angles, normalized to their values at 293 K, with *T*. (*Center*) The $O2\text{-}O2_{cw}$ cage-width variation with *T*. (*Bottom*) The $(O1\text{-}O1)_{12R}$ and $(O3\text{-}O4)_{12R}$ channel diameters, normalized to their values at 293 K, evolution with *T*.

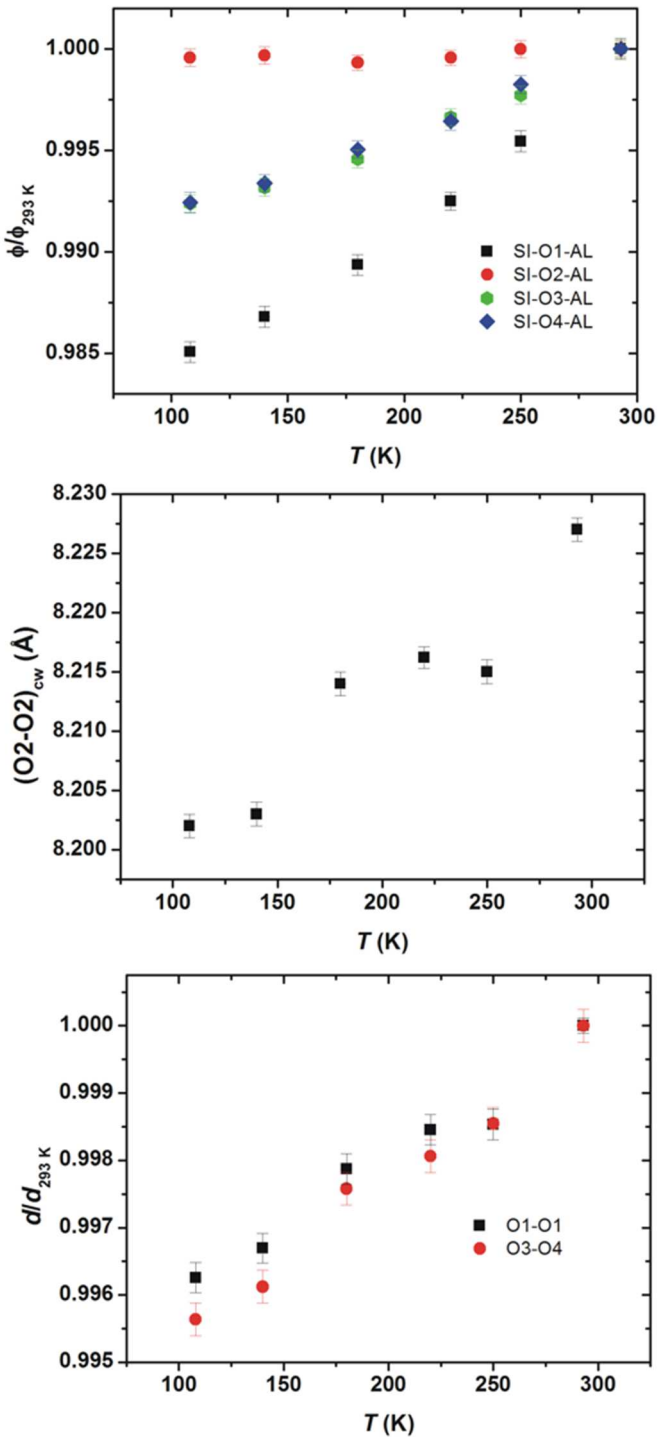

Figure 6.6 (*Left side*) The [CAN] framework viewed down [0001]. $(O1\text{-}O1)_{12R}$ is calculated as the projection onto the (0001) plane of the O1-O1 distance, as the involved O1 atoms are shifted along [0001] of 1/2**z*. (*Right side*) A column of *can* units.

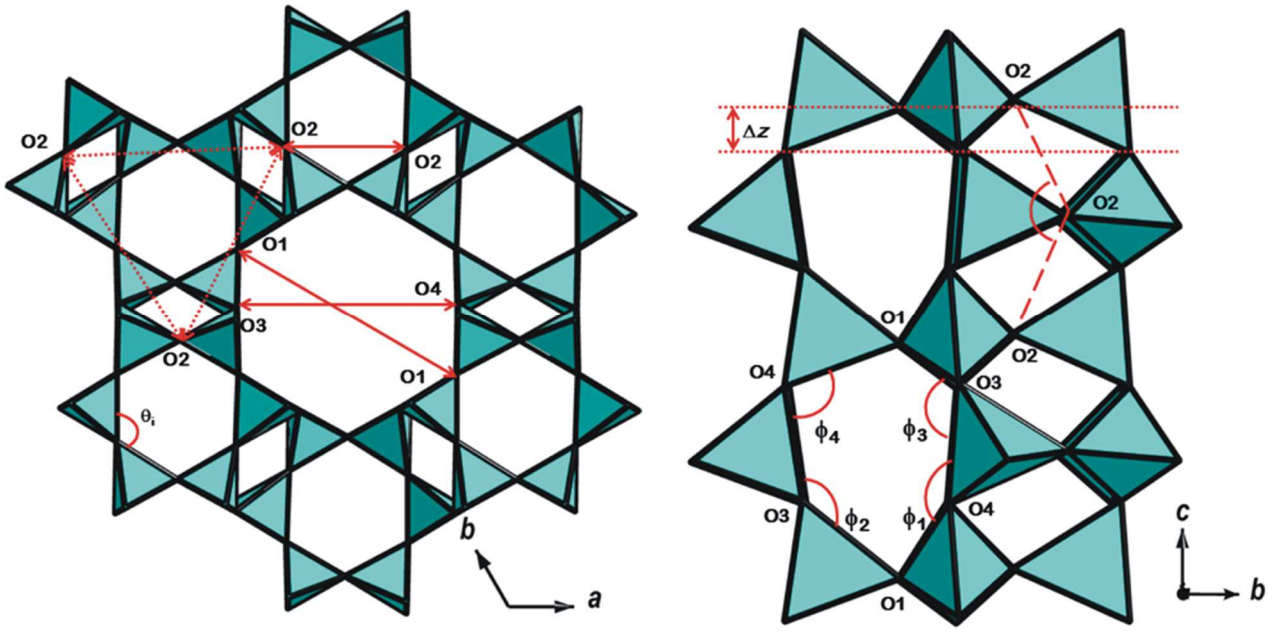

6.2 BALLIRANOITE BEHAVIOR AT HIGH PRESSURE

The experimental findings reported in the following paragraphs have been published in the following paper:

P. Lotti, G.D. Gatta, N. Rotiroti, F. Cámara, G.E. Harlow (2014) The high-pressure behavior of balliranoite: a cancrinite-group mineral. *Zeitschrift für Kristallografie*, **DOI 10.1515/zkri-2014-1626**.

6.2.1 Materials and experimental methods

The same sample of balliranoite from Mogok (Myanmar) used for low-*T* experiments (section 6.1) has been used for the high-*P* experiments. A single-crystal (160*100*70 μm^3), optically free of defects, was selected for the high-pressure diffraction experiments of this study. The crystal-chemical formula, from electron microprobe analysis in wavelength-dispersive mode, is reported in section 6.1.1 and in Table 6.2.

An X-ray diffraction intensity data collection was first performed with the crystal in air using an Oxford Diffraction Xcalibur diffractometer, operating at 50 kV and 40 mA, with a monochromatized Mo-Kα radiation and equipped with a CCD detector , 80 mm far from the sample position. A combination of ω/φ scans, with step scan 1° and exposure time 60 s per frame, was used to maximize redundancy and data coverage. A total of 19175 measured reflections showed a metrically hexagonal lattice with: a = 12.680(1) Å, c = 5.3141(5) Å and V = 739.9(1) $Å^3$. Systematic absences were compatible with the $P6_3$ space group and no superstructure reflections were observed. Intensity data were then integrated and corrected for Lorentz-polarization effects using the Crysalis software (Agilent 2012). Absorption due to the crystal was found to be not significant.

In-situ H*P*-experiments were performed with an ETH-type diamond anvil cell with Be backing plates (Miletich et al. 2000). A T301 steel foil was used as a gasket, with a micro-hole (diameter ~300 μm) drilled by spark-erosion as *P*-chamber, after a pre-indentation to a thickness of about 120 μm. A nominally anhydrous mixture (methanol:ethanol = 4:1) was used as hydrostatic *P*-transmitting medium (Angel et al. 2007), whereas a standard crystal of quartz, loaded along with the balliranoite sample in the *P*-chamber, was used as pressure calibrant (Angel et al. 1997). The balliranoite unit-cell parameters were measured from 0.0001 (crystal in the DAC without *P*-medium) to 6.77(2) GPa

(Table 6.6), by centering a list of 32 Bragg reflections with a KUMA-KM4 point-detector diffractometer. Operating conditions were 50 kV and 40 mA with a monochromatized Mo-Kα radiation. X-ray intensity data were collected at 0.0001, 0.85(3), 1.73(3), 2.62(4), 3.80(5), 4.95(3), 5.95(4) and 6.77(2) GPa using the Oxford Diffraction Xcalibur CCD-diffractometer at the same operating conditions used for the crystal in air. A combination of ω/φ scans was used for all the high pressure data collections, with step scan 0.5° and exposure time 60 s per frame. Reflections conditions compatible with $P6_3$ space group were always observed fo all the datasets within the *P*-range investigated. Intensity data were integrated and corrected for Lp-effects with the Crysalis software (Agilent 2012) and for absorption effects, due to the DAC, with the ABSORB software (Angel 2004). Further details pertaining to the data collections are in Table 6.7.

6.2.2 Structure refinement protocol

All the structure refinements were performed using the SHELXL-97 software (Sheldrick 1997, 2008), integrated in the WinGX suite of crystallographic programs (Farrugia 1999). The neutral atomic scattering factors of O, Si, Al, Na, Ca, Cl and C were taken from the *International Tables of Crystallography Vol. C* (Wilson and Prince 1999). The balliranoite structure refinement was first performed from the data collected with the crystal in air. First cycles were carried out starting from the framework coordinates reported by Chukanov et al. (2010b). The extraframework population was localized from the difference-Fourier synthesis of the electron density. The *can* units were filled by a Ca site (Ca), at the center of the S6R⊥[0001] on the 3-fold axis, and a Cl site (Cl), out of the 3-fold axis in three mutually exclusive positions (Fig. 6.1). The channel population was represented by two mutually exclusive cation sites (M1 and M2) near the channel walls, as also found by Chukanov et al. (2010b) and in low-*T* experiments (section 6.1), and two mutually exclusive configurations for the CO_3^{2-} groups (C1-O5 and C2-O6), with carbon atoms lying on the 6_3 axis at the channel center (Fig. 6.2). The difference-Fourier synthesis, calculated without the anionic groups, showed a highly disordered distribution of the electron density along the 6_3 axis (Fig. 6.3). This disorder hindered an unambiguous allocation of the SO_4^{2-} group, expected from the chemical analysis, as already reported in section 6.1 even from X-ray single-crystal diffraction data collected at 108 K. The configuration of the sulfate group in the holotype mineral (Chukanov et al. 2010b) was used, but unsuccessfully, suggesting that this configuration is not applicable to the balliranoite of this study. The M1 and M2 site occupancy factors (*sof*'s) were refined using the Na scattering factor, since a mixed Na/Ca curve

did not improve the figure of merit of the refinement. No restriction was applied to *sof*'s of the carbonate groups (C1-O5 and C2-O6, respectively), in order to refine any potential contribution from the sulfate group. The Ca and Cl sites were set to a full occupancy (1.0 and 1/3, respectively, since only one of the three Cl sites out of the 3-axis can be simultaneously occupied), as suggested by their early refinement. The first cycles were conducted with isotropic atomic displacement parameters (*adp*'s), which were subsequently set to anisotropic, except for the M2 site because of significant correlation between the refined parameters. The C1-C2 and O5-O6 atomic displacement parameters, respectively, were constrained to be equal in order to improve the refinement stability. A racemic twinning with components ratio 0.53(4):0.47(4) was found. A test refinement excluded the possibility that the material had the corresponding centrosymmetric space group $P6_3/m$. Convergence was achieved leading to an R_1 factor of 0.0447 for 1405 reflections with $F_o > 4\sigma(F_o)$ and highest/lowest residual peaks in the difference-Fourier maps: +0.83 and -0.67 $e/Å^3$.

The high-pressure structure refinements were performed starting from the model previously described. A set of restraints was applied in order to reduce the number of refined parameters, so as to compensate for the reduction in the number of observed reflections mainly due to the acces restrictions of the DAC. The site occupancy factors were all constrained to the values refined with the crystal in air and the atomic displacement parameters were all refined isotropic and constraining Si-Al, the framework oxygen sites, M1-M2, C1-C2 and O5-O6 to share the same values, respectively. Additionally, the C-O bond lengths were restrained to 1.300(5) Å and the carbonate oxygen sites (O5-O6) were constrained to share the same *x* and *y* coordinates, as they were found to be equal within 2σ from the refinement with the crystal in air. Convergence was always achieved with highest residual peaks in the difference-Fourier maps ≤ ±1.18 $e^-/Å^3$. Further details pertaining to the high-pressure structure refinements are in Table 6.7. Atomic coordinates, site occupancy factors and isotropic or equivalent atomic displacement parameters are in Table 6.8. Anisotropic displacement parameters from the refinement at $P_{0\text{-AIR}}$ are in Table 6.9.

6.2.3 Results

Elastic behavior

The balliranoite of this study is stable up to the highest pressure here investigated, *i.e.* 6.77(2) GPa, with no evidence of phase transition or change of the compressional behavior. The unit-cell volume

evolution as a function of P is shown in Fig. 6.7. The experimental data were fitted with a Birch-Murnaghan equation of state (Birch 1947; Angel 2000), truncated to the third order (III-BM EoS) and weighted for the experimental uncertainty in P and V, using the EoSFit v5.2 software (Angel 2000). The following parameters were obtained: V_0 = 735(1) Å^3, K_{V0} = 48(3) GPa and K_V' = 4.0(10). The refined K_V' value, supported by the horizontal trend of the normalized pressure as a function of the Eulerian strain (F_e-f_e plot) (Fig. 6.7), suggests that a truncation of the BM-EoS to the II-order, for which a K_V' = 4 is assumed (section 2.1.6), is adequate to describe the elastic behavior of balliranoite. The fit to the experimental data of a II-BM EoS gives the following parameters: V_0 = 735.5(7) Å^3, K_{V0} = 48.1(8) GPa, which compare well with the weighted linear regression of the F_e-f_e data, intercepting the F_e axis at 49(2) GPa (Fig. 6.7). The unit-cell edges evolution as a function of P is reported in Fig. 6.7: fitting the data with a "linearized" III-BM EoS (Angel 2000), weighted for the uncertainty in P and l, we obtained the following refined parameters: a_0 = 12.654(6) Å, K_{a0} = 54(4) GPa and K_a' = 4.6(14); c_0 = 5.305(2) Å, K_{c0} = 40(2) GPa K_c' = 3.3(6). The elastic anisotropy at ambient conditions can be represented by the ratio K_{a0}:K_{c0} = 1.35:1. The fit with a II-BM-EoS yielded the following parameters: a_0 = 12.652(4) Å, K_{a0} = 55(1) GPa; c_0 = 5.306(2) Å, K_{c0} = 37.6(5) GPa.

High-pressure structure evolution

The high-pressure structure evolution of this natural balliranoite can be described as mainly governed by the mutual tilting of the quasi-rigid framework tetrahedra. All of the Si-O-Al intertetrahedral angles decrease with pressure, though this deformation is significantly less intense for Si-O2-Al (Fig. 6.8; Table 6.10). The average <Si-O> and <Al-O> bond lengths at different pressures do not vary within the calculated standard deviations, even though a slight compression, especially for the AlO_4 tetrahedra, can be inferred (Table 6.10).

The pressure-induced tetrahedral tilting is reflected by several non-independent deformation mechanisms. Among those, within the (0001) plane can be represented by: 1) the ditrigonal rotation of the S6R⊥(0001) (described by the ditrigonal rotation angle, $\alpha_{S6R\perp[0001]}$), which induces the shortening along the S6R⊥(0001) O2-O2$_{S6R\perp[0001]}$ axis (Fig. 6.6; Table 6.10); 2) the *can* unit compression through the "cage width" O2-O2$_{cw}$ (dashed lines in Fig. 6.6) shortening (Fig 6.8; Table 6.10); 3) the channel compression through the shortening of both the symmetrically independent diameters O3-O4$_{12R}$ and O1-O1$_{12R}$ (the latter being calculated as the projection onto the (0001) plane of the O1-O1 distance, as the involved O1 atoms are shifted along [0001] of 1/2*z.) (Fig 6.6 and 6.8;

Table 6.10). Along the [0001] direction, the closure of the O3-O4-O3 angle (Table 6.10) reflects the compression of the double chain of tetrahedra (Fig. 6.6). The *dzc* compression also induces a ditrigonal deformation of the S6R∠(0001) windows and a decrease of the hexagonal layer *corrugation* Δz (Fig 6.6; Table 6.10).

The contribution of the cage- and channel-voids to the unit-cell volume evolution with pressure has been calculated following the same protocol reported in section 4.2.2. Their evolution with pressure has been fitted with a II-BM-EoS, yielding the following refined elastic parameters: V_{0ch} = 326.6(5) Å^3 and K_{V0ch} = 36.0(8) GPa, V_{0cg} = 206.7(4) Å^3 and K_{V0cg} = 66(3) GPa, for channel and cage volumes, respectively.

The Ca coordination shell within the *can* unit is a ditrigonal bipyramid (C.N. 8), where the S6R⊥[0001] oxygen atoms act as the basis and the neighboring Cl atoms as the apical vertices. A slight decrease with pressure of the three symmetrically related Ca-O2 and of both the independent Ca-Cl bond lengths is observed, whereas no significant deviation from the room-conditions value of the Ca-O1 bond distances occurs (Fig 6.1; Table 6.10). The pressure-induced evolution of the channel cations M-O bond lengths is also reported in Table 6.10. Both the average <M1-O_{fr}> and <M2-O_{fr}> bond lengths with framework oxygen atoms, along with the average <M1-O_c> bond lengths with carbonate oxygen, undergo a shortening with increasing pressure (Fig 6.2; Table 6.10).

6.2.4 Discussion

Elastic behavior: balliranoite and cancrinite

To the extent of our knowledge, this is the first study on the high pressure behavior of a davyne-subgroup mineral, specifically the (CO_3^{2-})-analogue balliranoite. No evidence of phase transition, structure collapse or change of the compressional behavior has been observed within the pressure range investigated (0.0001-6.77(2) GPa). The refined isothermal bulk modulus at ambient conditions (K_{V0} = 48(3) GPa) falls in the range so far reported for open-framework silicates (*i.e.* 18-70 GPa, Gatta 2008) and is comparable to that reported for natural cancrinite (45(2) GPa, section 4.2).

Balliranoite shows an anisotropic elastic behavior, with K_{a0}:K_{c0} = 1.35:1 at ambient pressure. It is worth noting that the [CAN]-framework can be seen as a “layered structure”, as described in section

1.1, and the most compressible direction is that perpendicular to the stacking plane of the hexagonal layers.

Cancrinite showed an apparent subtle change of the compressional behavior at 4.62(3) ≤ P (GPa) ≤ 5.00(2), as reported in section 4.2, with refined elastic parameters K_{V0} = 45(2) GPa and K_V' = 6(1) (within 0.0001-4.62(3) GPa), K_{V0} = 40(2) GPa and K_V' = 4 (fixed) (within 5.00(2)-6.62(3) GPa). Besides the refined isothermal bulk moduli, the balliranoite and cancrinite normalized unit-cell volumes (*i.e.* $V/V_{\text{room-}P}$) evolution with pressure, shown in Fig. 6.9, suggests that these isotypic minerals share a similar volume compressibility. However, as shown by the pressure-induced evolution of the normalized a and c unit-cell parameters ($l/l_{\text{room-}P}$) (Fig 6.9), balliranoite is characterized by a less pronounced anisotropic pattern: *i.e.*, compared to cancrinite, it presents a higher compressibility within the (0001) plane and a higher stiffness along the most compressible direction [0001]. These combined features lead to the aforementioned similar volume compressibility.

High-pressure structure evolution

Although a slight compression of the AlO_4 tetrahedra can be inferred from the average <Al-O> bond lengths (Table 6.10), the P-induced structure evolution of balliranoite is mainly driven by the tilting of the perfectly ordered framework, as shown by the Si-O-Al intertetrahedral angles (Fig 6.8; Table 6.10).

The shrinking of the unit-cell volume is accommodated along the softest [0001] crystallographic direction by the compression of the double chain of tetrahedra (*dzc* unit) (Fig 6.6, Table 6.10), whereas within the (0001) plane is accommodated by the combination of two concomitant mechanisms: 1) the *can* unit compression, through the $O2\text{-}O2_{cw}$ shortening (Fig 6.6 and 6.8; Table 6.10) and 2) the S6R⊥[0001] ditrigonal rotation, through the $O2\text{-}O2_{S6R\perp[0001]}$ contraction (Fig 6.6; Table 6.10). The refined elastic behavior of the cage- and channel-volumes shows that the bulk volume compression is mainly governed by the channel voids, as $K_{V0ch} : K_{V0cg} = 1 : 1.83$.

If we assume a full occupancy of the Ca and Cl sites within the *can* units, as suggested by the structure refinements, the chemical analysis of our balliranoite indicates that the composition of the channel population can be expressed as $Na_{4.47}Ca_{0.86}K_{0.11}(CO_3)_{0.78}(SO_4)_{0.33}$, which corresponds to 68.46 and 40.33 e^-/unit-cell, for cationic and anionic population, respectively. The structure refinement, based on the data collected with the crystal in air, has been performed using the neutral scattering curve of

Na for both the M1 and M2 sites, yielding the following site occupancy factors: 0.881(6) and 0.160(6), respectively. These values correspond to ((0.881+0.160)*6)*11 = 68.71 e^-/unit-cell, in excellent agreement with the chemical data. Assuming that all Ca^{2+} and K^+ occupy the M1 site, because of more favorable bond lengths (Table 6.10), the following composition is derived for M1: 59% Na, 14% Ca and 2% K with 25% of vacancies, whereas M2 is 16% occupied by Na. The refined electrons content from the modeled anionic groups (C1-O5 and C2-O6) is given by ((0.56+0.22)*2)*6 + ((0.575+0.165)*6)*8 = 44.88 e^-/unit-cell. The slight discrepancy between the refined anionic content and that expected from the chemical analysis is not surprising if we consider the highly disordered distribution of the electron density along the 6_3 axis, as shown by the difference-Fourier maps (Fig. 6.3). A comparable disorder was also reported by Della Ventura et al. (2007) for a natural sample of vishnevite, the SO_4^{2-} end-member of the cancrinite subgroup, along with a similar discrepancy between structure refinement and chemical analysis for the anionic groups. The refined anisotropic displacement parameters of the carbonate groups sites show unrealistically high U_{33} values (Table 6.9). This feature was already reported for cancrinite (Ballirano and Maras 2004; Della Ventura et al. 2009; section 4.1 of the present study) and in section 6.1 is shown that, in balliranoite, it is preserved at low-temperature at least down to 108 K. As proposed by several authors for cancrinite (*e.g.* Gatta et al. 2012; Grundy and Hassan 1982) and discussed in section 6.1 for balliranoite, the strong anisotropy exhibited by the displacement parameters of the (CO_3^{2-})-groups, along with the aplanarity between the average positions of the carbon and related oxygen atoms (Table 6.8), is a further hint of their positional disorder along the *c*-axis. The disorder of the extraframework population hinders a realistic refinement of the site occupancy factors and, thus, of the total electron content of the anionic groups.

The M1 and M2 cationic sites have the same configuration reported in section 6.1 and by Chukanov et al. (2010b). M1 lies closer to the channel center and is likely too far from O1 for an effective bond when it is occupied by Na. As a consequence, it is coordinated by 4 framework oxygen atoms on one side (5 with O1) and up to 3 carbonate oxygen atoms on the other side. However, the statistical distribution, the occurrence of vacancies and the positional disorder of the anionic population result in a non-univocal coordination environment. Conversely, the M2 site is closer to the channel walls and is coordinated by 5 framework oxygen atoms, whereas, according to the bond valence method (Brown 2002), the M2-(O5,O6) distances are too long for effective bonds. The loss of the contribution given to the total bond valence by the M-(O5,O6) bonds would be partially compensated by the shorter M2-O_{fr} distances with framework oxygen atoms, suggesting the occurrence of M2 likely

coupled with vacancies within the neighboring anionic sites. An inspection of the pressure-induced evolution of the M-O bond lengths (Table 6.10) shows that with increasing pressure: 1) O1 progressively falls within the Na(M1) coordination shell and 2) O5-O6 are more bound to M2. Furthermore, the distance between the M1 and M2 average positions continuously decreases (Table 6.10). In this light, test refinements have been performed in order to investigate a potential merging of the M sites. Although the full merging in a single site cannot be unambiguously proved, the decrease of the M1↔M2 distance and the very similar coordination environment shown by the M1 and M2 cations at the higher pressures suggest this tendency.

The configuration of the *can* units population is simpler than the channel one: three upwards and three downwards mutually exclusive Ca-Cl bonds can occur, due to the Cl positioning out of the 3-fold axis, but the ditrigonal bipyramid coordination is always preserved (Fig. 6.1). The *P*-induced evolution of the Ca-O and Ca-Cl bonds (Table 6.10) shows a slight re-arrangement related to the S6R⊥[0001] ditrigonalization and a compression of the Ca-Cl chains which follows that of the *dzc* units.

It is worth noting that, though with a significantly lower magnitude and, hence, without the effects pertaining to the channel cations coordination shells, the same deformation mechanisms have also been described for the low temperature ($108 \leq T$ (K) ≤ 293) structure evolution of the same natural balliranoite (section 6.1). A similar analogy between the effects induced by these "compressive" regimes (*i.e.* low-*T* and high-*P*), has been already reported for the isotypic cancrinite (sections 4.1 and 4.2).

Comparison with the cancrinite behavior at high pressure

The occurrence of Ca-Cl chains within the *can* units of balliranoite, in place of the Na-H_2O chains occurring in cancrinite, gives rise to an expansion of the [CAN]-framework, as shown by the higher unit-cell volume and by the higher values of all the Si-O-Al intertetrahedral angles in balliranoite at room conditions. The influence of the extraframework population is not only limited to the structure configuration at ambient conditions, but apparently plays a role also on the high-pressure structure evolution. In cancrinite, in fact, all the intertetrahedral angles decrease with pressure, whereas in

balliranoite only a slight deviation from the room-*P* value of the Si-O2-Al is shown (Fig 6.8; Table 6.10). The resulting different tetrahedral tilting shows the largest effects within the (0001) plane. Compared to cancrinite, the S6R⊥[0001] ditrigonal rotation angle in balliranoite is smaller at ambient conditions (α_{BAL} = 1.2(1)°, α_{CAN} = 8.8(2)°) and its increase with pressure is less pronounced. This is correlated to the different *P*-induced behavior shown by the cations-framework oxygen bonds of the cage population. In cancrinite, a strong compression of the shorter Na-O2 and a stretching of the longer Na-O1 bonds are observed at high pressure (section 4.2). In balliranoite, a less pronounced shortening of the Ca-O2 bonds occurs, whereas no significant changes of the Ca-O1 distances is observed (Table 6.10).

A considerably different deformation of the *can* unit can also be described between these isotypic compounds. In balliranoite, the shortening along the O2-$O2_{cw}$ ("cage width") is coupled with a same magnitude compression of the *dzc* unit along [0001]. As a consequence, no significant change of the cage flattening angle O2-O2-O2 (Fig 6.6 and 6.8; Table 6.10) is observed, so that the cage undergoes a homogeneous shrinking. In cancrinite, the *can* unit behavior is opposite: the compression of the double chain of tetrahedra is not counterbalanced by a shortening along O2-$O2_{cw}$ and the closure of O2-O2-O2 reflects the "flattening" of the *can* unit with pressure (section 4.2). Significant differences are also observed in the channel deformation. In our balliranoite, both the independent diameters are compressed with increasing pressure (Fig 6.8; Table 6.10), leading to a continuous shortening of the channel "free diameter" along O3-$O4_{12R}$ (*sensu* Baerlocher et al. 2007): from 5.58(1) Å at room-*P* to 5.25(1) Å at 6.77(2) GPa). Conversely, in cancrinite, only the O1-$O1_{12R}$ diameter undergoes a significant shortening, keeping almost constant the channel "free diameter" at the lower pressures, since, along the O3-O4 direction, compression is mainly accommodated by the S4R deformation (section 4.2). Furthermore, the different *can* units population leads to a stretching of the S4R along O3-$O4_{S4R}$ at ambient conditions in balliranoite, which is partially counterbalanced with a shorter O3-$O4_{12R}$ (*i.e.* a shorter channel free diameter, 5.58(1) Å in balliranoite, 5.78(1) Å in cancrinite).

Besides the significant differences observed within the (0001) plane, the same deformation mechanism is shown along [0001], *i.e.* the compression of the double chain of tetrahedra (*dzc* unit), even though with a different magnitude.

6.2.5 Conclusions

This study of a natural balliranoite from Mogok (Myanmar) represents, to the best of our knowledge, the first investigation on the high-pressure behavior of a davyne subgroup mineral. The studied sample is stable up to the highest pressure here investigated (6.77(2) GPa). The *P*-induced structure evolution is mainly governed by the tilting of the framework tetrahedra, acting as quasi-rigid units. This tilting is reflected within the (0001) plane by the ditrigonal rotation of the S6R⊥[0001] and by the cage compression through the O2-$O2_{cw}$ shortening, and along [0001] by the compression of the double chain of tetrahedra (*dzc* unit). An apparent slight re-arrangement of the channel cationic population occurs, described by the tendency of the two M sites to merge.

The comparison with the isotypic cancrinite (section 4.2) shows a similar volume compressibility, but a less pronounced elastic anisotropy. The observed different elastic behavior is due to different deformation mechanisms. The largest differences are observed within the (0001) plane, where different evolution of *can* units and channels occur.

The results obtained in this study and those from the low-*T* investigation of natural balliranoite (section 6.1) suggest that the nature of the extraframework population of the *can* units has a considerable influence on the structure deformation mechanisms at non-ambient conditions and, hence, on the thermo-elastic behavior of the cancrinite-group minerals. A discussion on this topic will be given in the chapter 8.

Figure 6.7 (*Top*) On the left: unit-cell volume evolution as a function of pressure. The solid line represents the fit with a II-BM EoS. On the right: the normalized stress ($Fe = P/[3fe(1 + 2fe)^{5/2}]$) *vs*. the Eulerian finite strain ($fe = [(V_0/V)^{2/3} - 1]/2$) plot. The estimated standard deviations have been calculated according to Heinz and Jeanloz (1984). The solid line represents a weighted linear fit through the data. (*Bottom*) The *a* and *c* unit-cell parameters evolution as a function of pressure. The solid lines represent the fit with "linearized" III-BM EoS

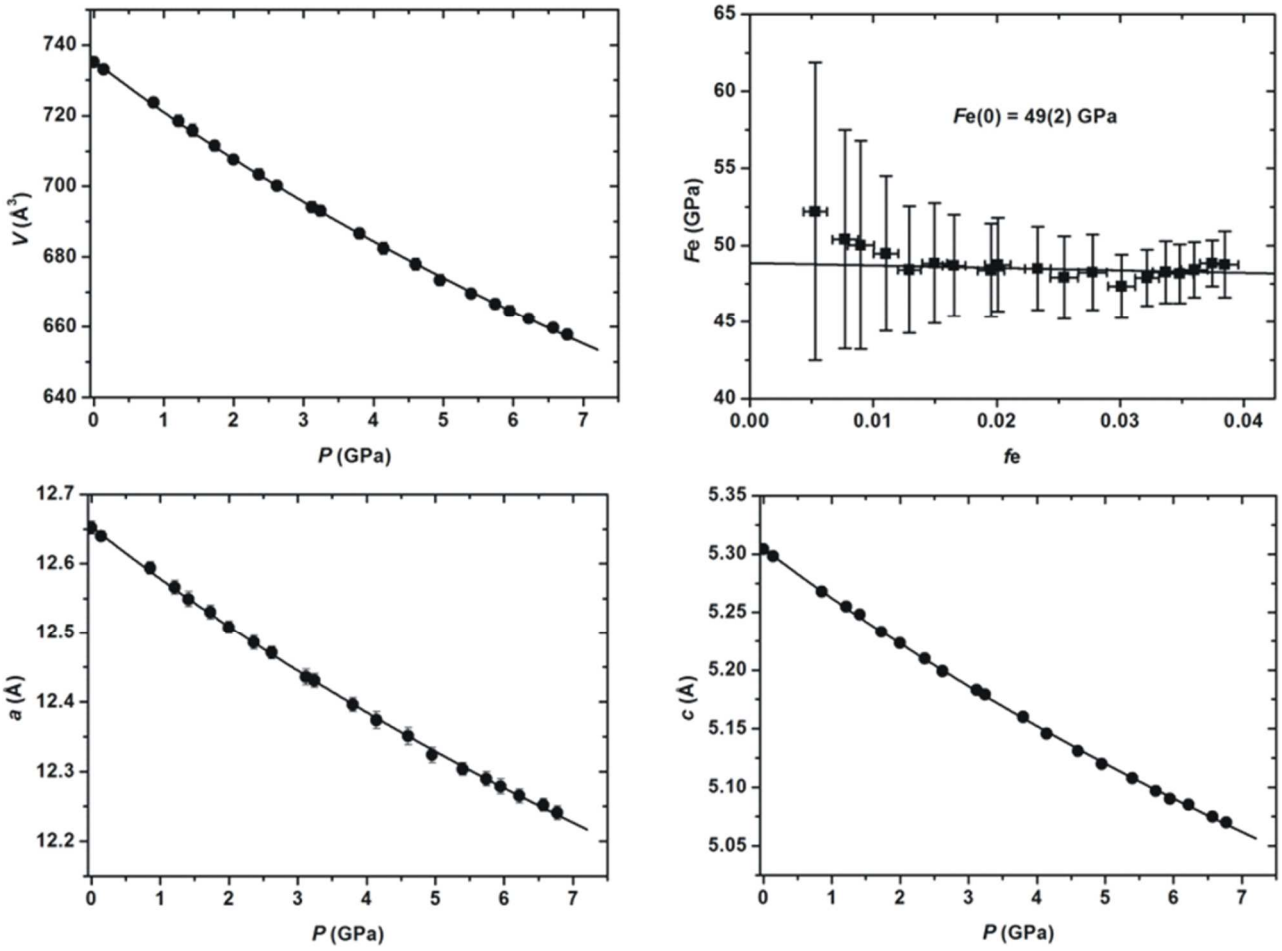

Figure 6.8 (*Top*) On the left: *P*-induced evolution of the intertetrahedral Si-O-Al angles, normalized to their room-*P* values. On the right: evolution as a function of pressure of the normalized O1-O1$_{12R}$ and O3-O4$_{12R}$ channel diameters. (*Bottom*) The *can* unit width O2-O2$_{cw}$ and flattening angle O2-O2-O2, normalized to their values at 0.0001 GPa, as a function of pressure in balliranoite (*left side*) and cancrinite (*righ sidet*).

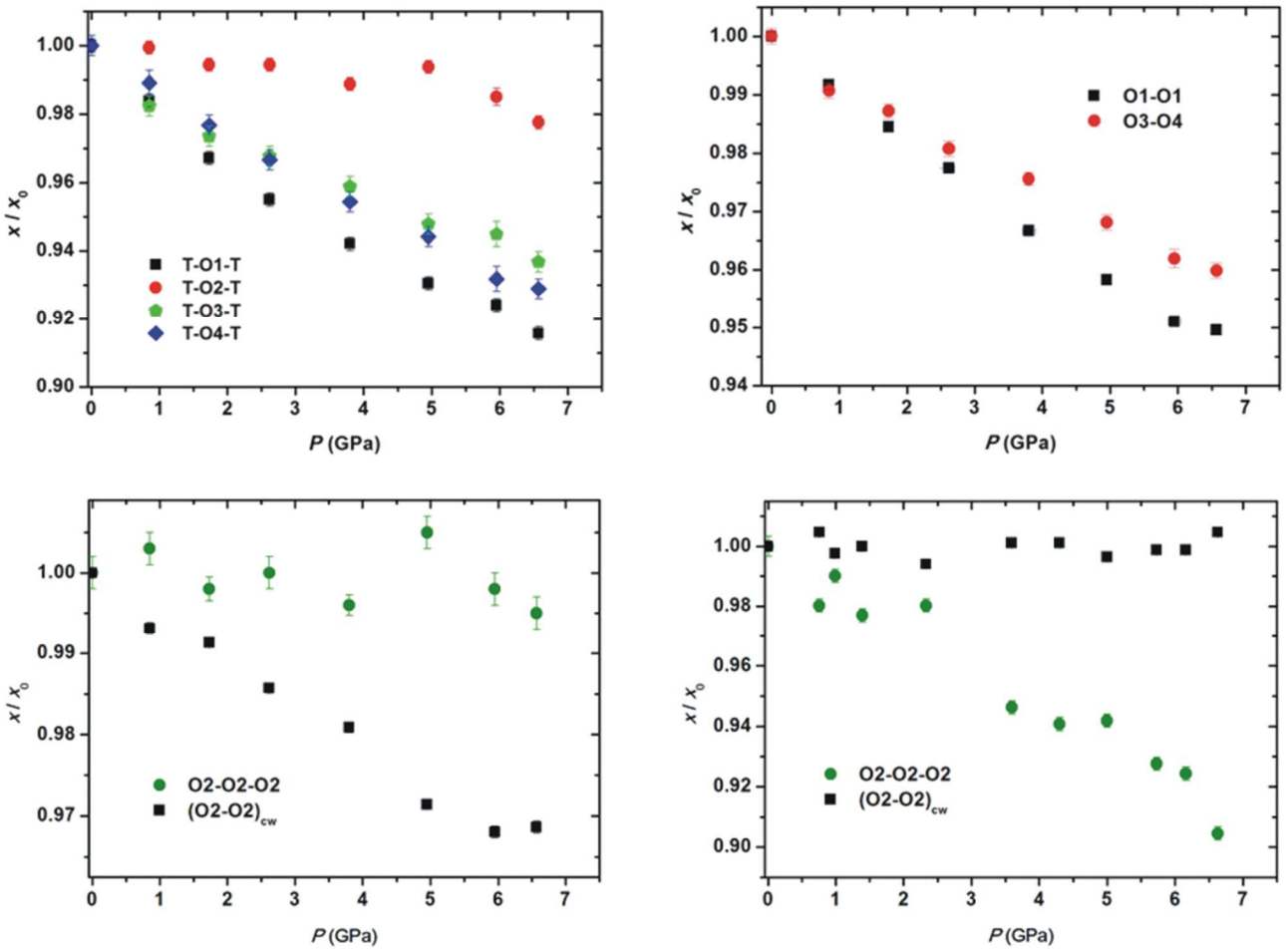

Figure 6.9 *P*-induced evolution of the normalized unit-cell volume, *a* and *c* parameters in balliranoite (circles) and cancrinite (triangles).

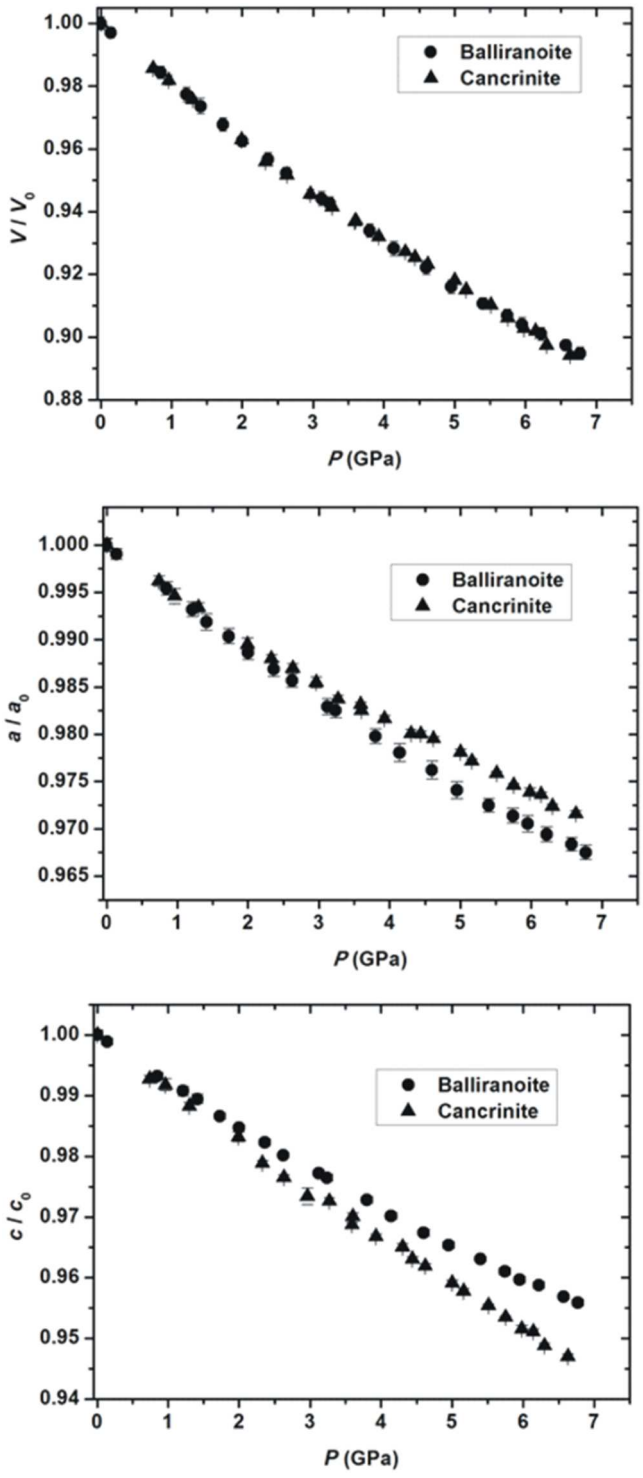

Chapter 7

Davyne

7.1 DAVYNE BEHAVIOR AT LOW TEMPERATURE

The experimental findings reported in the following paragraphs have been published in the following paper:

G.D. Gatta, P. Lotti, G. Nénert, V. Kahlenberg (2013) On the crystal structure and low-temperature behavior of davyne: A single-crystal X-ray and neutron diffraction study. *Microporous and Mesoporous Materials*, **185**, pp. 137-148.

7.1.1 Experimental methods

A large crystal of davyne (0.7 cm^3) from Mt. Vesuvius, Naples, Italy, free of defect under polarized microscope, was selected for this multi-methodological study. The crystal was cut in three fragments in order to perform the chemical analysis, the low-*T* X-ray diffraction and the room-*T* neutron diffraction experiments. Electron microprobe analysis in wavelength dispersive mode was performed using a JEOL 8200 microprobe operating at 15 kV acceleration voltage, 5 nA incident beam and 3 μm beam size. The following natural standards were used: omphacite (Na), realgar (S), anorthite (Ca, Al), K-feldspar (K), wollastonite (Si) and scapolite (Cl). The crystal (400*400*200 μm^3) was found to be chemically homogeneous. The average chemical formula, based on 20 point analyses and calculated on the basis of (Si + Al) = 12 atoms per formula unit, is the following: $(Na_{3.98}K_{1.79}Ca_{1.89}Mg_{0.02}Fe_{0.01})(Al_{5.99}Si_{6.01}O_{24})(SO_4)_{0.65}Cl_{1.96}$ (Table 7.1).

A further fragment of the original crystal (220*180*130 μm^3) was used in order to investigate the low-*T* behavior of davyne by *in situ* single-crystal X-ray diffraction. Six intensity data collections have been performed at 293 (room-*T*), 250, 220, 180, 140 and 110 K using an Oxford Diffraction Gemini Ultra diffractometer, equipped with a Ruby CCD detector and operating at 50 kV and 40 mA with monochromatized Mo-*K*α radiation. *In situ* low-*T* conditions were generated by cooling the crystal in air with a nitrogen gas flux using an Oxford Cryosystems 700 Plus device (temperature stability better than 0.2 K, absolute uncertainty within 2 K at the crystal position). No adsorption of nitrogen from the atmosphere, nor desorption of water, were detected at low-*T*. A combination of ω scans, with 1° step and 10 s exposure time per frame, was used to maximize the redundancy and data coverage. The diffraction pattern collected at any *T* showed weak, but indexable, superstructure reflections, compatible with the microsommite unit-cell. Least-squares refinement of the peak positions leads to the following super-cell parameters at room conditions: a = 22.1543(9) Å, c =

5.3469(2) Å and V = 2272.8(2) Å^3. The corresponding davyne subcell at room-T is given by a_{dav} = a_{mic}*($\sqrt{3}$)$^{-1}$ = 12.7908(5) Å, c_{dav} = c_{mic} = 5.3469(2) Å and V_{dav} = 757.59(6) Å^3. The 000l reflections were always found to be absent for l = 2n + 1, suggesting space group $P6_3$ within the T-range investigated, and so discarding the transition to the $P3$ (see sections 1.2.1 and 1.2.2 for further details). Intensity data at any T were integrated and corrected for Lorentz-polarization effects and absorption of the crystal (based on the empirical SCALE3 ABSPACK algorithm) using the CrysAlis software package (Agilent 2012). Analysis of all the intensity datasets showed that all the superstructure reflections (*i.e.*, those having $h - k \neq 3n$) were systematically "unobserved" (*i.e.*, $Fo \leq 4\sigma(Fo)$). As a consequence, a structure refinement in the microsommite super-cell cannot be performed. The intensity datasets were then re-indexed according to the davyne sub-cell, keeping only the reflections fulfilling the following condition in the microsommite metric: $h - k = 3n$.

Neutron intensity data were collected at 293 K on the high resolution four-circle diffractometer D9 at the Institut Laue Langevin, Grenoble (France), using a wavelength of 0.8242(1) Å obtained using the (220) reflection of a diamond monochromator operating in transmission geometry. Diamond crystal plates of high quality with dimensions of 1.5*1.5*0.17 cm^3 have a mosaic distribution of 0.15°. Composite diamond crystals, by stacking crystal plates on top of each other, were used. Such a technique allows the production of sufficiently thick diamond crystals with a controlled mosaic spread adapted to the instrument requirements. With an active area of 6*6 cm^2, it consists of 4 columns of 4 composite crystals that are approximately 0.55 cm thick with a global mosaic distribution of 0.3°. The crystals are mounted onto specific holders cut from a perfect silicon crystal in order to reduce instrumental background (Courtois et al. 2013). The wavelength was calibrated using a germanium single crystal. D9 is equipped with a small two-dimensional area detector (Lehmann et al. 1989), which allowed optimal separation of the peaks from the background. A preliminary X-ray data collection of the crystal used for the neutron diffraction did not show evidence of superstructure reflections expected for the microsommite metric. Accordingly, the neutron diffraction pattern did not show superstructure reflections. The data collection was then completed according to the davyne metric. A total number of 2362 reflections were collected up to $2\theta_{max}$ = 75.54°, giving 1351 unique reflections. For all data, background corrections following Wilkinson et al. (1988) and Lorentz corrections were applied. After corrections, the reliability factor among the symmetry related reflections was R_{int} = 0.0305 (Laue class 6/m). Least-squares matching of the observed and calculated centroids of the 482 strongest reflections gave a metrically hexagonal unit

cell with: $a = b = 12.7615(7)$ Å and $c = 5.3416(3)$ Å, with a primitive lattice. The reflection conditions agreed with the space group $P6_3$.

A summary of the details pertaining to the X-ray and neutron diffraction experiments are given in Table 7.2.

7.1.2 Results

Structure refinements

The X-ray structure refinements have been performed using the SHELXL-97 software (Sheldrick 1997, 2008). Neutral scattering factors for Si, Al, O, Na, K, Ca, Cl and S have been taken from the *International Tables for Crystallography Vol. C* (Wilson and Prince 1999). The framework site positions of balliranoite, from the refinement at 293 K (section 6.1), have been used as starting structure model for the first refinement cycles. The extraframework population was identified by difference-Fourier synthesis of the electron density. The cage content was found to be similar to that previously reported (*e.g.* Bonaccorsi et al. 1990, 1995, 2001; Hassan and Grundy 1990): a Ca site (Ca), centered on the S6R⊥[0001] cage-basis, alternated with a Cl anion occupying three symmetry-related and mutually exclusive positions (Cl), approximately at the center of the cage (Fig. 7.1). The channel content is given by cationic sites near the walls and sulfate groups at the center. A maximum (at 0.11, 0.22, 0.23) was interpreted as the "internal" K site (K, Table 7.3), whereas a slightly more broad distribution of electron density (Fig. 7.2) was modeled with two "external" Na sites (*i.e.*, Na1 at 0.15, 0.31, 0.23; Na2 at 0.17, 0.35, 0.24) (Fig. 7.3; Table 7.3). The short distances between these cationic sites suggest their mutual exclusivity. A strong maximum on the 6_3 axis (0, 0, 0.22) was assigned to a S atom (S, Table 7.3), while three maxima slightly out of the 6_3 axis at $z = 0.47$ were interpreted as three mutually exclusive positions of the apical oxygen atoms of the SO_4 tetrahedron (OA, Fig. 7.3; Table 7.3). Three coplanar and symmetrically related maxima were located at $z = 0.12$ and $z = 0.38$ and assigned to the oxygen atoms of the SO_4 tetrahedral basis (OB1 and OB2, Table 7.3), suggesting the presence of two possible configurations of the SO_4 tetrahedron: upward and downward (Fig. 7.3), as previously reported (Bonaccorsi et al. 1990, 1995, 2001). The first cycles of refinement were conducted with isotropic atomic displacement parameters (*adp*'s), which were then set anisotropic for all the framework, Ca and K sites. The two Na sites (*i.e.*, Na1-Na2, Table 7.3) and all the sulfate oxygen atoms (*i.e.*, OA, OB1 and OB2, Table 7.3) were restrained to share the same

isotropic *adp*'s, respectively. The refinements converged for all the low-*T* datasets, with no significant correlation between the refined parameters. The maxima in the difference-Fourier maps of electron density were lower than ± 1.09 $e^-/Å^3$ for all the datasets (Table 7.2). For the structure refinements based on the intensity data collected at 140 K and 110 K, the three mutually exclusive OA sites converged into a single site lying on the 6_3 axis on a 2*a* Wyckoff position (0,0,*z*) (Table 7.3). Refined atomic coordinates, occupancies and isotropic/equivalent atomic displacement parameters are listed in Table 7.3. Anisotropic atomic displacement parameters are in Table 7.4.

The neutron structure refinement was performed using the SHELXL-97 software, starting from the previously refined X-ray structure model. The neutron scattering lengths of Si, Al, O, Na, K, Ca, Cl and S were used according to Sears (1986). Correction for secondary isotropic extinction was performed according to the protocol of Larson (1967). After the first cycles of refinement, the difference-Fourier map of the nuclear density showed that the configuration of the SO_4-groups was more complex than that previously obtained by the X-ray refinement. S atoms appeared to be partially disordered along 0,0,*z* (Fig. 7.2). One apical oxygen site (*i.e.*, OA) and three other independent oxygen sites (*i.e.*, OB1, OB2 and OB3, Table 7.5) suggest the presence of three possible, and mutually exclusive, configurations of the SO_4 tetrahedron: one upward (*i.e.*, OB1*3 and OA) and one downward (*i.e.*, OB2 *3 and OA) as also observed by the X-ray refinement, and a third one upward (*i.e.*, OB3*3 and OA) with the 3*OB3 sites in a configuration similar to that observed in CO_3-group in balliranoite (Fig. 7.4). The first cycles of the structure refinement were then conducted with: a) Ca, Cl, Si, Al and all the framework oxygen sites (*i.e.*, O1, O2, O3 and O4, Table 7.5) refined anisotropically; b) K, Na1, Na2, S and all the oxygen sites belonging to the SO_4-group (*i.e.*, OA, OB1, OB2 and OB3) refined isotropically, c) unconstrained site occupancy for K, Na1, Na2, S, OA, OB1, OB2 and OB3. The convergence was rapidly achieved, with non-significant residuals in the difference-Fourier map of the nuclear density. However, a significantly high correlation between some of the refined parameters forced us to fix the values of the U_{ij} components in the last cycles of refinement. With such a configuration, the convergence was achieved and the shifts in all parameters were less than their *e.s.d.* values, the variance-covariance matrix showed no significant correlations, and the residuals in the difference-Fourier synthesis of the nuclear density were < ± 1.05 fm/$Å^3$. We obtained a final R_1 = 0.0684 for 1185 reflections with $Fo > 4\sigma(Fo)$. Site coordinates, occupancy factors and isotropic atomic displacement parameters are given in Table 7.5. Anisotropic atomic displacement parameters are in Table 7.4. Relevant bond lengths and angles are listed in Table 7.6.

Low-temperature elastic behavior

The evolution of the unit-cell parameters (*a*, *c*, *V*) of davyne with temperature is shown in Fig 7.5. The volume contraction follows a monotonic trend, with no evidence of phase transition nor change of the compressional behavior. The experimental data have been fitted to the equation (8) directly derived from the thermodynamic definition of the volume thermal expansion coefficient (*i.e.*, $\alpha_V = 1/V*(\partial V/\partial T)_P$): $V = V_r*\exp(\alpha_V*(T-T_r))$, where T_r is the reference temperature (in this case the lowest experimental T = 110 K) and V_r the volume at the reference temperature. This protocol was already to describe the low-*T* elastic behavior of the isotypic cancrinite and balliranoite (sections 4.1 and 6.1). The fit converged to the following refined parameters: V_r = 751.0(3) Å^3, α_V = 4.2(4)*10^{-5} K^{-1}. Similarly, the *a*- and *c*-edges evolution trends with temperature have been fitted to the "linearized" equation derived from the thermodynamic definition of the linear thermal expansion coefficient ($\alpha_l = 1/l*(\partial l/\partial T)_P$), $l = l_r*\exp(\alpha_l*(T-T_r))$, leading to the following refined parameters: a_r = 12.754(2) Å, α_a = 1.4(1)*10^{-5} K^{-1}; c_r = 5.3300(7) Å, α_c = 1.6(1)*10^{-5} K^{-1}. The resulting thermoelastic anisotropy is $\alpha_a : \alpha_c$ = 1 : 1.14. A fit using the equation (14) proposed by Pawley et al. (1996) yielded the following refined parameters: V_r = 751.4(2) Å^3, a_{0V} = 1.59(9)*10^{-4} K$^{-1/2}$; a_r = 12.757(1) Å, a_{0a} = 4.9(3)*10^{-5} K$^{-1/2}$; c_r = 5.3311(4) Å, a_{0c} = 5.8(2)*10^{-5} K$^{-1/2}$. The calculated thermal expansion coefficients at room-*T* are: $\alpha_{V,293K}$ = 6.6(4)*10^{-5} K^{-1}, $\alpha_{a,293K}$ = 2.0(1)*10^{-5} K^{-1} and $\alpha_{c,293K}$ = 2.41(8)*10^{-5} K^{-1}. The resulting thermoelastic anisotropy at room-*T* is is $\alpha_a : \alpha_c$ = 1 : 1.21.

Low-temperature structure evolution

As expected in open-framework silicates under "compressional" regimes (*i.e.*, low temperature or high pressure, Gatta 2008, 2010), the main deformation mechanisms observed in davyne at low temperature can be described in terms of tilting of the rigid (Al,Si)O_4 tetrahedra, suggested by the average <(Si,Al)-O> bond lengths reported in Table 7.6. This tilting is reflected by the intertetrahedral Si-O-Al angles, which all experience a closure with the exception of the Si-O2-Al angle (Fig. 7.6; Table 7.6). The effects of tetrahedral tilting on the framework can be followed through the behavior of the secondary building units. A slight increase of the ditrigonal rotation angle $\alpha_{S6R\perp[0001]}$ of the S6R⊥[0001] (Fig. 7.7, section 4.1.2) can be deduced from the data in Table 7.6, in analogy with the behavior shown by cancrinite (section 4.1) and balliranoite (section 6.1), even though this behavior is partially hindered by the experimental uncertainties. A deviation from planarity in response to cooling is also shown by the S6R⊥[0001], as suggested by the increasing of the *dz* between O1 and

O2 [$dz_{S6R\perp[0001]}$ = (z(O1) – z(O2))*c, Table 7.6]. In the [0001]-channel, a contraction of both the independent diameters O1-$O1_{12R}$ (projection on the (0001) plane) and O3-$O4_{12R}$ with decreasing temperature is observed (Fig. 7.6 and 7.7; Table 7.6), whereas the O3-$O4_{S4R}$ diameter of the S4R (Fig. 7.7; Table 7.6) do not vary within 1σ. The closure of the O3-O4-O3 angle (Fig. 7.7; Table 7.6) reflects the contraction of the double *zigzag* chains of tetrahedra along [0001]. Consistently with our previous studies on cancrinite-group minerals, we define as "corrugation" the deviation from planarity shown by the A- and B-planes of S6R⊥[0001] (Fig. 7.7, section 4.1.2). The "corrugation" parameter Δz shows a clear decrease towards the lowest temperatures (Table 7.6). The *can* unit deformation is described by the shortening of the three symmetrically related O2-$O2_{cw}$ diameters on the (0001) plane (dashed lines in Fig. 7.7) (Fig. 7.6; Table 7.6), which can be referred to as "cage width", as also reported in previous chapters, and the contraction of the double chains of tetrahedra along *c*-axis.

With the exception of the merging of the symmetrically related (and mutually exclusive) OA sites into a single position on the 6_3 axis at 140 and 110 K, no other significant changes affecting the configuration of the extraframework population are observed in response to low-*T*. However, contractions and elongations of several bond lengths can be followed with decreasing temperature. The Na bond distances with the framework oxygen O1, O3′ and O4′ undergo a shortening, whereas an elongation of Na1,2-O3″ and Na1,2-O4″ is observed (Table 7.6). Overall, the average <Na1,2-$O_{framework}$> bond lengths decrease with decreasing temperature (Table 7.6). A similar behavior is shown by the bond lengths between K and framework oxygen sites, but in this case no significant *T*-dependent changes of the average <K-$O_{framework}$> occurs (Table 7.6). For the extraframework population of the cage, only a shortening of the longer Ca-Cl″ bond length is significant (Table 7.6).

7.1.3 Discussion

This is the first study in which the crystal structure of davyne is refined on the basis of single-crystal X-ray and neutron diffraction data, and its low-*T* behavior is described by *in situ* single-crystal X-ray diffraction.

The davyne used in this study showed superstructure reflections, observed by the X-ray diffraction pattern only, which suggests a potential partial ordering of the extraframework population toward the structure model of microsommite. Moreover, as previously reported (section 7.1.1), all the superstructure reflections were systematically "unobserved" (*i.e.*, $Fo \leq 4\sigma(Fo)$). X-ray and neutron

structure refinements confirm the perfectly ordered Si/Al-distribution in the tetrahedral framework (Fig. 7.7; Tables 7.3 and 7.5). The extraframework configuration is similar to that previously reported for davyne (Bonaccorsi et al. 1990, 1995; Hassan and Grundy 1990) and microsommite (Bonaccorsi et al. 1995, 2001). The cages are occupied by chains of alternated Ca^{2+} and Cl^- almost equally spaced. In the channel, the "internal" K site is located far from the oxygen walls, in a position slightly closer to the centre if compared to the M1 site in balliranoite (*i.e.*, at 0.12 0.25 0.30 and occupied by Na^+ and Ca^{2+}, sections 6.1 and 6.2), likely in order to fit the longer K-O bonds. The broad distribution of electron and nuclear density closer to the channel walls (observed by X-ray and neutron diffraction data, Fig. 7.2) has been modelled with two Na sites (*i.e.*, Na1 and Na2, Tables 7.3 and 7.5). The K^+ cation is coordinated with 5 framework oxygen atoms and up to two OA apical oxygen (if adjacent upward and downwad SO_4 tetrahedra occur), whereas the Na^+ cations are coordinated by 4-5 framework oxygen and one OB basal oxygen of the sulfate tetrahedron at the same height (Fig. 7.3).

The crystal chemical formula deduced on the basis of the X-ray structure refinement is $(Na_{2.59}K_{2.70}Ca_2)(Al_6Si_6O_{24})(SO_4)_{0.68}Cl_2$, whereas that from neutron refinement is $(Na_{3.13}K_{2.65}Ca_2)(Al_6Si_6O_{24})(SO_4)_{0.70}Cl_2$. A good agreement between the EMPA-WDS chemical analysis [*i.e.*, $(Na_{3.98}K_{1.79}Ca_{1.89}Mg_{0.02}Fe_{0.01})(Al_{5.99}Si_{6.01}O_{24})(SO_4)_{0.65}Cl_{1.96}$] and structure refinements is shown for the cage population and the channel anions. The slight deficiency in Ca and Cl in EMPA-WDS data is not detected by the diffraction data, which lead to a full occupancy of the cage sites. As previously shown, the SO_4 tetrahedron can occur in at least two configurations: upward (involving the OB1 basal sites) and downward (involving OB2 sites). If the maximum amount of 1 SO_4 p.f.u. is reached, each channel is internally ordered, as discussed by Bonaccorsi et al. (2001) who pointed out that this is a necessary (but not sufficient) condition to lead toward the microsommite-like ordering. In our case, both the chemical analysis and the structure refinement show ~ 0.65-0.70 a.p.f.u. of S, allowing a disordered distribution of the anionic group into the channel due to site vacancies. An apparent discrepancy between the chemical formula based on the EMPA-WDS analysis and those from structure refinements is shown for the cationic population of the channel, suggesting an underestimation of the Na content and, in turn, an overestimation of K by the structure refinements. However, if the number of electrons at the cation sites is calculated, we obtain: (3.98*11) + (1.79*19) = 77.8 e^- for the EMPA-WDS analysis and (2.59*11) + (2.70*19) = 79.8 e^- for the X-ray structure refinement, showing an excellent agreement. This suggests that the discrepancy between the crystal chemical formulae is likely due to a partial substitution of K^+ by Na^+ at the K site and by a strong positional disorder of the Na1-Na2 population, as highlighted by the difference-Fourier map of

electron and nuclear density (Fig. 7.2). The neutron structure refinement leads to (3.13*11) + (2.65*19) = 84.8 e^- for the cationic population.

The Na1-Na2 positional disorder leads to a different coordination environment at a local scale. In this respect, the presence and the configuration (*i.e.*, upward or downward) of the sulfate tetrahedron can control the Na^+ positioning in order to fit the bonding environment energetically more favorable, with the cation closer to the walls when coupled with a S-vacancy. In this scenario, Na1 and Na2 positions should be considered as "virtual" sites, located in order to model an actually broad electron or nuclear density distribution. Similarly, the static disorder of the S site along 0,0,*z*, as well described by the nuclear density map shown in Fig. 7.2, leads to an underestimated S-O bond distances with the apical oxygen of the tetrahedron (*i.e.*, S-OA, Tables 7.3 and 7.5).

Low-temperature elastic behavior

The low number of datasets results in quite large uncertainties of the refined parameters. A good agreement is observed between the mean linear thermal expansion coefficients reported by Bonaccorsi et al. (1995) for a davyne up to 473 K (*i.e.*, α_a = 1.51(8)*10^{-5} K^{-1} and α_c = 1.6(4)*10^{-5} K^{-1}) and the experimental findings of this study. Although the linear thermal expansion coefficients of davyne and balliranoite are almost identical (*i.e.*, α_a = 1.4(1)*10^{-5} K^{-1}, α_c = 1.6(1)*10^{-5} K^{-1} in davyne; α_a = 1.4(2)*10^{-5} K^{-1} and α_c = 1.7(2)*10^{-5} K^{-1} in balliranoite), it is interesting to note that they are significantly different from those of cancrinite (*i.e.*, α_a = 0.7(2)*10^{-5} K^{-1}, α_c = 2.1(3)*10^{-5} K^{-1}). These data offer several potential interpretations: 1) From the crystal chemical point of view, davyne and balliranoite show strong structural similarities, as both belong to the davyne subgroup, and, in this respect, their similar elastic behavior is not surprising; 2) The ordering of the extraframework population within adjacent channels, giving rise to the microsommite superstructure, does not appear to affect the elastic behavior of davyne-like minerals, as shown by Bonaccorsi et al. (1995); 3) The significantly different elastic anisotropy shown by cancrinite, observed not only varying temperature (sections 4.1 and 4.3; Hassan et al. 2006) but also under isothermal high-pressure regime (section 4.2), suggests that the *can* units content might influence significantly the elastic behavior of the compounds sharing the [CAN]-topology.

The compatibility to the $P6_3$ space group, shown by the systematic absences within the entire *T*-range investigated in this study, suggests that no order-disorder phase transitions occurs in davyne at least down to 110 K.

Low-temperature structural evolution

The low-*T* induced structural evolution of davyne is mainly controlled by tilting of the rigid framework tetrahedra (Table 7.6). As in the CO_3 end-member balliranoite (section 6.1), all but the Si-O2-Al intertetrahedral angles undergo a closure with decreasing temperature (Fig. 7.6, Table 7.6). A different behavior is observed in cancrinite (section 4.1).

The deformation mechanisms observed in davyne at low-*T* are similar to those previously described in balliranoite (section 6.1). In the (0001) plane, the following non-independent mechanisms can explain the unit-cell contraction: the shortening along the O2-O2 direction through 1) the "cage width" contraction and 2) the decrease of the S6R⊥[0001] diameter (Figs. 7.6 and 7.7, Table 7.6), 3) the shortening of both the symmetrically independent channel diameters O1-$O1_{12R}$ and O3-$O4_{12R}$ (Fig. 7.6 and 7.7, Table 7.6) and 4) the S6R⊥[0001] deviation from planarity, as reflected by the increase of the $dz_{S6R\perp[0001]}$ (Table 7.6). The constant values shown by the O3-$O4_{S4R}$ diameter (Fig. 7.7; Table 7.6) suggest that this secondary building unit does not contribute to the *T*-induced decrease of the *a*-edge. Along the [0001]-axis, the deformation is accommodated by the contraction of the double *zigzag* chains of tetrahedra, which is correlated to S6R∠[0001] windows ditrigonalization and to the decrease of A- and B-planes "corrugation" Δz (Fig. 7.6 and 7.7; Table 7.6). If we consider the *T*-induced deformation of the *can* unit, it can be described as governed by the O2-$O2_{cw}$ "cage width" shortening and by the double chains contraction along [0001], both showing the same magnitude, as confirmed by the constant value of the O2-O2-O2 flattening angle (Fig. 7.7, Table 7.6). As in balliranoite (section 6.1), the *can* unit of davyne undergoes a homogeneous shrinking with decreasing temperature; a different behavior is observed in cancrinite and vishnevite, where a significant flattening of the cage occurs (section 4.1, chapter 5).

A comparison between our low-*T* structure evolution with the high-*T* behavior of davyne and microsommite (Bonaccorsi et al. 1995) shows, as expected, similar deformation mechanisms but opposite in sign (*i.e.* same mechanisms but with opposite trends if compared to the room-*T* conditions). In particular, at high-*T* davyne and microsommite show an expansion of the O1-$O1_{12R}$ channel diameter, of the O2-$O2_{cw}$ "cage width" and, in addition, of the double chains of tetrahedra towards the maximum geometrical limit, above which a displacive phase transition to the $P6_3/m$ space group occurs. The inverse phase transition from $P6_3/m$ to $P6_3$ will be discussed in the next section, where the high-pressure behavior of davyne will be reported.

The analysis of the evolution of the cation-oxygen bond lengths at low-*T* (Table 7.6) suggests that no significant change of the configuration of the extraframework population occurs, except for the apparent merging of the SO_4 tetrahedron apical oxygen into a single position onto the 6_3 axis (Table 7.3).

Figure 7.1 The Ca coordination environment within the *can* unit of davyne. Dashed lines represent the mutually exclusive Ca-Cl bonds.

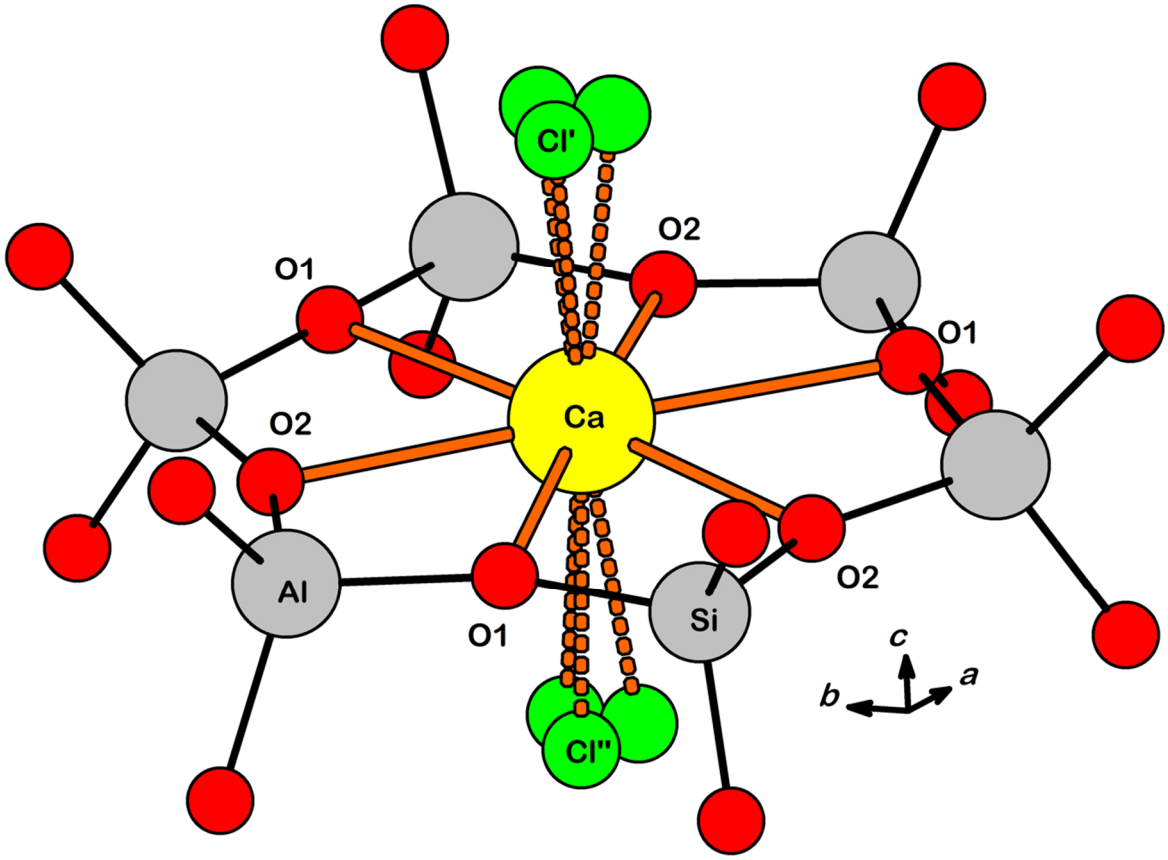

Figure 7.2 Difference-Fourier map of electron (A, in $e^-/Å^3$) and nuclear (B, in fm/$Å^3$) density on the (0001) plane at z ~ 0.23, phased without the channel population. The maxima of the "internal" and "external" cation sites and the broad distribution of electron/nuclear density are shown. (C) Difference-Fourier map of nuclear density along the 6_3 axis at the center of the 12R-channel, phased without the SO_4^{2-} groups.

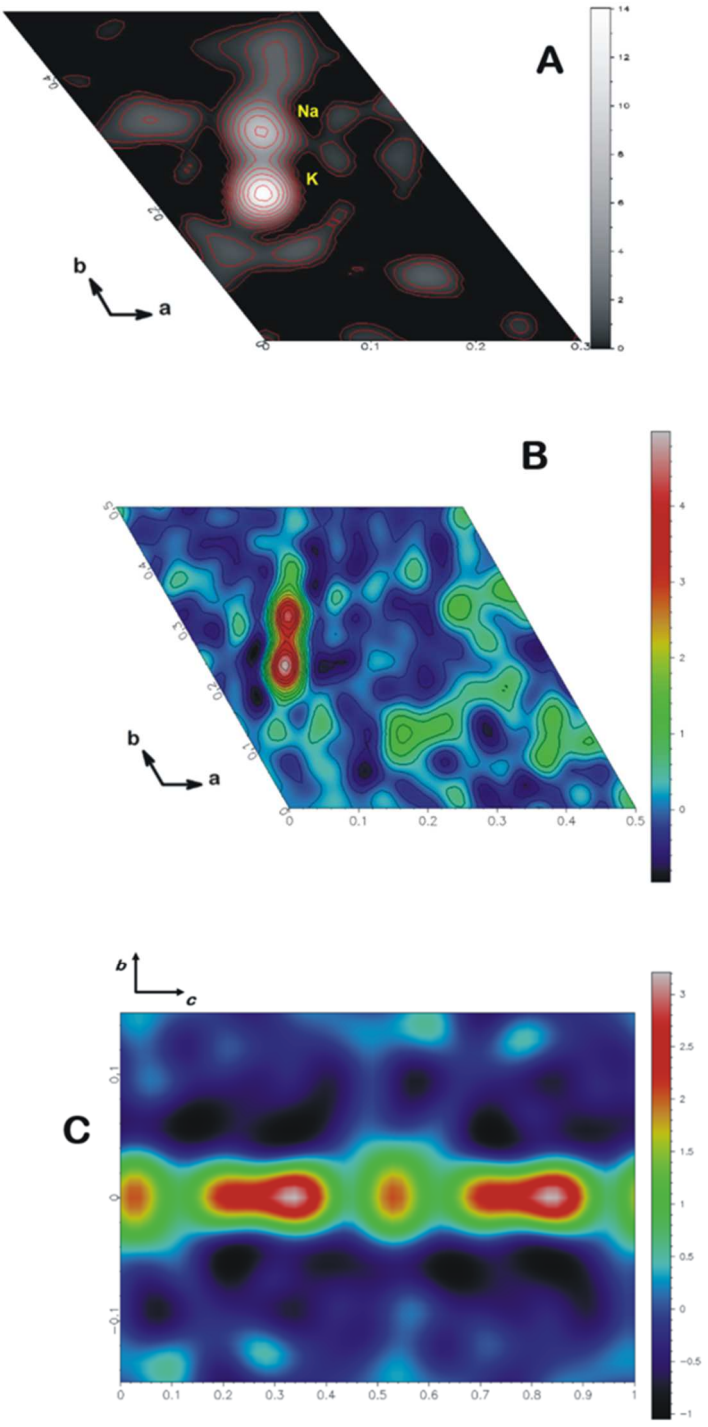

Figure 7.3 (*Left side*) The davyne channel population viewed down [0001]. (*Right side*) Bonding environment of the channel cations in davyne structure. Dashed lines represent the mutually exclusive bonds

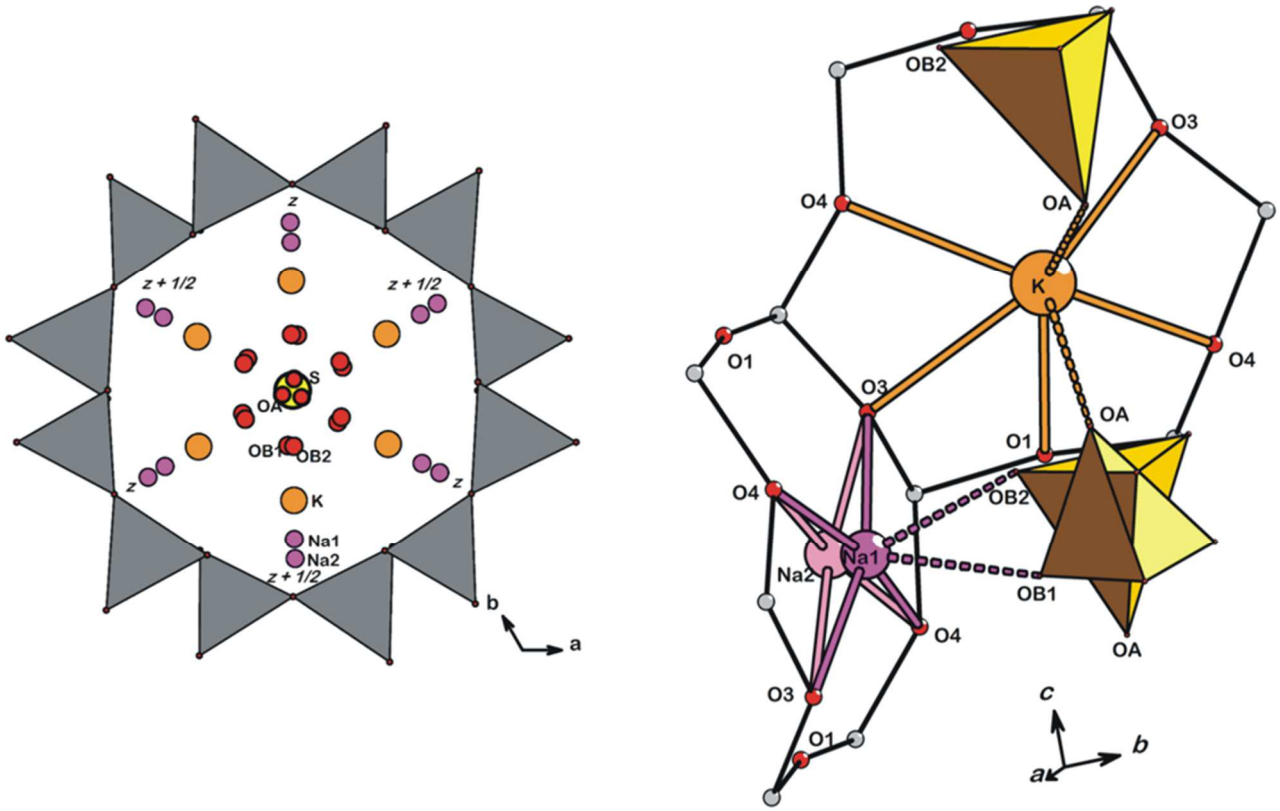

Figure 7.4 The complex (and mutually exclusive) configurations of the SO_4 group in davyne deduced from the neutron structure refinement. Two upwards (*i.e.*, S-OB1*3 and S-OB3*3, with the OA at the top) and one downward (*i.e.*, S-OB2*3 with the OA at the bottom) configurations occur.

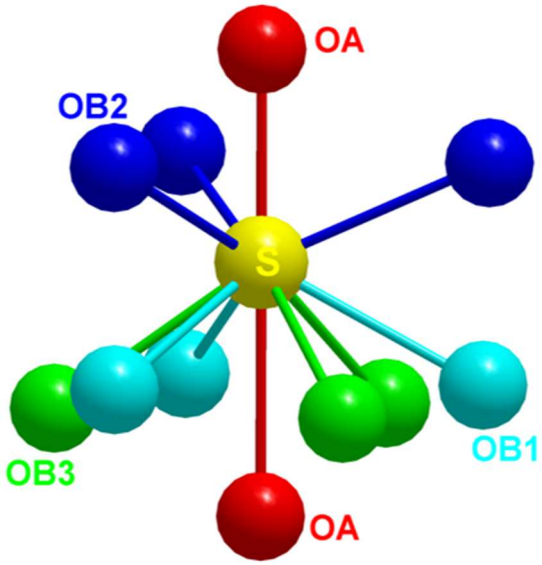

Figure 7.5 Evolution of the unit-cell parameters of davyne with temperature. The solid line represents the fits using the equations $V(T) = V_{Tr}*\exp[\alpha_V*(T-T_r)]$ and $l(T) = l_{Tr}*\exp[\alpha_l*(T-T_r)]$, respectively.

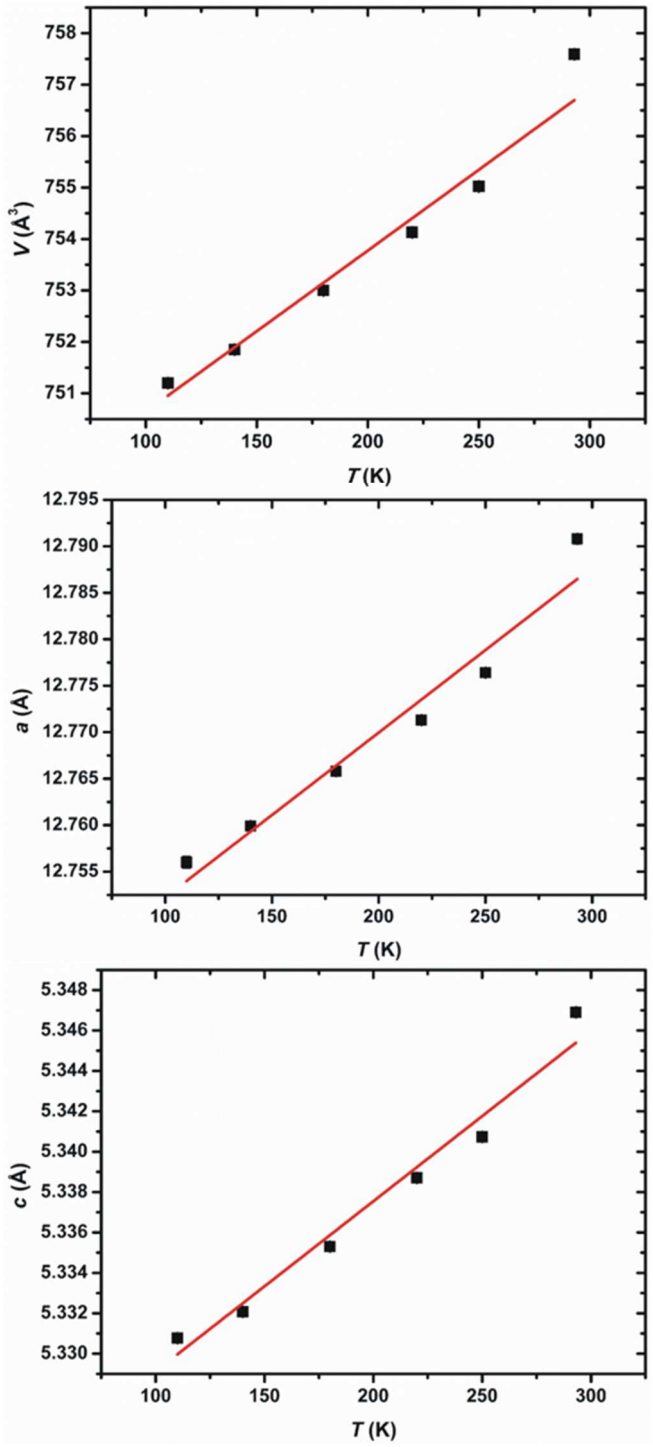

Figure 7.6 Evolution with *T* of: (A) the intertetrahedral Si-O-Al angles, normalized to their values at 293 K; (B) the 12R-channel independent diameters O1-O1$_{12R}$ and O3-O4$_{12R}$, normalized to their room-*T* values; (C) the O2-O2$_{cw}$ "*can* cage width"; (D) the Δ*z* "corrugation" of the A- and B-layers.

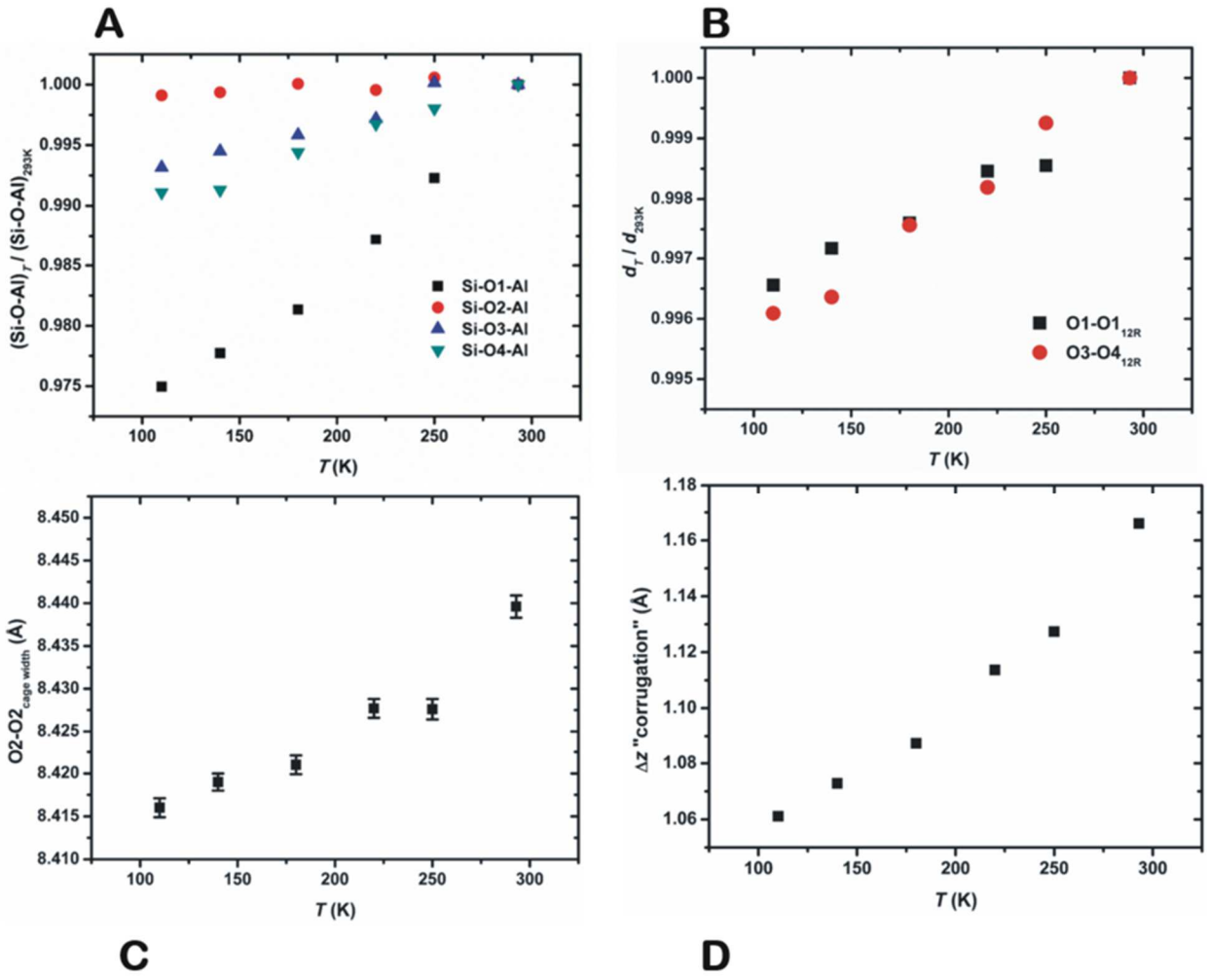

Figure 7.7 (*Top*) The [CAN]-framework viewed down [0001]. The 12mR channel is centred on the 6_3 axis and its symmetry-independent diameters are shown. The channel is surrounded by six columns of *can* units, of which, in this projection, are shown the S6R⊥[0001] bases and the S4R. The O1-$O1_{12R}$ diameter represents the projection onto the (0001) plane. (*Bottom*) A column of base-sharing *can* units. Relevant structural parameters are shown

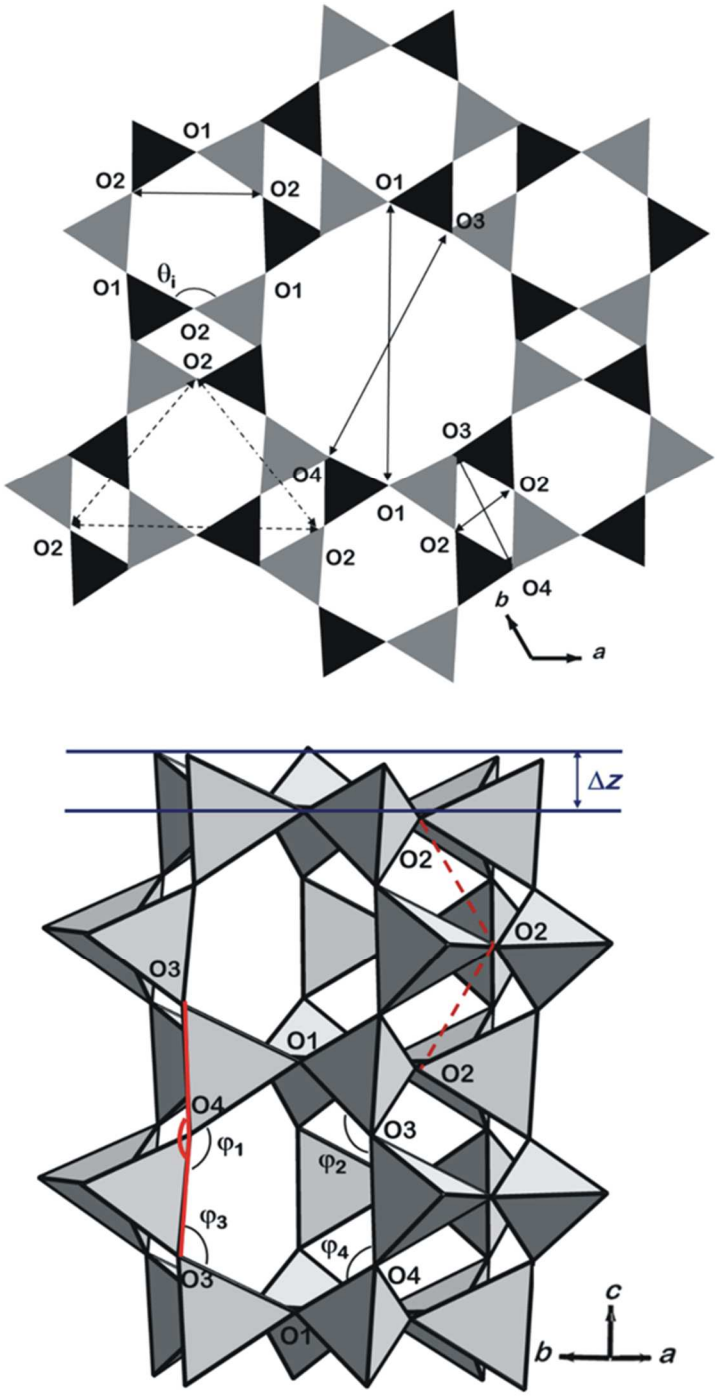

7.2 DAVYNE BEHAVIOR AT HIGH PRESSURE

7.2.1 Materials and experimental methods

A gem-quality crystal of davyne, found in a cavity of a skarn lithic block within volcanic deposits at Monte Somma (Naples, Italy), was selected for this high-pressure study. A fragment (~ 70*60*40 μm^3) was cut and used for the diffraction data collection at room-*P*. The diffraction experiments were performed at the ID09A beamline, at the European Synchrotron Radiation Facility (ESRF), Grenoble, France. A parallel monochromatic beam (E ~ 30 kEv, λ = 0.414 Å) was used. The beam was vertically focused by a spherical mirror and horizontally by a bent silicon-(111) monochromator, in order to have a beam-size at the sample of 30*30 μm^2. The diffraction pattern was collected by a MAR555 flat panel detector. The data collection strategy consisted in a rotation of the crystal about the vertical ω-axis, within the range -45° ≤ ω ≤ +45°, with 1° step scan and 1 s of exposure time per frame. The diffraction data were then indexed, showing a metrically hexagonal lattice, and integrated using the CrysAlis software (Agilent 2012). The unit-cell parameters were calculated by least-squares refinement from the indexed peak positions, leading to a = 12.7931(4) Å, c = 5.3495(1) Å and V = 758.23(5) $Å^3$, the systematic extinctions were compatible with the $P6_3/m$ or $P6_3$ space groups (see next paragraphs for a discussion on the space group symmetry). The intensity of the peaks was corrected for Lorentz-polarization effect and corrected for absorption effects using the ABSPACK routine implemented in the CrysAlis software.

A further smaller fragment (~ 40*40*20 μm^3) was cut from the davyne crystal and loaded into a membrane-controlled diamond anvil cell, with Boehler-Almax design, diamond culet-size 600 μm and cone-aperture of 60°. A stainless steel foil, pre-indented to ~ 70 μm, was used as a gasket; a hole, 250 μm in diameter, was drilled by spark-erosion to serve as a pressure chamber. Few ruby chips were loaded, along with the davyne crystal, into the chamber as *P*-calibrant (Mao et al. 1986). A 4:1 mixture of methanol:ethanol was used as hydrostatic *P*-transmitting fluid (Angel et al. 2007). Twenty-one data collections have been performed from 0.38(2) (P_1) to 7.18(6) GPa (P_{21}). At any *P*-point, the diffraction data were collected after 20 minutes in order to reach the strain relaxation. The same strategy was adopted for all the collections: a rotation about the vertical ω axis, within the range -30° ≤ ω ≤ +30°, with 1° step scan and 1 s exposure time per frame. Unit-cell parameters, at different pressures, were refined by least-squares method from the indexed peak positions and are listed in Table 7.7. Intensity data were always integrated using the CrysAlis software (Agilent 2012) and

corrected, for absorption using the ABSPACK routine implemented in the CrysAlis software. Systematic extinctions were always compatible to the $P6_3$ space group (see next paragraphs for a comprehensive discussion). Ten datasets have been selected to perform structure refinements. More details regarding the data collections are in Table 7.8.

A third fragment was cut from the large davyne sample, in order to perform the chemical analysis, using a JEOL 8200 microprobe operating at 15 kV acceleration voltage, 5 nA incident beam and 3 μm beam size. The following natural standards were used: omphacite (Na), realgar (S), anorthite (Ca, Al), K-feldspar (K), wollastonite (Si), scapolite (Cl), olivine (Mg), celestine (Sr) and sanbornite (Ba). The average chemical formula, based on 10 point analyses and calculated on the basis of (Si + Al) = 12 atoms per formula unit, is the following: $[(Na_{3.72}K_{1.86}Sr_{0.04}Mg_{0.02}Ba_{0.01})(SO_4)_{0.51}][Ca_{1.97}Cl_{2.00}][Si_{5.93}Al_{6.07}O_{24}]$ (Table 7.9).

7.2.2 Structure refinements and *P*-induced displacive phase transition

Structure refinements based on the room-*P* dataset and on the selected H*P*-datasets have been performed using the SHELXL-97 software (Sheldrick 1997, 2008) implemented in the WinGX suite of crystallographic programs (Farrugia 1999). Neutral scattering factors of O, Si, Al, Na, K, Ca, Cl and S have been taken from the *International Tables for Crystallography, Vol. C* (Wilson and Prince 1999).

Systematic absences of the room-*P* dataset showed 000*l* reflections to be always absent for $l = 2n+1$, with internal agreement factor for the 6/*m* Laue class $R_{int} = 0.0621$. Two space groups are compatible with these conditions (*International Tables for Crystallography, Vol. A*, Hahn 2002): the $P6_3/m$ and the $P6_3$, both reported in the literature for davyne samples (Bonaccorsi et al. 1990, 1995; Hassan and Grundy 1990). The Sheldrick's $|E^2-1|$ criterion (calculated value: 0.932; ideal values: 0.968 for centric, 0.736 for acentric structures) and the statistics of distribution of the normalized structure factors ("*E* statistics"), calculated using the WinGX suite of programs (Farrugia 1999), suggest as highly likely the centrosymmetric space group $P6_3/m$ (with 86.3% likelihood), for which a mirror plane is expected at $z = 0.25$ and $z = 0.75$ (Fig. 7.8). A structure refinement has been performed in this space group, starting from the framework coordinates of Bonaccorsi et al. (1990). The extraframework population has been identified through difference-Fourier synthesis of the electron density. The Ca^{2+} site (Ca) was found to occupy a special position on the 3-fold axis at (1/3,2/3,3/4), whereas a diffuse electron density around the 3-fold axis at $z = 1/4$ was modeled as three mutually

exclusive Cl^- sites (*x*,*y*,1/4). The configuration of the $[Ca\text{-}Cl]^+$ chains filling the *can* unit columns is, in this way, reproduced (see Fig. 7.1). Two symmetry-independent peaks were found near the channel walls: the "internal site" (M1, closer to the channel center) was assigned to K^+, whereas the "external one" (M2) was assigned to Na^+, as thoroughly reported in the literature for davyne subgroup minerals (Bonaccorsi et al. 1990, 1995, 2001; Ballirano et al. 1998; Chukanov et al. 2010b; sections 6.1, 6.2 and 7.1 of the present study). An intense peak at (0,0,0.25) was assigned to S^{6+} (S), whereas another peak at (0,0,0), slightly displaced from the 6_3 axis, was assigned to the apical oxygen of the SO_4^{2-} tetrahedron (OA). The refinement of the OA site out from the screw axis was tried, but unsuccesfully. A peak at ~ (0.06,0.11,0.36) was assigned to the basal oxygen atom (OB). The 6_3 screw axis and the mirror plane at $z = 0.25$ generate triangular symmetry-equivalent positions at $z \sim 0.14$ and $z \sim 0.36$, suggesting the existence of two mutually exclusive configurations for the sulfate group: downward and upward (see Fig. 7.3). In the first cycles, all the sites have been refined with isotropic atomic displacement parameters (*adp*'s), whereas in the last cycles, the *adp*'s of the framework sites and Ca were set to anisotropic. The OA and OB sites were constrained to share the same *adp*. Early refinements suggested a full occupancy for the Ca and the split Cl sites (*i.e.* 1.0 and 1/3, respectively). The analysis of the difference-Fourier maps of electron density, phased without the sulfate anion, showed a slight positional disorder of the tetrahedron along the *c* axis (Fig. 7.9). The real position of the S^{6+} atom could be slightly above or below the mirror plane at $z = 0.25$ (and $z = 0.75$), for the downward and upward configurations, respectively, as the short S-OA bonds also suggest. The refinement converged to a final $R_1 = 0.0733$ for 557 unique reflections with $F_o > 4\sigma(F_o)$, with no significant correlations between refined parameters: the highest residuals in the difference-Fourier maps were +1.65 and -2.25 $e^-/Å^3$. A discussion on these apparently high values will be given in the next paragraphs. Details on the structure refinements are in Table 7.8. Refined atomic occupancies, coordinates and isotropic/equivalent atomic displacement parameters are in Table 7.10. Relevant distances, bond angles and structural parameters in Table 7.11.

A test refinement in the space group $P6_3$ was also performed. The refinement converged to a final $R_1 = 0.0783$, for 939 unique reflections with $F_o > 4\sigma(F_o)$, and no significant correlations between the refined parameters. Apparently, there is no significant difference in the quality of the structure refinements using the $P6_3$ or the $P6_3/m$ space group. However, in the structure model refined in the $P6_3$ space group, all the sites which are expected to lie on the mirror planes in the space group $P6_3/m$ (*i.e.* all with the exception of O3, O4, OB1 and OB2), were found to have $z \sim 0.25$ (or 0.75). Moreover, unusually pronounced anisotropic atomic displacement parameters were obtained for the framework

oxygen sites, in particular for O3 and O4. In this light, and considering the distribution of the *E* statistical parameters the centrosymmetric $P6_3/m$ appears to be the most likely space group.

A significant contraction along the [0001] crystallographic direction is only possible if a compression, through tetrahedra tilting, of the *dzc* unit occurs (Fig. 7.8). This tilting necessarily induces a closure of the O3-O3-O3 angle (O3-O4-O3 in the $P6_3$ space group, Fig. 7.8). However, this angle is constrained by symmetry to 180° in the $P6_3/m$ space group. Therefore, any *P*-induced compression along [0001], driven by tetrahedra tilting, must induce a displacive phase transition from the $P6_3/m$ to the $P6_3$ space group. This has been confirmed by the structure refinements and by the *E* statistics calculations for the high-pressure datasets. The structure refinement from the P_1 [0.38(2) GPa] dataset was performed starting from the framework coordinates reported by Hassan and Grundy (1990) for a $P6_3$-davyne. The extraframework content was localized by difference-Fourier synthesis of the electron density. The cage population showed a different configuration, if compared to the room-*P* structure model. The Cl^- site (Cl) was found to be split into three mutually exclusive positions around the 3-fold axis at $z \sim 0.25$, as at room-*P*, but two distinct peaks were found for the Ca^{2+} cation, at ~ (1/3,2/3,0.71) and ~ (1/3,2/3,0.77), and modeled as two mutually exclusive split sites (Ca1 and Ca2). The configuration of the channel sites was found to be similar to that refined at room-*P* conditions: two mutually exclusive cationic sites (M1 assigned to K^+ and M2 to Na^+) and a tetrahedral sulfate group with upward or downward configurations (Fig. 7.3). The upward and downward triangular bases of the (SO_4^{2-})-tetrahedron are generated, in the $P6_3$ space group, by two symmetry-independent oxygen sites: OB1 (at $z \sim 0.15$) and OB2 (at $z \sim 0.35$). The structure refinement was performed with isotropic atomic displacement parameters for all the sites, restraining Ca1-Ca2, M1-M2 and OA-OB1-OB2 to share the same *adp*, respectively. The Cl^- and Ca^{2+} sites were constrained to the full allowed occupancy, modeling Ca1 and Ca2 as equally occupied (*i.e.* site occupancy factor = 0.5). The occupancy factors of the sulfate oxygen sites were restrained to that of the sulfur site, assuming the same probability for the upward (OB1) and downward (OB2) configurations. In order to stabilize the refinement, the S-OA and S-(OB1,OB2) bond lengths were restrained to 1.35(1) and 1.45(2) Å, respectively, and the (*x*,*y*)-coordinates of the OB1 and OB2 sites were fixed according to peak positions in the difference-Fourier maps of the electron density. The refinement converged to a final $R_1 = 0.0804$, for 565 unique reflections with $F_o > 4\sigma(F_o)$, and no significant correlations between the refined parameters. Residuals in the difference-electron density were $< \pm 1.38$ $e^-/Å^3$. Structure refinements from the selected high-pressure datasets have been performed starting from the model refined at P_1 (0.38(2) GPa), using the same strategy and constraining all the occupancies to the values

refined at P_1. All the refinements converged with no significant correlations between the refined parameters and no significant residuals in the difference-Fourier maps of electron density. Further details on the high-pressure structure refinements are given in Table 7.8. Atomic coordinates, occupancy factors and isotropic atomic displacement parameters are in Table 7.10. Relevant structural parameters in Table 7.11.

7.2.3 Results

Elastic behavior

The unit-cell volume evolution as a function of pressure is shown in Fig. 7.10 and the unit-cell parameters, refined at 21 pressures, are reported in Table 7.7. The studied sample of davyne is stable up to the highest pressure investigated of 7.18(6) GPa, with no significant evidence of change in the compressional behavior, nor of phase transition after that involving the symmetry change between room-*P* and 0.38(2) GPa. The elastic behavior of the studied sample of davyne has been modeled through the fit of a Birch-Murnaghan equation of state, truncated to the third order (III-BM EoS, Birch 1947, Angel 2000), to the experimental *V*-*P* data collected between 0.38(2) (P_1) and 7.18(6) GPa (P_{21}). The refined parameters are: V_0 = 761.6(5) Å^3, K_{V0} = 46.5(11) GPa and K_V' = 3.7 (3). The refined K_V' = 3.7(3) suggests that the truncation of the BM EoS to the second order (II-BM EoS), for which K_V' = 4 is assumed, is adequate for the studied davyne, leading to the following elastic parameter: V_0 = 761.9(3) Å^3, K_{V0} = 45.6(3) GPa. The same protocol was applied to the *a* and *c* unit-cell edges, for which the experimental *l*-*P* data have been fitted by "linearized" BM-EoS (Angel 2000). The fit with linearized III-BM EoS led to the following parameters for *a* and *c*, respectively: a_0 = 12.814(2) Å, K_{a0} = 50.3(9) GPa and K_a' = 4.0(3); c_0 = 5.3561(9) Å, K_{c0} = 40.3(7) GPa and K_c' 3.2(2). The fit with linearized II-BM EoS yelded: a_0 = 12.814(1) Å and K_{a0} = 50.4(3) GPa; c_0 = 5.3582(8) Å and K_{c0} = 38.2(3) GPa. Therefore, the elastic anisotropy at room-*P* conditions can be expressed as K_{a0} : K_{c0} = 1.25 : 1. Figure 7.10 and the refined K_l' values from linearized III-BM EoS show that the elastic anisotropy of davyne under study increases with increasing pressure. All the equation of state fits have been performed using the EoSFit v5.2 software (Angel 2000).

The response of the [CAN]-framework of the studied davyne to the applied pressure is mainly controlled by the tilting of tetrahedra. The average intratetrahedral Si-O and Al-O bond lengths are reported in Table 7.11 and suggest a quasi-rigid behavior, even though a slight compression, partially hindered by the *esd*'s, can be inferred. The evolution of the intertetrahedral Si-O-Al bond angles is shown in Fig. 7.11 and reported in Table 7.11: a strong closure of Si-O1-Al occurs, coupled with a less pronounced decrease of the Si-O3-Al and Si-O4-Al, whereas no unambiguous decreasing trend can be described for the Si-O2-Al. The tetrahedra tilting can also be described in terms of the deformation of the secondary and composite building units. The S6R⊥[0001] ditrigonal rotation angle $\alpha_{S6R\perp[0001]}$ (Fig. 7.7) slightly increases in response to the applied pressure, inducing a shortening of the O2-$O2_{S6R\perp[0001]}$ diameter. The cage-basis deformation is also described by the deviation from planarity $dz_{S6R\perp[0001]}$ = |z(O1) – z(O2)|**c*, which strongly increases at low pressure and tends towards a saturation at the highest pressures (Table 7.11). The compression within the (0001) plane is also achieved through the shortening of both the O1-$O1_{12R}$ and O3-$O4_{12R}$ symmetry-independent diameters of the 12-ring channel (Fig. 7.11, Table 7.11), whereas a less pronounced shortening with pressure is shown by the O3-$O4_{S4R}$ (Fig. 7.7; Table 7.11). The contraction along the *c* axis is described by the closure of the O3-O4-O3 angle (Fig. 7.7. and 7.8; Table 7.11), related to the compression of the *dzc* unit. As a consequence, a decrease of the "corrugation" of the (A,B)-planes of single six-membered rings (Fig. 7.7, section 4.1.2) is observed with pressure (Table 7.11). The *P*-induced deformation of the *can* unit can be described as a homogenous "shrinking", as the constant O2-O2-O2 angle (Fig. 7.7., Table 7.11) suggests.

Following the protocol already applied to the other cancrinite-group minerals, the channel volume (fraction occupying a unit-cell) and the cage volume of davyne have been modeled according to the protocol described in section 4.2.2 and their values are listed in Table 7.11. The channel and cage contributions to the bulk compressibility have been calculated by fitting the (V_{ch}, V_{cg}) *vs. P* data to a II-BM EoS using the EoSFit v.5.2 software (Angel 2000). The refined parameters for channel and *can* unit are: V_{ch0} = 338.2(6) Å^3, K_{Vch0} = 35.7(8) GPa; V_{cg0} = 212.1(4) Å^3, K_{Vcg0} = 56(2) GPa, respectively.

The displacive phase transition from the $P6_3/m$ to the $P6_3$ space group leads to a split of the Ca site into two subsites (Ca1 and Ca2), assumed to be equally occupied. These split sites show a similar behavior with increasing pressure. The Ca-O1 bond lengths do not vary within estimated standard

deviations, while a slight compression of the Ca-O2 bond lengths occurs (Table 7.11). The shorter Ca1-Cl_z and Ca2-$Cl_{z+1/2}$ bond lengths are constant with pressure, whereas the longer Ca1-$Cl_{z+1/2}$ and Ca2-Cl_z undergo a compression at the low-*P* regime and, then, reach a saturation at $P \geq 3.07(2)$ GPa (Table 7.11). The M1 channel site, assumed to be occupied by K^+, shows a slight decrease of the shorter M1-O3′ and M1-O4′ bonds, while the longer M1-O3″ and M1-O4″ are constant within the *P*-range investigated. A clear shortening of the M1 bond lengths with the OA sulfate apical oxygen at *z* – 0.5 and *z* + 0.5 is also observed (Table 7.11). The M2 site, assumed to be occupied by Na^+, shows a strong compression of its bonds to O1, O3′ and O4′ coupled with a slight elongation of the bonds to O3″ and O4″. The M2-OB bonds, to the neighboring sulfate basal oxygen atoms, clearly decrease with pressure (Table 7.11).

7.2.4 Discussion

Davyne structure model and *P*-induced displacive phase transition

The structure model refined from the room-*P* dataset is consistent with those so far reported in the literature (Bonaccorsi et al. 1990, 1995; Hassan and Grundy 1990; Rozenberg et al. 2009; Sapozhnikov 2010; Gatta et al. 2014). The *can* unit columns are stuffed by chains of equally spaced (by symmetry) Ca^{2+}-Cl^-, with the anion at one of three mutually exclusive positions out of the 3-fold axis. The channel population can be ideally described by the occurrence of two alternated clusters: $[M2_3(SO_4)]$ and $[M1_3]$, where M1 and M2 are assumed to be occupied by K^+ and Na^+, respectively (Fig. 7.3). The occurrence of vacancies in both the cation and anion sites prevents a long-range ordered alternation of these clusters and, therefore, does not allow the occurrence of a microsommite-type superstructure (Bonaccorsi et al. 2001).

The chemical formula deduced from the room-*P* refinement is the following: $[Na_{2.08}K_{3.08}(SO_4)_{0.60}][Ca_2Cl_2](Si_6Al_6O_{24})$. Compared to the EMPA-WDS chemical formula, an overestimated K^+ coupled with an underestimated Na^+ content are shown. However, if we compare the calculated number of channel cations electrons from the EMPA-WDS analysis and the X-ray structure refinement, 78.5 and 81.56 e^- respectively, a good matching is shown. A partial substitution of K^+ by Na^+ in the M1 site can be suggested. The slight mismatch between the cations electronic content from chemical and X-ray refinement formulae can be affected by the partial positional disorder of the Na^+ cation occupying the M2 site, as shown by the difference-Fourier map, phased

without the channel content, in Fig. 7.9. The positional disorder reflects the several potential configurations of the Na^+ coordination shell: the cation position closer to or farther from the channel wall likely depends on the presence of the neighboring sulfate anion occupying the same cluster, as discussed in the section 7.1. This positional disorder is also likely responsible for the high residuals in the difference-Fourier map of electron density: any attempt to model it (*e.g.* by applying anisotropic *adp*'s or by splitting the M2 site into two positions) led to unrealistic models of the channel extraframework configuration. The slight overestimation of the refined sulfate anion content, if compared to the EMPA-WDS value, can be due to several factors. The positional disorder shown by the sulfate tetrahedron along [0001] can partially affect the refinement of the *sof* parameter. Moreover, a contribution from channel H_2O molecules and CO_3^{2-} groups, which were found to be common in davyne subgroup minerals (Ballirano et al. 1996b, 1998; Binon et al. 2004), cannot be excluded. Therefore, the refined structure model of the studied davyne has to be considered as an "average model", based on a number of slightly different local configurations of the channel extraframework population.

As already discussed in the section 7.2.2, a *P*-induced compression along the *c* axis, driven by tetrahedra tilting, is only possible by breaking the mirrors at $z = 0.25$ and $z = 0.75$, allowing the closure of the O3-O3-O3 angle (O3-O4-O3 in the $P6_3$ space group) and, therefore, the compression of the *dzc* unit (Fig. 7.8). This is confirmed by the displacive phase transition from the $P6_3/m$ to the $P6_3$ space group observed at the first pressure point (P_1 = 0.38 GPa) investigated. This *P*-induced displacive phase transition leads to the split of the cage-Ca^{2+} into two sites, Ca1 and Ca2. If in the $P6_3/m$ structure the equally spaced Ca^{2+}-Cl^- chains are constrained by symmetry (*i.e.* both Ca and Cl lie on the mirror planes), in the $P6_3$ structure the downward (if Ca1 is occupied) or the upward (if Ca2 is occupied) Ca-Cl bonds are found to be slightly shorter, suggesting this configuration to be energetically more stable. A slightly different partitioning of electron density between the M1 and M2 sites is shown, if compared to the room-*P* dataset (Table 7.10). However, the calculated electronic content refined from room-*P* and P_1 datasets shows an excellent matching, being 81.56 and 82.40 *e*-, respectively. The *P*-induced displacive phase transition leads, at the low-*P* regime, to a migration of the sites out of the planes previously occupied by the mirrors ($z = 0.25$ and $z = 0.75$). This migration is particularly intense for the O1, Cl, M1, M2 and S, for which the "*z*" coordinates show a non linear trend, characterized by a decreasing rate with pressure (Fig. 7.11; Table 7.10). The deviation from planarity of the *can* unit bases ($dz_{S6R\perp[0001]}$) and the compression of the longer Ca-Cl bonds (Table

7.11), which show the same non linear trend, are strictly related to the migration of these sites and can be, therefore, at least partially related to the *P*-induced symmetry breaking.

High-pressure elastic behavior

If we exclude the *P*-induced change of symmetry (from $P6_3/m$ to $P6_3$), observed between room-*P* and 0.38(2) GPa, no other phase transition and no structure collapse or evident decrease of crystallinity are shown, suggesting the phase stability of davyne within the investigated *P*-range (0.0001 – 7.18(6) GPa). The II-BM EoS refined compressibility (K_{V0} = 45.6(3) GPa) falls in the middle of the range so far reported for zeolites and zeolite-like materials (18-70 GPa, Gatta 2008). Moreover, the refined isothermal bulk modulus is identical, within experimental uncertainty, to those reported for the isotypic balliranoite (48(3) GPa, section 6.2), cancrinite (45(2) GPa, section 4.2) and vishnevite (49(4) GPa, chapter 5).

The refined unit-cell linear elastic parameters and the derived elastic anisotropy at room conditions (K_{a0} : K_{c0} = 1.25 : 1) is almost overlapped with those reported for the carbonate end-member of davyne-subgroup, *i.e.* balliranoite (K_{a0} : K_{c0} = 1.35 : 1). On the contrary, a more pronounced elastic anisotropy is shown by the cancrinite-subgroup members, *i.e.* cancrinite *s.s.* and vishnevite. It is worth noting that davyne and balliranoite share a similar elastic behavior and the same difference in elastic anisotropy, compared to cancrinite-subgroup minerals, at low-*T* conditions too (sections 4.1, 5.1, 6.1 and 7.1). These data strengthen the hypotheses that the extraframework population filling the *can* unit columns affects the elastic behavior of the compounds sharing the alumino-silicate [CAN]-framework). A thorough discussion on this subject will be given in chapter 8.

The refined channel- and cage-volume elastic parameters suggest that the *P*-induced bulk volume compression is mainly accommodated by the channel voids.

High-pressure structure evolution

The high-pressure framework evolution is governed by the tilting of the quasi-rigid $(Si,Al)O_4$ tetrahedra, described by the closure of all the Si-O-Al angles, excluding Si-O2-Al. It is worth noting that the same Si-O-Al evolution with pressure was described for the (CO_3^{2-})-term balliranoite (section 6.2) and, even if with a lower magnitude, in response to low-*T* (down to 110 K) in balliranoite and davyne (sections 6.1 and 7.1). A different Si-O-Al behavior is shown by the isotypic cancrinite *sensu stricto* and vishnevite, at both high-*P* (section 4.2 and chapter 5) and low-*T* (section 4.1 and chapter

5). This suggests that the different elastic anisotropy, shown by the compounds belonging to these subgroups, is governed by different tilting mechanisms of the tetrahdera. The unit-cell volume contraction within the (0001) plane is accommodated by several non-independent deformation mechanisms: 1) along the O2-O2 axis by the shortening of the $O2\text{-}O2_{S6R\perp[0001]}$, induced by the slight ditrigonal rotation of the *can* unit basis, and by the compression of the $O2\text{-}O2_{cw}$ "cage width" (dashed lines in Fig. 7.7) (Table 7.11); 2) by the compression of both the independent channel diameters $O1\text{-}O1_{12R}$ and $O3\text{-}O4_{12R}$ (Fig. 7.7 and 7.11, Table 7.11) and 3) by the slight compression of the S4R diameter $O3\text{-}O4_{S4R}$ (Fig. 7.7, Table 7.11). The contraction along the [0001] direction is accommodated by the compression of the *dzc* unit, described by the closure of the O3-O4-O3 angle, which apparently follows a non linear trend with a decreasing rate at increasing pressure (Fig. 7.11), consistent with the elastic behavior of the *c* axis.

The channel and *can* unit evolution is governed by the same *P*-induced deformation mechanisms in both davyne and balliranoite. For the *can* unit, the compression within (0001) (through the $O2\text{-}O2_{cw}$ shortening) and along [0001] (through the compression of the *dzc* unit) have the same magnitude, leading to a homogeneous "shrinking" of the cage, as confirmed by the constant value of the O2-O2-O2 angle (Table 7.11). On the contrary, the different Si-O-Al *vs. P* behavior shown in cancrinite and vishnevite (chapters 4 and 5) leads to different tilting mechanisms of the tetrahedra and to a significant flattening of the *can* unit.

As in balliranoite, also in davyne no significant changes of the configuration of the channel population occur in response to pressure. Both the M1 and the M2 sites tend to move towards the center of the channel with increasing pressure (Table 7.10). At room-*P*, the Na^+ at M2 is bonded to four framework oxygen (O3′, O4′, O3″ and O4″) and one sulfate oxygen on the other side, whereas the K^+ or Na^+ at M1 are bonded to the aforementioned framework oxygen atoms and to one or two OA apical oxygen of the (SO_4^{2-})-group at z - 0.5 or z + 0.5. At increasing pressure, the O1 framework oxygen rapidly falls within the coordination shells of both M1 and M2 cations, while at higher pressures K^+ in M1 progressively shows potential bond distances with basal sulfate oxygen atoms (OB1 and OB2) at z + 0.5 or z – 0.5. More in general, both the $(Na,K)\text{-}O_{framework}$ and $(Na,K)\text{-}O_{sulfate}$ bonds decrease with pressure (Table 7.11).

7.2.5 Conclusions

To the best of our knowledge, this is the first study on the high-pressure behavior of davyne. Davyne is reported to crystallize in both the centric $P6_3/m$ (Bonaccorsi et al. 1990, 1995) and acentric $P6_3$ (Hassan and Grundy 1990; Bonaccorsi et al. 1995; Rozenberg et al. 2009; Sapozhnikov 2010) space groups. Bonaccorsi et al. (1995) reported the high-temperature behavior of two samples of davyne, the first showing $P6_3$ symmetry, the latter $P6_3/m$. These Authors reported different elastic behaviors along the *c* axis of the two samples. The ($P6_3/m$)-davyne was almost unexpandable along that direction, due to the symmetry-induced O3-O3-O3 = 180°. On the contrary, the ($P6_3$)-sample was highly expandable along [0001], until the O3-O4-O3 angle reached the geometric limit of 180° value, after which a further expansion driven by tetrahedra tilting was no more allowed (Bonaccorsi et al. 1995). The Authors suggested this corresponded to a displacive phase transition from $P6_3$ to $P6_3/m$. As consequence, the "inverse" phase transition would occur if pressure is applied on a ($P6_3/m$)-davyne.

Due to geometrical constraints, the compression along the [0001] direction in a ($P6_3/m$)-davyne is only possible by breaking the symmetry mirrors at $z = 0.25$ and $z = 0.75$ (Fig. 7.10). The *in situ* single-crystal diffraction study confirmed that a *P*-induced displacive phase transition, from the $P6_3/m$ to the $P6_3$ space group, occurs between room-*P* and 0.38(2) GPa, which corresponds to the first pressure point of this experiment. The structural constraints leading to this phase transition suggest that it would likely occur at a very low-pressure, as it is the only possible way to accommodate the strain through tetrahedra tilting, which is reported to be the most common mechanism in open-framework materials (Gatta 2010). The post-transition ($P6_3$)-davyne showed a large isothermal (293 K) stability field as function of pressure, being stable at least up to 7.18(2) GPa. The high-pressure elastic behavior has been described a II-BM EoS fit to the experimental data. The elastic anisotropy at room-*P* conditions can be described as $K_{a0} : K_{c0} = 1.25 : 1$, and was found to increase with pressure. The unit-cell volume compression is accommodated by [CAN]-framework of davyne mainly by tetrahedra tilting. The same deformation mechanisms already reported for balliranoite (section 6.2) were found for the studied davyne. On the contrary, a different different tilting mechanisms have been reported for cancrinite *sensu stricto* (chapter 4) and vishnevite (chapter 5). These data strengthen the hypothesis that the nature of the population of the *can* unit columns affect the (*T*,*P*)-induced tilting mechanisms and, therefore, the elastic behavior of the cancrinite-group compounds.

The role played by the extraframework population on the structure and elastic evolution of cancrinite-group compounds at non-ambient conditions should be taken into account if these materials will be used in future technological applications. In particular, concerning davyne, a special attention should be paid to the $P6_3/m \rightarrow P6_3$ displacive phase transition occurring at very low-*P* regime and to the "inverse" phase transition occurring with increasing temperature at about 473 K (Bonaccorsi et al. 1995).

Figure 7.8 A contraction along the *c* axis (governed by tetrahedral tilting) in the *P*6$_3$/*m* davyne is only possible by breaking the mirror planes at *z* = 0.25 and *z* = 0.75, for the symmetry-induced O3-O3-O3 = 180°

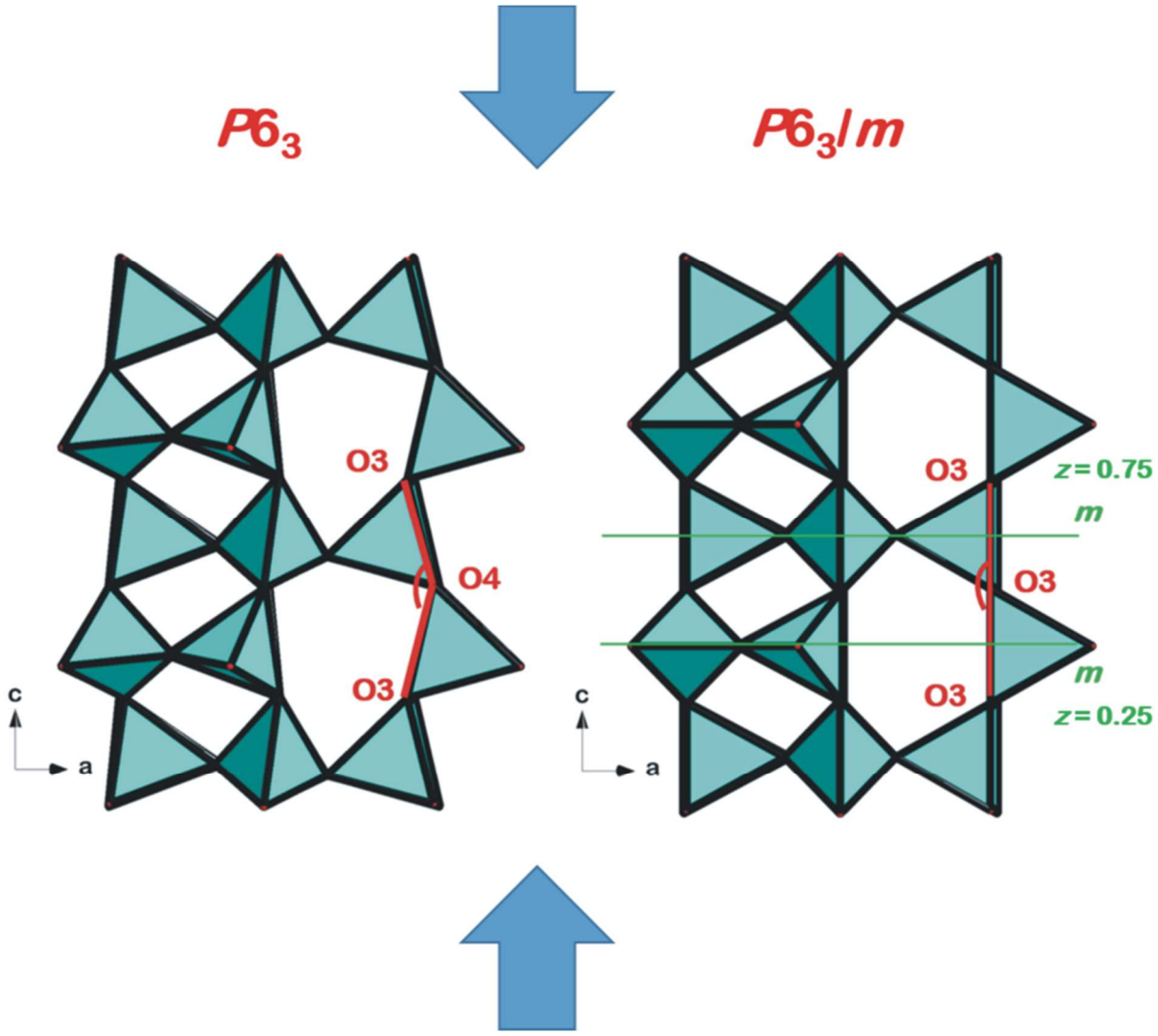

Figure 7.9 (*Top*) Difference-Fourier map of electron density along the 6_3 axis, at the center of the 12R-channel, phased without the SO_4^{2-} groups. (*Bottom*) Difference-Fourier map of electron density on the (0001) plane at z = 0.25, phased without the channel population. The maxima of the "internal" and "external" cation sites and the broad distribution of electron density related to the Na^+ cation in M2 are shown. Both the syntheses have been obtained from the room-*P* dataset in the $P6_3/m$ space group.

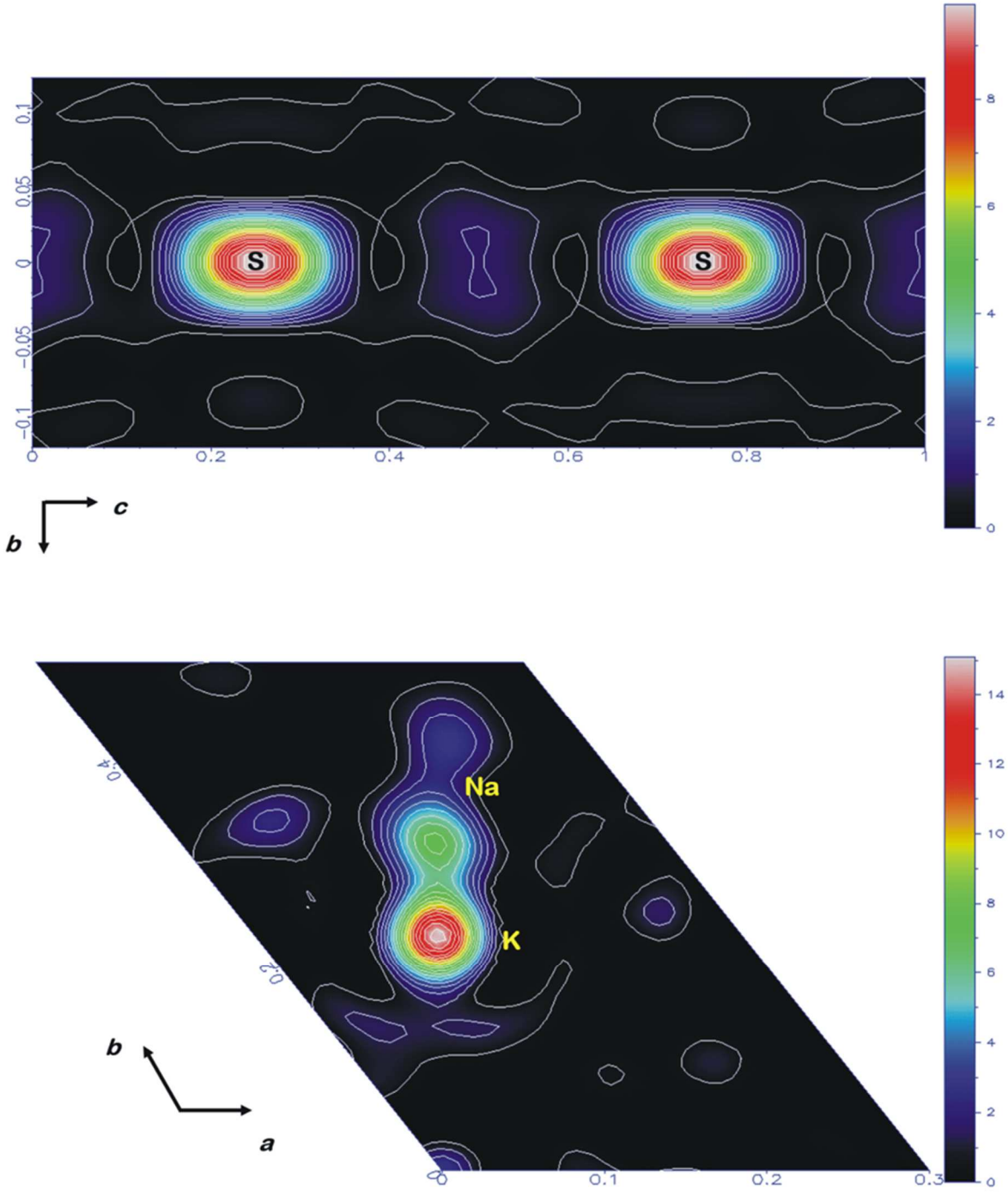

Figure 7.10 (*Left side*) The experimental unit-cell volume *vs*. pressure data, from P_1 (0.38(2) GPa) to P_{21} (7.18(6) GPa). The solid line represents the fit with a II-BM EoS. (*Right side*) The unit-cell *a* and *c* parameters normalized to their P_1 values, plotted against pressure. The solid lines represent the fit with III-BM "linearized" BM equations of state.

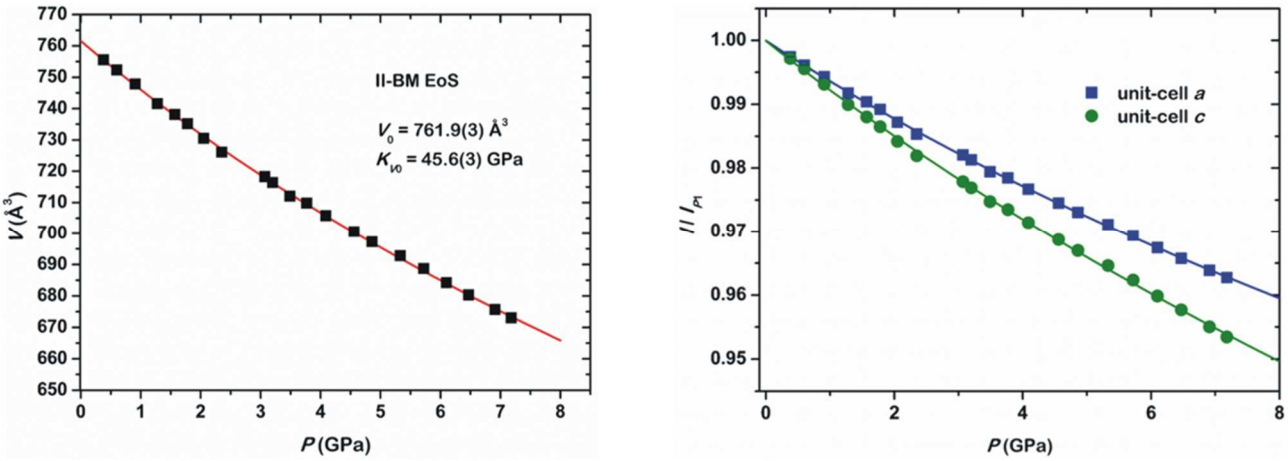

Figure 7.11 The pressure-induced evolution of: (A) the intertetrahedral Si-O-Al angles normalized to their P_1 values; (B) the O1-O1$_{12R}$ and O3-O4$_{12R}$ channel diameters normalized to their P_1 values; (C) the channel and *can* unit volumes (see text for further details) normalized to their P_1 values; (D) the *z* coordinates of the sites O1 [*z*(O1)-0.5], Cl, M1, M2 and S.

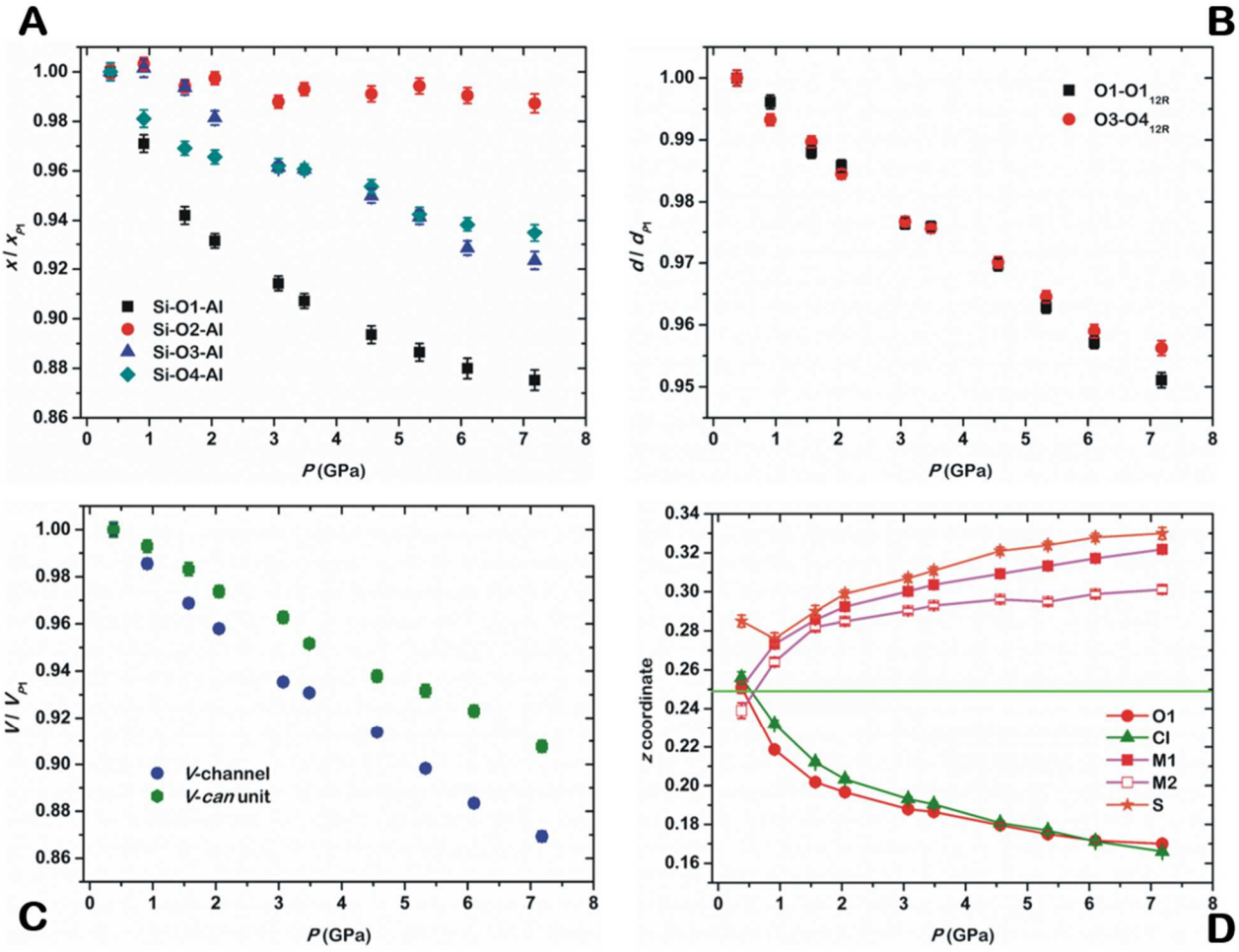

Chapter 8

Discussion

8.1 ISOTHERMAL ELASTIC BEHAVIOR

Figure 8.1 shows the evolution of the unit-cell volumes and linear parameters with pressure, normalized to the room-*P* values, of the studied cancrinite-group minerals. The refined elastic parameters, based on Birch-Murnaghan equations of state fits are reported in Table 8.1. The analysis of these parameters show that all the studied minerals share the same bulk compressibility, within 1 e.s.d., at ambient conditions. This compressibility (*i.e.* ~ 47 GPa) falls in the middle of the range so far reported for zeolites, 18-70 GPa (Gatta 2008). In addition, all the studied compounds show an anisotropic elastic behavior, where [0001] is the most compressible direction. Although they are tectosilicates, the cancrinite-group compounds can also be described as made by a "layered" structure, since the [CAN]-framework can be viewed as given by the stacking of planes made single six-membered rings (see section 1.1). It is interesting to note that the most compressible and expandable direction (further details are given later) coincides to the direction of layers stacking.

A visual inspection to Figure 8.1 and Table 8.1 highlights that the minerals belonging to the two subgroups are characterized by different elastic anisotropy. The refined linear bulk moduli K_{l0} underline that the anisotropic behavior is more pronounced for the cancrinite-subgroup minerals, being K_{a0}/K_{c0} equal to 1.53 (cancrinite), 1.51 (vishnevite), 1.35 (balliranoite) and 1.25 (davyne). In addition, Figure 8.1 and Table 8.1 show that, taking into account the estimated standard deviations, balliranoite and davyne share the same elastic behavior. On the contrary, a comparison among the cancrinite-subgroup minerals is not so simple. In chapter 5 it has been reported that vishnevite clearly undergoes a strong increase in compressibility with *P*, following a structural re-arrangement, at $P >$ 3.43(4) GPa. A subtle change in the elastic behavior, with a slight increase in compressibility, is also shown by cancrinite, in particular along the *a*-axis, but at a higher pressure (*i.e.* between 4.62(3) and 5.00(2) GPa). However, in the latter case no clear structural re-arrangement supports the change in the elastic behavior. As reported in section 4.2, the accuracy and precision of the data likely hinder an unambiguous interpretation of the phenomenon. On the basis of the results later obtained for vishnevite, an accurate re-investigation, focused to the *P*-range of interest, could help to clarify the scenario. Nevertheless, Figure 8.1 underlines that the two elastic discontinuities are barely comparable. In fact, the increase in compressibility, shown by all the unit-cell parameters of vishnevite, is higher if compared to cancrinite, suggesting the onset, if any, of a less pronounced structural re-arrangement in the cancrinite structure at $P >$ 4.62(3) GPa. Beside the different high-pressure elastic behavior, cancrinite and vishnevite share similar volume and linear compressibilities

at ambient conditions, as shown by the bulk moduli reported in Table 8.1 and, more in general, these minerals share a similar elastic behavior at low-pressure regime.

Overall, the davyne-subgroup minerals showed a significant stability at high pressure, somewhat surprising considering their nature of microporous materials widespread in the surface geological environments (see section 1.3). They appear to be stable up to ~ 7 GPa, with no evidence of structure collapse nor change in the compressional behavior. On the other hand, the cancrinite-subgroup minerals showed, at least vishnevite, a change in the elastic behavior with an increase in compressibility; the increase of pressure could act as a destabilizing factor. However, taking into account their typical geological environments and their potential technological applications (*e.g.* as waste-storage materials), it should be considered that the observed elastic discontinuities occur at very high pressures, being $P > 2.47(2)$ GPa in vishnevite and $P > 4.62(3)$ GPa in cancrinite. In addition, despite the observed change in the elastic behavior, both cancrinite and vishnevite are stable, under the elastic regime, up to the highest pressure investigated (~ 7 GPa), showing only at the very high pressures a decrease of the peak intensities and an increase of the peak halfwidths. Moreover, it seems worth noting that the reported phase stability fields at high pressure have been determined at 293 K. For an evaluation of the stability of a mineral in a real geological environment, the combined effect of temperature and pressure should be taken into account.

A comparison with the elastic parameters reported by Gatta and Lee (2008) for the isotypic $Na_6Cs_2[Ga_6Ge_6O_{24}]*Ge(OH)_6$ shows that this compound has a higher compressibility at ambient conditions. Therefore, the results obtained in this study confirm the hypothesis of Gatta and Lee (2008), who suggested a higher stiffness for the aluminosilicate cancrinites, for which a rigid behavior of the framework tetrahedra was expected, as confirmed by this study. Based on the elastic behavior of cancrinite and vishnevite at the low-*P* regime, the significantly high K′ values reported by Gatta and Lee (2008) could in part be related to the stiffening of the $(Ga,Ge)O_4$ tetrahedral compression with increasing pressure and in part to structural mechanisms, possibly comparable to those observed for the cancrinite-subgroup minerals. Oh et al. (2011) reported the high-pressure elastic behavior of a synthetic hydroxycancrinite, with a bulk modulus of 46(5) GPa (calculated by a II-BM EoS fit applied to the entire *P*-range investigated). Interestingly, the Authors reported that a subtle discontinuity was observed in the *P*-*V* data between 1.9 and 2.5 GPa, after which a III-BM EoS could be fitted (assuming a fixed V_0) yielding the following parameters: $K_{V0} = 46.9(9)$ and $K_V' = 4.0(4)$. Despite not reported by the Authors, a calculation from the published unit-cell parameters shows that

hydroxycancrinite shares the same elastic anisotropy of cancrinite and vishnevite (K_{a0}:K_{c0} ~ 54:31, 1.74:1), consistently to its nature of cancrinite-subgroup compound.

8.2 THERMOELASTIC BEHAVIOR AT CONSTANT PRESSURE

The refined thermo-elastic parameters of the studied minerals are reported in Table 8.2 and in chapters 4-7. For the low-*T* datasets of cancrinite, balliranoite and davyne, the experimental (*V*,*l*) *vs*. *T* data have been fitted by both the thermal equations of state (8), derived from the thermodynamic definition of the thermal expansion coefficient α_V, and (14), as proposed by Pawley et al. (1996) and adopted by Holland and Powell (1998) for their thermodynamic database (see section 2.1). A significant disagreement between the refined parameters from the two fits was found, showing systematic higher expansivities, at ambient conditions, from the fit with equation (14). A comparison to the thermo-elastic data reported by Hassan et al. (2006), for the high-*T* behavior of cancrinite, and Bonaccorsi et al. (1995), for the high-*T* behavior of davyne and microsommite, revealed that a better agreement is obtained by the constant α_V coefficients refined by equation (8) and reported in Table 8.2. If the large uncertainties, due to the low number and the scattering of the experimental data, are taken into account, similar conclusions to those reported in section 8.1 can be carried out. Cancrinite, balliranoite and davyne share the same volume expansivity, within 1σ, but with a different anisotropy, being higher in cancrinite. The *c*-axis corresponds to the most expandable direction, consistently to what reported in section 8.1. Despite the systematic higher values, the same conclusions, defining a different elastic anisotropy for the cancrinite- and davyne-subgroups, can be drawn by the analysis of the thermo-elastic parameters refined from equation (14), including the average thermal expansion coefficients calculated for vishnevite. Table 8.2 shows that davyne and balliranoite share an almost identical elastic behavior at low-*T*, down to ~ 110 K, whereas the lack of low-*T* data from vishnevite (chapter 5) makes a comparison between the two cancrinite-subgroup minerals impossible. A slight mismatch can be shown if the thermal coefficients of cancrinite (Table 8.2), refined from the low-*T* (section 4.1) and the high-*T* (section 4.3) datasets, are compared, being $\alpha_{V293K,1bar}$ equal to $3.8(7)*10^{-5}$ and $4.88(8)*10^{-5}$ K^{-1}, respectively. However, an excellent agreement is shown between our high-*T* data and those calculated from Hassan et al. (2006) for the range 298-769 K (*e.g.* $\alpha_{V293K,1bar}$ = $4.7(8)*10^{-5}$ K^{-1}). Due to the higher number, accuracy and precision of experimental data and the consistency to the literature data reported above, the high-*T* parameters more likely represents the thermo-elastic behavior of cancrinite.

8.3 HIGH-TEMPERATURE BEHAVIOR

The high-temperature behavior of cancrinite, reported in section 4.3, is characterized by a strong and slow dehydration process occurring at 748 K, after which a quasi-anhydrous phase was found to be stable up to the highest temperature investigated, *i.e.* 823 K. However, a decrease in the intensity and a broadening of the peaks suggested an impeding decomposition of the crystal. An interesting result was that the dehydration was found to be irreversible at the time scale of the experiment. The stability of the quasi-anhydrous form of cancrinite, which we observed at least in the range 748-823 K and, then, at room-*T* after the cooling of the crystal, has also been widely reported in the literature (see section 3.1) and is confirmed by the occurrence of a natural sample in volcanic deposits (Zubkova et al. 2011). Zubkova et al. (2011) described the re-distribution of Na^+ cations along the 3-fold axes, likely to minimize the electrostatic repulsion in response to the absence of H_2O molecules. Such a re-distribution was not directly observed by us, even though a strong increase in the anisotropic atomic displacement parameter of the cage-Na site could be partially explained by a positional re-arrangement coupled with an enhanced thermal displacement. The structure refinement performed at 748 K, when the dehydration was completed, clearly showed that a minor amount of H_2O molecules were still present within the cages. This could possibly be a necessary condition for the stability of the (quasi)-dehydrated form of cancrinite. The structure collapse, not observed in our experiment, is always reported in the literature to occur at higher temperatures than the dehydration and could be related both to the loss of channel anions "backbones" and/or to the loss of the residual cage-H_2O molecules. Overall, since the occurrence of natural (quasi)-anhydrous samples of cancrinite in volcanic deposits would likely be ascribable to the heating induced by the effusive process (Zubkova et al. 2011), a rigorous characterization of the dehydration process in cancrinite could allow a better characterization of the effusive process itself.

The results obtained in this study show a strong consistency to those reported by Sirbescu and Jenkins (1999) from a manual thermogravimetric study at equilibrium conditions. The temperature of the main dehydration peak that we observed (*i.e.* 748 K) is almost overlapped to that reported by Sirbescu and Jenkins (1999). In addition, the most interesting feature is likely the slow kinetics of the dehydration, since the isothermal process at 748 K took 12 days to be complete in our experiment, whereas Sirbescu and Jenkins (1999) reported that the full manual TG-analysis needed a total of 10 days. The results reported in section 4.3 allowed a careful determination of the dehydration temperature, which could be considered in the evaluation of cancrinite-group compounds as suitable

waste-disposal materials. Based on our results, those of Sirbescu and Jenkins and others reported in the literature (section 3.1), it appears that 700-750 K is the dehydration temperature of cancrinite at ambient pressure. A more detailed description of the structural re-arrangements induced by the dehydration in cancrinite will be given in sections 8.5 and 8.6.

The high-temperature behavior of vishnevite has not been studied here. However, a thermal study of the chemically analogous pitiglianoite is available in the literature (Bonaccorsi et al. 2007). Bonaccorsi et al. (2007) reported a dehydration, with unit-cell shrinking, in the range 499-676 K, but the most striking effect is the dehydration-induced cationic exchange between cage-Na^+ and channel-K^+. The larger K^+ cation was found to fully occupy the *can* unit in the dehydrated pitiglianoite, approximately at its center (Bonaccorsi et al. 2007) and having as the major consequence the inhibition of a long time-scale re-hydration of these units at ambient conditions. This suggetss the thermal transformation of pitiglianoite into a new compound. These data underline the fundamental role played by the extraframework constituents during (*T*,*P*)-induced re-arrangements. In particular, an interesting goal would be the characterization of the possibly enhanced thermal stability of the new (quasi)-anhydrous compound, having the *can* units mainly occupied by the large K^+ cations. In addition, the reproducibility of this thermal-induced cationic exchange in K-bearing cancrinite-subgroup compounds should be also investigated.

The high-temperature behavior of three davyne-subgroup minerals has been studied by Bonaccorsi et al. (1995). The Authors reported that davyne and microsommite samples, both sharing $P6_3$ symmetry, showed a comparable elastic behavior, which was, in turn, consistent to the low-*T* elastic parameters refined in this study. However, both the samples underwent an abrupt decrease in expansivity along the *c*-axis at 473 and 433 K, respectively, from $\alpha_c = 1.6(4)*10^{-5}$ K^{-1} to $0.2(1)*10^{-5}$ K^{-1}. This behavior was ascribable to a displacive phase transition from $P6_3$ to $P6_3/m$, for which the structural expansion along [0001], governed by tetrahedral tilting, was inhibited by the symmetry-constraint O3-O3-O3 = 180°, as already described in the previous chapters (see, for example, Fig. 3.1). This was confirmed in Bonaccorsi et al. (1995) by the elastic behavior shown by a davyne sample having $P6_3/m$ symmetry at room conditions. This sample showed an insignificant linear thermal expansion coefficient along [0001] within the entire *T*-range investigated, likely due to the limited tetrahedral expansion (Bonaccorsi et al. 1995). If the dehydration can be viewed as a destabilizing factor for cancrinite-subgroup compounds at high-temperature, in the nominally anhydrous davyne-subgroup compounds thermal instability is governed by the symmetry-induced limited expansion of the *dzc* chains, possibly influencing their potential use as storage waste-forms (Riley et al. 2012). In fact, davyne-subgroup

compounds show an expanded [CAN]-framework at ambient conditions, if compared to cancrinite-subgroup, with the O3-O4-O3 angle (Fig. 3.1) close to the highest allowed value of 180°. At O3-O4-O3 = 180°, a displacive phase transition to $P6_3/m$ occurs. In particular, the *dzc* chains are so expanded in davyne that both natural $P6_3$ and $P6_3/m$ samples can be found in Nature (see section 1.2.2). It is an obvious consequence that if the thermal-induced expansion will cause the $P6_3$ to $P6_3/m$ phase transition, the pressure-induced compression will cause the inverse phase transition, as it will be discussed below.

8.4 *P*-INDUCED $P6_3/m$ TO $P6_3$ PHASE TRANSITION

The structural reasons for the *P*-induced displacive phase transition from the $P6_3/m$ to the $P6_3$ space group in davyne have been thoroughly described in section 7.2. The studied crystal was found to be stable within the entire *P*-range investigated, up to 7.18(6) GPa. The displacive phase transition to the $P6_3$ space group causes a structural re-arrangement, with the migration of the sites far from the mirror planes at z = 0.25 and 0.75 in ($P63/m$, Fig. 7.11). However, the most striking effect of the symmetry change is the split of the cage-Ca^{2+} site, giving rise to two mutually exclusive and equivalent bonding configurations (Tables 7.10 and 7.11). In the $P6_3/m$ structure, both the upward and the downward Ca-Cl bonds (Fig 7.1) are constrained to be equal by symmetry; whereas in the $P6_3$ split configuration, one of the two Ca-Cl bonds is shorter.

8.5 THE DEFORMATION MECHANISMS OF THE [CAN]-FRAMEWORK

The [CAN]-framework deformation mechanisms at non-ambient conditions can be inferred from the relevant structural parameters reported in Tables 4.4, 4.9 and 4.16 (cancrinite), 5.6 (vishnevite), 6.5 and 6.10 (balliranoite), 7.6 and 7.11 (davyne).

First of all, as already discussed in the previous chapters, the substitution of $[Na\cdot H_2O]^+$ clusters (in cancrinite subgroup) by $[Ca\cdot Cl]^+$ (in davyne-subgroup minerals) induces a framework expansion, which is reflected by several structural parameters. The different coordination environment of the cage-Na^+, when compared to Ca^{2+}, leads to a more pronounced ditrigonalization of the S6R⊥[0001] basis of the *can* unit, as well described by the ditrigonal rotation angles: 8.44(3)° and 10.2(1)° in cancrinite and vishnevite, 1.02(3)° and 3.00(2)° in balliranoite and davyne, respectively (room-*T* data; Fig. 4.4, 5.6, 6.6 and 7.7). The expansion along [0001] is well represented by the values of the O3-O4-O3 angles, being 144.84(5)°, 152.6(2)°, 162.68(5)°, and 171.51(4)° in the four studied minerals, respectively. It is interesting to note the expansion due to the SO_4^{2-} anions (and the related K^+ cations) in vishnevite and davyne, when compared to the (CO_3^{2-})-rich terms. The framework expansion along the *c*-axis in the davyne-subgroup minerals also causes a lesser flattening of the *can* units at room conditions, as shown by the higher values of the O2-O2-O2 angles (Fig. 4.4, 5.6, 6.6 and 7.7). In addition, an expansion of the *dzc* chain width in (0001) is shown in davyne-subgroup minerals, by an elongation of the O3-$O4_{S4R}$ diameters of the S4R units, which is partially counterbalanced by shorter O3-$O4_{12R}$ channel diameters, with respect to the cancrinite-subgroup minerals. In the latter, longer

$O3\text{-}O4_{12R}$ also shorter $O1\text{-}O1_{12R}$ lengths are observed. The different O1-O1/O3-O4 ratios of channel diameters between the two subgroups have also implications in the shape of the channel sections. In fact, if in cancrinite-subgroup minerals the similar values of $O1\text{-}O1_{12R}$ and $O3\text{-}O4_{12R}$ give rise to an almost circular channel, in davyne-subgroup minerals the higher O1-O1/O3-O4 ratio results in an almost perfect hexagonal shape, with slightly shorter effective pore width, *sensu* Baerlocher et al. (2007), as is evident in Figures 4.4, 5.6, 6.6 and 7.7.

As can be observed on the basis of the structural data, the structure deformations induced by high and low temperature and by high pressure do not substantially affect the intratetrahedral (Si,Al)-O lengths. *Id est*, the temperature- and pressure-induced structure evolution of the studied cancrinite-group minerals is governed by the tilting of the substantially rigid $(Si,Al)O_4$ tetrahedra about the shared oxygen hinges. This mechanism is typical of open-framework materials showing a tridimensional tetrahedral structure and has been proposed as the energetically less costly way for accommodating the *T*- and *P*-induced strain (Gatta 2008, 2010).

An inspection of the Si-O-Al intertetrahedral angles *versus* temperature or pressure (Fig. 4.14, 5.5, 6.5, 6.8, 7.6 and 7.11) shows that two clearly different trends can be defined for the cancrinite- and davyne-subgroup minerals, respectively. In the first subgroup, all the four symmetry-independent Si-O-Al angles vary with *T* or *P*. In the second subgroup, no significant variations of the Si-O2-Al angle are observed and the Si-O1-Al angle always shows the strongest change with *T* or *P*. These different trends are the basis of the different deformation mechanisms between the two subgroups, which will be thoroughly described and discussed below and in the next sections. It is worth noting that the effects of the thermal-induced dehydration on the cancrinite structure evolution is clearly reflected by a change in the Si-O2-Al trend (Fig. 4.14), as will be discussed in section 8.6.

The framework deformation along [0001] is controlled by the tilting of the tetrahedra forming the *dzc* chains, around the O3 and O4 hinges (Fig. 4.4, 5.6, 6.6 and 7.7), which is reflected by the Si-O3-Al and Si-O4-Al intertetrahedral angles. The behavior of these angles does not show significant differences between the two subgroups of minerals. In fact, the same deformation mechanism is found to accommodate the strain along the *c*-axis: the expansion or compression of the *dzc* chains bordering the *can* units (see section 1.1), well described by the change in the O3-O4-O3 angle (see Fig. 3.1), which also causes the hexagonalization or ditrigonalization of the S6R∠[0001] linking channels and cages (Fig. 4.4, 5.6, 6.6 and 7.7) . When the maximum expansion limit of 180° for the O3-O4-O3

angle is reached, the displacive phase transition to the $P6_3/m$ space group occurs, as has been already discussed above.

The main differences between the two subgroups are shown by the mechanisms accommodating the strain within the (0001) plane, mainly governed by the tilting of the tetrahedra around the O1 and O2 hinges, reflected by the Si-O1-Al and Si-O2-Al intertetrahedral angles. In cancrinite and vishnevite, a strong variation in the ditrigonal shape of the S6R⊥[0001] occurs in response to *T* and *P*, as well described by the evolution of the ditrigonal rotation angle (Fig. 4.5, 4.9 and 5.5). The channel deformation is mainly accommodated by the O1-$O1_{12R}$ diameter, whereas the O3-$O4_{12R}$ shows none or significantly lower change (Fig. 4.5, 4.9 and 5.5). On the other hand, along the O3-O4 direction the strain is clearly accommodated by the O3-$O4_{S4R}$ diameter of the S4R units, in response to the rotation of the tetrahedra around the O2 hinges (Fig. 4.5 and 4.9). On the contrary, in balliranoite and davyne, beside a significantly lower ditrigonal shape at room conditions, a less intense variation in the ditrigonal rotation angle occurs, if compared to the cancrinite-subgroup minerals at the same conditions. A consequence of the constant Si-O2-Al intertetrahedral angle is represented by the inhibited rotation of the tetrahedra around O2 and, therefore, by the almost constant values of the O3-$O4_{S4R}$ diameters of the S4R units. On the other hand, in davyne-subgroup minerals, both the channel diameters show similar changes in response to *T* or *P* (Fig. 6.5, 6.8, 7.6 and 7.11).

The different deformation mechanisms acting on the (0001) have a large effect on the behavior of the *can* unit at non-ambient conditions. In cancrinite and vishnevite, the expansion/contraction along [0001], governed by the *dzc* chain, is not counterbalanced within the (0001) plane by a similar change in the O2-$O2_{cw}$ diameter ("cage width" in chapters 4-7, Fig. 4.4, 5.6, 6.6 and 7.7). Therefore, the *can* unit undergoes a flattening (when compressed) and a stretching (when expanded) as well described by the variation in the O2-O2-O2 angle (Fig. 4.9 and 5.5). On the contrary, in balliranoite and davyne, the strain along [0001] is counterbalanced by a similar strain in the (0001) plane of the cage, reflected by the variation in the O2-$O2_{cw}$ "cage width" (Fig. 6.5, 6.8 and 7.6), leading to a homogeneous shrinking of the *can* unit at low-*T* and high-*P*. The different behavior of the *can* unit, at non-ambient conditions, in cancrinite and balliranoite is shown in Figure 6.8.

The analysis of the evolution against temperature and pressure of the modeled channel- (V_{ch}) and cage-volumes (V_{cg}) shows that the bulk volume strain is mainly accommodated by the channel voids (Fig. 4.14, 5.5 and 7.11).

8.6 THE *can* UNIT EXTRAFRAMEWORK CONTENT

Two different kinds of extraframework population fill the *can* units of the species belonging to the cancrinite and davyne subgroups, respectively. The davyne-subgroup minerals show chains made by $[Ca \cdot Cl]^+$ clusters. The Ca^{2+} site lies close to the S6R⊥[0001] "plane" (even though O1 and O2 are not exactly coplanar) an is bounded to the three O2 and the three O1 atoms, showing similar bond lengths. Therefore, only a small deviation from the perfect hexagonal shape of the S6R⊥[0001] *can* unit basis is shown (Fig. 6.1 and 7.1), as reflected by the low ditrigonal rotation angles in these minerals. The Cl^- anion is placed approximately at the center of the cage in three mutually exclusive positions out of the 3-fold axis (Fig. 6.1 and 7.1). Each Ca^{2+} cation is bonded to the two neighboring Cl^-, giving rise to a slightly distorted hexagonal bipyramidal coordination shell (C.N. = 8). Despite the lengths of the two Ca-Cl bonds are similar in value, one is slightly shorter that the other and the splitting of Ca^{2+} sites, following the $P6_3/m$ to $P6_3$ displacive phase transition in davyne, suggests this configuration as energetically more favorable than with an equal displacement between Ca^{2+} and Cl^- in an expanded framework. In cancrinite-subgroup minerals, chains of $[Na \cdot H_2O]^+$ clusters occur. The Na^+ site is slightly displaced form the S6R⊥[0001] "plane" with a stronger bond to one of the neighboring water-oxygen sites, positioned out of the 3-axis approximately at the cage center (Fig. 4.3 and 5.1). Therefore, each H_2O molecule shows a shorter bond to one Na^+ cation and a longer bond to the other Na-neighbor, which, in turn, will be strongly bonded to the next H_2O molecule (Fig. 4.3 and 5.1). Similarly, Na^+ shows shorter bonds to the three O2 oxygen sites with respect to the three O1's. As a consequence, significant deviation from the hexagonal shape is shown by the S6R⊥[0001], as reflected by the higher ditrigonal rotation angles, if compared to those in balliranoite and davyne (Fig. 4.3 and 5.1). The Na^+ coordination environment can, therefore, be described as made by a first tetrahedral shell (3*O2 + Ow′) plus a second weaker tetrahedral shell (3*O2 + Ow″), giving rise to a distorted ditrigonal bipyramid (C.N. = 4 + 4). The vishnevite structure refined from the high-*P* datasets shows the cage-Na modeled in two split sites, for which the same considerations reported above can be carried out.

The different coordination environments shown by the cage cations in cancrinite- and davyne-subgroup members not only are the source for the different framework configurations at ambient conditions (described in the previous section), but also affect significantly their distortion with temperature or pressure. The high-*P* and low-*T* structure refinements of cancrinite and vishnevite showed that, in response to pressure or decreasing temperature, a compression of the shorter Na-O2

and an elongation of the longer Na-O1 bonds occurred, inducing an increase in the ditrigonal character of the S6R⊥[0001]. The substantially constant value of the Na-O1 bond at $P < 3.43(4)$ GPa in vishnevite, discussed in chapter 5, has tentatively been ascribed to be a secondary effect of the short contacts involving the channel cations shells, as will be further discussed in the next section. A less clear behavior is shown by the Na-Ow bonds, for which a constant or very low compression is observed from the low-*T* and high-*P* datasets. Overall, under "compressive" regimes (*i.e.* under low temperature and high pressure), a strong compression of the first tetrahedral shell of the cage-Na coordination environment occurs along with a distorted expansion of the second shell. In other words, the distortion of the ditrigonal bipyramidal polyhedron is further enhanced at high-*P* and low-*T* conditions, leading to an increasingly tetrahedral character of the Na-coordination environment.

On the contrary, an inspection of the Ca-O bonds behavior in balliranoite and davyne shows that only very minor changes occur at low-*T* conditions, whereas at high pressure only a slight decrease in the Ca-O2 bonds can be unambiguously described. Therefore, only a slight deviation from the room-conditions configuration of the S6R⊥[0001] is observed, as confirmed by the slight increase in their ditrigonal rotation angles. The shortening of both the Ca-Cl bonds follows the compression of the cages along the *c*-axis. The markedly different behavior between the Na-O_{fr} and the Ca-O_{fr} (O_{fr} stands for framework-oxygen) reflects the different *T* and *P* evolution of the Si-O2-Al intertetrahedral angle between the two subgroups. In fact, the inhibited tetrahedral rotation around the O2 hinge prevents the migration of this oxygen toward the Ca^{2+} cation (Tables 4.2, 4.8, 5.4, 6.3, 6.8, 7.3 and 7.10) and, therefore, a marked compression of the Ca-O2 bonds. Even though an unambiguous assignment is not straightforward, the different behavior could be ascribed to the nature of the channel cations. In fact, the longer ideal Ca-O bond length, if compared to Na-O, and the Ca^{2+} higher valence hinders the compression of the Ca-O2 bonds and a significant change of the quasi-hexagonal bipyramidal coordination, inhibiting the tetrahedral rotation around O2. Consequently, the observed marked differences in the framework deformation mechanisms within the (0001) plane (section 8.5) can be mainly ascribed to the different nature of the *can* units extraframework population and, in particular, to the different nature of the cations coordination environments.

The analysis of the high-temperature behavior of cancrinite showed that the same mechanisms, but opposite in sign, observed at low-*T* and high-*P* occur. In particular, in the hydrous regime preceding the dehydration, the increase in intertetrahedral angles reflects a distortion toward the hexagonal shape of the S6R⊥[0001]. As a consequence, an increase in Na-O2 and a decrease in Na-O1 occur.

One of the most interesting features emerging from the high-temperature study of cancrinite is the change in the trend of the Si-O2-Al intertetrahedral angle, following the dehydration process. In fact, the structure refinement based on the post-dehydration dataset suggested an inversion of this trend, with a closure of the intertetrahedral angle. This induces a compression of the $O3\text{-}O4_{S4R}$ diameter after an expansion in the hydrous regime, confirming the dependence of this parameter on Si-O2-Al (section 8.5). The change in the tilting mechanism, which apparently affects only Si-O2-Al, is likely driven by the tendency to minimize both the Na-O1 and Na-O2 bonds, in order to compensate the loss in bond valence due to the H_2O desorption. The availability of a mechanism able to partially counterbalance this loss could possibly concur to the stability (or metastability) of the observed quasi-anhydrous form of cancrinite.

In this light, we can conclude that the extraframework population filling the *can* units has the largest impact on the type of the framework deformation mechanisms in response to temperature and pressure and, therefore, on the bulk elastic behavior of this class of minerals. However, a markedly different configuration, from those here studied, can occur. In section 1.4 are reported synthetic cancrinite-group compounds having the cages filled by large monovalent cations (*e.g.* K^+ or Cs^+) (Lee et al. 2000; Colella and de' Gennaro 1989). Based on the results obtained in this study, it can be predicted that further different deformation mechanisms of the framework can govern the structure evolution in these materials at non-ambient conditions.

8.7 THE CHANNEL EXTRAFRAMEWORK CONTENT

If only two kinds of "geometrically simple" configurations occur in the *can* units of the studied minerals, the arrangement of the channel extraframework population is, by far, more complex. As described in sections 8.5 and 8.6, the different cage content results in a different framework configuration at ambient conditions. In particular, a different ratio between the O1-$O1_{12R}$ and O3-$O4_{12R}$ diameters leads to a markedly different shape of the channel section between the two subgroups (4.4, 5.6, 6.6 and 7.7). The cations sites lie close to the channel walls in one (cancrinite) or two mutually exclusive sites (vishnevite, balliranoite and davyne). However, an inspection of the Fourier-syntheses of the electron density, phased without the channel population (Fig. 5.2, 6.3, 7.2 and 7.9), shows that a disordered distribution is often found around the site maxima, suggesting a positional disorder (at least partial) of the cations. In balliranoite, two sites (Fig. 6.2 and 6.3) partially occupied by both Na^+ and Ca^{2+} have been found: even though a clear picture cannot be drawn, it is highly likely that Ca^{2+} and the minor K^+ occupy the internal one (M1, Tables 6.3 and 6.8) for the more favorable bond lengths (Tables 6.5 and 6.10). In cancrinite, both Na^+ and Ca^{2+} share the same single site (Tables 4.2, 4.8 and 4.15). Nevertheless, the same coordination environment can be described for all these cations: four or five bonds to the framework oxygen atoms on a side (2*O3 + 2*O4 ± O1) and up to three carbonate oxygen on the other side, for which more details are in chapters 4 and 6 (Fig. 4.3 and 6.2). The triangular (CO_3^{2-})-groups occupy the center of the channel in two mutually exclusive and iso-oriented configurations with the C site on the 6_3 axis, for which the neighboring cations face an edge of the anionic group, giving rise to two bonds to the closer oxygen atoms (Fig. 4.3 and 6.2). Due to the resulting short C-C contacts, not all the sub-cells can be occupied by the carbonate anions and thus vacancies and positional disorder occur along the channel (Fig. 4.12 and 6.3), as already reported in the literature (see sections 1.2.1, 4.1, 4.2 and 4.3). In vishnevite and davyne, two distinct clusters can be defined. The first is given by the Na^+ cations occupying the "external" M2 site, closer to the channel walls, and the sulfate tetrahedral group at the center of the channel. For both the studied minerals at ambient conditions, the triangular basis of the sulfate tetrahedron was found to point a vertex toward the neighboring Na^+ atoms, so that a single Na-Os bond occurs. On the other side, the Na^+ cations are bonded to four or five framework oxygen atoms (depending on the distance between M2 and O1), as described above. In the low-*T* study of davyne, the structure has been modeled with two mutually exclusive external Na^+ sites, in order to account for the observed positional disorder (Fig. 7.2, more details are in section 7.1). The second cluster is made by the "internal" M1 sites partially occupied by both K^+ and Na^+, sharing the same coordination to the framework oxygen as

M2. In order to avoid too short K-O bonds, a vacancy in the anionic sites is typically associated to these clusters and up to two M1-O bonds with the sulfate apical oxygen in the neighboring sub-cells can occur. Graphical representations of the above-mentioned clusters in the (SO_4^{2-})-rich terms are in Fig. 5.1, 5.3 and 7.3.

The construction of a model of the channel population behavior is also not straightforward. However, a general trend can be defined. The ditrigonalization of the S6R∠[0001] windows (Fig. 4.4, 5.6, 6.6 and 7.7), following the compression of the *dzc* unit at low-*T* and high-*P*, induces a migration of the O1, O3 and O4 oxygen sites, from which a compression of the shorter M-O3′ and M-O4′ and a stretching of the longer M-O3″ and M-O4″ bonds occur. A compression of the M-O1 is also observed, so that, if too far at ambient conditions, a progressive fall within the cation coordination shell at high-*P* occurs for the O1 oxygen.

In cancrinite, balliranoite and davyne, no substantial change in the bonds between the cations and the carbonate- and sulfate-oxygen atoms is observed at non-ambient conditions. Therefore, for these three studied mineralogical species, the channel extraframework population apparently does not have any significant influence on the structure deformation mechanisms in response to the applied temperature or pressure.

On the contrary, in vishnevite a re-arrangement of the channel population occurs at $P \geq 3.43(4)$ GPa, coupled with a drop in the bulk modulus of the material. An interpretation of the source for such a re-arrangement is provided in the section 7.2. The instability of the low-*P* channel configuration has been ascribed to the cations coordination environments. An inspection of the parameters reported in Table 7.11 shows that possibly too short Na-O (or K-O), contacts occur with increasing pressure. At $P \geq 3.43(4)$ GPa, an inspection of the Fourier-syntheses of electron density revealed that a rotation of the sulfate tetrahedron of approximately 60° around the 6_3 axis occur, toward the CO_3^{2-} configuration described above. Furthermore, a marked migration of both the M1 and M2 sites toward the channel center followed the re-configuration of the anionic group. The latter could be interpreted as a structural response to allow the migration of the cations far from the channel walls and so from the framework oxygen, which was possibly previously prevented by the facing sulfate basal oxygen atoms (Fig. 5.1, 5.3 and 7.3). In this light it can also be interpreted the constant Na-O1 bonds shown by the cage-Na before the structural re-arrangement: the O1 migration toward the channel cations (therefore far from the cage-Na, Fig. 4.4, 5.6, 6.6 and 7.7) could also be prevented to avoid a potential

overbonding of those cations. However, an inspection of the post-structural re-arrangement parameters, in Table 7.11, shows that unusually short K-O bonds occur with increasing pressure.

The results from the high-*P* study of vishnevite suggest that the channel extraframework population plays a key role on the structure evolution, elastic behavior and even on the phase stability of vishnevite at high pressure. In particular, the cations coordination environment seems to be the source for the instability which leads the structural re-arrangement at high-*P*. However, as already mentioned in the previous chapters, the pressure at which the discontinuity occurs is very high if compared to the typical geological environments of these minerals and their potential applications as waste-storage forms.

Figure 8.1 The pressure-induced evolution of the unit-cell volume, *a* and *c* parameters of cancrinite, vishnevite, balliranoite and davyne, normalized to their room-*P* values. The estimated standard deviations are of the same order of magnitude of the symbols.

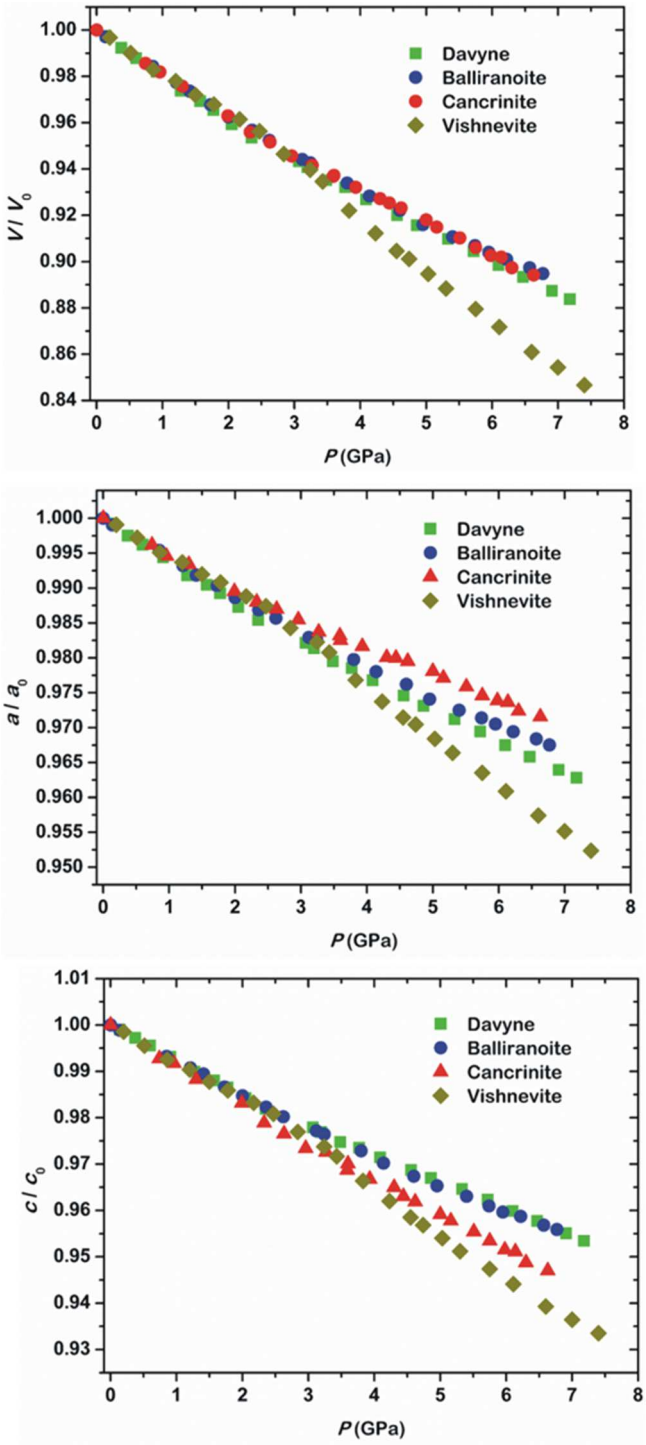

Chapter 9

Conclusions

The *in situ* high-pressure and low-temperature single-crystal X-ray diffraction studies of cancrinite, vishnevite, balliranoite and davyne, coupled with the *in situ* high-temperature single-crystal X-ray diffraction study of cancrinite, allowed to derive a model of the elastic and structural behavior of these cancrinite-group minerals. The following concluding remarks can be carried out.

- All the studied minerals share the same compressibility and, though with higher uncertainties on the refined parameters, the same thermal expansivity at ambient conditions.
- All the studied minerals show an anisotropic behavior, where the *c*-axis corresponds to the most expandable/compressible direction. It is interesting to note that the *c*-axis also corresponds to the stacking direction of the planes of single six-membered rings typical of the ABC-6 family of frameworks.
- Despite the similar elastic behavior at ambient conditions, the studied minerals show different elastic anisotropy, more pronounced for the cancrinite-subgroup minerals. In addition, both cancrinite and vishnevite show, in the low-*P* regime, higher $K' = (\partial K_0/\partial P)_T$ values, with respect to davyne and balliranoite.
- In vishnevite, a clear change in the compressional behavior, with a pronounced increase in compressibility, occurs between 2.47(2) and 3.83(9) GPa, which appears to be governed by a structural re-arrangement of the channel population at $P \geq 3.43(4)$ GPa. In cancrinite, a subtle increase in compressibility is observed between 4.62(3) and 5.00(2) GPa, but no concomitant change in the structural evolution was found.
- The structural evolution of the studied minerals was found to be mainly governed by the tilting of the rigid framework tetrahedra around the shared oxygen hinges.
- The extraframework population filling the columns of *can* units and, in particular, the nature of the cation coordination environment were found to affect not only the framework configuration at ambient conditions, but also its deformation in response to the applied *T* and *P*.
    - In cancrinite-subgroup minerals, a change in *T* or *P* induces a change in all the intertetrahedral Si-O-Al angles. Under “compressive” regimes (*i.e.* L*T* and H*P*) a shortening of the (shorter) Na-O2 and a stretching of the (longer) Na-O1 bonds occur, leading an increase in the ditrigonal shape of the S6R⊥[0001] and a compression of

the O3-$O4_{S4R}$ diameter. Those, along with the strong compression of the O1-$O1_{12R}$ channel diameter, accommodate the deformation in the (0001) plane. In the high-temperature hydrous regime, the same mechanisms, but opposite in sign, occur.

- In davyne-subgroup minerals, the nature of the Ca-coordination environment likely prevents a strong compression of the Ca-O2 bonds, inhibiting the tetrahedral rotation around the O2 hinge. Consequently, only a minor increase in the ditrigonal shape of the S6R⊥[0001] and none or minor O3-$O4_{S4R}$ compression occur. The strain in the (0001) plane is accommodated by the compression of the *can* unit along the O2-O2 diameters ("cage width") and by both the channel diameters.

- The strain along the [0001] direction is governed by the tetrahedral rotation around the O3 and O4 hinges, which does not significantly differ between the two subgroups of minerals. The same mechanism has been observed: the compression/expansion of the *dzc* unit, which induces a ditrigonalization/hezagonalization of the S6R∠[0001] windows, linking channels and cages.

- In cancrinite, balliranoite and davyne, the channel extraframework population apparently does not influence the *T*- and *P*-induced structural evolution.

- In vishnevite, at $P \geq 3.43(4)$ GPa, coordination environment of the channel cations likely induces a re-arrangement of the channel population, involving both the cations and the sulfate tetrahedra. However, short contacts and an unusual strong increase in compressibility suggest a metastable nature of the high-*P* configuration of vishnevite.

- For all the studied minerals, the bulk strain was found to be mainly accommodated by the channel voids, rather than by the *can* units.

- Despite the change in the compressional behavior shown by cancrinite and vishnevite, all the studied minerals proved to be stable and keep their crystallinity up the highest pressures investigated (~ 7 GPa), at room-*T* conditions, which is somewhat surprising considering their nature of microporous open-framework materials.

- Beside the previously described model of elastic behavior and structural evolution, this study allowed to determine the elastic parameters for all the studied minerals. These parameters could be implemented in the thermodynamic databases.

- The high-temperature study of cancrinite showed a drastic and slow dehydration process at 748 K, after which a quasi-anhydrous form was found to be stable (or metastable) at least up to 823 K and, then, at room conditions after the cooling of the crystal.

- The dehydration leads to a change in the tilting mechanism of the framework tetrahedra, likely governed by the tendency to minimize the cage Na-O1 and Na-O2 bonds to counterbalance the loss in bond valence due to H_2O desorption.

- The characterization of the thermo-elastic parameters could improve the study of the phase stability fields of cancrinite-group minerals in the natural geological environments, in which they occur. In conjunction with a thorough spectroscopic analysis of the volatiles composition, it could allow the characterization of the pressure, temperature and chemical conditions of crystallization environment.

- In the light of potential technological applications, for example as waste-storage forms, the obtained results revealed an apparent high stability of the studied compounds at the (low) pressures of interest. A careful evaluation of the high-temperature stability should be taken into account, in consideration of the dehydration shown by cancrinite-subgroup compounds at ~ 700-750 K. In addition, the stability of the davyne-subgroup compounds, related to the displacive phase transition from the P63 to P63/m space group, should also be evaluated. The structural characterization of the compression of the dzc unit at ambient conditions (through the O3-O4-O3 angle), coupled with the characterization of the thermoelastic behavior, could improve significantly such an evaluation.

Acknowledgements

My tutor, Prof. G. Diego Gatta, is gratefully thanked for having supervised the various steps of my PhD, for the many suggestions, for having supported my research activity and my participation to schools and congresses, for the supervision and support during my first attempts to write and publish my results. My co-tutor, Prof. Alessandro Pavese, is thanked for having supported my PhD activity and my participation to schools and congresses. Prof. Volker Kahlenberg (University of Innsbruck) is thanked for the low-temperature experiments on the studied cancrinite-group minerals. Dr. Marco Merlini (University of Milan) and Dr. Michael Hanfland (ESRF, Grenoble) are thanked for the support and assistance in the high-pressure experiments on vishnevite and davyne at ESRF. Dr. Nicola Rotiroti (University of Milan) is thanked for the assistance at the single-crystal X-ray diffraction laboratory, Earth Sciences Dept., Univ. of Milan. Prof. Fernando Cámara (University of Turin), Dr. Matteo Alvaro (University of Padua), Davide Comboni and Prof. Maria Chiara Domeneghetti (University of Pavia) are thanked for the high-temperature experiment on cancrinite. Dr. Pietro Vignola (CNR-Milano) and Andrea Risplendente (University of Milano) are thanked for the chemical analyses. Prof. Fernando Cámara (Univeristy of Turin) and Dr. George E. Harlow (Americam Museum of Natural History, New York) are thanked for sample of balliranoite. Dr. Fabio Bellatreccia (University of Roma Tre) is thanked for the samples of vishnevite and davyne. The PhD fellows Carla Tiraboschi, Irene Fantone, Lucia Pagliari and Andrea Bernasconi are thanked for the shared social (and scientific) meetings during the coffee breaks and lunches of the last three years.

The Italian Ministry of Education, MIUR-Project: ‘‘Futuro in Ricerca 2012 – ImPACT-RBFR12CLQD’’ is acknowledged.

Un ringraziamento particolare a Erika per aver condiviso con me questi tre anni e a mia madre e mio padre che hanno sempre condiviso e supportato gli studi che hanno preceduto questo dottorato, senza i quali non avrei potuto iniziare questo percorso.

Appendix

Tables

Appendix

Table 4.1 Details of data collections strategy and structure refinements of cancrinite at 293, 250, 220, 180, 140, 100 and 293 K (after the low temperature experiment).

T (K)	293 (T_0)	250 (T_1)	220 (T_2)	180 (T_3)	140 (T_4)	100 (T_5)	293* ($T_{0'}$)
a (Å)	12.6018(3)	12.5885(3)	12.5887(3)	12.5827(3)	12.5792(5)	12.5821(2)	12.6013(4)
c (Å)	5.1204(2)	5.1091(1)	5.1110(1)	5.0998(2)	5.1003(2)	5.0960(1)	5.1205(2)
V (Å^3)	704.21(2)	701.17(4)	701.46(4)	699.25(4)	698.93(6)	698.66(3)	704.16(6)
Maximum 2θ (°)	77.88	77.67	77.48	77.72	77.55	77.62	77.78
	-22≤h≤14	-18≤h≤21	-19≤h≤21	-21≤h≤18	-22≤h≤15	-17≤h≤22	-20≤h≤22
	-18≤k≤21	-21≤k≤21	-21≤k≤18	-21≤k≤21	-20≤k≤21	-22≤k≤21	-21≤k≤15
	-8≤l≤8	-8≤l≤8	-8≤l≤8	-8≤l≤8	-8≤l≤8	-8≤l≤8	-9≤l≤8
Measured reflections	11305	10843	11277	10761	11203	11670	11235
Unique eflections	2617	2518	2596	2509	2596	2614	2572
Unique reflections with $F_0 > 4\sigma(F_0)$	2260	2187	2303	2222	2292	2318	2163
R_{int}	0.0407	0.0408	0.0422	0.0433	0.0446	0.0451	0.0486
Number of l.s. parameters	99	97	97	97	97	97	99
R_1, $F_0 > 4\sigma(F_0)$	0.0378	0.0362	0.0339	0.0346	0.0346	0.0348	0.0381
R_1, all data	0.0478	0.0468	0.0421	0.0435	0.0441	0.0419	0.0512
wR^2	0.0586	0.0584	0.0571	0.0570	0.0576	0.0579	0.0614
Residuals (e^-/ Å^3)	+0.94/-0.67	+0.99/-0.68	+0.93/-0.75	+0.95/-0.73	+1.07/-0.82	+0.98/-0.73	+0.93/-0.70

ω/ϕ-scans; step scan = 1°; exposure time = 29 s; space group: $P6_3$; $Z = 1$

$R_{int} = \Sigma \mid F_{obs}^2 - F_{obs}^2(\text{mean}) \mid / \Sigma [F_{obs}^2]$

$R_1 = \Sigma(|F_{obs}| - |F_{calc}|)/\Sigma|F_{obs}|$; $wR_2 = [\Sigma[w(F^2_{obs} - F^2_{calc})^2]/\Sigma[w(F^2_{obs})^2]]^{0.5}$, $w = 1/ [\sigma^2(F_{obs}^2) + (0.01*P)^2]$, $P = (\text{Max}(F_{obs}^2, 0) + 2*F_{calc}^2)/3$

Table 4.2 Refined atomic coordinates, site occupancy factors (*sof*) and equivalent/isotropic atomic displacement parameters (Å^2) of cancrinite at 293, 250, 220, 180, 140, 100 and 293 K after the low temperature experiment. Ow site was refined with isotropic atomic displacement parameter.

T (K)	Site	Occ.	*x*	*y*	*z*	U_{iso}/ U_{eq}
293	Si	1.0	0.08266(3)	0.41076(3)	0.73332(8)	0.00694(6)
	Al	1.0	0.33706(3)	0.41216(3)	0.7342(1)	0.00695(7)
	O1	1.0	0.20182(9)	0.4050(1)	0.6425(2)	0.0139(2)
	O2	1.0	0.1145(1)	0.55067(9)	0.7108(3)	0.0187(2)
	O3	1.0	0.0444(1)	0.3589(1)	0.0278(2)	0.0148(2)
	O4	1.0	0.3210(1)	0.3509(1)	0.0450(2)	0.0144(2)
	Na1	0.957(6)	2/3	1/3	0.1177(3)	0.0275(5)
	Na2	0.894(4)	0.87422(5)	0.75144(6)	0.7765(1)	0.0246(3)
	Ca2	0.106(4)	0.87422(5)	0.75144(6)	0.7765(1)	0.0246(3)
	C1	0.345(9)	0	0	0.893(3)	0.032(3)
	Oc1	0.345(9)	0.0601(5)	0.1189(3)	0.880(2)	0.050(3)
	C2	0.472(9)	0	0	0.649 (3)	0.055(4)
	Oc2	0.472(9)	0.0616(3)	0.1193(3)	0.658(2)	0.052(2)
	Ow	0.33	0.3148(5)	0.6177(4)	0.168(1)	0.049(2)
250	Si	1.0	0.08271(3)	0.41078(3)	0.73328(8)	0.00602(6)
	Al	1.0	0.33708(3)	0.41223(3)	0.73431(9)	0.00606(7)
	O1	1.0	0.20144(9)	0.4043(1)	0.6410(2)	0.0120(2)
	O2	1.0	0.1150(1)	0.55100(9)	0.7102(3)	0.0167(2)
	O3	1.0	0.0447(1)	0.3592(1)	0.0285(2)	0.0135(2)
	O4	1.0	0.3208(1)	0.3511(1)	0.0455(2)	0.0127(2)
	Na1	0.957(6)	2/3	1/3	0.1172(3)	0.0227(3)
	Na2	0.894(4)	0.87411(5)	0.75142(6)	0.7768(1)	0.0223(2)
	Ca2	0.106(4)	0.87411(5)	0.75142(6)	0.7768(1)	0.0223(2)
	C1	0.36(1)	0	0	0.892(3)	0.030(3)
	Oc1	0.36(1)	0.0608(5)	0.1193(3)	0.878(2)	0.053(3)
	C2	0.46(2)	0	0	0.654(3)	0.055(5)
	Oc2	0.46(2)	0.0614(3)	0.1198(3)	0.657(2)	0.048(2)
	Ow	0.333	0.3143(5)	0.6165(4)	0.168(1)	0.043(1)
220	Si	1.0	0.08273(3)	0.41081(3)	0.73330(7)	0.00567(6)
	Al	1.0	0.33701(3)	0.41223(3)	0.73421(8)	0.00568(6)

	O1	1.0	0.20117(9)	0.40403(10)	0.6402(2)	0.0113(2)
	O2	1.0	0.1151(1)	0.55111(9)	0.7092(2)	0.0157(2)
	O3	1.0	0.0452(1)	0.3595(1)	0.0288(2)	0.0126(2)
	O4	1.0	0.3207(1)	0.3516(1)	0.0465(2)	0.0120(2)
	Na1	0.957(6)	2/3	1/3	0.1170 (3)	0.0204(3)
	Na2	0.894(4)	0.87414(5)	0.75131(6)	0.7766(1)	0.0211(1)
	Ca2	0.106(4)	0.87414(5)	0.75131(6)	0.7766(1)	0.0211(1)
	C1	0.349(9)	0	0	0.892(3)	0.029(3)
	Oc1	0.349(9)	0.0604(4)	0.1195(3)	0.882(2)	0.046(2)
	C2	0.480(8)	0	0	0.656(3)	0.057(4)
	Oc2	0.480(8)	0.0616(3)	0.1196(3)	0.660(2)	0.048(2)
	Ow	0.333	0.3139(5)	0.6157(4)	0.1673(9)	0.038(1)
180	Si	1.0	0.08277(3)	0.41074(3)	0.73330(8)	0.00509(6)
	Al	1.0	0.33699(3)	0.41216(3)	0.73423(9)	0.00510(7)
	O1	1.0	0.20122(9)	0.4039(1)	0.6392(2)	0.0102(2)
	O2	1.0	0.1156(1)	0.55122(8)	0.7086(2)	0.0142(2)
	O3	1.0	0.04549(9)	0.3598(1)	0.0301(2)	0.0117(2)
	O4	1.0	0.3206(1)	0.3517(1)	0.0471(2)	0.0109(2)
	Na1	0.957(6)	2/3	1/3	0.1155(3)	0.0171(2)
	Na2	0.894(4)	0.87426(5)	0.75151(5)	0.7765(1)	0.0191(1)
	Ca2	0.106(4)	0.87426(5)	0.75151(5)	0.7765(1)	0.0191(1)
	C1	0.384(9)	0	0	0.897(3)	0.036(3)
	Oc1	0.384(9)	0.0598(4)	0.1193(3)	0.882(2)	0.050(2)
	C2	0.447(9)	0	0	0.646(3)	0.047(4)
	Oc2	0.447(9)	0.0617(3)	0.1197(3)	0.657(1)	0.043(2)
	Ow	0.333	0.3131(4)	0.6153(3)	0.163(1)	0.034(1)
140	Si	1.0	0.08282(3)	0.41073(3)	0.73337(8)	0.00456(6)
	Al	1.0	0.33696(3)	0.41221(3)	0.73425(9)	0.00452(7)
	O1	1.0	0.20081(9)	0.4031(1)	0.6383(2)	0.0095(2)
	O2	1.0	0.1158(1)	0.55134(8)	0.7082(2)	0.0129(2)
	O3	1.0	0.0459(1)	0.3603(1)	0.0304(2)	0.0106(2)
	O4	1.0	0.3204(1)	0.3519(1)	0.0474(2)	0.0100(2)
	Na1	0.957(6)	2/3	1/3	0.1156(3)	0.0146(2)
	Na2	0.894(4)	0.87428(5)	0.75139(5)	0.7763(1)	0.0173(1)

	Ca2	0.106(4)	0.87428(5)	0.75139(5)	0.7763(1)	0.0173(1)
	C1	0.325(8)	0	0	0.894(3)	0.025(3)
	Oc1	0.325(8)	0.0602(4)	0.1194(3)	0.883(2)	0.037(2)
	C2	0.501(9)	0	0	0.659(3)	0.056(4)
	Oc2	0.501(9)	0.0620(3)	0.1203(3)	0.659(1)	0.047(2)
	Ow	0.333	0.3128(4)	0.6135(3)	0.1666(8)	0.028(1)
100	Si	1.0	0.08284(3)	0.41078(3)	0.73323(8)	0.00408(6)
	Al	1.0	0.33696(3)	0.41222(3)	0.73433(9)	0.00404(7)
	O1	1.0	0.20081(9)	0.40302(9)	0.6379(2)	0.0087(2)
	O2	1.0	0.11593(9)	0.55152(8)	0.7072(2)	0.0120(2)
	O3	1.0	0.04640(9)	0.3606(1)	0.0307(2)	0.0100(2)
	O4	1.0	0.32062(9)	0.3523(1)	0.0480(2)	0.0093(2)
	Na1	0.957(6)	2/3	1/3	0.1152(2)	0.0119(2)
	Na2	0.894(4)	0.87431(5)	0.75147(5)	0.7765(1)	0.0159(1)
	Ca2	0.106(4)	0.87431(5)	0.75147(5)	0.7765(1)	0.0159(1)
	C1	0.348(8)	0	0	0.894(3)	0.026(3)
	Oc1	0.348(8)	0.0606(4)	0.1196(3)	0.884(2)	0.039(2)
	C2	0.475(8)	0	0	0.658(3)	0.056(4)
	Oc2	0.475(8)	0.0616(3)	0.1199(2)	0.662(1)	0.044(2)
	Ow	0.333	0.3120(4)	0.6125(3)	0.1668(8)	0.0232(8)
293*	Si	1.0	0.08265(3)	0.41077(3)	0.7335(1)	0.00682(7)
	Al	1.0	0.33712(3)	0.41216(3)	0.7344(1)	0.00692(8)
	O1	1.0	0.2016(1)	0.4048(1)	0.6422(3)	0.0137(2)
	O2	1.0	0.1146(1)	0.55073(9)	0.7098(3)	0.0184(3)
	O3	1.0	0.0444(1)	0.3591(1)	0.0277(2)	0.0148(2)
	O4	1.0	0.3211(1)	0.3509(1)	0.0447(2)	0.0139(2)
	Na1	0.957(6)	2/3	1/3	0.1176(4)	0.0272(5)
	Na2	0.894(4)	0.87408(6)	0.75135(6)	0.7764(2)	0.0251(3)
	Ca2	0.106(4)	0.87408(6)	0.75135(6)	0.7764(2)	0.0251(3)
	C1	0.37(1)	0	0	0.896(3)	0.030(3)
	Oc1	0.37(1)	0.0603(5)	0.1190(3)	0.879(3)	0.055(4)
	C2	0.47(1)	0	0	0.651(4)	0.052(4)
	Oc2	0.47(1)	0.0616(4)	0.1195(3)	0.659(2)	0.053(3)
	Ow	0.333	0.3147(6)	0.6162(4)	0.169(1)	0.054(2)

* After the low-*T* experiment

Table 4.3 Anisotropic atomic displacement parameters (Å^2) of cancrinite sites at 293, 250, 220, 180, 140, 100 and 293 K after the low temperature experiment.

T_0 = 293 K

Atom	U_{11}	U_{22}	U_{33}	U_{12}	U_{13}	U_{23}
Si	0.0064(1)	0.0077(1)	0.0073(1)	0.0039(1)	0.0002(2)	0.0006(2)
Al	0.0064(2)	0.0078(2)	0.0072(2)	0.0039(1)	0.0003(2)	0.0007(2)
O1	0.0111(4)	0.0201(5)	0.0138(4)	0.0104(4)	0.0025(4)	0.0027(4)
O2	0.0194(5)	0.0105(4)	0.0290(6)	0.0094(4)	0.0039(6)	0.0020(5)
O3	0.0131(5)	0.0229(5)	0.0098(5)	0.0100(4)	0.0027(4)	0.0034(4)
O4	0.0164(5)	0.0222(5)	0.0097(5)	0.0134(4)	0.0009(4)	0.0036(4)
Na1	0.0201(5)	0.0201(5)	0.0424(9)	0.0101(3)	0.00000	0.00000
Na2	0.0158(3)	0.0274(4)	0.0342(5)	0.0134(3)	-0.0001(3)	0.0013(3)
Ca2	0.0158(3)	0.0274(4)	0.0342(5)	0.0134(3)	-0.0001(3)	0.0013(3)
C1	0.007(3)	0.007(3)	0.08(1)	0.003(1)	0.00000	0.00000
OC1	0.028(3)	0.011(2)	0.104(8)	0.005(2)	-0.002(4)	-0.004(3)
C2	0.014(2)	0.014(2)	0.14(1)	0.007(1)	0.00000	0.00000

T_1 = 250 K

Atom	U_{11}	U_{22}	U_{33}	U_{12}	U_{13}	U_{23}
Si	0.0055(1)	0.0067(1)	0.0063(1)	0.0034(1)	0.0002(2)	0.0004(2)
Al	0.0057(2)	0.0068(2)	0.0062(2)	0.0035(1)	0.0001(2)	0.0002(2)
O1	0.0101(4)	0.0187(5)	0.0110(4)	0.0101(4)	0.0016(4)	0.0020(4)
O2	0.0174(5)	0.0093(4)	0.0259(6)	0.0085(4)	0.0032(5)	0.0013(5)
O3	0.0113(5)	0.0208(5)	0.0087(5)	0.0084(4)	0.0024(4)	0.0041(4)
O4	0.0142(5)	0.0195(5)	0.0088(5)	0.0118(4)	0.0015(4)	0.0042(4)
Na1	0.0168(4)	0.0168(4)	0.0346(8)	0.0084(2)	0.00000	0.00000
Na2	0.0141(3)	0.0249(3)	0.0312(4)	0.0123(2)	0.0000(3)	0.0015(3)
Ca2	0.0141(3)	0.0249(3)	0.0312(4)	0.0123(2)	0.0000(3)	0.0015(3)
C1	0.010(3)	0.010(3)	0.070(9)	0.005(2)	0.00000	0.00000
OC1	0.026(3)	0.010(2)	0.117(9)	0.004(2)	-0.005(4)	-0.005(3)
C2	0.011(2)	0.011(2)	0.14(2)	0.006(1)	0.00000	0.00000

T_2 = 220 K

Atom	U_{11}	U_{22}	U_{33}	U_{12}	U_{13}	U_{23}
Si	0.0050(1)	0.0063(1)	0.0060(1)	0.0031(1)	0.0001(2)	0.0003(1)
Al	0.0052(1)	0.0063(2)	0.0059(1)	0.0031(1)	0.0001(2)	0.0003(2)
O1	0.0091(4)	0.0170(5)	0.0111(4)	0.0090(4)	0.0013(3)	0.0017(3)
O2	0.0162(5)	0.0087(4)	0.0243(5)	0.0078(4)	0.0028(5)	0.0014(4)
O3	0.0101(5)	0.0203(5)	0.0082(4)	0.0082(4)	0.0025(3)	0.0036(3)
O4	0.0138(5)	0.0183(5)	0.0083(4)	0.0114(4)	0.0015(3)	0.0037(3)

Na1	0.0152(4)	0.0152(4)	0.0307(6)	0.0076(2)	0.00000	0.00000
Na2	0.0127(2)	0.0238(3)	0.0298(4)	0.0114(2)	0.0000(2)	0.0015(2)
Ca2	0.0127(2)	0.0238(3)	0.0298(4)	0.0114(2)	0.0000(2)	0.0015(2)
C1	0.006(2)	0.006(2)	0.075(8)	0.003(1)	0.00000	0.00000
OC1	0.019(2)	0.010(2)	0.103(7)	0.005(2)	-0.003(3)	-0.008(2)
C2	0.016(2)	0.016(2)	0.14(1)	0.008(1)	0.00000	0.00000

T_3 = 180 K

Atom	U_{11}	U_{22}	U_{33}	U_{12}	U_{13}	U_{23}
Si	0.0046(1)	0.0056(1)	0.0053(1)	0.0029(1)	0.0000(2)	0.0003(2)
Al	0.0048(1)	0.0057(1)	0.0051(1)	0.0028(1)	0.0001(2)	0.0002(2)
O1	0.0081(4)	0.0162(5)	0.0092(4)	0.0084(4)	0.0013(3)	0.0015(4)
O2	0.0149(4)	0.0078(4)	0.0218(6)	0.0070(3)	0.0020(5)	0.0012(5)
O3	0.0098(4)	0.0189(5)	0.0074(4)	0.0080(4)	0.0021(3)	0.0036(4)
O4	0.0130(4)	0.0169(5)	0.0071(4)	0.0106(4)	0.0015(3)	0.0034(4)
Na1	0.0126(3)	0.0126(3)	0.0262(6)	0.0063(2)	0.00000	0.00000
Na2	0.0112(2)	0.0218(3)	0.0275(4)	0.0108(2)	-0.0002(2)	0.0011(3)
Ca2	0.0112(2)	0.0218(3)	0.0275(4)	0.0108(2)	-0.0002(2)	0.0011(3)
C1	0.014(3)	0.014(3)	0.08(1)	0.007(1)	0.00000	0.00000
OC1	0.022(2)	0.008(2)	0.115(8)	0.005(2)	-0.005(3)	-0.004(3)
C2	0.004(2)	0.004(2)	0.13(1)	0.0021(9)	0.00000	0.00000
OC2	0.014(2)	0.015(2)	0.102(6)	0.009(1)	0.004(2)	0.008(2)

T_4 = 140 K

Atom	U_{11}	U_{22}	U_{33}	U_{12}	U_{13}	U_{23}
Si	0.0041(1)	0.0051(1)	0.0047(1)	0.0025(1)	0.0001(2)	0.0004(2)
Al	0.0041(2)	0.0050(2)	0.0047(1)	0.0025(1)	0.0001(2)	0.0002(2)
O1	0.0087(4)	0.0141(5)	0.0084(4)	0.0078(4)	0.0014(3)	0.0015(4)
O2	0.0134(4)	0.0071(4)	0.0199(5)	0.0063(4)	0.0025(5)	0.0011(4)
O3	0.0095(5)	0.0178(5)	0.0062(4)	0.0082(4)	0.0017(3)	0.0030(4)
O4	0.0112(5)	0.0160(5)	0.0069(4)	0.0098(4)	0.0009(3)	0.0026(4)
Na1	0.0111(3)	0.0111(3)	0.0214(6)	0.0056(2)	0.00000	0.00000
Na2	0.0099(2)	0.0202(3)	0.0249(4)	0.0098(2)	0.0001(2)	0.0011(2)
Ca2	0.0099(2)	0.0202(3)	0.0249(4)	0.0098(2)	0.0001(2)	0.0011(2)
C1	0.004(3)	0.004(3)	0.065(8)	0.0021(13)	0.00000	0.00000
OC1	0.012(2)	0.003(2)	0.090(6)	-0.001(2)	-0.004(3)	-0.002(2)
C2	0.009(2)	0.009(2)	0.15(1)	0.005(1)	0.00000	0.00000
OC2	0.019(2)	0.017(2)	0.105(5)	0.010(1)	0.000(2)	0.001(2)

T_5 = 100 K

Atom	U_{11}	U_{22}	U_{33}	U_{12}	U_{13}	U_{23}

Si	0.0038(1)	0.0046(1)	0.0041(1)	0.0022(1)	0.0002(2)	0.0002(2)
Al	0.0038(1)	0.0045(1)	0.0041(1)	0.0023(1)	0.0001(2)	0.0003(2)
O1	0.0071(4)	0.0136(4)	0.0080(4)	0.0071(4)	0.0014(3)	0.0017(4)
O2	0.0125(4)	0.0067(4)	0.0181(5)	0.0058(3)	0.0022(4)	0.0009(4)
O3	0.0084(4)	0.0170(5)	0.0057(4)	0.0071(4)	0.0016(3)	0.0027(4)
O4	0.0107(4)	0.0147(5)	0.0062(4)	0.0092(4)	0.0015(3)	0.0029(4)
Na1	0.0092(3)	0.0092(3)	0.0174(5)	0.0046(2)	0.00000	0.00000
Na2	0.0089(2)	0.0192(3)	0.0230(4)	0.0096(2)	-0.0004(2)	0.0011(2)
Ca2	0.0089(2)	0.0192(3)	0.0230(4)	0.0096(2)	-0.0004(2)	0.0011(2)
C1	0.005(2)	0.005(2)	0.067(8)	0.003(1)	0.00000	0.00000
OC1	0.017(2)	0.007(2)	0.088(6)	0.002(2)	-0.002(3)	0.001(2)
C2	0.009(2)	0.009(2)	0.15(1)	0.005(1)	0.00000	0.00000
OC2	0.014(2)	0.012(1)	0.107(6)	0.008(1)	0.002(2)	0.008(2)

$T_{0'}$ = 293 K (after L*T* experiment)

Atom	**U_{11}**	**U_{22}**	**U_{33}**	**U_{12}**	**U_{13}**	**U_{23}**
Si	0.0062(1)	0.0075(2)	0.0072(2)	0.0038(1)	0.0000(2)	0.0002(2)
Al	0.0063(2)	0.0074(2)	0.0076(2)	0.0038(1)	0.0000(2)	0.0006(2)
O1	0.0109(5)	0.0205(5)	0.0135(5)	0.0108(4)	0.0017(4)	0.0021(5)
O2	0.0188(5)	0.0101(4)	0.0286(8)	0.0089(4)	0.0041(6)	0.0022(6)
O3	0.0132(5)	0.0224(6)	0.0101(6)	0.0098(5)	0.0026(4)	0.0038(5)
O4	0.0152(5)	0.0214(6)	0.0097(6)	0.0127(5)	0.0013(4)	0.0034(5)
Na1	0.0194(6)	0.0194(6)	0.043(1)	0.0097(3)	0.00000	0.00000
Na2	0.0157(3)	0.0268(4)	0.0359(6)	0.0130(3)	-0.0004(3)	0.0013(3)
Ca2	0.0157(3)	0.0268(4)	0.0359(6)	0.0130(3)	-0.0004(3)	0.0013(3)
C1	0.011(3)	0.011(3)	0.07(1)	0.006(2)	0.00000	0.00000
OC1	0.031(3)	0.016(3)	0.113(10)	0.008(2)	-0.004(4)	-0.004(3)
C2	0.014(3)	0.014(3)	0.13(2)	0.007(1)	0.00000	0.00000

Appendix

Table 4.4 Relevant bond distances (Å), diameters (Å), angles (°), S6R⊥[0001] ditrigonal rotation angle $\alpha_{S6R\perp[0001]}$(°), hexagonal layers corrugation Δ*z*(Å) and cage/channel-volumes (Å^3) of cancrinite at different temperatures.

	T	293 K (T_0)	250 K (T_1)	220 K (T_2)	180 K (T_3)	140 K (T_4)	100 K (T_5)	293§ K ($T_{0'}$)
Si-	O1	1.608(1)	1.608(1)	1.608(1)	1.609(1)	1.609(1)	1.611(1)	1.607(1)
	O2	1.605(1)	1.606(1)	1.607(1)	1.607(1)	1.607(1)	1.609(1)	1.605(1)
	O3	1.618(1)	1.617(1)	1.618(1)	1.619(1)	1.618(1)	1.618(1)	1.616(1)
	O4	1.617(1)	1.618(1)	1.619(1)	1.618(1)	1.620(1)	1.618(1)	1.618(1)
<Si-O>		1.612(1)	1.612(1)	1.613(1)	1.613(1)	1.614(1)	1.614(1)	1.612(1)
Al-	O1	1.726(1)	1.727(1)	1.729(1)	1.728(1)	1.729(1)	1.730(1)	1.729(1)
	O2	1.722(1)	1.720(1)	1.720(1)	1.723(1)	1.723(1)	1.723(1)	1.722(1)
	O3	1.745(1)	1.744(1)	1.747(1)	1.742(1)	1.744(1)	1.747(1)	1.745(1)
	O4	1.736(1)	1.733(1)	1.737(1)	1.735(1)	1.735(1)	1.735(1)	1.734(1)
<Al-O>		1.732(1)	1.731(1)	1.733(1)	1.732(1)	1.733(1)	1.734(1)	1.733(1)
Si-O1-Al		147.02(9)	146.46(8)	146.14(8)	145.85(8)	145.42(8)	145.32(7)	147.02(9)
Si-O2-Al		151.79(7)	151.45(10)	151.27(10)	150.9(9)	150.74(9)	150.56(9)	151.79(7)
Si-O3-Al		133.46(7)	133.26(7)	133.05(6)	132.83(7)	132.78(7)	132.55(7)	133.46(7)
Si-O4-Al		133.55(7)	133.26(7)	133.02(6)	132.85(7)	132.72(7)	132.66(7)	133.55(7)
Na1-	O1(x3)	2.858(1)	2.863(1)	2.866(1)	2.866(1)	2.873(1)	2.875(1)	2.860(1)
	O2(x3)	2.437(1)	2.429(1)	2.427(1)	2.421(1)	2.418(1)	2.416(1)	2.435(1)
	Ow'	2.364(6)	2.359(6)	2.366(5)	2.377(5)	2.364(4)	2.361(4)	2.364(7)
	Ow''	2.870(6)	2.869(6)	2.868(5)	2.847(5)	2.870(4)	2.873(4)	2.878(7)
Na2/Ca2-	O1	2.535(1)	2.519(1)	2.514(1)	2.508(1)	2.499(1)	2.495(1)	2.533(2)
	O3'	2.457(1)	2.453(1)	2.449(1)	2.444(1)	2.442(1)	2.441(1)	2.458(1)
	O4'	2.439(1)	2.432(1)	2.429(1)	2.425(1)	2.422(1)	2.423(1)	2.438(1)
	O3''	2.922(1)	2.921(1)	2.927(1)	2.931(1)	2.937(1)	2.942(1)	2.922(1)
	O4''	2.891(1)	2.893(1)	2.899(1)	2.900(1)	2.903(1)	2.907(1)	2.892(1)
	Oc1'	2.474(9)	2.476(9)	2.461(7)	2.457(8)	2.449(7)	2.445(7)	2.48(1)
	Oc1''	2.408(4)	2.409(4)	2.409(4)	2.400(4)	2.407(4)	2.409(4)	2.409(5)

	Oc1'''	2.411(5)	2.400(5)	2.410(4)	2.413(4)	2.411(4)	2.408(4)	2.408(5)
	Oc2'	2.411(7)	2.395(7)	2.411(5)	2.395(6)	2.401(5)	2.412(6)	2.413(9)
	Oc2''	2.442(4)	2.435(4)	2.437(3)	2.437(4)	2.434(3)	2.429(4)	2.439(4)
	Oc2'''	2.412(4)	2.418(4)	2.411(4)	2.409(4)	2.407(3)	2.406(4)	2.414(4)
Na2/Ca2-	C1	2.778(4)	2.773(3)	2.774(3)	2.777(4)	2.775(3)	2.774(3)	2.781(4)
	C2	2.791(4)	2.781(4)	2.781(3)	2.789(4)	2.774(4)	2.775(4)	2.788(4)
$O2\text{-}O2_{S6R\perp[0001]}$		4.142(2)	4.126(2)	4.123(2)	4.112(2)	4.108(2)	4.106(2)	4.137(2)
$O2\text{-}O2_{cw}$		8.467(2)	8.466(2)	8.469(2)	8.474(2)	8.476(2)	8.480(2)	8.468(2)
O2-O2-O2		91.16(5)	90.97(5)	90.91(3)	90.57(3)	90.48(3)	90.37(3)	91.21(5)
O3-O4-O3		144.84(2)	144.42(5)	143.98(4)	143.71(5)	143.37(5)	143.05(5)	144.8(5)
$O1\text{-}O1_{12R}$*		8.841(2)	8.815(2)	8.810(2)	8.802(2)	8.783(2)	8.783(1)	8.837(2)
$O3\text{-}O4_{12R}$		8.486(1)	8.471(1)	8.475(1)	8.472(1)	8.474(1)	8.480(1)	8.481(1)
$O3\text{-}O4_{S4R}$		4.129(3)	4.123(2)	4.120(2)	4.117(2)	4.111(2)	4.108(2)	4.127(2)
$\alpha_{S6R\perp[0001]}$		8.45(3)	8.66(3)	8.75(3)	8.87(3)	9.05(3)	9.09(3)	8.50(3)
Δz		0.937(3)	0.928(3)	0.922(2)	0.910(2)	0.907(2)	0.899(2)	0.932(3)

*calculated as the projection on the (0001) plane;

§ after the low-temperature experiment

Appendix

Table 4.5 Frequencies of Raman bands of cancrinite at room conditions

Bands	Frequency (cm^{-1})	
v_1	108	Intra-tetrahedral O-T-O bending and rotational modes, and lattice modes
v_2	115	
v_3	161	
v_4	231	
v_5	277	
v_6	293	
v_7	338	
v_8	350	
v_9	364	
v_{10}	401	
v_{11}	418	
v_{12}	440	
v_{13}	460	
v_{14}	469	
v_{15}	499	
v_{16}	631	Inter-tetrahedral *symmetric* T-O-T stretching modes and in-plane bending modes of CO_3-group
v_{17}	685	
v_{18}	768	
v_{19}	816	
v_{20}	938	Inter-tetrahedral *anti-symmetric* T-O-T stretching modes and symmetric stretching modes of CO_3-group
v_{21}	960	
v_{23}	976	
v_{24}	981	
v_{25}	1002	
v_{26}	1042	
v_{27}	1057	
v_{28}	3536	O-H stretching modes
v_{29}	3647	

Table 4.6 Details of the data collections strategy and structure refinements of cancrinite at different pressures.

P (GPa)	0.0001	0.0001*	0.76(2)	0.99(2)	1.39(2)	2.33(2)	3.59(2)	4.30(3)	5.00(2)	5.73(3)	6.16(2)	6.63(3)
X-ray radiation	Mo-*K*α	Mo-*K*α	Mo-*K*α	Mo-*K*α	Mo-*K*α	Mo-*K*α	Mo-*K*α	Mo-*K*α	Mo-*K*α	Mo-*K*α	Mo-*K*α	Mo-*K*α
Scan width (°/frame)	1	0.5	0.5	0.5	0.5	0.5	0.5	0.5	0.5	0.5	0.5	0.5
a (Å)	12.5976(6)	12.620(9)	12.580(9)	12.530(9)	12.514(9)	12.447(5)	12.386(3)	12.347(6)	12.322(4)	12.278(2)	12.266(3)	12.240(4)
c (Å)	5.1168(2)	5.083(4)	5.058(3)	5.072(5)	5.034(2)	5.006(2)	4.954(2)	4.935(3)	4.905(2)	4.876(1)	4.864(2)	4.843(2)
Maximum 2θ (°)	69.96	60.91	64.02	64.05	64.05	64.05	63.42	63.64	63.96	63.66	64.00	63.85
Measured reflections	19933	1545	1858	1932	2034	1838	1937	2238	2019	2000	2111	1945
Unique reflections	1980	685	789	769	771	722	728	834	780	752	799	704
Unique reflections with $F_0 > 4\sigma(F_0)$	1092	327	374	396	356	343	325	402	350	337	373	327
R_{int}	0.0581	0.1068	0.0958	0.1177	0.0936	0.0964	0.1088	0.0961	0.0900	0.0972	0.0884	0.0995
N. of refined parameters	87	45	45	45	45	45	45	45	45	45	45	45
R_1, $F_0 > 4\sigma(F_0)$	0.0560	0.0833	0.0888	0.0777	0.0656	0.0549	0.0634	0.0696	0.0606	0.0733	0.0830	0.0694
wR^2	0.0634	0.0925	0.1025	0.1192	0.0946	0.0775	0.0890	0.0958	0.0855	0.1045	0.0958	0.0881
Residuals (e^-/ Å^3)	+0.77/ -0.55	+0.71/ -0.85	+0.65/ -0.74	+0.66/ -0.72	+0.70/ -0.73	+0.77/ -0.51	+0.66/ -0.69	+0.60/ -0.87	+0.61/ -0.63	+0.79/ -0.96	+0.76/ -0.80	+0.89/ -0.72

* With the crystal in the DAC without any *P*-medium; ω/ϕ-scans; exposure time = 60 s; space group: $P6_3$; $Z = 1$

$R_{int} = \Sigma \mid F_{obs}^2 - F_{obs}^2(mean) \mid / \Sigma [F_{obs}^2]$; $R_1 = \Sigma(|F_{obs}| - |F_{calc}|)/\Sigma|F_{obs}|$; $wR_2 = [\Sigma[w(F^2_{obs} - F^2_{calc})^2]/\Sigma[w(F^2_{obs})^2]]^{0.5}$, $w = 1/ [\sigma^2(F_{obs}^2) + (0.01*P)^2]$, $P = (\text{Max}(F_{obs}^2, 0) + 2*F_{calc}^2)/3$

Appendix

Table 4.7 Unit-cell parameters of cancrinite at different pressures measured using a KUMA diffractometer

P (GPa)	*a* (Å)	*c* (Å)	*V* (Å^3)
0.0001*	12.598(8)	5.114(4)	702.6(8)
0.74(2)	12.550(7)	5.077(3)	692.5(7)
0.96(2)	12.530(9)	5.072(5)	690.0(9)
1.30(2)	12.515(6)	5.054(3)	685.6(6)
1.99(2)	12.466(8)	5.028(4)	676.6(8)
2.33(2)	12.447(5)	5.006(2)	671.7(5)
2.63(2)	12.434(6)	4.994(2)	668.7(5)
2.96(2)	12.415(7)	4.978(7)	664.0(9)
3.27(2)	12.393(5)	4.974(3)	661.6(5)
3.59(2)	12.386(3)	4.954(2)	658.3(3)
3.60(2)	12.378(6)	4.961(3)	658.5(6)
3.93(2)	12.367(4)	4.944(2)	654.9(4)
4.30(3)	12.347(6)	4.935(3)	651.5(6)
4.44(2)	12.346(4)	4.925(2)	650.1(4)
4.62(3)	12.340(3)	4.919(2)	648.6(3)
5.00(2)	12.322(4)	4.905(2)	645.0(4)
5.16(2)	12.310(3)	4.898(2)	642.9(3)
5.51(2)	12.294(2)	4.886(1)	639.6(2)
5.75(2)	12.278(2)	4.876(1)	636.6(2)
5.98(2)	12.269(5)	4.866(3)	634.2(5)
6.14(2)	12.266(3)	4.864(2)	633.7(3)
6.30(3)	12.250(3)	4.852(2)	630.5(3)
6.63(3)	12.240(4)	4.843(2)	628.3(4)

* With the crystal in the DAC without any *P*-medium.

Table 4.8 Atomic fractional coordinates, site occupancy factors (*sof*), and equivalent/isotropic atomic displacement parameters (Å^2) of cancrinite at different pressures.

Sites occupancies at P_0-AIR

Site	*sof*	Site	*sof*	Site	*sof*
Si	1.0	O4	1.0	Oc1	0.421(7)
Al	1.0	Na1	0.960(9)	C2	0.459(6)
O1	1.0	Na2(Na)	0.854(6)	Oc2	0.459(6)
O2	1.0	Na2(Ca)	0.146(6)	Ow	1.0
O3	1.0	C1	0.421(7)		

Site fractional coordinates and displacement parameters

P (GPa)	Site	*x*	*y*	*z*	U_{iso}/ U_{eq}
0.0001	Si	0.08267(7)	0.41096(7)	0.7338(2)	0.0090(2)
(P_0-AIR)	Al	0.33709(7)	0.41224(7)	0.7342(2)	0.0087(2)
	O1	0.2014(2)	0.4043(2)	0.6419(4)	0.0155(5)
	O2	0.1145(2)	0.5507(2)	0.7109(5)	0.0198(5)
	O3	0.0443(2)	0.3588(2)	0.0276(4)	0.0164(6)
	O4	0.3212(2)	0.3508(2)	0.0442(4)	0.0148(6)
	Na1	2/3	1/3	0.1159(5)	0.0294(9)
	Na2	0.8742(1)	0.7516(1)	0.7764(2)	0.0287(5)
	C1	0	0	0.914(4)	0.048(6)
	OC1	0.0562(7)	0.1184(4)	0.888(2)	0.052(3)
	C2	0	0	0.649(3)	0.021(4)
	OC2	0.0639(5)	0.1196(3)	0.664(1)	0.030(2)
	Ow	0.315(1)	0.6171(6)	0.171(1)	0.048(3)
0.0001	Si	0.0824(3)	0.4106(3)	0.7244(8)	0.0082(9)
(P_0-DAC)	Al	0.3372(3)	0.4126(3)	0.7231(9)	0.0087(9)
	O1	0.2007(7)	0.4027(7)	0.634(1)	0.013(2)
	O2	0.1140(6)	0.5520(7)	0.698(2)	0.019(2)
	O3	0.0462(8)	0.3590(8)	0.020(2)	0.012(3)
	O4	0.3199(8)	0.3517(7)	0.036(1)	0.007(2)
	Na1	2/3	1/3	0.108(2)	0.038(3)
	Na2	0.8746(4)	0.7519(4)	0.7673(5)	0.027(1)
	C1	0	0	0.91(1)	0.006(9)
	OC1	0.058(2)	0.1182(8)	0.881(6)	0.038(5)
	C2	0	0	0.652(9)	0.006(9)
	OC2	0.062(2)	0.1190(5)	0.662(4)	0.038(5)
	Ow	0.316(4)	0.617(2)	0.173(4)	0.039(9)
0.76(2)	Si	0.0828(3)	0.4112(3)	0.7347(7)	0.0095(7)
	Al	0.3373(3)	0.4126(3)	0.7348(9)	0.0111(8)

	O1	0.2009(7)	0.4022(7)	0.639(1)	0.015(2)
	O2	0.1175(6)	0.5542(6)	0.704(1)	0.019(2)
	O3	0.0491(7)	0.3632(7)	0.034(2)	0.014(2)
	O4	0.3212(7)	0.3540(7)	0.048(2)	0.010(2)
	Na1	2/3	1/3	0.112(1)	0.041(3)
	Na2	0.8754(4)	0.7517(4)	0.7779(6)	0.032(1)
	C1	0	0	0.90(2)	0.04(1)
	OC1	0.061(2)	0.1190(8)	0.883(6)	0.048(5)
	C2	0	0	0.672(4)	0.04(1)
	OC2	0.062(2)	0.1193(5)	0.672(4)	0.048(5)
	Ow	0.306(4)	0.613(2)	0.181(4)	0.054(9)
0.99(2)	Si	0.0826(3)	0.4108(3)	0.7376(6)	0.0139(7)
	Al	0.3374(2)	0.4121(3)	0.7389(7)	0.0133(8)
	O1	0.2000(7)	0.4017(7)	0.644(1)	0.020(2)
	O2	0.1163(6)	0.5513(6)	0.707(1)	0.020(2)
	O3	0.0457(7)	0.3588(7)	0.034(1)	0.015(2)
	O4	0.3191(7)	0.3512(7)	0.053(1)	0.017(2)
	Na1	2/3	1/3	0.115(1)	0.036(2)
	Na2	0.8733(3)	0.7497(4)	0.7820(6)	0.032(1)
	C1	0	0	0.91(1)	0.05(1)
	OC1	0.056(3)	0.119(1)	0.864(7)	0.069(6)
	C2	0	0	0.66(1)	0.05(1)
	OC2	0.063(2)	0.1200(5)	0.657(5)	0.069(6)
	Ow	0.309(3)	0.608(2)	0.173(4)	0.05(1)
1.39(2)	Si	0.0829(2)	0.4109(2)	0.7342(6)	0.0105(7)
	Al	0.3372(2)	0.4121(3)	0.7356(7)	0.0112(7)
	O1	0.2004(6)	0.4006(7)	0.635(1)	0.017(2)
	O2	0.1180(5)	0.5533(6)	0.702(1)	0.022(2)
	O3	0.0484(6)	0.3620(6)	0.035(1)	0.013(2)
	O4	0.3183(6)	0.3535(6)	0.054(1)	0.015(2)
	Na1	2/3	1/3	0.110(1)	0.040(2)
	Na2	0.8743(3)	0.7508(3)	0.7784(5)	0.032(1)
	C1	0	0	0.90(1)	0.028(9)
	OC1	0.058(2)	0.1200(6)	0.886(6)	0.052(5)
	C2	0	0	0.671(4)	0.028(9)
	OC2	0.063(2)	0.1203(5)	0.671(4)	0.052(5)
	Ow	0.305(3)	0.614(2)	0.178(4)	0.056(8)
2.33(2)	Si	0.0829(2)	0.4111(2)	0.7340(7)	0.0103(6)
	Al	0.3369(2)	0.4123(3)	0.7357(8)	0.0092(7)

	O1	0.2004(6)	0.4010(7)	0.634(1)	0.016(2)
	O2	0.1174(5)	0.5525(5)	0.699(1)	0.021(2)
	O3	0.0494(6)	0.3629(7)	0.0390(1)	0.014(2)
	O4	0.3181(6)	0.3529(6)	0.058(1)	0.016(2)
	Na1	2/3	1/3	0.107(1)	0.042(2)
	Na2	0.8749(3)	0.7524(3)	0.7792(5)	0.0283(9)
	C1	0	0	0.90(1)	0.032(8)
	OC1	0.052(2)	0.1193(7)	0.870(5)	0.053(5)
	C2	0	0	0.655(9)	0.032(8)
	OC2	0.067(2)	0.1198(6)	0.672(3)	0.053(5)
	Ow	0.319(4)	0.617(2)	0.176(3)	0.047(6)
3.59(2)	Si	0.0831(3)	0.4112(3)	0.7360(7)	0.0101(7)
	Al	0.3367(3)	0.4124(3)	0.7393(8)	0.0105(7)
	O1	0.1988(7)	0.3977(7)	0.631(1)	0.017(2)
	O2	0.1232(6)	0.5556(6)	0.697(1)	0.020(2)
	O3	0.0529(7)	0.3664(6)	0.047(1)	0.014(2)
	O4	0.3189(6)	0.3581(6)	0.062(1)	0.015(2)
	Na1	2/3	1/3	0.100(1)	0.038(2)
	Na2	0.8755(3)	0.7523(3)	0.7785(6)	0.028(1)
	C1	0	0	0.91(1)	0.05(1)
	OC1	0.066(3)	0.119(1)	0.860(5)	0.054(5)
	C2	0	0	0.686(9)	0.05(1)
	OC2	0.057(2)	0.1210(6)	0.664(4)	0.054(5)
	Ow	0.308(3)	0.615(2)	0.159(3)	0.031(7)
4.30(3)	Si	0.0835(2)	0.4111(3)	0.7345(7)	0.0120(6)
	Al	0.3369(2)	0.4126(3)	0.7366(8)	0.0125(7)
	O1	0.1981(6)	0.3957(7)	0.628(1)	0.019(2)
	O2	0.1243(5)	0.5566(6)	0.691(1)	0.020(2)
	O3	0.0539(6)	0.3675(6)	0.046(1)	0.015(2)
	O4	0.3181(6)	0.3579(6)	0.063(1)	0.017(2)
	Na1	2/3	1/3	0.095(1)	0.040(2)
	Na2	0.8754(3)	0.7523(3)	0.7756(6)	0.0291(9)
	C1	0	0	0.90(1)	0.026(8)
	OC1	0.055(2)	0.1204(9)	0.867(5)	0.053(5)
	C2	0	0	0.682(7)	0.026(8)
	OC2	0.067(2)	0.1216(5)	0.669(4)	0.053(5)
	Ow	0.311(3)	0.617(2)	0.155(2)	0.031(6)
	Si	0.0841(2)	0.4116(2)	0.7369(7)	0.0127(6)

Appendix

5.00(2)	Al	0.3372(2)	0.4131(3)	0.7384(8)	0.0123(7)
	O1	0.1984(6)	0.3978(6)	0.626(1)	0.016(2)
	O2	0.1235(6)	0.5554(6)	0.691(1)	0.024(2)
	O3	0.0546(7)	0.3666(6)	0.048(1)	0.014(2)
	O4	0.3182(6)	0.3584(6)	0.067(1)	0.017(2)
	Na1	2/3	1/3	0.094(1)	0.039(2)
	Na2	0.8757(3)	0.7527(3)	0.7795(6)	0.0276(9)
	C1	0	0	0.918(9)	0.025(8)
	OC1	0.054(2)	0.118(1)	0.857(5)	0.050(4)
	C2	0	0	0.659(8)	0.025(8)
	OC2	0.065(2)	0.1218(5)	0.665(4)	0.050(4)
	Ow	0.314(3)	0.614(2)	0.151(3)	0.045(8)
5.73(3)	Si	0.0839(3)	0.4118(3)	0.7377(8)	0.0123(7)
	Al	0.3377(3)	0.4137(3)	0.7415(9)	0.0131(8)
	O1	0.1955(7)	0.3916(8)	0.625(1)	0.020(2)
	O2	0.1259(7)	0.5560(7)	0.686(1)	0.027(2)
	O3	0.0574(8)	0.3702(6)	0.058(1)	0.014(2)
	O4	0.3196(7)	0.3617(7)	0.072(2)	0.017(2)
	Na1	2/3	1/3	0.085(2)	0.049(3)
	Na2	0.8760(4)	0.7531(4)	0.7764(7)	0.030(1)
	C1	0	0	0.90(1)	0.024(9)
	OC1	0.060(3)	0.121(1)	0.855(6)	0.047(5)
	C2	0	0	0.67(1)	0.024(9)
	OC2	0.064(2)	0.1226(5)	0.668(4)	0.047(5)
	Ow	0.308(4)	0.614(2)	0.151(3)	0.048(9)
6.16(2)	Si	0.0842(3)	0.4119(3)	0.7387(8)	0.0130(6)
	Al	0.3375(2)	0.4139(3)	0.7405(9)	0.0125(7)
	O1	0.1960(7)	0.3931(7)	0.627(1)	0.020(2)
	O2	0.1267(6)	0.5590(6)	0.686(1)	0.027(2)
	O3	0.0578(7)	0.3721(6)	0.055(1)	0.014(2)
	O4	0.3193(6)	0.3613(6)	0.070(1)	0.017(2)
	Na1	2/3	1/3	0.084(1)	0.047(2)
	Na2	0.8761(3)	0.7530(3)	0.7774(7)	0.031(1)
	C1	0	0	0.92(1)	0.016(8)
	OC1	0.060(2)	0.119(1)	0.853(5)	0.045(4)
	C2	0	0	0.676(7)	0.016(8)
	OC2	0.062(2)	0.1228(5)	0.666(4)	0.045(4)
	Ow	0.311(3)	0.614(2)	0.146(3)	0.048(9)

6.63(3)	Si	0.0841(2)	0.4123(3)	0.7392(8)	0.0126(6)
	Al	0.3373(2)	0.4142(3)	0.7424(9)	0.0137(7)
	O1	0.1959(6)	0.3910(7)	0.626(1)	0.022(2)
	O2	0.1302(6)	0.5576(6)	0.687(1)	0.027(2)
	O3	0.0572(7)	0.3721(6)	0.061(1)	0.018(2)
	O4	0.3199(6)	0.3620(6)	0.073(1)	0.019(2)
	Na1	2/3	1/3	0.077(2)	0.065(3)
	Na2	0.8762(3)	0.7527(3)	0.7758(7)	0.034(1)
	C1	0	0	0.90(1)	0.031(8)
	OC1	0.061(4)	0.121(1)	0.854(5)	0.055(4)
	C2	0	0	0.684(8)	0.031(8)
	OC2	0.062(3)	0.1225(6)	0.661(4)	0.055(4)
	Ow	0.308(3)	0.615(2)	0.141(3)	0.045(9)

Appendix

Table 4.9 Relevant bond distances (Å), diameters (Å), angles (°), S6R⊥[0001] ditrigonal rotation angle $\alpha_{S6R\perp[0001]}$(°), hexagonal layers corrugation Δ*z*(Å) and cage/channel-volumes (Å^3) of cancrinite at different pressures.

P (GPa)	0.0001 P_0-DAC	0.76(2)	0.99(2)	1.39(2)	2.33(2)	3.59(2)	4.30(3)	5.00(2)	5.73(3)	6.16(2)	6.63(3)
Si-O1	1.613(9)	1.620(8)	1.603(8)	1.618(7)	1.610(7)	1.611(8)	1.607(7)	1.598(7)	1.604(9)	1.596(8)	1.610(7)
Si-O2	1.627(8)	1.631(8)	1.600(7)	1.617(7)	1.599(6)	1.607(8)	1.619(7)	1.601(7)	1.598(8)	1.629(7)	1.595(7)
Si-O3	1.612(8)	1.604(8)	1.611(7)	1.610(6)	1.617(7)	1.621(8)	1.609(7)	1.603(7)	1.624(8)	1.597(8)	1.616(8)
Si-O4	1.628(8)	1.624(9)	1.615(8)	1.622(7)	1.602(7)	1.615(8)	1.615(7)	1.613(7)	1.604(9)	1.612(8)	1.603(8)
<Si-O>	1.620(8)	1.620(8)	1.607(8)	1.617(7)	1.607(7)	1.613(8)	1.613(7)	1.604(7)	1.608(9)	1.609(8)	1.606(8)
Al-O1	1.725(8)	1.723(8)	1.728(8)	1.721(7)	1.711(7)	1.709(8)	1.706(7)	1.716(7)	1.723(8)	1.716(8)	1.703(7)
Al-O2	1.701(9)	1.701(8)	1.723(7)	1.713(7)	1.708(6)	1.719(7)	1.711(7)	1.711(7)	1.719(8)	1.687(8)	1.730(7)
Al-O3	1.752(9)	1.755(9)	1.741(8)	1.736(8)	1.727(7)	1.729(8)	1.727(8)	1.734(8)	1.729(9)	1.734(8)	1.718(8)
Al-O4	1.734(8)	1.718(8)	1.734(8)	1.731(7)	1.742(7)	1.704(8)	1.715(8)	1.716(8)	1.708(9)	1.702(8)	1.697(9)
<Al-O>	1.728(9)	1.724(8)	1.732(8)	1.725(7)	1.722(7)	1.715(8)	1.715(8)	1.719(8)	1.720(9)	1.710(8)	1.712(8)
Si-O1-Al	147.5(7)	145.4(7)	145.9(7)	143.9(6)	143.6(6)	141.4(7)	140.7(6)	139.6(6)	137.6(7)	138.3(6)	137.3(6)
Si-O2-Al	151.8(6)	149.0(5)	149.5(5)	148.3(5)	148.5(4)	144.2(5)	143.3(5)	143.6(5)	140.9(5)	140.7(5)	138.6(5)
Si-O3-Al	131.4(6)	131.3(6)	132.2(5)	131.3(4)	130.4(4)	128.9(5)	128.6(5)	127.7(4)	126.0(5)	126.8(5)	126.4(5)
Si-O4-Al	132.5(5)	132.6(5)	131.5(5)	129.9(5)	129.4(4)	128.6(5)	127.8(5)	127.2(4)	126.5(5)	126.9(5)	126.8(5)
Na1-O1 (x 3)	2.888(8)	2.883(8)	2.879(8)	2.886(7)	2.867(7)	2.894(7)	2.902(7)	2.874(7)	2.931(8)	2.914(7)	2.932(7)
Na1-O2 (x 3)	2.441(7)	2.397(6)	2.403(6)	2.380(6)	2.374(6)	2.312(6)	2.286(7)	2.291(6)	2.262(7)	2.252(6)	2.219(6)
Na1-Ow'	2.28(2)	2.26(2)	2.34(2)	2.25(2)	2.23(2)	2.25(1)	2.24(1)	2.25(1)	2.19(2)	2.20(2)	2.18(1)
Na1-Ow''	2.92(2)	2.94(2)	2.90(2)	2.91(2)	2.90(2)	2.83(1)	2.81(1)	2.79(1)	2.82(2)	2.79(2)	2.79(1)

Na2-O1	2.515(9)	2.479(8)	2.467(8)	2.432(7)	2.425(6)	2.371(7)	2.353(7)	2.337(6)	2.294(8)	2.301(7)	2.280(7)
Na2-O3'	2.436(9)	2.426(9)	2.419(8)	2.406(7)	2.397(6)	2.357(7)	2.351(7)	2.334(7)	2.310(8)	2.329(7)	2.308(7)
Na2-O4'	2.429(9)	2.437(8)	2.390(8)	2.375(7)	2.359(6)	2.355(7)	2.327(7)	2.324(7)	2.315(8)	2.316(7)	2.308(7)
Na2-O3''	2.930(10)	2.980(9)	2.902(8)	2.947(8)	2.949(8)	2.995(8)	2.999(8)	2.985(8)	3.040(10)	3.043(9)	3.051(9)
Na2-O4''	2.903(9)	2.905(9)	2.884(8)	2.910(7)	2.902(7)	2.940(7)	2.940(7)	2.937(7)	2.976(8)	2.960(7)	2.964(8)
Na2-Oc1'	2.40(3)	2.42(3)	2.34(4)	2.38(3)	2.26(3)	2.44(3)	2.27(3)	2.25(3)	2.30(3)	2.30(3)	2.31(5)
Na2-Oc1''	2.44(3)	2.38(3)	2.41(3)	2.43(3)	2.46(3)	2.23(3)	2.14(3)	2.39(3)	2.32(3)	2.31(3)	2.29(5)
Na2-Oc1'''	2.42(3)	2.44(3)	2.56(3)	2.42(3)	2.48(2)	2.50(3)	2.43(3)	2.49(2)	2.45(3)	2.47(2)	2.44(3)
Na2-Oc2'	2.39(2)	2.37(2)	2.41(3)	2.38(2)	2.29(2)	2.41(3)	2.28(3)	2.31(2)	2.30(3)	2.33(2)	2.33(4)
Na2-Oc2''	2.43(2)	2.43(2)	2.46(3)	2.42(2)	2.45(2)	2.34(3)	2.42(3)	2.40(2)	2.36(3)	2.34(2)	2.34(4)
Na2-Oc2'''	2.45(2)	2.44(2)	2.37(2)	2.42(2)	2.40(2)	2.34(2)	2.37(2)	2.32(2)	2.32(2)	2.31(2)	2.29(2)
C1↔C1, C2↔C2	2.542(2)	2.529(2)	2.538(3)	2.517(1)	2.503(1)	2.477(1)	2.468(2)	2.453(1)	2.438(1)	2.432(1)	2.422(1)
C1↔C2	3.85(7)	3.8(1)	3.81(9)	3.63(7)	3.71(7)	3.55(8)	3.56(6)	3.72(6)	3.59(8)	3.60(6)	3.46(7)
$O2\text{-}O2_{S6R\perp[0001]}$	4.15(1)	4.07(1)	4.08(1)	4.04(1)	4.03(1)	3.91(1)	3.87(1)	3.88(1)	3.82(1)	3.80(1)	3.73(1)
$\alpha_{S6R\perp[0001]}$	8.8(2)	9.6(2)	9.5(2)	10.0(2)	9.8(2)	11.6(2)	12.2(2)	11.6(2)	13.2(2)	13.2(2)	14.3(2)
O2-O2-O2	91.1(3)	89.3(2)	90.2(2)	89.0(2)	89.3(2)	86.2(2)	85.7(2)	85.8(2)	84.5(2)	84.2(2)	82.4(2)
$*O1\text{-}O1_{12R}$	9.16(1)	9.12(1)	9.08(1)	9.04(1)	9.00(1)	8.88(1)	8.81(1)	8.837(9)	8.68(1)	8.70(1)	8.636(9)
$O3\text{-}O4_{12R}$	8.48(1)	8.51(2)	8.41(1)	8.432(9)	8.388(8)	8.405(8)	8.380(8)	8.351(8)	8.377(9)	8.386(8)	8.379(8)
$O3\text{-}O4_{S4R}$	4.15(1)	4.08(1)	4.13(1)	4.09(1)	4.07(1)	3.99(1)	3.97(1)	3.98(1)	3.91(1)	3.89(1)	3.87(1)
O3-O4-O3	142.9(4)	141.1(4)	143.1(3)	140.3(3)	140.1(3)	136.5(3)	135.7(3)	135.1(3)	133.1(4)	132.8(3)	133.0(3)
Δz	0.90(2)	0.86(2)	0.88(1)	0.84(1)	0.80(1)	0.74(1)	0.72(1)	0.70(1)	0.62(1)	0.64(1)	0.61(1)

Appendix

V_{ch}	298(1)	296(1)	292(1)	289.4(8)	285.0(7)	278.7(7)	274.6(8)	273.0(7)	267.1(7)	267.5(7)	264.1(7)
V_{cg}	157(3)	155(2)	154(3)	153(2)	151(2)	150(2)	150(2)	147(2)	149(2)	147(2)	148(2)

* calculated as the projection on the (0001) plane

Table 4.10 Anisotropic atomic displacement parameters (Å^2) of cancrinite sites from the structure refinement based on the data collected with the crystal in air

	$P_{0\text{-AIR}}$					
Atom	**U_{11}**	**U_{22}**	**U_{33}**	**U_{12}**	**U_{13}**	**U_{23}**
Si	0.0090(4)	0.0098(4)	0.0088(4)	0.0052(3)	0.0006(5)	0.0006(5)
Al	0.0081(4)	0.0091(4)	0.0089(4)	0.0043(4)	0.0005(6)	0.0018(6)
O1	0.012(1)	0.021(1)	0.018(1)	0.012(1)	0.0013(9)	0.0028(10)
O2	0.021(1)	0.010(1)	0.030(1)	0.010(1)	0.004(1)	0.0009(14)
O3	0.016(1)	0.022(1)	0.010(1)	0.009(1)	0.002(1)	0.0025(10)
O4	0.016(1)	0.023(1)	0.011(1)	0.014(1)	0.0020(9)	0.0031(10)
Na1	0.020(1)	0.020(1)	0.047(2)	0.0102(6)	0	0
Na2	0.0199(7)	0.0301(8)	0.0392(9)	0.0147(6)	0.0012(7)	0.0041(7)
Ca2	0.0199(7)	0.0301(8)	0.0392(9)	0.0147(6)	0.0012(7)	0.0041(7)

Appendix

Table 4.11 Unit-cell parameters of cancrinite with temperature

T (K)	*a* (Å)	*c* (Å)	*V* (Å^3)
291*	12.6207(3)	5.1260(1)	707.10(3)
303	12.6251(4)	5.1249(1)	707.43(4)
303	12.6243(4)	5.1260(1)	707.50(4)
323	12.6279(4)	5.1282(1)	708.20(4)
348	12.6310(4)	5.1317(2)	709.03(4)
373	12.6345(5)	5.1354(1)	709.93(5)
398	12.6378(5)	5.1398(1)	710.92(4)
423	12.6426(4)	5.1435(1)	711.97(4)
448	12.6454(6)	5.1468(2)	712.74(5)
473	12.6480(5)	5.1504(1)	713.54(5)
473	12.6485(5)	5.1501(2)	713.55(5)
498	12.6530(6)	5.1540(2)	714.61(6)
498	12.6525(6)	5.1545(2)	714.61(6)
498	12.6524(4)	5.1537(1)	714.49(4)
523	12.6564(6)	5.1578(2)	715.51(6)
548	12.6614(6)	5.1623(2)	716.70(6)
573	12.6647(4)	5.1658(2)	717.55(4)
598	12.6699(5)	5.1700(2)	718.73(5)
623	12.6737(5)	5.1742(2)	719.75(5)
648	12.6771(5)	5.1793(2)	720.84(5)
673	12.6817(6)	5.1829(2)	721.87(5)
698	12.6867(5)	5.1873(2)	723.06(5)
723	12.6909(5)	5.1915(1)	724.12(4)
748	12.6942(6)	5.1931(3)	724.72(6)
748†	12.6814(6)	5.1720(2)	720.32(6)
773†	12.6850(10)	5.1761(2)	721.29(9)
773†	12.6848(4)	5.1755(2)	721.19(4)
798†	12.6914(5)	5.1791(2)	722.44(5)
823†	12.6957(5)	5.1833(2)	723.52(5)
773**	12.690(1)	5.174(4)	721.6(6)
673**	12.658(8)	5.168(8)	717.1(1.3)
573**	12.658(4)	5.154(11)	715.2(1.5)
473**	12.645(9)	5.140(14)	711.7(2.1)
373**	12.626(4)	5.123(5)	707.4(8)
291**	12.611(6)	5.118(10)	705.0(1.4)

Note: *data collected with the crystal in air (no furnace, no silica vial), †data collected after the dehydration process, ** data collected during temperature decrease.

Appendix

Table 4.12 Unit-cell parameters of cancrinite with time at 748 K.

Time (min)	*a* (Å)	*c* (Å)	*V* (Å^3)
0	12.6942(6)	5.1931(3)	724.72(6)
131	12.6942(6)	5.1928(3)	724.67(6)
254	12.6933(5)	5.1927(2)	724.56(5)
334	12.6933(5)	5.1927(2)	724.56(5)
488	12.6933(7)	5.1913(3)	724.36(7)
1270	12.6933(5)	5.1910(2)	724.33(5)
1378	12.6935(5)	5.1897(3)	724.15(6)
1570	12.6907(5)	5.1894(2)	723.80(5)
1692	12.6911(5)	5.1886(3)	723.73(6)
2912	12.6870(6)	5.1817(3)	722.30(6)
3210	12.6870(4)	5.1815(2)	722.28(5)
3391	12.6869(5)	5.1812(3)	722.23(5)
3601	12.6868(4)	5.1807(2)	722.14(5)
4536	12.6871(6)	5.1798(3)	722.06(7)
5782	12.6860(6)	5.1791(3)	721.82(6)
5931	12.6851(5)	5.1782(3)	721.61(6)
6337	12.6843(10)	5.1779(2)	721.47(8)
6337	12.6857(5)	5.1779(2)	721.63(5)
6419	12.6825(9)	5.1775(2)	721.22(7)
6419	12.6849(5)	5.1774(2)	721.47(5)
12099	12.6849(5)	5.1774(2)	721.47(5)
15000	12.6824(1)	5.1786(8)	721.35(11)
15180	12.6820(5)	5.1730(2)	720.52(5)
15360	12.6812(5)	5.1727(2)	720.39(5)
15540	12.6807(6)	5.1726(2)	720.32(6)
15720	12.6814(6)	5.1726(2)	720.39(6)
15900	12.6798(5)	5.1718(2)	720.11(5)
16080	12.6787(5)	5.1722(2)	720.05(6)
16260	12.6822(5)	5.1727(2)	720.50(5)
16440	12.6801(5)	5.1725(2)	720.23(4)
16620	12.6812(5)	5.1726(2)	720.37(5)
16800	12.6821(5)	5.1723(2)	720.44(5)
16980	12.6803(6)	5.1718(2)	720.16(5)
17100	12.6814(6)	5.1720(2)	720.32(6)

Table 4.13 Results of the thermal equation of state fits, using the EoSFit software (courtesy of RJ Angel). Further details are given in the text.

	Volume	***a*-axis**	***c*-axis**
Pawley et al. (1996), T < 478K			
l_0(Å), V_0 (Å^3)	707.51(5)	12.6237(5)	5.1265(4)
$\alpha_{303,1bar}$(K^{-1})	4.6(2)*10^{-5}	1.14(7)*10^{-5}	2.5(1)*10^{-5}
a_0 (K^{-1})	8.63(4)*10^{-5}	1.7(1)*10^{-5}	5.2(3)*10^{-5}
a_1 (K$^{-1/2}$)	-1.7(5)*10^{-5}	-0.7(2)*10^{-4}	-2.7(6)*10^{-4}
Berman (1988), T < 478K			
l_0(Å), V_0 (Å^3)	707.50(5)	12.6237(3)	5.1264(3)
$\alpha_{303,1bar}$ = a_0 (K^{-1})	4.88(8)*10^{-5}	1.16(3)*10^{-5}	2.58(8)*10^{-5}
a_1 (K^{-1})	3.2(4)*10^{-8}	4.9(8)*10^{-9}	2.3(3)*10^{-9}
Berman (1988), T > 478K			
l_0 (Å), V_0 (Å^3)	705.5 (1.0)	12.618(9)	5.116(6)
$\alpha_{303,1bar}$ = a_0 (K^{-1})	3.1(6)*10^{-5}	0.6(3)*10^{-5}	1.9(5)*10^{-5}
a_1 (K^{-1})	6.4(1.4)*10^{-8}	2.1(9)*10^{-9}	2.1(1.0)*10^{-9}

Appendix

Table 4.14 Details pertaining to the data collection protocol and structure refinements of cancrinite at different temperatures

T (K)	303 (T_0)	478 (T_1)	748 (T_2)
a (Å)	12.6261 (4)	12.6554 (5)	12.6849 (5)
c (Å)	5.1257 (2)	5.1468 (1)	5.1774 (2)
V (Å^3)	707.66 (4)	712.74(4)	721.47 (5)
Maximum 2θ (°)	59.90	59.97	59.88
	0≤ h ≤11	0≤ h ≤12	0≤ h ≤11
	-17≤ k ≤15	-17≤ k ≤14	-17≤ k ≤14
	-7≤ l ≤7	-7≤ l ≤7	-7≤ l ≤7
Measured reflections	3408	3542	3470
Unique reflections	1366	1385	1393
Unique reflections with $F_0 > 4\sigma(F_0)$	1057	1003	949
R_{int}	0.0696	0.0718	0.0679
Number of l.s. parameters	90	84	84
R_1, $F_0 > 4\sigma(F_0)$	0.0525	0.0567	0.0596
R_1, all data	0.0743	0.0905	0.1016
wR_2	0.1330	0.1436	0.1587
Residuals (eÅ^{-3})	+0.64/-0.53	+1.09/-0.54	+0.85/-0.47

Note: $R_{int} = \Sigma|F^2_{obs} - (mean)|/\Sigma[F^2_{obs}]$; $R_1 = \Sigma||F_{obs}| - |F_{calc}||/\Sigma|F_{obs}|$; $wR_2 = \{\Sigma[w(F^2_{obs} - F^2_{calc})^2]/\Sigma[w(F^2_{obs})^2]\}^{0.5}$, $w = 1/[\sigma^2(F^2_{obs}) + (0.01\cdot P)^2]$, $P = [Max(F^2_{obs},0) + 2\cdot F^2_{calc}]/3$.

Table 4.15 Atomic fractional coordinates, site occupancy factors (*sof*) and isotropic/equivalent atomic displacement parameters (Å^2) of cancrinite at different temperatures.

Atom site	*T* (K)	Occupancy	*x*	*y*	*z*	U_{eq}/U_{iso}
Si	303	1.0	0.32814(9)	0.41065(9)	0.7019(8)	0.0079(2)
	478	1.0	0.3284(1)	0.4108(1)	0.6945(4)	0.0107(2)
	748	1.0	0.3286(1)	0.4119(1)	0.7304(4)	0.0163(3)
Al	303	1.0	0.0754(1)	0.4124(1)	0.7027(8)	0.0081(2)
	478	1.0	0.0748(1)	0.4121(1)	0.6952(4)	0.0106(2)
	748	1.0	0.0747(1)	0.4133(1)	0.7596(8)	0.0165(3)
O1	303	1.0	0.2038(3)	0.4052(3)	0.611(1)	0.0159(7)
	478	1.0	0.2040(2)	0.4064(3)	0.6089(7)	0.0199(7)
	748	1.0	0.2047(3)	0.4083(4)	0.6516(8)	0.032(1)
O2	303	1.0	0.1147(3)	0.5641(3)	0.679(1)	0.0205(7)
	478	1.0	0.1133(3)	0.5630(2)	0.6720(8)	0.0249(7)
	748	1.0	0.1157(4)	0.5641(3)	0.710(1)	0.038(1)
O3	303	1.0	0.0303(3)	0.3508(3)	0.013(1)	0.0147(7)
	478	1.0	0.0286(3)	0.3496(3)	0.0033(6)	0.0197(7)
	748	1.0	0.0247(4)	0.3483(4)	0.0331(8)	0.029(1)
O4	303	1.0	0.3142(3)	0.3585(3)	-0.005(1)	0.0144(6)
	478	1.0	0.3144(3)	0.3567(3)	-0.0143(6)	0.0192(7)
	748	1.0	0.3174(4)	0.3562(4)	0.0164(7)	0.0290(9)
Na1	303	1.0	2/3	1/3	0.088(1)	0.035(1)
	478	1.0	2/3	1/3	0.081(1)	0.048(1)
	748	1.0	2/3	1/3	0.111(2)	0.071(2)
Ow	303	1.0	0.315(2)	0.699(2)	0.137(4)	0.062(5)
	478	1.0	0.312(2)	0.697(2)	0.142 (4)	0.082(6)
	748	1.0	0.286(13)	0.696(13)	0.20(5)	0.082
Na2/Ca2	303	Na, 0.88(1) Ca, 0.12(1)	0.1232(2)	0.2499(2)	0.2451(9)	0.0265(7)
	478	"	0.1233(2)	0.2500(2)	0.2377(5)	0.0355(5)
	748	"	0.1240(2)	0.2516(3)	0.2693(7)	0.0554(8)
C1	303	0.37(1)	0	0	0.358(5)	0.044(5)
	478	0.351(9)	0	0	0.309(4)	0.042(3)
	748	0.36(1)	0	0	0.415(5)	0.035(4)
OC1	303	0.37(1)	0.1189(4)	0.061(1)	0.351(5)	0.059(4)

Appendix

	478	0.351(9)	0.1175(4)	0.058(1)	0.347(2)	0.044(2)
	748	0.36(1)	0.1175(5)	0.062(2)	0.394(4)	0.069(4)
C2	303	0.47(1)	0	0	0.113(6)	0.044(5)
	478	0.451(9)	0	0	0.099(4)	0.042(3)
	748	0.46(1)	0	0	0.142(5)	0.035(4)
OC2	303	0.47(1)	0.1191(4)	0.061(1)	0.125(4)	0.059(4)
	478	0.451(9)	0.1183(4)	0.0623(9)	0.128(2)	0.044(2)
	748	0.46(1)	0.1179(5)	0.061(1)	0.161(3)	0.069(4)

Table 4.16 Relevant bond distances (Å), diameters (Å), angles (°), ditrigonal rotation angle $\alpha_{S6R\perp[0001]}$ (°) of the S6R⊥[0001], and cage/channel-volumes (Å^3) of cancrinite at different temperatures.

	T (K)	303 (T_0)	478 (T_1)	748 (T_2)
Si-	O1	1.605(3)	1.607(3)	1.603(4)
	O2	1.608(3)	1.608(3)	1.610(4)
	O3	1.626(3)	1.624(3)	1.624(4)
	O4	1.614(3)	1.620(3)	1.616(4)
	<Si-O>	1.613(3)	1.615(3)	1.613(4)
Al-	O1	1.734(3)	1.730(3)	1.732(4)
	O2	1.726(3)	1.722(3)	1.717(4)
	O3	1.735(3)	1.737(3)	1.730(4)
	O4	1.756(3)	1.747(3)	1.746(4)
	<Al-O>	1.738(3)	1.734(3)	1.731(4)
	Si-O1-Al	147.2(2)	148.0(2)	151.2(3)
	Si-O2-Al	151.2(2)	152.5(2)	151.0(3)
	Si-O3-Al	133.4(2)	134.0(2)	136.1(3)
	Si-O4-Al	133.3(2)	134.1(2)	136.6(3)
Na1-	O1(x3)	2.862(3)	2.854(2)	2.846(3)
	O2(x3)	2.437(4)	2.455(3)	2.446(4)
	Ow'	2.38(2)	2.33(2)	2.3(2)
	Ow''	2.87(2)	2.94(2)	3.2(3)
Na2/Ca2	O1	2.532(6)	2.566(4)	2.623(6)
	O3′	2.432(6)	2.446(5)	2.476(7)
	O3′′	2.893(5)	2.880(4)	2.863(6)
	O4′	2.456(5)	2.466(4)	2.498(5)
	O4′′	2.914(6)	2.895(5)	2.885(7)
	OC1′	2.418(17)	2.421(8)	2.44(2)
	OC1′′	2.456(14)	2.439(11)	2.45(2)
	OC1′′′	2.48(2)	2.514(12)	2.48(2)
	OC2′	2.416(18)	2.409(12)	2.449(18)
	OC2′′	2.440(14)	2.474(9)	2.504(16)
	OC2′′′	2.451(9)	2.467(7)	2.471(11)
	<Na2/Ca2-O_{fr}>	2.645(6)	2.651(4)	2.669(6)
	<Na2/Ca2-O_{CO}^3>	2.441(15)	2.451(10)	2.471(16)
	C1-OC1	1.301(5)	1.302(5)	1.296(6)
	C2-OC2	1.304(5)	1.305(5)	1.299(6)
	O2-$O2_{S6R\perp[0001]}$	4.143(6)	4.176(6)	4.143(8)
	O2-$O2_{cw}$	8.487(6)	8.473(5)	8.545(7)
	O2-O2-O2	91.1(2)	92.0(1)	90.9(2)
	*O1-$O1_{12R}$	8.862(5)	8.901(5)	8.971(7)
	O3-$O4_{12R}$	8.487(4)	8.485(4)	8.536(5)
	O3-$O4_{S4R}$	4.145(6)	4.166(6)	4.155(8)
	O3-O4-O3	144.6(3)	146.39(16)	149.8(2)
	$\alpha_{S6R\perp[0001]}$	8.48(9)	7.99(8)	8.19(12)
	V_{cg}	202.4(2)	203.8(2)	204.9(3)
	V_{ch}	302.9(3)	305.2(3)	311.6(5)

* Calculated as the projection on the (0001) plane

Appendix

Table 4.17 Site anisotropic displacement parameters (Å^2) of cancrinite at different temperatures

Atom site	U_{11}	U_{22}	U_{33}	U_{12}	U_{13}	U_{23}
			T_0 (303 K)			
Si	0.0077(4)	0.0096(4)	0.0067(4)	0.0046(4)	0.0009(5)	0.0016(5)
Al	0.0078(5)	0.0083(5)	0.0077(4)	0.0036(4)	0.0007(6)	0.0013(6)
O1	0.012(2)	0.027(2)	0.013(1)	0.013(1)	0.001(1)	0.003(1)
O2	0.023(2)	0.011(1)	0.030(2)	0.010(1)	0.002(2)	0.004(2)
O3	0.014(2)	0.022(2)	0.008(1)	0.009(1)	0.002(1)	0.003(1)
O4	0.015(2)	0.021(2)	0.009(1)	0.010(1)	0.001(1)	0.004(1)
Na1	0.027(1)	0.027(1)	0.052(2)	0.0134(6)	0	0
Na2/Ca2	0.019(1)	0.031(1)	0.034(1)	0.0153(8)	-0.0007(8)	-0.0011(8)
C1-C2	0.014(3)	0.014(3)	0.10(2)	0.007(2)	0	0
OC1-OC2	0.026(3)	0.030(4)	0.12(1)	0.014(3)	0.005(7)	0.000(7)
			T_1 (448 K)			
Si	0.0107(4)	0.0121(4)	0.0099(4)	0.0063(3)	0.0017(5)	0.0014(5)
Al	0.0100(4)	0.0115(4)	0.0100(4)	0.0052(3)	0.0019(6)	0.0018(6)
O1	0.013(1)	0.030(1)	0.018(1)	0.013(1)	0.000(1)	0.003(1)
O2	0.027(1)	0.016(1)	0.034(2)	0.013(1)	0.005(2)	0.003(2)
O3	0.018(1)	0.030(2)	0.011(1)	0.012(1)	0.004(1)	0.004(1)
O4	0.023(1)	0.027(1)	0.013(1)	0.016(1)	0.001(1)	0.007(1)
Na1	0.036(1)	0.036(1)	0.073(3)	0.0179(7)	0	0
Na2/Ca2	0.0248(7)	0.0378(9)	0.048(1)	0.0184(6)	-0.0017(8)	-0.0016(9)
			T_2 (748 K)			
Si	0.0159(5)	0.0181(6)	0.0157(5)	0.0091(4)	0.0009(9)	0.0034(9)
Al	0.0159(6)	0.0181(6)	0.0150(6)	0.0083(5)	0.0022(9)	0.0030(9)
O1	0.020(2)	0.048(3)	0.034(2)	0.022(2)	0.001(2)	0.005(2)
O2	0.045(2)	0.025(2)	0.052(3)	0.023(2)	0.007(3)	0.006(3)
O3	0.027(2)	0.039(2)	0.020(2)	0.016(2)	0.009(2)	0.008(2)
O4	0.037(2)	0.038(2)	0.019(2)	0.024(2)	0.000(2)	0.008(2)
Na1	0.052(2)	0.052(2)	0.111(6)	0.026(1)	0	0
Na2/Ca2	0.041(1)	0.060(2)	0.072(2)	0.030(1)	-0.006(2)	-0.007(2)

Table 5.1 Chemical analysis of vishnevite (in wt.%) and atoms per formula unit, based on (Si + Al = 12), averaged from 5 point analyses

SiO_2	37.82
Al_2O_3	30.77
CaO	0.42
Na_2O	16.64
K_2O	7.94
SO_3	4.80
SrO	0.06
Total	98.45
Number of atoms per formula unit on the basis (Si+Al=12)	
Si	6.13
Al	5.87
Ca	0.07
Na	5.22
K	1.64
S	0.58
Sr	0.01

Appendix

Table 5.2 Unit-cell parameters of vishnevite measured at different pressures.

P (GPa)	*a* (Å)	*c* (Å)	*V* (Å^3)
0.0001*	12.7684(6)	5.2089(3)	735.44(9)
0.20(2)	12.750(2)	5.1935(5)	731.2(3)
0.52(2)	12.727(2)	5.1777(5)	726.3(3)
0.86(2)	12.700(1)	5.1622(5)	721.1(3)
1.20(3)	12.682(1)	5.1510(4)	717.4(3)
1.50(5)	12.660(1)	5.1374(5)	713.0(3)
1.78(5)	12.645(2)	5.1276(5)	710.0(3)
2.17(6)	12.619(2)	5.1137(5)	705.3(3)
2.47(2)	12.601(2)	5.1014(5)	701.5(3)
2.84(10)	12.562(1)	5.0810(5)	694.3(2)
3.24(9)	12.536(1)	5.0646(4)	689.3(2)
3.43(4)	12.517(1)	5.0536(4)	685.6(3)
3.83(9)	12.466(1)	5.0260(3)	676.4(3)
4.23(7)	12.427(1)	5.0034(4)	669.2(3)
4.55(5)	12.398(1)	4.9851(3)	663.6(4)
4.74(6)	12.385(1)	4.9765(4)	661.1(3)
5.03(6)	12.359(1)	4.9619(3)	656.3(3)
5.30(5)	12.3331(8)	4.9472(3)	651.7(3)
5.75(7)	12.2964(9)	4.9272(3)	645.2(3)
6.11(4)	12.2628(9)	4.9104(3)	639.5(3)
6.60(10)	12.2183(8)	4.8852(3)	631.6(3)
7.00(5)	12.190(1)	4.8704(4)	626.7(3)
7.40(4)	12.154(1)	4.8552(4)	621.1(4)
0.0001**	12.667(2)	5.1415(5)	721.2(2)

* Unit-cell parameters from the crystal collected in air

** Unit-cell parameters from the crystal collected in DAC at room-P after the H*P*-experiment

Table 5.3 Details of the data collections strategy and structure refinements of vishnevite at different pressures and temperatures

P (GPa)	0.0001 ($P_{0\text{-AIR}}$)	0.52(2) (P_2)	1.20(3) (P_4)	1.78 (5) (P_6)	2.47(2) (P_8)	3.24(9) (P_{10})	3.43(4) (P_{11})	4.23 (7) (P_{13})	4.74(6) (P_{15})	5.30(5) (P_{17})	6.11(4) (P_{19})	7.40(4) (P_{22})	0.0001 ($P_{0\text{-pos}}$)
a (Å)	12.7684(6)	12.727(2)	12.682(1)	12.645(2)	12.601(2)	12.536(1)	12.517(1)	12.427(1)	12.385(1)	12.3331(8)	12.2628(9)	12.154(1)	12.667(2)
c (Å)	5.2089(3)	5.1777(5)	5.1510(5)	5.1276(5)	5.1014(5)	5.0646(4)	5.0536(4)	5.0034(4)	4.9765(1)	4.9472(3)	4.9104(3)	4.8552(4)	5.1514(5)
V (Å^3)	735.44(8)	726.3(3)	717.4(2)	710.0(2)	701.5(2)	689.3(2)	685.6(1)	669.2(1)	661.1(1)	651.7(3)	639.5(1)	621.1(1)	715.8(2)
Maximum 2θ (°)	37.92	37.48	37.66	38.08	37.98	38.10	37.14	37.84	37.66	37.86	38.14	37.42	37.80
	$1 \le h \le 19$ $-16 \le k \le 0$ $-7 \le l \le 6$	$2 \le h \le 15$ $-10 \le k \le 0$ $-6 \le l \le 6$	$2 \le h \le 15$ $-10 \le k \le 0$ $-6 \le l \le 6$	$2 \le h \le 14$ $-9 \le k \le 0$ $-6 \le l \le 6$	$2 \le h \le 14$ $-10 \le k \le 0$ $-6 \le l \le 6$	$2 \le h \le 15$ $-9 \le k \le 0$ $-6 \le l \le 6$	$2 \le h \le 15$ $-9 \le k \le 0$ $-6 \le l \le 6$	$2 \le h \le 15$ $-9 \le k \le 0$ $-6 \le l \le 6$	$2 \le h \le 14$ $-9 \le k \le 0$ $-6 \le l \le 6$	$2 \le h \le 15$ $-9 \le k \le 0$ $-6 \le l \le 6$	$2 \le h \le 15$ $-9 \le k \le 0$ $-6 \le l \le 6$	$2 \le h \le 14$ $-9 \le k \le 0$ $-6 \le l \le 5$	$0 \le h \le 19$ $-15 \le k \le 0$ $-8 \le l \le 7$
Measured reflections	3138	1082	1051	1036	1018	1037	1064	1114	998	996	969	888	1111
Unique reflections	1294	743	726	712	685	699	705	697	659	661	623	586	720
Unique reflections with $F_0 > 3\sigma(F_0)$	758	479	474	444	441	484	524	498	454	448	384	270	514
R_{int}	0.0489	0.0443	0.0461	0.0479	0.0421	0.0413	0.0421	0.0450	0.0314	0.0325	0.0333	0.0486	0.0344
Number of l.s. parameters	85	41	41	41	41	41	40	40	40	40	40	40	40
R_1, $F_0 > 4\sigma(F_0)$	0.0548	0.0922	0.0844	0.0840	0.0869	0.0856	0.0865	0.0839	0.0847	0.0925	0.1008	0.1256	0.0797
R_1, all data	0.1048	0.1293	0.1198	0.1241	0.1193	0.1173	0.1092	0.1157	0.1120	0.1179	0.1376	0.2053	0.1069
wR^2	0.0538	0.0896	0.0836	0.0866	0.0877	0.0871	0.0988	0.0938	0.0920	0.1001	0.0976	0.1224	0.0889
Residuals (e^-/ Å^3)	+0.74/ -0.84	+0.88/ -0.86	+0.98/ -0.81	+0.75/ -0.80	+0.78/ -1.31	+0.85/ -1.10	+0.76/ -1.13	+0.90/ -0.86	+1.53/ -0.83	+0.70/ -1.28	+0.74/ -0.85	+1.27/ -1.21	+0.84/ -1.13
λ = 0.414 Å; ω-scan; step scan = 1°; exposure time = 1 s; space group $P6_3$; Z = 1													

T (K)	293(2)	110(2)
a (Å)	12.7613(7)	12.7223(6)
c (Å)	5.2231(2)	5.1918(3)
V (Å^3)	736.63(9)	727.75(8)
Maximum 2θ (°)	62.53	62.63
	$-5 \le h \le 18$ $-10 \le k \le 12$ $-6 \le l \le 7$	$-18 \le h \le 11$ $-10 \le k \le 15$ $-7 \le l \le 7$
Measured reflections	2575	2634
Unique reflections	1404	1431
Unique reflections	1221	1280

Appendix

with $F_0 >$ $4\sigma(F_0)$		
R_{int}	0.0369	0.0368
Number of l.s. parameters	86	82
R_1, $F_0 > 4\sigma(F_0)$	0.0536	0.0518
R_1, all data	0.0638	0.0614
wR^2	0.1234	0.1199
Residuals (e^-/ Å^3)	+0.82/ -0.63	+1.05/ -0.77

λ = 0.71073 Å; ω-scan; step scan = 1°; exposure time = 90 s; space group $P6_3$; Z = 1

Table 5.4 Atomic fractional coordinates, site occupancy factors (*sof*) and isotropic/equivalent atomic displacement parameters (Å^2) of vishnevite at different pressures and temperatures

Site	*P* (GPa) $^{§}T$ (K)	*sof*	*x*	*y*	*z*	U_{iso}/ U_{eq}
Si	0.0001$^{\#}$	1.0	0.0827(2)	0.4143(3)	0.740(2)	0.020(1)
	0.52(2)	1.0	0.0815(5)	0.4115(5)	0.735(2)	0.0252(6)
	1.20(3)	1.0	0.0819(5)	0.4115(5)	0.732(2)	0.0240(5)
	1.78(5)	1.0	0.0792(5)	0.4159(6)	0.730(2)	0.0252(6)
	2.47(2)	1.0	0.0801(6)	0.4154(6)	0.725(2)	0.0270(6)
	3.24(9)	1.0	0.0788(5)	0.4158(6)	0.733(2)	0.0219(5)
	3.43(4)	1.0	0.0780(5)	0.4154(5)	0.717(2)	0.0218(6)
	4.23(7)	1.0	0.0787(5)	0.4165(5)	0.723(2)	0.0212(6)
	4.74(6)	1.0	0.0789(5)	0.4158(5)	0.730(1)	0.0239(6)
	5.30(5)	1.0	0.0796(6)	0.4169(6)	0.710(2)	0.0289(7)
	6.11(4)	1.0	0.0838(6)	0.4102(6)	0.715(2)	0.0342(7)
	7.40(4)	1.0	0.0808(6)	0.4175(6)	0.764(4)	0.043(1)
	0.0001$^{\#\#}$	1.0	0.0829(5)	0.4113(5)	0.742(2)	0.0176(6)
	§293 K	1.0	0.0841(1)	0.4144(2)	0.7415(4)	0.0093(3)
	§110 K	1.0	0.0840(2)	0.4143(2)	0.7408(4)	0.0058(3)
Al	0.0001$^{\#}$	1.0	0.3377(3)	0.4160(3)	0.738(2)	0.020(1)
	0.52(2)	1.0	0.3381(6)	0.4163(6)	0.735(2)	0.0252(6)
	1.20(3)	1.0	0.3385(6)	0.4165(6)	0.732(2)	0.0240(5)
	1.78(5)	1.0	0.3312(7)	0.4125(7)	0.729(2)	0.0252(6)
	2.47(2)	1.0	0.3324(8)	0.4127(7)	0.724(2)	0.0270(6)
	3.24(9)	1.0	0.3302(7)	0.4121(6)	0.733(2)	0.0219(5)
	3.43(4)	1.0	0.3287(6)	0.4113(5)	0.714(2)	0.0218(6)
	4.23(7)	1.0	0.3280(6)	0.4095(6)	0.721(2)	0.0212(6)
	4.74(6)	1.0	0.3281(6)	0.4098(6)	0.728(1)	0.0239(6)
	5.30(5)	1.0	0.3276(7)	0.4099(7)	0.706(2)	0.0289(7)
	6.11(4)	1.0	0.3396(6)	0.4179(6)	0.714(2)	0.0342(7)
	7.40(4)	1.0	0.3326(6)	0.4143(7)	0.763(4)	0.043(1)
	0.0001$^{\#\#}$	1.0	0.3391(5)	0.4154(5)	0.739(2)	0.0176(6)
	§293 K	1.0	0.3387(2)	0.4149(2)	0.7415(4)	0.0096(4)
	§110 K	1.0	0.3387(2)	0.4153(2)	0.7408(4)	0.0066(4)
O1	0.0001$^{\#}$	1.0	0.1996(8)	0.4044(4)	0.668(1)	0.031(3)
	0.52(2)	1.0	0.2012(8)	0.4073(8)	0.658(2)	0.031(1)
	1.20(3)	1.0	0.2009(8)	0.4058(8)	0.651(2)	0.031(1)
	1.78(5)	1.0	0.1960(9)	0.4051(9)	0.645(2)	0.033(1)
	2.47(2)	1.0	0.1965(9)	0.4039(9)	0.637(2)	0.036(1)
	3.24(9)	1.0	0.1950(9)	0.4037(8)	0.644(2)	0.030(1)
	3.43(4)	1.0	0.1940(8)	0.4029(9)	0.620(2)	0.035(1)
	4.23(7)	1.0	0.1922(8)	0.3993(8)	0.621(2)	0.034(1)
	4.74(6)	1.0	0.1901(9)	0.3964(9)	0.629(2)	0.039(1)
	5.30(5)	1.0	0.1892(9)	0.3954(9)	0.612(2)	0.043(2)
	6.11(4)	1.0	0.1932(9)	0.389(1)	0.610(2)	0.050(2)
	7.40(4)	1.0	0.188(1)	0.389(1)	0.651(5)	0.058(3)
	0.0001$^{\#\#}$	1.0	0.2012(8)	0.4052(8)	0.657(2)	0.025(1)
	§293 K	1.0	0.2006(5)	0.4040(3)	0.6710(6)	0.0191(8)
	§110 K	1.0	0.2001(6)	0.4017(3)	0.6667(6)	0.0133(7)
O2	0.0001$^{\#}$	1.0	0.1215(3)	0.5549(9)	0.720(2)	0.036(3)

	0.52(2)	1.0	0.1183(6)	0.5518(7)	0.710(2)	0.031(1)
	1.20(3)	1.0	0.1185(6)	0.5515(7)	0.703(2)	0.031(1)
	1.78(5)	1.0	0.1209(7)	0.5581(8)	0.698(2)	0.033(1)
	2.47(2)	1.0	0.1218(6)	0.5577(9)	0.694(2)	0.036(1)
	3.24(9)	1.0	0.1235(7)	0.5596(8)	0.694(2)	0.030(1)
	3.43(4)	1.0	0.1217(7)	0.5594(8)	0.679(2)	0.035(1)
	4.23(7)	1.0	0.1229(8)	0.5605(8)	0.682(3)	0.034(1)
	4.74(6)	1.0	0.1256(8)	0.5620(8)	0.692(2)	0.039(1)
	5.30(5)	1.0	0.1252(8)	0.5619(9)	0.660(2)	0.043(2)
	6.11(4)	1.0	0.1292(9)	0.5549(9)	0.666(2)	0.050(2)
	7.40(4)	1.0	0.143(1)	0.5691(9)	0.708(5)	0.058(3)
	0.0001[##]	1.0	0.1175(7)	0.5520(7)	0.713(2)	0.025(1)
	[§]293 K	1.0	0.1212(3)	0.5535(5)	0.7177(8)	0.0240(8)
	[§]110 K	1.0	0.1221(3)	0.4143(2)	0.7408(4)	0.0170(8)
O3	0.0001[#]	1.0	0.0353(6)	0.3598(7)	0.020(2)	0.031(4)
	0.52(2)	1.0	0.039(1)	0.363(2)	0.023(2)	0.031(1)
	1.20(3)	1.0	0.040(1)	0.364(2)	0.023(2)	0.031(1)
	1.78(5)	1.0	0.041(1)	0.364(2)	0.022(2)	0.033(1)
	2.47(2)	1.0	0.042(1)	0.364(2)	0.017(2)	0.036(1)
	3.24(9)	1.0	0.045(1)	0.366(1)	0.032(2)	0.030(1)
	3.43(4)	1.0	0.044(1)	0.368(2)	0.011(2)	0.035(1)
	4.23(7)	1.0	0.0491(9)	0.372(1)	0.027(2)	0.034(1)
	4.74(6)	1.0	0.052(1)	0.372(2)	0.035(2)	0.039(1)
	5.30(5)	1.0	0.054(1)	0.373(2)	0.018(2)	0.043(2)
	6.11(4)	1.0	0.052(1)	0.368(2)	0.030(2)	0.050(2)
	7.40(4)	1.0	0.060(1)	0.382(2)	0.084(4)	0.058(3)
	0.0001[##]	1.0	0.0443(9)	0.364(1)	0.033(2)	0.025(1)
	[§]293 K	1.0	0.0362(4)	0.3607(5)	0.0237(6)	0.017(1)
	[§]110 K	1.0	0.0381(4)	0.3624(5)	0.0267(7)	0.012(1)
O4	0.0001[#]	1.0	0.3318(6)	0.3541(6)	0.042(2)	0.024(3)
	0.52(2)	1.0	0.328(1)	0.357(2)	0.046(2)	0.031(1)
	1.20(3)	1.0	0.327(1)	0.358(2)	0.046(2)	0.031(1)
	1.78(5)	1.0	0.325(1)	0.358(2)	0.044(2)	0.033(1)
	2.47(2)	1.0	0.326(1)	0.359(2)	0.039(2)	0.036(1)
	3.24(9)	1.0	0.321(1)	0.357(1)	0.053(2)	0.030(1)
	3.43(4)	1.0	0.322(1)	0.360(2)	0.037(2)	0.035(1)
	4.23(7)	1.0	0.317(1)	0.357(1)	0.048(2)	0.034(1)
	4.74(6)	1.0	0.320(1)	0.361(2)	0.056(2)	0.039(1)
	5.30(5)	1.0	0.319(1)	0.361(2)	0.041(2)	0.043(2)
	6.11(4)	1.0	0.324(1)	0.367(2)	0.051(2)	0.050(2)
	7.40(4)	1.0	0.319(2)	0.367(2)	0.105(4)	0.058(3)
	0.0001[##]	1.0	0.328(1)	0.355(1)	0.052(2)	0.025(1)
	[§]293 K	1.0	0.3304(6)	0.3517(5)	0.0416(6)	0.018(1)
	[§]110 K	1.0	0.3303(6)	0.3526(5)	0.0465(7)	0.015(1)
Na1	0.0001[#]	0.46(3)	1/3	2/3	0.573(4)	0.021(2)
	0.52(2)	0.41(3)	1/3	2/3	0.567(5)	0.013(3)
	1.20(3)	0.46(4)	1/3	2/3	0.567(6)	0.016(3)
	1.78(5)	0.43(5)	1/3	2/3	0.560(6)	0.018(3)
	2.47(2)	0.43(11)	1/3	2/3	0.56(1)	0.024(4)
	3.24(9)	0.33(5)	1/3	2/3	0.542(8)	0.016(3)
	3.43(4)	0.44(6)	1/3	2/3	0.539(7)	0.011(3)
	4.23(7)	0.47(3)	1/3	2/3	0.543(5)	0.009(3)
	4.74(6)	0.40(2)	1/3	2/3	0.529(5)	0.016(3)
	5.30(5)	0.37(2)	1/3	2/3	0.496(6)	0.028(4)
	6.11(4)	0.42(3)	1/3	2/3	0.518(7)	0.043(6)

	7.40(4)	0.55(6)	1/3	2/3	0.59(1)	0.10(1)
	0.0001[##]	0.57(9)	1/3	2/3	0.590(6)	0.015(3)
	[§]293 K	0.84(2)	1/3	2/3	0.611(1)	0.033(2)
	[§]110 K	"	1/3	2/3	0.6051(9)	0.0185(9)
Na2	0.0001[#]	0.35(3)	1/3	2/3	0.661(5)	0.021(2)
	0.52(2)	0.40(3)	1/3	2/3	0.656(5)	0.013(3)
	1.20(3)	0.35(4)	1/3	2/3	0.654(6)	0.016(3)
	1.78(5)	0.38(5)	1/3	2/3	0.647(6)	0.018(3)
	2.47(2)	0.38(11)	1/3	2/3	0.64(1)	0.024(4)
	3.24(9)	0.48(5)	1/3	2/3	0.626(6)	0.016(3)
	3.43(4)	0.38(6)	1/3	2/3	0.616(7)	0.011(3)
	4.23(7)	0.35(3)	1/3	2/3	0.641(5)	0.009(3)
	4.74(6)	0.41(2)	1/3	2/3	0.639(4)	0.016(3)
	5.30(5)	0.44(2)	1/3	2/3	0.626(4)	0.028(4)
	6.11(4)	0.39(3)	1/3	2/3	0.650(6)	0.043(6)
	7.40(4)	0.26(6)	1/3	2/3	0.74(3)	0.10(1)
	0.0001[##]	0.24(9)	1/3	2/3	0.66(1)	0.015(3)
	[§]293 K	-	-	-	-	-
	[§]110 K	-	-	-	-	-
Ow	0.0001[#]	0.31(1)	0.315(4)	0.696(4)	0.180(3)	0.064(9)
	0.52(2)	0.31	0.323(5)	0.699(5)	0.170(3)	0.038(9)
	1.20(3)	0.31	0.326(3)	0.702(3)	0.161(3)	0.025(7)
	1.78(5)	0.31	0.299(4)	0.676(4)	0.152(4)	0.030(8)
	2.47(2)	0.31	0.299(4)	0.677(5)	0.161(5)	0.04(1)
	3.24(9)	0.31	0.294(3)	0.670(4)	0.149(4)	0.03(1)
	3.43(4)	0.31	0.302(3)	0.676(4)	0.125(3)	0.012(7)
	4.23(7)	0.31	0.332(3)	0.709(3)	0.131(4)	0.017(7)
	4.74(6)	0.31	0.297(3)	0.673(4)	0.155(4)	0.03(1)
	5.30(5)	0.31	0.294(9)	0.68(1)	0.19(1)	0.11(2)
	6.11(4)	0.31	0.227(3)	0.716(3)	0.270(5)	0.03(1)
	7.40(4)	0.31	0.263(4)	0.745(5)	0.327(8)	0.04(1)
	0.0001[##]	0.31	0.331(3)	0.704(2)	0.177(4)	0.014(7)
	[§]293 K	0.33(2)	0.319(3)	0.699(3)	0.180(3)	0.055(7)
	[§]110 K	"	0.312(2)	0.695(2)	0.179(2)	0.030(3)
M1	0.0001[#]	0.563(4)	0.1178(8)	0.2293(4)	0.272(2)	0.029(1)
	0.52(2)	0.563	0.122(2)	0.2451(9)	0.280(3)	0.047(2)
	1.20(3)	0.563	0.121(3)	0.2433(9)	0.279(2)	0.044(2)
	1.78(5)	0.563	0.126(2)	0.2433(9)	0.278(3)	0.043(2)
	2.47(2)	0.563	0.127(3)	0.2450(9)	0.264(3)	0.045(2)
	3.24(9)	0.563	0.126(3)	0.2453(9)	0.276(3)	0.043(2)
	3.43(4)	0.563	0.126(3)	0.247(1)	0.252(3)	0.047(2)
	4.23(7)	0.563	0.125(4)	0.244(1)	0.259(4)	0.051(2)
	4.74(6)	0.563	0.122(3)	0.241(1)	0.256(4)	0.059(2)
	5.30(5)	0.563	0.118(4)	0.239(2)	0.244(4)	0.066(3)
	6.11(4)	0.563	0.111(4)	0.233(2)	0.245(4)	0.071(3)
	7.40(4)	0.563	0.117(3)	0.230(2)	0.267(7)	0.098(5)
	0.0001[##]	0.563	0.119(2)	0.2476(9)	0.279(3)	0.044(2)
	[§]293 K	0.340(6)	0.1165(6)	0.2292(4)	0.2791(3)	0.029(1)
	[§]110 K	"	0.1150(5)	0.2282(3)	0.2782(6)	0.0192(6)
M2	0.0001[#]	0.519(5)	0.1528(8)	0.3029(4)	0.263(2)	0.029(1)
	0.52(2)	0.519	0.150(3)	0.298(1)	0.256(3)	0.047(2)
	1.20(3)	0.519	0.149(3)	0.2970(9)	0.251(3)	0.044(2)
	1.78(5)	0.519	0.149(3)	0.296(1)	0.243(3)	0.043(2)
	2.47(2)	0.519	0.149(3)	0.294(1)	0.243(4)	0.045(2)

Appendix

	3.24(9)	0.519	0.150(3)	0.293(1)	0.245(3)	0.043(2)
	3.43(4)	0.519	0.143(3)	0.287(1)	0.235(4)	0.047(2)
	4.23(7)	0.519	0.140(4)	0.277(1)	0.241(4)	0.051(2)
	4.74(6)	0.519	0.135(4)	0.274(1)	0.262(5)	0.059(2)
	5.30(5)	0.519	0.133(4)	0.274(2)	0.235(5)	0.066(3)
	6.11(4)	0.519	0.133(4)	0.276(2)	0.245(4)	0.071(3)
	7.40(4)	0.519	0.155(3)	0.278(2)	0.311(8)	0.098(5)
	0.0001[##]	0.519	0.150(2)	0.294(1)	0.263(4)	0.044(2)
	[§]293 K	0.58(1)	0.1497(6)	0.2999(4)	0.2791(7)	0.29(1)
	[§]110 K	"	0.1489(6)	0.2987(3)	0.2687(7)	0.0184(7)
S1	0.0001[#]	0.251(6)	0	0	0.347(3)	0.071(3)
	0.52(2)	0.251	0	0	0.372(4)	0.071
	1.20(3)	0.251	0	0	0.371(4)	0.071
	1.78(5)	0.251	0	0	0.386(4)	0.071
	2.47(2)	0.251	0	0	0.417(4)	0.071
	3.24(9)	0.251	0	0	0.385(5)	0.071
	[§]293 K	0.172(6)	0	0	0.331(3)	0.037(3)
	[§]110 K	"	0	0	0.341(3)	0.037(2)
OB1	0.0001[#]	0.251(6)	0.081(2)	0.116(2)	0.462(5)	0.071(3)
	0.52(2)	0.251	0.081	0.116	0.493(4)	0.071
	1.20(3)	0.251	0.081	0.116	0.494(4)	0.071
	1.78(5)	0.251	0.081	0.116	0.511(5)	0.071
	2.47(2)	0.251	0.081	0.116	0.546(5)	0.071
	3.24(9)	0.251	0.081	0.116	0.517(5)	0.071
	[§]293 K	0.172(6)	0.059(5)	0.106(2)	0.424(6)	0.066(8)
	[§]110 K	"	0.067(3)	0.111(2)	0.419(5)	0.036(6)
S2	0.0001[#]	0.251(6)	0	0	0.208(3)	0.071(3)
	0.52(2)	0.251	0	0	0.195(4)	0.071
	1.20(3)	0.251	0	0	0.207(4)	0.071
	1.78(5)	0.251	0	0	0.209(4)	0.071
	2.47(2)	0.251	0	0	0.194(5)	0.071
	3.24(9)	0.251	0	0	0.217(5)	0.071
	[§]293 K	0.172(6)	0	0	0.257(3)	0.037(3)
	[§]110 K	"	0	0	0.267(3)	0.037(2)
OB2	0.0001[#]	0.251(6)	0.028(2)	0.115(2)	0.152(5)	0.071(3)
	0.52(2)	0.251	0.028	0.115	0.142(5)	0.071
	1.20(3)	0.251	0.028	0.115	0.149(5)	0.071
	1.78(5)	0.251	0.028	0.115	0.147(5)	0.071
	2.47(2)	0.251	0.028	0.115	0.125(5)	0.071
	3.24(9)	0.251	0.028	0.115	0.144(5)	0.071
	[§]293 K	0.172(6)	0.077(3)	0.099(3)	0.158(6)	0.066(8)
	[§]110 K	"	0.074(3)	0.097(2)	0.159(4)	0.036(6)
S	3.43(4)	0.502	0	0	0.206(3)	0.1
	4.23(7)	0.502	0	0	0.216(3)	0.1
	4.74(6)	0.502	0	0	0.216(3)	0.1
	5.30(5)	0.502	0	0	0.289(3)	0.1
	6.11(4)	0.502	0	0	0.282(3)	0.1
	7.40(4)	0.502	0	0	0.192(6)	0.1
	0.0001[##]	0.502	0	0	0.194(4)	0.1
OA	3.43(4)	0.502	0	0	0.482(3)	0.1
	4.23(7)	0.502	0	0	0.495(3)	0.1
	4.74(6)	0.502	0	0	0.497(3)	0.1

	5.30(5)	0.502	0	0	0.006(3)	0.1
	6.11(4)	0.502	0	0	0.567(3)	0.1
	7.40(4)	0.502	0	0	0.480(6)	0.1
	0.0001[##]	0.502	0	0	0.463(4)	0.1
OB	3.43(4)	0.502	0.12	0.06	0.102(3)	0.1
	4.23(7)	0.502	0.12	0.06	0.108(3)	0.1
	4.74(6)	0.502	0.12	0.06	0.109(3)	0.1
	5.30(5)	0.502	0.12	0.06	0.173(3)	0.1
	6.11(4)	0.502	0.12	0.06	0.165(3)	0.1
	7.40(4)	0.502	0.12	0.06	0.068(6)	0.1
	0.0001[##]	0.502	0.12	0.06	0.116(4)	0.1

[#] From the structure refinement based on the dataset collected with the crystal in air
[##] From the structure refinement based on the dataset collected with the crystal in DAC after the H*P*-experiment
[§] From the structure refinements based on the L*T*-experiment datasets

Appendix

Table 5.5 Site anisotropic displacement parameters (Å^2) of vishnevite from the room-*P*, room-*T* and 110 K datsets

			$P_{0\text{-AIR}}$			
Atom site	U_{11}	U_{22}	U_{33}	U_{12}	U_{13}	U_{23}
Si	0.017(2)	0.020(2)	0.022(2)	0.009(1)	0.004(2)	0.003(2)
Al	0.019(2)	0.018(2)	0.022(2)	0.009(1)	0.003(2)	0.003(2)
O1	0.026(4)	0.038(2)	0.032(3)	0.018(4)	0.003(4)	-0.001(2)
O2	0.036(2)	0.021(4)	0.048(3)	0.012(3)	0.006(3)	0.000(5)
O3	0.026(4)	0.050(5)	0.018(5)	0.020(3)	-0.003(3)	0.007(3)
O4	0.025(4)	0.021(4)	0.021(4)	0.007(3)	-0.006(3)	0.001(3)
			293 K			
Si	0.0071(8)	0.0081(8)	0.0116(8)	0.0031(6)	-0.001(1)	0.001(1)
Al	0.0088(8)	0.0133(9)	0.0079(8)	0.0066(8)	-0.001(2)	0.001(1)
O1	0.014(3)	0.028(2)	0.021(2)	0.015(3)	0.000(2)	-0.002(1)
O2	0.026(2)	0.012(2)	0.034(2)	0.009(2)	0.007(2)	0.005(3)
O3	0.013(2)	0.023(3)	0.013(3)	0.008(2)	-0.002(2)	0.005(2)
O4	0.023(2)	0.023(3)	0.013(3)	0.014(2)	-0.004(3)	0.000(2)
Na	0.019(2)	0.019(2)	0.062(4)	0.0094(9)	0	0
			110 K			
Si	0.0051(8)	0.0054(8)	0.0065(7)	0.0023(6)	0.002(1)	0.000(1)
Al	0.0065(8)	0.0084(9)	0.0053(8)	0.0041(8)	0.003(2)	0.001(1)
O1	0.009(3)	0.021(2)	0.012(1)	0.009(3)	0.000(2)	-0.001(1)
O2	0.016(2)	0.014(2)	0.026(2)	0.011(2)	0.009(2)	0.000(3)
O3	0.010(2)	0.019(3)	0.006(2)	0.008(2)	0.002(1)	0.006(2)
O4	0.024(2)	0.016(3)	0.011(3)	0.015(2)	0.000(3)	0.000(2)
Na	0.010(1)	0.010(1)	0.036(2)	0.0049(6)	0	0

Table 5.6 Relevant bond distances (Å), diameters (Å), angles (°), ditrigonal rotation angle $\alpha_{S6R\perp[0001]}$ (°) of the S6R⊥[0001], and cage/channel-volumes (Å^3) of vishnevite at different pressure and temperatures

P (GPa)		0.0001 ($P_{0\text{-AIR}}$)	0.52(2) (P_2)	1.20(3) (P_4)	1.78(5) (P_6)	2.47(2) (P_8)	3.24(9) (P_{10})	3.43(4) (P_{11})	4.23(7) (P_{13})	5.74(6) (P_{15})	6.10(8) (P_{17})	6.11(4) (P_{19})	7.40(4) (P_{22})	0.0001** ($P_{0\text{-post}}$)	293 K	110 K
Si-	O1	1.604(11)	1.602(14)	1.603(14)	1.609(15)	1.608(16)	1.604(14)	1.614(14)	1.611(14)	1.594(14)	1.579(15)	1.577(16)	1.60(2)	1.600(13)	1.600(7)	1.594(5)
	O2	1.609(11)	1.609(12)	1.602(11)	1.608(13)	1.604(13)	1.610(12)	1.612(11)	1.602(11)	1.613(11)	1.604(13)	1.590(13)	1.626(13)	1.615(11)	1.597(6)	1.600(6)
	O3	1.600(11)	1.601(14)	1.600(15)	1.608(15)	1.601(16)	1.608(16)	1.581(13)	1.597(12)	1.591(12)	1.591(13)	1.616(14)	1.60(3)	1.601(15)	1.611(4)	1.611(4)
	O4	1.600(9)	1.608(17)	1.608(17)	1.613(17)	1.606(18)	1.616(16)	1.610(17)	1.624(15)	1.613(16)	1.610(18)	1.59(2)	1.61(2)	1.589(15)	1.615(5)	1.594(5)
<Si-O>		1.603(11)	1.605(14)	1.603(14)	1.610(15)	1.605(16)	1.610(15)	1.604(14)	1.609(13)	1.603(13)	1.596(15)	1.593(16)	1.61(2)	1.601(14)	1.606(6)	1.600(5)
Al-	O1	1.733(11)	1.734(14)	1.733(14)	1.720(16)	1.717(17)	1.706(15)	1.704(14)	1.701(14)	1.705(14)	1.689(15)	1.724(14)	1.718(18)	1.737(13)	1.735(7)	1.726(7)
	O2	1.718(9)	1.718(11)	1.716(10)	1.714(12)	1.714(12)	1.715(11)	1.708(11)	1.714(11)	1.709(12)	1.704(13)	1.710(13)	1.718(16)	1.707(11)	1.740(7)	1.731(7)
	O3	1.749(13)	1.75(2)	1.74(3)	1.74(2)	1.74(3)	1.75(2)	1.74(2)	1.73(2)	1.75(2)	1.75(3)	1.71(3)	1.74(3)	1.75(2)	1.737(5)	1.734(6)
	O4	1.753(11)	1.758(16)	1.755(16)	1.744(16)	1.731(17)	1.745(17)	1.744(15)	1.745(13)	1.728(12)	1.750(14)	1.750(15)	1.74(3)	1.761(16)	1.746(4)	1.760(5)
<Al-O>		1.738(11)	1.740(15)	1.736(18)	1.730(16)	1.726(19)	1.729(16)	1.724(15)	1.723(15)	1.723(15)	1.723(18)	1.724(18)	1.73(2)	1.739(15)	1.740(6)	1.738(6)
Si-O1-Al		153.0(7)	151.9(9)	150.2(8)	149.0(9)	147.8(10)	147.4(9)	145.0(8)	143.1(8)	142.5(9)	143.3(9)	138.9(9)	136.2(10)	149.4(8)	153.3(2)	151.6(2)
Si-O2-Al		147.6(6)	149.1(6)	148.6(6)	146.8(7)	146.3(7)	144.3(7)	145.9(7)	144.5(7)	143.4(7)	142.6(7)	140.0(7)	130.0(7)	149.4(6)	147.4(3)	146.8(2)
Si-O3-Al		139.9(6)	138.3(9)	137.4(9)	135.8(8)	135.5(9)	132.6(8)	134.4(8)	131.5(7)	128.9(7)	128.0(8)	128.4(8)	125.1(13)	135.2(8)	140.6(4)	139.6(4)
Si-O4-Al		141.2(6)	137.2(8)	136.0(9)	136.0(9)	136.2(8)	132.6(8)	133.5(7)	130.0(7)	130.7(7)	129.5(8)	128.3(8)	125.2(14)	137.7(8)	140.2(4)	139.4(4)
Na1-	O1(x3)	2.942(6)	2.897(10)	2.898(10)	2.899(10)	2.892(12)	2.903(11)	2.889(10)	2.905(9)	2.943(10)	2.956(11)	2.984(11)	2.942(12)	2.889(10)	2.920(3)	2.937(3)
	O2(x3)	2.465(7)	2.485(10)	2.463(11)	2.432(11)	2.402(17)	2.408(15)	2.401(13)	2.367(11)	2.371(12)	2.367(13)	2.290(14)	2.078(17)	2.453(11)	2.411(4)	2.400(4)
	Ow'(*z*)	2.12(3)	2.11(3)	2.15(3)	2.15(4)	2.12(6)	2.06(4)	2.14(4)	2.13(3)	1.93(3)	1.63(7)	2.08(3)	2.03(5)	2.18(4)	2.312(18)	2.279(12)
	Ow''(*z*+1)	3.21(3)	3.16(3)	3.10(3)	3.08(4)	3.09(6)	3.12(5)	3.00(4)	2.99(3)	3.15(3)	3.49(6)	4.06(4)	3.89(6)	3.06(4)	3.019(17)	3.030(12)
Na2-	O1(x3)	2.901(4)	2.859(9)	2.865(9)	2.866(10)	2.868(10)	2.858(9)	2.861(9)	2.881(9)	2.901(10)	2.900(9)	2.956(10)	2.96(2)	2.868(9)	-	-
	O2(x3)	2.363(5)	2.388(7)	2.375(7)	2.341(8)	2.327(10)	2.304(9)	2.316(9)	2.274(9)	2.244(9)	2.229(9)	2.173(9)	2.008(15)	2.384(11)	-	-
	Ow'(*z*+1)	2.56(3)	2.56(3)	2.59(3)	2.47(4)	2.48(6)	2.47(4)	2.52(4)	2.51(3)	2.46(3)	2.24(6)	2.52(4)	2.54(12)	2.54(7)	-	-
	Ow''(*z*)	2.76(3)	2.71(3)	2.66(3)	2.64(4)	2.72(6)	2.70(4)	2.61(4)	2.61(3)	2.61(3)	2.83(6)	3.48(4)	3.25(13)	2.70(7)	-	-
M1	O1	2.830(9)	2.651(17)	2.619(14)	2.588(17)	2.578(17)	2.539(16)	2.513(17)	2.47(2)	2.50(2)	2.48(2)	2.44(2)	2.51(4)	2.604(16)	2.815(5)	2.779(5)
	O3′	2.714(13)	2.59(3)	2.58(3)	2.63(3)	2.57(3)	2.53(3)	2.52(3)	2.51(4)	2.44(4)	2.44(4)	2.36(4)	2.44(4)	2.46(3)	2.714(9)	2.692(9)
	O3′′	2.990(12)	2.98(3)	2.99(4)	3.01(3)	2.94(4)	2.97(4)	2.98(4)	3.03(4)	3.07(4)	3.09(5)	3.12(4)	3.22(4)	3.06(3)	3.005(8)	3.036(7)
	O4′	2.663(11)	2.57(2)	2.56(3)	2.50(2)	2.46(3)	2.40(3)	2.39(3)	2.33(4)	2.36(3)	2.39(4)	2.48(4)	2.31(3)	2.58(2)	2.677(8)	2.668(8)
	O4′′	3.038(13)	2.96(3)	2.96(4)	2.94(3)	3.02(4)	2.99(4)	3.01(4)	3.00(5)	3.04(4)	3.00(5)	3.02(5)	3.17(4)	2.88(2)	2.985(11)	2.991(10)
	OB1′(*z*+1/2)	2.51(2)	2.528(19)	2.50(2)	2.46(2)	2.34(2)	2.42(2)								2.82(3)	2.72(2)
	OB1′′(*z*+1/2)	2.95(3)	3.026(19)	2.99(2)	2.91(2)	2.81(2)	2.89(2)								2.92(4)	3.19(3)

Appendix

	OB2′															
	(*z*-1/2)	2.68(3)	2.72(2)	2.72(2)	2.69(2)	2.66(3)	2.68(3)								2.72(3)	2.76(2)
	OB2′′															
	(*z*-1/2)	3.17(3)	3.3(2)	3.29(2)	3.282(16)	3.28(2)	3.279(19)								3.07(3)	2.98(3)
	OB′(*z*)							2.43(2)	2.38(3)	2.35(2)	2.23(3)	2.15(3)	2.30(3)	2.471(15)		
	OB″ (*z*)							2.45(2)	2.41(3)	2.36(3)	2.24(4)	2.22(3)	2.32(3)	2.526(18)		
	OA(*z*)							2.290(13)	2.877(16)	2.849(16)	2.806(18)	2.939(19)	2.63(3)	2.878(13)		
	OA															
	(*z*-1/2)							3.006(14)	2.937(16)	2.888(17)	2.858(18)	2.627(17)	2.79(3)	3.167(13)		
<M1-O_{fr}>		2.851(12)	2.78(3)	2.77(4)	2.77(3)	2.75(4)	2.72(4)	2.73(4)	2.72(4)	2.73(4)	2.73(5)	2.75(4)	2.79(4)	2.75(3)	2.845(9)	2.833(8)
M2	O1	2.390(10)	2.403(18)	2.382(17)	2.386(18)	2.34(2)	2.352(18)	2.32(2)	2.32(2)	2.25(2)	2.27(2)	2.16(2)	2.04(4)	2.37(2)	2.393(5)	2.358(5)
	O3′	2.338(14)	2.30(4)	2.27(4)	2.26(4)	2.26(4)	2.22(4)	2.26(4)	2.28(4)	2.24(4)	2.19(5)	2.12(5)	2.37(4)	2.27(3)	2.338(9)	2.319(9)
	O3′′	2.851(13)	2.91(4)	2.93(4)	2.94(4)	2.93(4)	2.94(4)	2.96(4)	3.01(5)	3.02(5)	3.07(5)	3.02(5)	2.86(4)	2.92(3)	2.876(8)	2.897(9)
	O4′	2.342(12)	2.27(4)	2.25(4)	2.21(4)	2.22(4)	2.11(3)	2.19(3)	2.14(4)	2.23(4)	2.21(4)	2.24(4)	2.00(4)	2.27(3)	2.376(10)	2.355(10)
	O4′′	2.840(13)	2.91(4)	2.92(4)	2.94(4)	2.91(4)	2.97(4)	2.94(4)	2.95(5)	2.91(5)	2.91(5)	2.92(5)	3.10(5)	2.89(3)	2.791(11)	2.804(10)
	OB1	2.33(2)	2.372(17)	2.366(17)	2.42(2)	2.50(2)	2.38(2)								2.29(2)	2.22(2)
	OB2	2.19(2)	2.121(14)	2.101(13)	2.076(14)	2.084(15)	2.045(14)								2.32(4)	2.32(2)
	OB′(*z*)							2.783(18)	2.68(2)	2.65(2)	2.54(2)	2.55(2)	2.88(3)	2.926(15)		
	OB″ (*z*)							2.79(2)	2.66(3)	2.68(3)	2.58(3)	2.60(3)	2.73(3)	2.897(17)		
	OB															
	(*z*+1/2)							2.59(2)	2.49(2)	2.39(2)	2.72(3)	2.65(2)	2.09(3)	2.64(2)		
<M2-O_{fr}>		2.552(12)	2.56(4)	2.55(4)	2.55(4)	2.53(4)	2.52(3)	2.53(3)	2.54(4)	2.53(4)	2.53(4)	2.49(4)	2.47(4)	2.54(3)	2.555(9)	2.546(9)
S-OB1		1.45(2)	1.453(13)	1.452(14)	1.453(15)	1.455(15)	1.455(15)								1.46(3)	1.46(3)
S-OB2		1.36(3)	1.351(7)	1.351(7)	1.351(8)	1.354(9)	1.354(9)								1.46(3)	1.46(2)
S-OA								1.40(2)	1.40(2)	1.40(2)	1.40(2)	1.40(2)	1.40(4)	1.39(3)		
S-OB								1.403(9)	1.400(9)	1.393(8)	1.404(9)	1.398(9)	1.398(17)	1.376(9)		
$(O2\text{-}O2)_{S6R\perp[0001]}$		4.059(9)	4.108(12)	4.090(12)	4.030(14)	3.999(13)	3.946(14)	3.974(14)	3.923(16)	3.859(16)	3.850(16)	3.761(17)	3.47(2)	4.104(14)	4.064(4)	4.034(4)
$(O2\text{-}O2)_{cw}$		8.712(17)	8.623(14)	8.597(14)	8.616(16)	8.603(17)	8.590(16)	8.543(13)	8.504(16)	8.526(16)	8.483(17)	8.510(17)	8.688(18)	8.567(14)	8.702(7)	8.693(7)
O2-O2-O2		88.1(3)	89.4(3)	89.2(3)	88.1(3)	87.6(3)	86.7(3)	87.5(3)	86.8(3)	85.4(3)	85.5(3)	83.4(3)	77.7(5)	89.8(3)	88.4(1)	87.8(1)
$(O1\text{-}O1)_{12R}$*		8.943(7)	8.978(13)	8.913(14)	8.874(15)	8.816(15)	8.768(14)	8.737(15)	8.596(13)	8.506(15)	8.449(15)	8.260(16)	8.18(2)	8.894(14)	8.930(5)	8.852(5)
$(O3\text{-}O4)_{12R}$		8.750(8)	8.725(17)	8.695(18)	8.670(18)	8.642(18)	8.558(16)	8.594(17)	8.513(15)	8.493(17)	8.473(18)	8.43(2)	8.916(16)	8.656(15)	8.726(7)	8.715(6)
$(O3\text{-}O4)_{S4R}$		4.025(12)	4.01(2)	3.99(3)	3.98(2)	3.96(2)	3.98(2)	3.93(2)	3.92(2)	3.90(2)	3.87(3)	3.84(3)	3.71(3)	4.02(2)	4.042(10)	4.015(10)
ϕ1 (O1-O4-O3)		91.7(3)	87.4(5)	85.9(5)	84.8(5)	84.4(5)	82.2(5)	81.5(5)8	78.8(4)	77.7(5)	77.1(5)	75.4(5)	72.2(7)	86.2(5)	92.2(2)	90.5(2)
ϕ2 (O1-O3-O4)		91.8(3)	87.6(6)	86.1(5)	85.2(5)	84.6(5)	81.6(5)	81.1(5)	77.6(5)	76.8(5)	76.1(5)	75.9(6)	71.0(7)	85.9(5)	91.9(2)	90.3(2)
ϕ3 (O4-O3-O1)		152.5(4)	150.4(6)	151.6(6)	153.2(5)	153.4(6)	155.9(6)	157.0(5)	157.3(5)	159.8(5)	159.8(5)	160.9(6)	160.4(10)	152.6(6)	146.8(2)	148.0(2)
ϕ4 (O3-O4-O1)		152.5(4)	151.4(6)	152.8(6)	153.1(5)	153.7(6)	156.3(6)	155.6(5)	160.4(5)	160.1(5)	160.8(6)	160.1(6)	164.7(10)	152.0(5)	146.8(2)	148.5(2)
O3-O4-O3		152.5(4)	147.5(5)	146.2(5)	145.1(5)	144.8(5)	141.5(5)	141.5(5)	137.7(4)	136.0(4)	135(5)	135.3(5)	129.9(10)	146.5(5)	152.6(2)	151.2(2)
$\alpha_{S6R\perp[0001]}$		10.2(2)	9.0(2)	9.3(2)	10.0(3)	10.3(3)	10.8(3)	10.5(2)	11.4(3)	12.4(3)	12.7(3)	14.4(3)	17.5(4)	9.2(2)	10.2(1)	10.8(1)
Δz, corrugation		1.039(4)	1.017(5)	0.927(6)	0.902(6)	0.903(6)	0.820(5)	0.849(5)	0.772(4)	0.778(4)	0.703(5)	0.668(4)	0.602(7)	0.927(5)	1.013(2)	0.986(2)
V_{ch}		320.2(6)	318.6(11)	313.6(12)	309.9(12)	305.3(12)	298.5(10)	298.0(11)	287.6(10)	282.3(11)	278.2(11)	268.8(12)	278.5(12)	311.5(11)	319.7(5)	314.6(4)
V_{cg}		210.2(7)	203.8(7)	201.9(7)	200.1(7)	198.1(7)	195.4(6)	193.8(7)	190.8(7)	189.4(7)	186.8(7)	185.5(7)	171.2(8)	212.1(6)	208.5(3)	206.6(2)

*$(O1\text{-}O1)_{ch}$ is calculated as the projection onto the (0001) plane of the O1-O1 distance, as the involved O1 atoms are shifted along [0001] of 1/2**z*.

** Parameters from the structure refinement based on the data collected at room-*P* after the H*P*-experiment

Table 6.1 Details about the data collection protocol, unit-cell parameters and structure refinements of balliranoite at different temperatures.

T (K)	293 (T_0)	250 (T_1)	220 (T_2)	180 (T_3)	140 (T_4)	108 (T_5)
a (Å)	12.6701 (3)	12.6556 (4)	12.6560 (3)	12.6516 (3)	12.6383 (4)	12.6369 (4)
c (Å)	5.3178 (1)	5.3123 (2)	5.3102 (1)	5.3048(1)	5.3020 (1)	5.3017 (2)
V (Å^3)	739.30 (3)	736.85(4)	736.6 (3)	735.34 (3)	733.41 (3)	733.21 (4)
Maximum 2θ (°)	77.35	77.45	77.70	77.74	77.46	77.58
	-17≤ h ≤21	-15≤ h ≤22	-21≤ h ≤21	-21≤ h ≤21	-14≤ h ≤22	-19≤ h ≤22
	-21≤ k ≤21	-21≤ k ≤22	-22≤ k ≤16	-22≤ k ≤21	-21≤ k ≤22	-22≤ k ≤21
	-9≤ l ≤9	-8≤ l ≤9	-9≤ l ≤9	-8≤ l ≤9	-8≤ l ≤9	-7≤ l ≤9
Measured reflections	11535	11622	11596	11532	11806	10075
Unique reflections	2727	2718	2721	2612	2707	2640
Unique reflections with $F_0 > 4\sigma(F_0)$	2544	2559	2588	2486	2593	2545
R_{int}	0.0287	0.0280	0.0259	0.0258	0.0311	0.0274
Number of l.s. parameters	105	100	100	100	100	100
R_1, $F_0 > 4\sigma(F_0)$	0.0301	0.0298	0.0281	0.0298	0.0295	0.0287
R_1, all data	0.0333	0.0328	0.0305	0.0323	0.0316	0.0301
wR_2	0.0587	0.0592	0.0551	0.0577	0.0609	0.0583
Residues (eÅ^{-3})	+0.98/-0.57	+0.98/-0.59	+0.99/-0.60	+1.10/-0.62	+1.22/-0.57	+1.04/-0.66

λ: MoKα; ω-scan type; step scan = 1°; exposure time = 30 s; space group: $P6_3$; $Z = 1$

$R_{int} = \Sigma|F^2_{obs} - (\text{mean})|/\Sigma[F^2_{obs}]$

$R_1 = \Sigma||F_{obs}| - |F_{calc}||/\Sigma|F_{obs}|$; $wR_2 = \{\Sigma[w(F^2_{obs} - F^2_{calc})^2]/\Sigma[w(F^2_{obs})^2]\}^{0.5}$, $w = 1/[\sigma^2(F^2_{obs}) + (0.01 \cdot P)^2]$, $P = [\text{Max}(F^2_{obs},0) + 2 \cdot F^2_{calc}]/3$.

Appendix

Table 6.2 Chemical analysis of balliranoite (in wt%) and atoms per formula unit, based on (Si + Al = 12), averaged from 7 points

SiO_2	33.21
Al_2O_3	28.52
CaO	14.86
Na_2O	12.83
K_2O	0.46
SO_3	2.43
Cl	6.67
CO_2[§]	3.20
O = Cl	-1.50
Total	100.68
Number of atoms per formula unit on the basis (Si+Al=12)	
Si	5.964
Al	6.036
Ca	2.859
Na	4.466
K	0.105
C	0.780
S	0.328
Cl	2.029
Si/Al	0.988

[§]calculated from charge balance

Table 6.3 Atomic fractional coordinates, site occupancy factors (*sof*) and isotropic/equivalent atomic displacement parameters (Å^2) of balliranoite at different temperatures

Atom site	*T* (K)	*sof*	*x*	*y*	*z*	U_{eq}\U_{iso}
Si	293	1.0	0.32740(3)	0.40809(3)	0.75637(7)	0.00773(6)
	250	1.0	0.32726(3)	0.40797(3)	0.75690(7)	0.00664(6)
	220	1.0	0.32716(2)	0.40787(3)	0.75812(7)	0.00634(5)
	180	1.0	0.32712(3)	0.40783(3)	0.75763(7)	0.00565(6)
	140	1.0	0.32705(3)	0.40777(3)	0.75793(7)	0.00524(6)
	108	1.0	0.32698(3)	0.40771(3)	0.75823(7)	0.00485(6)
Al	293	1.0	0.06954(3)	0.40823(3)	0.75770(8)	0.00798(6)
	250	1.0	0.06953(3)	0.40816(3)	0.75836(8)	0.00687(6)
	220	1.0	0.06949(3)	0.40804(3)	0.75961(8)	0.00665(6)
	180	1.0	0.06945(3)	0.40798(3)	0.75913(8)	0.00593(6)
	140	1.0	0.06949(3)	0.40794(3)	0.75949(8)	0.00542(6)
	108	1.0	0.06944(3)	0.40786(3)	0.75990(8)	0.00506(6)
O1	293	1.0	0.21314(7)	0.42773(9)	0.7055(2)	0.0182(2)
	250	1.0	0.21313(8)	0.42759(9)	0.7037(2)	0.0161(2)
	220	1.0	0.21304(7)	0.42756(8)	0.7035(2)	0.0154(2)
	180	1.0	0.21310(8)	0.42746(9)	0.7011(2)	0.0138(2)
	140	1.0	0.21297(8)	0.42739(9)	0.7002(2)	0.0130(2)
	108	1.0	0.21291(8)	0.42725(9)	0.6995(2)	0.0122(2)
O2	293	1.0	0.09945(8)	0.55664(7)	0.7464(2)	0.0157(2)
	250	1.0	0.09935(8)	0.55661(7)	0.7463(2)	0.0140(2)
	220	1.0	0.09939(7)	0.55664(7)	0.7472(2)	0.0130(2)
	180	1.0	0.09943(8)	0.55663(7)	0.7465(2)	0.0117(2)
	140	1.0	0.09931(8)	0.55667(7)	0.7465(2)	0.0104(2)
	108	1.0	0.09930(8)	0.55659(7)	0.7467(2)	0.0096(2)
O3	293	1.0	0.01004(8)	0.32993(9)	0.0384(2)	0.0154(2)
	250	1.0	0.01093(9)	0.33024(9)	0.0401(2)	0.0134(2)
	220	1.0	0.01136(8)	0.33036(8)	0.0418(2)	0.0127(2)
	180	1.0	0.01197(8)	0.33057(9)	0.0421(2)	0.0115(2)
	140	1.0	0.01243(8)	0.33067(9)	0.0431(2)	0.0104(2)
	108	1.0	0.01243(8)	0.33067(9)	0.0431(2)	0.0096(2)
O4	293	1.0	0.31266(9)	0.33947(8)	0.0214(2)	0.0147(2)
	250	1.0	0.31216(9)	0.33995(9)	0.0232(2)	0.0126(2)
	220	1.0	0.31173(8)	0.33992(8)	0.0251(2)	0.0120(2)
	180	1.0	0.31142(8)	0.34022(9)	0.0252(2)	0.0108(2)
	140	1.0	0.31103(9)	0.34031(9)	0.0262(2)	0.0099(2)
	108	1.0	0.31075(9)	0.34040(9)	0.0269(2)	0.0090(2)

Ca	293	1.0	1/3	2/3	0.70754(8)	0.01387(8)
	250	1.0	1/3	2/3	0.70540(8)	0.01194(8)
	220	1.0	1/3	2/3	0.70518(7)	0.01133(7)
	180	1.0	1/3	2/3	0.70301(9)	0.00986(7)
	140	1.0	1/3	2/3	0.70195(8)	0.00892(7)
	108	1.0	1/3	2/3	0.70123(8)	0.00815(7)
Cl	293	1.0	0.3118(5)	0.657(2)	0.2105(2)	0.057(1)
	250	1.0	0.3134(6)	0.658(2)	0.2085(2)	0.052(1)
	220	1.0	0.350(3)	0.664(4)	0.2081(2)	0.045(2)
	180	1.0	0.339(4)	0.6852(5)	0.2062(2)	0.043(2)
	140	1.0	0.340(2)	0.656(2)	0.2054(2)	0.040(1)
	108	1.0	0.3168(5)	0.657(2)	0.2044(2)	0.037(1)
M1	293	0.859(4)	0.12142(6)	0.24909(9)	0.2994(2)	0.0230(3)
	250	0.854(4)	0.12134(7)	0.2490(1)	0.3014(2)	0.0199(2)
	220	0.851(3)	0.12131(6)	0.24892(9)	0.3032(2)	0.0185(2)
	180	0.850(4)	0.12136(7)	0.2488(1)	0.3036(2)	0.0165(2)
	140	0.850(4)	0.12134(7)	0.2489(1)	0.3044(2)	0.0148(2)
	108	0.859(4)	0.12150(7)	0.2490(1)	0.3049(1)	0.0141(2)
M2	293	0.158(4)	0.1530(4)	0.3130(6)	0.283(1)	0.026(1)
	250	0.160(4)	0.1519(4)	0.3105(6)	0.2848(9)	0.021(1)
	220	0.163(3)	0.1511(4)	0.3087(5)	0.2866(9)	0.021(1)
	180	0.160(4)	0.1493(4)	0.3066(6)	0.2872(9)	0.019(1)
	140	0.160(4)	0.1500(4)	0.3071(6)	0.2882(9)	0.017(1)
	108	0.155(4)	0.1495(4)	0.3067(6)	0.2898(8)	0.014(1)
C1	293	0.49(6)	0	0	0.159(2)	0.045(4)
	250	0.49	0	0	0.164(2)	0.042(2)
	220	0.49	0	0	0.164(2)	0.040(2)
	180	0.49	0	0	0.165(2)	0.039(2)
	140	0.49	0	0	0.166(2)	0.037(2)
	108	0.49	0	0	0.166(2)	0.035(2)
O5	293	0.544(4)	-0.0618(3)	0.0561(3)	0.163(1)	0.054(2)
	250	0.544	-0.0616(3)	0.0565(3)	0.166(1)	0.0504(9)
	220	0.544	-0.0614(2)	0.0563(2)	0.1662(9)	0.0492(8)
	180	0.544	-0.0617(2)	0.0565(2)	0.1649(9)	0.0456(8)
	140	0.544	-0.0618(2)	0.0560(2)	0.1678(9)	0.0437(8)
	108	0.544	-0.0615(2)	0.0563(2)	0.1683(9)	0.0429(8)
C2	293	0.24(2)	0	0	0.400(5)	0.053(8)
	250	0.24	0	0	0.412(4)	0.049(4)
	220	0.24	0	0	0.411(4)	0.047(4)
	180	0.24	0	0	0.414(4)	0.045(4)
	140	0.24	0	0	0.418(4)	0.044(4)

	108	0.24	0	0	0.418(4)	0.045(4)
O6	293	0.134(5)	-0.0571(11)	0.0585(11)	0.365(4)	0.054(2)
	250	0.134	-0.0576(11)	0.0569(11)	0.363(4)	0.0504(9)
	220	0.134	-0.0592(10)	0.0568(10)	0.362(4)	0.0492(8)
	180	0.134	-0.0595(10)	0.0565(10)	0.359(4)	0.0456(8)
	140	0.134	-0.0572(10)	0.0587(10)	0.364(4)	0.0437(8)
	108	0.134	-0.0586(10)	0.0573(10)	0.364(4)	0.0429(8)

Appendix

Table 6.4 Site anisotropic displacement parameters (Å^2) of balliranoite at different temperatures

Atom site	U_{11}	U_{22}	U_{33}	U_{12}	U_{13}	U_{23}
			T_0 (298 K)			
Si	0.0072(1)	0.0088(1)	0.0078(1)	0.00445(9)	0.0005(1)	0.0009(1)
Al	0.0075(1)	0.0087(1)	0.0081(1)	0.0043(1)	0.0002(1)	0.0005(1)
O1	0.0119(4)	0.0240(4)	0.0232(6)	0.0123(3)	0.0036(3)	0.0087(4)
O2	0.0181(4)	0.0110(3)	0.0197(5)	0.0087(3)	0.0006(4)	0.0000(3)
O3	0.0183(4)	0.0187(4)	0.0112(5)	0.0108(4)	0.0056(3)	0.0049(3)
O4	0.0165(4)	0.0170(4)	0.0104(4)	0.0082(3)	-0.0012(3)	0.0037(3)
Ca	0.0137(1)	0.0137(1)	0.0143(2)	0.00684(5)	0	0
Cl	0.053(2)	0.096(2)	0.0118(4)	0.031(2)	-0.001(1)	0.010(3)
M1	0.0129(3)	0.0281(6)	0.0335(5)	0.0144(3)	-0.0017(3)	-0.0026(3)
O5	0.033(1)	0.031(1)	0.108(3)	0.023(1)	-0.008(2)	0.002(2)
O6	0.033(4)	0.031(1)	0.108(1)	0.023(2)	-0.008(2)	0.002(3)
C1	0.018(2)	0.018(2)	0.10(1)	0.009(1)	0	0
C2	0.044(7)	0.044(7)	0.07(2)	0.022(3)	0	0
			T_1 (250 K)			
Si	0.0059(1)	0.0074(1)	0.0072(1)	0.0038(1)	0.0004(1)	0.0009(1)
Al	0.0063(1)	0.0074(1)	0.0073(1)	0.0037(1)	0.0002(1)	0.0004(1)
O1	0.0100(4)	0.0209(4)	0.0215(5)	0.0107(3)	0.0035(3)	0.0082(4)
O2	0.0157(4)	0.0095(3)	0.0175(4)	0.0075(3)	0.0008(4)	0.0001(3)
O3	0.0154(4)	0.0158(4)	0.0105(4)	0.0090(4)	0.0048(3)	0.0044(3)
O4	0.0143(4)	0.0147(4)	0.0092(4)	0.0076(4)	-0.0008(3)	0.0036(3)
Ca	0.0113(1)	0.0113(1)	0.0133(2)	0.00563(5)	0	0
Cl	0.048(2)	0.090(3)	0.0106(4)	0.029(2)	-0.001(1)	0.008(4)
M1	0.0101(3)	0.0241(5)	0.0307(4)	0.0124(3)	-0.0018(3)	-0.0022(3)
O5	0.026(1)	0.025(1)	0.107(3)	0.0175(9)	-0.006(2)	0.003(2)
O6	0.026(1)	0.025(1)	0.107(3)	0.0175(9)	-0.006(2)	0.003(2)
C1	0.016(2)	0.016(2)	0.093(7)	0.0079(8)	0	0
C2	0.040(6)	0.040(6)	0.07(1)	0.020(3)	0	0
			T_2 (220 K)			
Si	0.0056(1)	0.0071(1)	0.0070(1)	0.00362(9)	0.0005(1)	0.0009(1)
Al	0.0061(1)	0.0070(1)	0.0072(1)	0.0035(1)	0.0000(1)	0.0004(1)
O1	0.0095(3)	0.0202(4)	0.0200(5)	0.0101(3)	0.0029(3)	0.0078(3)
O2	0.0150(3)	0.0087(3)	0.0167(4)	0.0070(3)	0.0006(3)	-0.0002(3)
O3	0.0145(4)	0.0155(4)	0.0096(4)	0.0087(3)	0.0045(3)	0.0041(3)
O4	0.0135(4)	0.0143(4)	0.0089(4)	0.0074(3)	-0.0004(3)	0.0035(3)
Ca	0.01065(9)	0.01065(9)	0.0127(2)	0.0053(5)	0	0
Cl	0.074(7)	0.071(4)	0.0096(3)	0.051(6)	0.002(2)	0.001(3)
M1	0.0092(3)	0.0229(5)	0.0285(4)	0.0118(3)	-0.0017(2)	-0.0019(3)
O5	0.0249(9)	0.0251(9)	0.104(3)	0.0171(8)	-0.006(2)	0.003(2)
O6	0.0249(9)	0.0251(9)	0.104(3)	0.0171(8)	-0.006(2)	0.003(2)
C1	0.016(2)	0.016(2)	0.086(6)	0.0082(8)	0	0

C2	0.030(4)	0.030(4)	0.08(1)	0.015(2)	0	0

			***T*₃ (180 K)**			
Si	0.0052(1)	0.0065(1)	0.0060(1)	0.0035(1)	0.0004(1)	0.0009(1)
Al	0.0054(1)	0.0063(1)	0.0063(1)	0.0031(1)	-0.0000(1)	0.0002(1)
O1	0.0084(3)	0.0179(4)	0.0185(4)	0.0092(3)	0.0029(3)	0.0075(3)
O2	0.0135(4)	0.0081(3)	0.0149(4)	0.0066(3)	0.0006(3)	-0.0002(3)
O3	0.0127(4)	0.0145(4)	0.0085(4)	0.0077(3)	0.0040(3)	0.0038(3)
O4	0.0125(4)	0.0130(4)	0.0078(4)	0.0070(3)	-0.0004(3)	0.0030(3)
Ca	0.0093(1)	0.0093(1)	0.0109(2)	0.00466(5)	0	0
Cl	0.069(4)	0.038(1)	0.0078(3)	0.0150(14)	0.000(3)	0.0016(7)
M1	0.0077(3)	0.0204(5)	0.0261(4)	0.0106(3)	-0.0015(2)	-0.0018(3)
O5	0.0216(9)	0.0206(9)	0.099(3)	0.0138(9)	-0.005(2)	0.003(2)
O6	0.0216(9)	0.0206(9)	0.099(3)	0.0138(9)	-0.005(2)	0.003(2)
C1	0.014(2)	0.014(2)	0.089(6)	0.0069(7)	0	0
C2	0.034(5)	0.034(5)	0.07(1)	0.017(2)	0	0

			***T*₄ (140 K)**			
Si	0.0048(1)	0.0062(1)	0.0055(1)	0.0032(1)	0.0004(1)	0.0010(1)
Al	0.0050(1)	0.00589(1)	0.0056(1)	0.0029(1)	0.0000(1)	0.0002(1)
O1	0.0081(4)	0.0171(4)	0.0169(4)	0.0087(3)	0.0029(3)	0.0072(3)
O2	0.0120(4)	0.0073(3)	0.0129(4)	0.0056(3)	0.0005(3)	-0.0001(3)
O3	0.0112(4)	0.0127(4)	0.0078(4)	0.0064(3)	0.0035(3)	0.0036(3)
O4	0.0111(4)	0.0118(4)	0.0073(4)	0.0061(3)	-0.0002(3)	0.0027(3)
Ca	0.0084(1)	0.0084(1)	0.0100(2)	0.00419(5)	0	0
Cl	0.073(2)	0.064(2)	0.0073(3)	0.053(2)	-0.004(5)	-0.005(4)
M1	0.0066(3)	0.0194(5)	0.0231(4)	0.0100(3)	-0.0016(2)	-0.0021(3)
O5	0.020(1)	0.0202(9)	0.096(2)	0.0139(9)	-0.005(2)	0.003(2)
O6	0.020(1)	0.0202(9)	0.096(2)	0.0139(9)	-0.005(2)	0.003(2)
C1	0.013(2)	0.013(2)	0.086(6)	0.0065(8)	0	0
C2	0.030(5)	0.030(5)	0.07(1)	0.015(2)	0	0

			***T*₅ (108 K)**			
Si	0.0045(1)	0.0057(1)	0.0050(1)	0.0030(1)	0.0004(1)	0.0008(1)
Al	0.0046(1)	0.0056(1)	0.0053(1)	0.0027(1)	0.0001(1)	0.0002(1)
O1	0.0078(4)	0.0162(4)	0.0153(4)	0.0082(3)	0.0025(3)	0.0068(3)
O2	0.0109(4)	0.0070(3)	0.0119(4)	0.0052(3)	0.0011(3)	0.0003(3)
O3	0.0106(4)	0.0120(4)	0.0071(4)	0.0061(3)	0.0033(3)	0.0031(3)
O4	0.0103(4)	0.0110(4)	0.0067(4)	0.0060(3)	-0.0001(3)	0.0025(3)
Ca	0.0076(1)	0.0076(1)	0.0092(2)	0.00382(5)	0	0
Cl	0.029(1)	0.069(3)	0.0069(3)	0.019(1)	-0.0017(9)	-0.008(3)
M1	0.0060(3)	0.0190(5)	0.0222(4)	0.0098(3)	-0.0017(2)	-0.0021(3)
O5	0.018(1)	0.0186(9)	0.096(2)	0.0124(8)	-0.007(2)	0.002(2)
O6	0.018(1)	0.0186(9)	0.096(2)	0.0124(8)	-0.007(2)	0.002(2)
C1	0.012(2)	0.012(2)	0.082(6)	0.0061(8)	0	0
C2	0.029(5)	0.029(5)	0.08(1)	0.014(2)	0	0

Appendix

Table 6.5 Relevant bond distances (Å), diameters (Å), angles (°), S6R⊥[0001] ditrigonal rotation angle $\alpha_{S6R\perp[0001]}$ (°), hexagonal layers corrugation Δ*z* (Å) and cage/channel-volumes (Å^3) of balliranoite at different temperatures.

	T	293 K (T_0)	250 K (T_1)	220 K (T_2)	180 K (T_3)	140 K (T_4)	108 K (T_5)
Si-	O1	1.6098(8)	1.6083(9)	1.6101(8)	1.6079(8)	1.6098(9)	1.6099(9)
	O2	1.6022(8)	1.6017(9)	1.6029(8)	1.6035(8)	1.6012(9)	1.6028(9)
	O3	1.6213(9)	1.6213(9)	1.6224(9)	1.6225(9)	1.6221(9)	1.6222(9)
	O4	1.617(1)	1.6167(9)	1.6184(9)	1.6176(9)	1.6184(9)	1.6186(9)
<Si-O>		1.6126(9)	1.6120(9)	1.6135(8)	1.6129(9)	1.6129(9)	1.6134(9)
Al-	O1	1.7318(9)	1.7323(9)	1.7326(8)	1.7350(9)	1.7325(9)	1.7336(9)
	O2	1.7235(8)	1.7226(9)	1.7243(8)	1.7240(8)	1.7239(9)	1.7235(9)
	O3	1.742(1)	1.741(1)	1.7406(9)	1.741(1)	1.741(1)	1.741(1)
	O4	1.748(1)	1.749(1)	1.7488(9)	1.7488(9)	1.7489(9)	1.750(1)
<Al-O>		1.7363(9)	1.736(1)	1.7366(9)	1.7371(9)	1.7366(9)	1.737(1)
Si-O1-Al		155.98(8)	155.27(8)	154.81(7)	154.32(8)	153.92(8)	153.65(8)
Si-O2-Al		161.28(6)	161.28(7)	161.21(6)	161.17(6)	161.23(7)	161.21(7)
Si-O3-Al		136.44(6)	136.13(6)	135.98(6)	135.70(6)	135.51(6)	135.40(6)
Si-O4-Al		137.33(7)	137.09(6)	136.84(6)	136.65(6)	136.42(6)	136.29(7)
Ca-	O1(x3)	2.6218(9)	2.620(1)	2.6207(9)	2.6209(9)	2.619(1)	2.620(1)
	O2(x3)	2.5761(8)	2.5752(9)	2.5753(8)	2.5746(9)	2.5738(9)	2.5741(9)
	Cl'	2.654(1)	2.649(1)	2.650(2)	2.644(2)	2.640(1)	2.640(1)
	Cl''	2.685(1)	2.681(1)	2.681(2)	2.677(2)	2.676(1)	2.674(1)
M1	O1	2.917(1)	2.898(1)	2.890(1)	2.877(1)	2.867(1)	2.860(1)
	O3′	2.532(1)	2.525(1)	2.522(1)	2.519(1)	2.511(1)	2.509(1)
	O3′′	2.652(1)	2.653(1)	2.654(1)	2.655(1)	2.655(1)	2.654(1)
	O4′	2.568(1)	2.562(1)	2.557(1)	2.553(1)	2.547(1)	2.543(1)
	O4′′	2.661(1)	2.664(1)	2.665(1)	2.669(1)	2.668(1)	2.671(1)
	O5′	2.493(4)	2.485(3)	2.486(3)	2.488(3)	2.486(3)	2.484(3)
	O5′′	2.411(5)	2.408(5)	2.405(4)	2.392(4)	2.403(4)	2.403(4)
	O5′′′	2.460(3)	2.459(3)	2.461(3)	2.460(3)	2.453(3)	2.456(3)
	O6′	2.37(1)	2.38(1)	2.38(1)	2.38(1)	2.36(1)	2.37(1)
	O6′′	2.74(2)	2.76(2)	2.76(2)	2.78(2)	2.75(2)	2.75(2)
	O6′′′	2.42(1)	2.40(1)	2.40(1)	2.38(1)	2.41(1)	2.39(1)
<M1-O_{fr}>		2.666(1)	2.660(1)	2.658(1)	2.655(1)	2.650(1)	2.647(1)
<M1-O_{CO3}>		2.48(1)	2.48(1)	2.481(9)	2.480(9)	2.476(9)	2.476(9)
M2	O1	2.575(6)	2.569(5)	2.569(5)	2.565(5)	2.551(5)	2.542(5)
	O3′	2.325(5)	2.320(4)	2.318(4)	2.309(4)	2.306(4)	2.305(4)
	O3′′	2.585(5)	2.587(4)	2.590(4)	2.600(4)	2.596(4)	2.597(4)
	O4′	2.337(5)	2.329(5)	2.327(4)	2.333(4)	2.322(4)	2.325(4)

Appendix

O4″	2.605(5)	2.613(4)	2.615(4)	2.611(4)	2.616(4)	2.613(4)
<M2-O_{fr}>	2.485(5)	2.484(4)	2.484(4)	2.484(4)	2.478(4)	2.476(4)
M1↔M2	0.707(6)	0.679(5)	0.661(5)	0.639(5)	0.643(5)	0.636(5)
C1-O5	1.294(3)	1.295(3)	1.291(2)	1.295(3)	1.290(3)	1.289(3)
C2-O6	1.28(1)	1.28(1)	1.30(1)	1.30(1)	1.30(1)	1.30(1)
C1↔C2	3.94(3)	3.97(2)	3.97(2)	3.97(2)	3.99(2)	3.99(2)
$O2\text{-}O2_{S6R\perp[0001]}$	4.448(2)	4.444(2)	4.444(2)	4.442(2)	4.439(2)	4.439(2)
$O2\text{-}O2_{cw}$	8.227(1)	8.215(1)	8.2162(9)	8.214(1)	8.203(1)	8.202(1)
O2-O2-O2	101.06(4)	101.12(3)	101.07(3)	101.02(3)	101.11(3)	101.12(3)
$*O1\text{-}O1_{12R}$	9.387(1)	9.373(2)	9.372(2)	9.367(2)	9.356(2)	9.352(6)
$O3\text{-}O4_{12R}$	8.251(2)	8.239(2)	8.235(2)	8.231(2)	8.219(2)	8.215(2)
$O3\text{-}O4_{S4R}$	4.427(1)	4.424(1)	4.430(1)	4.428(1)	4.427(1)	4.429(1)
φ1 (O1-O4-O3)	137.55(5)	138.43(4)	138.84(4)	139.44(4)	139.89(4)	140.20(4)
φ 2 (O1-O3-O4)	137.40(5)	138.28(4)	138.69(4)	139.27(4)	139.75(4)	140.02(4)
φ 3 (O4-O3-O1)	101.47(5)	100.60(4)	100.15(4)	99.53(4)	99.09(4)	98.81(4)
φ 4 (O3-O4-O1)	101.43(4)	100.56(4)	100.12(4)	99.49(4)	99.06(4)	98.77(4)
O3-O4-O3	162.68(5)	161.81(4)	161.43(4)	160.85(4)	160.43(4)	160.18(4)
$\alpha_{S6R\perp[0001]}$	1.02(3)	1.03(3)	1.04(3)	1.07(3)	1.06(6)	1.08(3)
Δ*z*	1.197(2)	1.186(2)	1.180(2)	1.174(2)	1.168(2)	1.165(2)
V_{cg}	207.24(8)	206.7(1)	206.68(9)	206.39(9)	205.9(1)	206.0(1)
V_{ch}	324.8(1)	323.5(2)	323.2(2)	322.6(2)	321.5(2)	321.2(2)

*$(O1\text{-}O1)_{ch}$ is calculated as the projection onto the (0001) plane

Table 6.6 Unit-cell parameters of balliranoite at different pressures measured using a KUMA KM4 point-detector diffractometer

P (GPa)	*a* (Å)	*c* (Å)	*V* (Å^3)
0.0001*	12.652(9)	5.304(3)	735(1)
0.14(2)	12.640(7)	5.298(3)	733(1)
0.85(3)	12.594(9)	5.268(3)	724(1)
1.21(2)	12.566(10)	5.255(4)	719(2)
1.41(3)	12.549(11)	5.248(4)	716(2)
1.73(3)	12.530(10)	5.233(3)	712(2)
2.00(4)	12.508(9)	5.223(2)	708(1)
2.36(4)	12.486(10)	5.210(3)	703(2)
2.62(4)	12.471(9)	5.199(2)	700(1)
3.12(3)	12.436(11)	5.183(3)	694(2)
3.24(4)	12.431(10)	5.179(3)	693(2)
3.80(5)	12.396(10)	5.160(3)	687(2)
4.14(5)	12.374(12)	5.146(3)	682(2)
4.60(5)	12.351(12)	5.131(3)	678(2)
4.95(3)	12.324(11)	5.120(3)	673(2)
5.40(4)	12.304(9)	5.108(2)	670(1)
5.74(6)	12.290(10)	5.097(3)	667(1)
5.95(4)	12.279(11)	5.090(3)	665(2)
6.22(3)	12.265(10)	5.085(3)	662(1)
6.57(2)	12.252(9)	5.075(2)	660(1)
6.77(2)	12.241(10)	5.070(3)	658(1)

*With the crystal in the DAC without *P*-medium

Appendix

Table 6.7 Details pertaining to the intensity data collections, unit-cell parameters and structure refinements of balliranoite at different pressures

P (GPa)	0.0001 ($P_{0\text{-AIR}}$)	0.0001 ($P_{0\text{-DAC}}$)	0.85(3) (P_1)	1.73(3) (P_2)	2.62(4) (P_3)	3.80(5) (P_4)	4.95(3) (P_5)	5.95(4) (P_6)	6.77(2) (P_7)
Scan width (°/frame)	1	0.5	0.5	0.5	0.5	0.5	0.5	0.5	0.5
a (Å)	12.680(1)	12.669(3)	12.594(5)	12.558(3)	12.502(3)	12.426(3)	12.360(4)	12.289(4)	12.277(3)
c (Å)	5.3141(5)	5.3171(9)	5.284(1)	5.2518(8)	5.2199(9)	5.1780(8)	5.1348(9)	5.100(1)	5.095(1)
V (Å^3)	739.9(1)	739.1(4)	725.6(6)	717.3(4)	706.6(4)	692.4(4)	679.4(5)	667.1(5)	665.1(4)
Maximum 2θ (°)	72.61	61.01	60.64	60.98	60.97	61.01	60.95	60.75	60.82
Measured reflections	19175	3350	3300	3323	3378	3147	3183	3105	3072
Unique reflections	2085	973	964	974	952	930	903	894	884
Unique reflections with $F_0 > 4\sigma(F_0)$	1405	444	459	495	516	488	488	460	414
R_{int}	0.0621	0.0859	0.0811	0.0874	0.0766	0.0858	0.1007	0.1241	0.0963
Number of l.s. parameters	103	43	43	43	43	43	43	43	43
R_1, $F_0 > 4\sigma(F_0)$	0.0447	0.0517	0.0574	0.0556	0.0536	0.0571	0.0621	0.0729	0.0600
R_1, all data	0.0947	0.1236	0.1217	0.1141	0.1024	0.1110	0.1196	0.1411	0.1333
wR^2	0.0450	0.0682	0.0705	0.0724	0.0724	0.0698	0.0772	0.0971	0.0785
Residuals (e^-/ Å^3)	+0.83/ -0.67	+0.93/ -0.90	+0.71/ -0.71	+0.58/ -0.61	+0.67/ -0.71	+0.63/ -0.77	+1.06/ -0.77	+1.18/ -1.04	+0.93/ -0.91

λ: Mokα; ω/ φ-scan type; Exposure time: 60 s; Space group: $P6_3$; $Z = 1$

$R_{int} = \Sigma|F^2_{obs} - (\text{mean})|/\Sigma[F^2_{obs}]$; $R_1 = \Sigma||F_{obs}| - |F_{calc}||/\Sigma|F_{obs}|$; $wR_2 = \{\Sigma[w(F^2_{obs} - F^2_{calc})^2]/\Sigma[w(F^2_{obs})^2]\}^{0.5}$, $w = 1/[\sigma^2(F^2_{obs}) + (0.01\cdot P)^2]$, $P = [\text{Max}(F^2_{obs}, 0) + 2\cdot F^2_{calc}]/3$.

Table 6.8 Atomic fractional coordinates, site occupancy factors (*sof*) and isotropic/equivalent atomic displacement parameters (Å^2) of balliranoite at different pressures.

Site occupancy factors at P_0-AIR					
Site	Occ.	Site	Occ.	Site	Occ.
Si	1.0	O4	1.0	C1	0.56(1)
Al	1.0	Ca	1.0	O5	0.575(8)
O1	1.0	Cl	1/3	C2	0.22(1)
O2	1.0	M1	0.881(6)	O6	0.165(9)
O3	1.0	M2	0.160(6)		

Site fractional coordinates					
P (GPa)	Site	*x*	*y*	*z*	U_{iso}/ U_{eq}
0.0001	Si	0.32757(5)	0.40840(5)	0.7568(1)	0.0088(1)
($P_{0\text{-AIR}}$)	Al	0.06970(5)	0.40846(5)	0.7581(1)	0.0092(1)
	O1	0.2127(1)	0.4268(1)	0.7068(3)	0.0187(4)
	O2	0.0998(1)	0.5565(1)	0.7465(4)	0.0169(3)
	O3	0.0101(1)	0.3312(2)	0.0387(3)	0.0147(5)
	O4	0.3131(2)	0.3407(2)	0.0214(3)	0.0163(4)
	Ca	1/3	2/3	0.7074(1)	0.0156(2)
	Cl	0.323(2)	0.683(2)	0.2115(3)	0.051(2)
	M1	0.1226(1)	0.2514(2)	0.2987(2)	0.0291(6)
	M2	0.1583(7)	0.324(1)	0.281(2)	0.031(2)
	C1	0	0	0.148(3)	0.054(4)
	C2	0	0	0.396(7)	0.054(4)
	O5	-0.0626(5)	0.0548(5)	0.147(2)	0.076(3)
	O6	-0.062(2)	0.052(2)	0.339(6)	0.076(3)
0.0001	Si	0.3278(2)	0.4085(2)	0.7553(4)	0.0100(3)
($P_{0\text{-DAC}}$)	Al	0.0698(2)	0.4091(2)	0.7566(5)	0.0100(3)
	O1	0.2145(4)	0.4284(4)	0.7025(7)	0.0170(6)
	O2	0.1010(3)	0.5575(4)	0.7477(9)	0.0170(6)
	O3	0.0120(5)	0.3316(5)	0.0371(6)	0.0170(6)
	O4	0.3140(6)	0.3415(5)	0.0221(7)	0.0170(6)
	Ca	1/3	2/3	0.7067(3)	0.0160(7)
	Cl	0.322(1)	0.686(1)	0.2127(6)	0.029(2)
	M1	0.1216(3)	0.2499(3)	0.3022(5)	0.029(1)
	M2	0.158(2)	0.318(19)	0.267(4)	0.029(1)
	C1	0	0	0.170(6)	0.080(5)
	C2	0	0	0.42(1)	0.080(5)
	O5	-0.0625(8)	0.0557(8)	0.166(2)	0.057(9)
	O6	-0.0625(8)	0.0557(8)	0.435(7)	0.057(9)
0.85(3)	Si	0.3275(2)	0.4084(2)	0.7588(4)	0.0104(3)
(P_1)	Al	0.0696(2)	0.4085(2)	0.7593(5)	0.0104(3)
	O1	0.2139(5)	0.4274(4)	0.6963(7)	0.0166(6)
	O2	0.1006(4)	0.5560(4)	0.7456(8)	0.0166(6)
	O3	0.0156(5)	0.3315(5)	0.0464(7)	0.0166(6)
	O4	0.3115(6)	0.3433(5)	0.0289(7)	0.0166(6)
	Ca	1/3	2/3	0.6994(3)	0.0175(7)
	Cl	0.319(1)	0.687(1)	0.2065(5)	0.020(1)
	M1	0.1218(4)	0.2494(4)	0.3083(5)	0.028(1)
	M2	0.157(2)	0.318(2)	0.274(4)	0.028(1)
	C1	0	0	0.161(5)	0.041(7)
	C2	0	0	0.410(8)	0.041(7)
	O5	-0.0619(9)	0.0563(9)	0.182(2)	0.068(4)
	O6	-0.0619(9)	0.0563(9)	0.445(6)	0.068(4)
1.73(3)	Si	0.3269(2)	0.4075(2)	0.7622(4)	0.0109(3)
(P_2)	Al	0.0689(2)	0.4078(2)	0.7630(5)	0.0109(3)
	O1	0.2121(5)	0.4255(4)	0.6898(7)	0.0168(6)
	O2	0.1010(3)	0.5568(4)	0.7461(8)	0.0168(6)

	O3	0.0190(5)	0.3333(5)	0.0554(7)	0.0168(6)
	O4	0.3090(5)	0.3446(5)	0.0379(7)	0.0168(6)
	Ca	1/3	2/3	0.6914(3)	0.0187(7)
	Cl	0.322(1)	0.6885(9)	0.1981(5)	0.023(1)
	M1	0.1216(3)	0.2490(3)	0.3167(5)	0.024(1)
	M2	0.152(2)	0.306(2)	0.286(3)	0.024(1)
	C1	0	0	0.159(5)	0.038(6)
	C2	0	0	0.399(8)	0.038(6)
	O5	-0.0612(9)	0.0564(9)	0.196(2)	0.069(4)
	O6	-0.0612(9)	0.0564(9)	0.444(6)	0.069(4)
2.62(4)	Si	0.3264(2)	0.4071(2)	0.7649(4)	0.0110(3)
(P_3)	Al	0.0688(2)	0.4072(2)	0.7661(5)	0.0110(3)
	O1	0.2103(5)	0.4243(4)	0.6857(7)	0.0171(6)
	O2	0.1005(4)	0.5577(4)	0.7452(8)	0.0171(6)
	O3	0.0203(5)	0.3334(5)	0.0615(7)	0.0171(6)
	O4	0.3071(6)	0.3449(5)	0.0455(7)	0.0171(6)
	Ca	1/3	2/3	0.6844(3)	0.0176(7)
	Cl	0.328(1)	0.6926(8)	0.1920(5)	0.022(1)
	M1	0.1217(3)	0.2489(3)	0.3237(5)	0.022(1)
	M2	0.148(2)	0.300(2)	0.286(4)	0.022(1)
	C1	0	0	0.158(5)	0.042(7)
	C2	0	0	0.396(8)	0.042(7)
	O5	-0.0621(9)	0.0557(9)	0.204(2)	0.061(3)
	O6	-0.0621(9)	0.0557(9)	0.439(6)	0.061(3)
3.80(5)	Si	0.3259(2)	0.4064(2)	0.7677(4)	0.0118(3)
(P_4)	Al	0.0693(2)	0.4070(2)	0.7693(5)	0.0118(3)
	O1	0.2092(5)	0.4222(4)	0.6813(7)	0.0169(5)
	O2	0.1010(4)	0.5578(4)	0.7428(7)	0.0169(5)
	O3	0.0244(4)	0.3357(5)	0.0693(7)	0.0169(5)
	O4	0.3050(5)	0.3476(5)	0.0536(7)	0.0169(5)
	Ca	1/3	2/3	0.6770(3)	0.0194(7)
	Cl	0.327(1)	0.6928(8)	0.1852(5)	0.022(1)
	M1	0.1214(4)	0.2487(3)	0.3307(5)	0.0209(9)
	M2	0.143(2)	0.291(2)	0.287(4)	0.0209(9)
	C1	0	0	0.170(5)	0.050(7)
	C2	0	0	0.443(8)	0.050(7)
	O5	-0.0624(8)	0.0566(8)	0.214(2)	0.051(3)
	O6	-0.0624(8)	0.0566(8)	0.404(6)	0.051(3)
4.95(3)	Si	0.3253(2)	0.4065(2)	0.7700(5)	0.0091(3)
(P_5)	Al	0.0691(2)	0.4068(2)	0.7726(6)	0.0091(3)
	O1	0.2086(5)	0.4208(5)	0.6775(8)	0.0137(6)
	O2	0.0991(4)	0.5561(4)	0.7422(8)	0.0137(6)
	O3	0.0256(5)	0.3353(5)	0.0751(8)	0.0137(6)
	O4	0.3030(6)	0.3484(6)	0.0587(8)	0.0137(6)
	Ca	1/3	2/3	0.6702(4)	0.0176(7)
	Cl	0.323(1)	0.691(1)	0.1789(6)	0.021(1)
	M1	0.1214(4)	0.2469(3)	0.3366(6)	0.019(1)
	M2	0.143(2)	0.289(2)	0.298(4)	0.019(1)
	C1	0	0	0.166(5)	0.049(8)
	C2	0	0	0.456(8)	0.049(8)
	O5	-0.0607(9)	0.0584(9)	0.222(2)	0.046(3)
	O6	-0.0607(9)	0.0584(9)	0.410(7)	0.046(3)
5.95(4)	Si	0.3253(2)	0.4061(2)	0.7722(7)	0.0105(4)
(P_6)	Al	0.0691(3)	0.4069(3)	0.7733(7)	0.0105(4)
	O1	0.2083(6)	0.4200(6)	0.675(1)	0.0121(7)
	O2	0.1001(5)	0.5575(5)	0.7402(9)	0.0121(7)
	O3	0.0282(6)	0.3375(6)	0.078(1)	0.0121(7)
	O4	0.3011(7)	0.3477(6)	0.063(1)	0.0121(7)
	Ca	1/3	2/3	0.6648(5)	0.0189(9)
	Cl	0.326(2)	0.694(1)	0.1753(8)	0.025(2)

	M1	0.1219(6)	0.2475(5)	0.3408(7)	0.020(1)
	M2	0.137(3)	0.278(3)	0.288(6)	0.020(1)
	C1	0	0	0.187(7)	0.05(1)
	C2	0	0	0.45(1)	0.05(1)
	O5	-0.062(1)	0.059(1)	0.224(2)	0.040(4)
	O6	-0.062(1)	0.059(1)	0.422(8)	0.040(4)
6.77(2)	Si	0.3253(2)	0.4062(2)	0.7730(6)	0.0110(3)
(P_7)	Al	0.0690(3)	0.4065(2)	0.7762(7)	0.0110(3)
	O1	0.2082(5)	0.4198(6)	0.6731(9)	0.0146(7)
	O2	0.1008(4)	0.5576(5)	0.7376(8)	0.0146(7)
	O3	0.0296(5)	0.3372(5)	0.0794(9)	0.0146(7)
	O4	0.3003(6)	0.3490(5)	0.0647(9)	0.0146(7)
	Ca	1/3	2/3	0.6620(5)	0.0222(8)
	Cl	0.319(1)	0.689(1)	0.1738(7)	0.024(2)
	M1	0.1208(5)	0.2463(4)	0.3425(6)	0.020(1)
	M2	0.139(2)	0.278(2)	0.288(6)	0.020(1)
	C1	0	0	0.189(6)	0.06(1)
	C2	0	0	0.46(1)	0.06(1)
	O5	-0.0625(9)	0.0583(9)	0.230(2)	0.046(4)
	O6	-0.0625(9)	0.0583(9)	0.423(8)	0.046(4)

Appendix

Table 6.9 Site anisotropic displacement parameters (Å^2) of balliranoite at 0.0001 GPa ($P_{0\text{-AIR}}$)

	T_0 (298 K)					
Atom site	U_{11}	U_{22}	U_{33}	U_{12}	U_{13}	U_{23}
Si	0.0080(2)	0.0103(2)	0.0094(3)	0.0053(2)	0.0005(3)	0.0009(3)
Al	0.0085(3)	0.0098(3)	0.0090(3)	0.0044(2)	0.0002(3)	0.0005(3)
O1	0.0128(7)	0.0253(8)	0.021(1)	0.0120(6)	0.0036(7)	0.0083(7)
O2	0.0170(7)	0.0109(6)	0.0232(8)	0.0074(6)	-0.0002(8)	0.0006(8)
O3	0.0147(8)	0.0177(10)	0.012(1)	0.0083(8)	0.0050(6)	0.0037(6)
O4	0.0182(9)	0.0194(9)	0.014(1)	0.0118(8)	-0.0023(6)	0.0028(6)
Ca	0.0148(2)	0.0148(2)	0.0172(5)	0.00738(11)	0	0
Cl	0.073(4)	0.069(5)	0.0146(7)	0.037(2)	-0.017(3)	-0.010(3)
M1	0.0178(7)	0.043(2)	0.0353(8)	0.0222(7)	-0.0039(5)	-0.0051(6)
O5	0.044(3)	0.045(3)	0.153(8)	0.032(2)	0.003(3)	0.028(4)
O6	0.044(8)	0.045(3)	0.153(3)	0.032(3)	0.003(4)	0.028(8)
C1	0.040(4)	0.040(4)	0.083(10)	0.020(2)	0	0
C2	0.040(5)	0.040(5)	0.083(4)	0.020(2)	0	0

Table 6.10 Relevant bond distances (Å), diameters (Å), angles (°), S6R⊥[0001] ditrigonal rotation angle $\alpha_{S6R\perp[0001]}$ (°), hexagonal layers "corrugation" Δz (Å) and cage/channel-volumes (Å³) of balliranoite at different pressures.

P (GPa)		0.0001 ($P_{0\text{-DAC}}$)	0.85(3) (P_1)	1.73(3) (P_2)	2.62(4) (P_3)	3.80(5) (P_4)	4.95(3) (P_5)	4.95(4) (P_6)	6.77(2) (P_7)
Si-	O1	1.602(5)	1.599(6)	1.612(6)	1.624(6)	1.621(5)	1.611(6)	1.609(7)	1.611(6)
	O2	1.598(5)	1.607(5)	1.606(5)	1.591(5)	1.593(5)	1.595(5)	1.582(6)	1.584(6)
	O3	1.635(5)	1.637(5)	1.628(5)	1.618(6)	1.616(5)	1.611(6)	1.612(7)	1.624(6)
	O4	1.618(5)	1.607(5)	1.610(5)	1.619(5)	1.614(5)	1.610(5)	1.609(6)	1.607(5)
<Si-O>		1.613(5)	1.613(5)	1.614(5)	1.613(6)	1.611(5)	1.608(6)	1.603(7)	1.607(6)
Al-	O1	1.748(5)	1.743(6)	1.742(6)	1.724(6)	1.713(5)	1.715(6)	1.712(7)	1.716(6)
	O2	1.718(5)	1.698(5)	1.708(5)	1.722(5)	1.717(5)	1.698(5)	1.701(6)	1.705(6)
	O3	1.734(5)	1.745(5)	1.743(5)	1.743(5)	1.736(5)	1.734(5)	1.721(6)	1.713(6)
	O4	1.743(6)	1.745(6)	1.741(5)	1.733(6)	1.740(5)	1.743(6)	1.735(7)	1.751(7)
<Al-O>		1.736(5)	1.733(6)	1.734(5)	1.731(6)	1.727(5)	1.723(6)	1.717(7)	1.721(6)
Si-O1-Al		155.4(3)	152.9(3)	150.3(3)	148.4(3)	146.4(3)	144.6(3)	143.6(3)	142.3(3)
Si-O2-Al		160.3(3)	160.2(3)	159.4(3)	159.4(3)	158.5(3)	159.3(3)	157.9(4)	156.7(3)
Si-O3-Al		136.1(4)	133.7(4)	132.5(4)	131.7(4)	130.5(4)	129.0(4)	128.6(5)	127.5(4)
Si-O4-Al		137.9(4)	136.4(5)	134.7(4)	133.3(4)	131.6(4)	130.2(4)	128.5(5)	128.1(4)
Ca-	O1(x3)	2.614(4)	2.610(5)	2.623(4)	2.624(4)	2.631(5)	2.632(5)	2.626(7)	2.625(6)
	O2(x3)	2.560(4)	2.551(4)	2.544(4)	2.542(4)	2.525(4)	2.536(4)	2.513(5)	2.504(5)
	Cl'	2.650(4)	2.631(3)	2.616(3)	2.596(3)	2.573(3)	2.551(3)	2.526(4)	2.519(4)
	Cl''	2.712(4)	2.705(3)	2.686(3)	2.675(3)	2.657(3)	2.639(3)	2.632(5)	2.638(4)
M1	O1	2.893(5)	2.824(5)	2.744(5)	2.679(5)	2.604(5)	2.555(6)	2.505(8)	2.499(7)
	O3′	2.534(6)	2.481(6)	2.456(6)	2.436(6)	2.399(6)	2.386(7)	2.372(8)	2.356(7)
	O3″	2.584(6)	2.542(7)	2.509(6)	2.478(6)	2.444(6)	2.415(6)	2.379(8)	2.381(7)
	O4′	2.658(6)	2.655(6)	2.671(6)	2.658(6)	2.675(6)	2.654(6)	2.654(8)	2.661(7)
	O4″	2.670(7)	2.688(6)	2.703(6)	2.701(6)	2.720(6)	2.731(7)	2.716(9)	2.727(7)
	O5′	2.507(11)	2.467(11)	2.443(11)	2.440(11)	2.414(11)	2.367(11)	2.368(13)	2.350(12)
	O5″	2.414(9)	2.437(10)	2.453(10)	2.440(10)	2.426(8)	2.405(7)	2.374(10)	2.385(9)
	O5‴	2.462(11)	2.433(11)	2.417(11)	2.395(11)	2.378(10)	2.363(12)	2.348(12)	2.328(12)
	O6′	2.50(2)	2.481(14)	2.452(14)	2.435(14)	2.368(11)	2.323(12)	2.328(14)	2.317(13)
	O6″	2.43(3)	2.40(3)	2.42(3)	2.46(3)	2.61(3)	2.58(3)	2.53(4)	2.52(3)
	O6‴	2.457(14)	2.448(14)	2.426(13)	2.389(13)	2.331(11)	2.319(12)	2.308(14)	2.294(13)
<M1-O_{fr}>		2.668(6)	2.638(6)	2.617(6)	2.590(6)	2.568(6)	2.548(6)	2.525(8)	2.525(7)
<M1-O_{CO3}>		2.462(16)	2.444(15)	2.435(15)	2.427(15)	2.421(12)	2.393(14)	2.376(17)	2.366(15)
M2	O1	2.61(2)	2.53(2)	2.49(2)	2.49(2)	2.49(2)	2.40(2)	2.49(3)	2.48(3)
	O3′	2.29(2)	2.23(2)	2.22(2)	2.18(2)	2.14(2)	2.14(2)	2.11(3)	2.10(3)
	O3″	2.26(2)	2.22(2)	2.20(2)	2.18(2)	2.14(2)	2.12(2)	2.10(3)	2.06(3)
	O4′	2.63(2)	2.63(2)	2.64(2)	2.67(2)	2.70(2)	2.67(2)	2.73(3)	2.72(3)
	O4″	2.69(2)	2.70(2)	2.72(2)	2.73(2)	2.77(2)	2.76(2)	2.79(3)	2.83(3)
<M2-O_{fr}>		2.47(2)	2.45(2)	2.45(2)	2.44(2)	2.44(2)	2.42(2)	2.43(3)	2.43(3)
M1↔M2		0.77(2)	0.77(2)	0.64(2)	0.59(2)	0.50(2)	0.49(2)	0.42(3)	0.44(3)
C1-O5		1.297(4)	1.294(4)	1.294(4)	1.298(4)	1.301(5)	1.306(5)	1.300(5)	1.302(5)
C2-O6		1.301(5)	1.303(5)	1.300(5)	1.296(5)	1.297(5)	1.296(5)	1.296(5)	1.296(5)
C1↔C2		3.96(6)	3.96(5)	3.87(5)	3.85(5)	4.00(5)	4.06(5)	3.90(6)	3.92(6)
O2-$O2_{S6R\perp[0001]}$		4.418(7)	4.398(8)	4.379(7)	4.369(8)	4.333(8)	4.345(8)	4.302(10)	4.285(8)
O2-$O2_{cw}$		8.255(5)	8.198(6)	8.183(5)	8.137(5)	8.097(5)	8.019(5)	7.991(6)	7.996(6)
O2-O2-O2		100.2(2)	100.5(2)	100.0(2)	100.2(2)	99.8(1)	100.7(2)	100.0(2)	99.7(2)
*O1-$O1_{ch12R}$		9.400(7)	9.323(8)	9.255(8)	9.189(8)	9.087(8)	9.008(8)	8.940(10)	8.927(8)

Appendix

$O3\text{-}O4_{12R}$	8.279(11)	8.202(11)	8.173(10)	8.120(11)	8.077(9)	8.015(11)	7.964(13)	7.947(11)
$O3\text{-}O4_{S4R}$	4.400(10)	4.399(10)	4.392(10)	4.390(10)	4.357(10)	4.354(11)	4.333(12)	4.339(10)
φ1 (O1-O4-O3)	138.7(2)	142.2(2)	145.6(2)	147.6(2)	151.3(2)	153.4(2)	155.1(3)	156.4(2)
φ2 (O1-O3-O4)	138.2(2)	142(2)	145.6(2)	147.6(2)	151.3(2)	153.2(2)	154.8(3)	156.1(3)
φ3 (O4-O3-O1)	100.3(2)	96.9(2)	93.3(2)	91.2(2)	87.7(2)	85.7(2)	84(3)	83(2)
φ4 (O3-O4-O1)	100.6(2)	96.8(2)	93.3(2)	91.2(2)	87.6(2)	85.6(2)	84.1(2)	82.8(2)
O3-O4-O3	161.4(2)	157.7(2)	154.4(2)	152.8(2)	148.8(2)	146.9(2)	145.3(3)	143.8(2)
S6R⊥[0001] α	1.2(1)	1.4(1)	1.8(1)	1.9(1)	2.4(1)	2.3(2)	2.7(2)	2.9(2)
Δ*z*	1.200(9)	1.145(8)	1.093(8)	1.042(8)	0.980(7)	0.942(8)	0.903(10)	0.881(9)
V_{cg}	326.3(7)	318.6(8)	313.2(7)	307.1(7)	299.5(7)	292.2(7)	286.2(8)	284.8(7)
V_{ch}	206.4(6)	203.45(7)	202.1(6)	199.8(6)	196.4(5)	193.6(6)	190.5(7)	190.1(6)

*$(O1\text{-}O1)_{ch}$ is calculated as the projection onto the (0001) plane

Table 7.1 Chemical composition of the davyne used in L*T* X-ray and room-*T* neutron diffraction experiments, averaged from 20 EMPA-WDS data points.

	wt%
SiO_2	33.43
Al_2O_3	28.33
FeO	0.07
MgO	0.07
CaO	9.82
Na_2O	11.43
K_2O	7.82
SO_3	4.82
Cl	6.44
O=Cl	-1.45
Total	100.78
Number of atoms per formula unit on the basis of (Si + Al) = 12 apfu	
Si	6.01
Al	5.99
Fe	0.01
Mg	0.02
Ca	1.89
Na	3.98
K	1.79
S	0.65
Cl	1.96

Appendix

Table 7.2 Details pertaining to the data collection protocol, unit-cell parameters and structure refinements of davyne based on X-ray diffraction experiments at different temperatures and neutron diffraction (N.D.) at room-*T*.

T (K)	293 (T_0)	250 (T_1)	220 (T_2)	180 (T_3)	140 (T_4)	110 (T_5)	N.D.
a (Å)	12.7908(5)	12.7764(4)	12.7713(5)	12.7658(5)	12.7599(4)	12.7560(6)	12.7615(7)
c (Å)	5.3469(2)	5.3407(2)	5.3387(2)	5.3353(2)	5.3321(2)	5.3308(2)	5.3416(3)
V (Å^3)	757.59(6)	755.02(4)	754.13(5)	753.00(5)	751.85(4)	751.20(4)	753.36(7)
Maximum 2θ (°)	63.18	63.00	63.03	63.06	63.10	63.07	75.54
	-14≤ *h* ≤18	-11≤ *h* ≤17	-18≤ *h* ≤18	-18≤ *h* ≤14	-11≤ *h* ≤17	-18≤ *h* ≤18	-1≤ *h* ≤15
	-18≤ *k* ≤18	-18≤ *k* ≤14	-17≤ *k* ≤11	-18≤ *k* ≤18	-18≤ *k* ≤14	-18≤ *k* ≤11	-18≤ *k* ≤16
	-7≤ *l* ≤6	-7≤ *l* ≤6	-6≤ *l* ≤7	-7≤ *l* ≤7	-7≤ *l* ≤6	-6≤ *l* ≤7	-7≤ *l* ≤7
Measured reflections	6128	6104	6125	6148	6139	6141	2362
Unique reflections	1544	1538	1537	1540	1535	1532	1351
Unique reflections with $F_0 > 4\sigma(F_0)$	1428	1413	1420	1435	1451	1458	1185
R_{int}	0.0245	0.0250	0.0277	0.0295	0.0264	0.0275	0.0305
Number of l.s. parameters	95	92	92	92	90	90	69
R_1, $F_0 > 4\sigma(F_0)$	0.0422	0.0393	0.0406	0.0391	0.0367	0.0381	0.0684
R_1, all data	0.0467	0.0439	0.0450	0.0425	0.0399	0.0407	0.0806
wR_2	0.0756	0.0716	0.0765	0.0736	0.0705	0.0687	0.1132
Residuals (eÅ^{-3}; fmÅ^{-3})	+1.09/-0.95	+0.89/-0.77	+0.88/-0.79	+0.86/-0.68	+0.79/-0.69	+0.91/-0.63	+1.05/-0.91

LT experiment: ω-scan type; step scan = 1°; exposure time = 10 s. Space group: $P6_3$; $Z = 1$

Note: $R_{int} = \Sigma|F^2_{obs} - (\text{mean})|/\Sigma[F^2_{obs}]$; $R_1 = \Sigma||F_{obs}| - |F_{calc}||/\Sigma|F_{obs}|$; $wR_2 = \{\Sigma[w(F^2_{obs} - F^2_{calc})^2]/\Sigma[w(F^2_{obs})^2]\}^{0.5}$, $w = 1/[\sigma^2(F^2_{obs}) + (0.01\cdot P)^2]$, $P = [\text{Max}(F^2_{obs},0) + 2\cdot F^2_{calc}]/3$.

Table 7.3 Atomic fractional coordinates, site occupancy factors (*sof*) and equivalent/isotropic atomic displacement parameters (Å^2) of davyne at different temperatures. Structure refinements based on X-ray intensity data

Atom site	*T* (K)	*s.o.f.*	*x*	*y*	*z*	U_{eq}/U_{iso}
Si	293	1.0	0.32894(2)	0.41053(2)	0.74958(8)	0.00666(7)
	250	"	0.32885(2)	0.41050(2)	0.74914(7)	0.00580(6)
	220	"	0.32880(2)	0.41039(2)	0.74844(6)	0.00539(6)
	180	"	0.32876(2)	0.41036(2)	0.74791(6)	0.00481(5)
	140	"	0.32868(2)	0.41032(2)	0.74751(5)	0.00374(5)
	110	"	0.32860(2)	0.41022(2)	0.74742(5)	0.00375(5)
Al	293	1.0	0.07078(2)	0.41062(2)	0.74930(9)	0.00688(7)
	250	"	0.07077(2)	0.41051(2)	0.74838(8)	0.00607(7)
	220	"	0.07076(2)	0.41050(2)	0.74778(7)	0.00541(6)
	180	"	0.07073(2)	0.41042(2)	0.74716(6)	0.00504(6)
	140	"	0.07065(2)	0.41026(2)	0.74688(6)	0.00402(6)
	110	"	0.07056(2)	0.41020(2)	0.74668(6)	0.00390(6)
O1	293	"	0.21209(6)	0.42550(7)	0.7706(2)	0.0227(2)
	250	"	0.21188(6)	0.42536(7)	0.7758(2)	0.0201(2)
	220	"	0.21212(5)	0.42549(6)	0.7782(2)	0.0190(2)
	180	"	0.21188(5)	0.42531(5)	0.7815(1)	0.0170(2)
	140	"	0.21207(5)	0.42532(5)	0.7832(1)	0.0151(2)
	110	"	0.21198(5)	0.42519(5)	0.7848(1)	0.0142(2)
O2	293	"	0.10648(6)	0.55976(6)	0.7501(2)	0.0168(2)
	250	"	0.10635(6)	0.55962(6)	0.7520(2)	0.0151(2)
	220	"	0.10653(5)	0.55977(5)	0.7521(2)	0.0140(2)
	180	"	0.10637(5)	0.55963(5)	0.7531(2)	0.0129(2)
	140	"	0.10647(5)	0.55970(5)	0.7537(2)	0.0109(2)
	110	"	0.10645(5)	0.55969(5)	0.7542(2)	0.0106(2)
O3	293	"	-0.01723(8)	0.32252(8)	-0.0115(1)	0.0165(3)
	250	"	-0.01867(8)	0.32205(8)	-0.0131(1)	0.0148(3)
	220	"	-0.01992(6)	0.32111(6)	-0.0131(1)	0.0147(2)
	180	"	-0.02096(6)	0.32059(6)	-0.0145(1)	0.0138(2)
	140	"	-0.02159(6)	0.32018(6)	-0.0156(1)	0.0124(2)
	110	"	-0.02216(6)	0.31977(6)	-0.0162(1)	0.0116(2)
O4	293	"	0.33092(8)	0.33027(8)	-0.0271(1)	0.0177(3)
	250	"	0.33185(8)	0.32936(8)	-0.0286(1)	0.0164(3)
	220	"	0.33212(6)	0.32883(7)	-0.0289(1)	0.0153(2)
	180	"	0.33262(6)	0.32808(6)	-0.0301(1)	0.0148(2)
	140	"	0.33264(6)	0.32727(6)	-0.0311(1)	0.0137(2)
	110	"	0.33312(6)	0.32708(6)	-0.0319(1)	0.0134(2)
Ca	293	1.0	1/3	2/3	0.7689(1)	0.0200(1)
	250	"	1/3	2/3	0.7727(1)	0.0187(1)
	220	"	1/3	2/3	0.77514(9)	0.0175(1)
	180	"	1/3	2/3	0.77747(8)	0.0165(1)
	140	"	1/3	2/3	0.77983(8)	0.01465(9)
	110	"	1/3	2/3	0.78069(8)	0.01433(9)
Cl	293	1/3*	0.3151(2)	0.6355(1)	0.2609(3)	0.0455(3)
	250	"	0.3146(2)	0.6363(1)	0.2659(2)	0.0426(3)
	220	"	0.3153(2)	0.63671(8)	0.2698(2)	0.0399(3)
	180	"	0.3156(2)	0.63719(7)	0.2730(2)	0.0363(2)

Appendix

	140	"	0.3163(2)	0.63772(7)	0.2757(2)	0.0326(2)
	110	"	0.3164(1)	0.63811(7)	0.2767(2)	0.0308(2)
Na1	293	0.281(1)	0.1501(1)	0.3063(1)	0.2272(4)	0.0162(3)
	250	0.286(1)	0.1504(1)	0.3070(1)	0.2237(4)	0.0142(3)
	220	0.2877(9)	0.1505(1)	0.3070(1)	0.2224(3)	0.0120(2)
	180	0.2964(9)	0.15083(9)	0.3080(1)	0.2213(3)	0.0106(2)
	140	0.2870(9)	0.15033(9)	0.3068(1)	0.2183(3)	0.0085(2)
	110	0.2842(9)	0.14996(9)	0.3062(1)	0.2174(3)	0.0073(2)
Na2	293	0.152(1)	0.1692(2)	0.3475(3)	0.2386(9)	0.0162(3)
	250	0.147(1)	0.1692(2)	0.3483(3)	0.2343(8)	0.0142(3)
	220	0.1447(9)	0.1695(2)	0.3486(2)	0.2304(7)	0.0120(2)
	180	0.1360(9)	0.1705(2)	0.3500(2)	0.2261(6)	0.0106(2)
	140	0.1454(9)	0.1691(2)	0.3473(2)	0.2256(6)	0.0085(2)
	110	0.1482(9)	0.1689(2)	0.3470(2)	0.2242(5)	0.0073(2)
K	293	0.4493(8)	0.11033(5)	0.22594(7)	0.2313(2)	0.0407(2)
	250	"	0.11006(5)	0.22554(6)	0.2295(2)	0.0372(2)
	220	"	0.11009(4)	0.22537(5)	0.2279(2)	0.0351(2)
	180	"	0.11000(4)	0.22502(5)	0.2267(2)	0.0328(2)
	140	"	0.10976(4)	0.22446(5)	0.2250(2)	0.0300(2)
	110	"	0.10961(4)	0.22413(5)	0.2243(1)	0.0285(2)
S	293	0.342(1)	0	0	0.2212(4)	0.0253(4)
	250	"	0	0	0.2179(4)	0.0228(4)
	220	"	0	0	0.2175(3)	0.0234(3)
	180	"	0	0	0.2163(3)	0.0233(3)
	140	"	0	0	0.2140(3)	0.0217(3)
	110	"	0	0	0.2127(3)	0.0217(3)
OA	293	0.1138(5)**	0.023(1)	0.009(9)	0.467(2)	0.090(2)
	250	"	0.025(1)	0.011(7)	0.467(2)	0.079(2)
	220	"	0.018(1)	0.008(9)	0.454(1)	0.074(1)
	180	"	0.021(1)	0.009(6)	0.450(1)	0.064(1)
	140	0.342(1)	0	0	0.448(1)	0.065(1)
	110	"	0	0	0.448(1)	0.065(1)
OB1	293	0.1707(7)	0.0654(9)	0.1133(9)	0.125(2)	0.090(2)
	250	"	0.0650(9)	0.1145(9)	0.114(2)	0.079(2)
	220	"	0.0635(7)	0.1124(7)	0.102(2)	0.074(1)
	180	"	0.0636(6)	0.1136(6)	0.096(1)	0.064(1)
	140	"	0.0630(6)	0.1152(6)	0.091(2)	0.065(1)
	110	"	0.0623(6)	0.1156(6)	0.089(2)	0.065(1)
OB2	293	0.1707(7)	0.055(1)	0.115(1)	0.378(2)	0.090(2)
	250	"	0.0559(8)	0.1181(9)	0.364(2)	0.079(2)
	220	"	0.0591(7)	0.1181(7)	0.358(1)	0.074(1)
	180	"	0.0591(6)	0.1190(6)	0.358(1)	0.064(1)
	140	"	0.0595(6)	0.1165(6)	0.357(1)	0.065(1)
	110	"	0.0615(6)	0.1188(6)	0.356(1)	0.065(1)

* The highest occupancy for each of the three symmetrically equivalent and mutually exclusive Cl sites is 1/3
** The OA occupancy is constrained to be equal to that of S at 140 and 110 K, where both the sites lie on a 2*a* position; at *T* > 140 K, OA is split into three symmetrically equivalent and mutually exclusive sites, being *sof*(OA) = 1/3***sof*(S).

Table 7.4 Site anisotropic displacement parameters (Å^2) of davyne from X-ray diffraction refinements at different temperatures and from the neutron diffraction refinement at room-*T*

Atom site	U_{11}	U_{22}	U_{33}	U_{12}	U_{13}	U_{23}
			T_0 (298 K)			
Si	0.00588(9)	0.0079(1)	0.0067(1)	0.00383(7)	0.0002(2)	-0.0013(2)
Al	0.0069(1)	0.0077(1)	0.0067(1)	0.00412(8)	-0.0012(2)	-0.0008(2)
O1	0.0112(3)	0.0239(3)	0.0376(5)	0.0122(2)	-0.0039(5)	-0.0073(5)
O2	0.0162(3)	0.0106(3)	0.0246(4)	0.0074(2)	-0.0062(6)	-0.0008(5)
O3	0.0258(4)	0.0179(4)	0.0086(5)	0.0131(3)	0.0024(3)	-0.0012(3)
O4	0.0222(4)	0.0202(4)	0.0080(5)	0.0085(3)	-0.0071(3)	0.0010(3)
Ca	0.0133(1)	0.0133(1)	0.0334(3)	0.00666(6)	0	0
K	0.0234(2)	0.0570(3)	0.0516(5)	0.0277(2)	0.0029(5)	0.0055(5)
			T_1 (250 K)			
Si	0.00525(9)	0.00676(9)	0.0057(1)	0.00326(7)	0.0004(2)	-0.0009(1)
Al	0.0060(1)	0.0070(1)	0.0057(1)	0.00359(8)	-0.0008(2)	-0.0007(2)
O1	0.0105(3)	0.0223(3)	0.0320(5)	0.0116(2)	-0.0043(4)	-0.0072(5)
O2	0.0142(3)	0.0092(3)	0.0217(4)	0.0057(2)	-0.0031(5)	0.0008(5)
O3	0.0228(4)	0.0147(3)	0.0084(5)	0.0105(3)	0.0022(3)	-0.0010(3)
O4	0.0212(4)	0.0200(4)	0.0054(5)	0.0085(3)	-0.0063(3)	0.0013(3)
Ca	0.0121(1)	0.0121(1)	0.0321(3)	0.00604(6)	0	0
K	0.0212(2)	0.0513(3)	0.0484(4)	0.0250(2)	0.0030(4)	0.0042(5)
			T_2 (220 K)			
Si	0.00491(7)	0.00652(8)	0.0052(1)	0.00317(6)	0.0005(1)	-0.0009(1)
Al	0.00568(8)	0.00624(9)	0.0048(1)	0.00337(6)	-0.0008(1)	-0.0005(1)
O1	0.0104(2)	0.0201(3)	0.0298(4)	0.0103(2)	-0.0037(3)	-0.0072(4)
O2	0.0138(2)	0.0091(2)	0.0199(3)	0.0065(2)	-0.0031(4)	-0.0007(4)
O3	0.0211(3)	0.0136(3)	0.0101(4)	0.0092(2)	0.0038(3)	-0.0004(3)
O4	0.0189(3)	0.0162(3)	0.0066(4)	0.0057(2)	-0.0073(3)	0.0008(3)
Ca	0.01143(9)	0.01143(9)	0.0296(2)	0.00572(5)	0	0
K	0.0194(2)	0.0490(3)	0.0454(4)	0.0235(2)	0.0020(3)	0.0038(4)
			T_3 (180 K)			
Si	0.00449(7)	0.00583(8)	0.00447(9)	0.00285(6)	0.0004(1)	-0.0007(1)
Al	0.00523(8)	0.00644(8)	0.00423(1)	0.00345(6)	-0.0006(1)	-0.0004(1)
O1	0.0099(2)	0.0196(2)	0.0254(4)	0.0104(2)	-0.0042(3)	-0.0077(3)
O2	0.0118(2)	0.0079(2)	0.0184(3)	0.0046(2)	-0.0009(3)	0.0007(3)
O3	0.0204(3)	0.0137(3)	0.0091(4)	0.0098(2)	0.0037(3)	-0.0006(2)
O4	0.0171(3)	0.0149(3)	0.0089(4)	0.0054(2)	-0.0060(3)	0.0013(3)
Ca	0.01073(9)	0.01073(9)	0.0281(2)	0.00537(5)	0	0
K	0.0180(2)	0.0457(2)	0.0433(3)	0.0223(2)	0.0016(3)	0.0028(3
			T_4 (140 K)			
Si	0.00337(7)	0.00462(7)	0.00364(9)	0.00232(5)	0.0002(1)	-0.0006(1)

Appendix

Al	0.00393(8)	0.00484(8)	0.0036(1)	0.00243(6)	-0.0005(1)	-0.0004(1)
O1	0.0097(2)	0.0158(2)	0.0228(4)	0.0086(2)	-0.0033(3)	-0.0068(3)
O2	0.0106(2)	0.0064(2)	0.0160(3)	0.0044(2)	-0.0016(3)	-0.0004(3)
O3	0.0178(3)	0.0131(3)	0.0079(4)	0.0088(2)	0.0043(3)	0.0000(2)
O4	0.0152(3)	0.0127(3)	0.0086(4)	0.0036(2)	-0.0060(3)	0.0019(2)
Ca	0.00894(9)	0.00894(9)	0.0261(2)	0.00447(4)	0	0
K	0.01487(16)	0.0423(2)	0.0398(3)	0.01960(14)	0.0016(3)	0.0034(3)
			T_5 (110 K)			
Si	0.00344(7)	0.00431(7)	0.00370(9)	0.00207(5)	0.0005(1)	-0.0005(1)
Al	0.00360(8)	0.00482(8)	0.0036(1)	0.00233(6)	-0.0003(1)	0.0000(1)
O1	0.0087(2)	0.0159(2)	0.0214(4)	0.0088(2)	-0.0035(3)	-0.0064(3)
O2	0.0103(2)	0.0063(2)	0.0147(3)	0.0039(2)	-0.0013(3)	-0.0003(3)
O3	0.0181(3)	0.0110(2)	0.0072(3)	0.0085(2)	0.0037(2)	0.0000(2)
O4	0.0146(3)	0.0137(3)	0.0075(3)	0.0038(2)	-0.0057(3)	0.0017(2)
Ca	0.00830(8)	0.00830(8)	0.0264(2)	0.00415(4)	0	0
K	0.0145(2)	0.0388(2)	0.0391(3)	0.0185(1)	0.0014(3)	0.0033(3)
			Neutron diffraction refinement			
Si	0.0077(6)	0.0091(6)	0.0060(5)	0.0036(5)	0.0030(9)	-0.0004(9)
Al	0.0066(7)	0.0081(7)	0.0080(6)	0.0041(6)	-0.002(1)	-0.001(1)
O1	0.015	0.03	0.03	0.016	0.004	0.007
O2	0.011	0.011	0.026	0.001	0.001	0
O3	0.021	0.021	0.02	0.003	0.008	0
O4	0.022	0.02	0.015	0.006	0	0.008
Cl	0.063	0.061	0.03	0.017	0.004	0.006
Ca	0.0152(7)	0.0152(7)	0.035(2)	0.0076(4)	0	0

Table 7.5 Atomic fractional coordinates, site occupancy factors (*sof*) and equivalent/isotropic atomic displacement parameters (Å^2) of davyne from the structure refinement based on neutron diffraction intensity data at room-*T*

Atom site	*s.o.f.*	*x*	*y*	*z*	U_{eq}/U_{iso}
Si	1.0	0.3296(1)	0.4105(1)	0.7785(5)	0.0079(3)
Al	"	0.0709(2)	0.4100(2)	0.7779(7)	0.0074(3)
O1	"	0.2132(1)	0.4268(2)	0.7700(5)	0.0232
O2	"	0.4413(1)	0.5460(1)	0.7753(5)	0.0185
O3	"	0.3297(2)	0.3307(2)	0.5461(3)	0.0240
O4	"	0.3224(2)	0.3369(2)	0.0302(2)	0.0209
Ca	"	1/3	2/3	0.767(1)	0.0219(6)
Cl	1/3	0.3619(5)	0.685(1)	0.272(1)	0.0577
Na1	0.241(2)	0.135(1)	0.274(2)	0.254(3)	0.022(2)
Na2	0.28(1)	0.1600(6)	0.328(1)	0.297(3)	"
K	0.44(2)	0.1090(6)	0.2260(8)	0.298(2)	0.032(2)
S	0.35(2)	0	0	0.320(2)	0.015(3)
OA	0.35(2)	0	0	0.048(2)	0.081(4)
OB1	0.19(2)	0.060(2)	0.117(1)	0.191(4)	"
OB2	0.16(2)	0.060(3)	0.120(1)	0.429(5)	"
OB3	0.21(2)	0.108(1)	0.058(2)	0.162(3)	"

Appendix

Table 7.6 Relevant bond distances (Å), angles (°), diameters (Å), S6R⊥[0001] ditrigonal rotation angle $\alpha_{S6R\perp[0001]}$ (°) of davyne and deviation from planarity parameter $dz_{S6R\perp[0001]}$ (Å), A- and B-layers "corrugation" parameter Δz (Å) based on X-ray structure refinements at different temperatures and on neutron structure refinement (N.D.) at room-*T*

	T (K)	293 (T_0)	250 (T_1)	220 (T_2)	180 (T_3)	140 (T_4)	110 (T_5)	N.D.
	Si-O1-Al	166.15(7)	164.87(6)	164.02(5)	163.05(5)	162.45(5)	161.99(5)	165.7(2)
	Si-O2-Al	156.87(5)	156.96(5)	156.80(4)	156.88(4)	156.77(4)	156.73(4)	158.1(1)
	Si-O3-Al	141.83(7)	141.85(6)	141.43(5)	141.24(5)	141.05(5)	140.86(5)	141.0(2)
	Si-O4-Al	141.52(6)	141.24(5)	141.06(4)	140.73(4)	140.29(4)	140.26(4)	141.4(2)
Si-	O1	1.6030(9)	1.6042(9)	1.6032(8)	1.6061(8)	1.6036(7)	1.6042(7)	1.602(2)
	O2	1.6067(9)	1.6062(9)	1.6063(7)	1.6067(7)	1.6066(7)	1.6073(7)	1.600(2)
	O3	1.6436(9)	1.6388(9)	1.6302(8)	1.6283(7)	1.6281(8)	1.6274(7)	1.607(3)
	O4	1.5830(9)	1.5890(9)	1.5948(8)	1.5999(8)	1.6037(8)	1.6041(7)	1.615(3)
	<Si-O>	1.6091(9)	1.6095(9)	1.6086(8)	1.6103(8)	1.6105(8)	1.6108(7)	1.606(3)
Al-	O1	1.7238(9)	1.7222(9)	1.7254(7)	1.7245(7)	1.7274(7)	1.7283(7)	1.721(2)
	O2	1.7253(8)	1.7236(8)	1.7241(7)	1.7233(7)	1.7248(6)	1.7247(6)	1.723(2)
	O3	1.7041(8)	1.7073(8)	1.7180(7)	1.7203(6)	1.7196(6)	1.7213(6)	1.734(4)
	O4	1.7645(9)	1.7557(9)	1.7506(8)	1.7464(7)	1.7457(7)	1.7435(7)	1.724(3)
	<Al-O>	1.7294(9)	1.7272(9)	1.7295(7)	1.7286(7)	1.7294(7)	1.7295(7)	1.726(3)
Ca-	O1(x3)	2.6715(8)	2.6701(7)	2.6675(6)	2.6685(6)	2.6670(6)	2.6677(6)	2.652(2)
	O2(x3)	2.5162(7)	2.5153(7)	2.5129(6)	2.5140(6)	2.5121(6)	2.5117(6)	2.529(1)
	Cl'	2.653(2)	2.656(1)	2.662(1)	2.664(1)	2.6633(9)	2.6631(9)	2.664(10)
	Cl''	2.738(2)	2.728(2)	2.718(1)	2.711(1)	2.7074(9)	2.7053(9)	2.716(10)
Na1	O1	2.776(2)	2.728(2)	2.710(2)	2.681(2)	2.665(2)	2.655(2)	3.13(2)
	O3′	2.460(2)	2.455(2)	2.446(2)	2.437(2)	2.437(1)	2.435(1)	2.45(2)
	O4′	2.467(2)	2.454(2)	2.450(2)	2.435(2)	2.434(2)	2.430(2)	2.42(1)
	O3′′	2.588(2)	2.592(2)	2.597(2)	2.602(2)	2.603(2)	2.604(2)	2.71(2)
	O4′′	2.565(2)	2.571(2)	2.571(2)	2.580(2)	2.577(2)	2.583(2)	2.72(2)
	OB1	2.213(11)	2.213(11)	2.251(8)	2.254(7)	2.226(7)	2.216(7)	2.41(2)
	OB2	2.271(11)	2.220(10)	2.212(8)	2.213(7)	2.230(7)	2.199(7)	2.41(2)
	OB3′							2.65(3)
	OB3′′							2.73(2)
	<Na1-$O_{framework}$>	2.571(2)	2.560(2)	2.555(2)	2.547(2)	2.543(2)	2.541(2)	2.69(2)
	<Na-O3,O4>	2.520(2)	2.518(2)	2.516(2)	2.514(2)	2.513(2)	2.513(2)	2.58(2)
Na2	O1	2.647(5)	2.594(4)	2.560(4)	2.514(3)	2.512(3)	2.497(3)	2.70(2)
	O3′	2.416(4)	2.416(4)	2.413(3)	2.410(3)	2.401(3)	2.397(3)	2.46(1)
	O4′	2.410(4)	2.394(4)	2.398(3)	2.399(3)	2.385(3)	2.381(3)	2.47(1)
	O3′′	2.610(4)	2.610(4)	2.611(3)	2.616(3)	2.617(3)	2.619(3)	2.53(1)
	O4′′	2.608(4)	2.619(4)	2.612(3)	2.610(3)	2.613(3)	2.617(3)	2.52(1)
	OB1	2.671(11)	2.670(10)	2.706(8)	2.707(7)	2.667(8)	2.659(8)	2.41(2)
	OB2	2.686(11)	2.640(10)	2.640(8)	2.649(7)	2.647(7)	2.619(7)	2.41(2)
	<Na2-$O_{framework}$>	2.538(4)	2.527(4)	2.519(3)	2.510(3)	2.506(3)	2.502(3)	2.54(1)
	<Na2-O3,O4>	2.511(4)	2.510(4)	2.509(3)	2.509(3)	2.504(3)	2.504(3)	2.50(1)
K	O1	3.310(1)	3.280(1)	3.266(1)	3.247(1)	3.237(1)	3.2287(9)	3.321(10)
	O3′	2.725(1)	2.721(1)	2.7158(9)	2.7107(9)	2.7099(9)	2.7073(8)	2.717(11)
	O3′′	2.706(1)	2.696(1)	2.695(1)	2.689(1)	2.685(1)	2.6842(9)	2.735(11)
	O4′	2.809(2)	2.816(1)	2.817(1)	2.825(1)	2.827(1)	2.830(1)	2.777(8)
	O4′′	2.808(1)	2.816(1)	2.8141(9)	2.8189(9)	2.8183(9)	2.8238(8)	2.758(8)
	$OA'_{(z)}$	2.81(9)	2.81(7)	2.77(9)	2.77(6)	2.751(3)	2.749(3)	2.832(11)
	$OA''_{(z+0.5)}$	2.88(9)	2.87(7)	2.90(8)	2.90(6)	2.887(3)	2.880(3)	2.834(11)
	$OB1'_{(z+0.5)}$	2.929(9)	2.900(8)	2.862(7)	2.846(7)	2.840(7)	2.839(7)	2.98(2)
	$OB1''_{(z+0.5)}$	3.114(11)	3.068(11)	3.023(9)	2.998(8)	2.965(8)	2.948(8)	3.05(2)
	$OB2'_{(z-0.5)}$	2.869(13)	2.898(11)	2.912(7)	2.912(6)	2.886(6)	2.875(6)	2.90(3)
	$OB2''_{(z-0.5)}$	2.885(10)	2.931(8)	2.939(9)	2.928(8)	2.934(8)	2.939(8)	2.95(3)

<K-$O_{framework}$>		2.762(1)	2.763(1)	2.761(1)	2.761(1)	2.760(1)	2.7613(9)	2.862(10)
S	OA1	1.339(12)	1.357(10)	1.277(8)	1.269(7)	1.247(6)	1.256(6)	1.22(1)
	OB1	1.362(10)	1.386(9)	1.391(8)	1.413(7)	1.434(6)	1.440(6)	1.46(2)
	OA2	1.382(11)	1.371(10)	1.423(8)	1.438(7)	1.419(7)	1.409(7)	1.45(1)
	OB2	1.520(11)	1.521(9)	1.507(8)	1.517(7)	1.496(7)	1.521(7)	1.44(2)
	OB3							1.46(2)
S6R⊥[0001] α		3.00(2)	3.00(2)	3.00(2)	3.00(2)	3.02(2)	3.04(2)	2.35(4)
dz_{S6R}		0.110(2)	0.127(2)	0.139(2)	0.152(2)	0.157(2)	0.163(2)	0.082(5)
$O2\text{-}O2_{S6R}$		4.355(1)	4.352(1)	4.347(1)	4.348(1)	4.345(1)	4.344(1)	4.380(2)
$O2\text{-}O2_{cw}$		8.440(1)	8.428(1)	8.428(1)	8.421(1)	8.419(1)	8.416(1)	8.385(2)
O2-O2-O2		97.01(3)	97.08(3)	96.98(3)	97.06(3)	97.00(3)	97.01(3)	98.07(8)
$*O1\text{-}O1_{12R}$		9.427(1)	9.413(1)	9.412(1)	9.404(1)	9.400(1)	9.394(1)	9.433(3)
$O3\text{-}O4_{12R}$		8.467(1)	8.460(1)	8.4512(8)	8.4459(8)	8.4357(8)	8.4334(8)	8.422(3)
$O3\text{-}O4_{S4R}$		4.331(2)	4.323(2)	4.327(1)	4.327(1)	4.331(1)	4.329(1)	4.346(4)
φ1 (O1-O4-O3)		128.52(4)	130.19(4)	130.99(3)	132.13(3)	132.80(3)	133.41(3)	126.32(9)
φ2 (O1-O3-O4)		128.78(4)	130.35(4)	131.23(3)	132.33(3)	133.02(3)	133.60(3)	126.09(9)
φ3 (O4-O3-O1)		110.23(4)	108.64(4)	107.76(3)	106.65(3)	105.95(3)	105.39(3)	112.81(9)
φ4 (O3-O4-O1)		110.39(4)	108.74(4)	107.91(3)	106.76(3)	106.09(3)	105.50(3)	112.69(8)
O3-O4-O3		171.51(4)	169.96(4)	169.00(3)	167.92(3)	167.22(3)	166.65(3)	173.61(8)
Δz “corrugation”		1.1660(3)	1.1274(3)	1.1137(2)	1.0874(2)	1.0728(2)	1.0611(2)	1.1426(8)

* Calculated as the projection on the (0001) plane

Appendix

Table 7.7 Unit-cell parameters of davyne measured at different pressures

P **(GPa)**	***a*** **(Å)**	***c*** **(Å)**	***V*** **(Å^3)**
0.0001*	12.7931(4)	5.3495(1)	758.23(5)
0.38(2)	12.7822(7)	5.3399(2)	755.6(5)
0.60(2)	12.7654(7)	5.3312(2)	752.3(4)
0.91(3)	12.7421(6)	5.3183(2)	747.8(4)
1.28(2)	12.7093(5)	5.3011(1)	741.6(3)
1.57(5)	12.6919(6)	5.2908(2)	738.1(5)
1.78(4)	12.6764(5)	5.2828(1)	735.2(5)
2.05(6)	12.6509(6)	5.2704(1)	730.5(4)
2.35(6)	12.6271(6)	5.2582(2)	726.1(4)
3.07(2)	12.5853(5)	5.2366(1)	718.3(4)
3.20(2)	12.5752(5)	5.2314(1)	716.4(4)
3.49(2)	12.5513(5)	5.2198(1)	712.1(3)
3.77(4)	12.5390(5)	5.2131(1)	709.8(3)
4.09(6)	12.5165(5)	5.2020(1)	705.8(4)
4.56(7)	12.4884(6)	5.1874(2)	700.6(4)
4.86(6)	12.4696(5)	5.1782(1)	697.3(4)
5.33(8)	12.4451(5)	5.1655(1)	692.8(5)
5.72(7)	12.4223(8)	5.1533(2)	688.7(4)
6.10(8)	12.3976(5)	5.1340(1)	684.2(4)
6.47(7)	12.3761(5)	5.1284(1)	680.3(4)
6.91(8)	12.3519(5)	5.1142(2)	675.7(3)
7.18(6)	12.3373(5)	5.1058(1)	673.0(3)

* Unit-cell parameters from the crystal collected in air

Table 7.8 Details pertaining to the data collection protocol, unit-cell parameters and structure refinements of davyne at different pressures

P (GPa)	0.0001 ($P_{0\text{-AIR}}$)	0.38(2) (P_1)	0.91(3) (P_3)	1.57(5) (P_5)	2.05(6) (P_7)	3.07(2) (P_9)	3.49(2) (P_{11})	4.56(7) (P_{14})	5.33(8) (P_{16})	6.10(8) (P_{18})	7.18(6) (P_{21})
Space group	$P6_3/m$	$P6_3$	$P6_3$	$P6_3$	$P6_3$	$P6_3$	$P6_3$	$P6_3$	$P6_3$	$P6_3$	$P6_3$
a (Å)	12.7931(4)	12.7822(7)	12.7421(6)	12.6919(6)	12.6509(6)	12.5853(5)	12.5513(5)	12.4884(6)	12.4451(5)	12.3976(5)	12.3373(5)
c (Å)	5.3495(1)	5.3399(2)	5.3183(2)	5.2908(2)	5.2704(1)	5.2366(1)	5.2198(1)	5.1874(2)	5.1655(1)	5.1400(1)	5.1057(1)
V (Å^3)	758.23(5)	755.6(5)	747.8(4)	738.1(5)	735.2(5)	718.3(4)	712.1(3)	700.6(4)	692.8(5)	684.2(4)	673.0(3)
Maximum 2θ (°)	37.88	34.41	34.39	34.42	34.37	34.28	34.39	34.39	34.39	34.37	34.41
	$-14 \le h \le 15$	$-17 \le h \le 17$	$-17 \le h \le 17$	$-17 \le h \le 17$	$-16 \le h \le 17$	$-16 \le h \le 17$	$-16 \le h \le 17$	$-16 \le h \le 17$	$-16 \le h \le 17$	$-16 \le h \le 17$	$-15 \le h \le 16$
	$-16 \le k \le 17$	$-9 \le k \le 12$	$-9 \le k \le 12$	$-9 \le k \le 12$	$-9 \le k \le 13$	$-9 \le k \le 13$	$-9 \le k \le 13$	$-10 \le k \le 13$	$-10 \le k \le 13$	$-10 \le k \le 13$	$-10 \le k \le 13$
	$-7 \le l \le 7$	$-7 \le l \le 6$	$-7 \le l \le 6$	$-7 \le l \le 7$	$-7 \le l \le 6$	$-7 \le l \le 7$	$-7 \le l \le 7$	$-6 \le l \le 6$	$-6 \le l \le 6$	$-6 \le l \le 7$	$-6 \le l \le 6$
Measured reflections	3114	1090	1086	1016	1096	1082	1079	1043	1035	1031	1021
Unique reflections	823	722	711	652	687	676	673	651	647	649	648
Unique reflections with $F_0 > 4\sigma(F_0)$	557	565	596	570	607	587	591	580	579	575	581
R_{int}	0.0566	0.0440	0.0292	0.0284	0.0327	0.0324	0.0301	0.0279	0.0262	0.0281	0.0314
Number of l.s. parameters	53	48	46	46	46	46	46	46	46	46	46
R_1, $F_0 > 4\sigma(F_0)$	0.0733	0.0804	0.0734	0.0673	0.0644	0.0593	0.0594	0.0637	0.0640	0.0693	0.0756
R_1, all data	0.1060	0.1031	0.0882	0.0772	0.0728	0.0690	0.0677	0.0706	0.0704	0.0767	0.0825
wR^2	0.1534	0.1660	0.1438	0.1308	0.1279	0.1262	0.1154	0.1213	0.1226	0.1299	0.1400
Residuals (e^-/ Å^3)	+1.65/ -2.24	+1.38/ -1.28	+1.32/ -0.88	+1.00/ -0.91	+1.32/ -0.91	+1.37/ -1.03	+1.48/ -0.79	+1.37/ -0.77	+1.54/ -0.86	+1.34/ -0.96	+1.52/ -0.81

λ = 0.414 Å; ω- scan type; step scan; 1°; exposure time: 1 s; $Z = 1$

Note: $R_{int} = \Sigma|F^2_{obs} - (\text{mean})|/\Sigma[F^2_{obs}]$; $R_1 = \Sigma||F_{obs}| - |F_{calc}||/\Sigma|F_{obs}|$; $wR_2 = \{\Sigma[w(F^2_{obs} - F^2_{calc})^2]/\Sigma[w(F^2_{obs})^2]\}^{0.5}$, $w = 1/[\sigma^2(F^2_{obs}) + (0.01 \cdot P)^2]$, $P = [\text{Max}(F^2_{obs},0) + 2 \cdot F^2_{calc}]/3$.

Appendix

Table 7.9 Chemical composition of the davyne used for H*P* X-ray diffraction experiments, averaged from 20 EMPA-WDS analyses.

SiO_2	32.90
Al_2O_3	28.51
MgO	0.06
CaO	10.19
Na_2O	10.63
K_2O	8.09
SO_3	3.80
BaO	0.12
SrO	0.33
Cl	6.54
O=Cl	-1.48
Total	99.69

Number of atoms per formula unit on the basis (Si+Al=12)

Si	5.93
Al	6.07
Mg	0.02
Ca	1.97
Na	3.72
K	1.86
S	0.51
Ba	0.01
Sr	0.04
Cl	2.00

Table 7.10 Atomic fractional coordinates, site occupancy factors (*sof*) and equivalent/isotropic atomic displacement parameters (Å^2) of davyne at different pressures

Site occupancy factors at P_0-AIR

Site	Occ.	Site	Occ.	Site	Occ.
Si	1.0	Ca	1.0	S	0.30(1)
Al	1.0	Cl	1/3	OA	0.30(1)
O1	1.0	M1	0.514(8)	OB	0.30(1)
O2	1.0	M2	0.348(10)		
O3	1.0				

Site occupancy factors at P_1

Site	Occ.	Site	Occ.	Site	Occ.
Si	1.0	Ca1	1/2	S	0.26(2)
Al	1.0	Ca2	1/2	OA	0.26(2)
O1	1.0	Cl	1/3	OB1	0.132(9)
O2	1.0	M1	0.454(3)	OB2	0.132(9)
O3	1.0	M2	0.46(2)		
O4	1.0				

Site fractional coordinates

Site	*P* (GPa)	*x*	*y*	*z*	U_{iso}/ U_{eq}
Si	0.0001	0.3289(1)	0.4105(1)	3/4	
	0.38(2)	0.3290(2)	0.4109(2)	0.751(1)	0.0123(5)
	0.91(3)	0.3286(2)	0.4101(2)	0.7488(6)	0.0112(5)
	1.57(5)	0.3278(2)	0.4098(2)	0.7511(6)	0.0113(5)
	2.05(6)	0.3276(2)	0.4095(2)	0.7509(5)	0.0091(5)
	3.07(2)	0.3272(2)	0.4086(2)	0.7515(5)	0.0105(5)
	3.49(2)	0.3272(2)	0.4085(2)	0.7525(4)	0.0110(4)
	4.56(7)	0.3269(2)	0.4082(2)	0.7530(5)	0.0105(5)
	5.33(8)	0.3269(2)	0.4080(2)	0.7535(5)	0.0112(5)
	6.10(8)	0.3268(2)	0.4077(2)	0.7533(5)	0.0110(5)
	7.18(6)	0.3260(2)	0.4071(3)	0.7537(6)	0.0126(5)
Al	0.0001	0.0706(2)	0.4105(2)	3/4	
	0.38(2)	0.0708(2)	0.4110(2)	0.750(1)	0.0134(6)
	0.91(3)	0.0708(2)	0.4107(2)	0.7496(7)	0.0109(5)
	1.57(5)	0.0702(2)	0.4105(2)	0.7516(6)	0.0106(6)
	2.05(6)	0.0707(2)	0.4104(2)	0.7515(5)	0.0096(5)
	3.07(2)	0.0705(3)	0.4098(2)	0.7533(5)	0.0107(5)
	3.49(2)	0.0703(2)	0.4095(2)	0.7554(5)	0.0116(5)
	4.56(7)	0.0707(2)	0.4095(2)	0.7548(5)	0.0105(5)
	5.33(8)	0.0699(3)	0.4095(2)	0.7560(6)	0.0120(5)
	6.10(8)	0.0704(3)	0.4094(3)	0.7568(6)	0.0120(6)
	7.18(6)	0.0702(3)	0.4091(3)	0.7581(7)	0.0145(6)
O1	0.0001	0.2125(4)	0.4265(4)	3/4	
	0.38(2)	0.2109(6)	0.4252(6)	0.751(3)	0.033(2)
	0.91(3)	0.2106(6)	0.4249(6)	0.719(1)	0.027(2)
	1.57(5)	0.2103(6)	0.4231(6)	0.702(1)	0.027(2)
	2.05(6)	0.2107(5)	0.4235(6)	0.697(1)	0.023(2)

	3.07(2)	0.2098(5)	0.4217(6)	0.688(1)	0.025(2)
	3.49(2)	0.2104(5)	0.4226(5)	0.6865(9)	0.024(2)
	4.56(7)	0.2099(5)	0.4218(6)	0.682(1)	0.021(2)
	5.33(8)	0.2084(6)	0.4205(6)	0.675(1)	0.023(2)
	6.10(8)	0.2078(7)	0.4196(6)	0.672(1)	0.019(2)
	7.18(6)	0.2080(7)	0.4190(7)	0.670(1)	0.026(2)
O2	0.0001	0.1048(4)	0.5591(4)	3/4	
	0.38(2)	0.1062(6)	0.5599(5)	0.747(3)	0.023(1)
	0.91(3)	0.1055(6)	0.5592(5)	0.747(2)	0.025(1)
	1.57(5)	0.1069(6)	0.5606(5)	0.740(1)	0.027(2)
	2.05(6)	0.1065(6)	0.5589(5)	0.740(1)	0.023(2)
	3.07(2)	0.1078(6)	0.5602(5)	0.736(1)	0.026(2)
	3.49(2)	0.1064(6)	0.5604(5)	0.736(1)	0.026(2)
	4.56(7)	0.1059(6)	0.5596(5)	0.736(1)	0.028(2)
	5.33(8)	0.1048(7)	0.5595(6)	0.731(1)	0.028(2)
	6.10(8)	0.1054(7)	0.5603(6)	0.728(1)	0.026(2)
	7.18(6)	0.1058(8)	0.5603(8)	0.727(1)	0.033(2)
O3	0.0001	-0.0081(3)	0.3257(3)	0.0074(5)	
	0.38(2)	-0.0173(9)	0.3203(8)	-0.011(1)	0.019(3)
	0.91(3)	0.0052(6)	0.3327(7)	0.031(1)	0.022(2)
	1.57(5)	0.0109(6)	0.3361(6)	0.037(1)	0.020(2)
	2.05(6)	0.0124(6)	0.3351(5)	0.0402(9)	0.015(2)
	3.07(2)	0.0165(5)	0.3349(5)	0.0457(9)	0.015(2)
	3.49(2)	0.0171(5)	0.3356(5)	0.0491(8)	0.018(2)
	4.56(7)	0.0206(7)	0.3365(6)	0.0513(9)	0.019(2)
	5.33(8)	0.0215(7)	0.3365(6)	0.055(1)	0.021(2)
	6.10(8)	0.0240(8)	0.3364(7)	0.059(1)	0.023(2)
	7.18(6)	0.0262(8)	0.3377(8)	0.062(1)	0.026(2)
O4	0.0001	-	-	-	-
	0.38(2)	0.3343(8)	0.3312(8)	-0.027(1)	0.020(3)
	0.91(3)	0.3198(7)	0.3387(6)	0.016(1)	0.021(2)
	1.57(5)	0.3160(7)	0.3418(6)	0.022(1)	0.020(2)
	2.05(6)	0.3152(6)	0.3434(5)	0.0256(9)	0.016(2)
	3.07(2)	0.3141(6)	0.3456(5)	0.0296(9)	0.017(1)
	3.49(2)	0.3138(6)	0.3470(5)	0.0334(8)	0.017(1)
	4.56(7)	0.3129(6)	0.3478(6)	0.0341(9)	0.018(1)
	5.33(8)	0.3107(7)	0.3487(6)	0.039(1)	0.020(2)
	6.10(8)	0.3102(7)	0.3495(7)	0.042(1)	0.020(2)
	7.18(6)	0.3099(8)	0.3520(8)	0.047(1)	0.025(2)
Ca1	0.0001	1/3	2/3	3/4	
	0.38(2)	1/3	2/3	0.778(2)	0.020(1)
	0.91(3)	1/3	2/3	0.766(2)	0.0183(9)
	1.57(5)	1/3	2/3	0.734(2)	0.023(1)
	2.05(6)	1/3	2/3	0.728(1)	0.017(1)
	3.07(2)	1/3	2/3	0.713(1)	0.019(1)
	3.49(2)	1/3	2/3	0.706(2)	0.024(1)
	4.56(7)	1/3	2/3	0.701(2)	0.022(1)
	5.33(8)	1/3	2/3	0.698(1)	0.019(1)
	6.10(8)	1/3	2/3	0.693(1)	0.017(1)
	7.18(6)	1/3	2/3	0.683(2)	0.022(1)
Ca2	0.0001	-	-	-	-
	0.38(2)	1/3	2/3	0.714(2)	0.020(1)
	0.91(3)	1/3	2/3	0.693(1)	0.0183(9)

	1.57(5)	1/3	2/3	0.681(2)	0.023(1)
	2.05(6)	1/3	2/3	0.670(1)	0.017(1)
	3.07(2)	1/3	2/3	0.661(2)	0.019(1)
	3.49(2)	1/3	2/3	0.666(2)	0.024(1)
	4.56(7)	1/3	2/3	0.658(2)	0.022(1)
	5.33(8)	1/3	2/3	0.644(2)	0.019(1)
	6.10(8)	1/3	2/3	0.636(2)	0.017(1)
	7.18(6)	1/3	2/3	0.629(2)	0.022(1)
Cl	0.0001	0.321(1)	0.6888(9)	1/4	0.042(2)
	0.38(2)	0.322(1)	0.690(1)	0.256(3)	0.047(3)
	0.91(3)	0.323(2)	0.690(1)	0.232(2)	0.054(3)
	1.57(5)	0.322(1)	0.691(1)	0.212(1)	0.042(3)
	2.05(6)	0.322(1)	0.689(1)	0.203(1)	0.042(3)
	3.07(2)	0.323(1)	0.690(1)	0.193(1)	0.041(3)
	3.49(2)	0.3206(9)	0.6897(9)	0.190(1)	0.036(2)
	4.56(7)	0.324(1)	0.690(1)	0.184(1)	0.042(3)
	5.33(8)	0.357(1)	0.6985(9)	0.177(1)	0.041(3)
	6.10(8)	0.356(1)	0.6996(9)	0.171(1)	0.041(2)
	7.18(6)	0.356(2)	0.7021(8)	0.166(2)	0.042(3)
M1	0.0001	0.1137(4)	0.2321(5)	1/4	0.054(2)
	0.38(2)	0.1103(6)	0.2284(6)	0.251(3)	0.046(2)
	0.91(3)	0.1108(5)	0.2288(6)	0.273(1)	0.043(1)
	1.57(5)	0.1113(5)	0.2276(6)	0.286(1)	0.039(1)
	2.05(6)	0.1104(5)	0.2262(5)	0.2924(9)	0.034(1)
	3.07(2)	0.1096(5)	0.2261(5)	0.3003(9)	0.035(1)
	3.49(2)	0.1104(5)	0.2266(5)	0.3037(8)	0.036(1)
	4.56(7)	0.1096(5)	0.2252(5)	0.3066(9)	0.035(1)
	5.33(8)	0.1095(5)	0.2252(6)	0.3133(9)	0.035(1)
	6.10(8)	0.1091(6)	0.2248(6)	0.3172(9)	0.035(1)
	7.18(6)	0.1082(7)	0.2210(7)	0.322(1)	0.038(1)
M2	0.0001	0.1583(7)	0.3240(9)	1/4	0.030(3)
	0.38(2)	0.1585(9)	0.3224(9)	0.239(4)	0.045(3)
	0.91(3)	0.1588(9)	0.3239(9)	0.264(2)	0.043(1)
	1.57(5)	0.1565(9)	0.3203(9)	0.282(2)	0.039(1)
	2.05(6)	0.1562(8)	0.3165(9)	0.285(2)	0.034(1)
	3.07(2)	0.1550(8)	0.3132(9)	0.290(2)	0.035(1)
	3.49(2)	0.1533(8)	0.3098(9)	0.293(2)	0.036(1)
	4.56(7)	0.1525(9)	0.3074(9)	0.296(2)	0.035(1)
	5.33(8)	0.1507(9)	0.306(1)	0.295(2)	0.035(1)
	6.10(8)	0.149(1)	0.303(1)	0.299(2)	0.035(1)
	7.18(6)	0.147(1)	0.294(1)	0.301(2)	0.038(1)
S	0.0001	0	0	1/4	0.046(4)
	0.38(2)	0	0	0.285(3)	0.009(5)
	0.91(3)	0	0	0.276(3)	0.024(3)
	1.57(5)	0	0	0.290(3)	0.030(4)
	2.05(6)	0	0	0.299(2)	0.023(3)
	3.07(2)	0	0	0.307(2)	0.014(3)
	3.49(2)	0	0	0.311(2)	0.016(3)
	4.56(7)	0	0	0.317(2)	0.013(3)
	5.33(8)	0	0	0.324(2)	0.017(3)
	6.10(8)	0	0	0.328(2)	0.015(3)
	7.18(6)	0	0	0.330(3)	0.019(4)
OB1	0.0001	0.061(4)	0.109(4)	0.365(6)	0.10(1)

	0.38(2)	0.06	0.12	0.15(2)	0.038(8)
	0.91(3)	0.06	0.12	0.160(7)	0.026(6)
	1.57(5)	0.06	0.12	0.176(8)	0.049(8)
	2.05(6)	0.06	0.12	0.180(8)	0.057(9)
	3.07(2)	0.06	0.12	0.190(8)	0.08(1)
	3.49(2)	0.06	0.12	0.194(8)	0.08(1)
	4.56(7)	0.06	0.12	0.196(8)	0.09(2)
	5.33(8)	0.06	0.12	0.207(8)	0.08(1)
	6.10(8)	0.06	0.12	0.213(9)	0.10(2)
	7.18(6)	0.06	0.12	0.198(9)	0.08(6)
OB2	0.0001	-	-	-	-
	0.38(2)	0.06	0.12	0.35(2)	0.038(8)
	0.91(3)	0.06	0.12	0.368(7)	0.026(6)
	1.57(5)	0.06	0.12	0.390(8)	0.049(8)
	2.05(6)	0.06	0.12	0.408(8)	0.057(9)
	3.07(2)	0.06	0.12	0.420(9)	0.08(1)
	3.49(2)	0.06	0.12	0.433(8)	0.08(1)
	4.56(7)	0.06	0.12	0.434(9)	0.09(2)
	5.33(8)	0.06	0.12	0.443(8)	0.08(1)
	6.10(8)	0.06	0.12	0.445(9)	0.10(2)
	7.18(6)	0.06	0.12	0.462(9)	0.08(6)
OA	0.0001	0	0	1/2	0.10(1)
	0.38(2)	0	0	0.032(3)	0.038(8)
	0.91(3)	0	0	0.023(3)	0.026(6)
	1.57(5)	0	0	0.036(4)	0.049(8)
	2.05(6)	0	0	0.044(3)	0.057(9)
	3.07(2)	0	0	0.050(3)	0.08(1)
	3.49(2)	0	0	0.053(3)	0.08(1)
	4.56(7)	0	0	0.058(3)	0.09(2)
	5.33(8)	0	0	0.063(3)	0.08(1)
	6.10(8)	0	0	0.065(3)	0.10(2)
	7.18(6)	0	0	0.066(3)	0.08(6)

Table 7.11 Relevant bond distances (Å), angles (°), diameters (Å), S6R⊥[0001] ditrigonal rotation angle $\alpha_{S6R\perp[0001]}$ (°) and deviation from planarity parameter $dz_{S6R\perp[0001]}$ (Å), A- and B-layers "corrugation" parameter Δ*z* (Å), channel- and cage-volumes of davyne at different pressures.

P (GPa)		0.0001 ($P_{0\text{-AIR}}$)	0.38(2) (P_1)	0.91(3) (P_3)	1.57(5) (P_5)	2.05(6) (P_7)	3.07(2) (P_9)	3.49(2) (P_{11})	4.56(7) (P_{14})	5.33(8) (P_{16})	6.10(8) (P_{18})	7.18(6) (P_{21})
Si-	O1	1.601(5)	1.609(9)	1.614(9)	1.604(9)	1.601(8)	1.602(8)	1.599(8)	1.605(9)	1.610(9)	1.610(10)	1.593(10)
	O2	1.602(4)	1.598(5)	1.605(5)	1.599(5)	1.615(5)	1.611(5)	1.594(5)	1.587(6)	1.586(9)	1.579(6)	1.583(8)
	O3	1.615(3)	1.656(9)	1.583(9)	1.601(8)	1.598(7)	1.603(7)	1.592(7)	1.607(8)	1.594(8)	1.597(9)	1.594(10)
	O4	"	1.588(10)	1.658(8)	1.639(7)	1.640(6)	1.627(6)	1.626(5)	1.612(6)	1.615(6)	1.619(6)	1.614(7)
<Si-O>		1.608(4)	1.613(8)	1.615(8)	1.611(7)	1.614(7)	1.611(7)	1.603(6)	1.603(7)	1.601(8)	1.601(8)	1.596(9)
Al-	O1	1.722(5)	1.707(9)	1.706(9)	1.724(9)	1.719(8)	1.718(8)	1.720(7)	1.707(9)	1.711(9)	1.701(10)	1.703(10)
	O2	1.724(4)	1.722(7)	1.715(7)	1.721(7)	1.699(7)	1.710(7)	1.716(7)	1.716(8)	1.697(8)	1.702(9)	1.697(11)
	O3	1.730(3)	1.711(9)	1.760(8)	1.740(7)	1.750(5)	1.748(5)	1.743(5)	1.737(6)	1.742(6)	1.743(7)	1.731(7)
	O4	"	1.747(9)	1.695(7)	1.716(6)	1.711(5)	1.710(6)	1.707(5)	1.708(6)	1.710(6)	1.704(6)	1.699(7)
<Al-O>		1.727(4)	1.722(9)	1.719(8)	1.725(7)	1.720(6)	1.722(7)	1.722(6)	1.717(7)	1.715(7)	1.713(8)	1.708(9)
Si-O1-Al		167.7(3)	169.1(6)	164.2(6)	159.3(6)	157.5(5)	154.6(5)	153.4(5)	151.1(6)	149.9(6)	148.8(7)	148.0(7)
Si-O2-Al		158.1(3)	157.1(4)	157.6(4)	156.2(4)	156.7(4)	155.2(4)	156.0(4)	155.7(5)	156.2(5)	155.6(5)	155.1(6)
Si-O3-Al		142.0(2)	139.9(5)	140.1(5)	139.0(4)	137.3(4)	134.5(3)	134.4(3)	132.9(4)	131.7(4)	129.9(4)	129.2(5)
Si-O4-Al		"	142.6(5)	139.9(5)	138.2(4)	137.7(4)	137.2(4)	137.0(3)	136.0(4)	134.4(4)	133.8(4)	133.3(5)
Ca1-	O1(x3)	2.661(4)	2.676(7)	2.680(7)	2.683(7)	2.700(7)	2.674(7)	2.655(5)	2.649(7)	2.656(6)	2.655(6)	2.647(8)
	O2(x3)	2.533(4)	2.521(6)	2.517(5)	2.490(5)	2.487(5)	2.462(5)	2.473(5)	2.460(6)	2.470(6)	2.455(6)	2.443(8)
	Cl'(*z*+1)	2.702(1)	2.582(19)	2.509(14)	2.561(12)	2.536(9)	2.541(9)	2.559(11)	2.520(10)	2.600(9)	2.484(10)	2.497(11)
	Cl"(*z*)	"	2.814(19)	2.864(14)	2.790(12)	2.790(9)	2.749(9)	2.721(11)	2.719(10)	2.714(9)	2.706(10)	2.666(11)
Ca2-	O1(x3)		2.681(7)	2.672(7)	2.680(7)	2.668(7)	2.674(7)	2.656(5)	2.650(7)	2.658(7)	2.659(6)	2.655(8)
	O2(x3)		2.522(6)	2.532(6)	2.510(6)	2.513(6)	2.491(6)	2.495(6)	2.490(7)	2.505(7)	2.494(7)	2.483(9)
	Cl'(*z*)		2.477(19)	2.483(12)	2.512(11)	2.489(9)	2.478(10)	2.514(12)	2.473(11)	2.439(10)	2.418(11)	2.395(11)
	Cl"(*z*+1)		2.919(19)	2.890(12)	2.839(11)	2.837(9)	2.812(10)	2.766(12)	2.766(11)	2.775(10)	2.773(11)	2.768(11)
M1	O1	3.434(4)	3.446(19)	3.209(10)	3.077(9)	3.035(8)	2.944(8)	2.921(7)	2.860(8)	2.815(8)	2.774(8)	2.764(10)
	O3′	2.723(8)	2.650(13)	2.646(13)	2.647(12)	2.629(11)	2.575(10)	2.571(10)	2.548(11)	2.532(12)	2.501(13)	2.513(14)
	O3″	"	2.813(17)	2.811(9)	2.812(9)	2.794(9)	2.783(8)	2.775(8)	2.768(9)	2.763(9)	2.757(11)	2.758(12)
	O4′	2.723(5)	2.641(16)	2.684(10)	2.653(9)	2.655(8)	2.650(8)	2.633(7)	2.620(8)	2.607(8)	2.597(9)	2.599(10)
	O4″	"	2.892(13)	2.766(13)	2.792(12)	2.798(11)	2.791(11)	2.803(11)	2.805(12)	2.795(12)	2.792(13)	2.827(15)

Appendix

	OA(z)	2.899(5)	2.786(11)	2.854(10)	2.829(12)	2.803(9)	2.792(9)	2.789(9)	2.764(9)	2.750(10)	2.740(10)	2.699(10)
	OA (z+0.5)	"	2.941(13)	2.853(10)	2.831(12)	2.811(9)	2.790(9)	2.786(9)	2.772(9)	2.749(10)	2.729(10)	2.670(10)
	$^{+}$<M1-O_{fr}>	2.723(7)	2.749(15)	2.727(11)	2.726(11)	2.719(10)	2.700(9)	2.696(7)	2.685(10)	2.674(10)	2.662(12)	2.674(13)
M2	O1	2.906(4)	2.84(2)	2.662(13)	2.493(11)	2.467(10)	2.395(10)	2.392(10)	2.333(10)	2.319(11)	2.291(11)	2.310(13)
	O3′	2.496(9)	2.386(19)	2.366(15)	2.347(14)	2.336(13)	2.287(13)	2.281(13)	2.247(15)	2.207(15)	2.182(17)	2.189(18)
	O3′′	"	2.603(19)	2.613(15)	2.623(14)	2.600(13)	2.602(12)	2.605(12)	2.608(14)	2.629(14)	2.627(16)	2.621(17)
	O4′	2.503(9)	2.416(19)	2.367(15)	2.349(14)	2.312(12)	2.285(12)	2.274(12)	2.242(13)	2.223(13)	2.214(14)	2.196(15)
	O4′′	"	2.612(19)	2.608(15)	2.615(15)	2.648(13)	2.666(13)	2.678(13)	2.695(15)	2.691(15)	2.694(16)	2.736(18)
	OB1	2.46(5)	2.29(2)	2.317(13)	2.272(14)	2.223(14)	2.170(14)	2.127(14)	2.105(14)	2.056(14)	2.010(16)	1.931(18)
	OB2		2.32(3)	2.317(13)	2.275(15)	2.249(16)	2.213(17)	2.189(17)	2.181(19)	2.146(18)	2.10(2)	2.03(2)
	<M2-O_{fr}>	2.581(8)	2.571(19)	2.523(15)	2.485(14)	2.473(12)	2.447(12)	2.446(12)	2.425(13)	2.414(14)	2.402(15)	2.410(16)
	S-OA(z+0.5)	1.3374(1)	1.32(2)	1.31(2)	1.30(3)	1.291(19)	1.273(19)	1.263(19)	1.245(19)	1.235(19)	1.218(19)	1.20(2)
	S-OB1	1.36(4)*	1.51(5)	1.461(17)	1.450(19)	1.457(19)	1.444(18)	1.440(18)	1.437(18)	1.428(18)	1.42(2)	1.45(2)
	S-OA(z)		1.35(2)	1.35(2)	1.34(3)	1.344(19)	1.346(19)	1.347(19)	1.349(19)	1.348(19)	1.352(19)	1.35(2)
	S-OB2		1.37(3)	1.412(14)	1.421(17)	1.435(17)	1.44(2)	1.452(19)	1.44(2)	1.432(18)	1.42(2)	1.45(2)
	$\alpha_{S6R\perp[0001]}$	2.5(1)	3.0(2)	2.9(2)	3.6(2)	3.4(2)	4.0(2)	3.5(2)	3.6(2)	3.6(2)	3.9(2)	4.1(2)
	$(O2\text{-}O2)_{S6R\perp[0001]}$	4.388(8)	4.358(12)	4.357(12)	4.314(12)	4.306(12)	4.260(12)	4.275(12)	4.253(12)	4.269(12)	4.242(14)	4.214(16)
	S6R⊥[0001] dz	0	0.0214(1)	0.1532(4)	0.2042(4)	0.2266(4)	0.2535(1)	0.2563(3)	0.2718(4)	0.2872(4)	0.2894(5)	0.2900(6)
	$(O2\text{-}O2)_{cw}$	8.409(8)	8.429(11)	8.389(11)	8.383(11)	8.347(11)	8.329(7)	8.280(10)	8.241(12)	8.180(12)	8.161(12)	8.128(16)
	O2-O2-O2	97.9(2)	97.1(5)	97.4(3)	96.6(2)	96.8(2)	96.1(2)	96.7(2)	96.6(2)	97.5(2)	97.1(2)	96.8(3)
	$(O1\text{-}O1)_{12R}$*	9.451(6)	9.414(11)	9.377(10)	9.301(9)	9.280(9)	9.192(9)	9.187(8)	9.129(9)	9.064(9)	9.011(9)	8.953(11)
	$(O3\text{-}O4)_{12R}$	8.439(4)	8.460(11)	8.403(8)	8.373(8)	8.329(7)	8.264(7)	8.254(7)	8.207(8)	8.160(8)	8.113(9)	8.090(10)
	$(O3\text{-}O4)_{S4R}$	4.361(6)	4.328(11)	4.344(8)	4.325(8)	4.328(7)	4.327(11)	4.304(11)	4.287(14)	4.293(14)	4.290(15)	4.254(16)
	ϕ1 (O1-O4-O3)	119.6(1)	111.4(4)	107.2(3)	101.3(3)	99.1(2)	95.8(2)	94.5(2)	91.9(3)	90.4(3)	88.7(3)	86.7(3)
	ϕ2 (O1-O3-O4)	119.4(1)	111.7(4)	106.8(3)	101.1(3)	99.2(2)	95.7(2)	94.6(2)	91.8(2)	90.3(2)	88.6(3)	86.9(3)
	ϕ3 (O4-O3-O1)	119.6(1)	127.4(4)	132.1(4)	137.8(3)	139.6(3)	143.3(3)	144.2(2)	147.2(3)	148.7(3)	150.5(3)	152.3(4)
	ϕ4 (O3-O4-O1)	119.4(1)	127.6(4)	131.7(3)	137.8(3)	139.8(2)	143.0(3)	144.1(2)	146.6(3)	148.1(3)	149.7(3)	151.6(3)
	O3-O4-O3	180	170.1(4)	168.6(3)	162.6(3)	160.8(2)	157.3(2)	156.2(2)	153.2(2)	152.0(3)	150.2(3)	147.9(3)
	Δz	1.2978(9)	1.483(8)	1.080(4)	0.954(3)	0.902(2)	0.829(1)	0.799(2)	0.745(2)	0.705(2)	0.665(2)	0.630(2)
	V_{cg}	336.2(4)	335.0(9)	330.1(7)	324.5(7)	320.9(6)	313.3(6)	311.8(6)	308.0(6)	300.0(6)	295.9(6)	291.2(7)
	V_{ch}	211.0(2)	210.3(7)	208.8(5)	206.8(6)	204.8(5)	202.5(5)	200.2(4)	198.9(5)	196.0(6)	194.1(5)	190.9(5)

*$(O1\text{-}O1)_{ch}$ is calculated as the projection onto the (0001) plane of the O1-O1 distance

$^{+}$<Mi1-O_{fr}>: the M1-O1 bond distance has not been considered

Table 8.1 Isothermal (293 K) elastic parameters of cancrinite, vishnevite, balliranoite and davyne, obtained by fitting the high-pressure experimental data with Birch-Murnaghan equations of state, truncated to the II- or III-order

Isothermal elastic parameters

Unit-cell volume

	***P*-range (GPa)**	**V_0 (Å^3)**	**K_{V0} (GPa)**	**K_V'**	***P*-range (GPa)**	**V_0 (Å^3)**	**K_{V0} (GPa)**	**K_V'**
Cancrinite	0.0001-4.62	703.3(7)	45(2)	6(1)	5.00-6.63	715(4)	40(2)	4
Vishnevite	0.20-2.47	733.8(8)	49(4)	5.4(33)	3.83-7.40	757(6)	30(3)	2.6(5)
Balliranoite	0.0001-6.77	735(1)	48(3)	4.0(10)				
Davyne	0.38-7.18	761.6(5)	46.5(11)	3.7(3)				

Unit-cell linear parameters: *a*

	***P*-range (GPa)**	**a_0 (Å)**	**K_{a0} (GPa)**	**K_a'**	***P*-range (GPa)**	**a_0 (Å)**	**K_{a0} (GPa)**	**K_a'**
Cancrinite	0.0001-4.62	12.603(7)	52(6)	11(4)	5.00-6.63	12.63(2)	58(4)	4
Vishnevite	0.20-2.47	12.765(3)	56(4)	7.3(32)	3.83-7.40	12.844(19)	40(3)	1.8(4)
Balliranoite	0.0001-6.77	12.654(6)	54(4)	4.6(14)				
Davyne	0.38-7.18	12.814(2)	50.3(9)	4.0(3)				

Unit-cell linear parameters: *c*

	***P*-range (GPa)**	**c_0 (Å)**	**K_{c0} (GPa)**	**K_c'**	***P*-range (GPa)**	**c_0 (Å)**	**K_{c0} (GPa)**	**K_c'**
Cancrinite	0.0001-4.62	5.115(3)	34(2)	2.8(8)	5.00-6.63	5.196(16)	20.6(14)	4
Vishnevite	0.20-2.47	5.202(2)	37(2)	5.0(20)	3.83-7.40	5.33(3)	16(3)	3.6(5)
Balliranoite	0.0001-6.77	5.305(2)	40(2)	3.3(6)				
Davyne	0.38-7.18	5.3561(9)	40.3(7)	3.2(2)				

Appendix

Table 8.2 Thermoelastic parameters at constant pressure (0.0001 GPa) of cancrinite, vishnevite, balliranoite and davyne, obtained by fitting the low-temperature experimental data with the thermal equation of state (8) derived from the thermodynamic definition of the thermal expansion coefficient (further details are in section 2.1.3). For the high-temperature experimental data of cancrinite a different protocol was used (further details are in section 4.3)

Thermo-elastic parameters at 0.0001 GPa

Unit-cell volume

	***T*-range (K)**	V_0 (Å^3)	α_V (10^{-5} K^{-1})	***T*-range (K)**	V_0 (Å^3)	$\alpha_{V(303K,1bar)}$* (10^{-5} K^{-1})
Cancrinite	100-293	698.2(6)	3.8(7)	303-748	707.50(5)	4.88(8)
				748-823	705.5(10)	3.1(6)
Balliranoite	108-293	732.7(3)	4.6(4)			
Davyne	110-293	751.0(3)	4.2(4)			

Unit-cell linear parameters: *a*

	***T*-range (K)**	a_0 (Å^3)	α_a (10^{-5} K^{-1})	***T*-range (K)**	a_0 (Å^3)	$\alpha_{a(303K,1bar)}$* (10^{-5} K^{-1})
Cancrinite	100-293	12.580(3)	0.7(2)	303-748	12.6237(3)	1.16(3)
				748-823	12.618(9)	0.6(3)
Balliranoite	108-293	12.636(3)	1.4(2)			
Davyne	110-293	12.754(2)	1.4(1)			

Unit-cell linear parameters: *c*

	***T*-range (K)**	c_0 (Å^3)	α_c (10^{-5} K^{-1})	***T*-range (K)**	c_0 (Å^3)	$\alpha_{c(303K,1bar)}$* (10^{-5} K^{-1})
Cancrinite	100-293	5.096(2)	2.1(3)	303-748	5.1264(3)	2.58(8)
				748-823	5.116(6)	1.9(5)
Balliranoite	108-293	5.300(1)	1.7(2)			
Davyne	110-293	5.3300(7)	1.6(1)			

* Refined from the Berman (1988) equation of state, see section 4.3

References

References

Agilent (2012) Xcalibur CCD system, Crysalis software system.

Aleksandrov SM, Senin VG (2006) Genesis and composition of lazurite in magnesian skarns. *Geochem. Int*, **44**, 976-988.

Alvaro M, Cámara F, Domeneghetti MC, Nestola F, Tazzoli V (2011) H*T* $P2_1/c$-$C2/c$ phase transition and kinetics of Fe^{2+}-Mg order-disorder of an Fe-pure pigeonite: implications for the cooling history of ureilites. *Contrib. Mineral. Petrol.*, **162**, 599-613.

Anderson DL (1989) Themodynamics and equations of state. In: DL Anderson, *Theory of the Earth*, Blackwell Scientific Publications, Boston, Massachussets, USA, pp. 79-102.

Angel RJ (2000) Equations of state. In: RM Hazen, RT Downs (eds) *High-Temperature and High-Pressure Crystal Chemistry*, Reviews in Mineralogy and Geochemistry, Vol. 41, Mineralogical Society of America and Geochemical Society, Washington DC, USA, pp. 35-60.

Angel RJ (2001) *EOS-FIT v.5.2*, Virginia Tech, Blacksburg, Virginia, USA.

Angel RJ (2004) Absorption corrections for diamond-anvil cells implemented in the software package Absorb 6.0. *J. Appl. Crystallogr.*, **37**, 486-492.

Angel RJ, Allan DR, Miletich R, Finger LW (1997) The use of quartz as internal pressure calibrant in high-pressure crystallography. *J. Appl. Crystallogr.*, **30**, 461-466.

Angel RJ, Bujak M, Zhao J, Gatta GD, Jacobsen SJ (2007) Effective hydrostatic limits of pressure media for high-pressure crystallographic studies. *J. Appl. Crystallogr.*, **40**, 26-32.

Arletti R, Ferro O, Quartieri S, Sani A, Tabacchi G, Vezzalini G (2003). Structural deformation mechanisms of zeolites under pressure. *Am. Mineral.*, **88**, 1416-1422.

Arletti R, Vezzalini G, Morsli A, Di Renzo F, Dmitriev V, Quartieri S (2011) Elastic behavior of MFI-type zeolites: I. Compressibility of Na-ZSM-5 in penetrating and non-penetrating media. *Micropor. Mesopor. Mater.*, **142**, 696-707.

Armbruster T, Gunter ME (2001) Crystal structures of natural zeolites. In: DL Bish, DW Ming (eds) *Natural zeolites: occurrence, properties, applications*, Reviews in Mineralogy and Geochemistry, Vol. 45, Mineralogical Society of America and Geochemical Society, Washington DC, USA, pp. 1-67

Baerlocher C, McCusker LB, Olson DH (2007) *Atlas of zeolite framework types* (sixth ed), Elsevier, Amsterdam, The Netherlands.

Bailey DK, Hampton CM (1990) Volatiles in alkaline magmatism. *Lithos*, **26**, 157-165.

Ballirano P, Maras A (2004). The crystal structure of a "disordered" cancrinite. *Eur. J. Mineral.*, **16**, 135-141.

Ballirano P, Maras A, Caminiti R, Sadun C (1995) Carbonate-cancrinite: in situ real-time thermal processes studied by means of energy-dispersive X-ray powder-diffractometry. *Powder Diffr.*, **10**, 173-177.

Ballirano P, Merlino S, Bonaccorsi E, Maras, A (1996a) The crystal structure of liottite, a six-layer member of the cancrinite group. *Can. Mineral.*, **34**, 1021-1030.

Ballirano P, Maras A, Buseck PR (1996b) Crystal chemistry and IR spectroscopy of Cl^- and SO_4-bearing cancrinite-like minerals. *Am. Mineral.*, **81**, 1003-1012.

Ballirano P, Bonaccorsi E, Maras A, Merlino S (1997) Crystal structure of afghanite, the eight-layer member of the cancrinite-group; evidence for long-range Si,Al ordering. *Eur. J. Mineral.*, **9**, 21-30.

Ballirano P, Bonaccorsi E, Merlino S, Maras A (1998) Carbonate groups in davyne: structural and crystal-chemical considerations. *Can. Mineral.*, **36**, 1285-1292.

Ballirano P, Bonaccorsi E, Maras A, Merlino S (2000) The crystal structure of franzinite, the ten-layer mineral of the cancrinite group. *Can. Mineral.*, **38**, 657-668.

Bao Y, Grutzeck MW, Jantzen CM (2005) Preparation and properties of hydroceramic waste forms made with simulated Hanford low-acitivity waste. *J. Am. Ceram. Soc.*, **88**, 3287-3302.

Bariand P, Cesbron F, Giraud R (1968) Une nouvelle especie minerale: l'afghanite de Sar-e-Sang, Badakhshan, Afghanistan. Comparaison avec les mineraux du groupe de la cancrinite. *Boull. Soc. Fr. Mineral. Cristallogr.*, **91**, 34-42.

Barnes MC, Addai-Mensah J, Gerson AR (1999a) The kinetics of desilication of synthetic spent Bayer liquor seeded with cancrinite and cancrinite/sodalite mixed-phase crystals. *J. Cryst. Growth*, **200**, 259-264.

Barnes MC, Addai-Mensah J, Gerson AR (1999b). The mechanism of the sodalite-to-cancrinite phase transformation in synthetic spent Bayer liquor. *Micropor. Mesopor. Mater.*, **31**, 287-302.

Barnes MC, Addai-Mensah J, Gerson AR (1999c) The solubility of sodalite and cancrinite in synthetic spent Bayer liquor. *Colloid. Surface. A*, **157**, 101-116.

Barrer RM, Falconer JD (1956) Ion exchange in feldspathoids as a solid-state reaction. *Proc. Royal Soc.*, **236**, 227-249.

Bell K, Dunworth EA, Bulakh AG, Ivanikov VV (1996) Alkaline rocks of the Turiy peninsula, Russia, including type-locality turjaite and turjite: a review. *Can. Mineral.*, **34**, 265-280.

Belyankin DS (1931) Zur mineralogie und chemie eines feldspatvertreters aus der "Wishnewy Gory" [Vishevy Mountains] (Ural). *Centr. Min., Abt. A*, 190-196.

Berman RG (1988) Internally-consistent thermodynamic data for minerals in the system Na_2O-K_2O-CaO-MgO-FeO-Fe_2O_3-Al_2O_3-SiO_2-TiO_2-H_2O-CO_2. *J. Petrol.*, **29**, 445-522.

Bickmore BR, Nagy KL, Young JS, Drexler JW (2001) Nitrate-cancrinite precipitation on quartz sand in simulated Hanford tank solutions. *Environ. Sci. Technol.*, **35**, 4481-4486.

Bieniok A, Brendel U, Paulus EF, Amthauer G (2005) Microporous cobalto- and zinco-phosphates with the framework-type of cancrinite. *Eur. J. Mineral.*, **17**, 813-818.

Binon J, Bonaccorsi E, Bernhardt HJ, Fransolet AM (2004) The mineralogical status of “cavolinite” from Vesuvius, Italy, and crystallochemical data on the davyne subgroup. *Eur. J. Mineral.*, **16**, 511-520.

Birch F (1947) Finite elastic strain of cubic crystals. *Phys. Rev.*, **71**, 809-824.

Bonaccorsi E (2004) The crystal structure of giuseppettite, the 16-layer member of the cancrinite-sodalite group. *Micropor. Mesopor. Mater.*, **73**, 129-136.

Bonaccorsi E, Merlino S (2005) Modular Microporous Minerals: Cancrinite-Davyne Group and C-S-H Phases. In: G Ferraris, S Merlino (eds) *Micro- and Mesoporous Mineral Phases*, Reviews in Mineralogy and Geochemistry, Vol. 57, Mineralogical Society of America and Geochemical Society, Washington DC, USA, pp. 241-290.

Bonaccorsi E, Orlandi P (1996) Second occurrence of pitiglianoite, a mineral of the cancrinite-group. *Atti Soc. Tosc. Sc. Nat., Mem. Serie A*, **103**, 193-195.

Bonaccorsi E, Merlino S, Pasero M (1990) Davyne: Its structural relationship with cancrinite and vishnevite. *Neues Jb. Miner. Monat.*, 97-112.

Bonaccorsi E, Merlino S, Orlandi P, Pasero M, Vezzalini G (1994) Quadridavyne $[(Na_9K)_6Cl_2][Ca_2Cl_2][Si_6Al_6O_{24}]$, a new feldspathoid mineral from Vesuvius area. *Eur. J. Mineral.*, **6**, 481-487.

Bonaccorsi E, Comodi P, Merlino S (1995) Thermal Behaviour of Davyne-Group Minerals. *Phys. Chem. Minerals*, **22**, 367-374.

Bonaccorsi E, Merlino S, Pasero M, Macedonio, G (2001) Microsommite: crystal chemistry, phase transitions, Ising model and Monte Carlo simulations. *Phys. Chem. Minerals*, **28**, 509-522.

Bonaccorsi E, Della Ventura G, Bellatreccia F, Merlino S (2007) The thermal behaviour and dehydration of pitiglianoite, a mineral of the cancrinite-group. *Micropor. Mesopor. Mater.*, **99**, 225-235.

Bresciani-Pahor N, Calligaris M, Nardin G, Randaccio L (1982) Structure of a basic cancrinite. *Acta Cryst. B*, **38**, 893-895.

Brigatti MF, Guggenheim S (2002) Mica crystal chemistry and the influence of pressure, temperature, and solid solution on atomistic models. In A Mottana, FP Sassi, JB Thompson, S Guggenheim (eds) *Micas: Crystal Chemistry and Metamorphic Petrology*, Reviews in Mineralogy and Geochemistry, Vol. 46, Mineralogical Society of America and Geochemical Society, Washington DC, USA, pp. 1-98.

Brown ID (2002) *The Chemical Bond in Inorganic Chemistry. The Bond Valence Method*, Oxford University Press, Oxford, United Kingdom.

Buck EC, McNamara BK (2004) Precipitation of nitrate-cancrinite in Hanford tank sludge. *Environ. Sci. Technol.*, **38**, 4432-4438.

References

Buhl J-C, Stief F, Fechtelkord M, Gesing TM, Taphorn U, Taake C (2000) Synthesis, X-ray diffraction and MAS-NMR characteristics of nitrate cancrinite $Na_{7.6}[AlSiO_4]_6(NO_3)_{1.6}(H_2O)_2$. *J. Alloys Comp.*, **305**, 93-102.

Burton A, Feuerstein M, Lobo RF, Chan JCC (1999) Characterization of cancrinite sythesized in 1,3-butanediol by Rietveld analysis of powder neutron diffraction data and solid-state ^{23}Na NMR spectroscopy. *Micropor. Mesopor. Mater.*, **30**, 293-305.

Cámara F, Bellatreccia F, Della Ventura G, Mottana A (2005) Farneseite, a new mineral of the cancrinite-sodalite group with a 14-layer stacking sequence. Occurrence and crystal structure. *Eur. J. Mineral.*, **17**, 839-846.

Castaldi P, Silvetti M, Santona L, Enzo S, Melis P (2008) XRD, FTIR and thermal analysis of bauxite ore-processing waste (red mud) exchanged with heavy metals. *Clays Clay Mineral.*, **56**, 461-469.

Castaldi P, Silvetti M, Enzo S, Deiana S (2011) X-ray diffraction and thermal analysis of bauxite ore-processing waste (red mud) exchanged with arsenate and phosphate. *Clays Clay Mineral.*, **59**, 189-199.

Choi S, O'Day PA, Rivera NA, Mueller KT, Vairavamurthy MA, Seraphin S, Chorover J (2006) Strontium speciation during reaction of kaolinite with simulated tank-waste leachate: bulk and microfocussed EXAFS analysis. *Environ. Sci. Technol.*, **40**, 2608-2614.

Chorover J, Choi S, Amistadi MK, Kartikeyan KG, Crosson G, Mueller KT (2003) Linking Cesium and Strontium Uptake to Kaolinite Weathering in Simulated Tank Waste Leachate. *Environ. Sci. Technol.*, **37**, 2200-2208.

Chukanov NV, Pekov IV, Olysych LV, Massa W, Yakubovich OV, Zadov AE, Rastsvetaeva RK, Vigasina MF (2010a) Kyanoxalite, a new cancrinite-group mineral species with extraframework oxalate anion from the Lovozero alkaline pluton, Kola peninsula. *Geol. Ore Deposit*, **52**, 778-790.

Chukanov NV, Zubkova NV, Pekov IV, Olysych LV, Bonaccorsi E, Puschcharovsky DY (2010b) Balliranoite, $(Na,K)_6Ca_2(Si_6Al_6O_{24})Cl_2(CO_3)$, a new cancrinite-group mineral from Monte Somma – Vesuvio volcanic complex, Italy. *Eur. J. Mineral.*, **22**, 113-119.

Chukanov NV, Pekov IV, Olysych LV, Zubkova NV, Vigasina MF (2011) Crystal chemistry of the cancrinite-group minerals with an AB-type framework: a review and new data. II. IR spectroscopy and its crystal-chemical implications. *Can. Mineral.*, **49**, 1151-1164.

Colella C, de' Gennaro M (1989) Cancrinite crystallization from alkaline aluminosilicate systems containing large and small cations. In: ML Occelli, HE Robson (eds) *Zeolite synthesis*, ACS Symposium Series, Vol. 398, American Chemical Society, pp. 196-208

Coulson IM, Russell JK, Dipple GM (1999) Origins of the Zippa Mountain pluton: a late Triassic, arc-derived, ultrapotassic magma from the Canadian Cordillera. *Can. J. Earth Sci.*, **36**, 1415-1434.

Courtois P, Freund AK, Fernandez-Diaz MT, Nénert G, Schreck M, Gsell S, Fischer M, Link P (2013) *Proocedings of the international workshop on neutron optics and detectors (NOP&D 2013)*, Munich, Germany.

Crespi R, Gramaccioli CM, Liborio G, Pilati T (1981) Primo ritrovamento di un minerale della serie della cancrinite nella regione Alpina (Valmalenco, Sondrio). *Rend. Soc. Ital. Min. Petr.*, **37**, 677-682.

Dal Negro AT, Ungaretti L (1971) Refinement of the crystal structure of aragonite. *Am. Mineral.*, **56**, 768-772.

Davidson A (1970) Nepheline-K-feldspar intergrowth from Kaminak Lake, Northwest Territories. *Can. Mineral.*, **10**, 191-206.

De Villiers JP (1971) Crystal structures of aragonite, strontianite and witherite. *Am. Mineral.*, **56**, 758-767.

Deer WA, Howie RA, Zussmann J (1963) *Rock-forming Minerals. IV. Framework silicates.* Longmans, London, United Kingdom.

Deer WA, Howie RA, Wise WS, Zussman J (2004) *Rock-forming minerals. Framework silicates: silica minerals, feldspathoids and the zeolites* (Vol. 4B). The Geological Society, London, United Kingdom.

Della Ventura G, Bellatreccia F, Bonaccorsi E (2005) CO_2 in minerals of the cancrinite-sodalite group: pitiglianoite. *Eur. J. Mineral.*, **17**, 847-851.

Della Ventura G, Bellatreccia F, Parodi GC, Càmara F, Piccinini M (2007) Single-crystal FTIR and X-ray study of vishnevite, ideally $[Na_6(SO_4)][Na_2(H_2O)_2](Si_6Al_6O_{24})$. *Am. Mineral.*, **92**, 713-721.

Della Ventura G, Bellatreccia F, Piccinini M (2008) Channel CO_2 in Feldspathoids: New Data and New Pespectives. *Rend. Lincei-Sci. Fis.*, **19**, 141-159.

Della Ventura G, Gatta GD, Redhammer GJ, Bellatreccia F, Loose A, Parodi GC (2009) Single-crystal polarized FTIR spectroscopy and neutron diffraction refinement of cancrinite. *Phys. Chem. Minerals*, 36, 193-206.

Deng Y, Flury M, Harsh JB, Felmy AR, Qafoku O (2006) Cancrinite and sodalite formation in the presence of cesium, potassium, magnesium, calcium and strontium in Hanford tank waste simulants. *Appl. Geochem.*, **21**, 2049-2063.

Downs RT (2006) RRUFF database. *Program and abstracts of the 19th General Meeting of the International Mineralogical Association*, Kobe, Japan, pp. O03-13.

Duffy TS, Wang Y (1998) Pressure-volume-temperature equations of state. In: RJ Hemley (ed) *Ultrahigh-pressure mineralogy: physics and chemistry of the Earth's deep interior*, Reviews in Mineralogy, Vol. 37, Mineralogical Society of America, Washington DC, USA, p. 425-458

Dutta PK, Del Barco B (1985) Structure-sensitive Raman bands in hydrated zeolite A. *J. Chem. Soc. Chemical Communications*, 1297-1299.

Dutta PK, Puri M (1987) Synthesis and structure of zeolite ZSM-5 - A Raman spectroscopic study. *J. Phys. Chem.*, **91**, 4329-4333

Erd RC, Czamanske GK (1983) Orickite and coyoteite, two new sulfides minerals from Coyote Peak, Humboldt County, California. *Am. Mineral.*, **68**, 245-254.

Fall A, Bodnar RJ, Szabò C, Pàl-Molnàr E (2007) Fluid evolution in the nepheline syenite of the Ditrau alkaline massif, Transylvania, Romania. *Lithos*, **95**, 331-345.

Farrugia LJ (1999) WinGX suite for small-molecule single-crystal crystallography. *J. Appl. Crystallogr.*, **32**, 837-838.

Fechtelkord M, Stief F, Buhl J-C (2001a) Sodium cation dynamics in nitrate cancrinite: A low and high temperature ^{23}Na and ^{1}H MAS NMR study and high temperature Rietveld structure refinement. *Am. Mineral.*, **86**, 165-175.

Fechtelkord M, Posnatzki B, Buhl J-C, Fyfe CA, Groat LA, Raudsepp M (2001b) Characterization of synthetic Cs-Li cancrinite grown in a butanediol-water system: an NMR spectroscopic and Rietveld refinement study. *Am. Mineral.*, **86**, 881-888.

Fechtelkord M, Posnatzki B, Buhl J-C (2003) Characterization of basic cancrinite synthesized in a butanediol-water system. *Eur. J. Mineral.*, **15**, 589-598.

Fei Y (1995) Themal expansion. In: TJ Ahrens (ed) *Mineral physics and crystallography, a handbook of physical constants*, American Geophysical Union, Washington DC, USA.

Ferrari S, Nestola F, Massironi M, Maturilli A, Helbert J, Alvaro M, Domeneghetti MC, Zorzi F (2014) *In-situ* high-temperature emissivity spectra and thermal expansion of *C*2/*c* pyroxenes: implications for the surface of Mercury. *Am. Mineral., in press*.

Foit FF, Peacor DR, Heinrich EW (1973) Cancrinite with a new superstructure from Bancroft, Ontario. *Can. Mineral.*, **11**, 940-951.

Frost RL, Bahfenne S, Graham JE (2009) A Raman spectroscopic study of the antimony mineral klebelsbergite $Sb_4O_4(OH)_2(SO_4)$. *J. Raman Spectrosc.*, **40**, 855-860.

Fulignati P, Panichi C, Sbrana A, Caliro S, Gioncada A, Del Moro A (2005) Skarn formation at the walls of the 79 AD magma chamber of Vesuvius (Italy): mineralogical and isotopic constraints. *N. Jb. Miner. Abh.*, **181/1**, 53-66.

Gatta GD (2008) Does porous mean soft? On the elastic behaviour and structural evolution of zeolites under pressure. *Z. Kristallogr.*, **223**, 160-170.

Gatta GD (2010) Extreme deformation mechanisms in open-framework silicates at high-pressure: Evidence of anomalous inter-tetrahedral angles. *Micropor. Mesopor. Mater.*, **128**, 78-84.

Gatta GD, Lee Y (2006) On the elastic behavior of zeolite mordenite. A synchrotron powder diffraction study. *Phys. Chem. Minerals*, **32**, 726-732.

Gatta GD, Lee Y (2007) Anistropic elastic behavior and strctural evolution of zeolite phillipsite at high-pressure: a synchrotron powder diffraction study. *Micropor. Mesopor. Mater.*, **135**, 239-250.

References

Gatta GD, Lee Y (2008) Pressure-induced structural evolution and elastic behaviour of $Na_6Cs_2Ga_6Ge_6O_{24}$*$Ge(OH)_6$ variant of cancrinite: A synchrotron powder diffraction study. *Micropor. Mesopor. Mater.*, **116**, 51-58.

Gatta GD, Lotti P (2011) On the low-temperature behavior of the zeolite gobbinsite: a single-crystal X-ray diffraction study. *Micropor. Mesopor. Mater.*, **143**, 467-476.

Gatta GD, Comodi P, Zanazzi PF (2003) New insights on high-pressure behaviour of microporous materials from X-ray single crystal data. *Micropor. Mesopor. Mater.*, **61**, 105-111.

Gatta GD, Comodi P, Zanazzi PF, Boffa Ballaran T (2005). Anomalous elastic behavior and high-pressure structural evolution of zeolite levyne. *Am. Mineral.*, **90**, 645-652.

Gatta GD, Lotti P, Kahlenberg V, Haefeker U (2012) The low-temperature behaviour of cancrinite: an *in situ* single-crystal X-ray diffraction study. *Mineral. Mag.*, **76**, 933-948.

Gatta GD, Lotti P, Kahlenberg V (2013) The low-temperature behavior of balliranoite (CAN topology): an *in-situ* single-crystal X-ray diffraction study. *Micropor. Mesopor. Mater.*, **174**, 44-53.

Gatta GD, Lotti P, Nénert G, Kahlenberg V (2014). On the crystal structure and low-temperature behaviour of davyne: a single-crystal X-ray and neutron diffraction study. *Micropor. Mesopor. Mater.*, **185**, 137-148.

Gatta GD, Comboni D, Alvaro M, Lotti P, Cámara F, Domeneghetti MC (2014) Thermoelastic behavior and dehydration process of cancrinite. *Phys. Chem. Minerals*, in press.

Gelencsér A, Kováts N, Turóczi B, Rostási A, Hoffer A, Imre K, Nyirö-Kósa I, Csákberényi-Malasics D, Tóth A, Czitrovszky A, Nagy A, Nagy S, Acs A, Kovács A, Ferincz A, Hartyáni Z, Pósfai M (2011) The red mud accident in Ajka (Hungary): characterization and potential health effects of fugitive dust. *Environ. Sci. Technol.*, **45**, 1608-1615.

Giacovazzo C (1992) The diffraction of X-rays by crystals. In: C Giacovazzo (ed) *Fundamentals of crystallography*, Oxford University Press, Oxford, United Kingdom, pp. 153-226.

Gies H, Kirchner R, Van Konigsveld H, Treacey MJ (1998) Faulted zeolite framework structures. In: MJ Treacey, MBK Marcus, ME Bisher, JB Higgins (eds) *Proc. 12th International Zeolite Conference, Baltimore, Maryland, USA*, Materials Reasearch Society, Warrendale, Pennsylvanya, USA, pp. 2999-3029.

Gomes CV, Velazquez VF, Azzone RG, Paula GS (2011) Alkaline magmatism in the Amambay Area, NE Paraguay: the Cerro Sarambì complex. *J. S. Am. Earth Sci.*, **32**, 75-95.

Grundy HD, Hassan I (1982) The crystal structure of a carbonate-rich cancrinite. *Can. Mineral.*, **20**, 239-251.

Hackbarth K, Gesing TM, Fechtelkord M, Stief F, Buhl J-C (1999) Synthesis and crystal structure of carbonate cancrinite $Na_8[AlSiO_4]_6CO_3(H_2O)_{3.4}$, grown under low-temperature hydrothermal conditions. *Micropor. Mesopor. Mater.*, **30**, 347-358.

Hahn T (2002) *International Tables for Crystallography. Volume A: Space-group symmetry*. Springer, Dordrecht, The Netherlands.

Harlow GE, Bender W (2013) A study of ruby (corundum) composition from the Mogok Belt, Myanmar: searching for chemical fingerprints. *Am. Mineral.*, **98**, 1120-1132.

Hassan I (1996a) Thermal expansion of cancrinite. *Mineral. Mag.*, **60**, 949-956.

Hassan I (1996b) The thermal behavior of cancrinite. *Can. Mineral.*, **34**, 893-900.

Hassan I, Grundy HD (1984) The character of cancrinite-vishnevite solid-solution series. *Can. Mineral.*, **22**, 333-340.

Hassan I, Grundy HD (1990) Structure of davyne and implications for stacking faults. *Can. Mineral.*, **28**, 341-349.

Hassan I, Grundy HD (1991) The crystal structure of basic cancrinite, ideally $Na_8[Al_6Si_6O_{24}](OH)_2$*$3H_2O$. *Can. Mineral.*, **29**, 377-383.

Hassan I, Buseck PR (1992) The origin of the superstructure and modulations in cancrinite. *Can. Mineral.*, **30**, 49-59.

Hassan I, Antao SM, Parise JB (2006) Cancrinite: Crystal structure, phase transitions, and dehydration behavior with temperature. *Am. Mineral.*, **91**, 1117-1124.

Hazen RM, Sharp ZD (1988) Compressibility of sodalite and scapolite. *Am. Mineral.*, **73**, 1120-1122.

Heinz DL, Jeanloz R (1984) The equation of state of the gold calibration standard. *J. Appl. Phys.*, **55**, 885-893.

Hoffmann SK, Lijewski JG, Olejniczak I, Jankowska A, Zeidler S, Koperska N (2012) S_3^- radicals in epsilon-cages of cancrinite: Spectroscopic and magnetic resonance studies. *Micropor. Mesopor. Mater.,* **151**, 70-78.

Holland TJB, Powell R (1998) An internally consistent thermodynamic dataset for phases of petrological interest. *J. Metamor. Geol.,* **16**, 309-343.

Holland TJB, Redfern SAT, Pawley, AR (1996) Volume behavior of hydrous minerals at high pressure and temperature: II. Compressibilities of lawsonite, zoisite, clinozoisite, and epidote. *Am. Mineral.,* **81**, 341-348.

Isupova D, Ida A, Kihara K, Morishita T, Bulka G (2010) Asymmetric thermal vibrations of atoms and pyroelectricity in cancrinite. *J. Miner. Petrol. Sci.,* **105**, 29-41.

Jarchow O (1965) Atomanordnung und strukturverfeinerung von cancrinit. *Z. Kristallogr.,* **122**, 407-422.

Khomyakov AP, Semenov EI, Pobedimskaya EA, Nadezhina TN, Rastsvetaeva RK (1991) Cancrisilite $Na_7[Al_5Si_7O_{24}]CO_3*3H_2O$: a new mineral of the cancrinite-group. *Zap. Vses. Mineral. Obs.,* **120**, 80-84.

Klaska R, Jarchow O (1977) Synthetischer sulfat-hydrocancrinit von mikrosommit-typ. *Naturwissenschaften,* **64**, 93.

Kurdakova SV, Grishchenko RO, Druzhinina AI, Ogorodova LP (2013) Thermodynamic properties of synthetic Ca-free carbonate cancrinite. *Phys. Chem. Minerals*, **41**, 75-83.

Lacroix A (1907) Etude mineralogique des produits silicates de l'eruption du Vesuve (Avril 1906). *Nouvelles Archives du Musèum,* **9**, 1-172.

Larsen ES (1942) Alkalic rocks of Iron Hill, Gunnison County, Colorado. *U.S. Geol. Surv. Prof. Paper,* **197-A**, 1-64.

Larson AC (1967) Inclusion of secondary extinction in least-squares calculations. *Acta Cryst.,* **23**, 664-665.

Latham K, Williams CD, Duke CVA (1996) The synthesis of iron cancrinite using tetrahedral iron species. *Zeolites,* **17**, 513-516.

Leardini L, Quartieri S, Vezzalini G (2010) Compressibility of microporous materials with CHA topology: I. Natural chabazite and SAPO-34. *Micropor. Mesopor. Mater.,* **127**, 219-227.

Lee Y, Parise JB, Tripathi A, Kim SJ, Vogt T (2000) Synthesis and crystal structures of gallium and germanium variants of cancrinite. *Micropor. Mesopor. Mater.,* **39**, 445-455.

Lehmann MS, Larsen FK (1974) A method for location of the peaks in step-scan measured Bragg reflexions. *Acta Cryst. A,* **30**, 580-584.

Lehmann MS, Kuhs W, McIntyre GJ, Wilkinson C, Allibon J (1989) On the use of a small two-dimensional position-sensitive detector in neutron diffraction. *J. Appl. Crystallogr.,* **22**, 562-568.

Leoni L, Mellini M, Merlino S, Orlandi P (1979) Cancrinite-like minerals: new data and crystal chemical considerations. *Rend. Soc. Ital. Mineral. Petrol.,* **35**, 713-719.

Linares CF, Simon C, Weller MT (2011) Synthesis and characterization of the oxalate cancrinite-type zeolite. *Micropor. Mesopor. Mater.,* **137**, 32-35.

Lindner GG, Massa W, Reinen D (1995) Structure and properties of hydrothermally synthesized thiosulfate cancrinite. *J. Solid State Chem.,* **117**, 386-391.

Lindner GG, Hoffmann K, Witke K, Reinen D, Heinemann C, Koch W (1996) Spectroscopic properties of $Se_2^{(2-)}$ and $Se_2^{(-)}$ in cancrinite. *J. Solid State Chem.,* **126**, 50-54.

Liu Q, Xu H, Navrotsky A (2005) Nitrate cancrinite: Synthesis, characterization, and determination of the enthalpy of formation. *Micropor. Mesopor. Mater.,* **87**, 146-152.

Lotti P, Gatta GD, Rotiroti N, Càmara F (2012) High-pressure study of a natural cancrinite. *Am. Mineral.,* **97**, 872-882.

Lotti P, Gatta GD, Rotiroti N, Cámara F, Harlow GE (2014) The high-pressure behavior of balliranoite: a cancrinite-group mineral. *Z. Kristallogr.*, DOI 10.1515/zkri-2014-1626

Mao HK, Xu J, Bell PM (1986) Calibration of the ruby gauge to 800 kbar under quasihydrostatic conditions. *J. Geophys. Res.,* **91**, 4673-4676.

McCusker LB, Liebau F, Engelhardt G (2001) Nomenclature of structural and compositional characteristics of ordered microporous and mesoporous materials with inhorganic hosts. *Pure Appl. Chem.,* **73**, 381-394.

References

Merlino S, Mellini M, Bonaccorsi E, Pasero M, Leoni L, Orlandi P (1991) Pitiglianoite, a new feldspathoid from southern Tuscany, Italy: chemical composition and crystal structure. *Am. Mineral.,* **76**, 2003-2008.

Miletich R, Allan DR, Kuhs WF (2000) High-Pressure Single-Crystal Techniques. In: RM Hazen, RT Downs (eds) *High-Temperature and High-Pressure Crystal Chemistry*, Reviews in Mineralogy and Geochemistry, Vol. 41, Mineralogical Society of America and Geochemical Society, Washington DC, USA, pp. 445-520

Miyake M, Akachi T, Matsuda M (2005) Preparation, structure and photocatalytic properties of cancrinite encapsulating lead and sulfide ions. *J. Mater. Chem.,* **15**, 791-797.

Mon J, Deng Y, Flury M, Harsh JB (2005) Cesium incorporation and diffusion in cancrinite, sodalite, zeolite, and allophane. *Micropor Mesopor. Mater.,* **86**, 277-286.

Monticelli T, Covelli N (1825) *Prodromo della mineralogia vesuviana*, Napoli, Italy.

Mozgawa W (2001) The relation between structure and vibrational spectra of natural zeolites. *J. Mol. Struct.,* **596**, 129-137.

Murnaghan FD (1937) Finite deformations of an elastic solid. *Am. J. Math.,* **49**, 235-260.

Nakamoto K, Fujita J, Tanaka S, Kobayashi M (1957) Infrared spectra of metallic complexes IV. Comparison of the infrared spectra of unidentate and bidentate metallic complexes. *J. Am. Chem. Soc.,* **79**, 4904-4908.

Norby P, Krogh Andersen IG, Krogh Andersen E, Collela C, de' Gennaro M (1991) Synthesis and structure of lithium cesium and lithium thallium cancrinites. *Zeolites*, **11**, 248-253.

North ACT, Phillips DC, Mathews FS (1968) A semi-empirical method of absorption correction. *Acta Cryst. A,* **24**, 351-359.

Ocanto F, Alvarez R, Moy B, Brikgi M, Urbina de Navarro C, Linares CF (2008) Study of the influence of the basicity and chromate-chloride anionic composition in the synthesis of the cancrinite-sodalite system. *J. Mater. Sci.,* **43**, 190-196.

Ocanto F, Figueredo E, Brikgi M, Urbina de Navarro C, Linares CF (2009) Oxydation-reduction reactions: a novel method in the synthesis of nitrate cancrinite type zeolites. *Mater. Lett.,* **63**, 11-14.

Ogorodova LP, Mel'chakova LV, Vigasina MF, Olysych LV, Pekov IV (2009) Cancrinite and cansilite in the Khibina-Lovozero alkaline complex: thermochemical and thermal data. *Geochem. Int,* **47**, 260-267.

Oh JE, Monteiro PJM, Jun SS, Choi S, Clark SM (2010) The evolution of strength and crystalline phases for alkali-activated ground blast furnace slug and fly ash-based geopolymers. *Cem. Concr. Res.,* **40**, 189-196.

Oh JE, Clark SM, Monteiro PJM (2011) Determination of the bulk modulus of hydroxycancrinite, a possible zeolitic precursor in geopolymers, by high-pressure synchrotron X-ray diffraction. *Cement Concrete Comp.,* **33**, 1014-1019.

Olysych LV, Vigasina MF, Mel'chakova LV, Ogorodova LP, Pekov IV, Chukanov NV (2011) Thermal evolution and thermochemistry of the cancrinite-group carbonate-oxalate mineral. *Geochem. Int,* **49**, 731-737.

Palomo A, Grutzeck MW, Blanco MT (1999) Alkali-activated fly ashes: a cement for the future. *Cem. Concr. Res.,* **29**, 1323-1329.

Pascal ML, Katona I, Fonteilles M, Verkaeren J (2005) Relics of high-temperature clinopyroxene on the join Di-CaTs with up to 72 mol.% $Ca(Al,Fe^{3+})AlSiO_6$ in the skarns of Ciclova and Magureaua Vaţei, Carpathians, Romania. *Can. Mineral.,* **43**, 857-881.

Pauling L (1930) The structure of some sodium and calcium aluminosilicates. *Proc. Natl. Acad. Sci.,* **16**, 453-459.

Pawley AR, Redfern SAT, Holland TJB, (1996) Volume behavior of hydrous minerals at high pressure and temperature: I. Thermal expansion of lawsonite, zoisite, clinozoisite, and diaspore. *Am. Mineral.,* **81**, 335-340.

Peacor DR, Rouse RC, Ahn,J-H (1987) Crystal structure of tiptopite, a framework beryllophosphate isotypic with basic cancrinite. *Am. Mineral.,* **72**, 816-820.

Pekov IV, Olysych LV, Chukanov NV, Zubkova NV, Pushcharovsky DY (2011a) Crystal chemistry of cancrinite-group minerals with an AB type framework: a review and new data. I. Chemical and structural variations. *Can. Mineral.,* **49**, 1129-1150.

Pekov IV, Olysych LV, Zubkova NV, Chukanov NV, Van KV, Pushcharovsky DY (2011b) Depmeierite $Na_8[Al_6Si_6O_{24}](PO_4,CO_3)_{1-x}*3H_2O$ (x<0.5): a new cancrinite-group mineral species from the Lovozero alkaline pluton of the Kola peninsula. *Geol. Ore Deposit,* **53**, 604-613.

Petricek V, Dusek M, Palatinus L (2006) *JANA2006. The crystallographic computing system*, Institute of Physics, Prague, Czech Republic.

Piermarini GJ, Block S, Barnett JD (1973) Hydrostatic limits in liquids and solids to 100 kbar. *J. Appl. Phys.,* **44**, 5377-5382.

Pilipiuk AN, Ivanikov VV, Bulakh AG (2001) Unusual rocks and mineralization in a new carbonatite complex at Kandaguba, Kola peninsula, Russia. *Lithos,* **56**, 333-347.

Pobedimskaya EA, Lepa E, Terent'eva LF, Sapozhnikov AN, Kashaev AA, Dorokova GI (1991) Crystal structure of bystrite. *Soviet Physics Doklady,* **36**, 553-555.

Poborchii VV, Lindner GG, Sato M (2002) Selenium dimers and linear chains in one-dimensional cancrinite nanochannels: Structure, dynamics, and optical properties. *J. Chem. Phys.*, **116**, 2609-2617.

Poirier JP, Tarantola A (1998) A logarithmic equation of state. *Phys. Earth Planet. Int.,* **109**, 1-8.

Quartieri S, Montagna G, Arletti R, Vezzalini G (2011) Elastic behavior of MFI-type zeolites: compressibility of H-ZSM-5 in penetrating and non-penetrating media. *J. Solid State Chem.,* **184**, 1505-1516.

Rastsvetaeva RK, Pekov IV, Chukanov NV, Rozenberg KA, Olysych LV (2007) Crystal Structures of Low-Symmetry Cancrinite and Cancrisilite Varieties. *Crystallogr. Rep.,* **52**, 811-818.

Redhammer GJ, Cámara F, Alvaro M, Nestola F, Tippelt G, Prinz S, Simons J, Roth G, Amthauer G (2010) Thermal expansion of high-temperature $P2_1/c$-$C2/c$ phase transition in clinopyroxene-type $LiFeGe_2O_6$ and comparison to $NaFe(Si,Ge)_2O_6$. *Phys. Chem. Minerals,* **37**, 685-704.

Riley BJ, Crum JV, Matyas J, McCloy JS, Lepry WC (2012) Solution-Derived, Chloride-Containing Minerals as a Waste Form for Alkali Chlorides. *J. Am. Ceram. Soc.,* **95**, 3115-3123.

Rivera NA, Choi S, Strepka C, Mueller KT, Perdrial N, Chorover J, O'Day PA (2011) Cesium and strontium incorporation into zeolite-type phases during homogeneous nucleation from caustic solution. *Am. Mineral.,* **96**, 1809-1820.

Rosé G (1839) Beschreiben einiger neu mineral vom Ural. *Ann. Phys. Chem.*, **47**, 779.

Rozenberg KA, Sapozhnikov AN, Rastsvetaeva RK, Bolotina NB, Kashaev AA (2004) Crystal structure of a new representative of the cancrinite group with a 12-layer stacking sequence of tetrahedral rings. *Crystallogr. Rep.,* **49**, 635-642.

Rozenberg KA, Rastvetaeva RK, Chukanov NV (2009) Crystal structures of oxalate-bearing cancrinite with an unusual arrangement of CO_3 groups and sulfate-rich davyne. *Crystallogr. Rep.,* **54**, 793-799.

Santona L, Castaldi P, Melis P (2006) Evaluation of the interaction mechanisms between red muds and heavy metals. *J. Hazard. Mater.,* **B136**, 324-329.

Sapozhnikov AN (2010) Crystal chemical features of davyne from Tultui lazurite deposit (Baikal region). *J Struct. Chem.,* **51**, 507-513.

Scacchi A (1872) Notizie preliminari di alcune specie mineralogiche rinvenute nel Vesuvio dopo l'incendio di Aprile 1872. *Rend. Sci. Fis. Mat. Napoli* , 210-213.

Sears VF (1986) Neutron Scattering Lengths and Cross-Sections. In: K Sköld, DL Price (eds) *Neutron Scattering*, Methods of Experimental Physics, Vol. 23A, Academic Press, New York, U.S.A, pp. 521-550.

Sheldrick GM (1997) *SHELX-97. A Program for crystal structure refinement.* University of Goettingen, Goettingen, Germany.

Sheldrick GM (2008) A short history of SHELX. *Acta Cryst. A,* **64**, 112-122.

Shirinova AF, Khrustalev VN, Samedov HF, Chiragov MI (2006) Hydrothermal Synthesis and the Crystal Structure of Borate Cancrinite $(Na,Ca)_2[Na_6(AlSiO_4)_6]BO_3*2H_2O$. *Crystallogr. Rep.,* **51**, 37-41.

Sindern S, Kramm U (2000) Volume characteristics and element transfer of fenite aureoles: a case-study from the Iivaara alkaline complex, Finland. *Lithos,* **51**, 75-93.

References

Sirbescu M, Jenkins DM (1999. Experiments on the stability of cancrinite in the system Na_2O-CaO-Al_2O_3-SiO_2-CO_2-H_2O. *Am. Mineral.*, **84**, 1850-1860.

Stewart FH (1941) On sulphatic cancrinite and analcime (eudnophite) from Loch Borolan, Assynt. *Mineral. Mag. J. M. Soc.*, **26**, 1-8.

Vinet P, Ferrante J, Smith JR, Rose JH (1986) A universal equation of state for solids. *J. Phys. C: Solid State*, **19**, L467-L473.

Vinet P, Ferrante J, Rose JH, Smith JR (1987) Compressibility of solids. *J. Geophys. Res.*, **92**, 9319-9325.

Vopenka B, Freeman JJ, Nikisher T (1998) Raman spectroscopic identification of fibrous natural zeolites. *Appl. Spectrosc.*, **52**, 54-63.

Wang G, Um W (2013) Facilitated strontium transport by remobilization of strontium-containing secondary precipitates in Hanford site subsurface. *J. Hazard. Mater.*, **248-249**, 364-370.

Wilkinson C, Khamis HW, Stansfield RFD, McIntyre GJ (1988) Integration of single-crystal reflections using area multidetectors. *J. Appl. Crystallogr.*, **21**, 471-478.

Wilson AJC, Prince E (1999) *International Tables for Crystallography volume C, Mathematical, Physical and Chemical Tables* (2nd ed.), Kluwer, Dordrecht, The Netherlands.

Xu B, Smith P, Wingate C, De Silva L (2010) The effect of calcium and temperature on the transformation of sodalite to cancrinite in Bayer digestion. *Hydrometallurgy*, **105**, 75-81.

Yakubovich OV, Karimova OV, Mel'nikov OK (1994) A new representative of the cancrinite family $(Cs,K)_{0.33}(Na_{0.18}Fe_{0.16}(H_2O)_{1.05})(ZnPO_4)$: preparation and structure. *Crystallogr. Rep.*, **39**, 564-568.

Zambonini F (1906) Notizie mineralogiche sull'eruzione vesuviana dell'Aprile 1906. *Atti R. Acc. Sci. Fis. Mat. Napoli*, **13**, 1-40.

Zhao H, Deng Y, Harsh JB, Flury M, Boyle JS (2004) Alteration of kaolinite to cancrinite and sodalite by simulated Hanford tanks waste and its impact on cesium retention. *Clays Clay Mineral.*, **52**, 1-13.

Zubkova NV, Chukanov NV, Pekov IV, Pushcharovskii DY (2011) Low-Hydrous Cancrinite: Atomic Structure and Indicative Importance. *Dokl. Earth Sci.*, **439**, 998-1001.